Weir Advanced Research Centre
Department of Mechanical and Aerospace Engineering
Faculty of Engineering
University of Strathclyde

Development and Validation of a Fatigue-Resistant Cladding Technology

Gladys Schnier

Submitted in fulfilment of the requirements for the degree of

Doctor of Philosophy

2015

Abstract

Knowledge and understanding of residual stresses has been and remains a complex area of study, the determination of these stresses crucial in appreciating the state of the component both prior to and during operation. In the case of dissimilar joints, the interaction of materials increases the complexity of the residual stress state resulting due to the applied joining process. A fatigue-resistant cladding technology is presented in this thesis, with the aim of inducing compressive residual stresses in the clad layer. Through the generation of these beneficial compressive residual stresses an improvement in fatigue performance can be achieved in an erosive-corrosive environment. Characterisation of clad and substrate materials allows an understanding of the interaction of materials and the resulting residual stress distribution due to a weld cladding process, both experimentally and through finite element modelling. Finite element modelling of the weld cladding process utilised an elastic-perfectly plastic material model throughout the investigation of the modelling process. Good correlation between experimental and simulation residual stresses is presented, with factors influencing residual stress distributions discussed. The accurate capturing of residual stresses due to weld cladding is a complex process due to, for example, material metallurgy and properties. Laser cladding provides an alternative method of generating residual stresses indicating that the fatigue-resistant cladding technology is not limited to weld cladding. Furthermore, weld cladding is not a process that must be applied exclusively, with the application of autofrettage post-cladding providing a means of favourably modifying tensile residual stresses obtained through the weld cladding process. The fatigue-resistant weld cladding technology has been successfully developed and validated, with recommendations provided for further development and the implementation of this concept. Although this research was primarily focussed on the weld cladding of a hydraulic fracturing pump, the application of this technology is not limited to this component therefore presenting the potential to improve the fatigue performance of any component operating under cyclic loading conditions in an erosive-corrosive environment.

This thesis is the result of the author's original research. It has been composed by the author and has not been previously submitted for examination which has led to the award of a degree.

Signed:

Date:

Acknowledgements

First and foremost, I would like to express my sincere thanks and gratitude to my supervisor, Dr. Jim Wood. Your passion and enthusiasm is incredibly inspiring and your unwavering support, guidance and encouragement has made it a joy to undertake this research. Thank you for entrusting me with the task of developing the concept and for your continuous championing of the research. It has truly been an honour and a privilege to have had the opportunity to learn and benefit from your knowledge over the last three and a half years.

A special thanks also to my second supervisor, Dr. Alex Galloway, for your expertise in the materials and welding aspects of the project and for leading the production of the weld clad specimens central to the research.

Thank you to my colleagues in the Weir Advanced Research Centre, it has been a pleasure to work alongside you all and watch the centre grow. Thanks in particular to Prof. Donald MacKenzie, David Cunningham and Ian MacQueen for your continuing support in facilitating the dissemination of the research.

I would like to thank my Weir Champion, Alastair Pearson, for his metallurgical expertise and for allowing me to accompany you in the furthering of the concept. It has been a pleasure to work in conjunction with the Weir Group and I am very grateful for the support in the development of the research, both technically and financially, particularly regarding the presentation of the research, the travel opportunities and the filing of the patent.

The experimental aspects of this research would not have been possible without the support and expertise of the technical support staff within the department, particularly the following individuals: Drew Irvine, Chris Cameron, Dr. Fiona Sillars, James Gillespie, James Kelly and Jim Docherty. Thank you for providing the means to undertake an experimental program far exceeding initial expectations and for entertaining the many, many specimens requiring machining, testing, examination and transportation.

For the advice and guidance with the finite element modelling and associated IT aspects, thank you to Dr. James Ure, Dr. Yevgen Gorash, Dr. Xingguo Zhou and Alex Cairney.

A special thanks also to Dr. Salah Rahimi at the Advanced Forming Research Centre for the opportunity to undertake further research additional to the program outline. Thank you for enabling exposure to an array of knowledge and resources and for your time, expertise and passion in developing the research.

I would like to thank IODS Ltd. for providing the weld clad specimens and Laser Cladding Technology Ltd. for providing the laser clad specimens. I would also like to thank Dr. Phil Whitehead at Stresscraft Ltd. for the residual stress measurements using the incremental centre hole-drilling method and Dr. Sanjooram Paddea at the Open University for the residual stress measurements using the contour method.

Thank you also to the various undergraduate students who supported the completion of this research: Amy Waughman, Jacob Roszak, Greg Barnard, Mhairi Scott, David Webb, Russell Baxter, Jacquelyn Gray, Mark Johnston, Matthew McSorley and Angus Simpson. I am truly thankful for and appreciative of your contributions to the research.

Last but certainly not least, I would like to thank my wonderful family and friends for their continuous support and encouragement throughout my studies. It is not possible to express in words how grateful I am to you all for your company on the long journey resulting in this thesis. To my brother, Phil, for being the best *little* brother a sister could ask for, whether far or near. To my husband, Yousef, for embracing residual stresses and for sharing with me the bringing of this chapter to a close as a new one begins. And most of all, vielen Dank Liebe Mama, ohne dich hätte ich es nie geschafft.

Contents

List of Figures

List of Tables

List of Symbols and Acronyms

α	Thermal diffusivity
α_W	Thermal expansion coefficient of welded material
$\circ$	Circularity
$\Delta\alpha$	Difference between CTE values
ΔL	Measured change in sample length
ΔL_T	Measured change in sample length at specified temperature
ΔT	Temperature difference
$\varnothing$	Diameter
$\varnothing_{m_{centre}}$	Mean centre diameter
$\varnothing_{m_{grip}}$	Mean grip diameter
$\dot{\sigma}$	Rate of axial stress
$\dot{T}(c)$	Cooling rate
$\dot{T}(h)$	Heating rate
$\dot{T}$	Rate of temperature
ϵ_{hkl}	Strain considering interplanar spacing
λ	Thermal conductivity
λ	X-ray wavelength
μ	Ductility parameter
ν	Poisson's ratio
ρ	Density
ρ_{ref}	Density of solid at reference temperature
ρ_T	Density of solid at specified temperature
σ	Stress
σ^1	Type 1 residual stress

σ^2	Type 2 residual stress
σ^3	Type 3 residual stress
$\sigma_{a,UTS}$	Tensile strength of coating
σ_a	Stress amplitude with mean stress
$\sigma_{b,UTS}$	Tensile strength of substrate
σ_m	Mean stress
σ_R	Stress amplitude with zero mean stress
σ_{test}	Required test stress
σ_{UTS}	Ultimate tensile strength
σ_y	Yield stress
θ	Angle between the incoming ray and the crystal lattice plane
ε_E	Strain component due to elastic loading
$\varepsilon_{fracture}$	True strain at fracture
ε_f	Fracture ductility
ε_P	Strain component due to plastic loading
ε_{Total}	Total strain
ε_{TRP}	Strain component due to transformation plasticity
ε_T	Strain component due to thermal loading
ε_{VOL}	Strain component due to volumetric change
A	Cross-sectional area
$AISI$	American Iron and Steel Institute
Al	Aluminium
$ASTM$	American Society for Testing and Materials
B	Boron
BHN	Brinell hardness
C	Carbon
C_p	Specific heat capacity
CCT	Continuous cooling transformation
CMM	Coordinate measurement machine
CNC	Computer numerical controlled
CO_2	Carbon dioxide

$CoCrWC$	Cobalt chromium tungsten carbide
Cr	Chromium
CTE	Coefficient of thermal expansion
Cu	Copper
CVD	Chemical vapour deposition
d^0_{hkl}	Interplanar spacing in the stress-free state
d_{hkl}	Interplanar spacing in the stressed state
DLC	Diamond-like coating
DMA	Dynamic Mechanical Analyser
DSC	Differential Scanning Calorimetry
DSC	Vertical displacement between specimen/sample holder and sapphire DSC thermal curves at given temperature
E	Young's modulus
E_W	Young's modulus of welded material
EDM	Electro-discharge machining
F	Force
$F_{applied}$	Applied force
F_{max}	Maximum load
F_{min}	Minimum load
F_{UTS}	Ultimate tensile load
F_y	Yielding load
Fe	Iron
$GMAW$	Gas metal arc welding
$GTAW$	Gas tungsten arc welding
H	Height
H_2S	Hydrogen sulfide
H_V	Vickers hardness
HAZ	Heat-affected zone
HIC	Hydrogen induced cracking
$HVAF$	High-velocity air-fuel
$HVOF$	High-velocity oxy-fuel
$ICHD$	Incremental centre hole-drilling

L	Length
L_1	Grip length
L_{arm}	Force arm length
L_{gauge}	Gauge length
L_o	Initial sample length
MIG	Metal inert gas
Mn	Manganese
Mo	Molybdenum
MR	Machinability rating
N	Number of cycles
n	Positive integer
$NaCl$	Sodium chloride
Nb	Niobium
Ni	Nickel
$NiCrBSi$	Nickel chromium boron silicium
$NiCrMo$	Nickel chromium molybdenum
$NiCrMoSiB$	Nickel chromium molybdenum silicon boron
P	Phosphorus
PH	Precipitation hardening
PTA	Plasma transferred arc
PVD	Physical vapour deposition
$PWHT$	Post-weld heat treatment
$PWSR$	Post-weld stress relief
R	Tangential fillet radius
r	Radius
RA	Percentage area reduction
rpm	Revolutions per minute
S	Sulphur
S_e	Endurance limit
S_f	Fatigue strength
SCC	Stress corrosion cracking

SEM	Scanning electron microscope
Si	Silicon
STA	Simultaneous Thermal Analyser
T_{Int}	Interpass temperature
T_{PH}	Preheat temperature
T_{ref}	Reference temperature
Ta	Tantalum
TBC	Thermal barrier coating
TG	Thermogravimetry
Ti	Titanium
TIG	Tungsten inert gas
TS	Tensile strength
W	Mass
W	Width
WC	Tungsten carbide
$WCCo$	Tungsten carbide cobalt
$WCCoCr$	Tungsten carbide cobalt chromium
$WCNi$	Tungsten carbide nickel
XRD	X-ray diffraction
YS	Yield strength

Chapter 1

An Overview of Residual Stresses Relating to Fatigue Performance

"Residual stresses in metals operate under a cloak of mystery, as they have neither been seen in the laboratory nor detected by means of the microscope. In spite of their phantom-like nature, they frequently exert metallurgical effects that cannot be ignored." - Kent R. Van Horn (1)

"In fact, residual stresses can be particularly insidious because they offer no external evidence of their existence and yet often have magnitudes on the order of the material yield stress." - Michael B. Prime (2)

1.1 Introduction

The presence of stresses in engineering components due to various processes prior to loading in service is an area of great interest. The effects of these stresses, known as residual stresses, depend on the level of work experienced by the component and will invariably affect fatigue performance. Any pre-service process, whether a joining process, mechanical working, heat or chemical treatment, will result in residual stresses in the component and it is the understanding and determination of these stresses which forms a large area of research today.

Residual stresses are a common issue in many structures and components across a range of engineering applications, from the industries of aerospace to medical engineering, automotive to oil and gas. An area of great interest is that of residual stresses arising through the joining of materials, the result of which requires not only the knowledge of each material separately, but also knowledge of the interaction of those materials throughout the joining process. In this study, focus is placed solely on metals, examining the arising residual stresses due to cladding processes. A joining process utilised very commonly is that of welding, often the application of a material at a temperature such that the material is molten in order to allow the fusing of this material to another. Clearly, in this case, effects arise through not only mechanical interactions, but also through thermal effects. Knowledge is then required of material behaviour with temperature and consequently through the joining of materials, knowledge of the material properties arising due to the joining process in the vicinity of the join. This creates a complex case, due to alloying and diffusion of materials, the variation of thermal and mechanical properties with temperature and the creation of stress gradients at the joining of materials.

Joining processes are applied with the intention of improving an engineering product, additional factors such as cost, availability and performance will naturally vary with intended purpose, however, the investigation of such factors is critical in ensuring an applicable solution for the requirements of industry. Weld cladding, the area of focus of this research, presents an attractive option due to process adaptability, catering for the modification of the process, welding materials and consumables, to suit the geometry and application of the component. It should be highlighted that although weld cladding is utilised as a term here, in fact weld cladding includes a range of processes, such as centricast pipe, co-extruded pipe, explosive bonding, hot roll bonding and weld overlay cladding (3). Therefore, from here on in the use of the term weld cladding will be used to refer solely to weld overlay cladding.

As there is a great emphasis on material behaviour and interaction, the outcomes of

this research are restricted to weld cladding and the particular materials and geometries investigated.

In this chapter, an introduction to residual stresses will be given, detailing the main causes and effects of residual stresses. The effects of residual stresses on the fatigue life of structures and components will be presented, leading then onto the beneficial effects of compressive residual stresses and methods through which these beneficial stresses can be induced. A selection of cladding and coating technologies will be discussed, allowing an insight into the process leading to the selection of weld cladding as the area of interest in this research. The material selection process will then be detailed prior to a summary of the aims and objectives of the research presented in this thesis.

1.2 Residual stresses

Residual stresses are commonly defined as the stresses that exist in a component post-manufacture without the presence of external loading or constraints. These stresses will vary depending on manufacturing processing methods and durations and are elastic, self-equilibrating, although the mechanisms through which they result may be due to plastic deformation. Therefore tensile and compressive residual stresses will both exist in a component and any processes that alter residual stresses in a certain region of a component must result in a balancing of stresses throughout the component. These residual stresses can be beneficial or detrimental in terms of fatigue and fracture mechanics. It is well known that tensile residual stresses have a negative effect on the fatigue life of a component, while compressive residual stresses improve fatigue life. The effects of residual stresses must be evaluated and are very much dependent on the processes experienced by the component.

Residual stresses can be defined as macro or micro (4) with both types requiring consideration when evaluating the state of a component. Macro, often denoted as type 1 (σ^1) residual stresses, vary at a scale larger than grain or microstructural scales. Micro residual stresses can be divided into type 2 (σ^2) and type 3 (σ^3) stresses and arise due to the microstructure of the material, the former being characterised at grain-size scale and the latter at atomic scale. These stresses are influenced by material phases and therefore can change greatly over distances comparable to the grain size of the material. As type 2 stresses can vary across grains these stresses can exist both in single-phase materials due to grain anisotropy and multi-phase materials due to differing phases. Type 3 stresses exist within grains and are therefore influenced by factors such as dislocation and other crystalline effects.

Figure 1.1 illustrates the schematically the three types of residual stress.

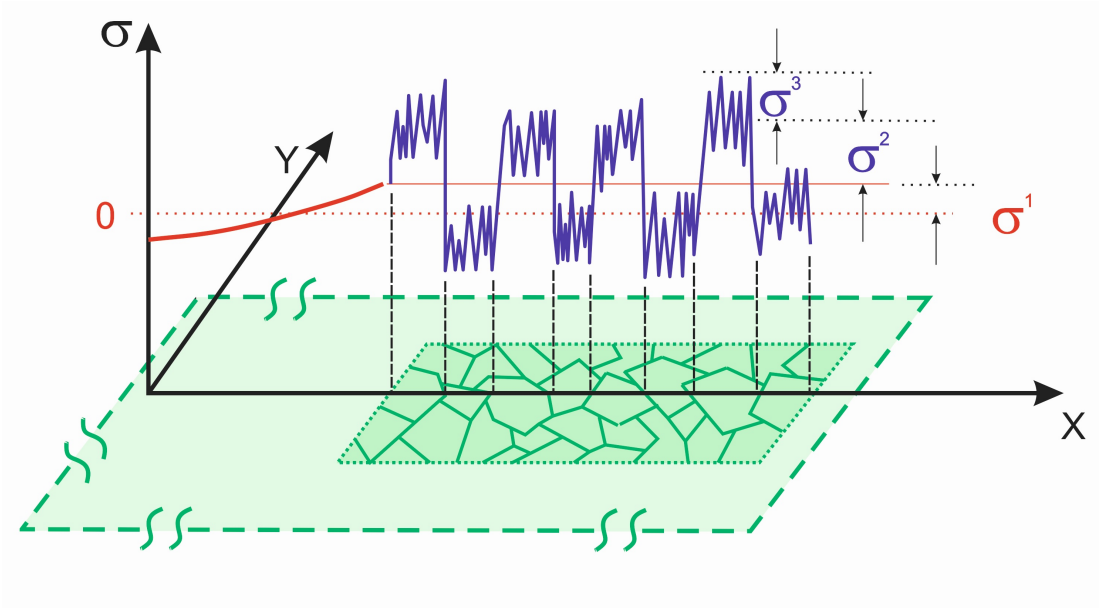

Figure 1.1: Categorisation of residual stress according to scale - Modified from (4).

Figure 1.2 details various characteristics of residual stresses. The causes of residual stresses are many, for example, joining processes may induce distortion and ultimately failure. The potential for distortion of a component due to residual stress is particularly crucial when these stresses are not controlled. The possibility of reducing residual stress levels will be discussed in 11.5. Withers and Bhadeshia describe residual stresses as arising through misfits between regions, different parts or different phases (5). This statement makes it understandable that joining processes will result in residual stresses in a component. From a mechanical point of view, aspects such as the mechanism of plastic deformation, machining, grinding, peening, burnishing and autofrettage will induce residual stresses. These methods of influencing the residual stress state may be intentional or unintentional. Constraint on thermal expansion and non-uniform heating and cooling through quenching, welding, brazing and material dissimilarity induce residual stresses as can chemical reactions, volume changes, precipitation hardening, phase transformations, nitriding and carburizing. The points described here do not account for all possibilities and so it is clear that there are many factors that must be taken into consideration when evaluating residual stresses.

As can be concluded from the previous paragraph, residual stresses arise from numerous sources and therefore these stresses will invariably be present in unprocessed raw materials, with manufacturing processes creating additional sources of residual stress.

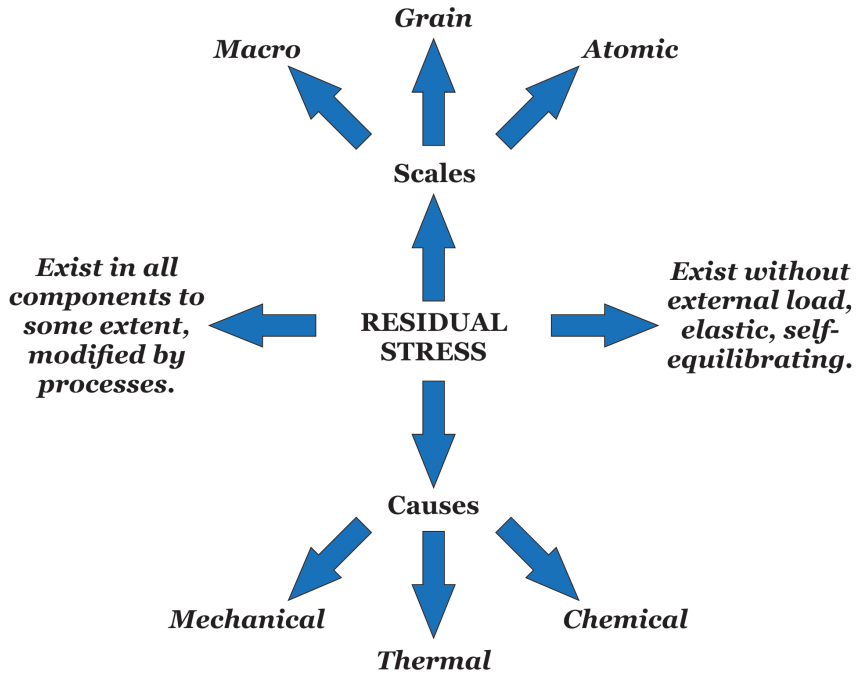

Figure 1.2: Residual stress characteristics and causes - Schematic illustrating various aspects of residual stress, such as scale, causes and nature.

1.2.1 Major parameters involved in inducing residual stresses

In weld cladding, stresses will arise due to mechanical, thermal and chemical mechanisms. The nature of stresses will be dependent on the thermal mechanisms and degree of material dissimilarity. Welding processes and dissimilar joints typically induce a complex residual stress field involving both significant tensile and compressive residual stresses and therefore shorten fatigue life. Weld cladding can be thought of as a dissimilar joint in essence, with thermally generated residual stresses arising due to the non-uniform heating and cooling operations during welding, producing constraints on thermal expansion and contraction in a component at a macroscopic level and possibly also phase transformations. Thermally induced stresses can also arise through processes such as brazing and quenching for example. Microscopically, material mismatch such as between coefficient of thermal expansion values between phases or constituents will cause thermally induced residual stresses to develop. The effects of three major parameters on residual stress distribution due to weld cladding are considered as highlighted in figure 1.3. Firstly, the global pre-heat shrink-fit effect is investigated, which accounts for the effective shrinking of cladding relative to substrate, affected by material and temperature dissimilarity. Secondly, changes in microstructure due to phase transformations and chemical reactions are considered. Chemically generated residual stresses can develop due to volume changes associated with chemical reactions, precipitation or phase transformation. It will be seen that these heavily influence material properties and ultimately the nature of residual

stresses arising in a component, particularly when changes are sudden and abrupt. Thirdly, the spatial and temporal variation of the clad deposition process and the subsequent cooling of the component. The variation in temperature of both materials will affect cooling rates and thus constraint levels within the component.

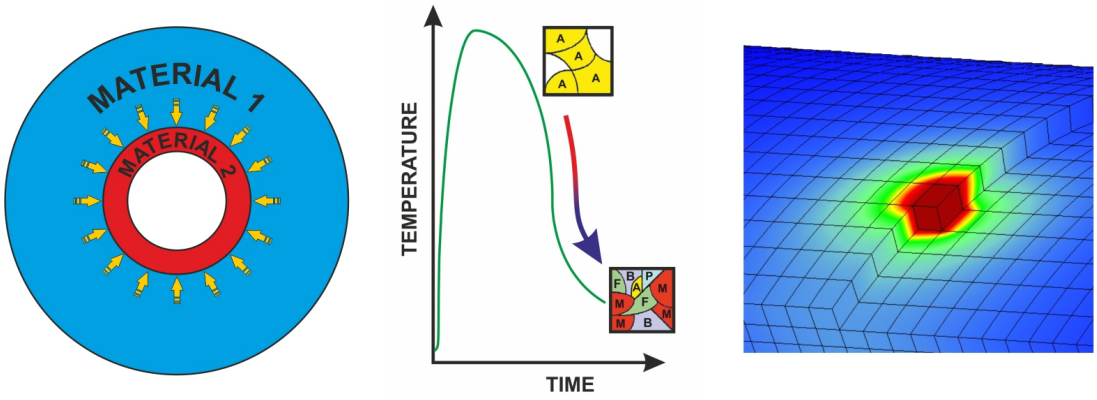

Figure 1.3: Major parameters affecting residual stress distribution - Major parameters affecting residual stresses due to weld cladding.

The influence of a thermal transient process creates a dependence on differing thermal expansion rates with material properties changing with temperature as time progresses. Stresses will remain in the post-cooled component due to the constraint being a function of stiffness and plastic flow. The mechanical properties of yield stress and Youngs modulus will develop in the component during cooling from melt to room temperature, with values differing in elements and therefore resulting in a variation in thermal stresses.

1.3 Residual stress effects on failure mechanisms

Residual stresses arise from locked-in elastic strain energy in the material's lattice structure and can affect both crack initiation and propagation stages, for example enhancing crack propagation rates. Prior to discussing methods of inducing residual stress to positively impact fatigue life, or number of cycles prior to failure, the process of fatigue will be briefly detailed. Cyclic loading of a component, provided the stress levels are below the tensile strength of the material, can lead to fatigue failure.

The three stages of fatigue failure are as follows:

- Stage I: Crack initiation, which can account for the majority of the life in a non-welded component, often occurs at the surface of a component, in areas of flaws or damage which bring about an increase in stress.

- Stage II: Crack propagation, during which shear slip causes crack growth in each cycle for a cyclically loaded component, hence resulting in incremental crack growth.
- Stage III: Fatigue failure, occurring when the critical crack length is reached.

The fatigue life of a component, as well as the time spent in the crack initiation stages, is dependent on the microstructure of the material in the vicinity of the crack. Grain boundaries in a refined microstructure possess the ability to hinder crack propagation and therefore crack growth rate is accelerated in the case of a rough grain structure due to the lack of such *barriers*. Material properties will generally influence fatigue life, along with the cyclic stress state and the surface finish of the component. The presence of inclusions or notches for example act as crack initiation locations, therefore shortening this phase and allowing crack propagation to dominate.

Therefore improvement in fatigue life is often achieved through focussing on beneficially altering the stress state, through influencing the mean stress in a component, either during or post-manufacture. This is of particular interest where operational stresses will be highest, usually at the surface of components and structures. To improve fatigue performance, ideally the entire stress cycle would be in the compressive range when operational stresses are superimposed on residual stresses as shown in figure 1.4. However, any level of compressive residual stress would be beneficial in drawing the combined stress cycle closer to the compressive region. If the compressive residual stresses present in the component are of a high enough level, cracks will tend not to propagate from flaws, corrosion pits or stress concentrations. It is also recognised that compressive residual stresses can improve corrosion performance and stress corrosion cracking performance for some materials (6). Additionally, microstructural changes are likely to occur due to any processes a component experiences to alter its' stress state and the effects of these changes on fatigue life, not only crack growth, but also material properties, must also be considered.

As can be seen from figure 1.4, a component which experiences a tensile operating stress, a compressive residual stress effectively lowers the mean stress level. With reference to the three stages of fatigue failure, compressive residual stresses will decrease the rate of crack propagation, however are said to have little or no effect on the crack initiation stage (7).

Residual stresses will vary depending on the materials present in a component and the processes that have been implemented. Additionally once the component fulfils its purpose in operation and experiences loading these stresses will also differ. The combination of residual stresses and operational stresses will determine potential failure mechanisms. Residual stresses can be, as previously highlighted, large

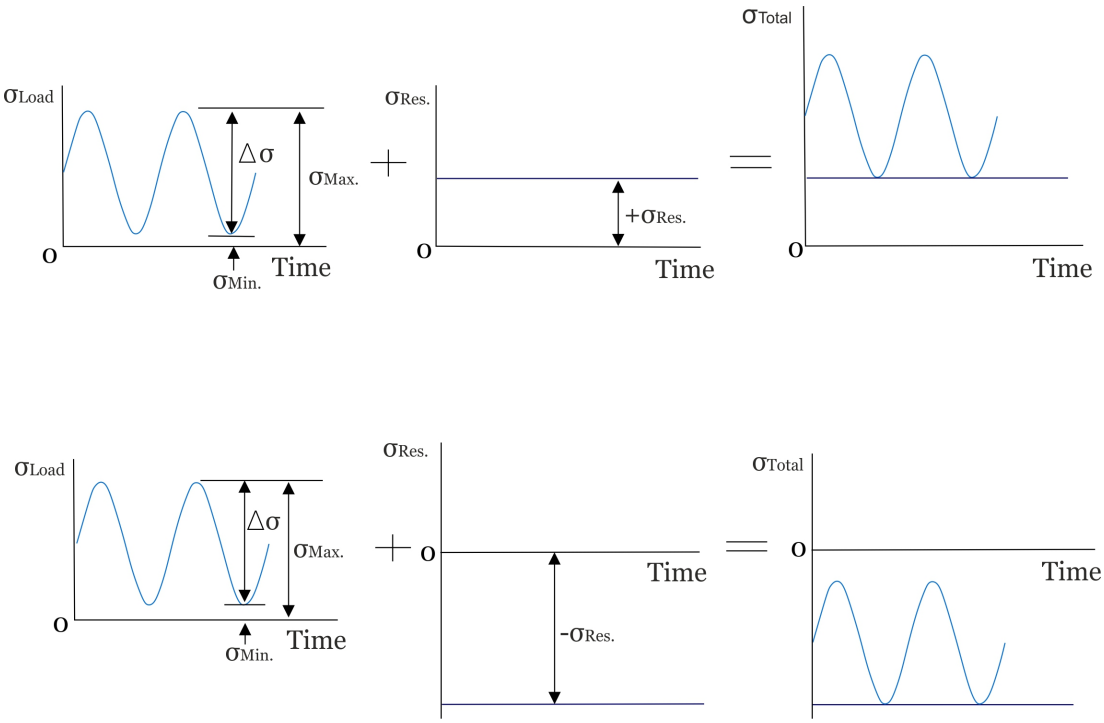

Figure 1.4: Principal of superposition of residual and operational stresses - Top set showing effect of tensile residual stress, bottom set showing effect of compressive residual stress.

enough to severely affect the performance of engineering components and therefore it is a serious error to assume a stress-free state in the fatigue design of ductile and brittle materials and the static design of brittle materials. The performance of components and the relevance of failure mechanisms should be considered taking into account the distribution and magnitude of residual stresses. The first important factor is the ductile or brittle behaviour of materials. Connecting this to a coating or cladding, or indeed any dissimilar joint, the dissimilarity and the residual stresses arising through this factor can result in failure in the vicinity of the join, whether at the join or in the joining materials. The complex nature of a dissimilar joint increases the complexity of the assessment of the thermal and mechanical material properties and the microstructure and therefore experimental testing is a common method of assessing performance, allowing the effects of combined residual stresses and operational loading to be determined.

The effects of residual stresses are most significant in the failure mechanisms of fatigue and fracture. Considering the effects of residual stresses on fatigue, it is generally the case that tensile residual stresses present at the surface of a component in operation often contribute to fatigue failure, while an increase in fatigue strength can be achieved through the presence of compressive residual stresses. In particular in dissimilar joints, and therefore applicable in this investigation of cladding, is the potential presence of high discontinuity stresses at the interface between dis-

similar materials, therefore creating a region in which fatigue failure can also occur. The strength of the bond is a key issue, as the potential for cracking is high when the bond is poor. Another major failure mechanism which is related to dissimilar joints is that of stress corrosion cracking, with the presence of residual stresses and the metallurgy of the join potentially affecting stress corrosion cracking. Fatigue can also be impacted by surface straining and rate of corrosion interactions. Brittle failure can occur in components due to the combination of residual stresses and operational stresses or solely due to the presence of residual stresses post-manufacture. Compressive residual stresses can increase the fatigue strength and static bending strength of brittle materials and therefore the presence of these beneficial stresses in the surface layers of a component, where operational stresses are often highest, would offer resistance to brittle failure. Brittle fracture, stress corrosion cracking and fatigue failure most commonly occur in a state of tensile residual stress at the surface of a component. Residual stresses could influence buckling as this mechanism is assessed considering the stress state in a body, including the potential for failure through buckling of a cladding or coating due to poor adhesion as mentioned above. Residual stresses should be considered in modelling ratcheting behaviour due to the considerations of local stress concentrations, with initial plastic straining and subsequent accumulation influenced by the presence of residual stresses. Residual stresses do not generally affect plastic collapse due to the self-equilibrating nature of the stresses and stress concentrations can generally be neglected. In conclusion, it is important to consider the scale at which residual stresses are to be modelled and accounted for in order to accurately assess their effects on component performance and failure mechanisms.

1.4 Methods of influencing residual stresses

There are many methods through which residual stresses can be influenced. As the overall objective of this research is to develop a fatigue-resistant technology focus will be placed on methods through which compressive residual stresses result and ultimately through which an improvement in fatigue life can be achieved.

Another key factor in this investigation is the depth to which beneficial residual stresses are obtained, as in many cases compressive residual stresses are obtained in relatively thin layers, as is shown in (8). Herein shot peening of Inconel 625 is shown to induce compressive residual stresses to a depth of around 0.3 mm while laser peening results in compressive residual stresses to a depth just greater than 1 mm. It is clear from these values that in erosive and corrosive environments such amounts of material will quickly be removed, removing therefore also the benefits induced by such treatments.

1.4.1 Machining induced residual stresses

During the manufacture of a component, residual stresses will be induced through machining processes, the extent of which depends on the level of plastic deformation, the properties of the material, particularly at the surface, and any metallurgical transformation occurring due to the machining process and the machining process itself. The mechanics of residual stress require two aspects to be examined: the causes and the sources of residual stress. In machining processes, the sources can be due to mechanical, thermal or transformational effects (9).

Machining processes can be tailored to induce compressive residual stresses, such as quenching, milling, rolling and combining particular steps of the drawing process (9). Grinding typically induces tensile residual stresses, however modifying aspects such as the cutting speed and feed rates allows stress levels to be altered. Low-stress or stressless grinding of 4300 steel fatigue specimens induced compressive residual stresses of around -500 MPa in the axial direction with these beneficial stresses decreasing rapidly with depth. Axial fatigue testing of these specimens concluded that these compressive residual stresses did not benefit fatigue performance, porosity dictating the fatigue behaviour (10).

Further discussion on residual stresses produced through grinding will be discussed in section 6.3.1.1. It should be ensured that any beneficial effects of compressive residual stresses induced through a particular process are not then removed by subsequent machining of the component. This action not only decreases fatigue life but also increases corrosion susceptibility and therefore experimental procedures are recommended to achieve beneficial residual stress states and maintain corrosion resistance (11).

Electro-discharge machining (*EDM*) is an example of a machining processes which is influenced by thermal means. This process induces tensile residual stresses in a thin surface layer, which decrease quickly with increasing depth from the surface. The EDM process will also be further discussed in section 4.4.1.

Although it is critical to attain knowledge of residual stresses due to machining processes, the depth penetration of such stresses is generally only some hundredths of millimetres (9). In the case of thin components this will obviously account for a much greater portion of the specimen and larger effects on deformation may be experienced.

It should also be borne in mind throughout that the self-equilibrating nature of residual stresses results in a balancing of stresses throughout the component such that tensile and compressive residual stresses are present in the component. Methods of influencing residual stresses will alter the nature and location of residual stresses,

for example the modification of surface stresses in turn altering the residual stress further into the component.

1.4.2 Shot peening

Compressive residual stresses can be induced in the surface of a component through the cold-work shot peening process, up to a depth of around 400 μm depending on peening conditions (9). This method increases the hardness of the material, however is limited primarily by shallow penetration depth. In another review, peening is described as controlled pre-stressing with potential benefits for stress corrosion and corrosion fatigue amongst other failure mechanisms. Herein, compressive residual stresses are defined as generally being in the region of 60% of the ultimate tensile strength of a material with the potential of the presence of these stresses to depths of 0.05 mm to 2.5 mm (12).

Shot peening is a cold-work, mechanical process involving controlled high speed impact of small spherical particles, commonly steel, ceramic or glass, at speeds in the range of 40-70 m/s (13), on the surface of a component which results in plastic deformation and ultimately improves crack initiation resistance during the operation of the component and therefore increases fatigue performance. The application of this process can also increase resistance to stress corrosion cracking. The dimples formed in the surface through these shots causes tensile yield of the material, however the bulk material restricts movement of the surface material and therefore a compressive residual stress results. It should be noted that a surface can be 'over-peened' which can result in crack formation on the surface, however it has been shown that these cracks do not generally affect fatigue life (14).

Notable differences have been observed in the creation of compressive residual stresses by shot peening in the cases of static compression and dynamic impact testing with a single steel ball (15). In steel plates tensile residual stresses arose at the center of the indentation with dynamic impact of the ball, contrary to the general assumption of the generation of compressive residual stresses through shot peening. However, repeated impact in the area of indentation transformed these stresses into compressive residual stress, illustrating the creation of a superposition effect to obtain this final residual stress state.

The level of compressive residual stresses arising due to the shot peening process is dependent on various parameters, such as the shot velocity, size, material, intensity and impact angle. A higher intensity is shown to produce compressive residual stresses, both to a greater depth and to a higher level in a shot peened aluminium alloy, however the resulting compressive residual stress state is not able to translate directly into the level of fatigue life improvement (16). The work-hardened layer

increases the flow stress and will slow crack initiation and decrease the rate of crack propagation.

Investigating the effects of shot peening on 4340 low alloy carbon steel also demonstrates an increase in compressive residual stresses and a deepening of the stress field with increased peening intensity. However this compressive residual stress did not always equate to an increase in fatigue life in this steel (17). It is also noted that shot peening can impact the location of crack initiation, also dependent on the conditions of low or high cycle fatigue.

The modification of surface roughness which occurs due to this process should normally be taken into account as this is a factor that can hasten crack initiation and therefore have a negative effect on fatigue life. However, in cyclic fatigue systems where residual stresses and strain hardening dominate, the effect of this parameter on fatigue life is likely to be negligible (18). Micro-cracking arises through the shot peening process, yet, again, it is said that if the compressive residual stress is of a large enough level, unavoidable stress redistribution effects of micro-cracks will not impact fatigue performance (19).

To quantify the increase in fatigue performance, it is shown that peened steel specimens experience an increase in life by a factor of 5 in comparison with unpeened specimens, this measure is dependent however on the stress amplitude in question (20).

A variation of this method is water jet peening also producing compressive residual stresses, investigated numerically and experimentally using an austenitic stainless steel plate. Compressive residual stresses were obtained at the surface of the component using two values of external loading, with maximum stresses around -600 MPa (21). Like shot peening, this process also provides an increase in fatigue performance and resistance to stress corrosion cracking.

1.4.3 Autofrettage

Components operating under high pressure conditions are often subjected to the autofrettage process, with the aim of inducing plastic deformation at the inner surface of the component to a particular depth. This is achieved through the application of a hydrostatic pressure, which is applied and increased until plastic deformation occurs to the desired depth and hence compressive residual stresses arise. This autofrettage process is known as mechanical or hydraulic autofrettage. Although more uncommon, thermal autofrettage is also an effective, but possibly impractical, means to creating compressive residual stresses through temperature reduction.

Subjecting a compound cylinder to mechanical autofrettage results in that cylinder possessing a higher fatigue resistance compared with a homogeneous cylinder of the same dimensions (22). A study into thick-walled quenched and tempered steel cylinders concluded that mechanical autofrettage significantly reduces stress intensity factors and operating stresses at the inner surface while also extending the critical crack size by 100% (23).

Studies have shown that compressive residual stresses induced through the autofrettage process do not further increase in an alloy steel after an autofrettage percentage of 60% with open ends and the outer radius double that of the inner (24). Yielding to the geometric mean radius is generally the maximum allowable autofrettage radius presented in the standards (25).

Autofrettage has also successfully been paired with wire-winding to produce compressive residual stresses throughout a wire-wound autofrettaged cylinder (26).

Swage autofrettage works in a similar manner to cold expansion, the process using a mandrel which is forced through the component bore. This tool has a greater diameter than the bore of the component to bring about expansion of the bore when the mandrel is forced through the inner diameter of the component. Through this process of plastic expansion of the bore a compressive residual stress arises. Mandrel geometry heavily influences the level of residual stress, typically the mandrel takes the form of two conical sections with a cylindrical section joining these two end pieces. Finite element simulation studies have concluded that rear mandrel slopes are thought to have a larger impact on the final compressive residual stress level present (27). The required forming load has also been investigated using finite element simulations, concluding that tool cone angles, land lengths and lubricant types have the greatest influence on friction levels and therefore the required forming load (28).

Autofrettage will be further discussed as a method of improving fatigue performance in section 9.1.

1.4.4 Thermochemical treatments

Methods which utilise a heating process can effectively harden the surface of materials while also producing substantial residual stress gradients. There are various types of these hardening methods under the umbrella of gas nitriding, such as nitriding, carburising, nitrocarburising and carbonitriding. As the name suggests, these process use nitrogen and/or carbon and a heating process of typically 500-1000°C to facilitate diffusion in the vicinity of the surface to increase the hardness of the surface. Carburising for example increases the carbon content, hardening the component surface

while toughness and ductility remains. It must be ensured therefore that the materials treated can withstand these heat treatments without experiencing negative effects on the material properties.

Another form of nitriding, known as plasma nitriding, uses a plasma energy source to diffuse nitrogen into the surface of the component. This method requires the use of a vacuum chamber in which the component is placed with then an electrical potential difference introduced between vessel wall and component to produce the plasma. This method has great potential in alloy steels and has the added benefit of shorter time periods and lower temperatures than the processes described above, typically below 600 °C. Furthermore, adding an oxidation step can enhance corrosion resistance to produce an oxide layer on top of the introduced hardened zone. This method is again suited for low alloy steels.

The plasma or ion nitriding process has been shown to induce compressive residual stresses in 4140 low alloy carbon steel, resulting in a 12% increase in fatigue strength in comparison with liquid nitriding (29). This study discusses the increase in strength, fatigue life and wear resistance of steels due to ion nitriding and highlights that the differentiation arises due to the period over which nitrogen diffusion takes place.

1.4.5 Laser shock processing

As mentioned, the depth to which compressive residual stresses can be induced through shot peening is a significant limitation of the method. Laser shock processing, or peening, often implemented in gas turbines, is also limited in depth penetration with potential beneficial stresses to depths in the region of 1 mm (30).

Laser shock processing uses a Q-switched laser to impact the metal surface with a high energy pulse which in turn results in pressure pulses in the material. Material is laid onto the component to act as an ablation and a thermal insulation layer, which allows a smoother surface finish. Without the presence of this protective layer, severe surface roughness can result due to vaporization and melting. In addition to the benefits of compressive residual stresses, this surface finish will naturally also contribute to an increase in fatigue performance. Plastic deformation is produced when the shockwave pressure exceeds the Hugoniot Elastic Limit, bringing about microstructural and material property changes. In a similar manner to shot peening, the area of plastic deformation is constrained elastically by the surrounding material and this creates a compressive residual stress at the surface. Again compressive residual stresses will be generally highest at the surface with a decrease with depth below the surface.

Increasing numbers of laser impacts increases compressive residual stresses and surface micro-hardness (31). This increase in hardness will be present in the entire region that has been subjected to laser shock processing, the level of increase being dependent on the process parameters and material characteristics. Studies show that laser shock processing can increase fatigue strength in steels, aluminium alloys and titanium alloys (32). It is reported that notched 4340 steel specimens experienced a 60-80% increase in fatigue life due to laser shock processing (32). Stress corrosion cracking resistance is also improved in 304 stainless steel due to the beneficial effects of the compressive residual stress and grain refinement resulting from laser shock processing (33). A method of using smaller spots and overlapping these spots is said to be important due to the complex laser generation systems utilised (34), with high costs being the major disadvantage of this process.

1.4.6 Low plasticity burnishing

Low plasticity burnishing produces compressive residual stresses using a ball supported hydrostatically by a constant volume flow of fluid with the aim of minimising cold work (35). Hydrostatic support means that a friction-free rolling contact is established and therefore a high pressure can be applied. The rolling of this ball across a surface creates plastic deformation and results in thermally stable compression while also improving surface finish. This process is commonly used for conventional and *CNC* machine tools and in the aerospace industry, presenting an attractive option for the repair and refurbishment of aircraft components (36).

Studies into the use of low plasticity burnishing on 4340 steel concluded that compressive residual stresses resulted to a depth of 1.25 mm, a depth 2-3 times greater than that achieved through conventional shot peening with magnitudes also being greater (36). In this investigation it is also stated that compression levels at the surface and to considerable depth are greater perpendicular to the ball travel path while the level of compressive residual stresses at greater depths are greater parallel to the ball path.

Low plasticity burnishing applied to aluminium alloy 7075-T6 was also shown to increase fatigue life by an order of magnitude, investigating also the effects of salt fog on fatigue life and the consequential improvement in fatigue life after application of the low plasticity burnishing process (37).

Low plasticity burnishing costs are lower in comparison to those of laser shock processing, and therefore as compressive residual stresses can be achieved at similar depths and magnitudes, this process is favourable. A range of materials have been shown to benefit from the low plasticity burnishing process: steel alloys, nickel-based superalloys, aluminium alloys and titanium alloys. It has also been shown that 17-4

stainless steel specimens treated by low plasticity burnishing could withstand erosion and foreign object damage to depths of 1 mm (38).

Aluminium alloy 74745-T7351 showed greater resistance to pitting and stress corrosion cracking damage after low plasticity burnishing in comparison to shot peening, with increased corrosion fatigue life and damage tolerance (39). This can be attributed to the greater depth to which low plasticity burnishing induces compressive residual stresses, where as in the case of shot peening, corrosion pits will be of similar depths to the depths of compressive residual stresses induced.

1.4.7 Ultrasonic processes

Compressive residual stresses can result from a variety of ultrasonic processes, some of which will be covered briefly in this section. Plastic deformation is again the mechanism through which these stresses are induced.

Ultrasound-aided deep rolling, similar to the conventional deep rolling process, and ultrasonic nanocrystal surface modification provide the greatest stress magnitudes and depths.

Ultrasound-aided deep rolling drives a rolling ball subjected to ultrasonic waves into the surface of a component which is also experiencing static pressure. This ball impinges and rolls the surface to produce plastic deformation. A friction-free impact ensures no residual shear stress and a polished finish. Ultrasound-aided deep rolling produced compressive residual stresses of -950 MPa to a depth of 1 mm in titanium alloy Ti-6Al-4V and an improvement in high cycle fatigue strength of 65% (40).

Ultrasonic nanocrystal surface modification induces a nanocrystal microstructure through the impact of a ball connected to an ultrasonic device, with 20,000 or more impacts per second and 1000 to 10,000 shots per square millimetre. At a similar level, compressive residual stresses of -1100 MPa were present in ultrasonic nanocrystal surface modified 304 austenitic steel to a depth of 0.4 mm, although it does not result in as great an improvement in fatigue life in comparison with deep rolling (41).

Ultrasonic shot peening uses an ultrasonic generator and a spherical medium to impact the surface of a material and induce a compressive residual stress. Ultrasonic shot peening produces lower compressive residual stresses to a depth similar to those created above by ultrasonic nanocrystal surface modification (42). As with the majority of the processes that involve impact, the extent of plastic deformation is dependent on the frequency and intensity of the shots and the process duration. Depending on component material, joint type and external loading, ultrasonic peening has the potential to increase fatigue limits by 50-200% in low-carbon steel butt joints and high-strength steel T-joints (43).

Ultrasonic surface mechanical attrition is used obtain a nano-crystalline material structure whilst maintaining the chemical composition of the material. This is achieved through incremental refinement of the grains, from a coarse to a nanometre scale, through high vibration frequency repeated impact resulting in plastic deformation. However, studies on titanium sheets have shown that this process can have adverse effects on the ductility of the material due to the high stressing of the material (44).

Ultrasonic cavitation involves the attachment of the specimen to an ultrasonic vibrator, described as resulting in similar effects to the shot peening process and when applied to materials that experience high work-hardening there will be no erosive effects due to the process. Depending on the temperature of the cavitation liquid in which the specimen is immersed, residual stress levels can be in the range of -650 MPa for 304 stainless steel (45).

Ultrasonic impact treatment induces plastic deformation through ultrasonic frequency impact in the region of 27,000 Hz (46). Investigation into the increase in fatigue strength of structural steel welded joints subjected to ultrasonic impact treatment, shot peening, hammer peening and *TIG* dressing concluded that specimens subjected to ultrasonic impact treatment experienced the greatest increase in fatigue life at a value of 65-75% (47).

1.4.8 Cold expansion

Cold expansion is a manufacturing process that can be utilised to induce compressive residual stresses, often applied to fastener holes in the aerospace industry. Drawing a mandrel and split sleeve through the hole such that their diameter are greater than that of the hole, plastic deformation occurs and consequently an area of compressive residual stress exists in the vicinity of the hole with near constant magnitude (48). This removes the tendency for crack initiation and growth in the vicinity of the hole, typically an area of local stress concentration. The geometry of the mandrel again heavily influences the arising residual stress state, research showing that a tapered pin with a mating tapered split sleeve produces fatigue life improvement factor of 4-5 in comparison with a parallel split sleeve in aluminium alloy Al 7075-T6 (49).

Simulation studies of the cold expansion process applied to an aluminium alloy sheet showed that the maximum values of compressive residual stresses achieved were approximately -100 ksi with these stress levels present to a depth of 0.125 inches (50).

In another study of aluminium alloy Al 2024 the split sleeve technique with taper pin and the split sleeve technique with ball technique were compared, concluding that a 200% increase in fatigue life was achieved with the former in comparison with the latter (51).

In aluminium alloy LY12-CZ compressive residual stresses of around -300 MPa were obtained both through simulation and experimental means using X-ray diffraction to a depth of approximately 3 mm from the edge of the hole after application of the cold expansion process, resulting in an improvement in fatigue performance by a factor of six in comparison with specimens that had not undergone cold expansion (52).

Likewise titanium alloy TC4 was treated using the cold expansion process, studies of which showed that fatigue performance was improved by a factor of 1.5-3 through the process, additionally a corner crack formed in cold-expanded holes at the entrance face in comparison with a face crack at the mid-plane in unexpanded holes (53)

1.4.9 Combining processes to further enhance fatigue performance

Lastly, it is of course possible to combine these methods to achieve the most favourable results, whether creating a series of processes or applying certain processes in certain areas of a component. Through careful consideration of residual stress state alteration through these methods and the order in which to apply these methods, it is possible to achieve a further improvement in fatigue performance.

Carburising was combined with shot peening and low plasticity burnishing on 9310 steel to assess the effectiveness of these combinations. Combining low plasticity burnishing and carburising proved more effective than shot peening, a maximum compressive residual stress of approximately -1800 MPa being obtained to a depth of 3 times greater compared with the shot peening and carburising combination through which maximum stresses obtained were approximately -1500 MPa (54).

Plasma-carburising and deep-rolling combined achieved both wear resistance through the former and compressive residual stresses through the latter in a titanium alloy. This study showed however, that maximum compressive residual stresses through the combination of these processes were in the same region as the stresses produced solely through the deep-rolling process and that little difference was observed in fatigue performance. Therefore the key added benefit of carburising in this case is the increase in wear resistance (55).

Although some cases have been presented, due to the specialist nature of combining processes, there is little literature available on particular material and process combinations.

1.4.10 Summary

Various methods of influencing residual stresses with a focus on generating compressive residual stresses have been discussed, highlighting the potential for tailoring of

the residual stress magnitude and distribution depending on component requirements. Consideration must be given to the materials in question and the effects that any such processes will have on material properties and metallurgy. Great potential is shown for the alteration of process variables to obtain the desired residual stress state. A major factor remains of the assumption of an initially stress-free component, a case that will not occur in reality. Residual stress distributions obtained can vary greatly with depth and adequate steps must be taken to determine this distribution throughout the component to thoroughly understand the consequences of these stresses on aspects such as fatigue performance. Methods of measuring residual stress will be discussed in 6.2. Great difficulty arises in assessing the effects of the combination of residual stresses and operational stresses, the most effective means being experimental testing paired with finite element simulation modelling of the particular case in question.

Ultimately, processes must be evaluated with a view of their applicability to the particular component and operation, with economic considerations also playing a major role. Autofrettage is largely utilised in pressurised components for example. As has been demonstrated, lower cost processes, such as shot peening, while effective in producing compressive residual stresses, do so only to a very shallow depth. Other aspects such as effects on surface finish must also be considered, as the introduction of surface roughness will not be negligible even if beneficial residual stresses are present. Beneficial effects on surface finish are achieved through laser shock processing, however this presents higher costs. Fatigue and wear properties on the other hand can also be improved and so there are processes such as thermochemical treatments which will provide multiple benefits. The combination of processes must be carefully considered, as this will not necessarily provide greater benefits to the residual stress state and overall fatigue performance.

1.5 Research aims and objectives

The aim of the introduction provided is to illustrate the need for an understanding of the causes of residual stresses and investigation into solutions for industry in dealing with the potentially detrimental effects of residual stresses. This is the core of this research: the development and validation of a fatigue-resistant cladding technology.

As the title suggests, an improvement in fatigue performance will be sought through the implementation of a cladding technology. Through process modification and material selection, the generation of beneficial compressive residual stresses will be investigated in clad components.

This will be achieved through the following:

- Selection of specific material combinations and deposition processes to induce compressive residual stresses.
- Investigation of temperature dependent thermal and mechanical material properties of weld clad layers, heat affected zones and substrate.
- Simulation of residual stress distributions arising through the cladding process using Abaqus and assuming elastic-perfectly plastic material behaviour and in doing so developing an understanding of the importance of model accuracy and assumptions.
- Experimental validation of residual stress distributions arising through the cladding process.
- Examination of the roles of process variables, such as cladding methods, in producing compressive residual stresses to significant depths.
- Effects of the cladding process on metallurgy and material properties and ultimately residual stresses.
- Introduction of methods of modifying the commonly obtained tensile residual stress distribution due to weld cladding with certain material combinations using mechanical autofrettage to increase fatigue performance.
- Understanding the applicability of the technology and identifying challenges.

Chapter 2

Corrosion Fatigue Performance of Unclad Low Alloy Carbon Steel

Validation of the hypothesis of the beneficial effects of a compressive mean stress on the corrosion fatigue performance of a material was obtained through the corrosion of low alloy carbon steel 4330 fatigue specimens. Tensile testing allowed the construction of a four-point bending diagram to provide an indication the fatigue strength of 4330 low alloy carbon steel. The importance of specimen quality for the purpose of fatigue testing is discussed and evaluated. Uncorroded specimen quality was assessed through measuring parameters such as surface roughness and referring to required standards for fatigue testing. Axial fatigue testing and R.R. Moore rotating beam fatigue testing was undertaken with varying corrosion methods investigated and issues in obtaining adequate corrosion discussed. Uncorroded specimens were subjected to cyclic axial fatigue with a tensile mean stress, after which corroded specimens were subjected to a tensile mean stress. This enabled confirmation of the detrimental effects of corrosion on fatigue life. Following this, corroded specimens were subjected to a compressive mean stress. The expectation of a compressive mean stress reducing the negative effects of corrosion fatigue was confirmed and hence the potential benefits of compressive surface residual stresses for fatigue performance of corroded steel introduced.

2.1 Introduction

Corrosion effects can have a major impact on fatigue life, with 4140 heat treated steel experiencing corrosion degradation factors of three to four (56). The negative effects of these mechanisms must be taken into account when evaluating fatigue life. Analysis carried out on a failed hydraulic fracturing pump confirmed the contribution of the mechanisms of erosion and corrosion in fatigue failure. The extent of these mechanisms can be observed in figure 2.1. Methods of combating these effects in engineering components is a common area of investigation. In the case of hydraulic fracturing pumps, one method would be to manufacture the entire pump body out of corrosion resistant material. Although this is an advantageous solution, it is likely to substantially increase manufacturing costs.

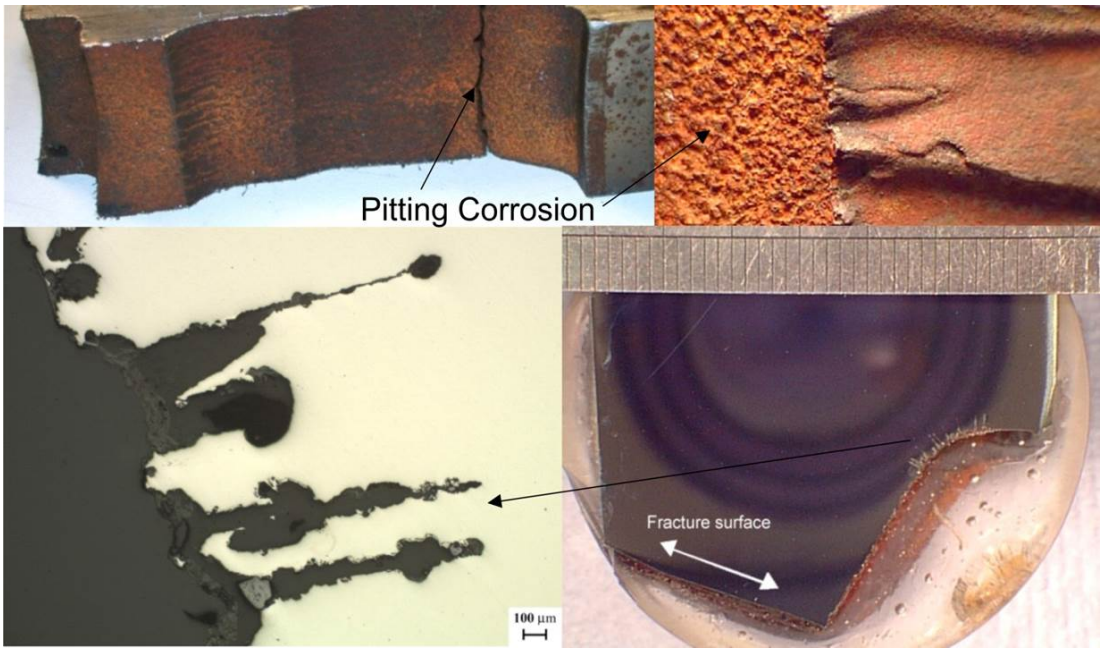

Figure 2.1: Corrosion pitting and failure in hydraulic fracturing pump - Analysis of section of 4330 hydraulic fracturing pump showing cracked bore surface, erosion and corrosion pitting.

When engineering components and structures experience cyclic loading at levels below yield strength, crack initiation can occur, followed by propagation and ultimately fatigue failure. With 90% of service failures in metal parts being attributed to fatigue (57), it is crucial to evaluate the effects of fatigue of component performance. In determining the effects of residual stresses on fatigue life, the interaction of these stresses with operational loads must be investigated to determine the effects on crack initiation and potential residual stress relaxation (13).

Clearly a tensile residual stress increases the mean stress and the maximum stress level which will be reached during operation. Each cycle experienced causes an in-

crease in fatigue damage through crack growth until a critical crack length is reached leading to crack propagation and failure of the component. Tensile residual stresses utilise a greater portion of the ductility of the material as the increased stress level results in the reaching of a higher point on the stress-strain curve. Compressive residual stresses act as a means of increasing the portion of the stress-strain curve that can be utilised through decreasing the mean stress and peak stress and effectively facilitating an increase in ductility and fracture strength of the material (58). With regards to crack propagation, compressive residual stresses, if present to a high enough level, limit crack growth due to the lack of the tendency of crack faces to open during a stress cycle.

Empirical relationships exist for the effects of mean stress on fatigue strength, for example the Modified Goodman equation 2.1:

$$\frac{\sigma_a}{\sigma_R} + \frac{\sigma_m}{\sigma_{UTS}} = 1 \tag{2.1}$$

In the Modified Goodman equation σ_a is the stress amplitude in the presence of a mean stress and σ_R is the stress amplitude in the presence of a zero mean stress for the same life as in the case of σ_a. σ_m is the mean stress that corresponds to the stress amplitude in the presence of a mean stress and σ_{UTS} is the ultimate tensile strength.

Depending on the material and whether crack initiation or propagation is dominant, mean stress effects will vary. Furthermore, if the specimen is notched, the type of notch will also influence the fatigue strength, or endurance limit, with welded joints being described as effectively severely notched specimens, in which crack propagation is dominant. At this endurance limit, the material has the ability to resist fatigue failure regardless of the number of cycles it experiences. Results comparing notched and welded mild steel specimens at 10^6 cycles showed little difference in cyclic stress limit versus mean stress. For plain mild steel, the effects of mean stress on crack initiation are of greater interest while the effects of mean stress on crack propagation are less influential when the stress cycle is fully tensile (59). Fatigue performance is measured by the number of cycles endured by a material. The term high cycle fatigue is assigned to the case where the number of cycles N involved are greater than 10^5 (60). High cycle fatigue involves an elastically applied stress at low amplitude with the development of cracks generally occurring in a transgranular manner. In low cycle fatigue, with high amplitude plastic strain characteristics, cracks develop in an intergranular manner (61).

This chapter presents the effects of a compressive mean stress on the corrosion fatigue performance of 4330 low alloy carbon steel to mimic the beneficial effects of compressive residual stresses on corrosion fatigue performance. Corrosion of fatigue specimens was undertaken using two methods due to the inability of the first method

in achieving adequate corrosion. Corroded and uncorroded specimens were tested under a tensile mean stress to prove the detrimental effects of corrosion on fatigue performance. Corroded specimens were then subjected to a compressive mean stress to highlight that corrosion fatigue performance benefits from the presence of compressive residual stresses.

2.2 Mechanism of corrosion

The effects of corrosion during component operation can have catastrophic consequences if not considered and accounted for. There have been many studies into the causes of failure of engineering components and structures, and it has long been known that fatigue is the major failure mechanism in aircraft, chemical and offshore process plants and boilers and pressure vessels (62). Corrosion follows fatigue closely as the major mechanism leading to failure and the coupling of these two mechanisms is also a major contributor. In 2002, a study concluded that the total annual estimated direct cost of corrosion in the U.S. was $276 billion (63).

Corrosion involves an electrochemical process at the surface of a component when a material is exposed to moisture and oxygen causing oxidation. In the case of steel, iron reacts with oxygen to form iron oxide Fe_2O_3, commonly known as rust. The creation of electrons and metal ions allows a reduction reaction, with the presence of an electrolyte solution. Hydroxide ions are formed through the conversion of oxygen and water, the combining of these hydroxide ions with iron ions present in the iron or iron alloy material forming hydrated oxides. The rate of corrosion is dependent on the conductivity of the ions present, acceleration or deceleration being controllable through the electrolyte and solution oxygen content and salinity. For example, corrosion rates are increased in marine environments as electrolytes are present in the form of chlorides in seawater.

The corrosion process alters the mechanical properties of a material. For example, rusted steel loses the ability to protect the material from further oxidation and further damage occurs. The decrease in cross-sectional area of a component presents the risk of failure of a component. As shown in figure 2.1 pitting corrosion is observed in the component in question, this being a type of localised corrosion where specific areas of the component are more aggressively affected by the electrolyte. Increased material removal occurs with increasing levels of oxidation ultimately leading to a potential failure of the component.

2.3 Immersion corrosion method

2.3.1 Axial fatigue specimens

Specimens for axial fatigue testing were machined from bulk 4330 low alloy carbon steel material blocks according to the British Standards for Tensile Testing (64) using a CNC machine on a lathe, adequate for fatigue testing in this case. The specimen dimensions are shown in table 2.1 with figure 2.2 illustrating the placement of these dimensions.

D (mm)	15.9
R (mm)	12.5
L_{gauge} (mm)	50
L_1 (mm)	70

Table 2.1: Fatigue specimen dimensions

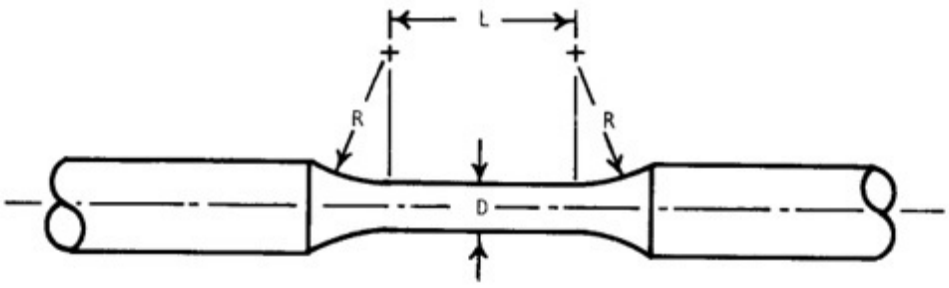

Figure 2.2: Tangentially blended fillet fatigue specimen with circular cross section - Figure as shown in (65).

Initial testing plans included the cycling of the specimen from a tensile to a compressive value hence passing through zero and so the specimens were machined with threaded ends to prevent slackness in the grips. Furthermore, the diameter of the specimens was increased compared with that provided in the standard to prevent buckling of the specimen.

Specimens were hand polished to finish using emery cloth.

2.3.2 Tensile test

The required cyclic load value was determined through a tensile test using a Denison-Mayes servo-hydraulic universal testing machine, resulting in yielding occurring at a

load of 195.6 kN and the ultimate tensile load being 216 kN. Table 2.2 displays the obtained results and yield and ultimate tensile stresses calculated using the relationship between force and area (equations 2.2 and 2.3).

$$A = \pi r^2 \tag{2.2}$$

$$\sigma = F/A \tag{2.3}$$

$\varnothing$ (mm)	15.945
A (mm^2)	199.68
F_{σ_y} (kN)	195.6
F_{UTS} (kN)	216
σ_y (MPa)	979.56
UTS (MPa)	1081.7

Table 2.2: 4330 tangentially blended fillet fatigue specimen tensile test results

2.3.3 Four-point method

It is often difficult to obtain fatigue performance data due to the length of time and number of specimens required and therefore methods have been developed to predict fatigue performance.

Using the data obtained from the tensile test, the four-point method using the strain-based approach was applied to provide an indication of the fatigue strength of the material (66). This requires the plotting of the elastic and plastic strain life lines.

Point A corresponds to the UTS at N=$\frac{1}{4}$ cycles, assuming that the tensile test is representative of a quarter of a single, completely reversed fatigue cycle.

Point B is the fatigue endurance limit. For ferrous alloys this is generally around 10^7 or 10^6 cycles, where the fatigue curve becomes a horizontal line, signalling the stress level below which fatigue failure will not occur. If the endurance limit cannot be determined for the material, which is often the case in materials which do not experience work hardening, then an endurance strength can be estimated as the failure stress at a large number of cycles, for example at N=10^7 cycles, or through using tensile test data using equation 2.4 to calculate the ductility parameter. For common structural alloys, this value can then be used to find the corresponding ratio of endurance to yield strength $\frac{S_f}{\sigma_y}$ (67). A distinct endurance limit around 50% of the UTS exists for ferrous alloys such as 4330, while some materials, such as aluminium,

do not have an endurance limit, with eventual failure occurring at a low stress level (60). Multiplying this value by the yield stress obtained from the tensile test provides an estimation of the endurance strength S_e. The values obtained for 4330 are documented in table 2.3. The joining of points A and B provides the elastic limit line.

$$\mu = 1 - \frac{\sigma_y}{UTS} \tag{2.4}$$

σ_y (MPa)	979.56
UTS (MPa)	1081.7
μ	0.094
$\frac{S_f}{\sigma_y}$	0.5
S_e (MPa)	489.78

Table 2.3: Estimation of endurance strength of 4330 using four-point method

Point C is known as the fracture ductility ε_f, which can also be obtained through a tensile test as the natural log of the true strain at fracture $\varepsilon_{fracture}$. The value of fracture ductility can also be estimated using equation 2.5.

$$\varepsilon_f = ln\left[\frac{100}{100 - RA}\right] \tag{2.5}$$

$\varepsilon_{fracture}$	3.567 E-02
E (GPa)	185
ε_{PointA}	0.00584324
ε_{PointB}	0.00264703
ε_{PointC}	3.33344528
ε_{PointD}	0.00324324

Table 2.4: Strain values as plotted for the strain-based four-point method using tensile test data obtained for 4330

The theory of *universal slopes* dictates that the elastic and plastic strain curves intersect at N=10^4 cycles and therefore point D is plotted on the elastic curve at N=10^4 cycles and the plastic curve created through the joining of points C and D. The fatigue strength estimation curve can then be plotted as the arithmetic summation of the elastic and plastic curves.

Figure 2.3 illustrates the resulting diagram for the strain-based four-point method using tensile test data obtained for 4330.

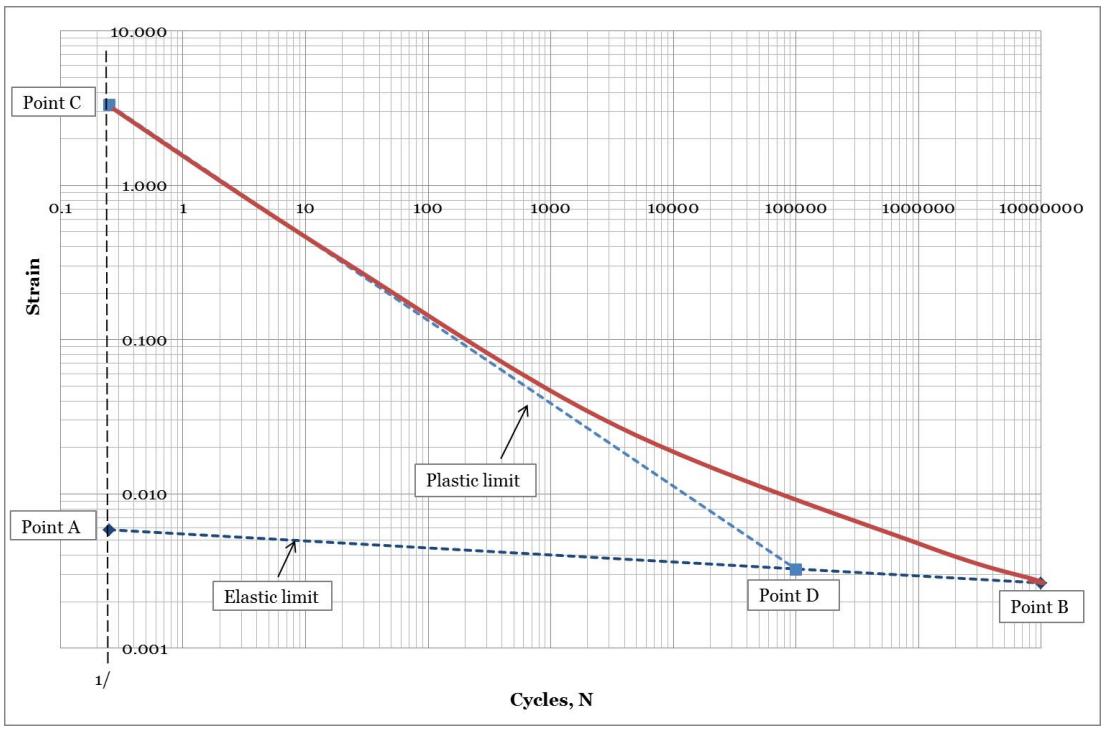

Figure 2.3: Approximation of fatigue strength of 4330 - Applying four-point method using the strain-based approach.

2.3.4 Specimen quality

Design and machining of specimens was found to be a key factor in this investigation, as failure occurred in areas of machining defects in the threaded region or at the tangential fillet between the thread and the gauge length. For example, a specimen failed in the threaded region at 31,500 cycles when tested at a stress range of 5%-95% σ_y with figure 2.4 illustrating degradation of the material surface due to tool chatter.

Crack initiation occurred in middle region of figure 2.5 with crack propagation progressing towards the left and right edges of the image where tearing can be seen to have occurred.

A second batch of specimens was machined to ensure that chatter would not create areas of stress concentration in the threads. However, it was found that failure occurred in these specimens at the tangential radius and the gauge length with the presence of a cusp, common in the milling process due to the requirement for a number of adjacent cuts to achieve the desired finish. This defect was detected through microscopic examination of the specimen, with the region shown in figure 2.6. The presence of this cusp along with stress concentration due to machining marks created an area of stress concentration large enough to move the point of failure to this location as opposed to in the centre of the gauge length.

The diameter of the specimens was reduced to 15 mm and the radius increased to

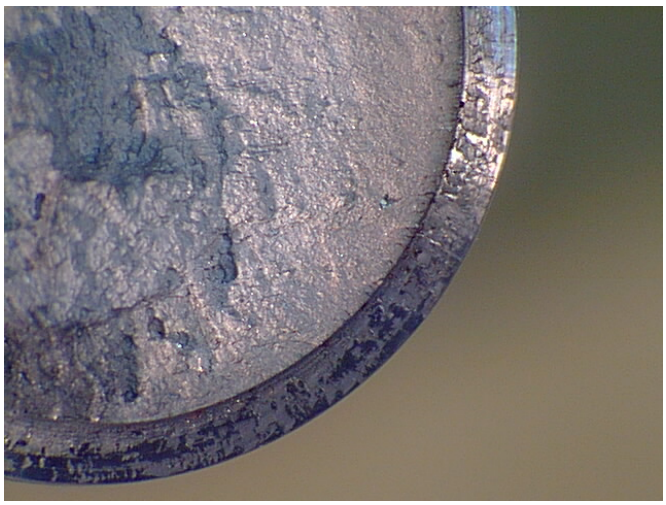

Figure 2.4: Thread chatter in 4330 uncorroded tangentially blended fillet specimen - Degradation of material surface due to tool impact causing chatter.

Figure 2.5: Crack initiation point on 4330 uncorroded tangentially blended fillet specimen - Crack initiation in middle region of figure, with crack propagation progressing towards left and right edges of the figure.

Figure 2.6: Cusp fracture and example of machining marks on 4330 tangentially blended fillet specimen - Stress concentration effects due to machining process on 4339 axial fatigue specimens.

15 mm to eliminate the cusp and the threads of the specimens of the third batch flattened. For screw fasteners, rolling is the preferred method of creating threads as threads that are machined using a cutting process are known to possess a lower endurance strength (68). Thread roots experience plastic deformation under static loading, risking local over-stressing in cyclic conditions leading to potential fracture (69).

As the presence of *obvious abnormalities* is unacceptable in specimens (65), these specimens were deemed to be of unacceptable standards. Furthermore, the standard requires the fillet radius R to be eight times the test section diameter D. Table 2.5 notes the dimensions for the first and second batches of specimens highlighting that this requirement has not been met. A decrease in the test section diameter is required along with an increase in the fillet radius. Simultaneously the diameter of the test section must not be less than 5.08 mm and the test section length must be two to three times the test section diameter.

	Batch 1	Batch 2
D (mm)	15.9	15
R (mm)	12.5	15

Table 2.5: Specimen dimensions for batches 1 and 2 of 4330 tangentially blended fillet specimens

Additionally, surface finish is required to be of an acceptable standard, although as previously emphasised, this does not necessarily mean that machining processes have not induced tensile residual stresses or micro-cracking. Polishing, preferred to be in the longitudinal direction, is standard practice as the final step in specimen prepara-

tion. In this case rotational polishing was applied. It must be ensured that any steps applied throughout the specimen preparation process do not alter the metallurgy of the material or induce residual stresses (70). The use of appropriate coolant in the machining process for example is crucial to ensure that heat treatment effects do not alter the metallurgical properties of the material. If residual stresses are thought to have been induced through the machining process then attempts should be made the quantify these, as will be discussed in section 6.3.1.1.

Finite element simulations undertaken in separate studies confirmed the detrimental effects of the presence of a cusp modelled through the elimination of the tangential curve, where stress concentrations were observed to become infinitely high in the vicinity of the cusp. The tendency for high stress concentration factors in the threads encourage failure in these regions. These findings are in agreement with the experimental results, failure having occurred at N=21,783 cycles in the radius and gauge length in a specimen of batch 1 tested at a stress range σ_R of 5%-95% $sigma_y$ as was highlighted in figure 2.6. Examining the results from the specimens of these batches, three of the four specimens tested under a tensile mean stress failed in the section between the radius and the gauge length. The elimination of cusps would likely move the point of failure to the threaded section due to the removal of the stress concentration in this area and the focus then on the stress concentration in the threaded region. Both of these failure locations ultimately indicated that failure in the gauge length in the centre of the specimen is unlikely under the given machining quality and specimen design.

Taking into account the need to overcome stress concentration effects in the threaded region, table 2.6 presents an example of suggested dimensions to conform with requirements of the ASTM standard (65). The requirements according to the standards are noted in equations 2.6, 2.7 and 2.8.

$$R = 8D \tag{2.6}$$

$$L_{gauge} = 3D \tag{2.7}$$

$$A_{Grip} / A_{GaugeLength} \geq 4 \tag{2.8}$$

These suggested specimens would yield a specimen with a circular bar and a tangentially blended fillet. Alternatively a constant fillet radius section could be machined, with similar requirements as previously stated. Threaded ends would ideally be eliminated to in turn eliminate the issue of chatter and stress concentration and would in fact not be required for testing under tensile or compressive mean stresses.

D_{Grip} (mm)	31.6
$D_{GaugeLength}$ (mm)	10
R (mm)	80
L_{gauge} (mm)	30

Table 2.6: Suggested amended tangentially blended fillet specimen dimensions

On completion of the machining of specimens for the purpose of fatigue testing, it would be desirable to receive information regarding the machining process utilised, including machining speeds, tooling and surface finishing techniques. As observed, surface finishes obtained are not consistent and this is a cause for concern.

2.3.5 Summary

The primary issue in the early investigation into the corrosion fatigue performance of 4330 related to the corrosion of the axial fatigue specimens. An immersion corrosion method utilised a carousel modified as shown in figure 2.7 to allow specimens to be immersed and rotating in an eight litre bath of 3.5% saline solution to imitate salt water conditions (71). Nylon inserts enabled the specimens to be screwed into the holders and a motor utilised to allow variable speed of rotation. Each specimen holder was rotated via a rod connected to a number of gears. A pump was installed at the bottom of the bath to increase the oxygen content of the water. Increased corrosion rates can be attained through this manner of aeration, as well as through modification of the temperature or concentration of the solution (72).

Visual inspection allowed observation of the effects of corrosion as illustrated in figure 2.8. Discolouration occurred through the immersion corrosion method and it can be seen that material removal has occurred and pit formation has commenced. The formation of pits is recognisable through small holes appearing on the material surface indicating localised corrosion. Careful inspection of these pits is crucial, as they cannot be solely characterised through visual inspection and may be difficult to observe due to the presence of oxide layers. Pits may be of many forms, with cross-sectional shapes varying from elliptical to narrow and deep or wide and shallow, undercutting to subsurface and horizontal to vertical (73). Stress concentrations arise at the base of a pit, creating the potential for crack initiation and fatigue failure if the component experiences cyclic loading.

Optical microscopy allowed further examination of the effects of corrosion utilising the discs attached to the specimens. The discs were sectioned using a water-cooled Struers cut-off grinder, followed by grinding with silicone carbide paper with varying levels of grit (220-1200 μm), water coolant and a machine speed of 300 rpm to remove

Figure 2.7: Immersion corrosion experimental rig - Set-up illustrates specimens suspended above saline solution with a pump to induce bubbling to increase oxygen content.

Figure 2.8: Visual inspection of corroded 4330 tangentially blended fillet fatigue specimen - Corrosion seen to have affected threaded region of specimen.

any machining effects due to the sectioning. Polishing of the surface ensured a mirror finish using a 3 μm diamond pad and an alcohol lubricant and finally a 0.05 μm colloidal silica polishing pad prior to mounting of these discs in Bakelite using a hydraulic press.

After a period of five days, pitting was not found to be present as can be seen in figure 2.9, although general corrosion is visible on the surface of the disc.

Figure 2.9: Magnified image of 4330 corroded disc surface - Magnification factor: x1000.

After a period of five weeks, an etched sample was examined under the optical microscope. The etching process uses a 2% Nital solution to enable the grain structure to be examined. From figure 2.10 it can be seen that a potential pit was observed with a crack emanating from the base of the pit.

Figure 2.10: Magnified image of pit and potential crack on 4330 corroded disc surface - Magnification factor: x100.

Increasing the magnification further enabled the investigation of areas of potential pitting, with the conclusion that a wide, shallow pit was forming, shown in figure 2.11.

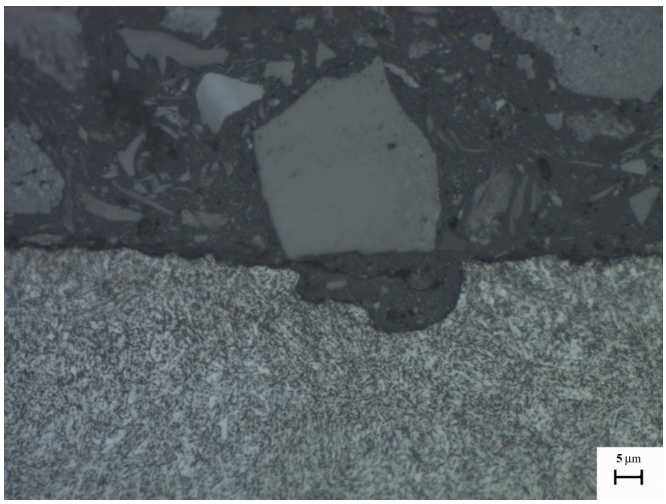

Figure 2.11: Magnified image of shallow, wide pit on 4330 corroded disc surface - Magnification factor: x1000.

Inspection of these discs illustrated the early stages of corrosion pitting, however there were too few areas of pitting for methods of evaluation such as number of pits per unit area or average pit size or depth. Furthermore, this investigation was undertaken on the discs attached to the specimens, as the specimens could not be inspected as sectioning would clearly utilise material intended for fatigue testing. Additionally, corrosion inspection could be achieved through measuring mass or geometrical reduction to quantify material loss.

The attempts of observing corrosion signalled the difficulty in obtaining adequate levels of corrosion and so one month prior to ending the corrosion process, specimens were raised out of the saline solution on a daily basis in an attempt to increase the level of localised corrosion. On examination of a third disc, an increase in the level of pitting was not observed and so the corrosion process was brought to an end. In fact, protection may be offered to the material through the growth of the oxide layer formed during the corrosion process, and hence the level of corrosion decelerates with time. Although methods of accelerating corrosion are available, due to the set-up of the carousel, the options of modifying the corrosive fluid or increasing the temperature could not be realised.

Results of this study did conclude that a compressive mean stress does have beneficial effects on the fatigue performance of corroded, or notched, 4330 steel. This was illustrated by increased fatigue performance, with specimens not failing under a compressive mean stress, while under a tensile mean stress failure occurred at 20,000-40,000 cycles.

It would be recommended that future testing would include a larger number of specimens to ensure representative data and to allow the effects of different load levels to

be assessed. Furthermore, the specimen dimensions were later deemed to be inappropriate for fatigue testing, thought to be the cause of the scatter in the results for uncorroded specimens. Comparing the uncorroded specimens tested under a tensile mean stress, failure occurred in one case after 1.7 million cycles and in another at the stress range after 161,208 cycles. Unnecessary stress concentrations arose in the threaded region and the surface finish was found to be of a low quality, highlighting the need for amendments to the specimen design and machining process.

Adequate corrosion levels were not obtained using the immersion pre-corrosion method, indicating the need for modification of the pre-corrosion method or the means of investigating the interaction between corrosion and fatigue during testing, guidelines for this type of testing provided in (74). Possible modifications to the corrosion method include elevated temperature and high velocity impinging flow or a combination of both, studies having illustrated the capability of these parameters in facilitating the breakdown of passivity and in turn the effects of the corrosion behaviour of stainless steels and related Ni-base and Co-base alloys (75). Applying a method of impingement would not only produce increased corrosion and pitting but potentially also greatly decrease corrosion time.

Due to the poor machining quality and lack of adequate corrosion levels, further studies were then undertaken utilising an aeration corrosion method and a different specimen geometry.

2.4 Aeration corrosion method

Much of the available corrosion data relates to fatigue testing of pre-corroded specimens. The interaction between corrosion and fatigue, however, is crucial in accurately assessing fatigue performance. The time dependence of corrosion means that the frequency of fatigue testing involving corrosion is an important parameter. Longer time periods and lower frequency testing allow increased interaction between corrosion and fatigue and a larger number of pits and cracks can form prior to failure. The initiation of cracks in areas of corrosion pitting severely reduce fatigue performance of components subjected to cyclic loading due to the presence of stress concentrations. Cyclic loading also increases the rate of corrosion as the protection offered by the material is decreased through continued loading of the material and exposing of material below the surface. There is a correlation between the density of pitting and the level of stress applied and cyclic strain enhanced dissolution encourages the formation and growth of corrosion pits (76).

In continuing the examination of the hypothesis of the beneficial effects of a compressive residual stress in a corrosive environment, fatigue specimens were corroded

using a dripping mechanism to achieve adequate levels of pitting with the initiation of fatigue cracks (77). Specimens were corroded in four-point bending fatigue using a custom-designed corrosion rig in an R.R. Moore rotating beam fatigue testing machine. Pre-corroded specimens were then tested under a compressive mean stress in a uni-axial fatigue testing machine whilst subjected to a corrosive environment. Comparisons were drawn with the results of specimens tested under a tensile mean stress as previously, with the finding that even pre-corrosion was adequate to cause failure after a short period of time without the requirement to corrode during the test. Uncorroded specimens tested under a tensile mean stress allowed the effects of corrosion on fatigue performance to be determined. Ultimately the method of corrosion and testing proved more successful in comparison with the previous immersion corrosion method.

2.4.1 Test specimens

Specimens were machined on a CNC lathe from bars of 4330 low alloy carbon steel according to the British Standards ISO 1143 for rotating bar bending fatigue testing specimens (78). Care was taken to avoid issues with the previous batch of fatigue specimens by utilising a continuous radius between the ends of the specimen as shown in figure 2.12 and eliminating the parallel gauge length and the threaded grips required when passing through a zero stress value. This effectively removed the areas of stress concentration to encourage failure in the centre of the specimen.

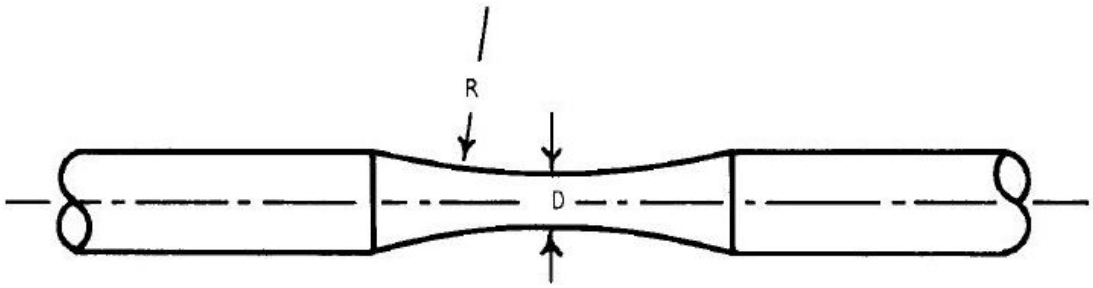

Figure 2.12: Continuous radius fatigue specimen with circular cross section - Figure as shown in (65).

Dimensions of the specimens are shown in figure 2.13.

2.4.2 Measuring surface roughness

Corrosion pitting obtained through pre-corrosion was expected to result in deeper penetration than machining marks and therefore no polishing was undertaken during the machining process. However, consistency between specimens was emphasised as

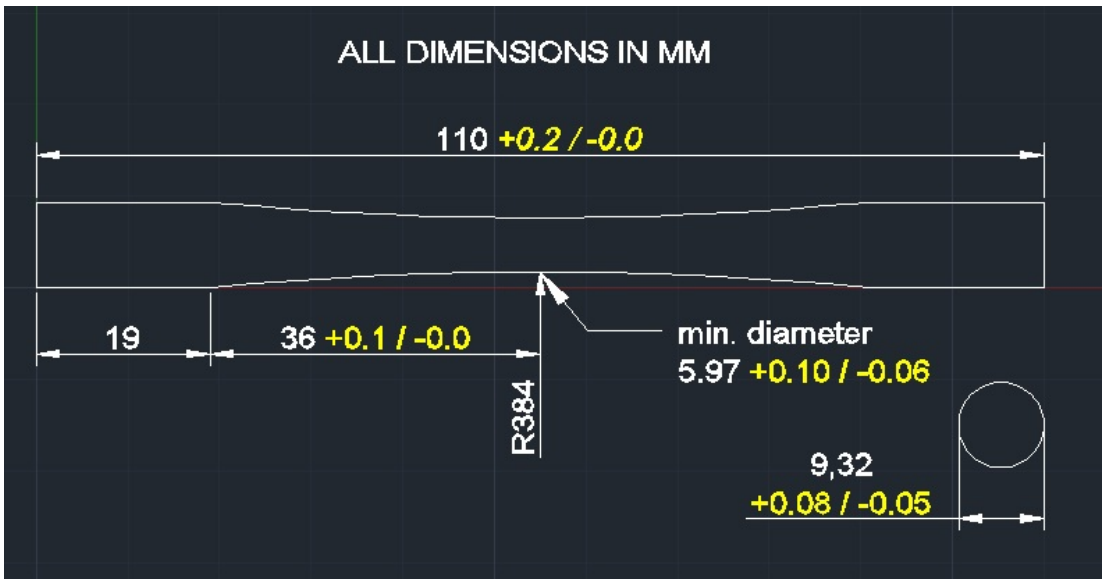

Figure 2.13: Continuous radius fatigue specimen dimensions - Dimensions requested for machined specimens, illustrating also required tolerance values.

an important aspect to allow similar corrosion behaviour and comparison of results when specimens are subjected to the same loading cycles.

A Mitutoyo Surftest SV-2000 (figure 2.14) was utilised to measure values of the arithmetic mean roughness R_a and the distance between maximum peak height and maximum valley depth R_y on uncorroded specimens as shown in figure 2.15. Readings were obtained across five 0.8 mm segments at angles of 0° and 90° around the centre circumference. The maximum speed of measurement, 0.5 mm/s, was used.

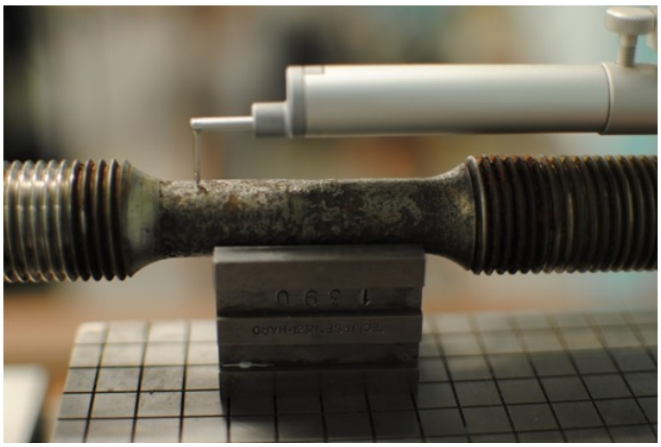

Figure 2.14: Surface roughness measurement of corroded 4330 tangentially blended fillet fatigue specimen - Measurements obtained using Mitotoyo Surftest SV-2000.

Figure 2.16 shows a path plot along the specimen illustrating the peaks and valleys present on an as-machined specimen.

Table 2.7 displays the values for minimum, maximum, mean and standard deviation for R_a and R_y for the batch of specimens. The large differences in the minimum

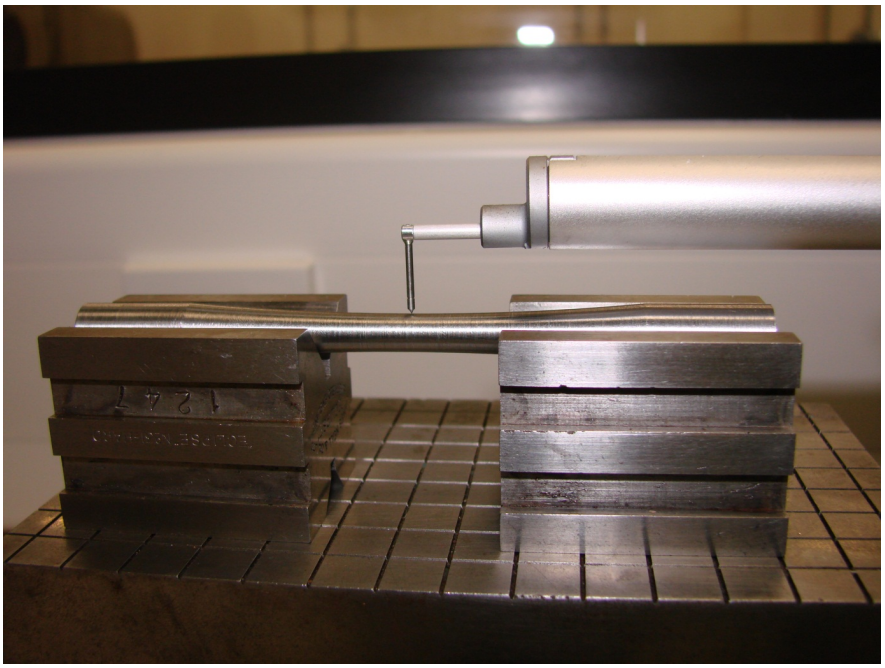

Figure 2.15: Surface roughness measurement of 4330 continuous radius fatigue specimen - Measurements obtained using Mitotoyo Surftest SV-2000.

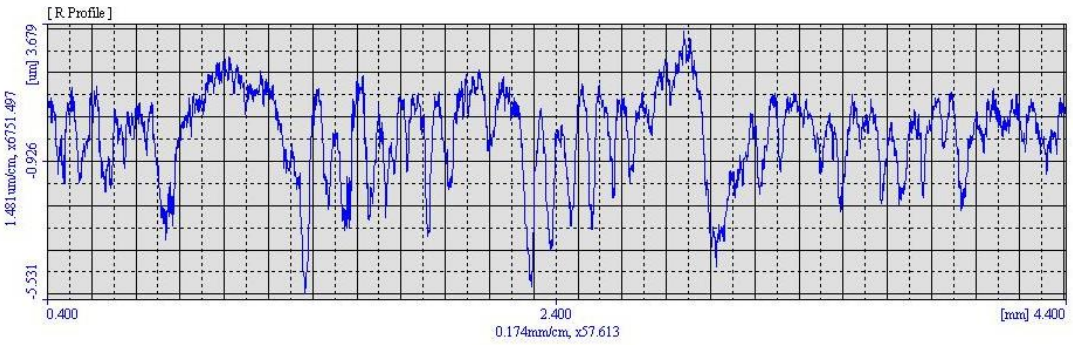

Figure 2.16: Surface roughness data for 4330 continuous radius fatigue specimen - Peaks and valleys shown on surface of specimen number 1.

and maximum values is alarming and highlights a lack of consistency in the machining process. Scatter in the results for surface roughness will need to be taken into consideration, as this will translate into scatter in experimental results.

	R_a (μm)	R_y (μm)
Minimum	0.430	2.966
Maximum	2.206	9.917
Mean	0.964	5.973
Standard deviation	0.361	1.713

Table 2.7: 4330 continuous radius fatigue specimens - Batch surface roughness values

Machining marks were visible by eye, figure 2.17 showing circumferential marks lengthwise along the specimen resulting from rotation in the *CNC* lathe. Diagonal marks are a result of an attempted polishing process, likely during rotation of the specimen.

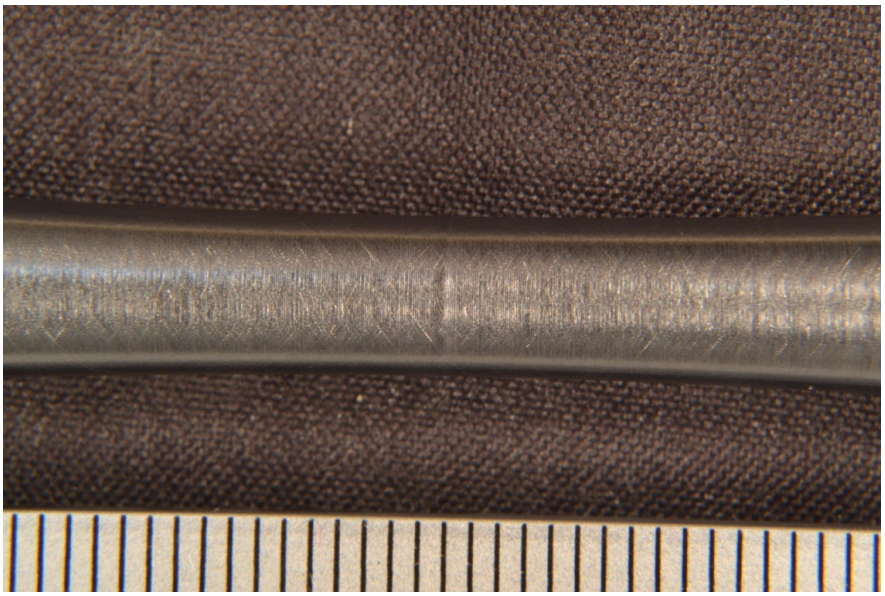

Figure 2.17: 4330 continuous radius fatigue specimen - Magnification factor: x10. Millimetre scale shown below specimen.

2.4.3 Measuring specimen dimensions

To allow calculation of the loading required to provide stressing of the material, the centre diameter of each specimen was measured to calculate the minimum cross-sectional area. The diameter of the grip was also measured on each specimen to ensure that a secure fit would be achieved between specimen and R.R. Moore rotating beam fatigue testing machine collets. This avoids rotation of the specimen in the

collets during testing which would alter the number of cycles the specimen experiences. A 3D *CNC* Mitutoyo Vision Measuring Machine provided measurements to an accuracy of 0.001 mm. The average of two centre diameter measurements $\varnothing m_{centre}$ at an angle of 90° to one another was obtained with center circularity ∘ calculated as the difference between the two values. One measurement for the grip diameter was obtained at each end of the specimen. Values obtained for as-machined specimens are shown in table 2.8.

	$\varnothing m_{centre}$ (mm)	∘ (mm)	$\varnothing m_{grip}$ (mm)
Minimum	5.917	0.000	9.281
Maximum	6.065	0.095	9.376
Mean	5.971	0.021	9.317
Range	0.148	0.095	0.096
Standard deviation	0.030	0.020	0.019

Table 2.8: 4330 continuous radius fatigue specimens - As-machined dimensions

Measurements obtained demonstrated that the dimensions and tolerances shown in figure 2.13 requested dimensions were obtained.

2.4.4 Tensile test

To determine the maximum allowable stress for fatigue testing, the yield stress σ_y of the 4330 low alloy carbon steel, again a tensile test was performed. Obtaining the *UTS* also provides an approximation of the endurance limit S_e for the material. This value is typically around half of the *UTS* for ferrous alloys as previously mentioned in section 2.3.3. An Instron 5969 with a load capacity of 50 kN was used to conduct two tensile tests, shown in figure 2.18.

Mean yield stress and ultimate tensile strength values obtained are shown in table 2.9.

σ_y (MPa)	885
UTS (MPa)	1035

Table 2.9: 4330 continuous radius fatigue specimen tensile test results

Figure 2.19 shows a plot of applied load versus elongation for one of the specimens, with yielding observed at a load of 24 kN. To increase the accuracy of the results, a larger number of specimens would ideally be tested.

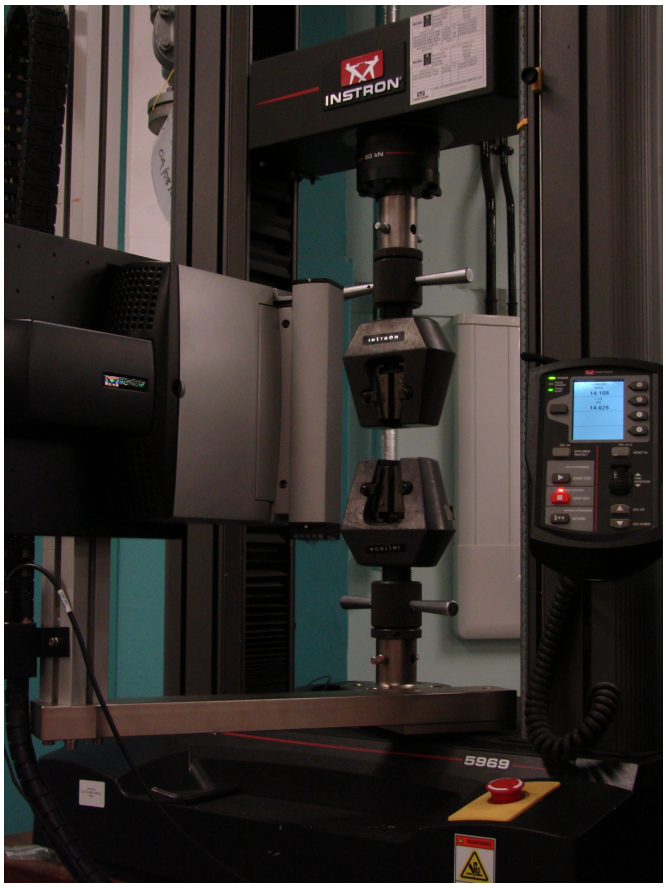

Figure 2.18: Instron 5969 dual column tabletop universal testing system - Load capacity: 50 kN.

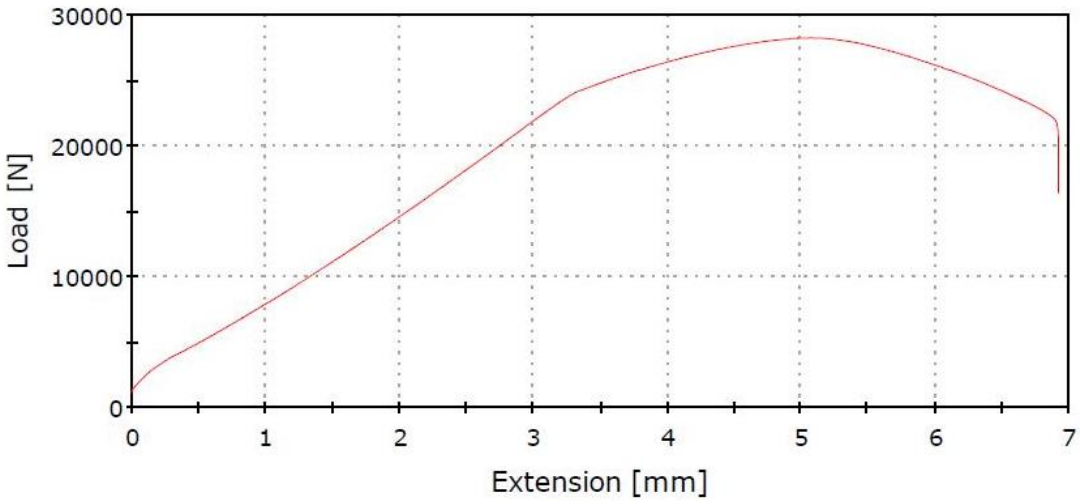

Figure 2.19: 4330 continuous radius fatigue specimen tensile test result - Load versus extension obtained from tensile test using Instron 5969 testing machine.

2.4.5 Pre-corrosion of specimens

Due to the poor levels of corrosion obtained using the immersion corrosion method, an alternative method of corrosion was applied. Early studies utilising a custom built corrosion rig attached to an R.R. Moore rotating beam bending fatigue testing machine proved that the dripping of saline solution onto the centre of the specimen as it rotated experiencing minimal frequency fatigue resulted in much greater corrosion levels including pitting. This method increases the oxygen content during corrosion and also captures the interaction between corrosion and fatigue. However in this pre-corrosion stage, loads were maintained at a level and number of cycles such that significant pitting occurred with the potential of fatigue crack growth whilst ensuring fatigue failure did not occur. An example of the corrosion achieved using this method is shown in figure 2.20.

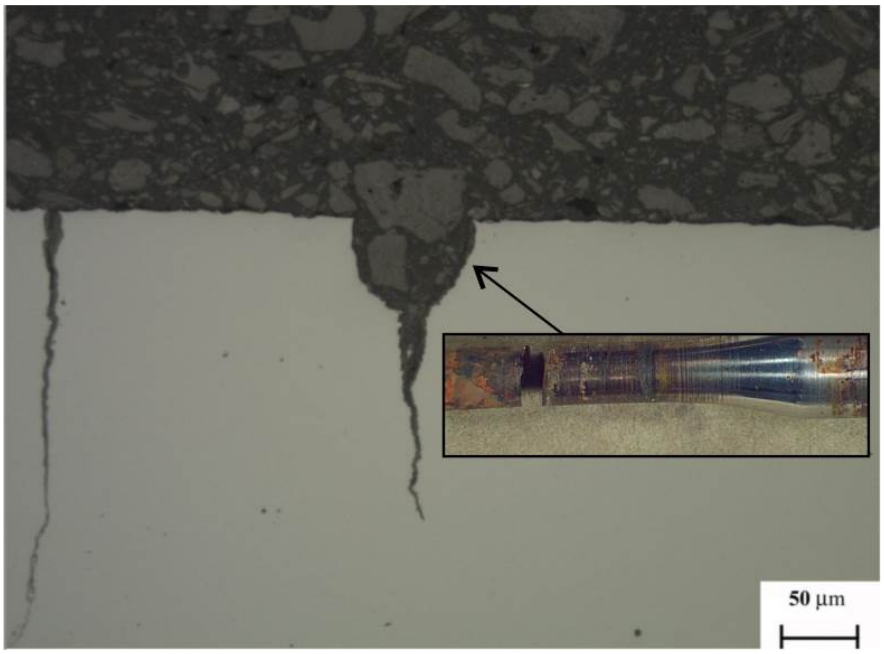

Figure 2.20: Corrosion pitting and cracking of 4330 continuous radius fatigue specimen - Magnification factor: x200. Crack protrusion from pit is observable using corrosion rig and dripping mechanism to achieve pre-corrosion of fatigue specimens.

Corrosion rates in seawater decrease with time for iron and steel components due to the build up of corrosion products inhibiting interaction between the corrosive fluid and the material and pitting can occur to several times the depth of that occurring due to general corrosion when the corrosive fluid flows over the material (79). Therefore a short corrosion period with a dripping mechanism was considered to be appropriate. The specimen is fitted into the 3D prototype shown in figure 2.21 and the combination mounted in the R.R. Moore testing machine. The corrosion rig was developed and custom-manufactured for the purpose of this research (80).

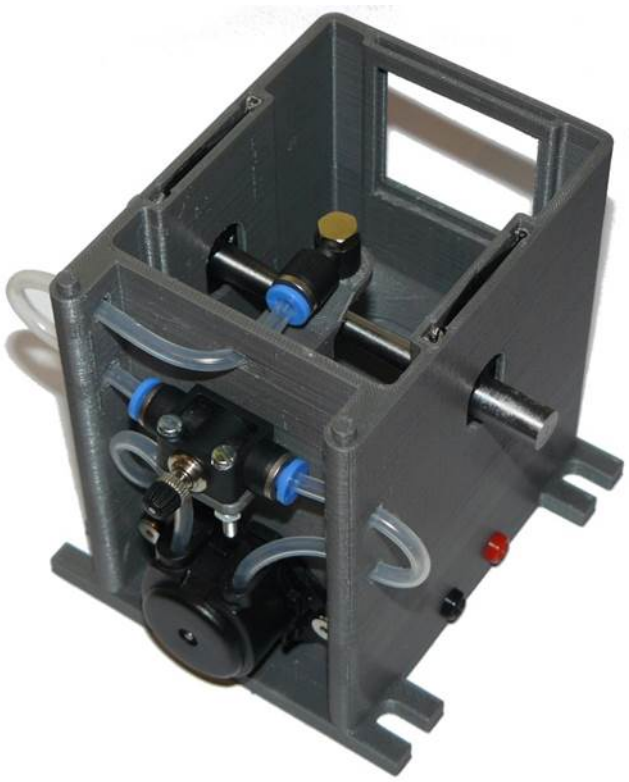

Figure 2.21: Custom-built corrosion rig for use with R.R. Moore rotating beam bending fatigue testing machine - Fatigue specimen placed in corrosion rig with brushes inserted into slots and rubber rings fitted to prevent the travel of saline solution into machine collets.

Corrosive fluid is filled into the reservoir and drawn upwards by a pump to a tap which allows it to drop onto the specimen. A 5% $NaCl$ solution was achieved through the mixing of water and salt to achieve a fluid resembling seawater, typically around 3.5% $NaCl$. It was expected that as corrosion progresses, the concentration of the solution would fluctuate as the $NaCl$ crystals evaporate. However, it was assumed that this effect would be fairly constant in all tests. A specimen undergoing pre-corrosion is shown in figure 2.22. Rubber rings were fitted to prevent the solution travelling onto the grip regions of the specimens to avoid corrosion in these regions and potentially damaging the test machine.

Figure 2.22: Corrosion of 4330 continuous radius fatigue specimen - Fatigue specimen corroding in suitable saline environment.

The rotating beam principle of the R.R. Moore machine means that the specimen is mounted and acts like a beam loaded symmetrically at two points such that a load hangs in the centre to impart a bending stress. The mass that imparts this load can be altered and controlled as necessary to an accuracy of 0.05 kg. The maximum speed of the testing machine is 10,000 rpm, however noise levels at this value were considered too high and therefore a lower speed was used. Tensile stresses exist in the lower region of the specimen and compressive in the upper region with rotation of the specimen causing these stresses to reverse and therefore for every rotation a full stress cycle is experienced by the specimen. The mean stress of zero resulting from this process makes this test unable to be utilised for the testing of the hypothesis of the beneficial effects of a compressive mean stress. A mechanical mechanism halts the test upon failure and outputs the number of cycles.

The applied load required was calculated for every specimen using equation 2.9, taking into account the diameter of the particular specimen and re-arranging the equation given for the required test stress for a specimen subjected to two-point bending in an R.R. Moore rotating bar bending fatigue test (78). The weight of the

hanging mass was 31.1 N, which was subtracted from the term $F_{applied}$ to provide the additional force and therefore additional mass required.

$$\sigma_{test} = \frac{16 F_{applied} L_{arm}}{\pi \varnothing^3} \tag{2.9}$$

Different combinations of stress level, cycle speed and test duration were applied until failure to investigate the resulting severity of pre-corrosion. The gauge length region of failed specimens were sectioned using a water-cooled Struers cut-off grinder and mounted in Bakelite using a hydraulic press. A water-cooled grinding process using grit 220 - 1200 μm was applied with a speed of 300 rpm followed by a polishing procedure using a 3 μm diamond pad and an alcohol lubricant and lastly a 0.05 μm colloidal silica pad to provide a mirror finish and prepare the specimen for optical microscopy examination. The four specimens examined in this way are shown in figure 2.23 with test details given in table 2.10.

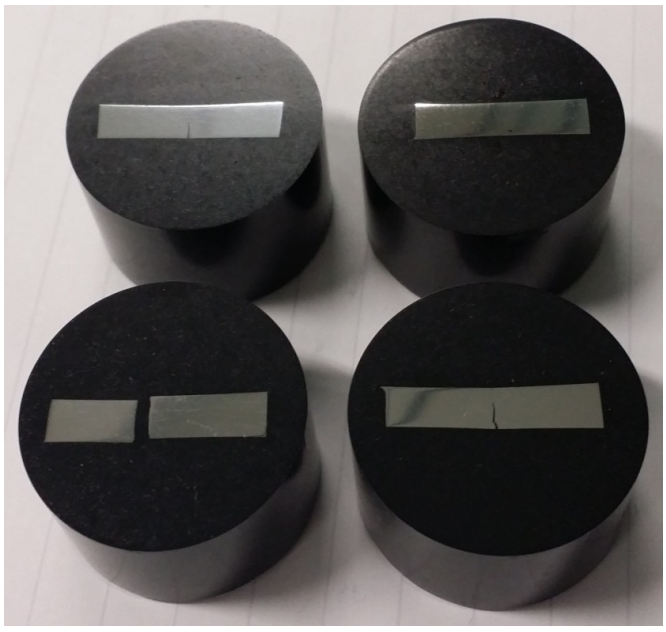

Figure 2.23: Corroded 4330 continuous radius fatigue specimens prepared for optical microscopy - Clockwise from top left: numbers 32, 49, 33 and 43.

The level of pitting resulting in the specimens varied, with the first pre-corrosion test, using the highest stress, resulting in the greatest level of pitting along with the initiation of fatigue cracks. Failure is most likely to have occurred at a region of pit formation followed by crack initiation and propagation. The fourth pre-corrosion test echoed that of the first, without reaching failure, and it was this method that was then implemented for the remaining twelve specimens to be tested on the uni-axial machine. Inspecting surface roughness values showed a significant increase through the pre-corrosion process, with an average increase in R_a and R_y of 83% and 84% respectively and a maximum increase in R_y of 196% in one specimen.

Pre-corrosion run no.	Specimen no.	% σ_y	σ (Pa)	Cycles	Duration (mins)	R.R. Moore speed (Hz)	Result
Test 1	43	62.70	5.55E+08	30020	90	5	Failed
Test 2	32	46.31	4.10E+08	51031	330	2.58	Failed
Test 3	33	48.84	4.32E+08	57456	720	1.33	Failed
Test 4	49	62.70	5.55E+08	22502	73	5	Intact
1	28	62.70	5.55E+08	22538	75	5	Intact
2	24	62.70	5.55E+08	22500	75	5	Intact
3	10	62.70	5.55E+08	22500	74	5	Intact
4	9	62.70	5.55E+08	22541	75	5	Intact
5	17	62.70	5.55E+08	22500	75	5	Intact
6	11	62.70	5.55E+08	22501	73	5	Intact
7	31	62.70	5.55E+08	22506	75	5	Intact
8	1	62.70	5.55E+08	22501	75	5	Intact
9	46	62.70	5.55E+08	22505	74	5	Intact
10	34	62.70	5.55E+08	22516	75	5	Intact
11	37	62.70	5.55E+08	22511	75	5	Intact
12	27	62.70	5.55E+08	22499	75	5	Intact

Table 2.10: Pre-corrosion data for 4330 continuous radius fatigue specimens

Evidence of the pitting and cracking occurring in the fourth pre-corrosion test is shown in figures 2.24-2.27. Despite the short duration of pre-corrosion, pitting was achieved along with the emanation of cracks from the base of pits. The majority of pits were observed to be wide, shallow pits with depths of approximately 20-30 μm, although subsurface, undercutting and narrow, deep pits were also present. Crack initiation is shown to occur during corrosion fatigue in high strength steels at pits depths of 30-60 μm (81) and therefore cracks were expected in these corroded specimens. Non-destructive evaluation of the cracking could not be obtained, however from the section obtained it was shown that minimum crack lengths were in the region of 300 μm. Oxidation in the cracks further proved the success of the corrosion method in penetrating through the material. Locally, oxidation will likely alter the residual stresses due to the modification of material volume and properties in this region. If the alteration of the stresses results in a tensile residual stress then this could facilitate crack propagation even when the specimen is subjected to a compressive mean stress. The depth of compressive residual stresses must be analysed with a view of the depth of corrosion pitting and cracking to effectively draw conclusions as to the beneficial nature of a compressive residual stress both locally and generally in a component.

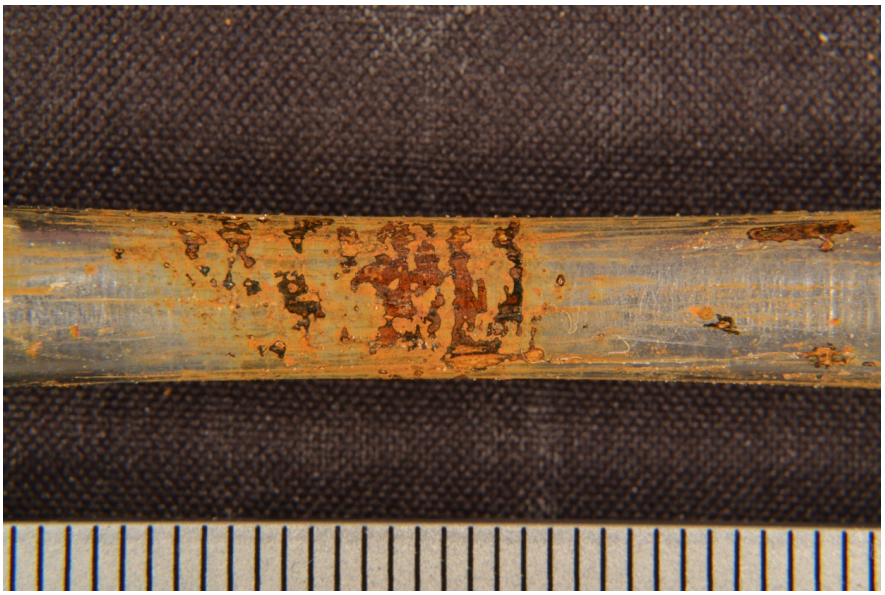

Figure 2.24: Corrosion visible on 4330 continuous radius fatigue specimen - Magnification factor: x10. Specimen number: 49.

2.4.6 Capturing the interaction between corrosion and fatigue

Although the method of pre-corrosion achieved a satisfactory level of corrosion, it was desirable to capture the interaction between corrosion and fatigue in order to test the hypothesis that a significant compressive mean stress could prevent fatigue cracks

Figure 2.25: Numerous pits and cracks seen in 4330 continuous radius fatigue specimen - Magnification factor: x50. Specimen number: 49.

Figure 2.26: Various types of corrosion pits seen in 4330 continuous radius fatigue specimen - Magnification factor: x200. Specimen number: 49.

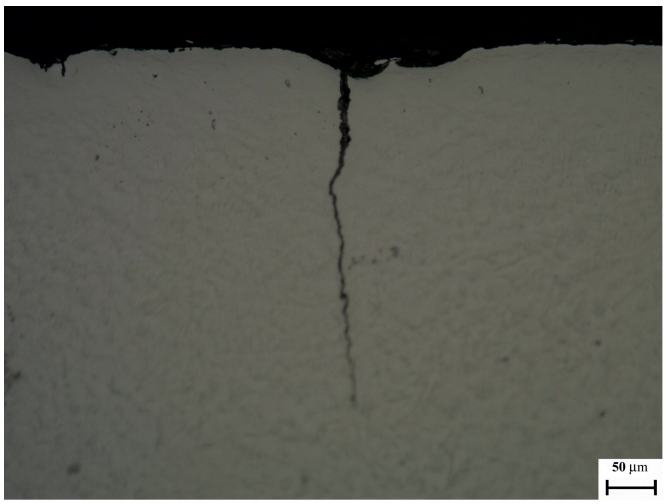

Figure 2.27: Fatigue crack initiating at corrosion pit seen in 4330 continuous radius fatigue specimen - Magnification factor: x200. Specimen number: 49.

developing for a corrosion pitted surface. This interaction is present in reality and therefore methods were sought to account for this during testing. The rig produced for use with the R.R Moore machine was not suitable as it is only capable of testing at a zero mean stress. Therefore the next stage of the experiment would utilise a vertical uni-axial fatigue testing machine to enable the generation of a compressive mean stress to simulate a high compressive residual stress. In creating a method of obtaining corrosion during testing, it was important to take into consideration that the machine must be protected from the corrosive fluid and therefore leakage must be avoided. The specimen must also still experience adequate oxygen levels. The specimen was fitted into a funnel and silicone sealant used to provide a fit between specimen and funnel and avoid leakage. Previous work has indicated the success of using a sponge soaked in saline solution to achieve the desired conditions in rotating bending tests (82). However, it is more difficult to maintain a dripping mechanism in a vertical test set-up and the option of spraying saline solution would require the design of a more complex corrosion chamber to avoid damage to the testing machine. Capillary matting is used successfully in home applications when water retention is required and therefore this material was soaked in the saline solution and fitted around the specimen inside the funnel as shown in figure 2.28. This provides a corrosive environment for the specimen whilst allowing oxygen exposure. The machine was also protected from potential damage through the corroding of the specimen using WD-40.

If further testing were to be conducted it would be recommended that a more complex corrosion chamber be manufactured to capture the dripping or spraying mechanism similar to that used for the R.R. Moore machine.

2.4.7 Fatigue testing

The Denison-Mayes $\pm$600 kN uni-axial testing machine with a maximum frequency of 5 Hz was used with the machining of adapters to prevent movement of the specimen when applying the compressive loading. Adapters were machined to fit the diameter of 9.3 mm with tolerance $\pm 0.01/0.03$ and therefore accuracy in the machined specimen dimensions was crucial as fitting the specimens into the adapters by mechanical means would risk damage and alteration of the residual stress state in the specimen.

Table 2.11 shows the final testing plan and figure 2.28 an example of the test set-up showing a specimen, the corrosion attachment and the adapters fitted into the testing machine. To achieve the necessary loading a frequency of 4.3 Hz was set providing a loading cycle of approximately 2.1-18.4 kN. A minimum yield stress therefore refers to 9% σ_y and a maximum yield stress to 74% σ_y.

Specimen	F_{min} (kN)	F_{max} (kN)	σ_m
46	2.13	18.4	Compressive
17	2.19	18.0	Compressive
9	2.23	18.3	Tensile
37	2.21	18.2	Tensile

Table 2.11: 4330 continuous radius specimen fatigue testing plan

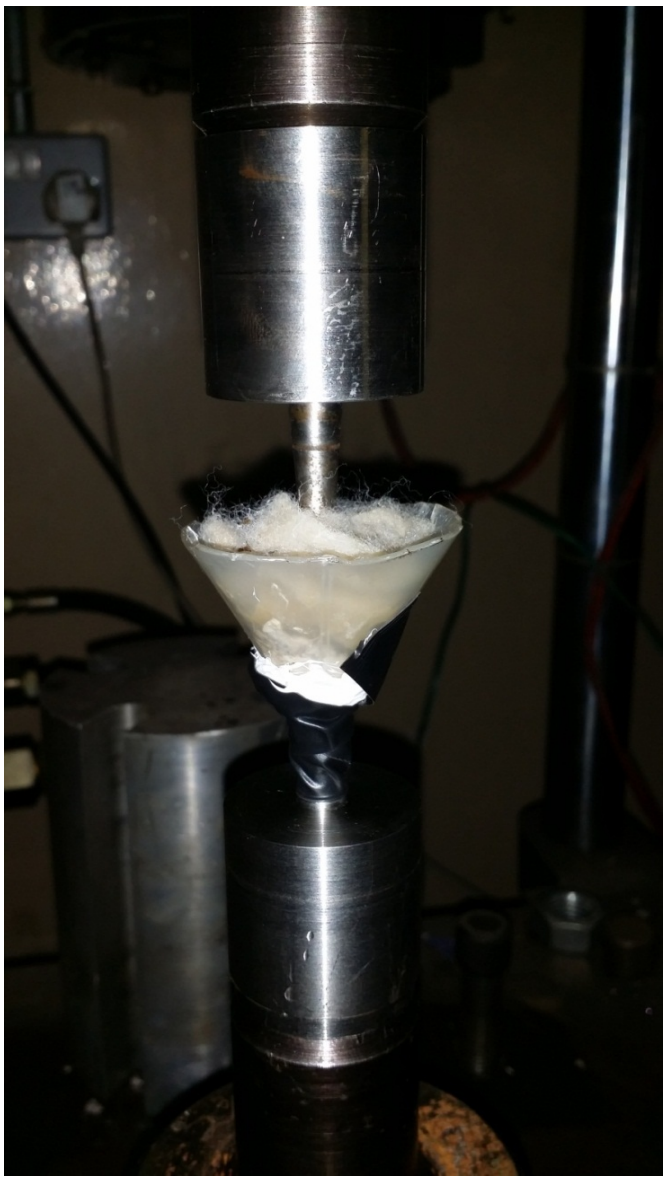

Figure 2.28: 4330 continuous radius specimen in Denison-Mayes servo-hydraulic universal testing machine - Corrosion attachment and adapters also shown in image.

No.	Pre-corroded	σ_m	σ_R (% σ_y)	Corrosion rig	Cycles	Duration	Result
46	YES	-	9-74	YES	3,016,750	183.1 hrs	Run-off
37	YES	-	9-74	YES	2,164,003 +	129.1 hrs	Run-off
9	YES	+	9-74	NO	2582	4.3 mins	Failure in centre
1	YES	+	9-74	NO	3044	5.1 mins	Failure in centre
8	NO	+	9-74	NO	1,000,000 +	27.8 hrs	Run-off

Table 2.12: 4330 continuous radius specimen uni-axial fatigue test results

The two tests subjecting pre-corroded specimens to a tensile mean stress were carried out on a 250 kN servo-hydraulic machine with loads equivalent to those used on the 600 kN machine. The maximum frequency of the machine was 10 Hz and the specimens failed after 4.3 and 5.1 minutes. Therefore the corrosion attachment was not fitted during these tests. A final uncorroded specimen was also tested on this machine using the same stress range to compare with corroded specimen results.

Results of the uni-axial fatigue tests are shown in table 2.12. A compressive mean stress is denoted - while a tensile mean stress is denoted +.

The average number of cycles achieved when pre-corroded specimens were subjected to a tensile mean stress emphasises the success of the corrosion method, especially when comparing this with the uncorroded specimen subjected to a tensile mean stress for which the test was halted at 10^6 cycles. In this case the applied tensile stress range did not cause stresses large enough for crack initiation, propagation or failure to occur in the duration of the test. Pit formation and crack propagation during the corrosion process resulted in the presence of damage and accumulating this with crack propagation occurring through the application of a tensile load would encourage accelerated failure. For this reason it was expected that corroding during testing would make little difference to the overall result, the duration of the tests indicating further that the interaction between corrosion and fatigue during testing was not necessarily required to provide accelerated failure.

Contrary to early methods of pre-corrosion, testing presented in this section captured the interaction between corrosion and fatigue through the use of the corrosion attachment. The two specimens subjected to a compressive mean stress demonstrated the inability for cracks to propagate as the crack faces were not encouraged to open during the test and therefore the beneficial effects of a compressive mean stress on corrosion fatigue performance of 4330 low alloy carbon steel.

2.5 Summary

Specimens of 4330 low alloy carbon steel were successfully pre-corroded through dripping a 5% $NaCl$ solution onto the specimens subjected to bending fatigue in an R.R. Moore rotating beam bending fatigue testing machine. Pit depths were found to increase with increased stress levels and the corrosion procedure was successful in producing not only corrosion pitting but also fatigue crack initiation at the base of pits.

Results have shown the detrimental effects of corrosion on the fatigue life of 4330 low alloy carbon steel when subjecting the material to a tensile mean stress. Pre-corroded specimens tested under a tensile mean stress failed after an average of 2813 cycles. On the other hand, the application of a compressive mean stress indicated beneficial effects on the fatigue performance of corroded 4330 low alloy carbon steel. Pre-corroded specimens tested under a compressive mean stress for 3,016,750 and 2,164,003 cycles respectively did not fail. Therefore, the presence of compressive residual stresses at the surface of a component, if of a large enough magnitude to ensure that the entire cycle during fatigue remains in the region of compression, eliminates the negative effects of corrosion on the fatigue performance of the material. The depth of compressive residual stresses should be greater than the depths of corrosion pitting to avoid the presence of tensile residual stresses at crack tip locations, which would in turn facilitate crack propagation and fatigue failure regardless of the presence of a compressive residual stress.

Improved corrosion could be achieved through modifying the corrosion process, introducing aspects such as corroding at high temperatures or utilising acids in the corrosive fluid. Alternative methods of producing corrosion could also be investigated, such as the use of spark erosion to create pitting (83). A larger number of specimens should be tested if further studies were to be undertaken, a minimum of three for each data point is suggested, allowing the investigation of differing stress ranges and the effects of lower test frequencies on the interaction between corrosion and fatigue. Development of the corrosion attachment for axial fatigue testing is recommended, utilising a spraying method and ensuring the protection of the machine from corrosion, primarily the machine grips. Post-testing, destructive testing could be used to assess crack propagation in corroded specimens that did not experience failure under a compressive mean stress. This should then be compared with the levels of crack initiation and propagation observed in corroded specimens prior to fatigue testing. In the future, in line with the main aim of this project, corrosion fatigue testing of clad specimens would also be desirable.

The findings of these studies prove the mileage in developing cost-effective methods of achieving high compressive residual stresses at the surface of a component to as great a depth as possible to improve the fatigue performance of the material in corrosive environments.

Ultimately, inducing surface compressive residual stresses to a significant depth in non-clad components manufactured from a corrosive material has demonstrated the ability to drastically reduce the detrimental effect of corrosion on fatigue life therefore proving the hypothesis presented herein.

Chapter 3

Weld Cladding of Low Alloy Carbon Steel

Residual stress effects on dissimilar joints are discussed in this chapter to allow an insight into considerations when moving from a component consisting of a single material to a combination of materials. This results in a dissimilarity in materials and therefore properties, in turn affecting residual stresses and ultimately fatigue performance. A concept of using a cladding or a coating process to deposit material onto an 4330 low alloy carbon steel to improve the fatigue performance forms the basis for this research. Several coating and cladding processes were reviewed, with a particular interest in the resulting residual stresses and the erosion and corrosion performance of the resulting coating/cladding. Naturally factors such as deposition methods, required equipment, ease of deposition, material selection and cost were also considered. The weld cladding process was identified as a key method of interest. Weld overlay cladding of two materials, Inconel 625 and 17-4 PH stainless steel, onto a 4330 low alloy carbon steel substrate was undertaken. A short discussion on the material selection process indicates the reasons and benefits of the choice of clad materials. Weld cladding process considerations are highlighted to ensure a clad of acceptable quality and fitness for purpose. The effects of geometry, pre-heat temperature and post-weld stress relief were also of interest and measures were taken to ensure these aspects could be investigated.

3.1 Introduction

The proven beneficial effects of compressive residual stresses on the corrosion fatigue performance of 4330 low alloy carbon steel (77) led to the desire to induce these stresses in the surface of a component which would be subjected to cyclic loading in an erosive and corrosive environment. As discussed in the introductory chapter, there are many methods of inducing compressive residual stresses. Processes such as machining and welding however typically induce damaging tensile residual stresses, through which stresses in the region of yield can result. Compressive residual stresses of 800 MPa have been reported in thermal barrier coatings at the interface (4). Danger also lies in welding processes due to the potential to shorten or by-pass the crack initiation stage and alter the material properties of the substrate. For this reason an in-depth understanding of the effects of welding processes on the residual stress state, material properties and fatigue performance of a component is required. This is the basis of this research: the development and validation of a fatigue-resistant cladding technology. In the early stages of the research, coating technologies were also of interest and therefore these will also be examined in the course of this chapter.

It can be said that coatings and claddings are effectively dissimilar joints in terms of residual stress states as the process of creating the material substrate and coating/cladding combination results in residual stresses throughout the component due to the thermal process, of which most importance are those stresses at the surface and interface. However, some coating and cladding processes do not entail such a thermal process, such as high-velocity oxy-fuel (*HVOF*) coatings which acts in more of a peening manner inducing compressive residual stresses at the surface due to this action. Severe discontinuity stresses and areas of stress concentration can arise at the interface of the two dissimilar materials, potentially damaging the performance of the coating/cladding material. The causes of residual stresses have been discussed previously, alongside their characteristics and influence on failure mechanisms. Methods of influencing residual stresses have been introduced, with the focus now on cladding and coating methods in particular. Cladding and coating processes will be discussed and the residual stress distributions arising through these processes reviewed and assessed with regards to fatigue performance.

In seeking to improve corrosion resistance, it is often the case that residual stresses arising through these protective measures are not considered heavily, especially in the sense of maximising a compressive residual stress with a view of increasing fatigue life. Given the extremely detrimental effect of corrosion pitting on fatigue life it may be that measures to improve corrosion resistance alone would be sufficient, regardless of the resulting residual stress state. However, it is believed that in harnessing the benefits of compressive residual stresses, while also potentially improving erosion

and corrosion resistance provides an all-encompassing solution for the performance of components in erosive and corrosion environments subjected to cyclic loading.

If compressive residual stresses are present in the component then even if erosion and corrosion are occurring, the benefits of a compressive residual stress layer will delay the negative effects experienced due to these mechanisms.

3.2 Effects of dissimilar joints on residual stresses

The nature of resulting residual stresses is dependent on the component state pre-, during and post-process. Figure 3.1 illustrates key influences in resulting residual stresses in thermal spray coatings. These factors are applicable in a general sense to cladding and joining processes. The suggestion is made that the ratio of coefficient of thermal expansion (CTE) is a dominant factor (84). As will be discussed later in this thesis, metallurgical effects on residual stresses are also of great importance and therefore related factors such as the cooling rate for example is especially important in terms of precipitate formation and phase transformation in martensitic materials.

The nature of residual stresses due to the weld cladding process are dependent on the thermal mechanisms and the degree of material dissimilarity. Residual stresses generated through welding arise due to two main mechanisms: poor joint alignment and structural mismatch or uneven distribution of non-elastic mechanical and thermal strains (14). Factors such as manufacturing processes, material properties, component geometry, external fixtures, welding procedures, post-weld heat treatments and applied service loading will influence the residual stress state of a component. Investigation of residual stresses in the three orthogonal directions is also essential as potential variations with respect to the weld can in turn affect the constraint on thermal expansion (85). However this is generally of greater concern in the case of joining materials as opposed to cladding or coating processes, though stress generation and potential shrinkage between welding passes would require this to be verified.

Cladding, buttering and post-weld heat treatment were investigated in dissimilar metal welded pipes, concluding that yield strength in the cladding zone will heavily impact the level of residual stress present at the inside surface of the pipe, however the outside surface is generally unaffected by the yield strength of the cladding zone (86). In considering residual stresses throughout a component it should always be borne in mind that the self-equilibrating nature of residual stresses will also affect the variation in residual stresses. If residual stresses are heavily influenced in one region, the requirement for self-equilibration will dictate the consequent effect of residual stresses elsewhere. The component geometry will also have an impact, for example residual stress distributions varying in thick and thin pipes.

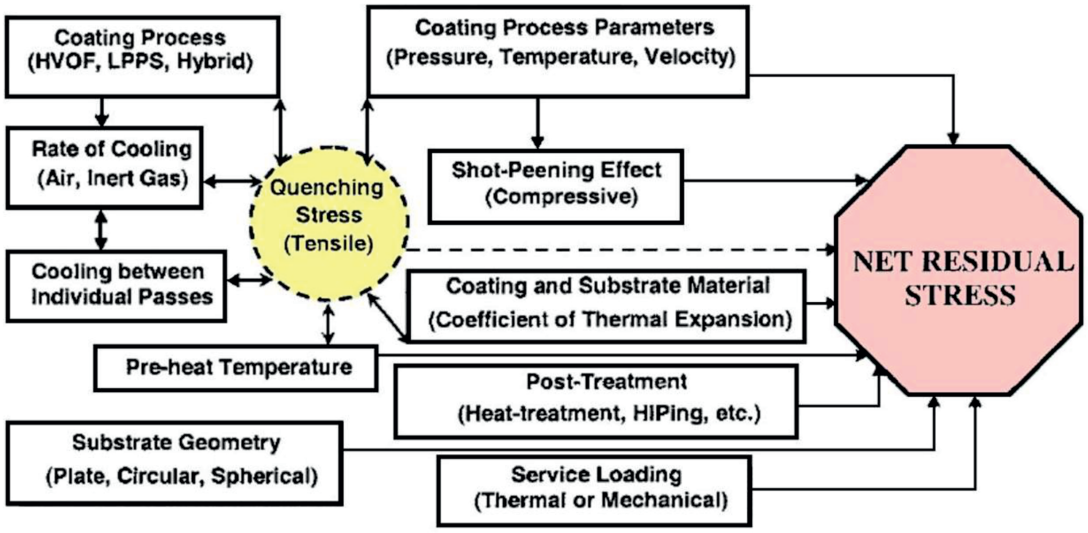

Figure 3.1: Influential factors in residual stress generation due to thermal spray coating processes - Modified from (84).

Residual stresses in dissimilar ferritic and austenitic steel pipe joints were investigated, along with the effect of a buttering layer of Inconel 82. These studies concluded that the buttering layer was effective in reducing heat-affected zone (HAZ) residual stresses, in turn decreasing failure potential due to the residual stresses present in these welded joints (87). Material surrounding the weld or coating will experience an increase in temperature during the welding or coating process. This region is known as the heat-affected zone, HAZ, and material in this region will undergo microstructural and material property changes.

3.3 Residual stress effects on failure mechanisms in coatings and claddings

The interface between the clad/coating material and the substrate is a key area of interest due to the potential for high discontinuity stresses in this region, which can affect performance of a component in operation and failure mechanisms. Numerous studies have shown that often, there is a transition from high tensile residual stresses in the clad layer or coating to compressive residual stresses in the substrate. This has been investigated with respect to various residual stress measurement techniques on clad steel and it was found that although the magnitude and transition may vary, the overall nature of tensile to compressive transformation can be identified using the measurement techniques of neutron diffraction, ring-core and deep-hole measurements (88). This study also highlights the difficulties in simulating residual stress

distribution mainly due to the inability to easily capture the change in material properties.

An interfacial crack present can either penetrate or deflect depending on material fracture energies and energy release rates (89). Residual stresses play a large part in energy release rates due to thermal expansion ratios of substrate and coating materials and have been found to be especially influential in the case of thin films and layered materials, affecting the quality of the interface.

Crack behaviour investigations using the Gurson micromechanical material model for austenitic cladding on a ferritic substrate concluded that crack penetration in the clad layer occurs with increasing load, however substrate crack extension is limited with good correlation between numerical analysis and experiment (90).

It is widely accepted that a high compressive mean stress will inhibit fatigue damage, although most fatigue test results generally relate to alternating loading or a tensile mean stress. A previous study by Saal noted in (59) found that crack propagation would only take place under a fully compressive stress cycle if a tensile residual stress field was present around the crack tip.

A study of the influence of compressive residual stresses in nano nitride composite coating of steel illustrated that cracks initiating due to corrosion were suppressed at weak interfaces. This was due to the presence of compressive residual stresses and allowed structural integrity to be retained. Furthermore, defects already present were not worsened and therefore protected the substrate and the interface from corrosion damage (91).

Coating failure can of course occur regardless of the nature of the residual stress. It is commonly known that tensile residual stresses often cause fracture of the coating perpendicular to the interface, however compressive residual stresses can induce buckling upon exceeding a critical stress, which can then lead to spalling (92). The spallation of thermal spray coatings is confirmed in an investigation of tungsten carbide coatings for jet engine applications (93) and hence the criterion should be that the coating possesses adequate compressive residual stresses without inducing spallation while maintaining crack resistance.

In thermal barrier coatings, which are thick, durable, insulating materials capable of withstanding high thermal gradients, compressive residual stresses are in fact the reason for failure. This is due to the increasing influence of defects in the vicinity of the interface connected with the thermal oxide layer (94). Crack initiation in zirconia-based multilayer thermal barrier coatings is described as being due to stress relaxation of the coating surface, with compressive residual stresses transforming to tensile residual stresses as the coating cools (95). Using mullite however, stresses remain in compression reducing the chance of crack initiation.

The effect of residual stresses in cracking of steel is discussed in (96) concluding that the formation of cracks will only occur at the bottom of a pit in areas of tensile residual stress. The stress levels for cracks are required to be moderate at the surface with little reduction with depth, while pitting occurs in areas with the highest surface tensile residual stresses. However residual stresses can also transform active cracks into dormant cracks when there is a change in stresses from high tensile to low tensile or even compressive stresses.

Two methods of stress corrosion cracking resistance investigated, namely *anti-welding heat treatment* and *explosion treatment*, both induce compressive residual stresses. Explosion treatment uses an explosive deformation energy and anti-welding heat treatment induces a negative temperature field to relieve stresses and induce compressive residual stresses. Using metal inert gas (MIG) welded SS400 steel it was found that both processes induced compressive residual stresses therefore preventing stress corrosion cracking and improving fatigue life (97). Stress corrosion cracking (SCC) is highlighted in (98) for its accompanying apparent unpredictability. The role of tensile residual stress in SCC is discussed.

Tungsten Inert Gas (TIG) 316L steel cladding of a portion of the inner wall of a 304 stainless pipe was presented as a means of preventing intergranular stress corrosion cracking (99). The pipe was welded to a thick carbon steel plate with an Inconel outer clad. The authors reported high tensile residual stresses on the 316L clad layer on the inner surface of the pipe.

Surface finish can affect component integrity, which can be quantified through surface resistance to pitting and stress corrosion cracking. Studies have been carried out on steel surfaces to investigate the effect of sand blasting and wire brushing which through inducing compressive residual stresses benefit fatigue life (100). Wire brushing is often used as a cleaning technique, the wires of the circular brush in this study being rotated at speeds between 280 and 900 rpm. In the case of coatings, this is of concern primarily at the interface between coating and substrate. Unpolished surfaces subjected to sand blasting and wire brushing were found to generate compressive residual stresses of -175 MPa and -125 MPa respectively, these maximum values being present at the component surface. High-velocity oxy-fuel ($HVOF$) sprayed components can be sand-blasted prior to $HVOF$ spraying acting as a surface preparation technique (101).

Stress corrosion cracking was studied using tensile test specimens fabricated with various levels of compressive and tensile surface residual stresses exposed to a neutral pH aqueous soil environment in combination with an applied cyclic stress (102). The formation of micro-pitting was found to occur preferentially in areas where the tensile residual stresses were the highest at around 300 MPa, while SCC initiation

occurred in areas where the surface residual stress was in the range 150-200 MPa. $HVOF$ coatings are at risk of crack initiation at the coating surface due to the formation of a brittle structure attributed to oxidation, while failure can also occur at the interface between coating and substrate due to plastic strains arising from the differential mechanical properties. This was shown to be the case through three-point bend tests of an Inconel 625 $HVOF$ coating deposited onto a mild steel substrate (103), where coating failure occurred not only due to the brittle oxide areas but also due to the high discontinuity of stresses at the interface exceeding yield. Increased bending caused crack growth and deformation as part of a multi-cracking process.

Studies of tungsten carbide cobalt chromium $WCCoCr$ $HVOF$ coatings found that a thinner coating provided increased corrosion resistance whereas low adhesion was reported in thicker coating samples (104).

The ability of fixtures to influence residual stress states is noted in a study aiming to develop a fixture which would not cause a clamping load. This included the examination of $WCCo$ coatings and showed that increasing the coating thickness led to a transformation from tensile to compressive surface residual stress, with a stress-free state determined at a thickness of 365 μm (105).

Erosion resistance studies of $WCCo$ thermal spray coatings highlighted that thermal spray processes generally require both high material temperature and high velocity of particles to ensure high levels of adhesion (106).

Cracked clad ferritic steel specimens showed that brittle failure in the HAZ of the substrate is of greater concern than ductile failure consisting of crack formation and growth within the clad layer. The cladding remained intact while cracks propagated in the substrate material, further confirmed by numerical simulations showing cladding failure as being secondary to substrate brittle failure (107). Failure occurring primarily in the HAZ was also reported while investigating ferritic and austenitic steel dissimilar pipe joints (87). Simulation models have also been used to investigate failure mechanisms during welding and heat treatment processes (108).

Welding residual stresses examined using finite element simulation of a gas-shielded arc weld joint of HQ130 grade high strength steel reported high discontinuity stresses at the fusion boundary which may require adjustment of the welding procedure to prevent cracking at the interface (109).

3.4 Altering residual stresses arising due to dissimilar joints

Effects on material properties must be investigated to ensure that components subjected to joining processes adhere to any required standards. In the oil and gas

industry, for example, there are certain requirements on hardness values of the substrate and weld material post-welding (110). If these requirements are not met, then post-weld treatments must be considered. Post-weld heat treatment can be utilised as a measure to decrease hardness in the HAZ. Tempering can successfully decrease hardness in the HAZ while maintaining corrosion resistance of the clad material. Utilising a thermal stress relief process is however not always successful in the case of dissimilar joints due to the dissimilarity of the materials used. This will be discussed in section 4.2 with a focus on the effects on metallurgy and section 6.4 focussing on the effects on residual stresses.

3.5 Coating processes

Many coating processes have a degree of similarity in that they are applied in the form of molten material using a spraying process with thermal input from an electric arc or an oxy-fuel combustion. Process parameter selection is key to achieving the desired coating quality. The coating can be applied at different temperatures and velocities as required and this along with the desired coating thickness and material properties will often govern the choice of process. Generally coating thicknesses are in the region of hundreds of micrometres and processes are restricted in their application to complex geometries due to their line-of-sight nature. Developments allow coating in some cases at angles or coating of internal surfaces, however spray gun sizes do impose limitations in these cases. The powder used in these processes can be manufactured by various means with chemical variations and particle sizes altering the characteristics of the powder and in turn the deposited coating. Post-deposition machining or grinding, using diamond grinding for example, is generally required to remove the rough surface finish and prepare the component for service.

3.5.1 High-velocity oxy-fuel

High-velocity oxy-fuel ($HVOF$) coatings are the most common thermal spray coatings and although costly are generally considered to provide the most superior quality for corrosion and wear resistance. A powder is used for the coating material in the $HVOF$ process with a gas flame accelerating the powder to impact the substrate with high kinetic energy. The high-velocity gas is created through a mixture of fuel and oxygen in a combustion chamber prior to passing through a nozzle. Through this a coating with low porosity, high density and good adhesion is formed, adhesion also facilitated by the grit blasting process the substrate experiences prior to coating. Robotic control, portability and a variety of spray guns are available to cater for the

specific component requirements. Coating materials include metals, alloys and cermets and the fuel can be of gas or liquid form such as propane, propylene, kerosene and hydrogen.

Poor bond quality can be a major disadvantage of the $HVOF$ process as the coating does not bond metallurgically but remains as a surface coating due to the softening of the particles upon acceleration towards the substrate. Therefore component application must be considered to assess the suitability of this method and those resulting in similar adhesion. It may be that processes such as weld cladding are more suitable where adhesion is essential.

Typical coatings utilised for their resistance to wear mechanisms are tungsten carbide-based cermets, chromium carbide-based cermets, nickel chromium boron silicium alloys and cobalt-based alloys. The latter are most often used for corrosive wear resistance in the form of Stellite, most notably Stellite 6, Ultimet and Tribaloy alloys. Modification of the composition of these alloys can achieve particular requirements. For example, traditionally Stellite 6 is utilised in the cobalt chromium tungsten form, however substituting molybdenum for tungsten giving Stellite 706 yields a composition with improved erosion and erosion-corrosion resistance due to secondary carbide formation (111). Tungsten carbide (WC) coatings are commonly added to using cobalt or chromium to increase corrosion and wear resistance. The distribution of chromium between carbides can result in beneficial wear resistance while chromium distribution within the metallic matrix can result in corrosion resistance. The benefits of chromium and cobalt in providing slurry erosion resistance are highlighted in the results of erosion-corrosion testing of tungsten carbide hard metals subjected to erosion-corrosion testing in a silica-water slurry, with cobalt and nickel binders alone performing poorly in comparison with tungsten carbide nickel chromium cobalt and nickel chromium grades, the addition of chromium increasing corrosion resistance (112). Nickel chromium boron silicon grade cermets are favoured due to their low melting temperature as well as post-coating fusion process options to decrease porosity. From this point of view, $WCNi/Cr/Si/B/C$ coatings may be more advantageous than $WCCo$-base coatings. Vacuum-fusion was shown to improve erosion-corrosion resistance with a significant decrease in material loss in austenitic stainless steel $HVOF$ coated with $NiCrMoSiB$ under liquid and solid-liquid impingement conditions in saline water (113).

Post-coating may be necessary to seal the coating, for example through a polymer-resin sealing treatment or laser surface remelting, to prepare for operation in a corrosive environment due to porosity. Although this may benefit porosity levels at the surface of the component, depth penetration is less effective. Laser surface remelting of Inconel 625 $HVOF$ coatings illustrated the elimination of porosity (114).

When combining laser treatment with *HVOF* for tungsten carbide cobalt chromium (*WCCoCr*) coatings, care must be taken to ensure low irradiance to provide a uniform microstructure, low porosity and increased hardness (115)

In producing *HVOF* coatings, corrosion effects must be considered. Due to the bimetallic nature of the coating and substrate combination, there are risks of corrosion at the interface if the interface is porous. However, if appropriately applied the coating should provide protection to the substrate and thus the main concern is the corrosion resistance of the material utilised for the coating. Cermet coatings suffer from metal binder attack due to microstructural inhomogeneities which in turn results in low corrosion resistance. Galvanic corrosion was shown to be the cause for performance differences in bulk and *HVOF* sprayed coatings (114).

Application of *HVOF* coatings for the aerospace industry has been investigated with the issue of spalling highlighted in *WC*-based coatings under high cyclic loading (116).

Lee et al. found that the highest fracture toughness of *WCCoCr HVOF* coatings on a steel substrate resulted when a small fraction of coarse powder was mixed with fine powder, wear resistance also being of the highest value in this case. This was due to the low level of porosity resulting through this method (117).

Regardless of these issues, the fact remains that corrosion resistance offered by these coatings is greater than than of uncoated materials. Clearly the thickness of the coating and the metal binder used will determine the protection offered by the coating.

Fatigue life of Inconel 625 *HVOF* coatings on carbon and stainless steel was greater than that of carbon steel coated components when corroded in an aqueous solution for specific periods of time prior to fatigue testing (101). Residual stresses arising in the coating will be due to a combination of the micro-stresses due to the quenching effect, the stresses arising from the splatting effect of the sprayed particles (which also enhances the surface hardness) and also the macro-stresses resulting from the differing material properties. The effect of hot isostatic pressing as a form of post-treatment of an *HVOF* sprayed cermet (*WCCo*) coating showed that this increased the hardness, modulus, adhesion and cohesion of the coating while also decreasing the sharp stress discontinuity at the coating-substrate interface (84). The *WC* content has been shown to affect both the mechanical properties, temperature gradient and the level of residual stress (118), (119).

High-velocity air-fuel (*HVAF*), a variation of *HVOF*, utilises compressed air as suggested in place of oxygen. The advantages of this over the *HVOF* process are lower costs and deposition temperatures. Detonation gun spraying is also similar to the

HVOF process, however uses shock waves or deformation induced through spark-plugs to deposit a powder onto the substrate at lower velocities but higher temperatures.

3.5.2 Plasma transferred arc

A plasma created using a high-voltage electric arc can be used to melt a powder substance in preparation for deposition using a nozzle. This is known as the plasma transferred arc (*PTA*) process. The plasma can be created by a pilot arc between a tungsten cathode and a copper anode followed by an arc between the cathode and the component. This process uses a higher temperature than *HVOF* but a lower velocity. Three gases: the plasma gas, most often argon, carrier gas, containing the powder, and shielding gases are used in the deposition process. The resulting coating is dependent on parameters such as the powder feed rate and travel speed and the arc current and voltage. The stand-off distances and the gun sizes for the *PTA* process are less than those for the *HVOF* process, therefore presenting opportunities for complex geometries, particularly coating of internal surfaces. A study of the potential for plasma spraying of internal surfaces presented the possibility of miniaturised equipment, with the aim of the development of guns to allow coating of internal diameters of less than three inches, a gun identified as being able to coat inner diameters of 1.6 inches (120). Variations on the *PTA* process include atmospheric plasma spraying and vacuum plasma spraying.

The *PTA* process allows the deposition of not only metals but also ceramics and metal matrix composites, therefore providing potential for increased wear resistance. Metal matrix composites such as *WCNi* are often used. However, ceramics also present the issue of brittle cracking and the plasma spray process also has the disadvantage of high levels of porosity therefore questionable for use in a corrosive environment. This will ultimately decrease protection of the substrate, however low levels of dilution are obtainable using this process and therefore a single pass can provide a satisfactory coating. Plasma spraying of Inconel 718 onto a mild steel substrate resulted, however, in minimal porosity and good bond strength, with good slurry test performance in 3.5% *NaCl* solution (121).

Research into various alloys deposited using *PTA* on steel substrates focussed on erosion resistance, emphasising that no relationship was found between room temperature hardness and elevated temperature erosion resistance (122). Therefore materials required for high-temperature use should not be selected based on hardness values. There are various material properties often consulted when assessing material applicability. It should be ensured that correct procedures in material selection are undertaken.

The *PTA* process can also use materials which could not be used in a thermal spray process, such as oxides, due to the inability to melt them using *HVOF* for example. Due to metallurgical bonding through the *PTA* process, adhesion is less of a concern than with a thermal spray process. The high temperatures involved in *PTA* requires an in-depth knowledge of the consequent effects on coating material properties and composition to ensure that perceived material benefits are not lost in an attempt to attain a wear-resistant coating. The use of carbide-based cermet coatings, *WC* for example, results in carbide degradation upon high energy input and therefore high temperature presence, which decreases corrosion performance (123).

Hot isostatic pressing of plasma sprayed ceramic coatings was shown to be of benefit, with hardness values being retained and residual stresses reduced (124).

3.5.3 Thermal barrier coatings

Thermal barrier coatings (*TBC*), the material of which is as suggested thermally insulating, have four parts: a ceramic coating, a thermally grown oxide, forming and thickening with system cycling, a bond coat for oxidation resistance and a substrate. These coatings are deposited through either electron beam physical vapour deposition or air plasma spraying. *TBC*'s produce stress gradients through the coating thickness, an increase in substrate temperature transforming tensile residual stresses in a zirconia coating to compressive residual stresses. Furthermore thermal history was found to be a factor in the final residual stress state, with thermal cycling relieving stresses to an in-plane biaxial compressive stress state (125).

3.5.4 Physical vapour deposition

Physical vapour deposition (*PVD*) is a line-of-sight coating process that deposits a metal vapour using a cathodic arc source in a vacuum chamber at temperatures of 150-200°C. A depositing compound is formed due to the presence of a gas in the vacuum chamber, typically nitrogen, oxygen or a carbon containing gas. The substrate must be electrically conductive and the resulting thin coating, typically 2-5 μm, whether of a single or multi-pass system, has good adhesion qualities. However, due to the very thin coating layer, concerns naturally arise as to the appropriateness of this method in erosive and corrosive environments where components are subjected to cyclic loading.

The vapour can be produced in various ways, for example electron beam evaporation or resistance evaporation. An ion plasma is commonly used to target the material towards the substrate. Magnets can similarly be used.

Multi-layered coatings can provide low elastic modulus and high hardness properties, which results in deformation without cracking and a lower degree of de-adhesion.

The overall performance and quality of the coating can be assessed through investigation of the residual stress state. A brittle coating can arise if large residual stress magnitudes are present, presenting possible issues with delamination. If residual stresses are low, high levels of wear resistance can avoid cracking and material mechanical properties will be satisfactory.

PVD results in residual stresses due to various factors, both thermal and mechanical, such as the thermal expansion differential between coating and substrate. A high compressive residual stress arises in the coating which, case-dependent, can be in the region of 10-17 GPa (126). Due to the self-equilibrating nature of residual stresses, tensile residual stresses will be present elsewhere in the component.

3.5.5 Chemical vapour deposition

Chemical vapour deposition (CVD) relies on a chemical reaction to deposit the material onto the substrate, with the presence of gases in a reaction chamber. If a thermal means is to be utilised, much higher temperatures than PVD are required, in the region of 500-1000°C or greater. The thickness of coatings obtained through this process is similar to that of PVD. A plasma-assisted CVD process uses a plasma discharge to prompt the chemical reaction, therefore lowering the temperature required.

3.5.6 Diamond-like coatings

Diamond-like coatings (DLC) can be obtained using the PVD or CVD processes along with a gas containing carbon to coat metals and even rubber. Typical coating thicknesses can vary from as thick as 1-5μm and there are no line-of-sight limitations for this process. The amorphous (non-crystalline) nature of these coatings results in a non-brittle coating and allows for *metal doping*, the addition of elements into the coating. Material properties are dictated by the bonding present, diamond tetrahedral bonds aiming to be maximised for the highest performance, the resulting coatings known as tetrahedral amorphous carbon. On the other hand, the presence of a planar graphite structure decreases performance of the coating due to the impact on hardness. The presence of hydrogen can likewise decrease hardness, the presence of this being due to the gas utilised in the CVD process.

As with all coating processes, various parameters of the coating process will further impact the final coating quality and properties. Adhesion can be poor, and therefore a two-stage coating process can be utilised to introduce an intermediate layer to

grade the transition between the substrate and the coating material. This could be for example a PVD followed by a plasma-assisted CVD method, the first of a hard material layer such as chromium carbide, chromium nickel or silicon carbide, acting as the intermediate layer, followed by the DLC layer. Various forms of multi-layer methods are available to avoid adhesion issues, with the possibility of also utilising a specific adhesion layer.

3.5.7 Cold spray process

Unlike the previous processes which utilise high temperatures, the cold spray process uses a high velocity to deposit a solid-state coating avoiding the high tensile residual stresses induced by many coating processes. This removes the issues of thermal degradation and residual stress effects limiting coating thickness. A supersonic jet of compressed air is used to accelerate the coating in powder form through a nozzle to velocities in the range of 500-1500 m/s, the coating material remaining in a solid state to minimise oxidation. Coatings formed using this process are often in compression as opposed to tension. Post-spraying heat treatments can be required to increase the low ductility of the coating in the as-sprayed condition. Many materials can be used in the cold spray method. As mentioned previously, when high temperatures are involved, it is crucial to understand temperature effects on material properties and composition. Therefore the cold spray process is ideal for materials that are highly sensitive to temperature changes, where for example phase or grain structure changes cause notable changes in the material. It has been shown, for example, that cold spraying of $WCCo$ results in particle refinement with coating thicknesses in the range of 20-500 μm highlighted (127).

3.5.8 Infiltration brazing

Infiltration brazing uses a porous structure and a molten filler metal rolled into a cloth to be applied to a component which is then subjected to high-temperature, in excess of melting, vacuum-brazing to create a coating. The porous structure is a powder consisting of tungsten carbide particles, the resulting coating therefore containing fine WC particles. This thermal process results in metallurgical bonding with again limitations in applicability due to high-temperature effects on material properties. Standard $ASTM$ erosion, abrasion, and corrosion tests concluded that infiltration brazed tungsten carbide performed better than 1018 low carbon steel, chrome carbide weld overlay, 400 Brinnell heat-treated hard-plate and solid tungsten carbide (128).

3.5.9 Friction surfacing

A coating material can be rotated against a substrate under constant axial force to create a coating through the process known as friction surfacing. Localised heating occurs due to this process and therefore plastic deformation of the coating material. Metallurgical bonding occurs although this is a solid-state coating method. Again this removes issues with dilution levels and thermal degradation. Solid state bonding was shown to be excellent between austenitic stainless steel and a low carbon steel substrate due to discontinuous dynamic recrystallisation of the deposited material, improving corrosion and wear resistance (129).

3.5.10 Electroplated chromium

Commonly used chromium coatings can suffer from microcracking and therefore decreased corrosion resistance. A chromium electroplate paired with a sublayer of nickel can improve corrosion resistance by protecting the substrate. However, health and safety concerns require thorough consideration of the application of electroplated chromium.

3.6 Cladding processes

It is common practice to utilise a surfacing technique to deposit corrosion-resistant alloys onto substrate materials if premature degradation is of concern in erosive and corrosive environments. Arc welding has been utilised since its invention between 1939 and 1941, with conventional processes including submerged arc, gas metal arc and tungsten inert gas. Weld overlay cladding is the term used to describe the laying of corrosion resistant alloys using these methods. This process is popularly used in thick-walled vessels although components of thicknesses in the region of 30-50 mm can also be weld clad. In the case of thin components, heat sink removal will be required and potential distortion effects accounted for. These processes are continually developing to account for the requirements of industry to utilise new materials, adapt to more complex geometries and maintain a cost-effective result. Consideration must also be given to the process variables, as high heat input may initially seem beneficial, however effects on iron dilution, for example, may then require the laying of an additional layer, and thus the perceived benefit in shorter process times is in fact misleading.

The method of weld cladding was selected to test the hypothesis of the beneficial effects of compressive residual stresses on fatigue performance. This would provide

a means of reducing the use of expensive erosion and corrosion resistant materials, although would add an additional cost for the cladding process itself.

Weld cladding is widely used in industry, with great popularity in the oil and gas industry to improve the performance of components operating in an erosive-corrosive environment such as the geometry shown in figure 3.2. Using this process, relatively thick layers of corrosion-resistant alloys can be deposited. However, this is often not adopted with a view of maximising the benefits of the presence of compressive residual stresses. Through obtaining weld clad components, residual stresses arising through this process would be determined and the effects of cladding parameters investigated. Residual stresses arising at the surface of the component through the weld cladding process should ideally be compressive in nature, with as great a magnitude and to as large a depth as possible.

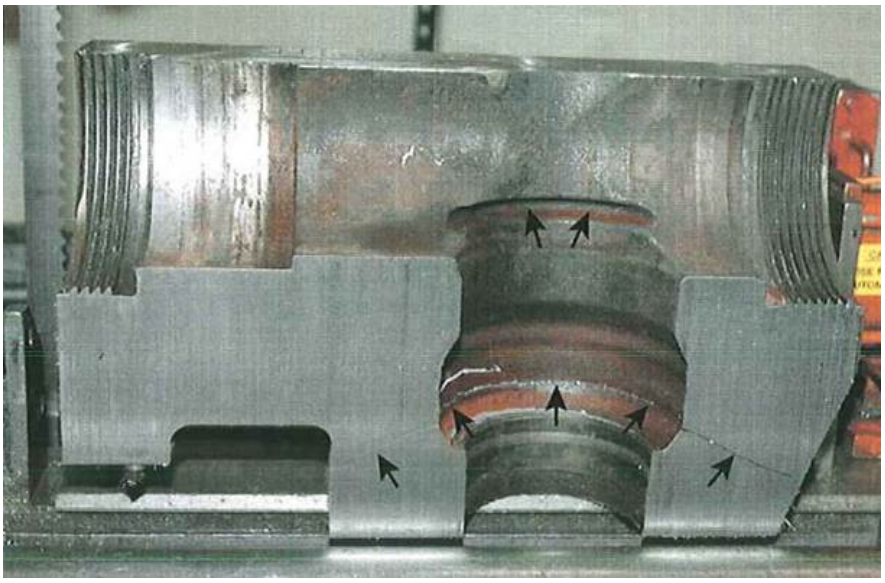

Figure 3.2: Example component geometry for weld cladding deposition - Photo courtesy of Weir SPM.

3.6.1 Weld overlay cladding

Weld overlay cladding can be achieved using hot wire Gas Tungsten Arc Welding (*GTAW*) to deposit a layer of clad material onto a substrate to create a bond between the two materials. Hot wire *GTAW*, or Tungsten Inert Gas (*TIG*) welding, is a development of conventional *GTAW* during which the melting of the filler wire, located at the leading edge of the weld pool, requires energy from the arc. This decreases the efficiency of the process and therefore in hot wire *GTAW* resistance heating of the filler wire to the region of melt prevents decrease in weld pool temperature when the filler metal is added to the weld pool behind the tungsten resulting in a smooth weld bead. As the energy from the welding arc is not required to heat the filler wire,

it can be utilised almost solely to penetrate the weld pool and generate fusion and therefore this process has a travel speed two to three times greater than conventional cold wire *GTAW* as shown in figure 3.3.

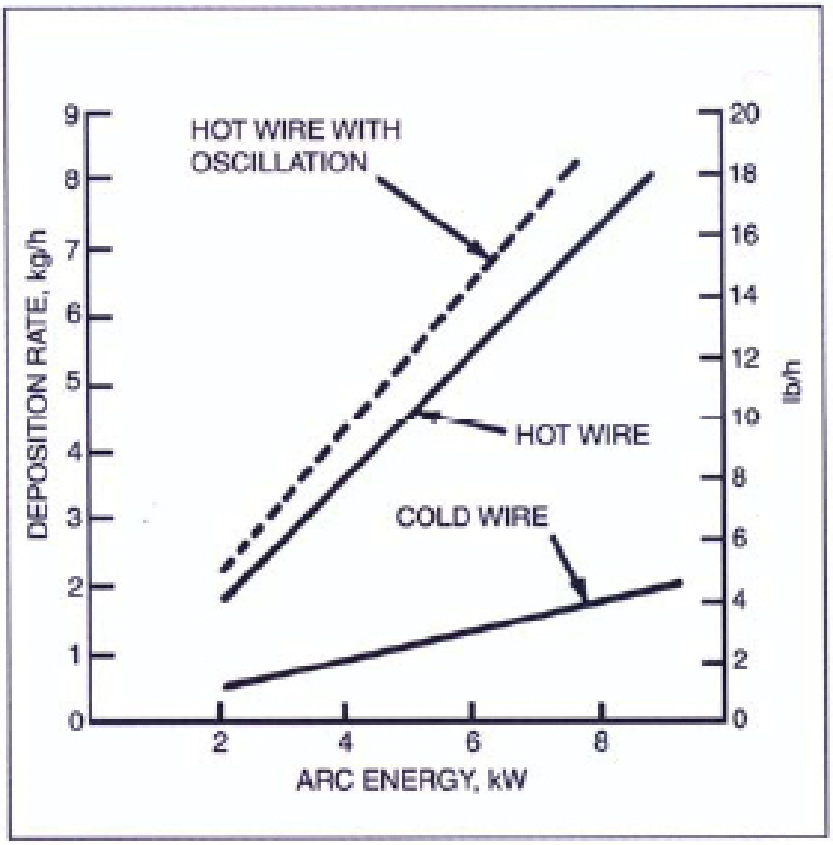

Figure 3.3: Comparison of deposition rates versus arc energy for cold and hot wire GTAW - Figure as provided in (130).

The required components for the hot wire *GTAW* process are shown in figure 3.4. The power source on the left provides a current to the *GTAW* torch to create the arc. The power supply on the right provides a current to a circuit from the contact tube, through which the wire is fed until it meets the weld pool. The wire is resistance heated through the power differential across the wire extension, the level of which depends on the length of wire protruding from the contact tube and the diameter of the wire (131). Figure 3.5 shows the equipment utilised in the weld cladding process.

Upon removal of the arc the two materials solidify and a bond is created. Contamination of the weld could result in decreased weld strength and this is prevented through the use of compressed inert gas, most often argon, which reaches the weld pool through a shroud surrounding the tungsten electrode (figure 3.6).

The capability of the technology to utilise digital data acquisition and multi-servo control allows unique torch configuration and therefore suitability for a wide range of geometries.

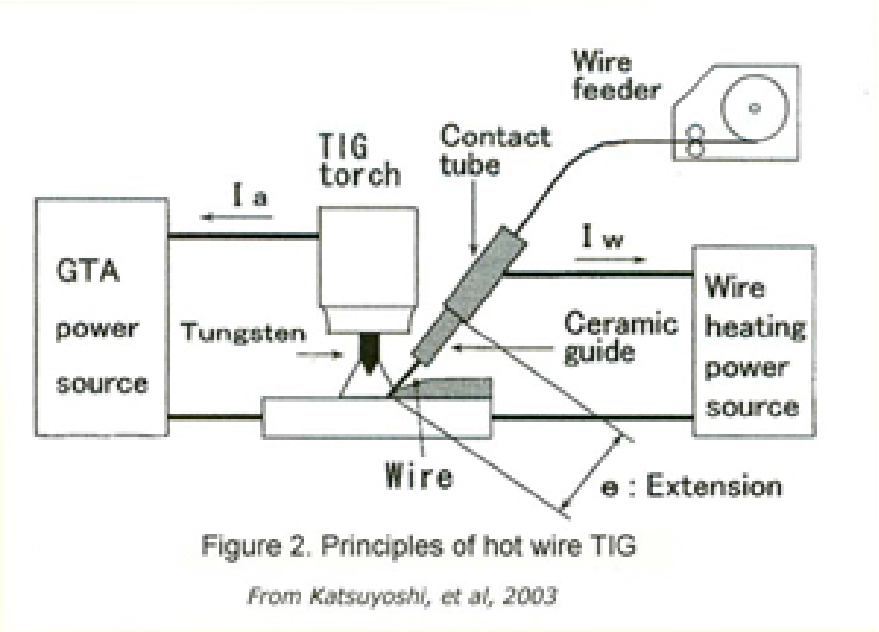

Figure 3.4: Hot wire TIG principles - Figure as provided in (132).

Using hot wire *GTAW*, as well as cold wire *GTAW* or pulsed Gas Metal Arc Welding (*GMAW*), enables positional welding and the ability to modify process variables to control dilution and therefore presents this as an attractive option.

3.6.2 Laser cladding

Laser cladding is an overlay process which uses a laser beam to melt a powder supply or a wire of the clad material onto the component surface. Although this process is more expensive than weld overlay cladding, lower heat input into the substrate and therefore a shallower *HAZ* results due to the increased heating and cooling rates facilitated by the laser. Many materials can be laid using laser cladding to increase corrosion resistance, such as steels and stainless steels, nickel-based alloys and cermets. Tungsten carbide (*WC*) is often used to provide wear and corrosion resistance. The materials that can be used are very similar to those that can be used in *HVOF* coatings, however, laser cladding provides greater layer thickness and improved metallurgical bonding in comparison with thermal spray coatings and therefore improved adhesion, critical in service loading. The application of the component must be considered to judge the appropriateness of the cladding material, as hard particles in cermets for example can perform poorly in impingement conditions, however would be appropriate in abrasive conditions.

The laser cladding process will be further discussed in chapter 8, where results of laser cladding will also be presented.

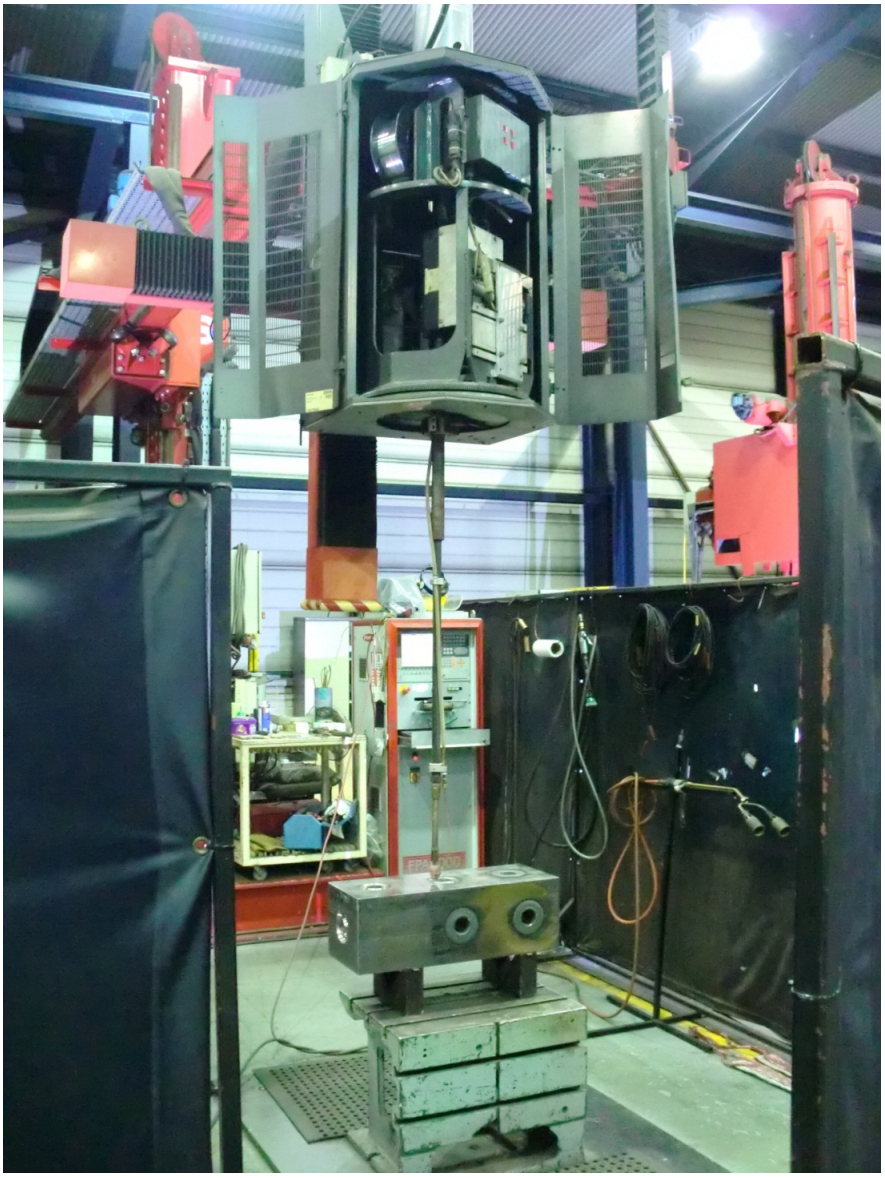

Figure 3.5: Hot wire GTAW equipment utilised - Weld cladding undertaken by IODS Pipeclad, East Kilbride.

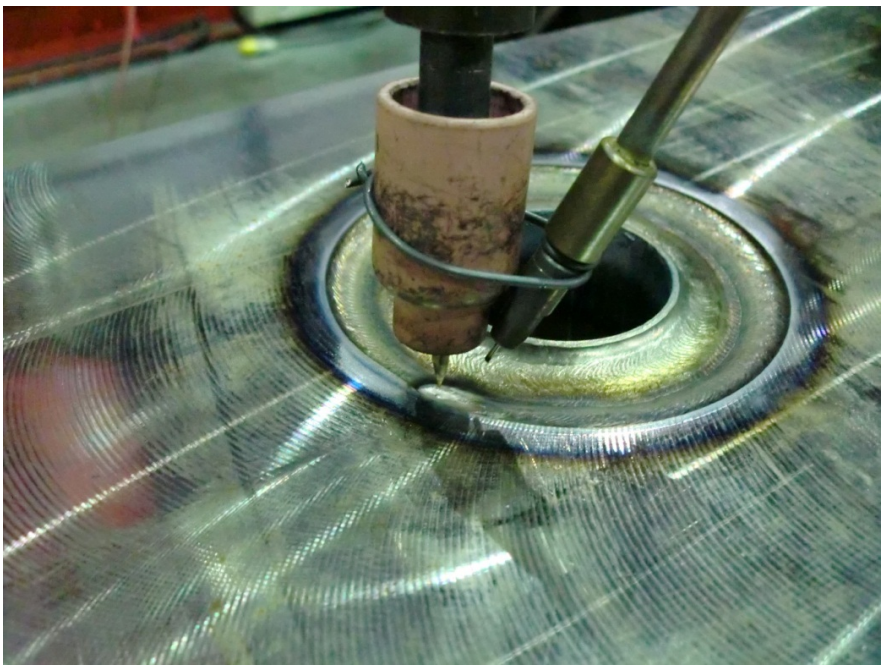

Figure 3.6: Tungsten electrode, shroud and filler wire of hot wire GTAW equipment utilised - Weld cladding undertaken by IODS Pipeclad, East Kilbride (133).

3.7 Weld overlay cladding of representative material and geometry

3.7.1 Material selection

In selecting the weld overlay cladding process, limitations are set on the materials with which this can be achieved. The weld material must have the ability to be drawn into a solid wire and coiled such that the material can be continuously fed into the welding head. Otherwise manual feeding of the wire could be considered and would allow a larger range of materials to be utilised, for example ceramics and cermets.

Additionally service conditions must be taken into account to ensure that materials will provide satisfactory performance in their application. In oil and gas applications, hydrogen sulfide (H_2S), dissolved carbon dioxide (CO_2) and chloride presence in fuels must be considered. At high temperatures, corrosive effects will dominate, whereas at high pressure, erosion will be of greater concern. In scenarios where erosion and corrosion will occur, component manufacture is especially critical. In this instance it must be assessed as to whether procedures such as coating or cladding provides adequate performance for the cost benefit, or whether a more beneficial solution would be to manufacture the entire component from a corrosion-resistant material. Corrosion-resistant alloys such as austenitic and ferritic/martensitic steels, duplex stainless steels and nickel chromium alloys provide the greatest protection in

corrosive environments. Stellite 6, a cobalt chromium tungsten carbide ($CoCrWC$) alloy is increasingly popular in weld overlay cladding due to its' resistance to wear and corrosion over a range of temperatures as a result of the large fraction of carbides present in the material. Effectiveness in resisting cavitation erosion, surface deterioration and material loss as a result of vapour generation inside a liquid flow, and galling, a form of adhesive wear between two sliding surfaces, further add to the benefits of using this material in corrosive and erosive environments, particularly in pump liners, shaft sleeves and valve trims.

For the present research, the greatest driver in material selection, and process selection, was to obtain a material combination which would induce compressive residual stresses through the weld cladding process, particularly at the surface, the location at which operational stresses are of the highest level.

Low alloy carbon steel The substrate material was chosen to be *AISI* (American Iron and Steel Institute) 4330 low alloy carbon steel, discussed and investigated in the previous chapter.

Nickel chromium-based superalloy Nickel-based alloys, as well as duplex steels, are unique in that the level of strength they possess when welded matches that of carbon steels. Material availability and process costs would result in difficulty in manufacturing entire components from these materials with the need also for specific welding procedures to harness these benefits. Using a carbon steel substrate on the other hand facilitates ease in material and process selection providing a larger scope in component geometry to which this can be applied. Using a stainless steel or nickel chromium alloy is common in protecting against corrosion. Depositing a layer of these materials can provide similar performance in service as manufacturing an entire component using these materials, leading to a significant cost-saving while maintaining component performance.

Nickel chromium molybdenum ($NiCrMo$) alloys, known an Inconel, offer resistance against corrosion and oxidation and these are therefore popular choices in oil and gas applications. Large components would incur great costs were these to cast from these materials and again this highlights the benefit of a cladding process. Repair of components is also often achieved using such a process, firstly machining the area requiring repair and then laying the corrosion-resistant weld material using an automated or manual welding process, enabling further operation of the component.

Due to the above benefits of nickel chromium-based superalloys and the popular use of Inconel 625 in particular, this was chosen as the first clad material to be applied to the 4330 low alloy carbon steel substrate.

The typical nominal composition of Inconel 625 welding wire is shown in table 3.1 (134).

Ni	58% min.
Cr	20-23%
Mo	8-10%
Nb+Ta	3.15-4.15%
Fe	5% max.
Al	0.4% max.
Ti	0.4% max.
C	0.1% max.
Mn	0.5% max.
Si	0.5% max.
Cu	0.5% max.
P	0.015% max.
S	0.015% max.

Table 3.1: Typical nominal chemical composition of Inconel 625 welding wire

One of the considerations in producing a weld overlay cladding of Inconel 625 is the formation of oxides on the weld bead if additional shielding gas is not utilised and the weld pool reaches further than the region protected by the torch shielding gas, resulting in poor weld quality due to arising porosity (135). The particular study in which this is discussed pertains exactly to the use of nickel-based alloys deposited on carbon or mild steel and therefore this provided guidance on the use of trailing shields in obtaining a corrosion-resistant high quality weld clad as desired.

Martensitic stainless steel With the wide range of stainless steel materials available and their common use due to high strength and corrosion resistance, a stainless steel clad was also considered. More specifically precipitation hardening martensitic stainless steel is often used when these performance measures are required.

17-4 PH stainless steel is one of the types of this alloy that is commonly used.

However, stress corrosion cracking (SCC) and corrosion fatigue have been highlighted as potential issues associated with the use of precipitation hardening martensitic stainless steels (38).

The typical nominal composition of 17-4 PH stainless steel welding wire is shown in table 3.2 (136).

C	0.05% max.
Ni	4.50-5.00%
Cu	3.25-4.00%
P	0.03% max.
Mo	0.75% max.
Nb/Ta	0.15-0.30%
Cr	16.0-16.75%
Mn	0.25-0.75%
Si	0.75% max.
S	0.03% max.
Fe	Balanced

Table 3.2: Typical nominal chemical composition of 17-4 PH welding wire

Utilising a martensitic material in the welding process is known to produce compressive residual stresses and it was the aim of this research to exploit this characteristic. It is the volume change associated with the martensitic transformation upon cooling of a martensitic steel that induces the compressive residual stress (137), (138). The use of a 17-4 stainless steel clad and the effects of metallurgy and material properties of martensitic steels on residual stresses will be discussed in detail in chapter 7.

3.7.2 Geometry

Weld cladding of two representative geometries was undertaken, allowing the effects of substrate geometry to be assessed. Substrate material was obtained from unused production quality material from the industrial research partner as detailed in figures 3.7 and 3.8. The components are representative of the thicknesses and dimensions of the body of a hydraulic fracturing pump to which this technology is to be applied.

The outer diameter of the cylinder was clad to provide ease of residual stress measurement. Plates were clad on one of the largest faces. It was believed and results show that in this type of thick component the nature of residual stress is not significantly dependent on the substrate geometry. These results will be discussed in section 6.4.

3.7.3 Process considerations

The deposition of a weld material onto the base material requires a high level of heat input to create a liquid region through which the dissimilar material bond and fusion

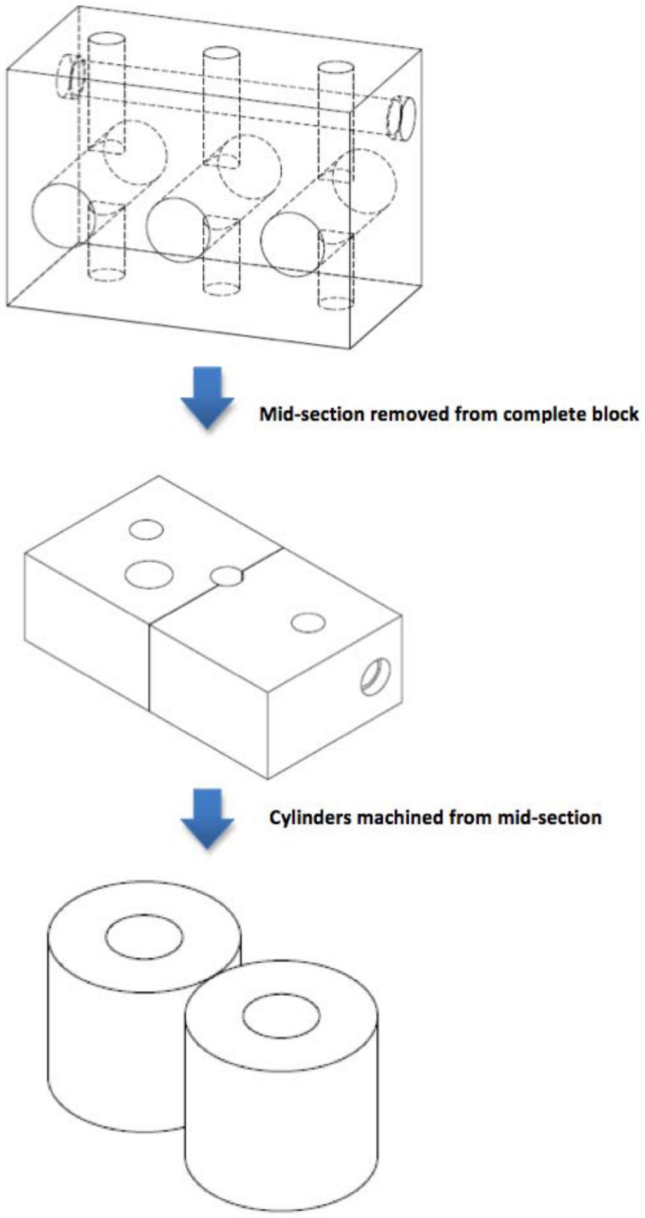

Figure 3.7: Section detail for cylindrical components - Photo courtesy of Weir SPM.

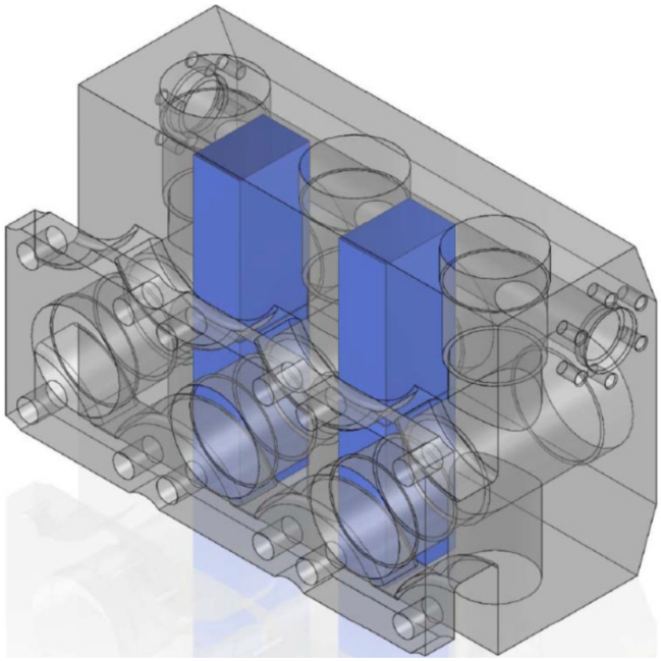

Figure 3.8: Section detail for rectangular components - Photo courtesy of Weir SPM.

of both materials is facilitated. In weld overlay cladding, the deposited material behaves like a protective layer, as opposed to fusion welding processes which utilise a filler material to strengthen the joining of two base materials. The generation of heat during this process can distort the component, as well as alter the material properties of the base metal in the *HAZ*. Dilution levels should be taken into consideration as welding qualification procedures often dictate acceptable levels of dilution of elements such as iron. Weld-metal dilution is said to be influenced by arc power and the feed rate of the filler metal, with the level of dilution decreased when arc power was decreased and/or the volumetric feed rate of the filler material increased in *GTAW* welding of a superaustenitic stainless steel with two nickel-based filler metals (139).

The heating of the material in the vicinity of the weld causes microstructural changes which in turn result in material property changes. A significant decrease in *HAZ* toughness for example can cause cracking, common in the formation of brittle martensite. Measures to avoid such cracking include the use of pre- and post-weld heat treatments. In the weld cladding process, two pre-heat temperatures were monitored and recorded: 150°C and 300°C. These are the values to which the substrate material was heated prior to commencing the weld cladding process. The aim of the investigation of the effects of pre-heat temperature were to determine not only the effects of pre-heat temperature on residual stresses but also on the metallurgy of the clad and substrate post-cladding. Clearly from an economic perspective a lower pre-heat temperature would be favourable. Additionally maximum interpass temperatures were set at 100°C above the pre-heat temperatures. This is the temperature to which the component must cool prior to the laying of the second pass of clad material.

A two pass system was utilised to control the levels of iron dilution. In studies of a superaustenitic stainless steel fusion weld with both Inconel 625 and Inconel 622, modifying arc power and filler-metal feed rate resulted in varying volumetric melting rates of the filler metal and in turn weld dilution levels. These studies concluded that decreasing the arc power and increasing the volumetric filler-metal feed rate brought about a decrease in the level of dilution (139).

The use of a substrate pre-heat temperature also decreases the cooling rate after each weld pass. The thickness of the substrate also influences the cooling rate, a greater substrate thickness encouraging more rapid cooling. It is this quenching effect that promotes martensite formation through microstructure shear transformation, prohibiting the natural transformation from austenite to ferrite and iron carbide upon cooling. Cooling temperatures were also monitored and recorded.

The cylinders were insulated during the cladding process with cooling post-welding occurring solely through the internal bore (figure 3.9).

Figure 3.9: Controlled cooling of cylindrical components - Cylinders wrapped in rock-wool.

Plates were also wrapped in insulating materials during the welding process and cooled post-welding from the clad face only, with the block immersed in a bed of vermiculite (figure 3.10), often utilised when high temperature insulation is required.

Two plates were also subjected to post-weld stress relief, with investigation of the microstructure before and after this process of a soak temperature of 530°C $\pm$ 5°C and a minimum soak time of 2.5 hours. The most effective stress relief temperature is a temperature in the region of the recrystallization temperature of the substrate, at which point removal of deformation occurs with the formation of a new microstructure.

Figure 3.10: Controlled cooling of rectangular components - Thick plates in bed of vermiculite.

Sample ID	Description	Welding consumable	T_{PH} (°C)	$T_{Int.}$ (°C)	Controlled cooling
Strath01	Cylinder	Inconel 625	300	400	Yes
Strath02	Cylinder	17-4 PH	300	400	Yes
Strath03	Plate	Inconel 625	300	400	Yes
Strath04	Plate	17-4 PH	300	400	Yes
Strath05	Plate	Inconel 625	150	250	Yes
Strath06	Plate	17-4 PH	150	250	Yes
Strath07	Plate	Inconel 625	150	250	Yes then $PWSR$
Strath08	Plate	17-4 PH	150	250	Yes then $PWSR$

Table 3.3: Weld cladding sample details

A top hat thyristor controlled, fan assisted furnace was used with direct computer network data download capability. Post-weld heat treatment is utilised to reduce damaging tensile residual stresses induced through the welding process along with the benefit of tailoring material properties, for example encouraging an increase in toughness post-martensite formation. The relative success of the stress relieving process is discussed in sections 4.2 and 6.4 for both clad materials.

3.7.4 Clad components

Details of the samples weld clad are provided in table 3.3 and examples of the clad cylindrical and rectangular specimens shown in figures 3.11 and 3.12.

Figure 3.11: Weld clad 4330 cylinder - Cylinder dimensions: $\varnothing_{outer}$=12″, $\varnothing_{inner}$=5″, L=10″.

Figure 3.12: Weld clad 4330 block - Block dimensions: L=12″, W=6″, H=4″. Image showing strain gauge locations for ICHD residual stress measurement.

3.8 Summary

Coating and cladding processes inevitably induce residual stresses due to the manufacturing methods used to deposit additional materials on the substrate of engineering components. Ideally residual stresses should be tailored to avoid severe discontinuity stresses which are often produced at the interface between the substrate and clad/coating materials. The presence of stress concentrations can heavily influence the residual and operational stresses and appropriate evaluation of these effects is critical in ensuring satisfactory performance of the particular purpose of the component. Partnering optimum performance in cyclic applications and the creation of an acceptable dissimilar joint is a difficult task. Erosion, corrosion and thermal performance are examples of additional factors which may require assessment, with ultimately the overall life of the component being of utmost importance.

High compressive residual stresses are desirable through the entire thickness of the coating or cladding and preferably well into the substrate to facilitate increased fatigue performance even in erosive and corrosive environments. At the interface, discontinuity stresses should be as low as possible to avoid static bond failure or premature sub-surface fatigue failure. To successfully obtain a fatigue-resistant clad therefore requires an understanding of the effects and modification of variables influencing the generation of compressive residual stresses as well as the levels of discontinuity stress. It is understood that the majority of processes inducing compressive residual stresses achieve this in a similar manner: plastic deformation of a small region of material constrained by a larger surrounding elastic region of material, which dominates upon removal of the load forcing the plastically deformed area into a state of compression (58). The mechanism for thermal processes is dependent upon the heating and cooling of materials. Material properties arising through the dissimilar joining process must also be satisfactory in the substrate, HAZ and clad/coating. In considering the application of this technology in an industrial context, naturally cost-effectiveness is also a factor.

Chapter 4

Investigating Weld Clad Metallurgy and Temperature-Dependent Material Properties

Following the weld cladding of 4330 low alloy carbon steel with both Inconel 625 and 17-4 PH stainless steel, investigation into the resulting metallurgy and material properties commenced. Metallurgical studies provided insight into the quality of fusion arising through the weld cladding process and the resulting microstructure in both substrate and clad regions. Chemical analysis provided knowledge of the resulting composition of materials and the variation in composition due to the application of a two-pass cladding process. These results provided understanding of aspects of the cladding process which would benefit from weld procedure refinement. Temperature-dependent thermal and mechanical properties were investigated, with specimens produced from the weld clad components to ensure that properties arising through the cladding process would be captured. It will be shown that published data does not provide satisfactory information on the behaviour of these materials, especially due to the effects of alloying and dilution impacting material properties. Upon completion of an extensive materials testing program, an array of experimental data was obtained, which served as the input into the finite element simulation to ensure accurate modelling of the residual stresses resulting through weld cladding with the materials under investigation. Recommendations for potential continuation of the materials testing program are provided.

4.1 Introduction

Due to the nature of the weld cladding process, although a degree of alloying and diffusion will occur, attention should be given to abrupt changes in material properties which can result in large discontinuity stresses. These stresses arising through the cladding process can then further be altered due to operational stresses. To appropriately assess fatigue performance, a thorough understanding of all contributing factors must be acquired.

It is therefore clear, that if the material properties of the clad and substrate materials play a major role in the stress state of the component, materials characterisation is essential. Experimental testing of thermal and mechanical temperature dependent material properties was undertaken to understand and simulate material behaviour during cladding process. The data obtained served as input into the finite element models which will be discussed in chapter 5. Metallurgical studies also provided great insight into the effects of the cladding process and the influence of certain parameters on the resulting metallurgy and residual stress states.

As described in the previous chapter, the substrate material is a low alloy carbon steel of the grade 4330. The two clad materials are nickel-chromium-based superalloy Inconel 625 and martensitic precipitation hardening stainless steel 17-4 PH.

4.2 Metallurgical examination

The cladding process results in metallurgical changes which require investigation with regards to their effects on material properties and residual stresses and to identify necessary refinement to the weld cladding process. The aspects which can affect the mechanical and thermal material properties are those of microstructural changes, elemental diffusion and alloying effects. Furthermore, differences in metallurgical structures will result from varying pre-heat temperatures prior to welding and cooling rates during welding using the hot wire *GTAW* process, cladding materials and post-weld heat treatments.

Specimens were prepared from the weld clad blocks Strath03-Strath08, detailed in table 3.3 using Kalling's etchant, providing the opportunity to assess the *as-clad* microstructures and the effects of pre-heat temperature, clad material and stress relief.

Figure 4.1 shows an example of a macrosection with the two clad passes, two *HAZ*'s and substrate material clearly visible. Measurements of the locations of these points of interest were taken on the samples as provided in table 4.1.

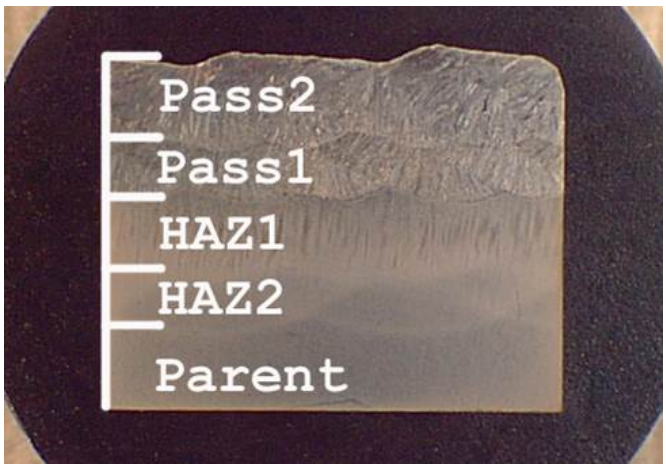

Figure 4.1: General macrosection of clad and substrate - Example of two clad passes, two HAZ's and substrate material.

As can be observed from the data, the first pass was 3-4 mm in depth, with the second pass bringing the total clad layer depth to 5-6 mm. The HAZ's extended almost as deep, however as these measurements are approximate, it is concluded that a good level of consistency was achieved in the request for a 6 mm clad layer deposited in two passes.

ID	Strath03	Strath04	Strath05	Strath06	Strath07	Strath08
			Depth in mm			
Pass 2	3.4	3.8	3.5	3.2	3.2	3.2
Pass 1	5.1	5.8	5.4	5.2	4.8	5.6
HAZ 1	8.6	8.9	7.9	7.4	7.1	7.7
HAZ 2	9.9	10.7	9.3	9.3	8.5	9.8

Table 4.1: Depth of weld clad passes and HAZ's from clad surface

Pre-cladding, the 4330 substrate material possessed a tempered martensitic structure with visible alloy segregation (figure 4.2), which typically arises through the production process of casting and forging. Areas of upper bainite, that is an incomplete transformation of martensite, were also found. Although these areas will have little effect on the mechanical properties on the whole, effects on residual stresses could be significant. This will be further discussed in chapter 7. The light and dark banding illustrates this alloy segregation. Non-metallic inclusions were observed as small black spots in some areas. These inclusions could accelerate degradation in a corrosive environment and therefore must be taken into consideration with regards to potential fatigue cracking and failure.

Figure 4.2: Substrate microstructure pre-cladding - Non-metallic inclusions observed in the substrate pre-cladding. Magnification factor: x50.

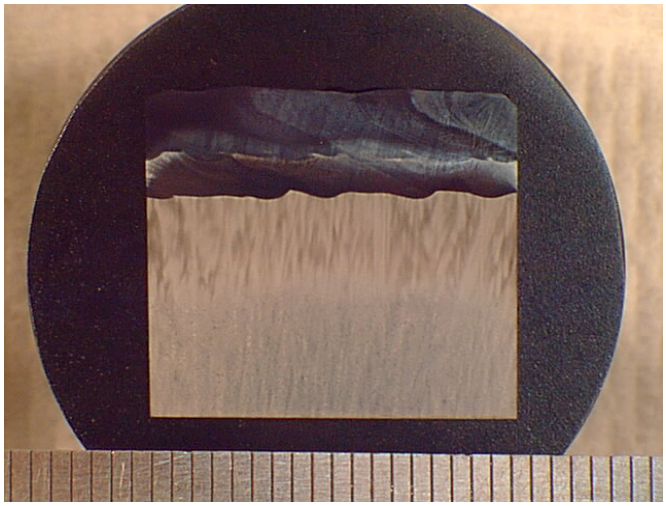

Figure 4.3: General macrostructure of Inconel 625 cladding - ID: Strath03 - Heavy alloy segregation in the HAZ.

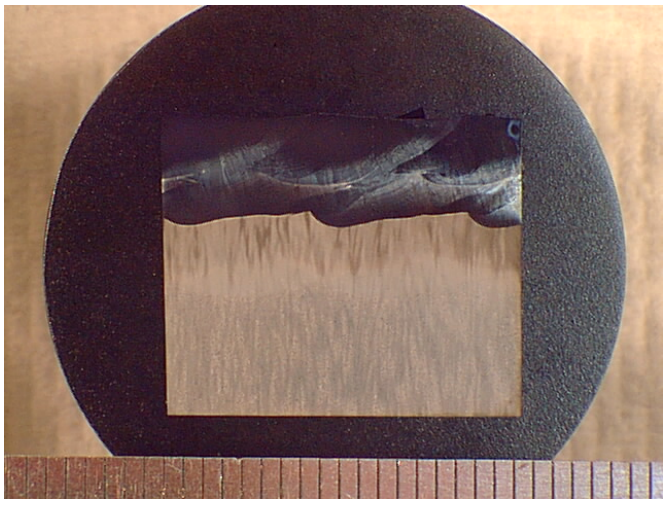

Figure 4.4: General macrostructure of Inconel 625 cladding - ID: Strath05 - Moderate alloy segregation in the HAZ.

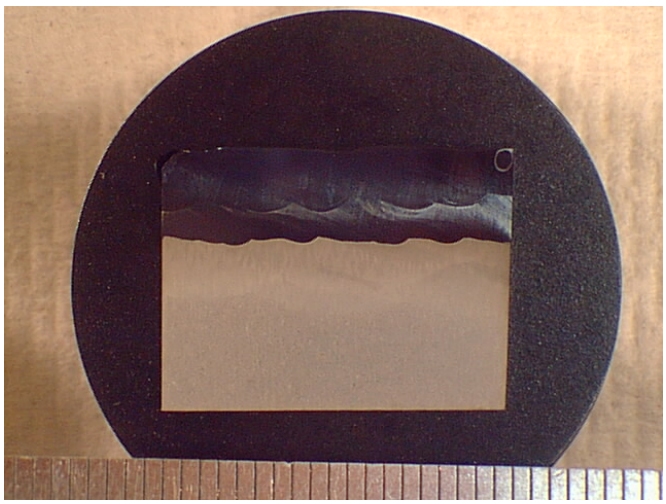

Figure 4.5: General macrostructure of Inconel 625 cladding - ID: Strath07 - Low alloy segregation in the HAZ.

4.2.1 Inconel 625 clad on 4330

Observing the three images showing the macrostructure of the Inconel 625 cladding, it can be seen that varying degrees of alloy segregation are present in the HAZ. In figure 4.3 heavy alloy segregation can be observed. In figure 4.4 the level of alloy segregation is moderate and finally in figure 4.5 only minor alloy segregation is visible. Alloy segregation will be dictated to a large extent by the cooling rate experienced post-cladding. As the components are of substantial thickness, slow cooling rates will be encountered. The temperatures chosen as pre-heat and interpass temperatures, as described in table 3.3, will also serve in slowing the rate of cooling to encourage solid state diffusion, for example of chromium and nickel.

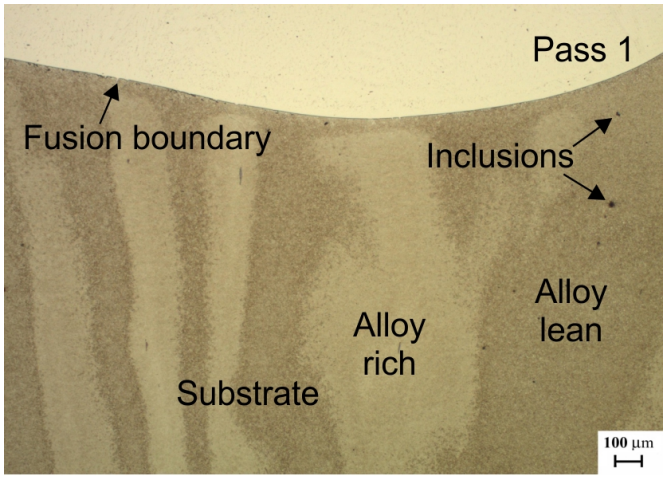

Figure 4.6: Fusion boundary of Inconel 625 cladding - ID: Strath05 - Magnification factor: x50.

The fusion between clad and substrate materials shows that good levels of penetration are obtained through the cladding process.

Examining the microstructure of the fusion boundary of the Inconel 625 cladding, heavy micro-segregation is observed in the *HAZ* as shown in figure 4.6. The substrate tempered martensitic microstructure has been changed through the welding process and strong banding is observable in the *HAZ*. The lighter areas are regions of alloy richness whereas the dark bands signify alloy lean regions. The driving factor behind the post-weld heat treatment is to increase the homogeneity of the structure, aiming to remove the bands of alloy segregation. Figure 4.7 shows that the *PWHT* has successfully increased the homogeneity of the structure, the segregation bands visibly no longer present.

Near-equilibrium cooling conditions were achieved by soaking at 530°C for 2.5 hours. Non-metallic inclusions are present in the substrate, however these are not connected to the cladding process as these inclusions were observed pre-cladding as highlighted in figure 4.2.

Drawing conclusions of the effects of pre-heat temperature and post-weld heat treatment in considering alloy segregation, it is clear that stress relief has a positive effect in increasing homogeneity, as the decrease in alloy segregation between figures 4.4/4.6 and 4.5/4.7 illustrates. These samples were both clad with a pre-heat temperature of 150°C with sample Strath07 subjected to post-weld heat treatment. *PWHT* will be further discussed in sections 6.4 and 11.5. Comparing figures 4.3 and 4.4, the former clad with a pre-heat temperature of 300°C and the latter 150°C, alloy segregation is lower in the case of the lower pre-heat temperature.

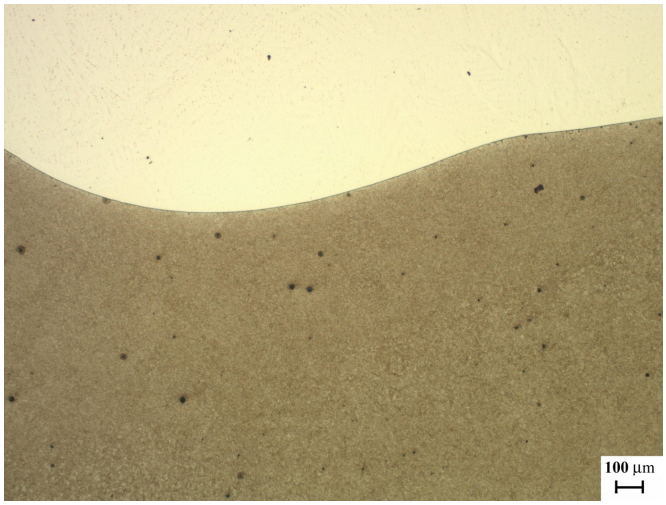

Figure 4.7: Fusion boundary of Inconel 625 cladding - ID: Strath07 - Post-weld heat treatment successfully increases homogeneity of HAZ microstructure. Magnification factor: x50.

Comparing the two passes of an Inconel 625 clad shows a tempered structure in the first pass (figure 4.8) and a cored columnar microstructure in the second (figure 4.9). This is to be expected due to the two-pass system as the tempering effect occurs

with the weld deposition and the final pass adopts the microstructure typical of cast structures. The dispersed carbide precipitates present in the first pass in figure 4.8 arise through the melting of the substrate into a liquid form, the carbon elements present in the substrate then diffusing into the clad material. Therefore upon laying of the second pass, it would be expected that these carbides will reduce as the diffusion will occur between the first and second passes of the clad. This is shown in figure 4.9.

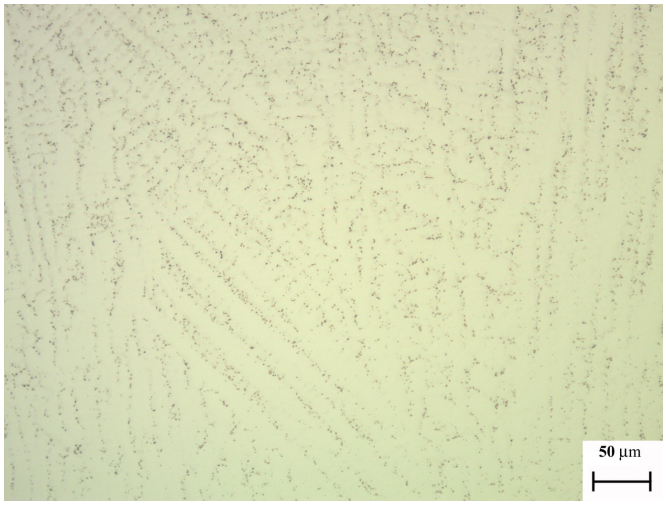

Figure 4.8: Pass 1 microstructure of Inconel 625 cladding - ID: Strath03 - Single-phase solid solution with dispersed carbides present. Magnification factor: x200.

Figure 4.9: Pass 2 microstructure of Inconel 625 cladding - ID: Strath03 - Single-phase solid solution, classical cast dendrite and coring features present with no evidence of carbide precipitation. Magnification factor: x200.

4.2.2 17-4 PH clad on 4330

Similarly, examining the macrostructure of the 17-4 PH cladding, alloy segregation levels in the *HAZ* differ. Heavy alloy segregation is observed in figure 4.10, alloy

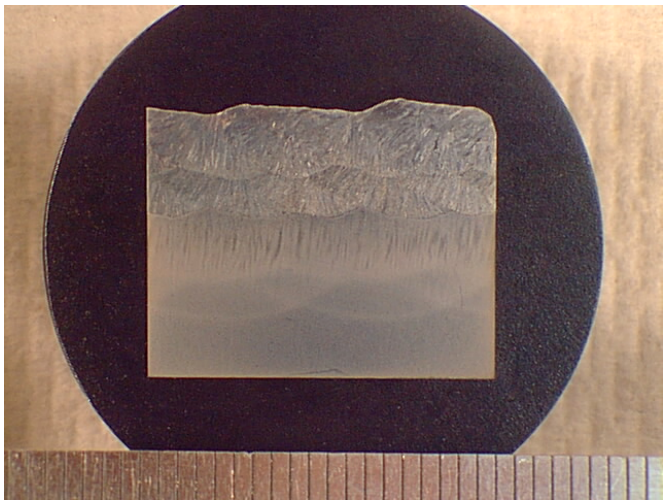

Figure 4.10: General macrostructure of 17-4 PH cladding - ID: Strath04 - Heavy alloy segregation in the HAZ.

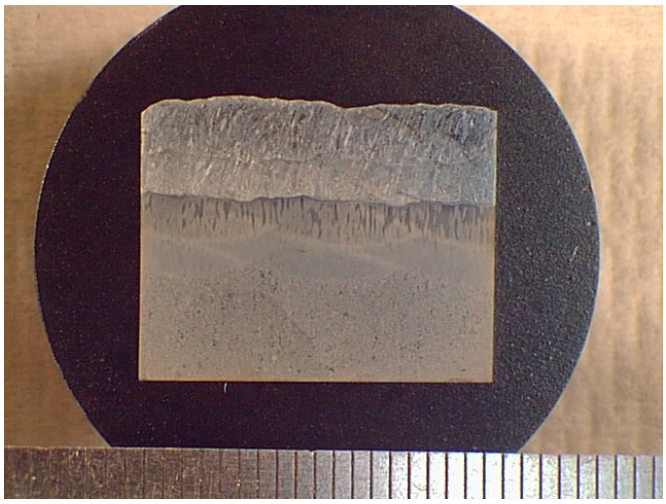

Figure 4.11: General macrostructure of 17-4 PH cladding - ID: Strath06 - Moderate alloy segregation in the HAZ.

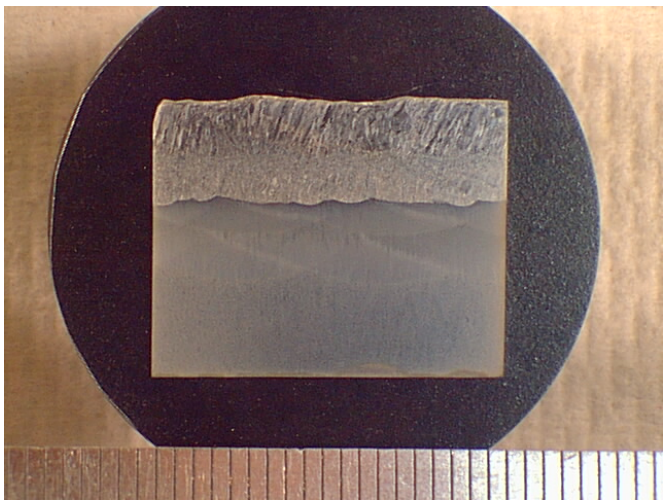

Figure 4.12: General macrostructure of 17-4 PH cladding - ID: Strath08 - Minor alloy segregation in the HAZ.

segregation levels decrease in figure 4.11, with the lowest level of alloy segregation in figure 4.12.

Therefore, the same conclusions can be drawn as to the effects of pre-heat temperature and post-weld heat treatment effects. A lower pre-heat temperature lowers the extent of alloy segregation, illustrated in comparing figures 4.10 and 4.11, while stress relief also decreases alloy segregation, shown by the lower level of alloy segregation in figure 4.12 in comparison with figure 4.11.

Generally martensite is observed as a triangular form in the microstructure with a grouping of the martensitic needles, highlighted in figure 4.13. Due to the hexagonal, close-packed structure of 17-4 PH this is commonly observed. In this image, non-metallic inclusions are also visible, again requiring attention and refinement of the weld cladding procedure to avoid degradation of material properties and therefore component performance.

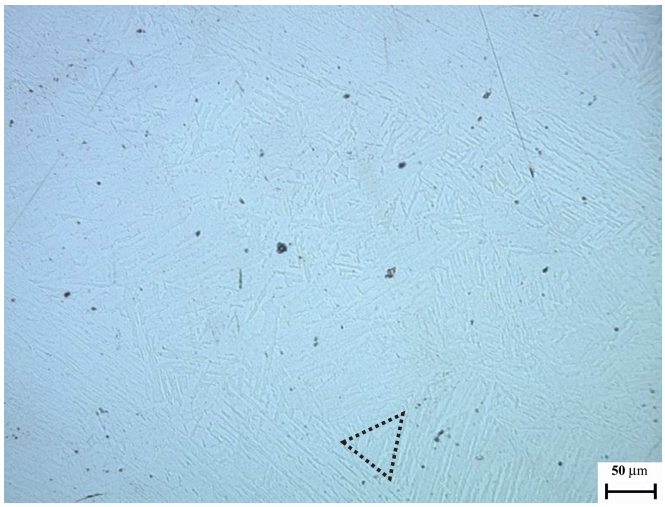

Figure 4.13: Microstructure of 17-4 PH cladding - ID: Strath04 - Triangular form of martensitic needles in 17-4 PH cladding highlighted by dashed lines. Magnification factor: x200.

As in the case of the Inconel 625 cladding, the 17-4 PH cladding also experienced variations between the first and second passes in terms of microstructure. Examining the microstructure post-cladding illustrates that through the solidification phase coarse dendritic growth occurs in the clad material, expected to be observed during any welding process as the molten metal cools.

The first pass was tempered by the laying of the second pass with coring more heavily present in the second pass. The first pass contains non-continuous regions of inter-dendritic δ-ferrite and martensite in the form of columnar grains, as shown in figure 4.14. Figure 4.15 shows a greater amount of coring and continuous grain boundary δ-ferrite. The presence of δ-ferrite in both passes is to be highlighted, as the presence of this phase is known to decrease corrosion resistance in stainless steel.

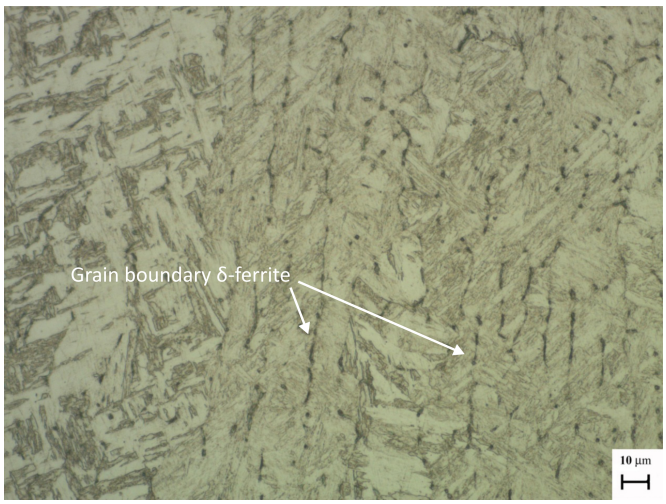

Figure 4.14: Pass 1 microstructure of 17-4 PH cladding - ID: Strath04 - Columnar grains of martensite and small non-continuous regions of inter-dendritic, grain boundary δ-ferrite present. Magnification factor: x500.

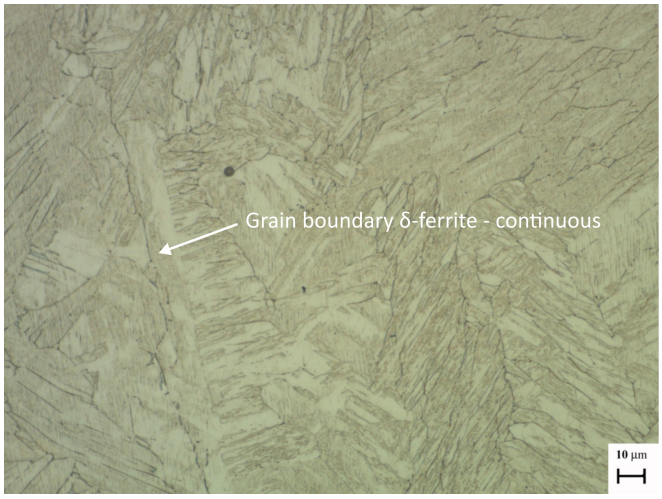

Figure 4.15: Pass 2 microstructure of 17-4 PH cladding - ID: Strath04 - Increased coring and greater level of continuous grain boundary second phase δ-ferrite observed in the martensitic matrix. Magnification factor: x500.

Examining the substrate post-cladding reveals areas of martensite and bainite (figure 4.16). This was found to be the case in samples Strath04, Strath06 and Strath08.

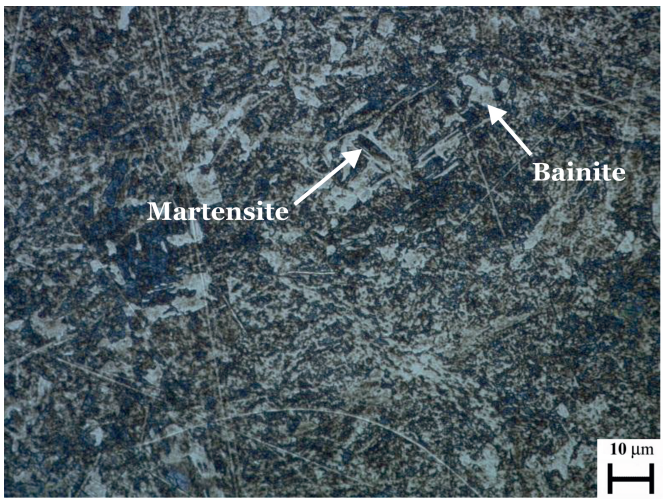

Figure 4.16: Microstructure of 4330 substrate clad with 17-4 PH - ID: Strath06 - Columnar grains of martensite and small non-continuous regions of inter-dendritic, grain boundary δ-ferrite present. Magnification factor: x500.

4.3 Chemical analysis

Elemental composition and therefore the extent of weld dilution can be assessed by carrying out chemical analyses in a line and spot testing manner. This was undertaken using a tungsten filament scanning electron microscope (SEM) with energy dispersive X-ray spectroscopy capability. An electron beam is directed towards the specimen with X-rays emitted from the specimen detected and the energy assessed to determine the elemental composition of the region in which the electron beam is acting.

The SEM results also allowed areas of alloy micro-segregation to be observed.

4.3.1 Inconel 625 clad on 4330

Chemical analysis of 4330 clad with Inconel 625, with emphasis on the weight percentage content of iron, showed that in travelling further from the clad and substrate interface towards the clad surface, the level of iron present decreased. This illustrates that iron dilution from the substrate material does occur, with the level of iron greater in the first clad pass than in the second. This highlights the reasoning for a multi-pass clad process. The low level of iron present in the second pass and therefore at the surface of the component ensures satisfactory corrosion resistance.

Clear variations in the chemical composition are observed in traversing from the clad surface down to the fusion boundary. Table 4.2 shows that the iron content of the clad material at the surface is around 7%, whereas at the fusion boundary this value is around 26%. This is expected as the gradual decrease in iron content towards the clad surface signifies a decrease in diffusion from the HAZ. Therefore in the chemical composition of the second pass the iron content is much lower. Chromium is diffused from the Inconel 625 clad into the substrate which will increase HAZ hardness values, increasing cracking susceptibility. As highlighted a two-pass deposition method was utilised for this very reason to ensure satisfactory corrosion resistance as hydrogen induced cracking (HIC) is more likely to be an issue if high dilution rates occur. To ensure satisfactory corrosion performance, industry requirements suggest that the maximum iron dilution level should be 5%. On the other hand, fusion is required between the substrate and the clad and therefore a certain degree of diffusion should occur. A dilution level of 0% iron is therefore not the aim. This pattern in decreasing iron levels was observed in all cases of Inconel 625 clad on 4330. The crossing from clad into substrate material can be clearly observed through the vast differences in chemical composition.

	% Cr	**% Fe**	**% Mn**	**% Mo**	**% Ni**	**% Si**
Clad surface	22.4	7.42	0	7.14	63.05	0
	21.32	11.03	0	6.73	60.92	0
	17.89	25.92	0	5.63	50.57	0
	20.39	16.28	0	6.77	56.56	0
Fusion boundary	18.24	26.2	0	5.99	49.57	0
	1.04	95.91	0.4	0	2.43	0.21
	1.29	95.37	0.56	0	2.52	0.27
	1.19	95.35	0.55	0	2.67	0.23
	1.07	95.86	0.44	0	2.42	0.21
	1.26	95.43	0.56	0	2.49	0.25
	1.2	95.3	0.56	0	2.69	0.25
	1.36	94.13	0.63	0.92	2.69	0.28
	1.46	95.1	0.63	0	2.54	0.27
Substrate	1.11	95.74	0.48	0	2.45	0.22

Table 4.2: Chemical composition in Inconel 625 clad approaching fusion boundary - ID: Strath05

Comparing the chemical composition in table 4.2 with that in table 3.1, it is observed that chromium values obtained for the as-clad material generally follow the guidelines given in the nominal composition for the Inconel 625 welding wire. A 58% min-

imum value is given in the nominal chemical composition for nickel and although values obtained are not vastly different, some values obtained are lower. Molybdenum values are lower in the as-clad condition than the typical nominal composition. Iron values are higher than the maximum 5% typical value. Manganese and silicon values obtained agree with the typical composition.

It should be noted that the chemical composition provided in table 3.1 is for the typical nominal chemical composition of Inconel 625 welding wire, prior to welding. Values in table 4.2 are representative of the as-clad material hence the arising variations. These values will also differ depending on the substrate materials due to diffusion effects. The 5% maximum level given for iron is also not reflected in the as-clad chemical composition, problematic also due to industry recommendations to ensure adequate corrosion resistance.

The following ten spot analyses in tables 4.3 and 4.4 were taken vertically in the HAZ demonstrate the variation in chemical composition between the parallel alloy rich and alloy lean areas.

% Cr	% Ni	% Fe	% Mn
1.08	2.56	95.93	0.42
1.07	2.62	95.96	0.35
1.1	2.62	95.73	0.55
1.09	2.51	95.7	0.43
1.15	2.77	95.55	0.54
1.07	2.45	95.92	0.56
1.13	2.59	95.84	0.43
1.19	2.6	95.71	0.51
1.13	2.67	95.46	0.47
1.21	2.6	95.46	0.46

Table 4.3: Chemical composition in alloy lean region of 4330 HAZ clad with Inconel 625 - ID: Strath05

In the alloy lean areas, shown as dark bands in the microstructure in figure 4.6, it can be seen that chromium and nickel content is lower than in the alloy rich areas, the light segregation band regions. The greater alloy content will later be seen to reflect higher hardness values due to the larger quench effect experienced by the HAZ.

4.3.2 17-4 PH clad on 4330

A line analysis was also carried out on the 17-4 PH cladding on 4330, from the clad surface through the HAZ and into the substrate. The main constituent elements in

% Cr	% Ni	% Fe	% Mn
1.23	2.44	94.59	0.5
1.16	2.67	95.63	0.53
1.18	2.64	95.35	0.52
1.21	2.67	95.24	0.58
1.28	2.72	95.14	0.52
1.31	2.79	95.02	0.6
1.36	2.7	94.71	0.61
1.39	2.96	94.73	0.59
1.56	2.99	94.43	0.64
1.45	3.00	94.23	0.61

Table 4.4: Chemical composition in alloy rich region of 4330 HAZ clad with Inconel 625 - ID: Strath05

table 4.5 are different in this case due to the composition of the clad material. The first clad layer closer to the substrate possesses lower levels of chromium and copper due to a greater level of diffusion with the substrate. This is also indicated by the increased levels of iron in the first clad pass diffused from the substrate into the clad. It is clear to see at which point the boundary between clad and substrate is crossed, especially when observing the levels of copper, and to a lesser extent nickel. These values highlight that these elements are not involved in the diffusion process.

Comparing the as-clad 17-4 PH material with the typical nominal chemical composition of 17-4 PH welding wire in table 3.2, silicon and manganese values follow the typical nominal composition provided. Chromium and copper values follow the typical composition values at the clad surface however towards the fusion boundary these values decrease and are less than those in table 3.2. Nickel values obtained for the as-clad condition of 17-4 PH are slightly less than those of the typical chemical composition. Again the variation in chemical composition arising through the weld cladding process in the clad and substrate materials and in the vicinity of the join is to be expected.

4.4 Materials characterisation

It has previously been highlighted that material properties affect the residual stress state arising due to the weld cladding process. Therefore a material testing program was undertaken to determine the thermal and mechanical temperature dependent material properties to provide an understanding of material behaviour and to serve

	% Si	% Cr	% Mn	% Fe	% Ni	% Cu
Clad surface	0.45	16.41	0.57	74.65	4.53	3.39
	0.44	16.69	0.58	74.75	4.32	3.21
	0.44	15.9	0.6	75.43	4.4	3.22
	0.44	14.99	0.56	76.94	4.16	2.91
Fusion boundary	0.41	13.47	0.62	78.73	4.05	2.73
	0.26	1.3	0.64	95.12	2.67	0
	0.28	1.3	0.66	95.02	2.74	0
	0.28	1.34	0.67	94.99	2.73	0
	0.24	1.16	0.54	95.46	2.6	0
	0.22	1.07	0.47	96.02	2.22	0
	0.26	1.3	0.59	95.37	2.47	0
	0.25	1.19	0.55	95.52	2.48	0
	0.23	1.14	0.5	95.73	2.39	0
Substrate	0.24	1.1	0.48	95.81	2.36	0

Table 4.5: Chemical composition in 17-4 PH clad approaching fusion boundary - ID: Strath06

as input into the finite element simulation of the weld cladding process.

In commencing the materials characterisation program for substrate and clad materials, published data availability was investigated. Published data availability is very limited for wrought materials with regards to temperature ranges and specific materials. Had complete data sets been available for these materials, properties in the wrought condition would also not necessarily represent the correct grades of material and would certainly not account for the effects of welding on the resulting properties and microstructure. Material properties of the welding wire will alter after the material has been deposited and cools to room temperature, forming the clad layer on the substrate on which it was deposited. The joining of the two materials will further alter the properties of both materials, with solid-solid phase transformations in respective materials also resulting in microstructural changes and therefore it is clear that characterisation is a complex process.

Examples of temperature-dependent data sets for thermal conductivity, specific heat capacity, thermal expansion coefficient and Young's modulus for a low alloy steel, a stainless steel and a nickel-chromium-based superalloy were provided in a report comparing experimental residual stress measurements with finite element simulations (140). This study highlighted the sensitivity of the finite element simulation results with regards to the input of material properties. Thermo-physical properties,

varying with temperature but not causing a change in chemical identity of a material, include coefficient of thermal expansion, thermal diffusivity, thermal conductivity and specific heat capacity. The study highlighted that there can be variations in material properties assumed, especially around the Curie temperature where a phase change alters the magnetic or ferroelectric properties of a material. Variability in physical properties at high temperature, stated as above 800°C in (140), is unlikely to heavily affect stress states due to the low strength a material possesses at these high temperatures.

All published data referred to and plotted in the following sections was obtained from a materials database (141), unless otherwise stated.

Experimental data was relatively easily obtained at room temperature. It was desired to obtain data from room temperature to the melt temperature for each material. These values are provided in table 4.6. Due to the inability of the testing equipment to allow materials to be tested at melt temperature, data was obtained up to 1200-1250°C in the case of thermal properties. Temperature range limitations will be discussed further in section 4.4.2 focussing on obtaining coefficient of thermal expansion (CTE) data, highlighting the importance of ensuring that the temperature range captures phase changes occurring upon heating and cooling.

Material	Melt temperature (°C)
4330	1427
Inconel 625	1350
17-4 PH	1440

Table 4.6: Melt temperatures of materials under investigation

4.4.1 Preparation of specimens for thermal property testing

A wire electro-discharge machining (EDM) process is a CNC process which utilises an electric current and a fine wire to allow the cutting of conductive materials. Deionised water is used to cool the material during the cutting process, the component being submerged in this water to ensure minimal stresses are induced and a fine surface finish is obtained. The cutting of the material is facilitated by the wire, however the cutting is actually due to the sparks emitted between the cutting wire and the material which causes erosion of the material.

4.4.2 Coefficient of thermal expansion

A Netzsch DIL 402C pushrod dilatometer was used to obtain the linear coefficient of thermal expansion (CTE) in accordance with the $ASTM$ standard (142). The speci-

Figure 4.17: Machining of clad and HAZ layers from clad cylinder - Machined from 1 inch cylinder offcut using wire EDM process.

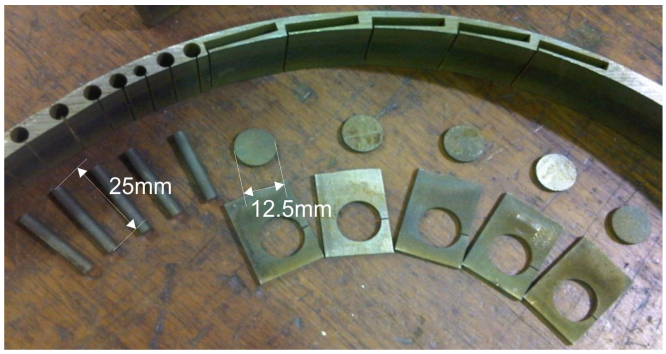

Figure 4.18: Specimens obtained for testing of thermal temperature-dependent material properties - Machined from clad and HAZ layers using wire EDM process.

mens took the form of thin rods, as shown in figure 4.18, with a length of 25 mm and a diameter of 4 mm.

Measurements were obtained in a continuous manner from room temperature to 1200°C initially for the heating phase. This upper temperature limit was chosen to ensure no damage to the equipment in approaching melt temperature of the materials. The effects of heating rate were investigated using unclad 4330 specimens. Figure 4.19 shows various readings using two heating rates $\dot{T}(h)$: 10K/min and 20 K/min. From a room temperature value until pre-phase change around 750°C there are slight variations in CTE values, with the bottom four curves being those for the higher heating rate and the top four curves being for the lower heating rate. At the phase change these curves are seen to group together and post-phase change remain so. It was concluded that in the heating phase the heating rate does not greatly affect results and so to decrease experiment duration a heating rate $\dot{T}(h)$ of 20 K/min, or °C/min, was utilised.

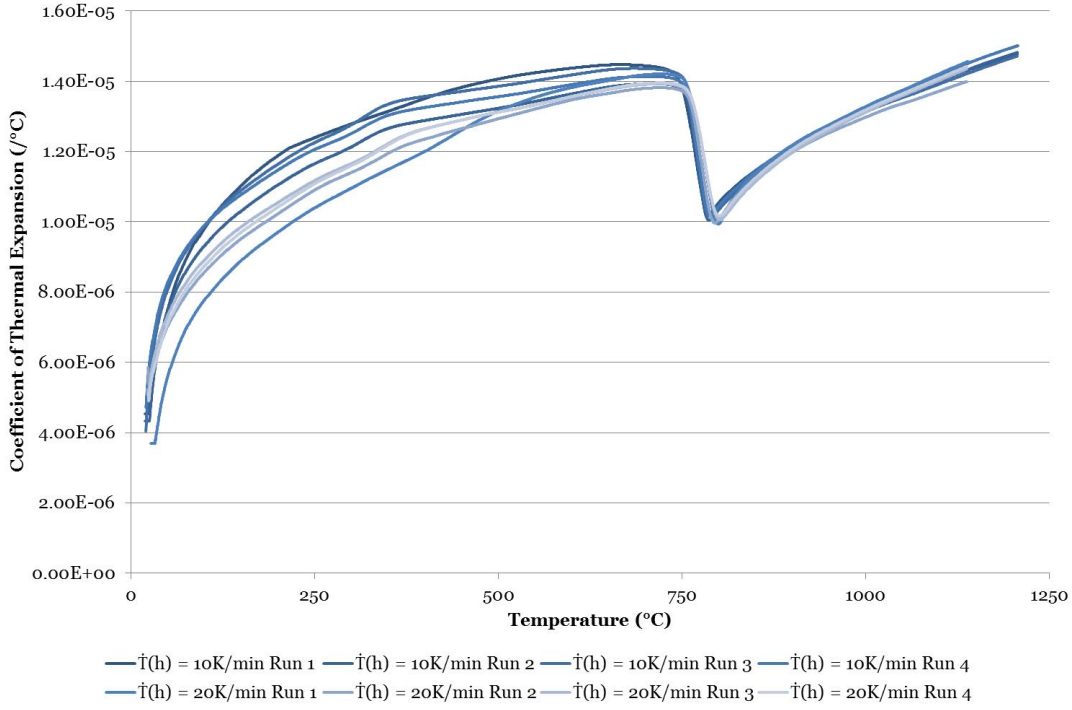

Figure 4.19: Heating rate effects on CTE of unclad 4330 - Data experimentally obtained upon heating using a Netzsch DIL 402C pushrod dilatometer.

The ASTM standard highlights the need to conduct repeated measurements using the same specimen to ensure that data obtained represents thermally stable data. This was thought to be especially crucial in the case of the clad materials and substrate where complex residual stress states would be present due firstly to the weld cladding process and secondly due to subsequent machining to obtain the specimens for thermal property characterisation. Repeating measurements would ensure that

any effects due to residual stress changes through thermal cycling would not affect the data obtained.

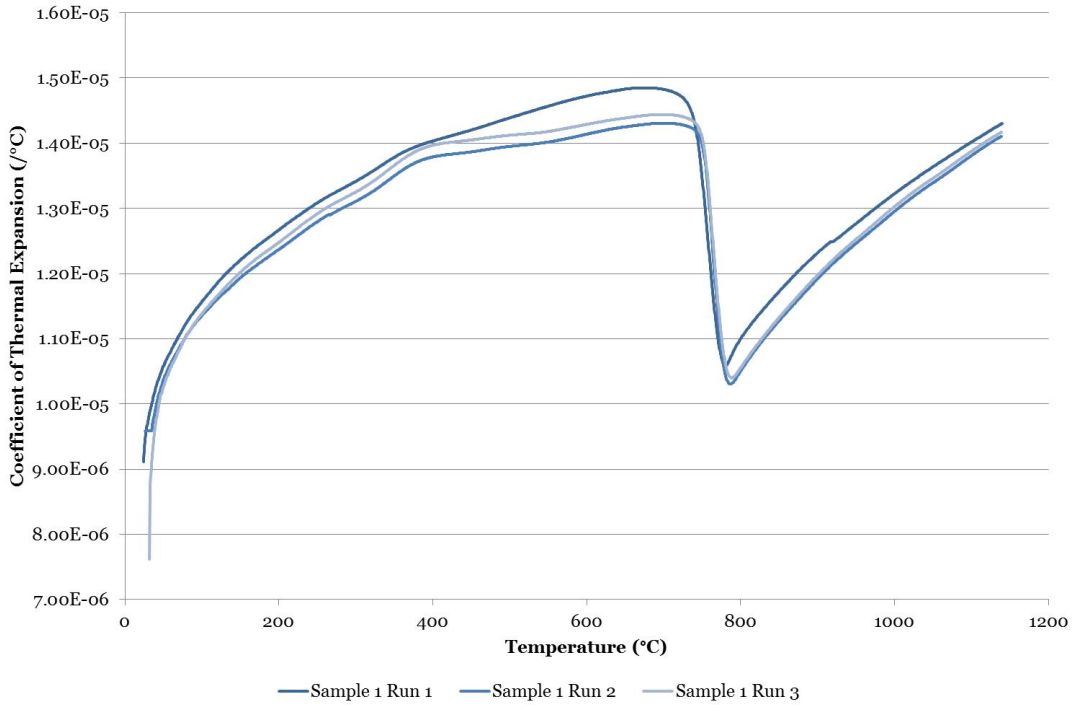

Figure 4.20: Repeated measurement effects on CTE of 4330 (HAZ of 4330 clad with Inconel 625) - Data experimentally obtained upon heating using a Netzsch DIL 402C pushrod dilatometer.

Referring to figure 4.20 these effects are observed with notable changes between the first and second measurements of a HAZ sample of 4330 clad with Inconel 625 in the vicinity of the phase change. A much smaller degree of variation is observed between measurements two and three. This was the general trend observed in all cases and so data was utilised for the finite element analysis from the second measurements of all samples. Again around the phase change the data groups together, with slight changes post-phase change between the first run and the second and third.

Cooling rates were also investigated with particular interest in the case of 4330 and 17-4 PH. Limited data was however obtained due to the incapability of the dilatometer to perform controlled cooling to ambient temperature. This is illustrated in the measurement obtained for 17-4 PH with a cooling rate $\dot{T}(c)$ of 25 K/min. The equipment ended the measurement at a temperature of 312.4°C due to the time expected to reach room temperature with the chosen cooling rate. The data obtained showed that this was not the case. Therefore data was obtained for cooling rates $\dot{T}(c)$ of 5 K/min and 10 K/min, however even in these cases ambient temperature was not reached. Final temperatures varied depending on the set cooling rate. Table 4.7 shows the temperatures reached for respective cooling rates for all materials.

Material	Lower bound temperature (°C)		
	$\dot{T}(c)$=5 K/min	$\dot{T}(c)$=10 K/min	$\dot{T}(c)$=25 K/min
Inconel 625	80.3	140.0	-
17-4 PH	81.6	140.4	312.4
4330 HAZ (Inconel 625 clad)	80.7	147.7	-
4330 HAZ (17-4 PH clad)	80.8	145.0	-

Table 4.7: Lower bound temperature variation upon cooling in CTE experimental measurements

Figure 4.21 shows the experimental data for heating and cooling of the 4330 *HAZ* when clad with Inconel 625. It should be noted that below the lower bound temperatures highlighted in table 4.7 data was extrapolated, as with data above 1200°C. This is the case with all *CTE* measurements.

Published material data was only available up to 600°C, completely neglecting phase changes and loss of strength of the materials approaching melt.

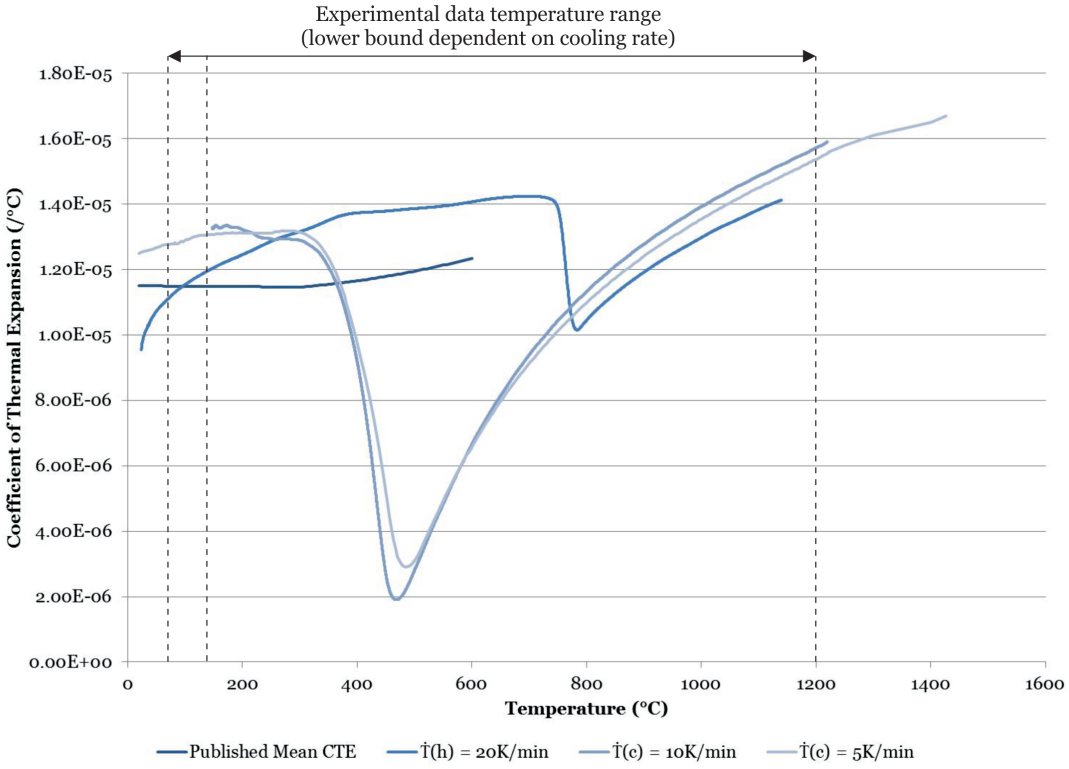

Figure 4.21: Coefficient of thermal expansion of 4330 (HAZ of 4330 clad with Inconel 625) - Data experimentally obtained upon heating and cooling using a Netzsch DIL 402C pushrod dilatometer.

Data was extrapolated to melt temperature and down to room temperature when required to provide a complete data set for input into the finite element model. This was done observing the shape of the curve post-phase change and estimating the

expected data to maintain this curve for the 4330 and 17-4 PH materials, as it was clear that a linear extrapolation would not be appropriate. A linear extrapolation was used in the case of the Inconel 625 due to the observed linear trend in CTE data.

Experimental data obtained for 4330 clad with 17-4 PH is shown in figure 4.22. Values are similar to those of the 4330 HAZ clad with Inconel 625, however upon cooling at the phase change it is seen that 4330 clad with 17-4 PH drops to a lower CTE value for both cooling rate values.

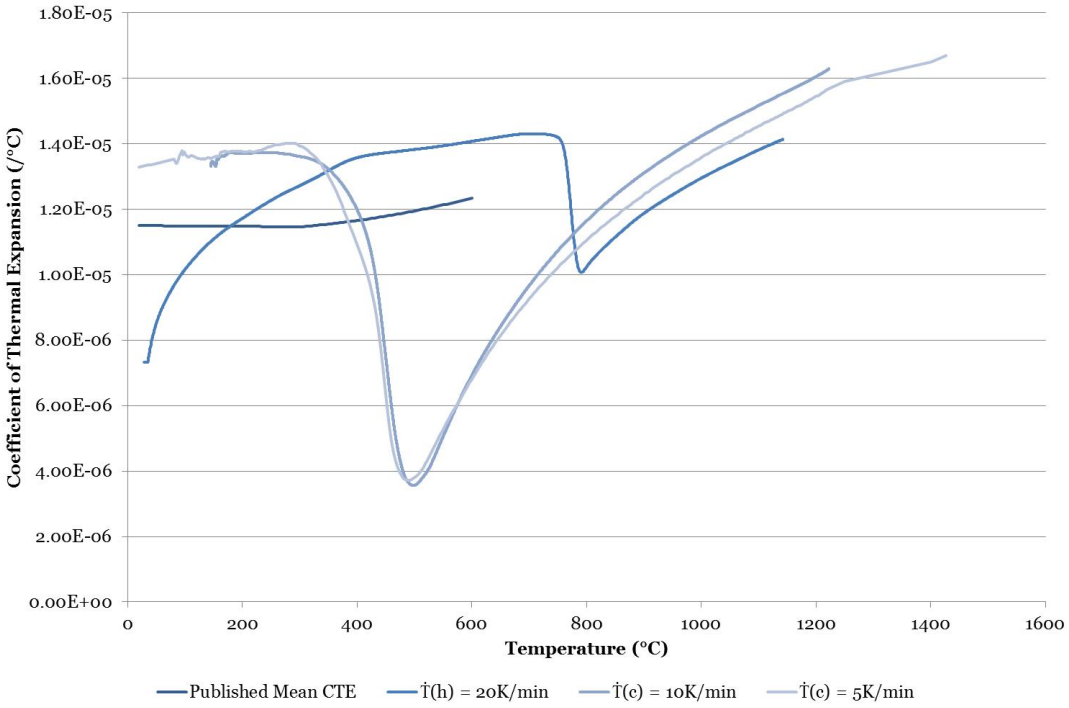

Figure 4.22: Coefficient of thermal expansion of 4330 (HAZ of 4330 clad with 17-4 PH) - Data experimentally obtained upon heating and cooling using a Netzsch DIL 402C pushrod dilatometer.

Specimens were also machined from unclad 4330 to investigate the variation in CTE due to the weld cladding process. Comparing CTE values for the unclad and clad HAZ cases in the heating phase, unclad 4330 possesses a lower CTE than both HAZ's. There are slight differences as already mentioned between the CTE values for 4330 clad with Inconel 625 and 17-4 PH, the former having the largest CTE value at room temperature, before the data sets gather towards in approaching the phase change (figure 4.23).

From figure 4.24 it is clear that Inconel 625 does not exhibit a phase change. Published and experimental data does not present the same large variations observed in the cases of 4330 shown previously. This is the expected reason for the increased correlation between simulation and experimental residual stresses throughout these studies, as 4330 and 17-4 PH are much more sensitive to material property changes

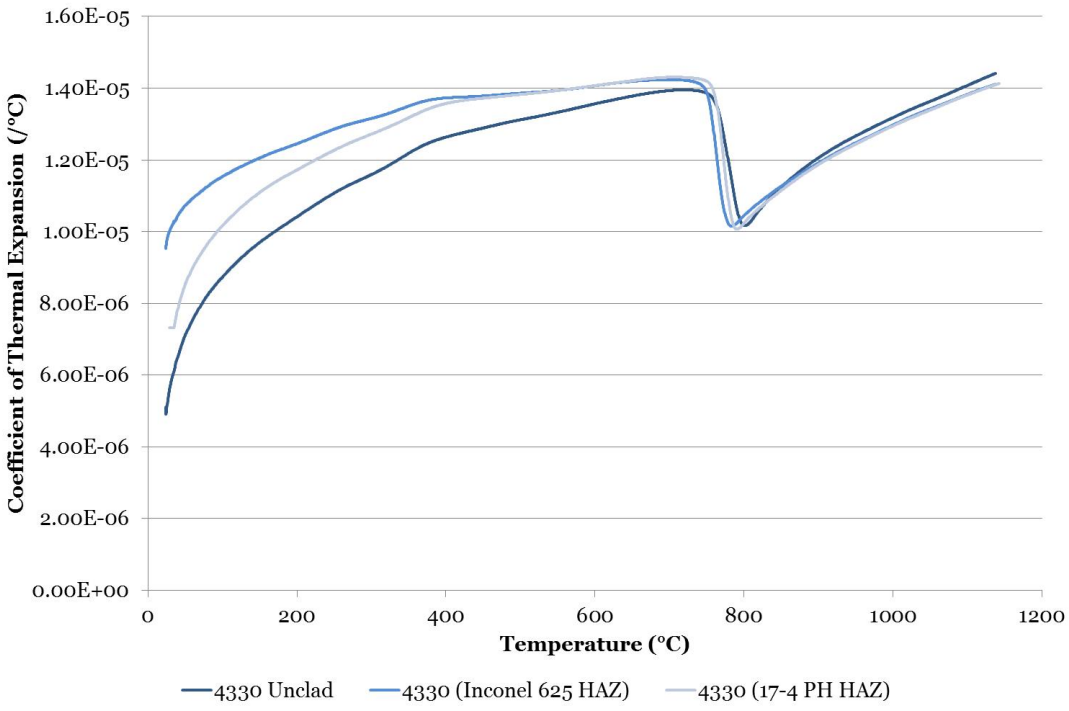

Figure 4.23: Comparison of coefficient of thermal expansion of 4330 (HAZ of 4330 clad with Inconel 625 or 17-4 PH) - Data experimentally obtained upon heating using a Netzsch DIL 402C pushrod dilatometer.

and possess more complex behaviours. Data for the heating and cooling phases of Inconel 625 on the other hand are very similar as illustrated.

An added complication arose in the initial lack of agreement in experimental and simulation residual stress states for the stainless steel clad and low alloy carbon steel substrate combination. This was due to the martensitic transformation occurring upon cooling which presents extremely large changes in material properties and the arising residual stress state. This is clearly observed in figure 4.25, with a decrease into the negative region for CTE as the martensitic transformation takes place upon cooling.

The correlation between simulation and experimental residual stresses, as well as the effects of material characteristics on residual stresses will be discussed in chapters 5, 6 and 7.

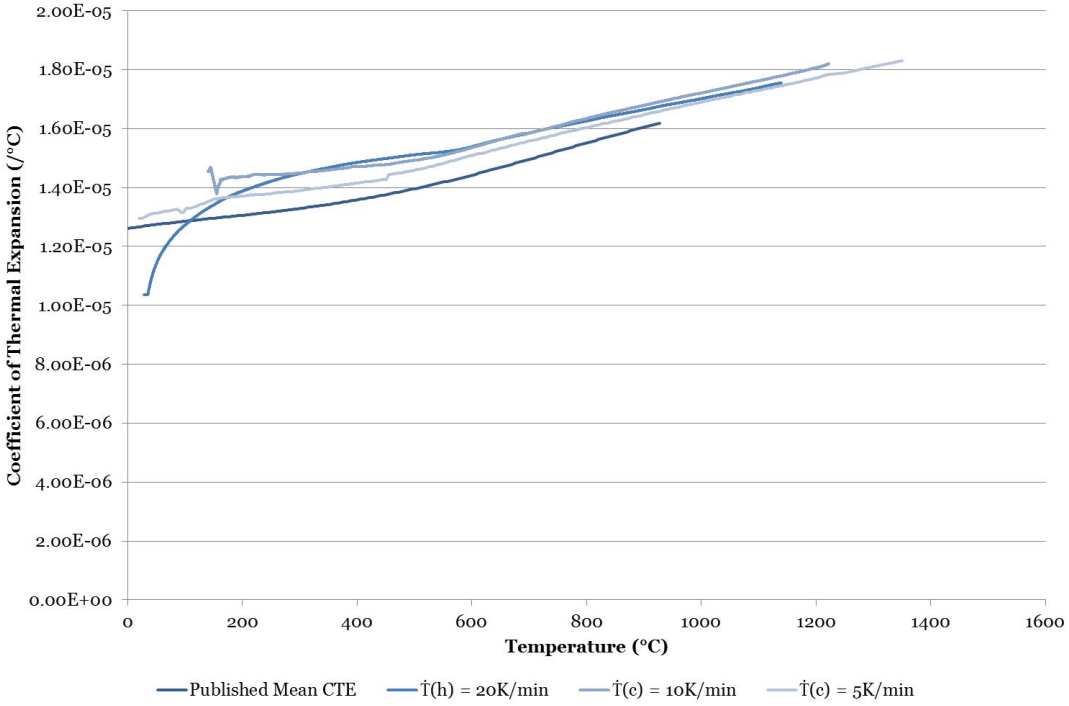

Figure 4.24: Coefficient of thermal expansion of Inconel 625 (Clad on 4330) - Data experimentally obtained upon heating and cooling using a Netzsch DIL 402C pushrod dilatometer.

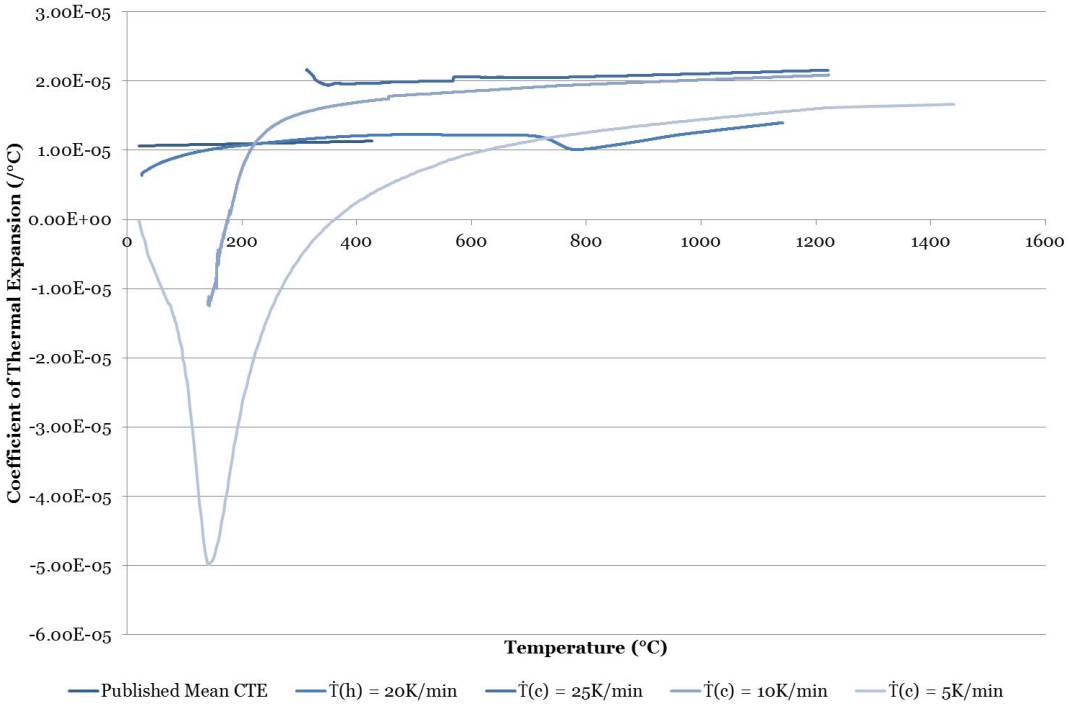

Figure 4.25: Coefficient of thermal expansion of 17-4 PH (Clad on 4330) - Data experimentally obtained upon heating and cooling using a Netzsch DIL 402C pushrod dilatometer.

4.4.3 Thermal diffusivity

Thermal diffusivity being a thermal transient property is important in temperature assessment of materials and components. Data for the materials investigated was not readily available and therefore this data was obtained using Netzsch LFA 427 laser flash apparatus using the disc specimens shown in figure 4.18 in accordance with the ASTM standard (143). These were 12.5 mm in diameter and 2-2.5 mm thick. The exact dimensions were input into the software for each particular measurement.

As the name suggests, the specimen is subjected to short bursts of high intensity radiant energy pulses and a temperature increase occurs at the rear face due to the energy absorbed on the front face. Thermal diffusivity can be calculated using the specimen thickness and the amount of time taken for the underside of the specimen temperature to reach a certain temperature. As thermal diffusivity was to be obtained over a temperature range, the standard dictates that readings should be repeated at every increment. Therefore three shots were set for every temperature increment.

Initially measurements were obtained from ambient temperature to 1200°C in 50°C increments in the heating phase alone. Latter experiments focussed on the importance of the cooling phase and therefore measurements were obtained in 100°C increments in the heating phase and 50°C increments in the cooling phase.

Figures 4.26-4.29 present the thermal diffusivity data for both 4330 $HAZ's$, Inconel 625 and 17-4 PH. Again clear variations are observed in the heating and cooling phases of 4330 and 17-4 PH, while Inconel 625 data does not vary in this manner. Large variations were present in measurements obtained post-phase change and therefore the material data presented is for the measurement deemed to provide the data with the lowest level of scatter.

For the purpose of the finite element simulation, thermal diffusivity was not directly utilised. However it is this property that is primarily measured using the laser flash apparatus. It is defined as the thermal conductivity divided by the product of the specific heat capacity and density of a solid material as noted in equation 4.1.

$$\alpha = \frac{\lambda}{C_p \cdot \rho} \tag{4.1}$$

From this relationship, the thermal conductivity could be calculated as will be presented in section 4.4.7. This relationship between material properties also provides a means of ensuring experimentally obtained data is correct.

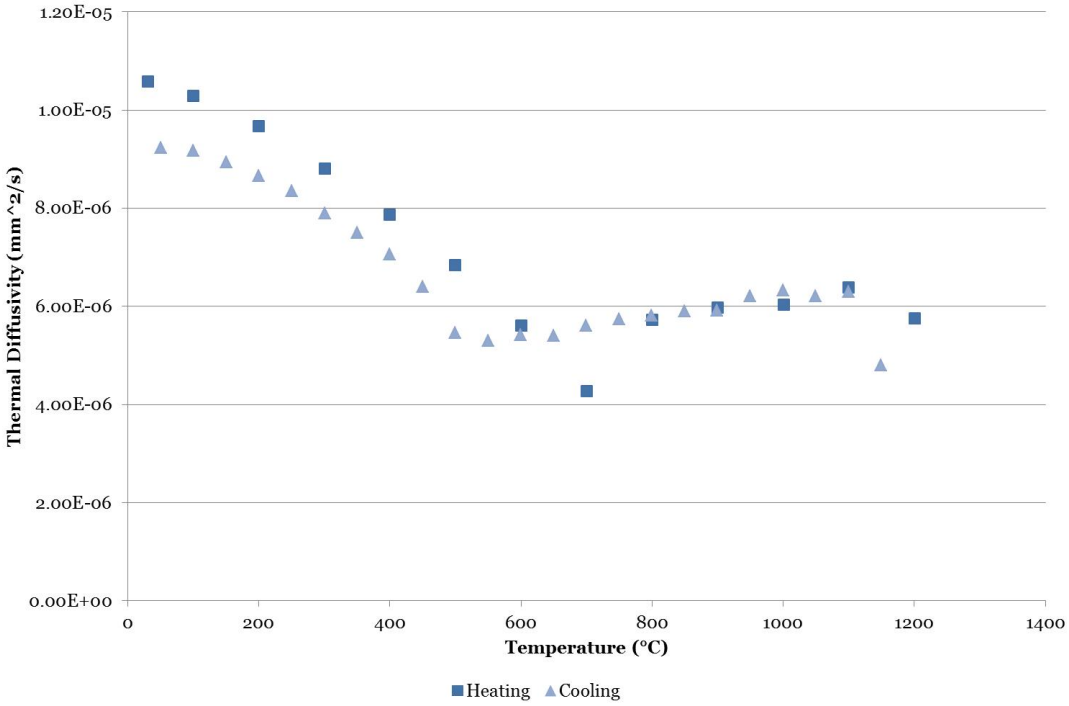

Figure 4.26: Thermal diffusivity of 4330 (HAZ of 4330 clad with Inconel 625) - Experimentally obtained using Netzsch LFA 427 laser flash apparatus.

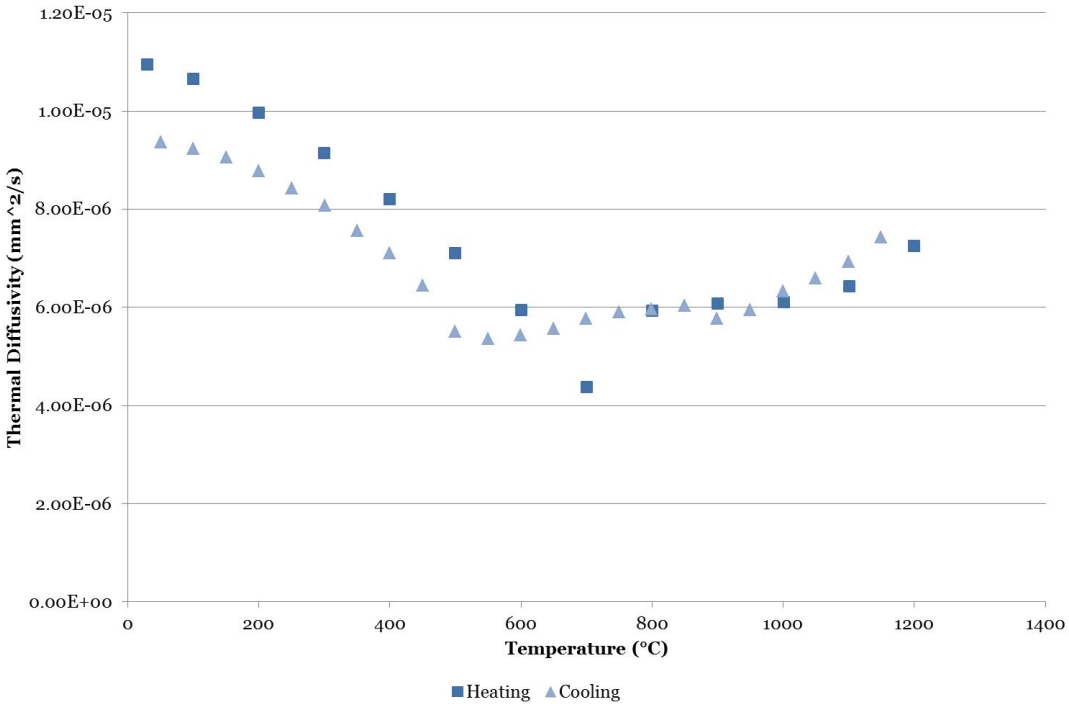

Figure 4.27: Thermal diffusivity of 4330 (HAZ of 4330 clad with 17-4 PH) - Experimentally obtained using Netzsch LFA 427 laser flash apparatus.

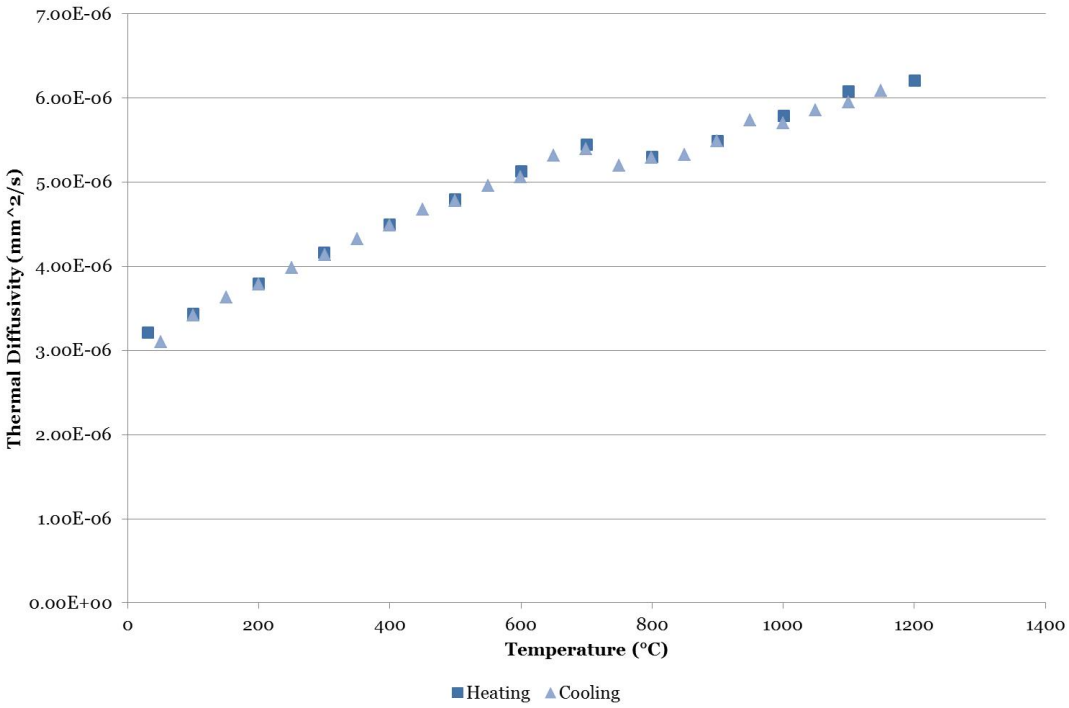

Figure 4.28: Thermal diffusivity of Inconel 625 (Clad on 4330) - Experimentally obtained using Netzsch LFA 427 laser flash apparatus.

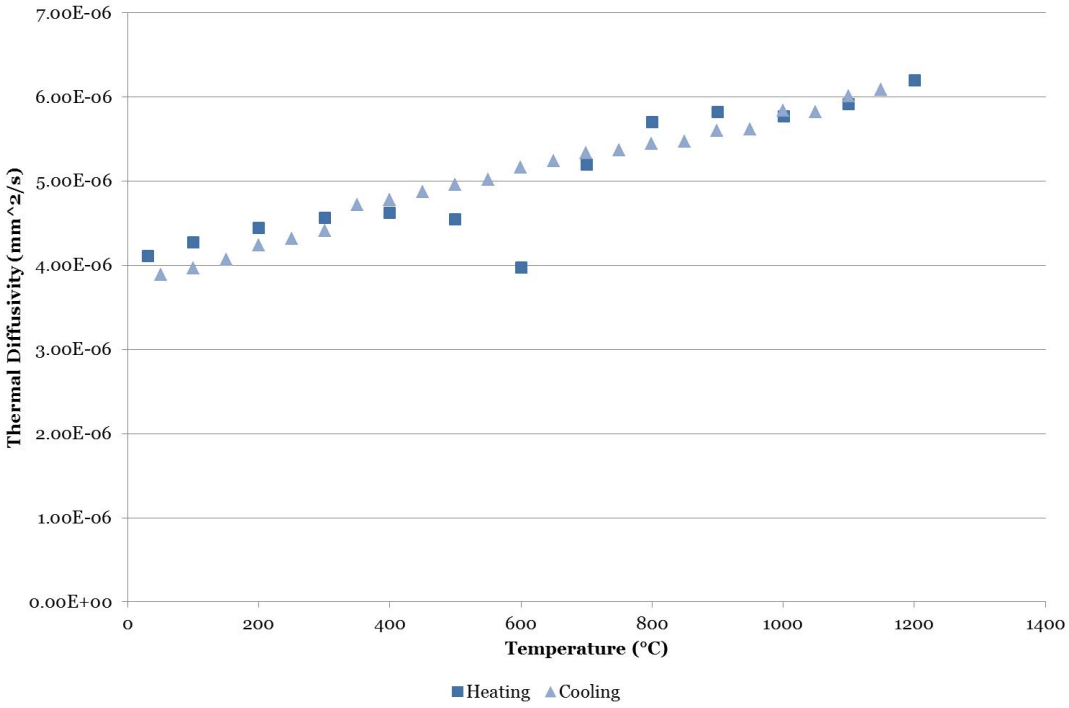

Figure 4.29: Thermal diffusivity of 17-4 PH (Clad on 4330) - Experimentally obtained using Netzsch LFA 427 laser flash apparatus.

4.4.4 Specific heat capacity

Specific heat was initially calculated using the thermal diffusivity data obtained from the laser flash equipment. However, due to issues with the data post-phase change producing large amounts of scatter, alternative measurements were obtained.

A Netzsch STA 449 F1 Jupiter simultaneous thermal analyser (*STA*) was utilised, advantageous for the combination of thermogravimetry (*TG*) and differential scanning calorimetry (*DSC*). The former observes mass changes and the latter, the method of interest in this case, observes the associated heat required to increase the temperature of a sample in comparison with a reference material. The temperature range was maintained as in previous experiments to ensure that equipment was not damaged, yet obtaining data close to the melt temperature of all materials. The areas of most interest are around the phase changes occurring in the low alloy carbon steel and stainless steel materials, and these have been adequately captured in the experiment.

Upon heating, specific heat capacity values were calculated within the software using the obtained experimental data and the specific heat capacity standard curve for the sapphire reference material. Although this was not possible upon cooling, the method could be applied manually, using the temperature dependent specific heat capacity for the standard material and the application of a logarithmic curve fit as shown in figure 4.30.

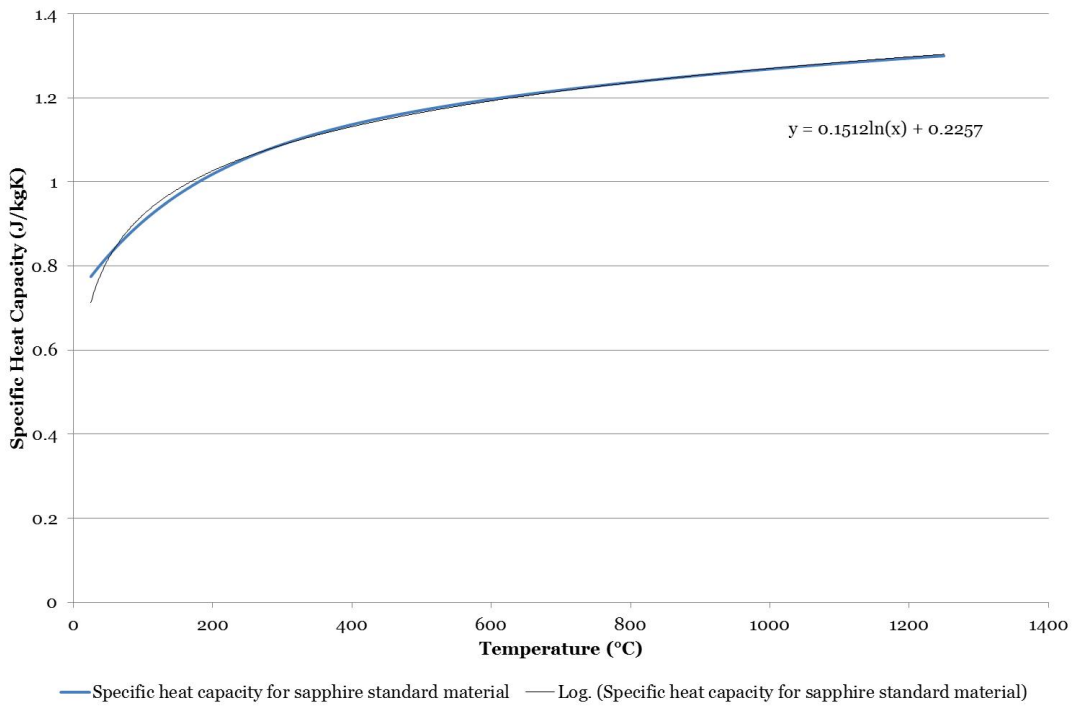

Figure 4.30: Specific heat capacity standard - Sapphire recommended in the ASTM standard (144) for the heat flow calibration standard in heating and cooling experiments.

Utilising the data for specific heat capacity of the standard material at the required temperatures allowed the use of the relationship provided in the ASTM standard (144). The specific heat capacity of the specimen using the mass and *DSC* data for the sample and standard materials could then be calculated using equation 4.2.

$$C_{p,specimen} = C_{p,standard} \cdot \frac{DSC_{specimen} \cdot W_{standard}}{DSC_{standard} \cdot W_{specimen}} \tag{4.2}$$

Figures 4.31-4.34 show the obtained experimental data for the heating of all materials and the calculated cooling data. Figure 4.34 illustrates two sharp peaks upon cooling for 17-4 PH. This was not observed in figure 4.25 for obtained *CTE* data, however limitations in reaching ambient temperature and appropriate cooling rates when using the dilatometer have been discussed. Therefore it would be desirable to further investigate the behaviour of 17-4 PH upon cooling to ensure thorough understanding of the phase changes occurring and the effects on material properties.

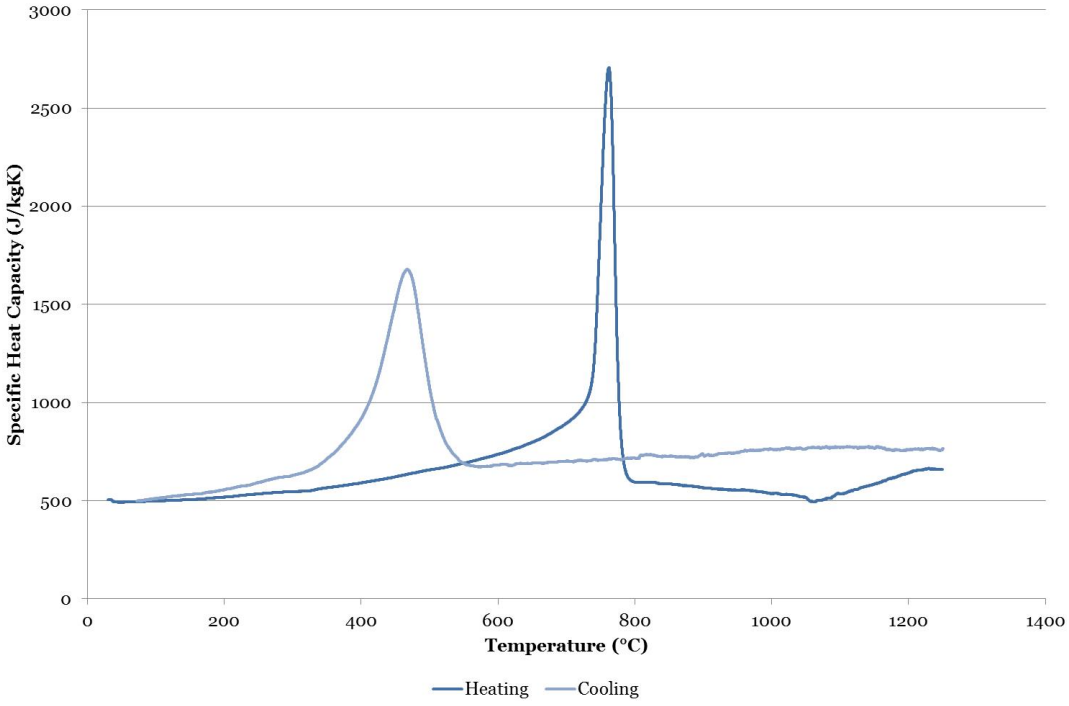

Figure 4.31: Specific heat capacity of 4330 (HAZ of 4330 clad with Inconel 625) - Experimentally obtained using a Netzsch STA 449 F1 Jupiter simultaneous thermal analyser.

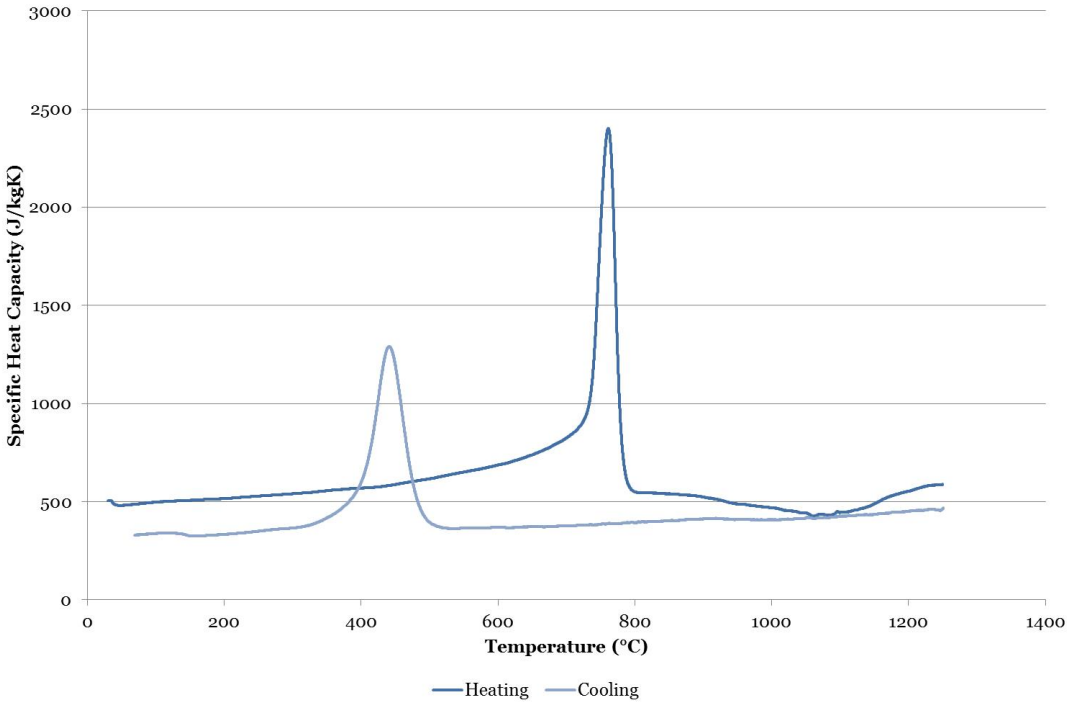

Figure 4.32: Specific heat capacity of 4330 (HAZ of 4330 clad with 17-4 PH) - Experimentally obtained using a Netzsch STA 449 F1 Jupiter simultaneous thermal analyser.

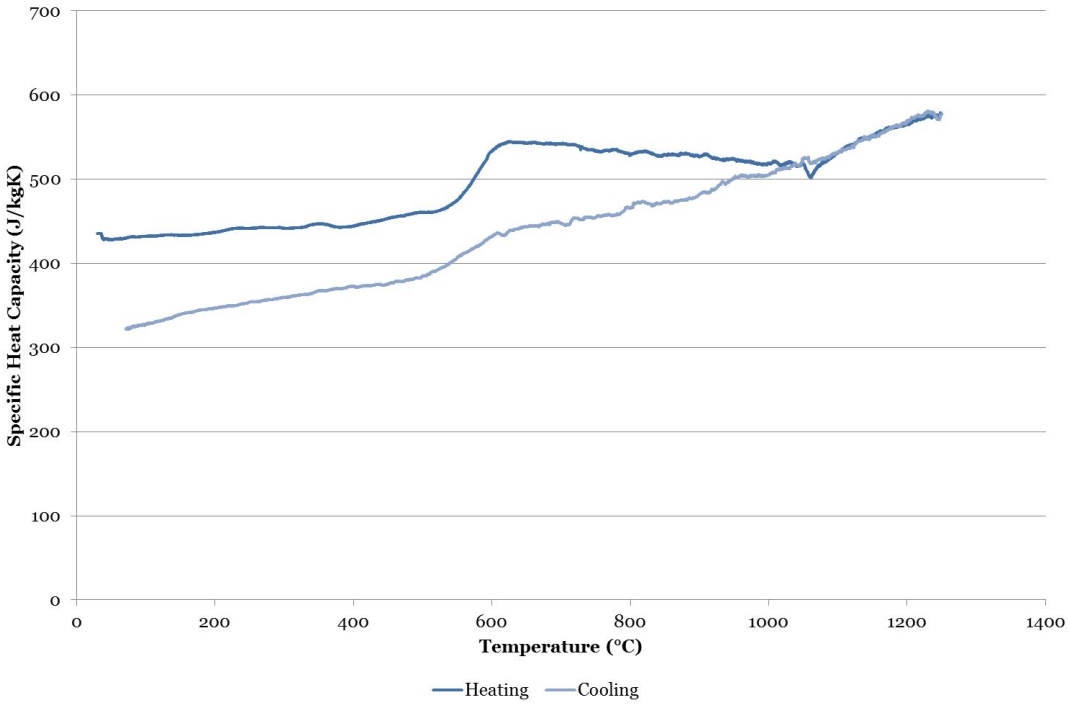

Figure 4.33: Specific heat capacity of Inconel 625 (Clad on 4330) - Experimentally obtained using a Netzsch STA 449 F1 Jupiter simultaneous thermal analyser.

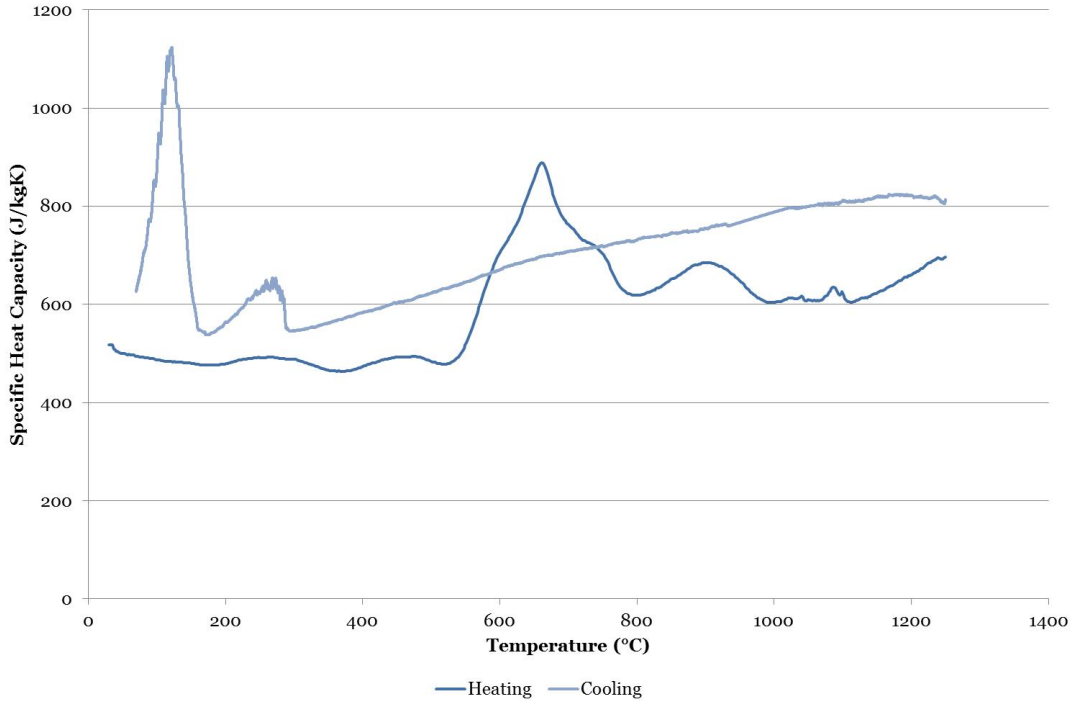

Figure 4.34: Specific heat capacity of 17-4 PH (Clad on 4330) - Experimentally obtained using a Netzsch STA 449 F1 Jupiter simultaneous thermal analyser.

4.4.5 Density

Published data for the density of the materials was obtained and plotted. Using the data obtained from dilatometry experiments, described in section 4.4.2, it is possible to calculate the density of a material at a particular temperature.

Calculating density for an isotropic solid is achieved using equation 4.3.

$$\rho_T = \rho_{ref} \cdot \frac{\left(1 + \frac{\Delta L_{T_{ref}}}{L_o}\right)^3}{\left(1 + \frac{\Delta L_T}{L_o}\right)^3} \tag{4.3}$$

The values obtained for temperature dependent density values for the materials under investigation are presented in figures 4.35-4.38.

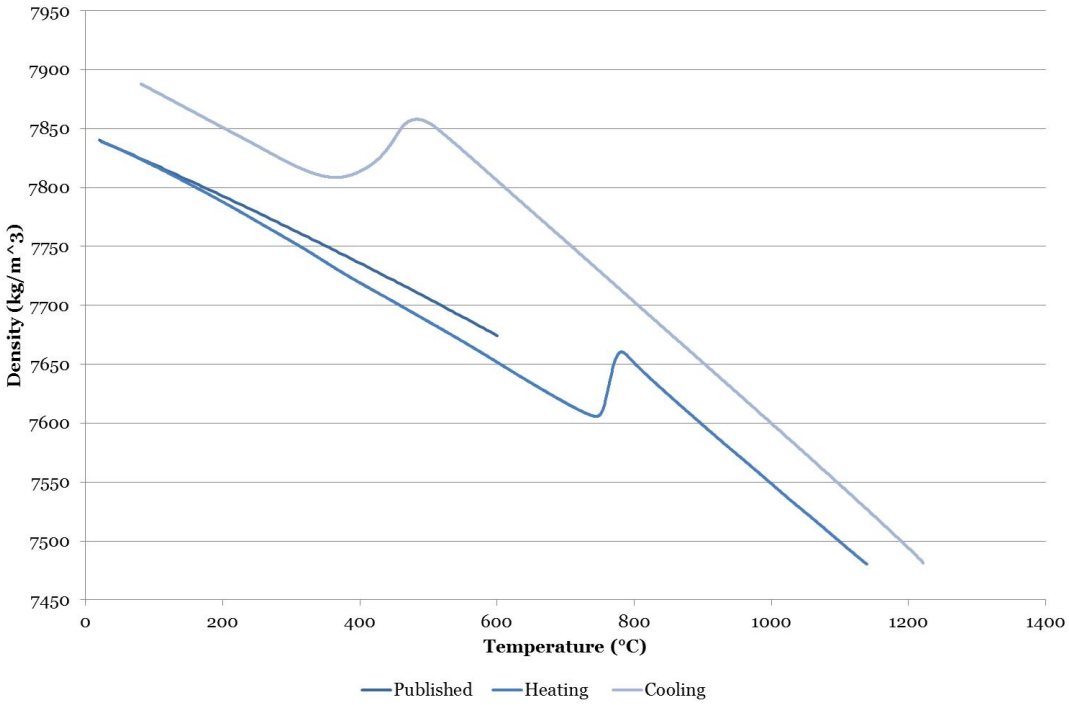

Figure 4.35: Density of 4330 (HAZ of 4330 clad with Inconel 625) - Calculated utilising room temperature density value and experimentally obtained dilatometry data.

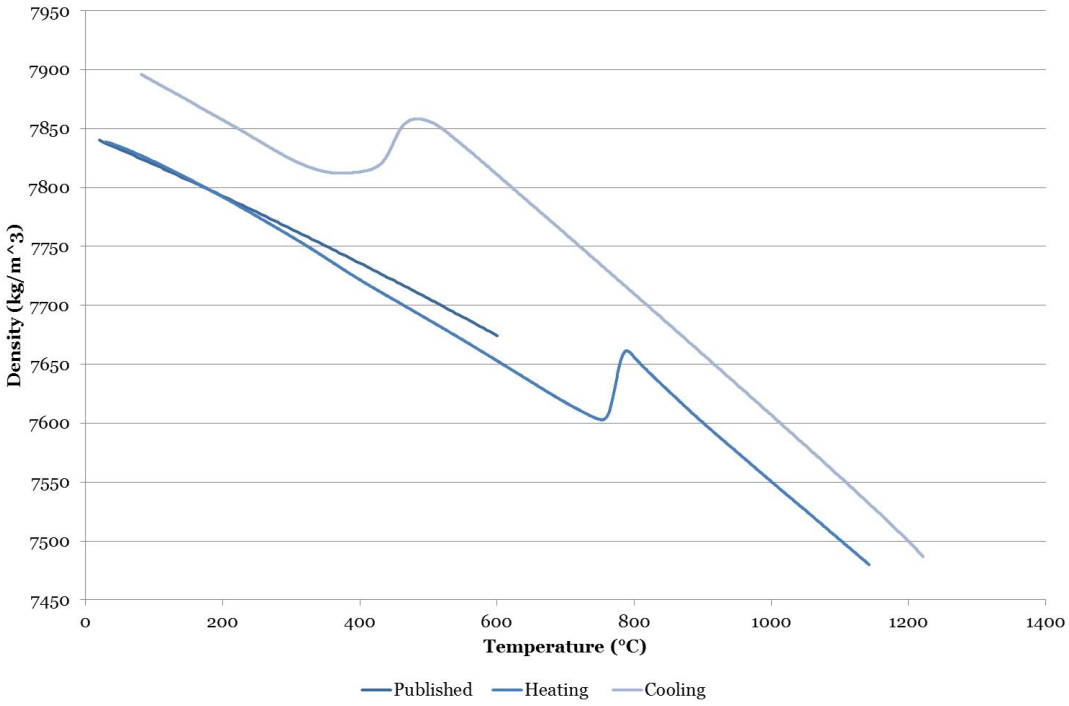

Figure 4.36: Density of 4330 (HAZ of 4330 clad with 17-4 PH) - Calculated utilising room temperature density value and experimentally obtained dilatometry data.

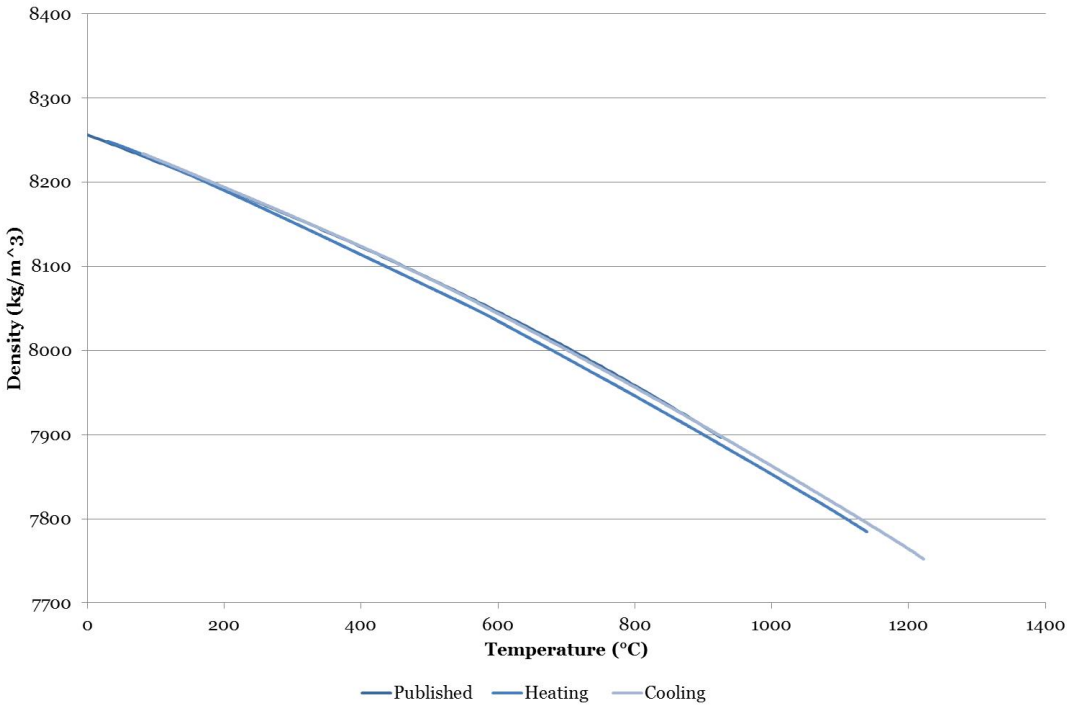

Figure 4.37: Density of Inconel 625 (Clad on 4330) - Calculated utilising room temperature density value and experimentally obtained dilatometry data.

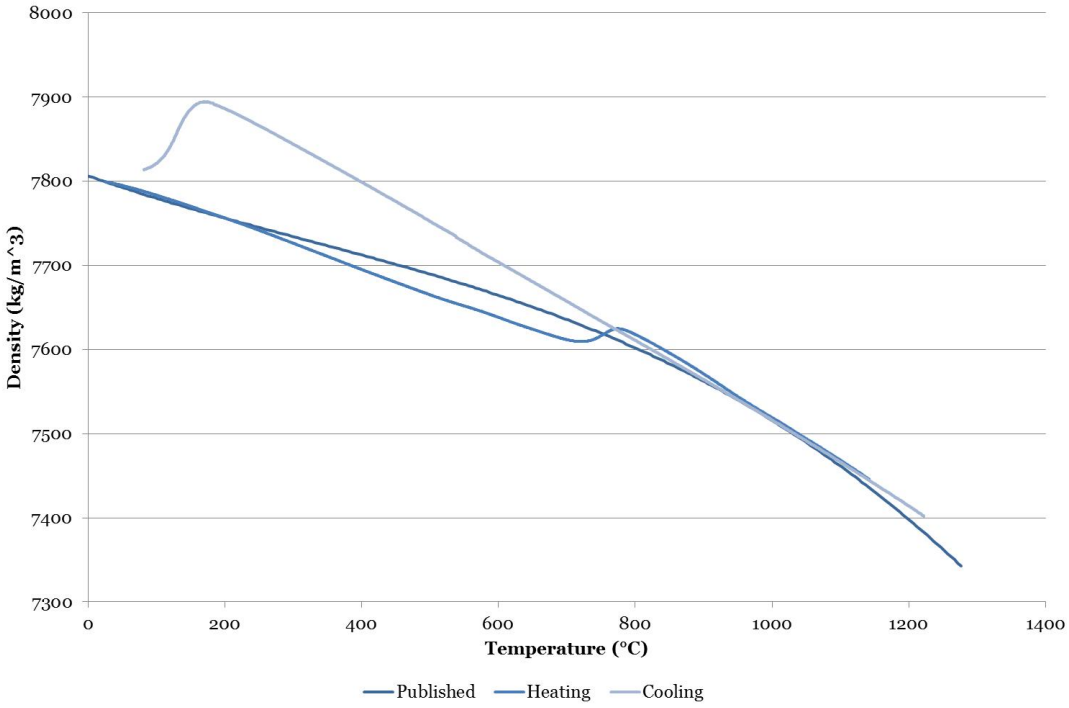

Figure 4.38: Density of 17-4 PH (Clad on 4330) - Calculated utilising room temperature density value and experimentally obtained dilatometry data.

4.4.6 Poisson's ratio

Initially Poisson's ratio was assumed constant with temperature in the finite element model which will be presented in the following chapter. However, due to the importance of capturing material property behaviour and the desire to obtain the most accurate residual stress state, Poisson's ratio variation was also utilised as provided in a material properties database (141).

Again, published data availability was limited. In the case of 4330, there was no data available and therefore the data available for 4340 was utilised. Data was extrapolated in figure 4.39 as was deemed appropriate observing the trend of the data. Data was in this case available to a high temperature.

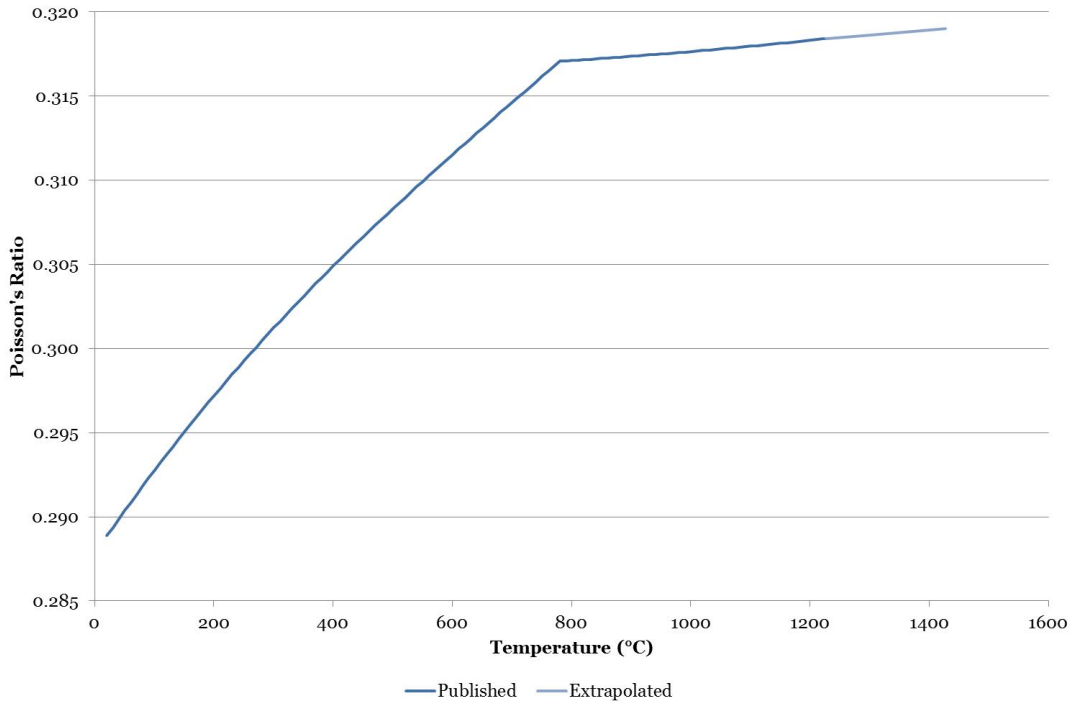

Figure 4.39: Poisson's ratio utilised in simulation for 4330 HAZ (clad with both Inconel 625 and 17-4 PH) - Published data for 4340 steel obtained from (141) extrapolated to melt temperature.

Published data was available for Inconel 625 to a fairly high temperature and the data appeared to follow an almost linear trend. Therefore extrapolation was undertaken making the assumption that this trend would continue to melt temperature as shown in figure 4.40.

Upon investigating the variation of Poisson's ratio for stainless steels, it was found that there is a complex temperature-dependence. This is illustrated in figure 4.41. The data obtained from the British Stainless Steel Association (145) for austenitic stainless steels 304, 316 and 310 highlighted an increase to a point prior to around 400°C followed by a sharp decrease to a point around 500°C. This was followed by

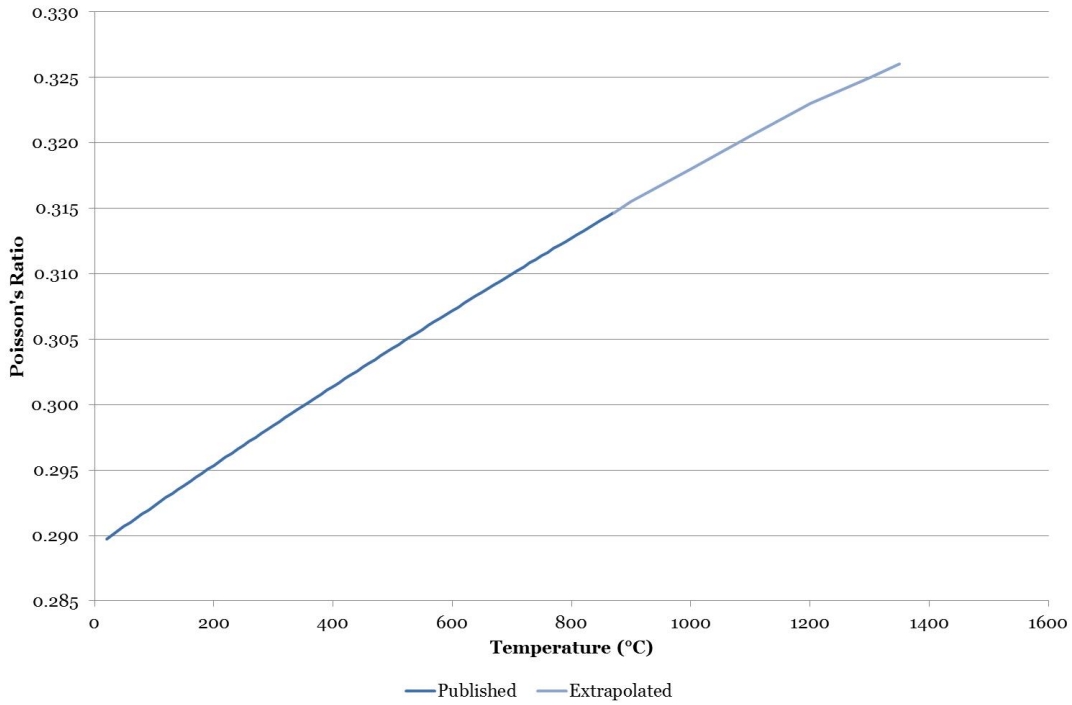

Figure 4.40: Poisson's ratio utilised in simulation for Inconel 625 - Published data for 4340 steel obtained from (141) extrapolated to melt temperature.

an increase to 600°C before the curve decreases sharply to the maximum temperature at which this data is available. Data to represent the variation of 17-4 PH, namely that available for 17-7 PH was plotted in figure 4.42 to draw comparisons in the expected form for the variation in Poisson's ratio with temperature accounting for the fluctuation around 500°C and consequent decrease.

Figure 4.42 shows the data set constructed for the variation with temperature of Poisson's ratio for 17-4 PH. Published data is available to a temperature of 481.85°C. The gradient of the curve at this point is very large and therefore extrapolation did prove difficult.

It should be highlighted that the steels investigated in the course of this research were not austenitic and that it has also been shown elsewhere that Poisson's ratio in steels continually increases with temperature (146). Therefore it is deemed inaccurate to utilise the data set created in figure 4.42 and more appropriate to in fact assume a continual increase in Poisson's ratio to a maximum value of 0.5 in the plastic state.

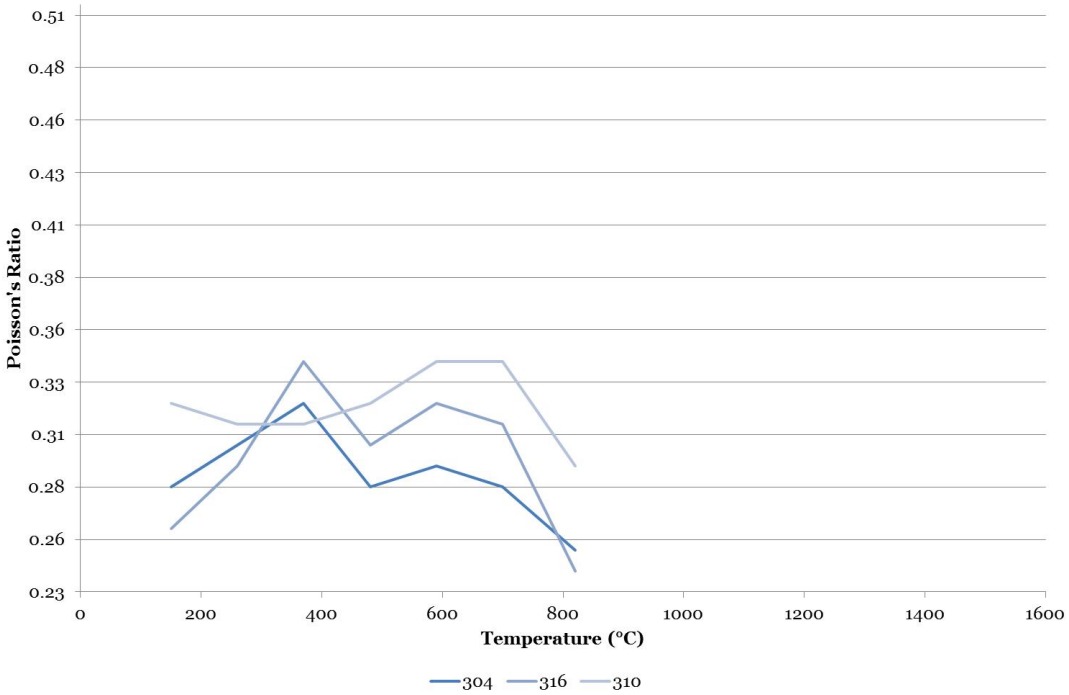

Figure 4.41: Poisson's ratio trends for stainless steel - Published data for 304, 316 and 310 stainless steel obtained from (145).

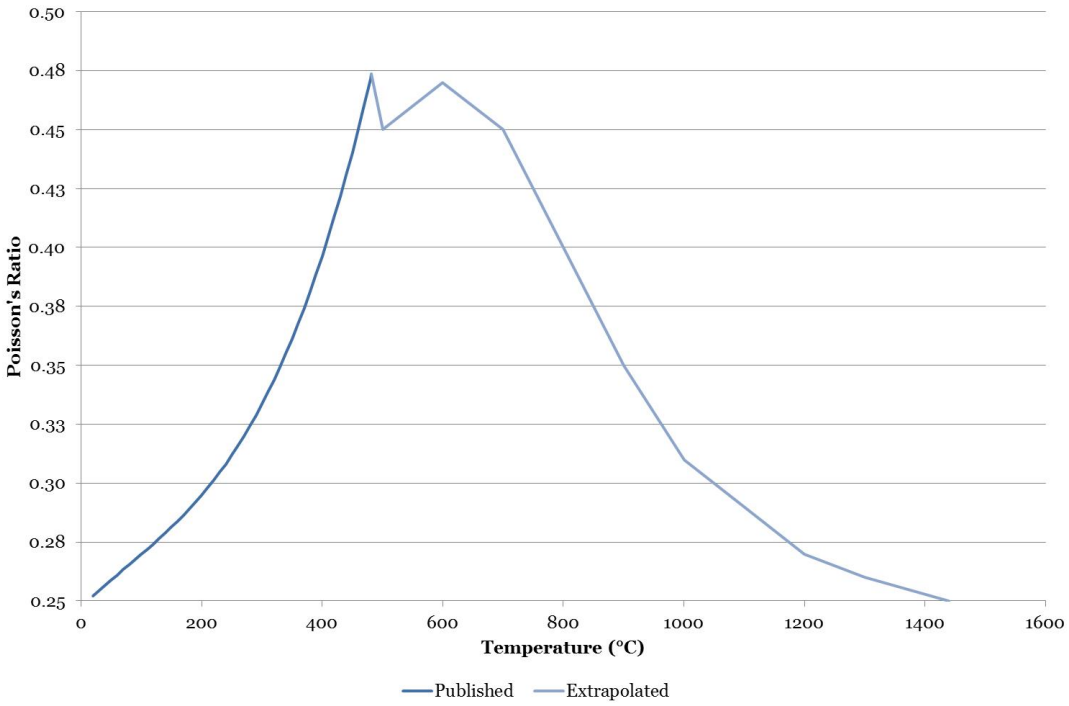

Figure 4.42: Poisson's ratio variation constructed for 17-4 PH - Published data for 17-7 PH steel obtained from (141) extrapolated to melt temperature.

4.4.7 Thermal conductivity

Thermal conductivity λ can be calculated using the relationship 4.4 previously presented in section 4.4.3 using thermal diffusivity, specific heat capacity and density.

$$\lambda = \alpha \cdot C_p \cdot \rho \tag{4.4}$$

Utilising the data obtained experimentally, temperature dependent thermal conductivity values calculated are shown in figures 4.43-4.46. Figures 4.43 and 4.44 illustrate phase changes at the same temperature upon cooling for 4330 *HAZ* when clad with both materials. However, it is noticeable that the maximum values of thermal conductivity reached upon cooling differ. Heating data is similar in both 4330 *HAZ* cases, though phase changes are not visible as was the case in the *CTE* data for example. Slight fluctuations are visible in phase change regions in figure 4.45 showing data obtained for Inconel 625. Heating and cooling data does not differ greatly for Inconel 625 as also previously observed in other obtained properties. Figure 4.46 showing data obtained for 17-4 PH indicates two possible phase changes upon heating, although as mentioned issues were encountered with data scatter post-phase change. Slight peaks are observed in thermal diffusivity data for 4330 HAZ as shown in figures 4.26 and 4.27 and so further testing would allow evaluation of the data to deduce whether two peaks are in fact arising in thermal conductivity data upon heating of 17-4 PH. As was highlighted in figure 4.34, two peaks were also observed upon cooling in the specific heat capacity data. Due to the use of this data in calculating thermal conductivity these peaks are also present in this data.

As observed in (140), effects of phase changes are notable also in certain materials. Published data plotted alongside the experimentally obtained data highlights the inability of the published data to again accurately characterise the materials under investigation.

Experimental results for 4330 highlight the variation in heating and cooling data, both material data sets producing a gradual decrease upon heating, with a notable rapid increase at high temperature for the HAZ 4330 when clad with 17-4 PH. Upon cooling, the phase change around 400°C is heavily reflected in thermal conductivity values, especially again in the case of the HAZ 4330 when clad with 17-4 PH. The linear trend observed in the published data is roughly followed by the Inconel 625 upon heating and cooling, however variations in data values are observed in heating and cooling, along with observable minor peaks around 700°C. The data obtained for 17-4 PH illustrates that the data is highly sensitive to phase change effects reflected in two peaks upon heating (around 700°C and 900°C) and two peaks upon

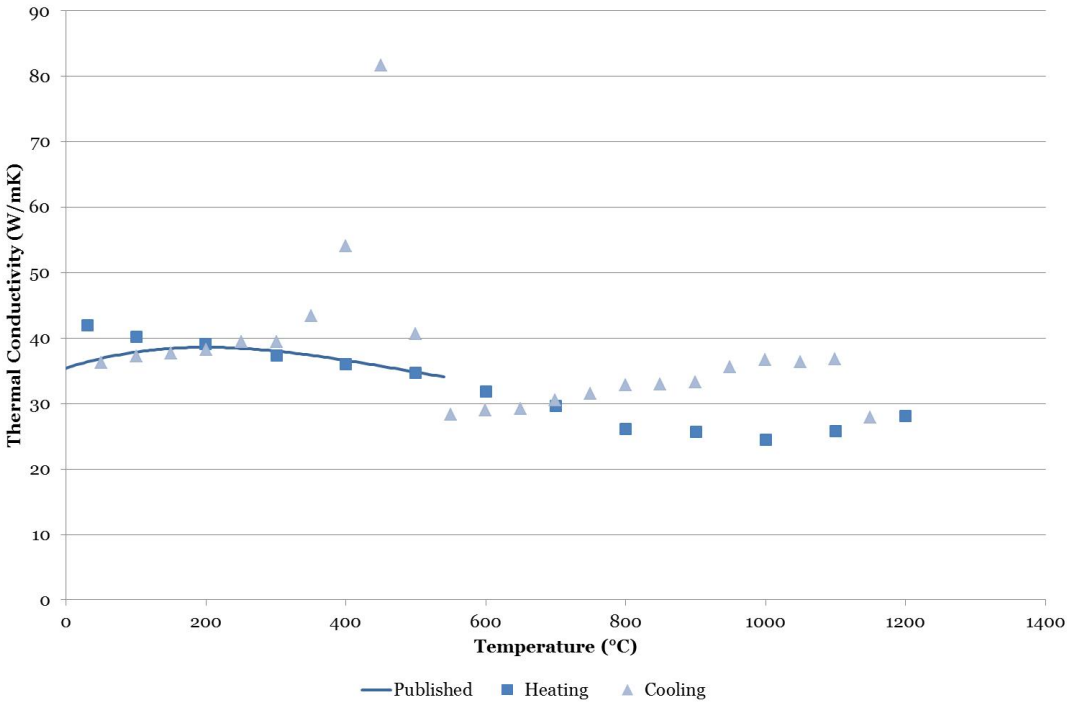

Figure 4.43: Thermal conductivity of 4330 (HAZ of 4330 clad with Inconel 625) - Calculated using experimentally obtained thermal diffusivity, specific heat capacity and calculated density.

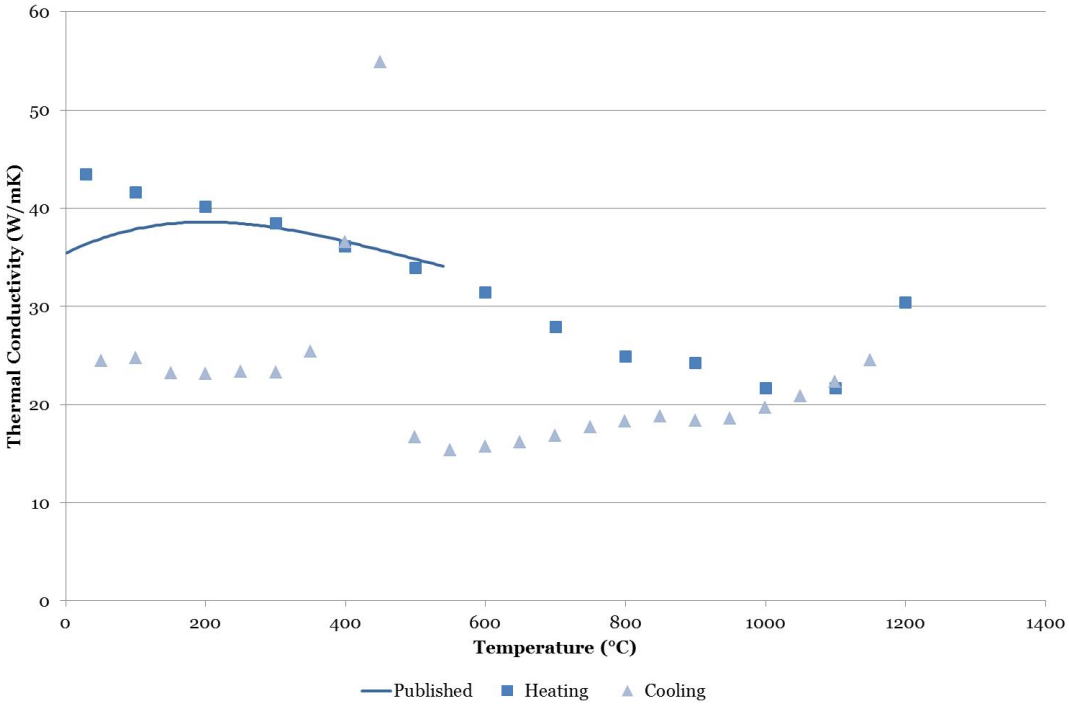

Figure 4.44: Thermal conductivity of 4330 (HAZ of 4330 clad with 17-4 PH) - Calculated using experimentally obtained thermal diffusivity, specific heat capacity and calculated density.

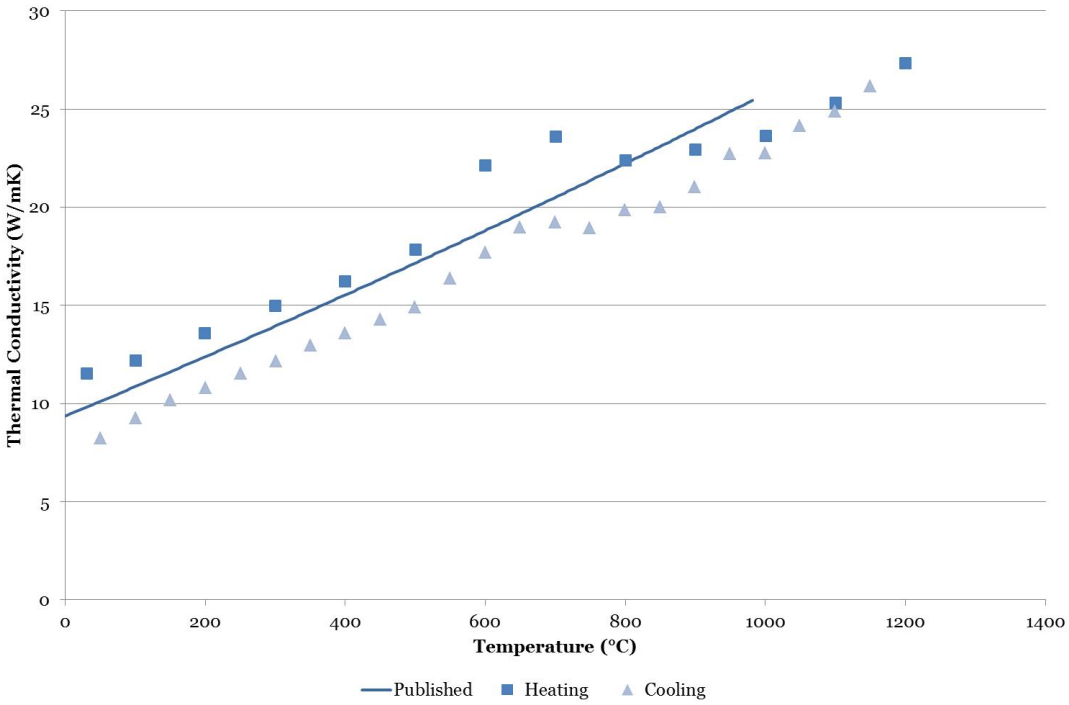

Figure 4.45: Thermal conductivity of Inconel 625 (Clad on 4330) - Calculated using experimentally obtained thermal diffusivity, specific heat capacity and calculated density.

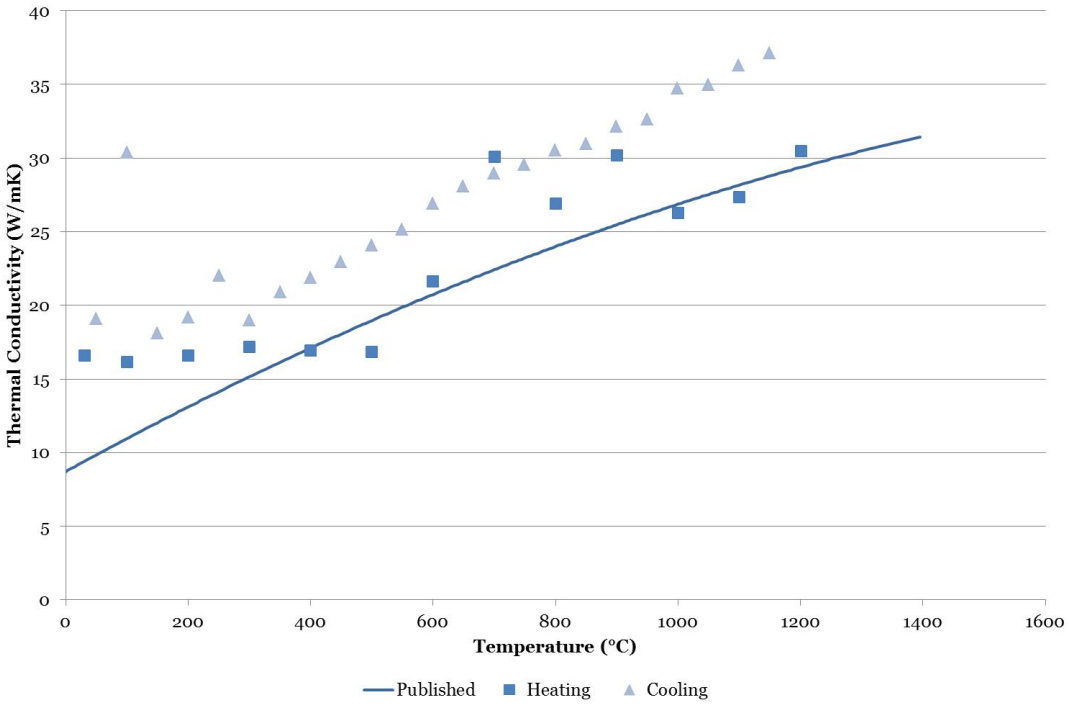

Figure 4.46: Thermal conductivity of 17-4 PH (Clad on 4330) - Calculated using experimentally obtained thermal diffusivity, specific heat capacity and calculated density.

cooling (around 100°C and 250°C), with the most pronounced during the martensitic transformation upon cooling.

4.4.8 Hardness

Measurement of micro-hardness values throughout the clad, HAZ and substrate were obtained for both clad and substrate combinations using a Vickers diamond indenter and a 200 g load.

Variation in hardness values is indicative of the effects of the welding process on arising material properties. Factors such as pre-heat temperature, heat input during welding, cooling rate and post-weld heat treatment will potentially alter material properties resulting from the welding process. The combination of clad and substrate materials will also play a role in the resulting material properties. Generally, welding high-strength low alloy steels is known to result in high hardness values often also indicative of low ductility and therefore obtaining measurements of the resulting hardness values due to the weld cladding process was especially necessary.

In the case of an Inconel 625 clad on 4330, chromium dilution from the clad material into the HAZ will increase hardness values in the HAZ, in turn presenting issues with increased risk of cracking. Alloy segregation in the HAZ due to solid-state diffusion was highlighted in section 4.3.1 and this in turn presents variation in hardness values depending on the levels of chromium and nickel present. These elements possess high hardenability characteristics and therefore hardness values increased with increased presence of these elements.

Figure 4.47 shows the extreme variation in hardness values in alloy lean and alloy rich areas. To decrease hardness values and to minimise the variation in values in the substrate, weld procedure refinement is required. Higher hardness values were found in the alloy rich areas, the areas of lighter banding, as shown in figure 4.47. It is suspected that the diffusion of chromium from the clad layer into the substrate encourages the formation of martensite in the HAZ which will create a brittleness of the material. Although these hardness values are extremely high in the alloy rich areas, the average HAZ hardness values will be lower and therefore the effects of the extreme hardness values are likely be less influential. Refinement of the weld procedure would allow these values to be decreased to abide by certain requirements, for example the standards as defined by NACE International, the National Association of Corrosion Engineers (110).

The variation in hardness values for an Inconel 625 clad, through the clad layer and traversing into the HAZ is shown in figure 4.48. More extreme increases in hardness values are observed in this material combination upon crossing the boundary

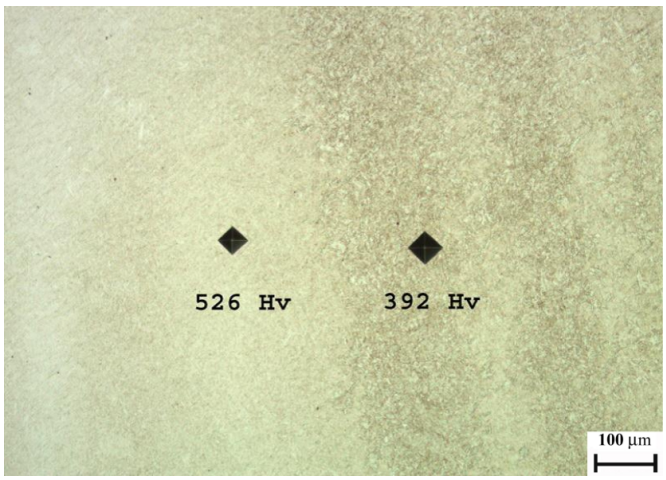

Figure 4.47: Extreme hardness variation in HAZ (Clad with Inconel 625) - ID: Strath05 - Measured using a Vickers diamond indenter with a 200 g load.

between the clad and substrate materials.

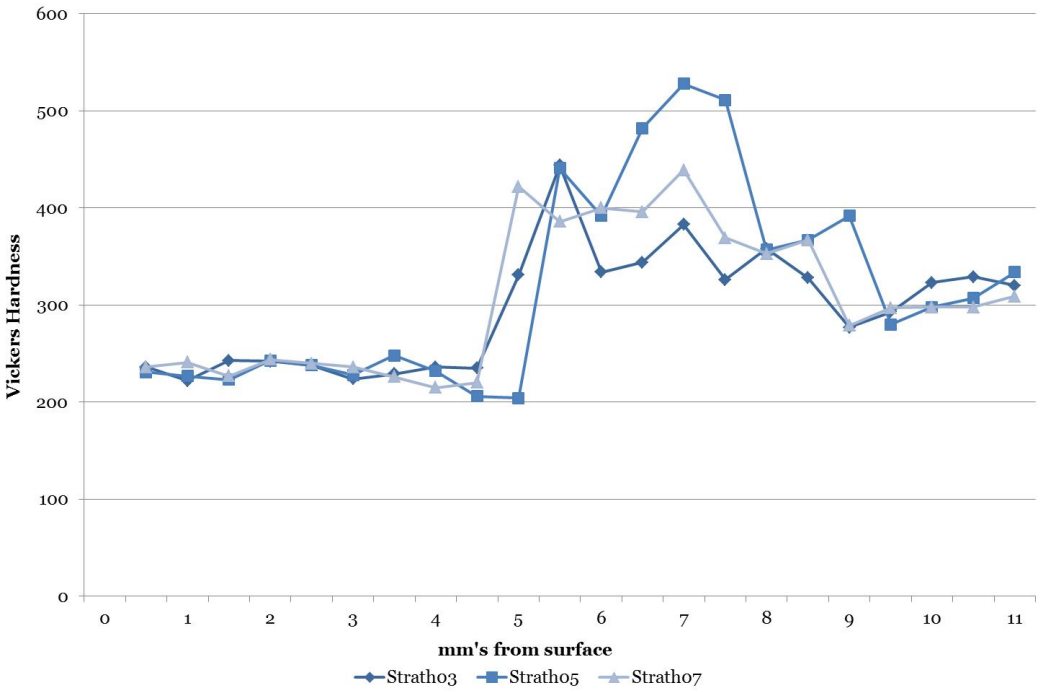

Figure 4.48: Hardness variation in Inconel 625 clad layer and 4330 HAZ - Measured using a Vickers diamond indenter with a 200 g load.

Variation in hardness values through a 17-4 clad layer and into the 4330 *HAZ* is shown in figure 4.49. Throughout the two clad passes variations in hardness values can be observed, with higher levels in the first pass.

Increased hardness values are often observed in the *HAZ* of the substrate material due to welding processes due to the quenching effect. The hardness measurements presented confirm high hardness values in the *HAZ*, with a greater degree of vari-

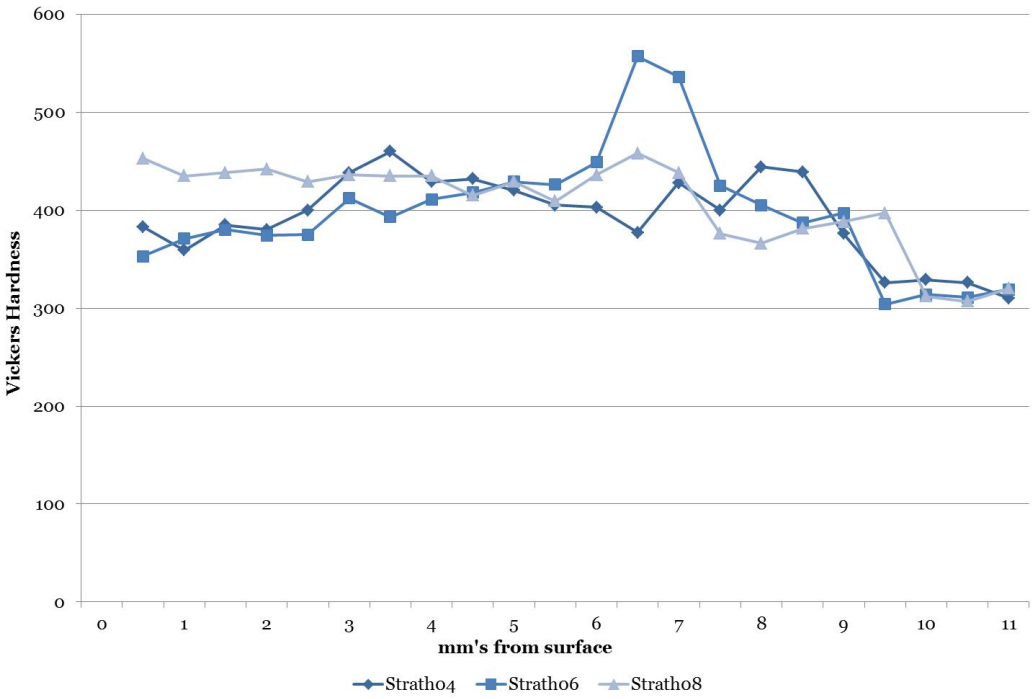

Figure 4.49: Hardness variation in 17-4 PH clad layer and 4330 HAZ - Measured using a Vickers diamond indenter with a 200 g load.

ation in the case of an Inconel 625 clad on 4330 due to the greater degree of material dissimilarity. Regarding pre-heat temperatures, higher hardness values were observed in samples Strath05 and Strath06. As noted in table 3.3, these samples were clad with the lower pre-heat temperature of 150°C and were not subjected to post-weld heat treatment (*PWHT*). A lower pre-heat temperature increases the effect of quenching on the *HAZ*. Values in these samples exceeded 500 HV. Such high hardness values reduce the toughness of the material, a cause for concern due to the consequential increase in brittleness.

In a tensile stress field, high hardness regions could prove problematic due to resulting decreased toughness. *NACE* standards, relating to oil and gas applications (110), state that welding processes should be controlled such that hardness values in the weldment, HAZ and base metal do not exceed 22 HRC, approximately 250 HV.

4.4.9 Yield stress

Residual stresses are greatly influenced by mechanical properties due to the correlation between, for example, yield stress and strain hardening and the magnitude of residual stresses (140).

The large selection of low alloy steels presents a wide range of potential material properties. As shown in figure 4.50, for 4330 low alloy carbon steel yield and tensile strength values can vary greatly although all grades of 4330 have the same chemical elements. The resulting properties are dependent on the production process of the material, with slow cooling often implemented to avoid the formation of stress cracks due air hardening. Heat treatment processes can further improve the properties of the material, for example tempering.

Published yield stress values for 4330 low alloy carbon steel values were obtained through manipulation of 4340 published data from the material properties database (141). A multiplication factor was calculated based on knowledge of the yield stress for 4330 at room temperature and the entire data set for 4330 was then produced using this multiplication factor and the published data for 4340 to obtain representative data. The published data for 4340 along with the calculated data for 4330 is shown in figure 4.51. As can be seen from this figure values at melt temperature are assumed to be the same.

Preparation of specimens for mechanical property testing With reference to figure 3.12, it can be seen that limited material was available from which to manufacture specimens to obtain mechanical properties. Flat tensile specimens were machined from the clad and HAZ layers, which were extracted as before using a wire EDM.

Due to the residual stresses present in the layers, a number of specimens experienced deformation during machining. Straightening of the specimens would entail alteration of the residual stresses within the material and as highlighted above, residual stresses are strongly correlated with the mechanical properties of the material. In the case of extreme bowing, the specimens were straightened manually in a vice and it is noted that cold working of this type will induce residual stresses. Further specimen deformation was experienced during grinding of the specimens. Distortion during machining due to the relief of residual stresses is common and is the basis of the contour and slitting methods, however heating during the machining process may also influence distortion. Specimen bowing was reduced through the replacement of the cooling jet with a larger size jet to enable cooling of the entire specimen surface.

The specimen geometry was obtained from the ASTM standard (148). Two tabs at either end of the specimen allowed gripping of the specimen with the gauge length in

Standard Designation	Grade, Class, Type, Symbol or Name	Steel Number	UNS Number	Product Form/Heat Treatment	Thickness		Yield Strength, min		Tensile Strength, min		Elongation	Other
					t, mm	t, in.	N/mm² or MPa	ksi	N/mm² or MPa	ksi	min, %	
ASTM A 958-00	SC 4330 Class 65/35	---	---	NT	---	---	240	35	450	65	24	---
	SC 4330 Class 70/36	---	---	NT	---	---	250	36	485	70	22	---
	SC 4330 Class 80/40	---	---	NT	---	---	275	40	550	80	18	---
	SC 4330 Class 80/50	---	---	NT	---	---	345	50	550	80	22	---
	SC 4330 Class 90/60	---	---	NT or QT	---	---	415	60	620	90	18	---
	SC 4330 Class 105/85	---	---	QT	---	---	585	85	725	105	17	---
	SC 4330 Class 115/95	---	---	QT	---	---	655	95	795	115	14	---
	SC 4330 Class 130/115	---	---	QT	---	---	795	115	895	130	11	---
	SC 4330 Class 135/125	---	---	QT	---	---	860	125	930	135	9	---
	SC 4330 Class 150/135	---	---	QT	---	---	930	135	1035	150	7	---
	SC 4330 Class 160/145	---	---	QT	---	---	1000	145	1105	160	6	---
	SC 4330 Class 165/150	---	---	QT	---	---	1035	150	1140	165	5	---
	SC 4330 Class 210/180	---	---	QT	---	---	1240	180	1450	210	4	---
JIS G 5111:1991	SCNCrM 2A	---	---	NT	---	---	590	---	780	---	9	223 HB min
	SCNCrM 2B	---	---	QT	---	---	685	---	880	---	9	269 HB min
DIN 17205:1992	GS-33 CrNiMo 7 4 4	1.6740	---	NT	≤ 150	---	600	---	800-950	---	12	see standard for impact data
					150 < t ≤ 400	---	550	---	750-900	---	12	
	GS-33 CrNiMo 7 4 4, Class I	1.6740	---	QT	≤ 100	---	700	---	850-1000	---	16	
	GS-33 CrNiMo 7 4 4, Class II	1.6740	---	QT	≤ 100	---	950	---	1050-1250	---	10	
	GS-33 CrNiMo 7 4 4, Class I	1.6740	---	QT	100 < t ≤ 250	---	700	---	850-1000	---	14	
	GS-33 CrNiMo 7 4 4, Class I	1.6740	---	QT	250 < t ≤ 400	---	650	---	800-950	---	10	
AFNOR NF A 32-054:1994	G30NiCrMo8	---	---	N	28 ≤ t < 50	---	550	---	750	---	15	32 J at RT
					50 ≤ t <100	---	550	---	750	---	12	32 J at RT
					100 ≤ t < 150	---	550	---	750	---	12	32 J at RT
					150 ≤ t < 250	---	500	---	700	---	12	32 J at RT
				QT2 (TR2)	28 ≤ t < 50	---	700	---	850	---	15	50 J at RT
					50 ≤ t <100	---	700	---	850	---	14	50 J at RT
					100 ≤ t < 150	---	650	---	850	---	12	35 J at RT
					150 ≤ t < 250	---	650	---	820	---	10	27 J at RT

Figure 4.50: Variation in mechanical properties of cast alloy steels - Figure modified from (147).

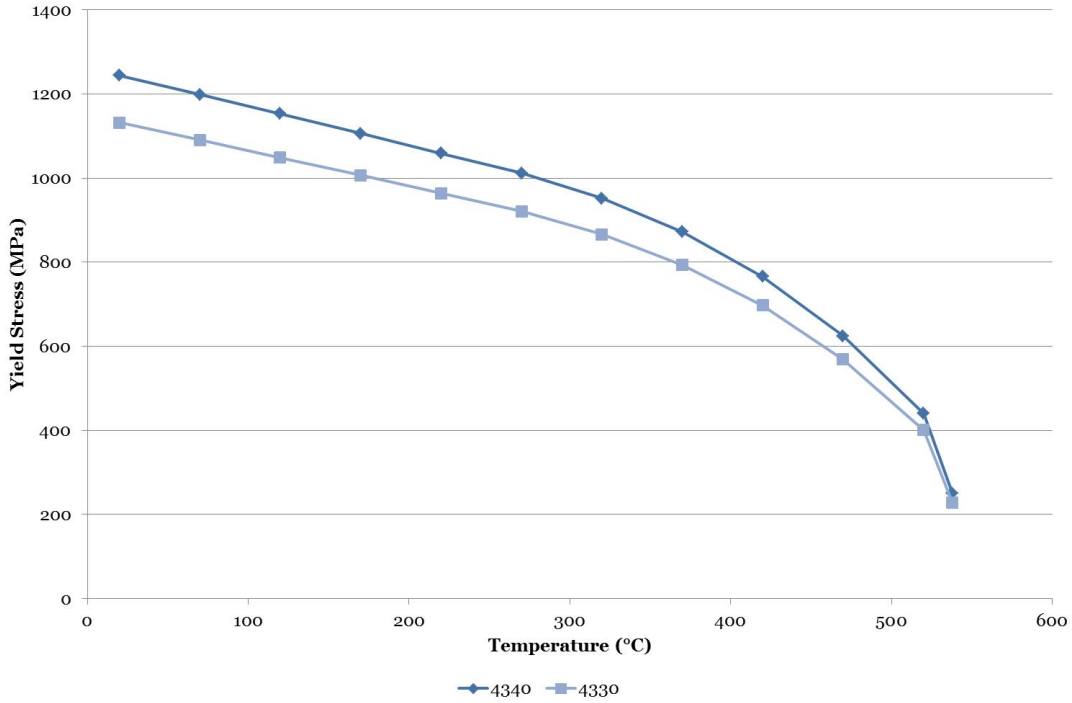

Figure 4.51: Comparison of yield stress values of published 4340 data and calculated 4330 data - Utilising multiplication factor accounting for known room temperature yield stress value of 4330 low alloy carbon steel.

the centre providing a region of uniform stress distribution and the eventual failure region. The specimen geometry and dimensions are shown in figure 4.52.

To avoid failure outwith the gauge length, the radii and surface roughness of the specimen were considered. Failure at the radii could occur if this dimension were to be too small and likewise too high a surface roughness could encourage failure outwith the gauge length. Surface roughness should therefore be minimised in the gauge length region and at the radii of the meeting of the gauge length and the tabs to ensure that failure is not encouraged through stress concentrations, but rather through internal defects. This is highlighted in the ASTM standard as being of particular importance for high strength materials and therefore a surface roughness value of $R_a = 2\mu m$ was adopted as desirable in the gauge length and at the radii of these specimens.

Specimen dimensions were measured to ensure consistency and adherence to the ASTM standard. The location of these measurements in illustrated in figure 4.53. These measurements would also provide the required cross-sectional area for the calculation of the ultimate tensile strength (UTS).

An example of the obtained values for the 17-4 PH specimens and corresponding 4330 HAZ are tabulated in table 4.8. An analysis of the uncertainties during testing will be presented in the discussion of the tensile testing program.

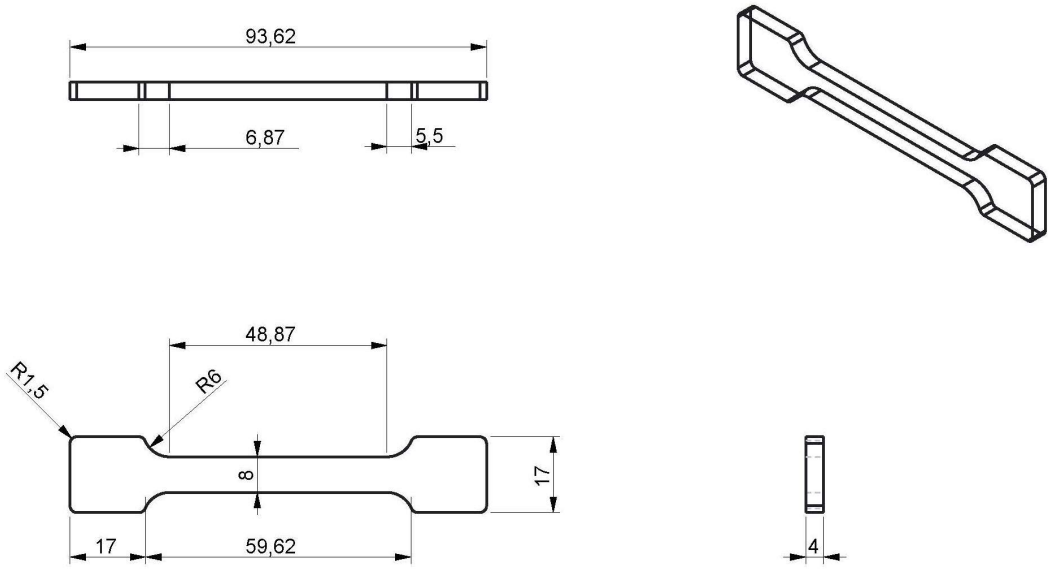

Figure 4.52: Tensile specimen geometry and dimensions - Specimen dimensions in millimetres, derived from ASTM standard (148).

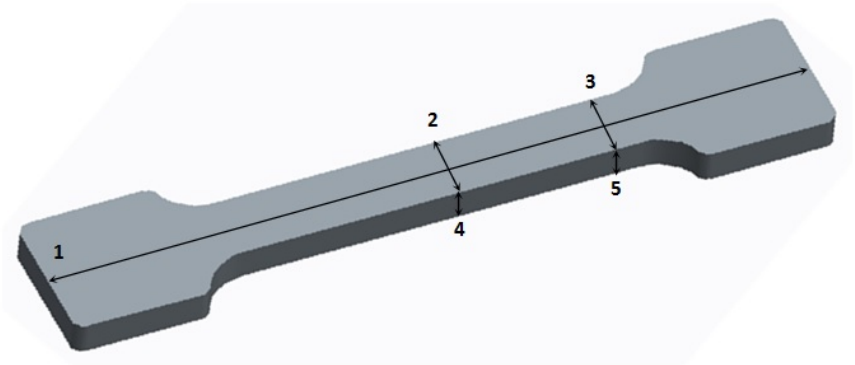

Figure 4.53: Location of measurements of tensile specimen dimensions - Specimen dimensions measured in the highlighted locations using vernier callipers to ensure consistency and adherence to the ASTM standard.

	Testing	Measurement number				
	temperature	1	2	3	4	5
Specimen	**(°C)**	Length (mm)	Width (mm)		Thickness (mm)	
Clad	25	93.82	4.06	4.06	8.00	8.00
Clad	25	93.76	4.04	4.06	8.00	8.00
Clad	25	93.78	4.04	4.06	8.06	8.06
Clad	150	93.78	4.04	4.06	8.00	8.00
Clad	300	93.74	4.00	4.00	8.00	8.00
Clad	450	93.76	4.06	4.08	8.00	8.00
Clad	600	93.84	4.02	4.02	8.04	8.04
Clad	780	93.52	4.06	4.06	8.02	8.00
Clad	820	93.84	4.04	4.04	8.06	8.06
HAZ	25	93.76	4.06	4.06	8.02	8.04
HAZ	25	93.72	4.04	4.04	8.00	8.00
HAZ	25	93.66	4.02	4.04	8.06	8.04
HAZ	150	93.76	4.02	4.04	8.04	8.04
HAZ	300	93.76	4.06	4.06	8.04	8.04
HAZ	450	93.72	4.02	4.04	8.08	8.08
HAZ	600	93.64	4.06	4.04	8.00	8.00
HAZ	780	93.72	4.04	4.04	8.02	8.02
HAZ	820	93.78	4.08	4.06	8.00	8.02

Table 4.8: Comparison of measured specimen dimensions for 17-4 PH and corresponding 4330 HAZ tensile specimens

The obtained measurements should be compared with the dimensions dictated in figure 4.52. Along with the specified tolerance values in table 4.9, it could then be determined whether the dimensions adhered to the required tolerance values by examining the maximum variation between dictated and measured dimensions. It can be seen that the maximum variation in the length of the specimen is greater than the desired tolerance value. However, the length does not affect the cross-sectional area of the specimen and therefore this will not affect the results with regards to stress in the specimen.

	Measurement number				
	1	2	3	4	5
	Length (mm)	Width (mm)		Thickness (mm)	
Average	93.62	4.00	4.00	8.00	8.00
Tolerance	$\pm$0.1	$\pm$0.1	$\pm$0.1	$\pm$0.1	$\pm$0.1
Maximum variation	+0.22	+0.08	+0.08	+0.08	+0.08

Table 4.9: Calculation of average dimensions, tolerances and maximum variation for 17-4 PH and corresponding 4330 HAZ tensile specimens

Preliminary testing Preliminary testing was undertaken to calibrate the furnace and the machine load cell.

Calibration of the furnace With the desire for temperature-dependent material properties, tensile testing was to be carried out at various temperatures. This would be achieved using an Instron three-zone furnace with a maximum temperature of 1000°C. Temperature values in the three zones are displayed as measured by thermocouples in the walls of the furnace. To determine the temperature of a specimen in the furnace compared with the temperature indicated by the furnace controller, a specimen was positioned in the furnace. Three thermocouples were positioned along the gauge length of the specimen as shown in figure 4.54. These thermocouple temperature measurements allowed evaluation of the differences in furnace and controller temperatures.

The first calibration test was carried out at a furnace temperature of 100°C. Points of interest are as follows: the temperature of the specimen along the gauge length, the temperature of the furnace in the three zones and the difference in temperatures of the furnace and the specimen. Thermocouple readings were taken to determine the difference in temperature between the furnace and the specimen. The results are shown in figure 4.55.

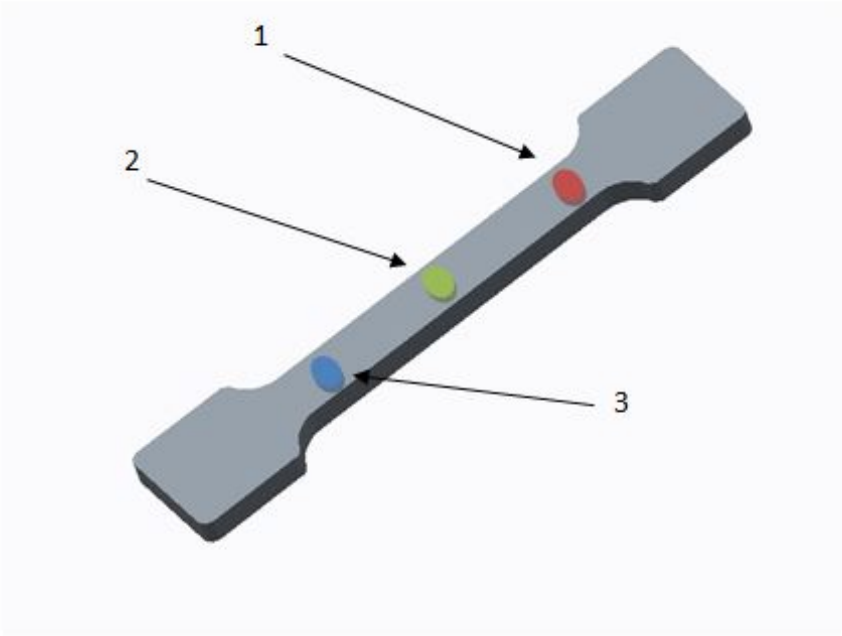

Figure 4.54: Positioning of thermocouples on tensile testing specimens - Location of thermocouples along gauge length of specimen to enable monitoring of temperature during testing.

It can be seen that the temperature of the specimen varies along the gauge length, with the highest temperature experienced at the location of thermocouple 1, decreasing to the lowest temperature at the location of thermocouple 3. The maximum difference between temperatures at thermocouples 1 and 3 was 11°C, possibly due to variant cooling at these locations or due to the phenomena of heat travelling upwards. At the end of the test, thermocouple 1 provided a temperature reading 5°C higher than that at thermocouple 3.

Investigating the measurements of the three controllers reveals that the temperature at the centre of the furnace is less than at the top and bottom. Furnace and controller temperatures in locations 1 and 3 were 2-3°C higher than location 2 in the middle of the furnace, which is questionable due to the earlier finding of the specimen temperature being lowest at location 3.

Calculation of the average thermocouple reading and comparing this curve with that of the average furnace temperature illustrates that the average thermocouple reading is much lower than the average furnace temperature reading, as shown in figure 4.56.

The furnace reaches 100°C within 30 minutes, however at this point in time, the specimen temperature is 35°C. The furnace was held at 100°C for a further 260 minutes allowing the specimen temperature to increase to an average of 61°C. It can be seen that the increase in specimen temperature decreases towards the end of this time period and therefore it was deemed that a steady state temperature distribution had

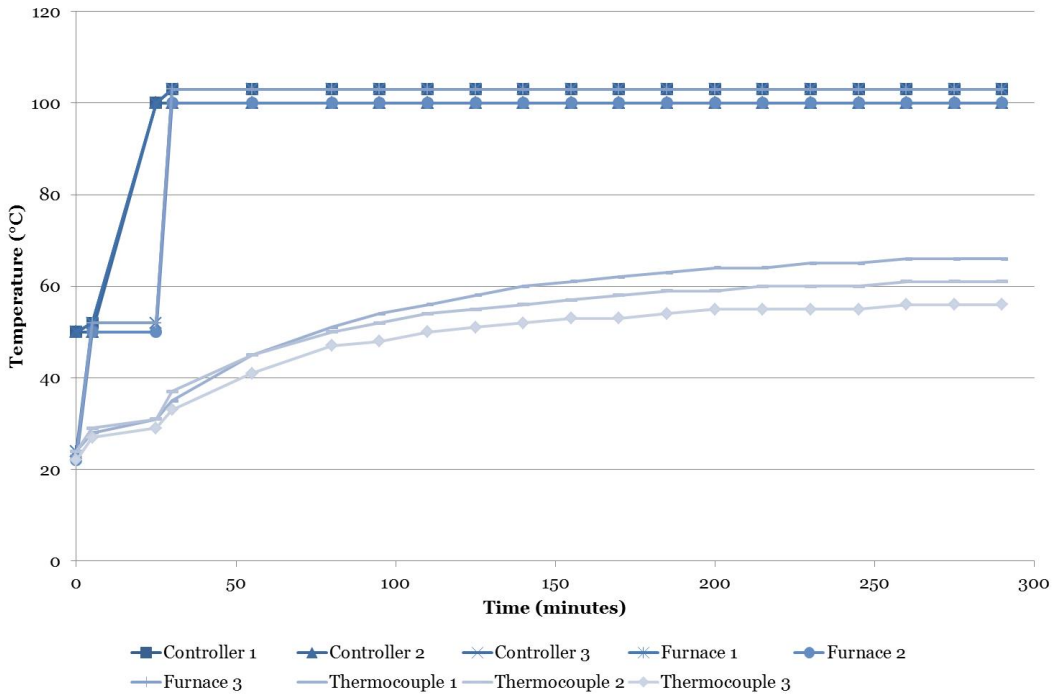

Figure 4.55: Comparison of furnace, controller and thermocouple temperatures at 100°C - Using a three-zone furnace and three thermocouples attached to the tensile specimen.

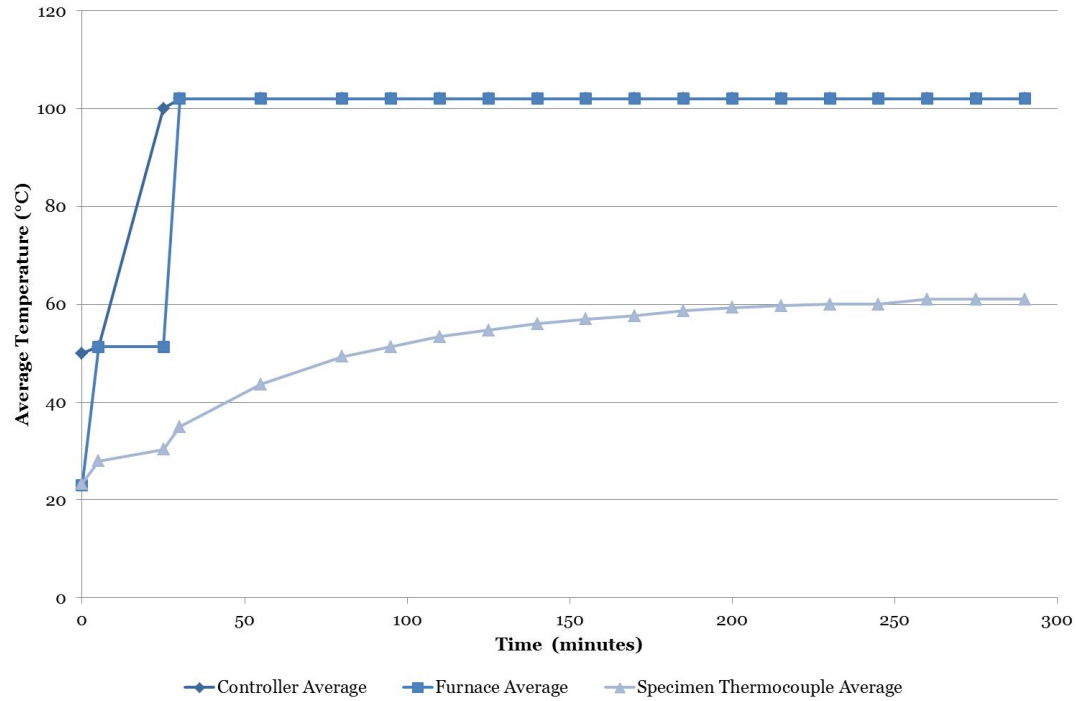

Figure 4.56: Comparison of average furnace, controller and thermocouple temperatures at 100°C - Average values for furnace, controller and thermocouple temperature values calculated from the obtained data at the specified temperature.

effectively been reached. At a furnace temperature of 100°C, the specimen temperature could therefore be assumed to be approximately 40°C lower.

A similar calibration experiment was conducted at a furnace temperature of 200°C with the data obtained displayed in figure 4.57.

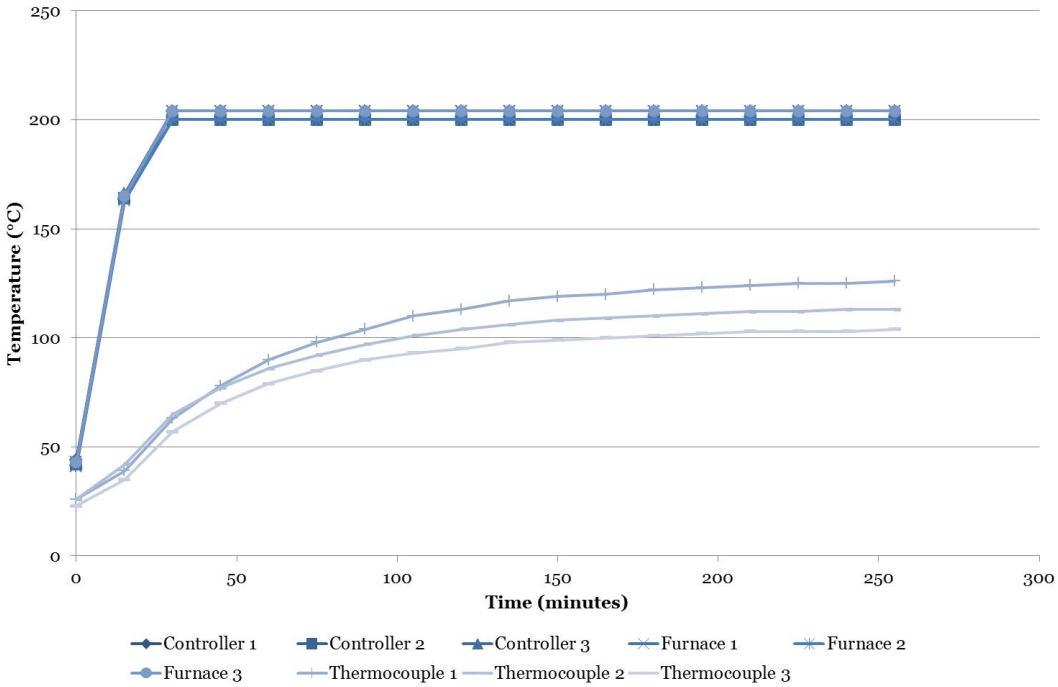

Figure 4.57: Comparison of furnace, controller and thermocouple temperatures at 200°C - Using a three-zone furnace and three thermocouples attached to the tensile specimen.

The results of this experiment also illustrated that the desired furnace temperature was obtained after 30 minutes of heating, at which point the specimen temperature was on average 62°C. After an additional 225 minutes the specimen temperature had converged to an average of 114°C (figure 4.58).

At a furnace temperature of 200°C, the specimen temperature according to the thermocouple readings is over 80°C lower than that of the furnace, with again temperatures varying at thermocouple locations.

Differing specimen heating rates were utilised in these tests: a heating rate of 0.1°C/min at a furnace temperature of 100°C and a heating rate of 0.234°C/min at a furnace temperature of 200°C. If the furnace temperature were to be increased to a higher temperature, it would therefore require a shorter time period to attain the desired specimen temperature. Maintaining the same furnace and specimen temperature is the key issue in this experiment, as this would be required for the duration of the test and throughout the gauge length of the specimen.

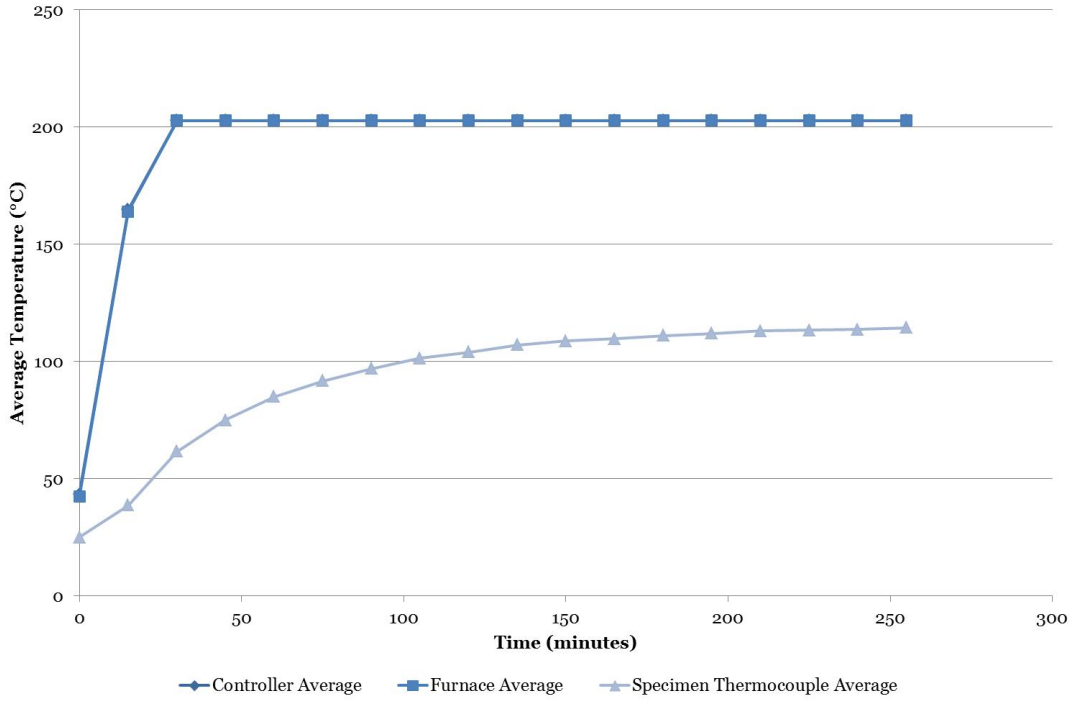

Figure 4.58: Comparison of average furnace, controller and thermocouple temperatures at 200°C - Average values for furnace, controller and thermocouple temperature values calculated from the obtained data at the specified temperature.

To account for testing at various temperatures, experiments were undertaken at various temperatures with the furnace temperature set to a higher value than the desired specimen temperature. It was hoped that using this method the specimen temperatures required would be attained. Upon achieving the specimen temperature, the furnace temperature was decreased and the experiment continued for ten minutes as an indication of the time duration for a tensile test. The results of this experiment are shown in figure 4.59. The maximum specimen temperature attained can be seen to be 820°C when the furnace temperature is at the maximum level of 1000°C. It was found that throughout the test, at a specified furnace temperature, the specimen temperature was approximately 250°C less.

An alternative to the process of producing a calibration curve would also have been to attach a thermocouple to all specimens and to attach this to the controller.

Another concern during this experiment was that of increased cooling rates of the specimen during the ten minute time period at which the furnace temperature was held at that of the desired specimen temperature. This indicated the need to conduct the testing at a satisfactory cross-head speed to ensure that testing did not exceed a time period of ten minutes and in turn allow as great a level of consistency in temperature as possible.

Quantification of the assessment of the capability of the specimen retaining the re-

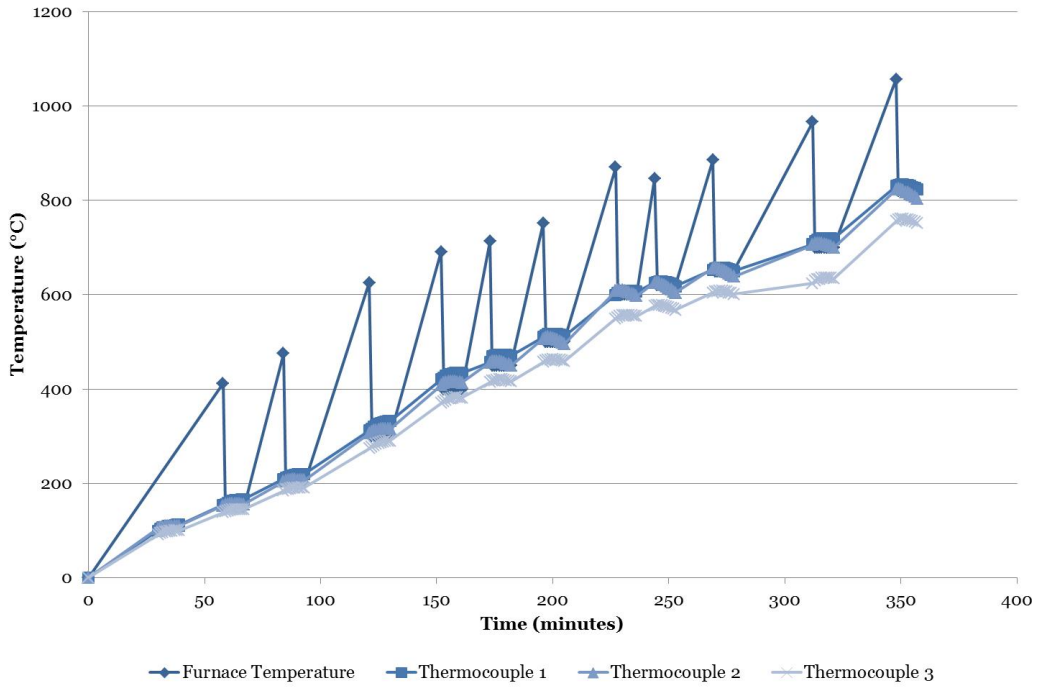

Figure 4.59: Comparison of furnace and thermocouple temperatures at 1000°C - Using a three-zone furnace and three thermocouples attached to the tensile specimen.

quired temperature during testing was provided through heating a specimen to the desired temperature. This temperature measurement was obtained from the middle thermocouple. The temperature of the furnace was then decreased to the same temperature and readings obtained from the middle thermocouple every minute for ten minutes. The results of this experiment are shown in table 4.10. These results provided information on the likely variation in specimen temperature during the tensile test and enabled the quantification of the error associated with this factor depending on the duration of the test. This was not required in the case of tests carried out at room temperature due to the furnace not being utilised in these tests.

The resulting temperature errors at the testing temperatures for the tests undertaken are provided in table 4.11.

Concluding the calibration test, it is clear that there are issues maintaining the required specimen temperature and that the temperature of the furnace is higher than that of the specimen. The calibration data obtained through these experiments were utilised throughout the tensile testing program to provide specimen temperature in relation to furnace temperature.

Calibration of the extensometer To allow measurement of the elongation of the gauge length of the tensile specimen, a high-temperature Instron extensometer was utilised during testing. This would in turn allow the Young's modulus of the material

	Furnace temperature (°C)					
	150	300	450	600	780	820
Time (minutes)	**Specimen temperature (°C)**					
1	153	306	456	607	780	823
2	155	309	458	610	788	824
3	156	312	459	610	791	823
4	157	313	458	609	793	821
5	157	314	458	608	794	817
6	157	315	457	606	795	817
7	157	315	455	605	794	814
8	157	315	453	602	792	811
9	156	315	452	600	792	808
10	156	315	449	597	791	804

Table 4.10: Furnace and specimen temperature correlation experiment

to be determined. As the accuracy of the extensometer readings directly impacts the determination of Young's modulus, calibration of the extensometer was required. Expansion or contraction of the extensometer during testing would affect Young's modulus values and therefore the extensometer was tested in the furnace without a specimen in place.

Figure 4.60 shows the measured extension values of the extensometer with increasing temperature plotted alongside the temperature of the furnace zones as experimental time progressed. It can be seen that one sharp peak in extension measurement occurs close to the beginning of the experiment, however in general very little extension is observed with increasing temperature and therefore it was deemed that error due to expansion or contraction of the extensometer would not majorly affect results.

Temperature limitations of the extensometer were such that the strain gauge should remain at a maximum temperature of 200°C, although applications with which the extensometer can be used allow a maximum temperature of 1000°C. The extensometer when inserted into the internal surface of the wall of the furnace was cooled using a computerised fan.

Tensile testing

Theory Applying an axial tensile load to the specimens and utilising an extensometer to measure the extension of the specimen allows the determination of the yield

Material	Specimen temperature (°C)	Test duration (minutes)	Temperature variation (°C)
Clad	25	3	N/A
Clad	25	4	N/A
Clad	25	3	N/A
Clad	150	3	±6
Clad	300	2	±9
Clad	450	2	±8
Clad	600	2	±10
Clad	780	3	±11
Clad	820	5	±4
Substrate	25	2	N/A
Substrate	25	3	N/A
Substrate	25	3	N/A
HAZ	150	3	±6
HAZ	300	3	±12
HAZ	450	3	±9
HAZ	600	3	±10
HAZ	780	6	±15
HAZ	820	8	±9

Table 4.11: Resulting specimen temperature variation during tensile testing for 17-4 PH clad, corresponding HAZ and substrate materials

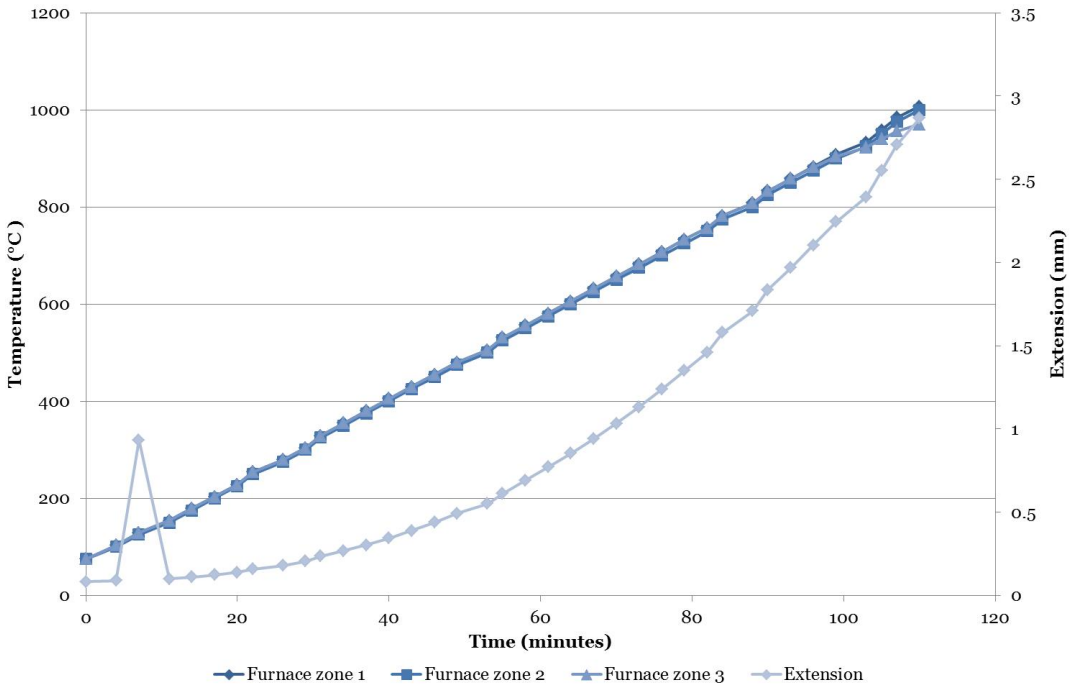

Figure 4.60: Calibration of high-temperature extensometer - Using a three-zone furnace for heating only and high-temperature extensometer.

stress and Young's modulus of the material. The typical behaviour of a ductile material during a tensile test is illustrated in figure 4.61.

The linear portion of the curve from a zero stress and strain value until the proportional limit is the elastic region. In this region the material undergoes elastic deformation and therefore with load removal the material adopts the original shape once again. The modulus of elasticity, known as Young's modulus, is calculated as the gradient of the line in the elastic region of the stress-strain curve.

The point at which deviation from linearity occurs is known as the proportional limit. At this point deformation remains elastic. Loading beyond the elastic limit produces plastic, or permanent deformation. At the yield point, a rapid increase in strain occurs without a major increase in stress.

The yield strength labelled in figure 4.61 is defined by an offset strain, utilised in the case where the yield point is not clear. This value is often 0.2%. The ultimate strength is the maximum stress value in the stress-strain diagram and the point of fracture can occur at this point or following decrease in the stress-strain curve. This is often observed by *necking* of the specimen, a visible elongation and decrease in area of the central section of the specimen.

The conversion of load to stress is carried out by dividing the load by the original cross-sectional area. The extension of the specimen is observed by comparing the length at a certain load with the original length of the specimen. The strain is then

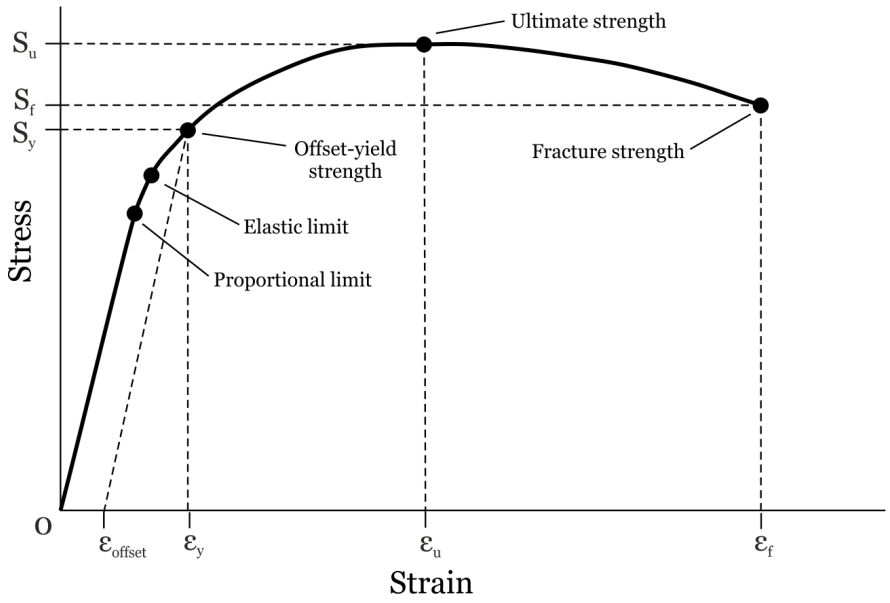

Figure 4.61: Typical stress-strain curve obtained through tensile testing - Stress-strain curve illustrating behaviour of a ductile material during a tensile test. Figure modified from (68).

calculated by dividing the change in length by the original length. This allows a stress-strain diagram to be plotted upon completion of the tensile test. The *true* measure of stress is obtained through measurement of the load and area during the test. Utilising the original cross-sectional area and the load at a specific time in the test does not account for the change in cross-sectional area during the test. For example, using the decrease in area after the point of ultimate strength would provide a higher stress value than calculating the stress at that point utilising the original cross-sectional area. Likewise, the *true* strain accounts for the total incremental elongation that has occurred until the point in question divided by the gauge length at that point. *True* stress is observable by a continual increase to the fracture point. In general, these stresses are described as *engineering* stresses to highlight that they are utilised in engineering calculations, however utilise the original unchanged cross-sectional area.

Testing procedure An Instron 8801 servo-hydraulic fatigue testing system was utilised for the tensile testing program, with a force capability of $\pm 100kN$. As previously mentioned an Instron three-zone furnace with a maximum temperature of 1000°C was also used to enable testing at elevated temperatures with the production of customised Inconel 625 grips to enable gripping of the flat tensile specimens and test endurance at elevated temperatures. During testing, the grips were cooled using a water pumping system. The addition of these grips into the system along with the cooling system applied to the grips introduced a heat sink effect. It has already been

highlighted that there were difficulties in attaining and maintaining the required temperatures and this will also have contributed to this. These grips are shown in figure 4.62. The specimens slotted into the recess shown and were clamped using a plate and bolts.

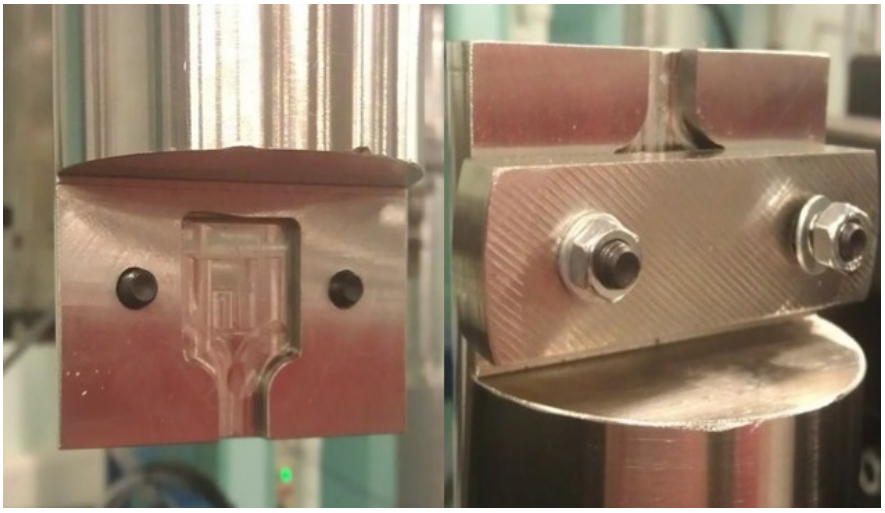

Figure 4.62: Tensile testing custom machined grips - Grips manufactured in-house for use with the Instron 8801 servo-hydraulic fatigue testing system.

The specimens were vertically positioned in the tensile testing machine as shown in figure 4.63 and the load applied through the application of a load cell serving to displace the specimen from the lower tab in a downwards manner.

The chosen elevated test temperatures are provided in tables 4.12 and 4.13. All materials were also tested at room temperature. These temperatures were chosen to adequately capture the change in yield stress across a wide temperature range, also taking into account the findings of the furnace calibration of the maximum specimen temperature reached. Slight variations in test temperatures were applied for the 4330 and 17-4 PH compared with the Inconel 625 to allow for phase change effects to be observed. These phase changes upon heating were clearly highlighted in figures 4.21-4.25.

Cross-head speed values were increased at elevated temperature tests in order to maintain better uniformity of temperature for the specific test with the resulting increase in strain rate deemed insignificant. The increase in cross-head speed was especially crucial in the case of Inconel 625 due to the ductility of this material. The increase in cross-head speed was applied at a displacement of 5mm/min.

Results Upon completion of the tensile testing program, the stress-strain diagrams obtained through testing at room temperature were analysed to determine the modulus and yield points for all materials and temperatures. This provided yield stress

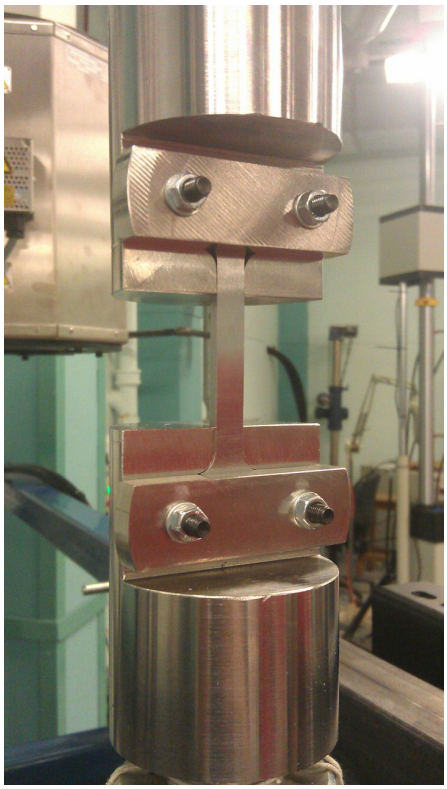

Figure 4.63: Tensile specimen positioned in custom machined grips - Grips manufactured in-house for use with the Instron 8801 servo-hydraulic fatigue testing system.

Test temperature (°C)	Initial cross-head speed (mm/min)	Increased cross-head speed (mm/min)
150	3	10
300	3	10
450	3	10
600	3	10
780	3	10
820	3	10

Table 4.12: Tensile test temperatures and corresponding cross-head speeds for 4330 and 17-4 PH

Test temperature (°C)	Initial cross-head speed (mm/min)	Increased cross-head speed (mm/min)
150	2	10
300	2	10
450	3	10
560	3	10
700	3	10
820	3	10

Table 4.13: Tensile test temperatures and corresponding cross-head speeds for Inconel 625

values. Three tests were conducted for all materials at room temperature with average values calculated and provided in tables 4.14-4.17. Creep effects were assumed negligible over the duration of the test.

Measurement	$\sigma_y(MPa)$
1	857
2	879
3	871
Average	869

Table 4.14: Resulting average room temperature yield stress of 4330 (HAZ of 4330 clad with Inconel 625)

Measurement	$\sigma_y(MPa)$
1	800
2	863
3	905
Average	856

Table 4.15: Resulting average room temperature yield stress of 4330 (HAZ of 4330 clad with 17-4 PH)

At elevated temperatures, issues were encountered in utilising the high-temperature extensometer and therefore stress-strain diagrams could not be obtained and consequently modulus measurements were impacted. Although the extensometer was capable of operating in the temperature range utilised, the internal electronic system in the extensometer experienced melting during the first test. An alternative measure of utilising the data of the load and cross-head displacement enabled determination

Measurement	$\sigma_y(MPa)$
1	468
2	479
3	474
Average	473.67

Table 4.16: Resulting average room temperature yield stress of Inconel 625 (Clad on 4330)

Measurement	$\sigma_y(MPa)$
1	990
2	985
3	1006
Average	993.67

Table 4.17: Resulting average room temperature yield stress of 17-4 PH (Clad on 4330)

of the yield point of the specimen using the expression for stress of load divided by area. Therefore when referring to extension, this is in reality displacement of the cross-head. Figures 4.64 and 4.65 provide examples of the load versus extension (cross-head displacement) and consequent calculated stress versus extension (cross-head displacement) curves to obtain the yield stress for each material.

The discrete data points obtained at various temperatures are shown in figures 4.66-4.69. Published data available for the materials under investigation was also plotted on the same figure to allow comparison with experimental data. The linear portion of the curves is where data has been extrapolated from the last available data point to the melt temperature value, at which point the yield stress is assumed to be effectively zero due to the loss in stiffness of the material at melt temperature. Maximum temperatures at which published data was available in the software utilised (141) are noted in table 4.18. The maximum temperature at which experimental data was obtained was 820°C. Above this temperature data was extrapolated for all data sets.

Material	Maximum temperature (°C)
4330	537.9
Inconel 625	981.9
17-4 PH	539.9

Table 4.18: Maximum temperature of available published yield stress data

The data for the 4330 HAZ when clad with Inconel 625 shown in figure 4.66 illustrates a slight increase in yield stress at a temperature of 450°C. This data point

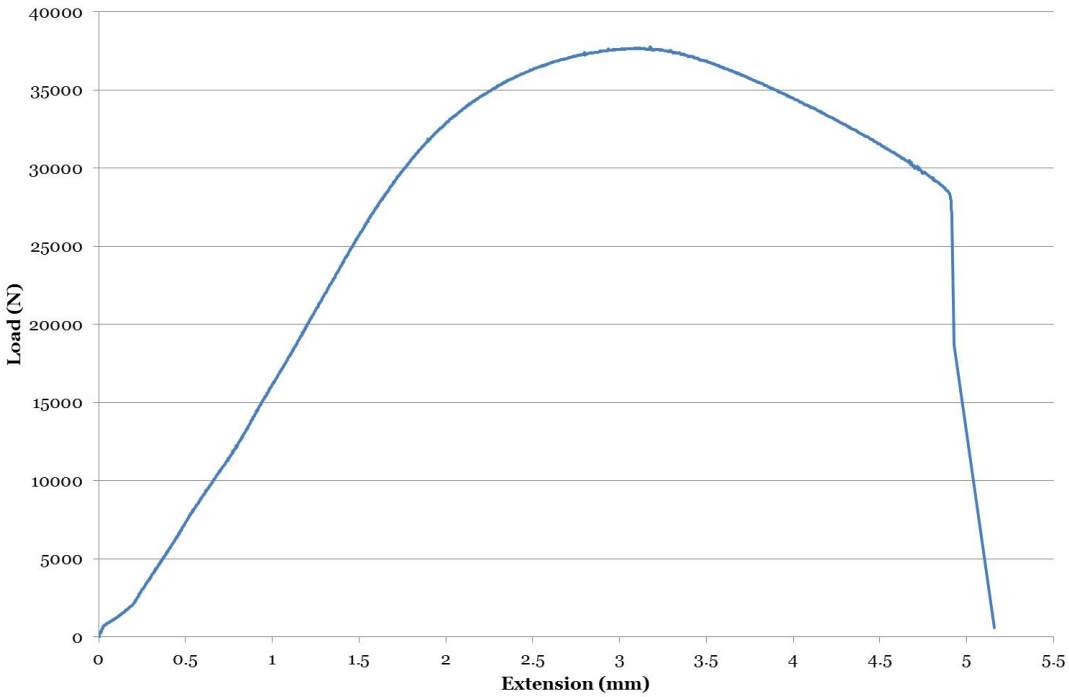

Figure 4.64: Load versus extension experimental data for 17-4 PH (Clad on 4330) - Experimentally obtained at room temperature using an Instron 8801 servo-hydraulic fatigue testing system and three-zone furnace. Extension denotes cross-head displacement.

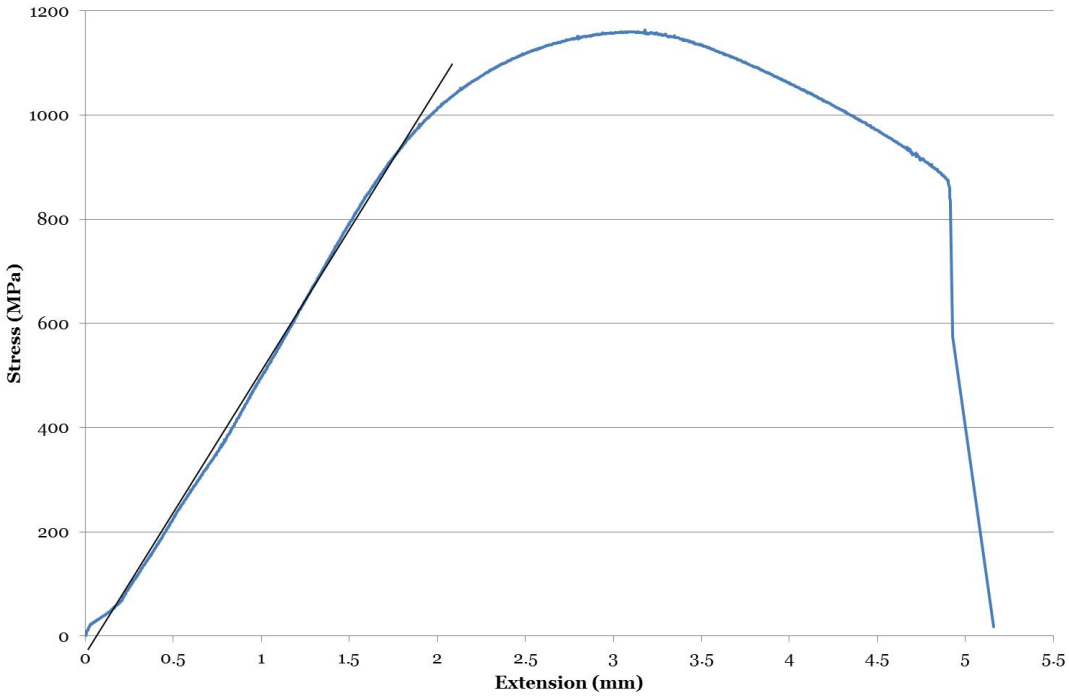

Figure 4.65: Stress versus extension experimental data for 17-4 PH (Clad on 4330) - Experimentally obtained at room temperature using an Instron 8801 servo-hydraulic fatigue testing system and three-zone furnace. Extension denotes cross-head displacement.

was modified for input into the finite element simulation as shown in figure 4.66 decreasing the value as it was deemed that any peaks in material properties could cause inaccuracies in resulting residual stresses. This also occurred at a temperature of 300°C in the case of the low alloy carbon steel *HAZ* when clad with 17-4 PH. It should again be highlighted that the data plotted as published 4330 data is in fact data manipulated from available published data for 4340 steel, as described in section 4.4.9.

It can be observed that the experimental data for 4330 is lower than the published data available. There is little difference in the values for yield stress when this material is clad with different materials. It may have been expected that the yield stress of the 4330 *HAZ* when clad with Inconel 625 would be lower than when the low alloy carbon steel is clad with 17-4 PH due to the much lower yield of the nickel-chromium-based superalloy and the effects of alloying and dilution. However it should also be considered that upon heating the specimens machined from the clad blocks the microstructure may undergo changes, for example possibly altering the martensitic phase, and therefore potentially alter material properties. This again emphasises the sensitivity of material microstructure and properties and the need for accurate material property testing.

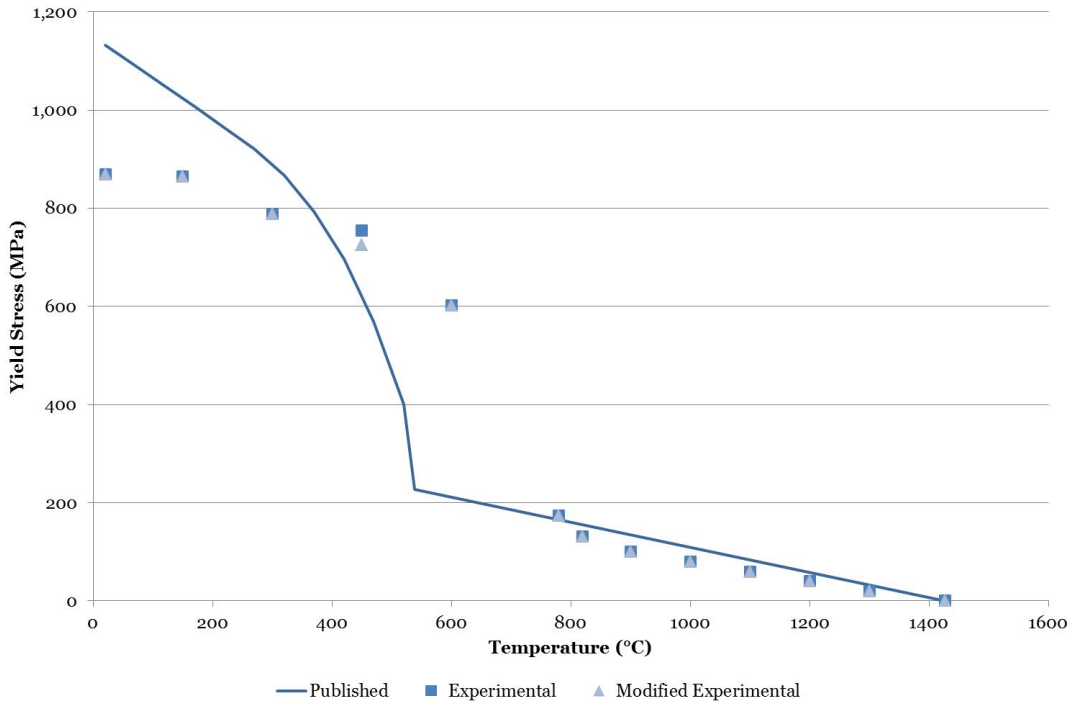

Figure 4.66: Yield stress of 4330 (HAZ of 4330 clad with Inconel 625) - Experimentally obtained using an Instron 8801 servo-hydraulic fatigue testing system and three-zone furnace.

Figure 4.68 comparing experimental and published temperature-dependent yield stress values for Inconel 625 illustrates that the experimental data follows the same

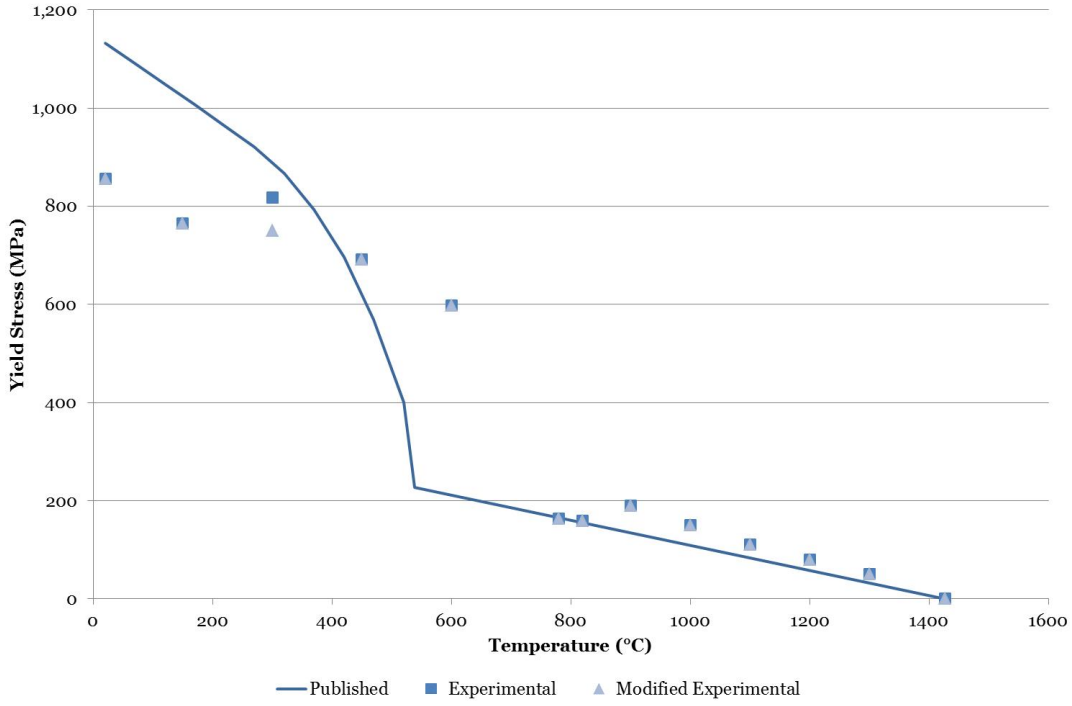

Figure 4.67: Yield stress of 4330 (HAZ of 4330 clad with 17-4 PH) - Experimentally obtained using an Instron 8801 servo-hydraulic fatigue testing system and three-zone furnace.

shape as that of the published data, however experimental values are higher than published values. This is most likely due to the effects of alloying and diffusion from the high-strength low alloy carbon steel substrate. The availability of published data for Inconel 625 has been highlighted as being available to a much greater temperature, as noted in table 4.18.

In figure 4.69, it can be seen that two points have been slightly adjusted to ensure a more intuitive and smoother experimental variation, most notably the data point obtained at a temperature of 150°C. The likely reasons for such a perturbation are unknown however it is believed that experimental variation has also impacted results.

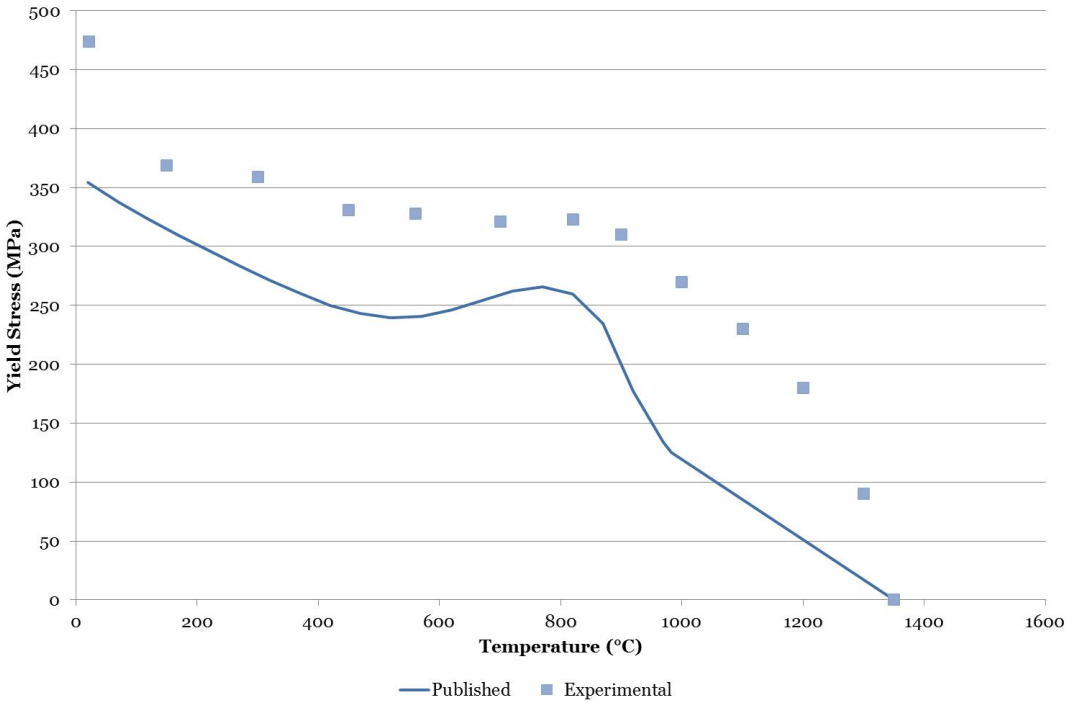

Figure 4.68: Yield stress of Inconel 625 (Clad on 4330) - Experimentally obtained using an Instron 8801 servo-hydraulic fatigue testing system and three-zone furnace.

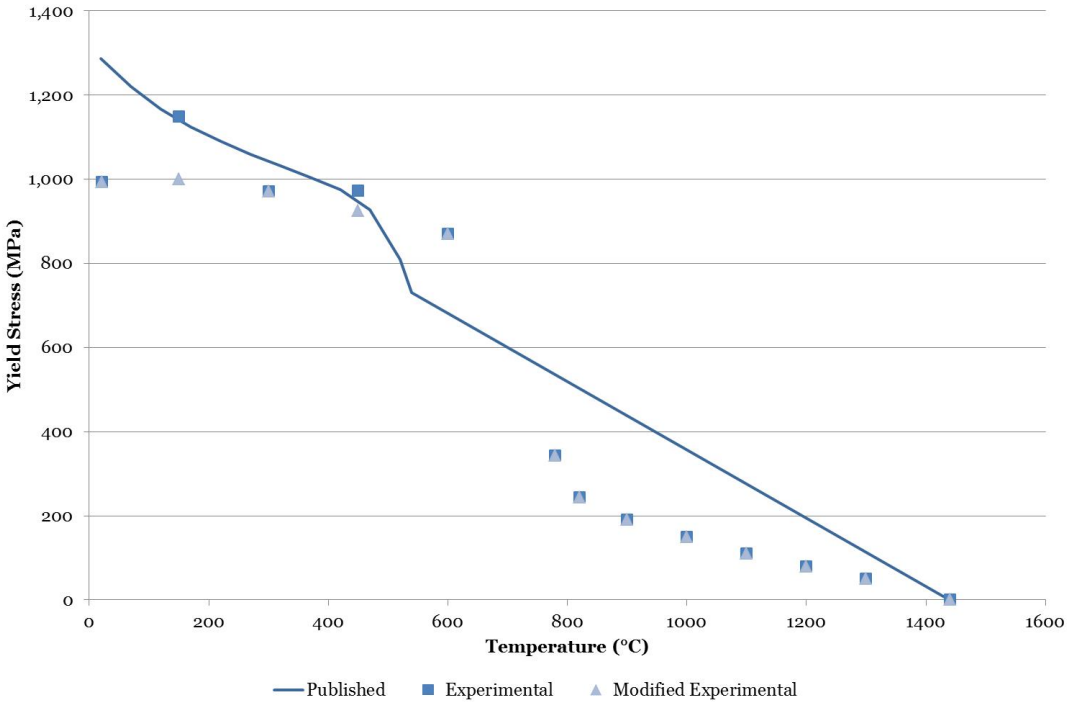

Figure 4.69: Yield stress of 17-4 PH (Clad on 4330) - Experimentally obtained using an Instron 8801 servo-hydraulic fatigue testing system and three-zone furnace.

Discussion As previously mentioned, mechanical properties influence greatly the residual stresses in a material. Although experimental data has been obtained for the yield stress values of clad and substrate materials, these have been obtained as single values across the 6 mm clad and *HAZ* regions, neglecting effects of diffusion and alloying through the thickness of these areas. This will also impact the material properties and ultimately the residual stresses in these region and therefore the specimens utilised do not allow for the characterisation of the variation of mechanical properties and ultimately residual stresses through these layers. This will be reflected in the finite element simulation results in chapter 5, where it will be seen that the input of material properties for the entire clad layer is indeed reflected in the inability to capture variation in resulting residual stress distribution through this clad layer. Further testing would require machining of thinner specimens to allow the variation in properties across the clad layer and *HAZ*'s to be deduced.

Uncertainty analysis It is clear that there were many difficulties encountered during the testing program and therefore the consideration of errors and uncertainties is of importance. These may arise from various aspects of the test and are highlighted in table 4.19. Efforts have been made through the preliminary testing results to assign values to these highlighted sources of uncertainty.

The calculated error values at elevated temperature vary depending on the deviation of the temperature from the desired temperature, as was investigated in the furnace calibration testing program. Results of this experiment were shown in table 4.11. The in-built error accounts for the variation in temperatures at the three thermocouples within the three-zone furnace. This has been assigned the value obtained at the end of the test as described in section 4.4.9, thermocouple 1 providing a temperature reading 5°C higher than that at thermocouple 3.

Affected result	Instrument	Uncertainty type	Value (°C)
Specimen Temperature	Furnace	Calculated	±4 - ±15
		Reading	±1
	Thermocouples	Reading	±1
		In built	±5
		Total error (elevated temp.)	±11 - ±22
		Total error (room temp.)	±7

Table 4.19: Estimation of uncertainties affecting temperature values in tensile testing program

It has also been mentioned that due to time limitations and inadequacies in the testing procedure only a small number of samples were tested and therefore to increase the

reliability of obtained data and ensure statistical significance it would be desirable to undertake testing of further specimens.

Metallurgical effects As will be highlighted throughout this research, the phase changes of most importance are those upon cooling. The yield stress values obtained through experiment are for discrete temperatures, achieved through heating of the material to these temperature values. Therefore the results of the experimental tensile testing program do not capture phase change effects, unlike the thermal properties obtained where continuous data upon cooling captures phase changes providing a more complete illustration of material behaviour.

During testing of the Inconel 625 specimens, the effect of slip was observed in the gauge length due to the ductility of the material. This is shown in figure 4.70. Inconel 625 possesses a face-centred cubic structure, and it is these structures which typically experience the occurrence of slip due to the presence of many slip planes. This specimen also illustrated fracture in a location displaced from the centre of the gauge length. This issue arose due to misalignment of the grips, with the grips subsequently altered to encourage adequate fit and symmetry of the specimen in the grips. Stability of the grips during testing was also monitored to ensure that the design of the grips did not introduce any additional error. Poor fit of the specimen in the grips would entail an initial adjustment of the specimen in the grips at the commencement of the test. This was observed by an initial zero gradient in the obtained data curves. Different coefficients of thermal expansion for grip and specimen materials could also contribute to poor fit of specimens in the grips due to varying expansion and cooling rates of respective materials. An appropriate fit at room temperature does not ensure satisfactory fit at elevated temperatures.

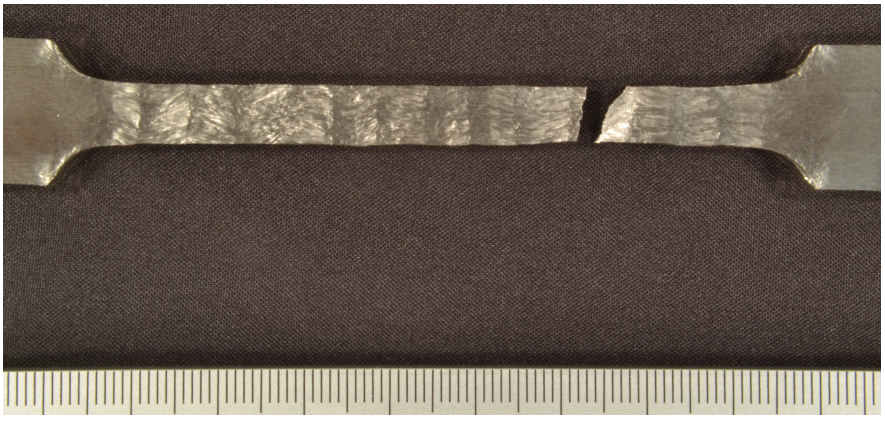

Figure 4.70: Fracture location of Inconel 625 tensile specimen - Tensile test conducted at room temperature. Occurrence of slip visible, the direction of slip dictated by the close-packing of atoms.

Testing at elevated temperatures produced oxide layers on the specimen, clearly visible at the two highest testing temperatures. The heat tint observed varies depending on the temperature experienced by the material. Figure 4.71 shows a specimen tested at 820°C. Inspection of the fracture surface indicates varying levels of discolouration, arising accordingly dependent on the fracture location.

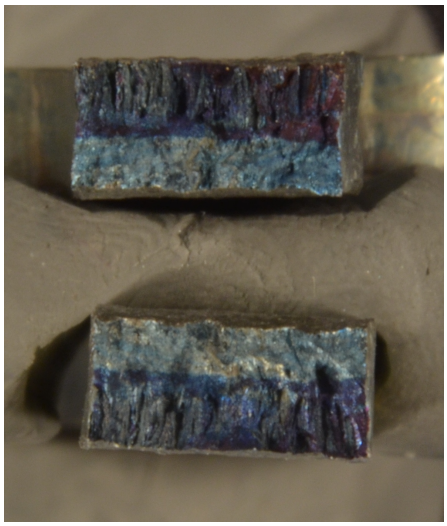

Figure 4.71: Fracture surface of Inconel 625 (Clad on 4330) specimen - Tensile test conducted at 820°C. Illustration of the presence of heat tint.

Straining due to the gripping arrangement is clearly visible, as illustrated in figure 4.72 due to poor fitting of the specimens in the grips depending on the dimensions of the machined specimen. Grips were machined such that specimens could be comfortably fitted into the grips, however this resulted in gaps between the grips and the specimen. Furthermore if the specimen varies from the specified dimensions additional gaps result. This is more clearly visible in the tab positioned in the upper grip due to the movement of the tab downwards as the lower grip begins to pull the specimen downwards at the commencement of the test. However, failure in the gauge length of the specimens meant that results were not deemed to be adversely affected. As highlighted previously, slip was observed in the Inconel 625 due to the high level of ductility, but also in the other two materials, although not as prevalent.

Figure 4.72: Fracture location of 4330 (HAZ of 4330 clad with Inconel 625) tensile specimen - Tensile test conducted at 450°C. Occurrence of slip visible, although to a lesser extent than with Inconel 625.

Figure 4.73 shows that specimens were subjected to varying temperatures across the gauge length, clear from the colour variance indicating variance in heat tint. This was expected due to the earlier findings of temperatures varying at the three thermocouple locations. However, refinement of the testing procedure to ensure consistent temperatures would be desirable.

Figure 4.73: Variation in heat tint in 4330 (HAZ of 4330 clad with Inconel 625) tensile specimen - Tensile test conducted at 300°C. Variance in heat tint illustrated indicating variation in temperature levels experienced in specimen.

Reduction in yield strength with temperature With reference to the results for yield stress of the materials under investigation, it can be seen from figures 4.66 and 4.67 that the yield stress of 4330 rapidly decreases with temperature to the maximum testing temperature of 820°C. This can similarly, although not as extremely, be seen in 17-4 PH. At a temperature of 150°C, the point of the curve has been manipulated due to the value being much higher than surrounding data points. It should however be noted that this point occurs around the martensitic transformation temperature and therefore could in fact reflect accurate variation in properties. Further investigation of the effects of this occurrence on material properties would be desirable to examine whether modification of such data points is the correct course of action. The strength of this material arises from the carbon atoms present in martensite, however this also creates a sensitivity to changes in temperature. This is the reason for the decrease in strength at elevated temperatures post-diffusion of the carbon atoms.

Inconel 625 exhibits a somewhat constant decrease in yield stress with temperature, with the sharpest decrease occurring between room temperature and the first test at elevated temperature.

Orientation of tensile specimen with respect to clad passes Tensile specimens were machined from the layers of clad and HAZ in a manner to maximise the number of specimens. The majority of specimens were harvested perpendicular to the clad pass orientation. However, the 4330 block clad with 17-4 PH with a pre-heat temperature of 150°C had been sectioned for the purpose of residual stress measurement and therefore a number of specimens were obtained parallel to the clad passes

although the effect of this has not been investigated due to the inability to draw statistical conclusions with the small number of specimens available.

4.4.10 Tensile strength

In a similar manner to the determination of the yield stress, tensile strength was also determined from the experimental data. A critical point to note is that the correlation between ultimate tensile strength (UTS) and fatigue strength is no longer applicable upon welding steel. Therefore, what may be perceived as advantageous in material selection, namely utilising a higher strength steel, is in fact irrelevant in the case of welded materials. This is an often overlooked factor in material selection for this purpose.

As can be seen from figures 4.74-4.77, the experimental results follow a similar trend to the published data, with the experimental values lower in all cases. At the highest temperatures, the published and experimental data curves intersect and there is a sharp decrease in published data, which is not reflected in the experimental results. This is observed in all materials, but most notably Inconel 625.

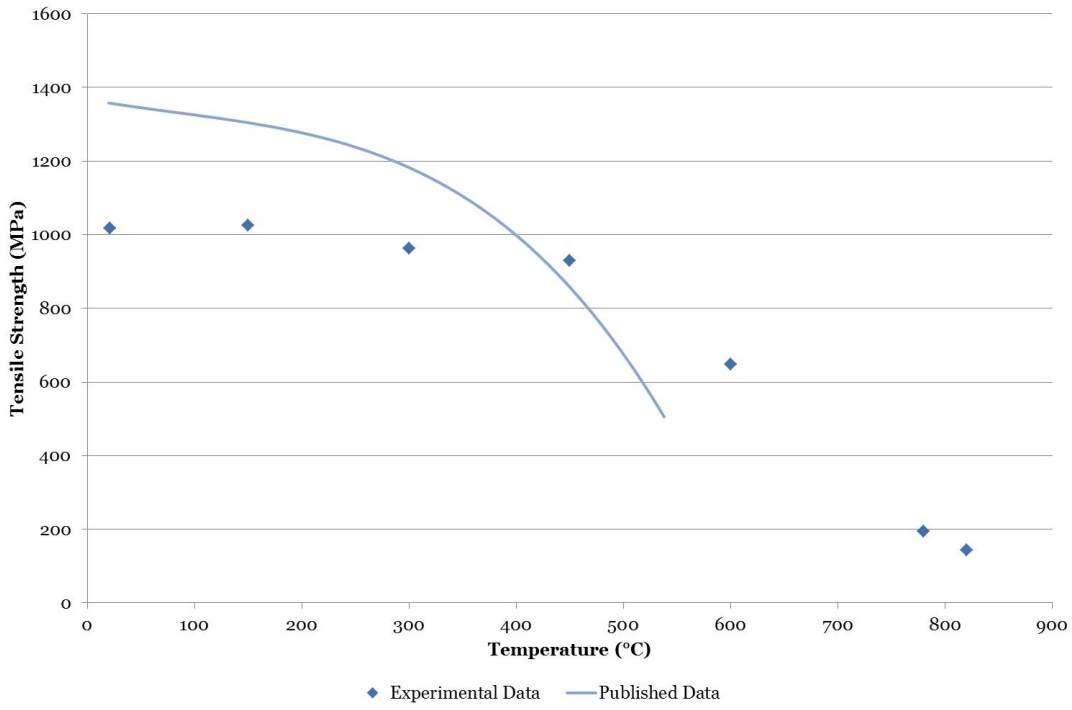

Figure 4.74: Tensile strength of 4330 (HAZ of 4330 clad with Inconel 625) - Experimentally obtained using an Instron 8801 servo-hydraulic fatigue testing system and three-zone furnace.

Another method of determining the tensile strength of a material is to utilise hardness values obtained for the material and apply the correlation between hardness and tensile strength for plain carbon and low-alloy steels. Data correlating these two

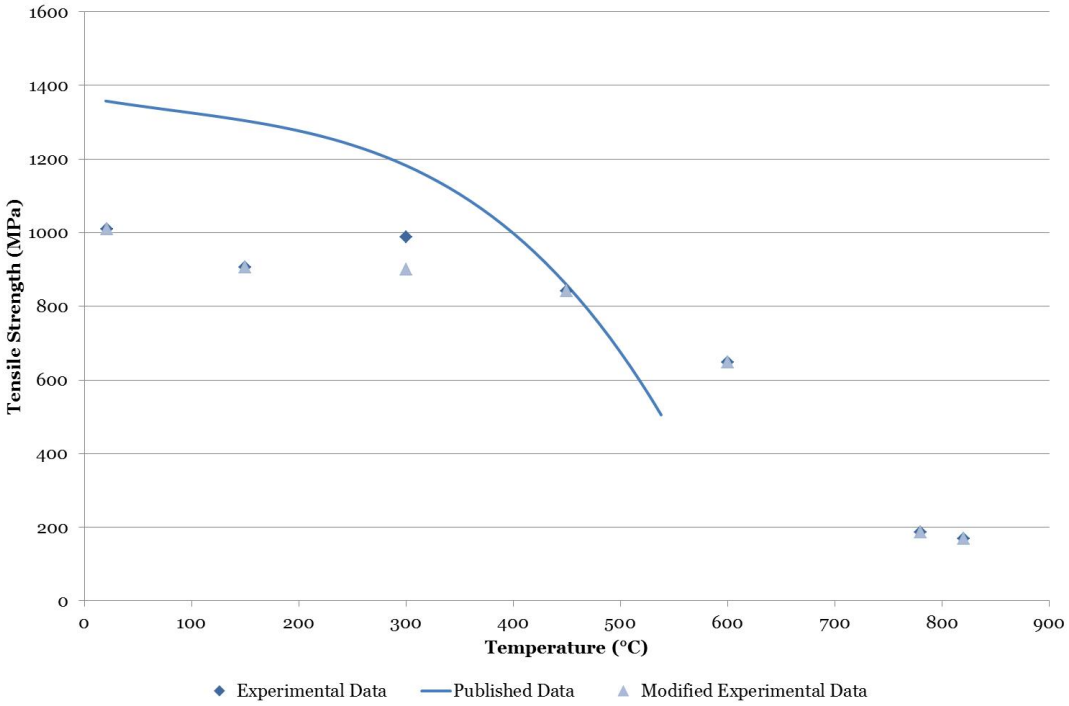

Figure 4.75: Tensile strength of 4330 (HAZ of 4330 clad with 17-4 PH) - Experimentally obtained using an Instron 8801 servo-hydraulic fatigue testing system and three-zone furnace.

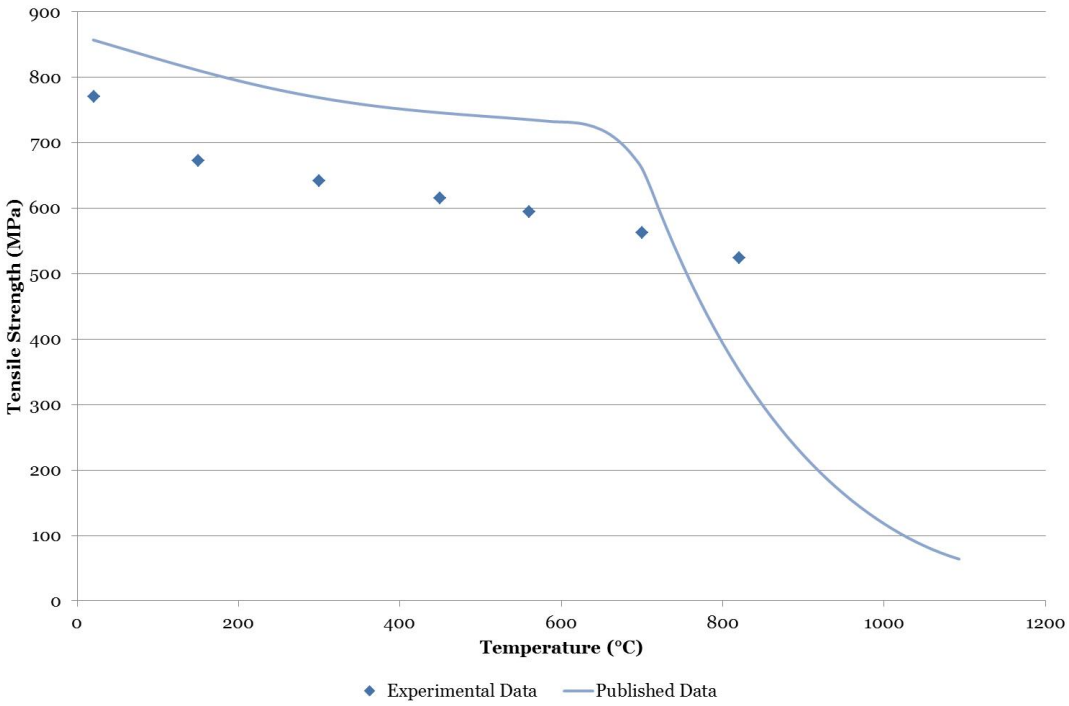

Figure 4.76: Tensile strength of Inconel 625 (Clad on 4330) - Experimentally obtained using an Instron 8801 servo-hydraulic fatigue testing system and three-zone furnace.

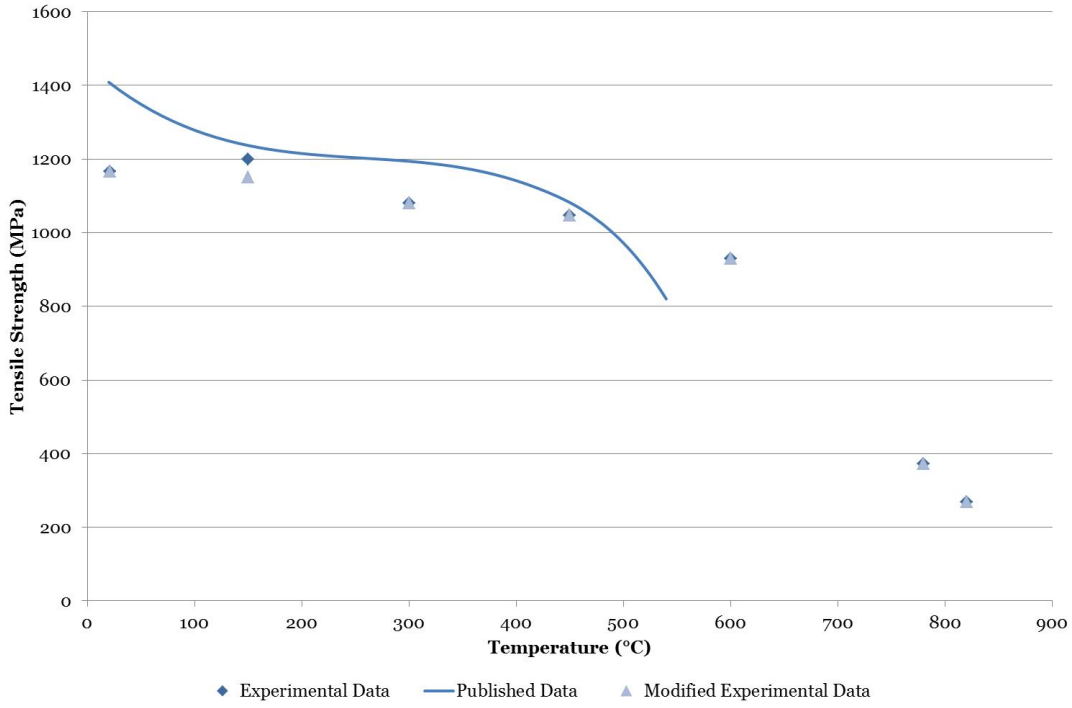

Figure 4.77: Tensile strength of 17-4 PH (Clad on 4330) - Experimentally obtained using an Instron 8801 servo-hydraulic fatigue testing system and three-zone furnace.

properties is found in (149) and applied utilising the Vickers hardness data obtained in section 4.4.8. The correlation between Vickers hardness and tensile strength is illustrated in figure 4.78.

Figures 4.79 and 4.80 show the resulting tensile strength values for 4330 and 17-4 PH with depth through the clad and *HAZ* layers utilising the correlation between tensile strength and Vickers hardness. It can be seen in figure 4.79 that as depth increases the variation in tensile strength decreases. This is due to travelling further from the *HAZ*, the effects of alloying and diffusion being greatest closer to the clad layer. Therefore further from the clad layer the microstructure will be more consistent with the original substrate material and variations in properties arising due to alloying and diffusion decrease.

Plotting the derived data for tensile strength for 4330 and 17-4 PH with depth on the same figure illustrates the change in tensile strength upon crossing the clad boundary into the substrate material. This is shown in figure 4.81. It can be observed that in general values for 17-4 PH are more tightly grouped together, however it should be noted that the data plotted for 4330 includes both that of 4330 clad with 17-4 PH and Inconel 625, samples 4, 6 and 8 being clad with 17-4 PH and 3, 5 and 7 clad with Inconel 625.

Table 4.20 lists the experimental and derived values for all materials, indicating the range in the case of the derived data. The hardness values and therefore derived

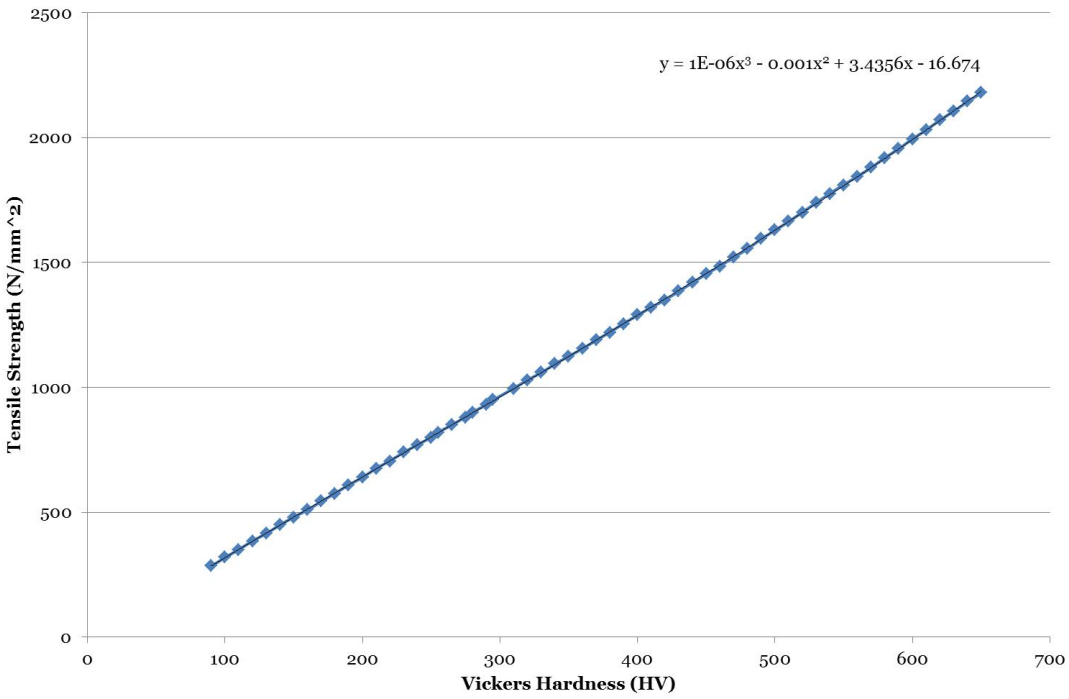

Figure 4.78: Correlation between tensile strength and Vickers hardness - Data obtained from (149). Correlation applies to plain carbon and low alloy steels, cast steels and limited high alloy and or/work hardened steels.

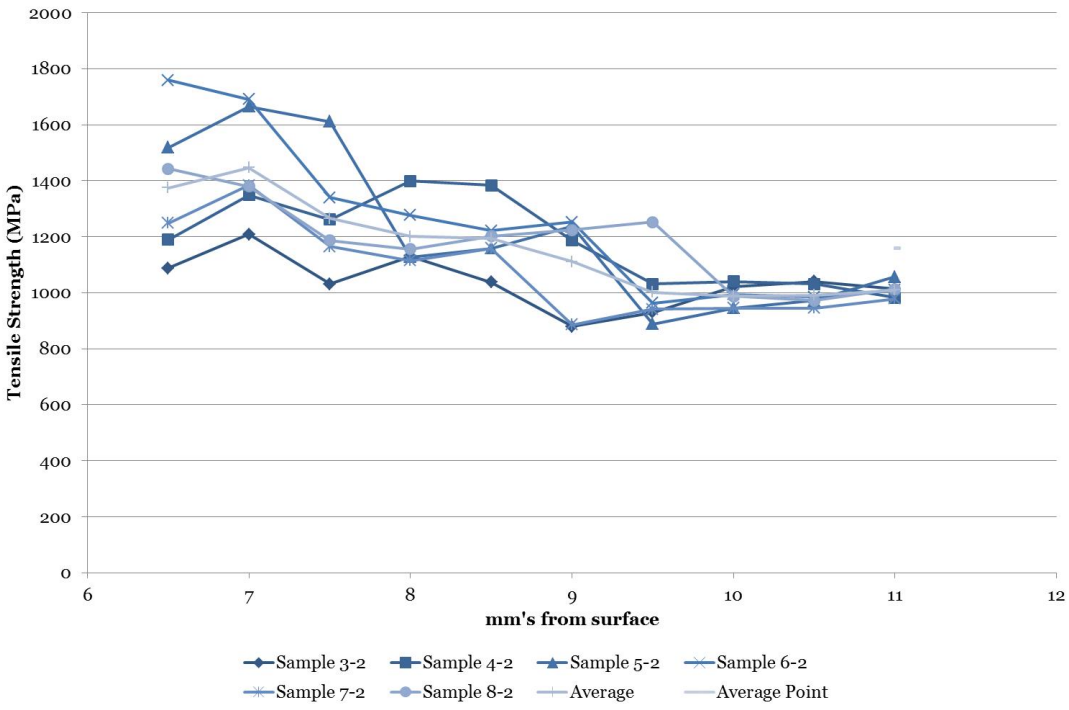

Figure 4.79: Tensile strength of 4330 (HAZ of 4330 clad with 17-4 PH or Inconel 625) - Samples 3, 5 and 7 indicate 4330 clad with Inconel 625. Samples 4, 6 and 8 indicate 4330 clad with 17-4 PH. Derived from correlation between tensile strength and Vickers hardness using data obtained experimentally from microhardness measurements.

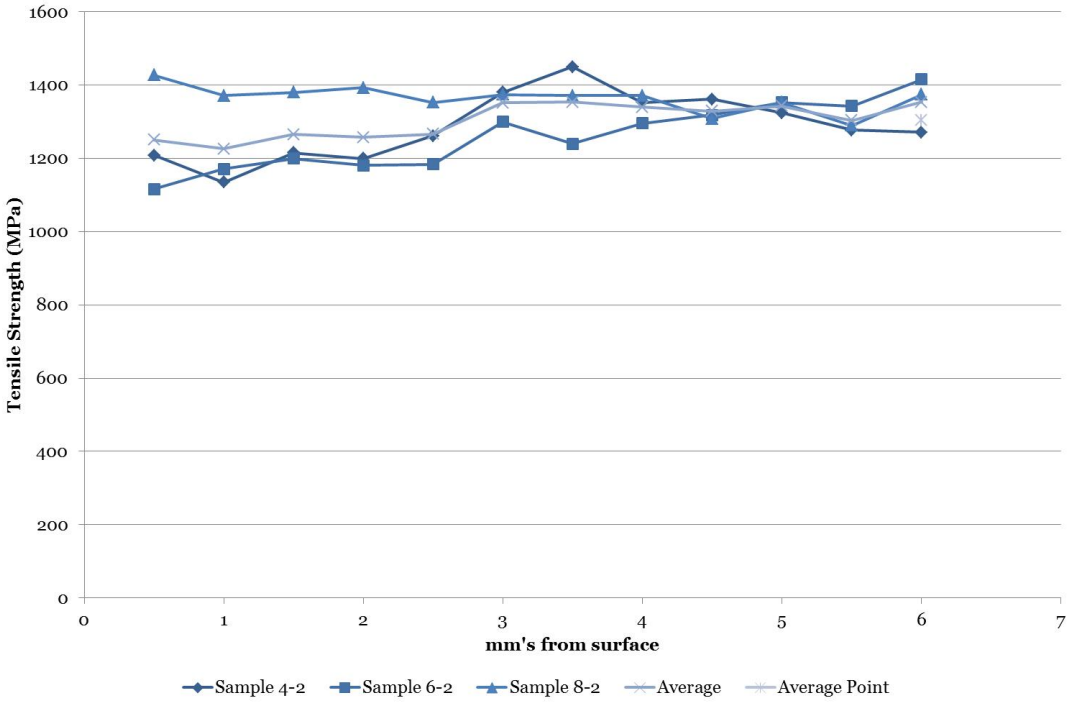

Figure 4.80: Tensile strength of 17-4 PH - Derived from correlation between tensile strength and Vickers hardness using data obtained experimentally from microhardness measurements.

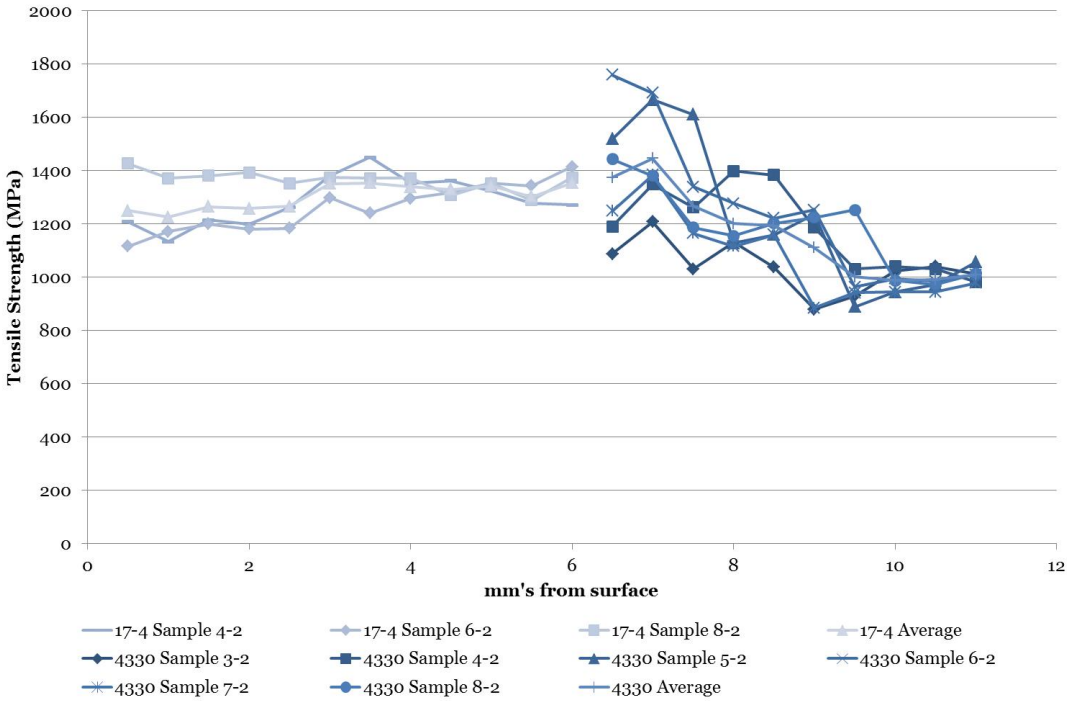

Figure 4.81: Tensile strength of 4330 (HAZ of 4330 clad with 17-4 PH or Inconel 625) and 17-4 PH - Derived from correlation between tensile strength and Vickers hardness using data obtained experimentally from microhardness measurements.

tensile strength values may be influenced by the cladding parameters such as pre-heat temperature and consequent effects such as the level of alloying and dilution. Tensile strength for 4330 is lower when clad with Inconel 625, which is to be expected due to the lower tensile strength values of Inconel 625 in comparison with 17-4 PH. The range of tensile strength values for 4330 is very large, signalling that the HAZ is very sensitive to the welding process and this is reflected in resulting hardness values and therefore also in derived tensile strength values. Experimental and derived values correlate well in the case of 17-4 PH. Experimental values lie in the lower region of the range for 4330.

Data presented herein for tensile strength was not utilised for the purpose of the weld cladding simulation in this case. However in future it would be recommended that a bilinear material model is implemented in the finite element model ideally utilising data from experimentally obtained stress-strain curves.

	Tensile strength (MPa)	
Material	**Experimental**	**Derived**
Inconel 625	770	-
17-4 PH	1167	1115-1150
4330 HAZ (Inconel 625 clad)	1017	886-1666
4330 HAZ (17-4 PH clad)	1010	963-1760

Table 4.20: Comparison of experimental and derived tensile strength values at room temperature

4.4.11 Young's modulus

Due to the issues encountered with the extensometry during the tensile testing program, the determination of Young's modulus was undertaken separately. This was undertaken for all materials under investigation using a TA Instruments Dynamic Mechanical Analyser (DMA) Q800. Using a single sample, Young's modulus values are obtained at specified temperatures through the application of a three-point bending load to the beam-like specimen. The dimensions of the specimen are measured prior to testing, with deflection of the beam measured throughout the experiment. The specimen geometry is shown in figure 4.82. These specimens were machined from remaining tensile test specimens as shown in figure 4.83. As yield is not exceeded during testing, the same specimen could be utilised to obtain yield over the entire temperature range.

The maximum load of the machine is 18 N, with this value being reached using a 3 N/min ramp rate. Stress-strain diagrams can then be constructed using the obtained

data and the Young's modulus calculated by determination of the gradient of the stress-strain curve. Creep effects were again assumed negligible over the duration of the test.

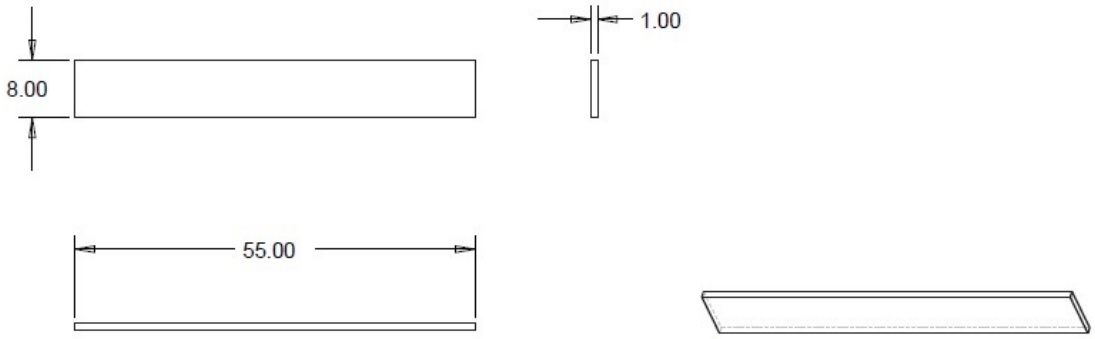

Figure 4.82: DMA specimens for experimental determination of Young's modulus - Dimensions in millimetres.

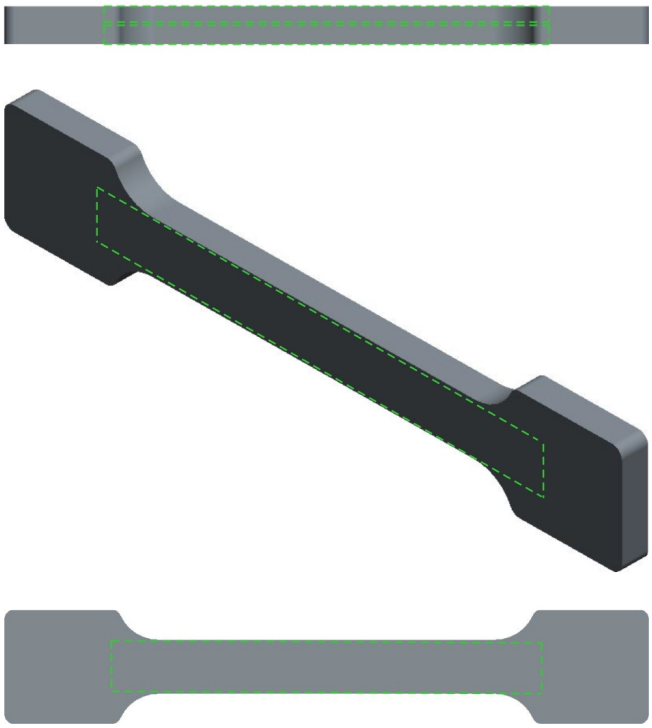

Figure 4.83: Machining of DMA specimens for experimental determination of Young's modulus - Specimens machined from remaining tensile test specimens using wire EDM.

Readings could only be obtained upon heating and cooling the specimen from room temperature to 500°C due to the limited temperature range of the equipment. Measurements were obtained in 100°C increments to observe effects with increasing temperature.

For the purposes of the finite element simulation, Young's modulus values were extrapolated to melt temperature, assuming a zero value at the melt temperature.

Values were extrapolated in a manner such that the values of Young's modulus decreased consistently to a value of effectively zero stiffness at melt temperature. This was deemed appropriate due to previous studies on the characterisation of weld metal indicating that the stiffness of the material decreased gradually with increasing temperature (150).

Minimal variation would be expected in heating and cooling data for Inconel 625 and this is indeed the case. There is also minimal variation in heating and cooling data for 4330. Notable variation is observed for 17-4 PH, with slightly increased stiffness values upon cooling.

The values extrapolated along with the experimental results and the available published data are shown in figures 4.84-4.87.

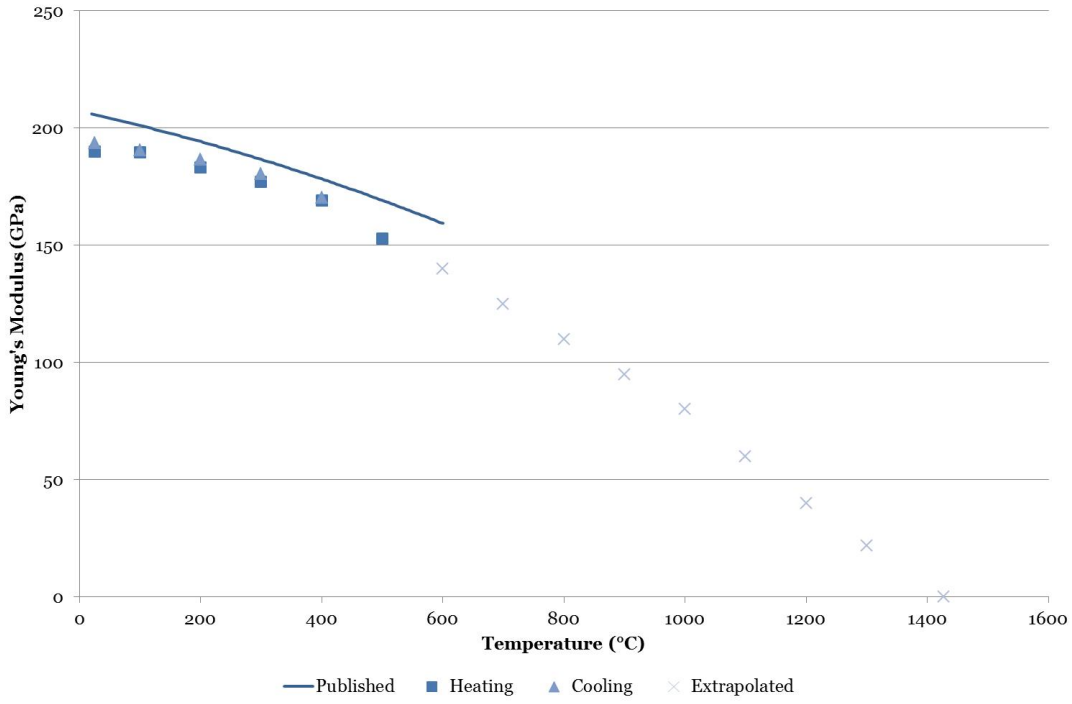

Figure 4.84: Young's modulus of 4330 (HAZ of 4330 clad with Inconel 625) - Experimentally obtained using a TA Instruments Q800 DMA.

Previous studies of austenitic stainless steel cladding on ferritic steel reactor pressure vessels revealed that the Young's modulus of as-clad material deviate from the bulk modulus, the degree of variance depending on the orientation to the cladding plane (151). This is attributed to effects from the texture arising during solidification and the presence of the δ-phase. Through annealing, the δ-phase is dissolved and the deviation from the bulk modulus decreases. Earlier discussions highlighted that some tensile specimens were machined parallel to the orientation of clad passes, while the majority were machined perpendicular to the clad passes. The specimens machined for the purposes of obtaining Young's modulus were obtained from the same

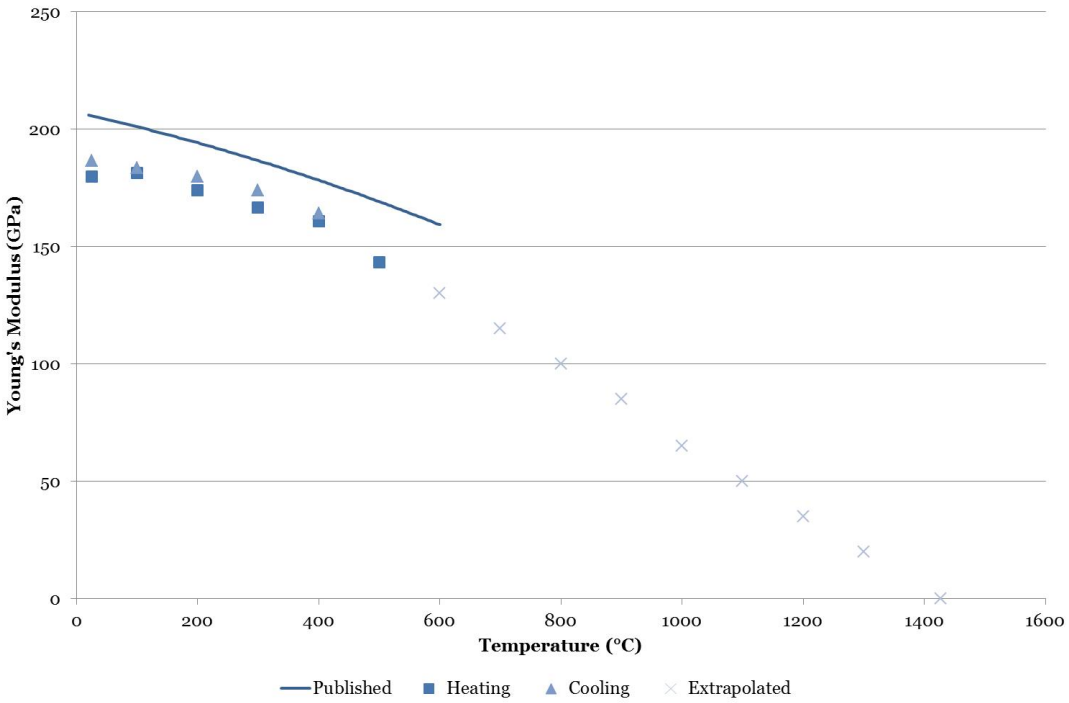

Figure 4.85: Young's modulus of 4330 (HAZ of 4330 clad with 17-4 PH) - Experimentally obtained using a TA Instruments Q800 DMA.

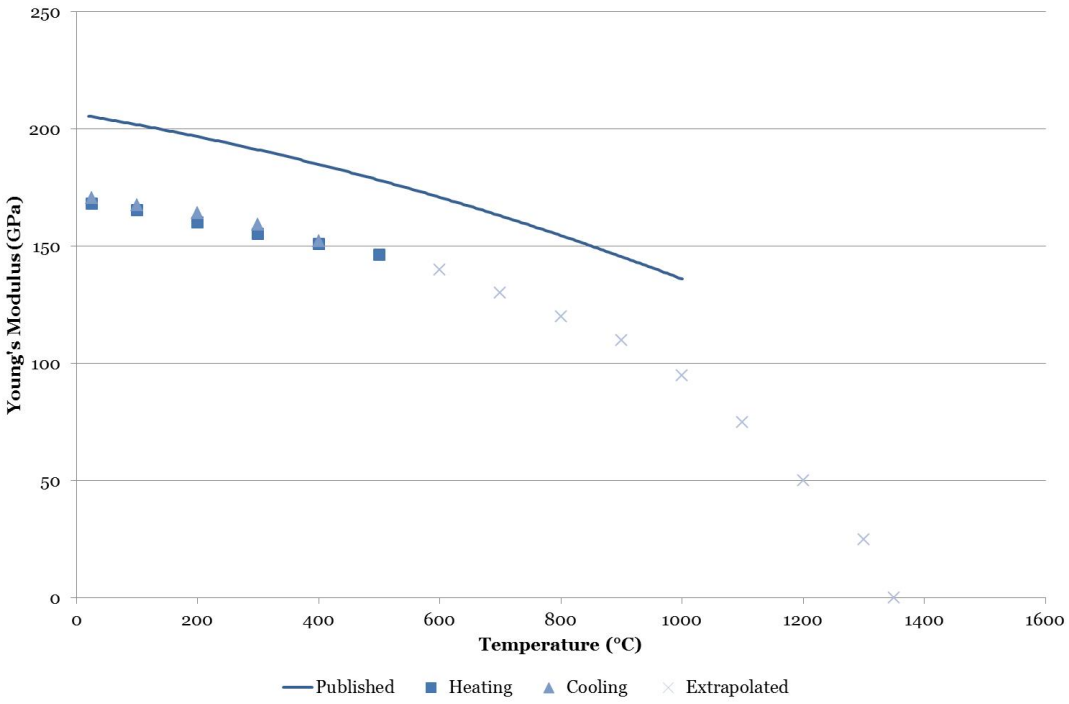

Figure 4.86: Young's modulus of Inconel 625 (Clad on 4330) - Experimentally obtained using a TA Instruments Q800 DMA.

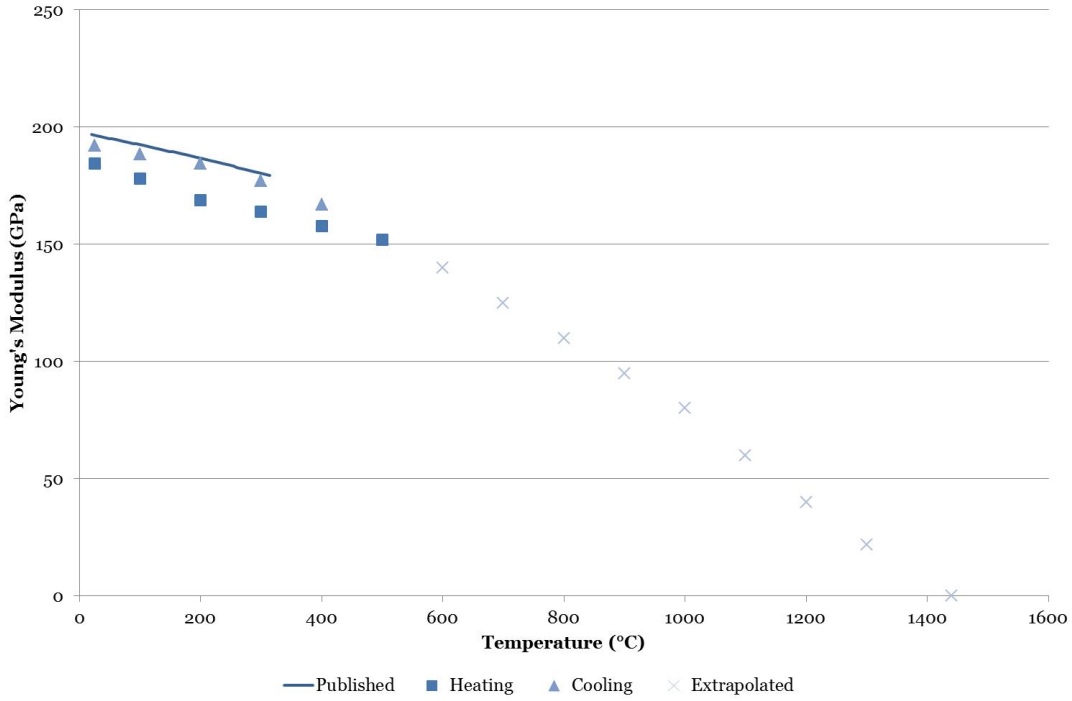

Figure 4.87: Young's modulus of 17-4 PH (Clad on 4330) - Experimentally obtained using a TA Instruments Q800 DMA.

material. Unfortunately , however, due to the small number of specimens tested, conclusions could not be drawn as to the presence of anisotropy of Young's modulus. These findings do however illustrate that effects of the cladding process on material properties should also be considered.

4.4.12 Toughness

For the purpose of the finite element simulation and therefore the validation of the model with experimental residual stresses, toughness values were not utilised. However, as the weld cladding process will impact toughness values it would be of interest to investigate resulting toughness values. Commonly weld consumables would be tested to obtain this property. In the same way as the thermal and mechanical properties were obtained as described in this chapter, it would be possible to experimentally obtain toughness values for the clad, HAZ and substrate regions of the materials under investigation. Although this was not the focus of this research, the potential testing method was considered.

With concerns over brittleness of the HAZ, the Charpy test would provide further insight into this, with the aim of this test being to indicate the energy absorption required to cause material fracture. A weighted mass is used to impact a notched specimen on the surface opposite to that on which the notch is machined, causing fracture of the specimen. The energy required for fracture is determined by assessing

the height reached by the mass post-impact. This value of energy and cross-sectional area of the specimen are then used to determine the toughness of the material.

The dimensions for standard Charpy specimens would require a length of 55 mm with 10 mm square ends. The limitation of available material led to the investigation of the preparation of sub-size or miniaturized specimens. Appropriate dimensions for miniaturized specimens were obtained from the ASTM standard (152). These specimens would require the machining of customised shims to enable testing as the testing equipment available has a minimum standard depth requirement of 10 mm in line with the standard Charpy specimen dimensions as provided in the ASTM standard (153). The miniaturized specimens dictated a depth of 4.83 mm and therefore the specimen would be required to be brought forward to allow the mass to impact the specimen at the required location. Sub-size specimen dimensions as provided in the appendices of the ASTM standard (153) and shown in figure 4.88 were selected as the most appropriate. With the thickness of these specimens being less than the standard specimens, shims would also require machining to allow the specimen to be impacted in the correct location and ensure that the weighted mass does not begin to travel upwards prior to impacting the specimen. Surface finish requirements are also provided in the standard.

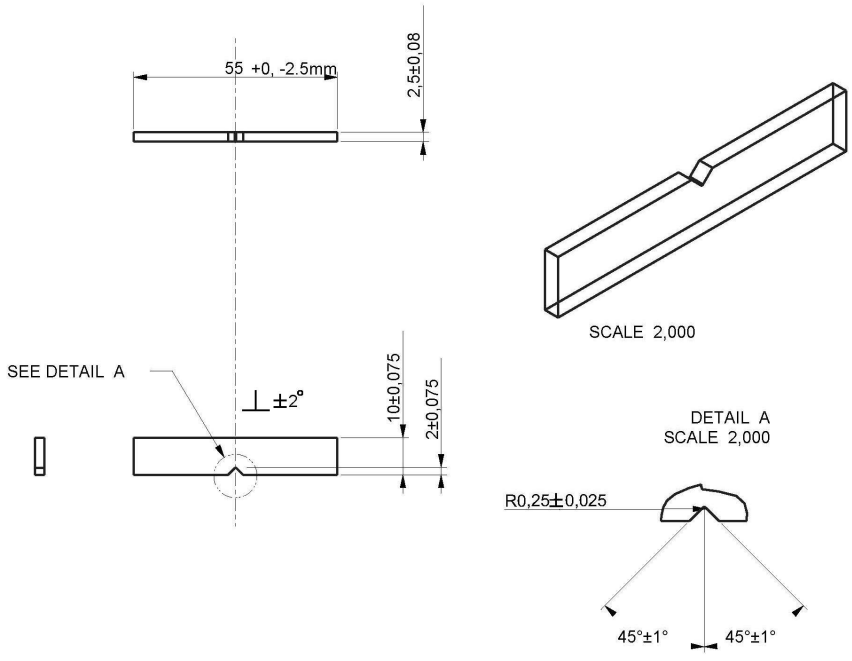

Figure 4.88: Sub-size Charpy specimen geometry and dimensions - Specimen dimensions in millimetres, derived from ASTM standard (153).

A consideration of undertaking testing utilising miniaturized specimens would be that results from the standard Charpy specimens would not be directly comparable to results of the miniaturized Charpy specimens. Therefore, miniaturized specimens

of unclad materials would also be required to allow comparison and conclusion as to the effects of the welding process on the toughness of these materials.

It would also be of interest to assess the change in ductility of the materials with temperature, also possible through the Charpy test. This is not of importance in the operation of the weld clad components, but certainly is of interest with regards to potential weld process refinement to ensure the most satisfactory material properties arise through the cladding process.

Furthermore, studies have been undertaken to assess the toughness of the interface of as-sprayed specimens subjected to the *HVOF* coating process (154). These studies examining coating adhesion of chromium carbide coatings indicated that toughness of the interface of as-sprayed components varied inversely with the square root of the coating thickness. Annealed components on the other hand appeared to possess toughness values independent of coating thickness. Similar research could be carried out in the case of the clad specimens to examine the effects of clad thickness, *PWHT* and material combinations on interface toughness.

Alternatively, Izod testing could be undertaken, with the specimen fixture differing to that of the Charpy test. Izod testing would also be restricted to testing at room temperature due to the method of fixing the specimen. The facilitation of sub-size specimens for Charpy testing and access to testing equipment would present Charpy testing as the most favourable option.

4.5 Summary

At the beginning of this chapter, metallurgical studies showed that the weld cladding process produced good fusion between clad and substrate materials. Neither non-metallic inclusions nor weld defects were found to be present. However, non-metallic inclusions were observed in the substrate material, present prior to application of the cladding process. The use of such material should be minimised, particularly in demanding applications involving fatigue and corrosion. The two-pass system applied produced variation in the microstructure in both passes due to the tempering of the first pass upon deposition of the second pass. This is beneficial due to the increased levels of homogeneity arising through this tempering.

Alloy segregation in the HAZ has been highlighted, creating alloy rich and alloy lean regions, increasing hardness values in areas of increased chromium and nickel content. $PWHT$ was found to decrease alloy segregation, therefore also beneficial in decreasing hardness values. Care must be taken when investigating the HAZ properties, as the supposition of average hardness values being adequate would not account for the range of values that has been shown to result through the weld cladding process. The *NACE* standard states that values exceeding the maximum hardness values provided are acceptable if several readings in the same region result in an average lower than the maximum permitted value, however the number of measurements required is not specified (110). Bearing this in mind, the weld cladding process requires further investigation and refinement to minimise regions of high hardness, but also generally to ensure satisfactory resulting material properties. Iron dilution levels should also be monitored. Iron dilution was found to be greater in the first pass of an Inconel 625 clad in comparison with the second as expected, with a recommendation of iron dilution levels of less than 5% at the clad surface so as not to impact corrosion resistance benefits of Inconel 625. A martensitic structure resulted upon welding with 17-4 PH, with the effects of heating and cooling rates known to affect the resulting microstructure in such materials. Therefore, it would be beneficial to refine the welding process for 17-4 PH clad on 4330 to ensure that the resulting microstructure and material properties are satisfactory. As will be discussed in a later chapter, the welding process applied when utilising 17-4 PH as the clad material also heavily impacts the resulting residual stress state and therefore there are likely to be contradictory requirements to ensure adherence to standards whilst also maintaining a desirable stress state.

Investigation of the thermal and mechanical properties of the materials selected for the purposes of this research has illustrated the wide range of considerations when undertaking the weld cladding process. The relationship between properties of the

clad and substrate materials can heavily influence resulting properties, with potentially large variations as the interface between the clad and substrate is traversed. The 17-4 PH and 4330 materials are *better matched* due to both being high strength, martensitic materials with similar yield stress values and a body-centred cubic lattice structure. Inconel 625 on the other hand possesses a face-centred cubic lattice structure, has a lower yield stress and does not exhibit phase changes upon heating and cooling. This is clearly illustrated in the results of the material property characterisation program presented in this chapter, especially in the case of the temperature-dependent thermal properties.

Results of the material characterisation program have been presented in this chapter, with details of the production of specimens, the testing procedure and issues encountered documented. Based on the program conducted, recommendations have been provided for future studies to further improve knowledge and understanding of the effects of the welding process and the arising material properties.

Capturing the thermal behaviour of materials is crucial for the accurate simulation of residual stress generation. Coefficient of thermal expansion has been said to be a dominant factor in the generation of residual stresses (84), with 4330 and 17-4 PH possessing similar characteristics upon heating and cooling. The effects of CTE on resulting residual stresses will be further investigated and discussed in section 7.4.1. It is clear when reflecting upon the results showing the variation in CTE values upon heating and cooling that input of respective material data sets would result in a very different residual stress state in a thermal transient analysis. Moreover, it has been proven that in all cases available published material properties are inadequate for input into a finite element model if accurate stresses are desired. Early studies have been undertaken and presented as to the effects of the cooling rate on CTE values and it would clearly be beneficial to investigate higher cooling rates to capture expected effects of cooling rate on material properties. It is realised that cooling rates examined in this testing program are not indicative of the cooling rates that will occur during the weld cladding process, particularly in the early stages of cooling immediately after the weld cladding process has been completed. This is discussed in section 5.6. A major limitation of the characterisation of the materials is the inability to capture the cooling rates that will be experienced in the early stages of the cladding process as the molten metal is deposited onto the pre-heated substrate.

Usually, material selection is driven by the desire for higher strength materials to ensure a higher UTS and therefore increased fatigue strength. It has been mentioned in this chapter, that the correlation between UTS and fatigue strength is lost upon application of a welding process. It should also be highlighted that fatigue consists of the crack initiation and propagation stages. In the crack initiation stage, the correlation

with UTS is applicable in non-welded applications. However, in the crack propagation stages, correlation exists between fatigue strength and toughness. In non-welded scenarios, the majority of the lifetime of a component can be spent in the crack initiation phase. In the case of welding, defects that arise due to the welding process can behave in a similar manner to initiated cracks and therefore welding can produce a bypassing of the crack initiation phase (155), entering the crack propagation phase at an early stage of component operation. This is of course undesirable and can cause fatigue failure at a much earlier stage than anticipated if not correctly assessed and accounted for. A suitably tough material with the capability of minimising crack propagation rates would be most appropriate in this case. These factors illustrate the importance of understanding material behaviour in specific scenarios, as this can very much alter the points of importance in material considerations.

In future, to further increase understanding and appreciation of the effects of the weld cladding process on material properties, it would be of interest to investigate the effects of pre-heat temperature, cooling rates and $PWHT$ on resulting material properties. Other aspects such as welding speed and the number of passes could also be investigated but it is clear that this would require a large number of specimens to undertake such a testing program to ensure that all results are sound from a statistical point of view.

Chapter 5

Simulating the Weld Cladding Process

Simulation of the weld cladding process was undertaken in Abaqus, investigating initial axisymmetric models through the deposition of one-pass. The modelling process was developed to account for the deposition of two passes and weld beads in an axisymmetric model, likewise in a planar model and finally a three-dimensional model developed accounting for the temporal deposition process and the thickness of the weld beads. It was found that the nature of residual stresses arising in all models remained the same, allowing the conclusion to be drawn that increasing the complexity of the weld clad model is not strictly necessary in this case. The reasons for this are discussed herein. Material properties were emphasised as more crucial in capturing the correct residual stress state in the clad layer. The effects of pre-heat temperature are discussed, results illustrating that a higher pre-heat temperature successfully decreases the discontinuity stress arising in the vicinity of the interface. This would be desirable from a fatigue perspective. Cooling rates at various nodes in the model are examined to provide an indication of the temperature history experienced throughout the substrate and clad materials. The need for further investigation of the microstructure and experimental testing for material properties using representative cooling rates is discussed. Ultimately, initial axisymmetric models successfully capture the development of residual stresses in the weld clad cylinder and provide results with which to compare experimental residual stress measurements to gauge correlation and allow validation of the finite element model.

5.1 Introduction

The nature and distribution of residual stresses in dissimilar joints resulting due to the application of thermal processes such as welding and brazing, are invariably important for fatigue life assessment. Dissimilar material joining influences these residual stresses as discussed in chapter 3 and therefore the development of the fatigue-resistant weld cladding concept requires the residual stress state to the examined.

Simulation of residual stresses and dissimilar joints requires in-depth knowledge of the behaviour of both substrate and joining material. This proves to be one of the greatest challenges as heavily emphasised in the previous chapter due to the poor availability of temperature-dependent material property data from room temperature up to melting point, particularly for the as-clad material as opposed to the welding consumable and substrate material, more commonly available. The importance of this data should not be underestimated, as phase transformations in particular are integral to capturing the behaviour of the dissimilar joint. This is discussed in a study by Katsuyama et al. (156) demonstrating that neglecting this aspect can deny the compressive nature of stresses in the substrate completely. Capturing phase changes in the solid-state of a material is therefore highlighted as crucial in both the joining and post-weld heat treatment processes. This was the driving factor for the in-depth investigation of the temperature-dependent material properties in the previous chapter. Having obtained experimental data for the clad and substrate materials, modelling of the weld cladding process was investigated. Simulation of the weld cladding process presented in this chapter was modelled in Abaqus utilising the geometry of the weld clad components presented in chapter 3 and the material properties presented in chapter 4.

5.2 Complexity of weld clad modelling

The mechanisms involved in inducing residual stresses were discussed in section 1.2.1. In the simulation of the weld cladding process it is crucial to capture all factors contributing to the final residual stress state arising due to the weld cladding process. One of the key findings in the previous chapter was the influence of heating and cooling on the temperature-dependent material properties, particularly illustrated in the experimentally obtained thermal material properties. With the thermal transient nature of the weld cladding process, it is clear that the heating and subsequent cooling of the component will influence the residual stresses arising due to specific material behaviour such as phase transformations.

Due to the complexity of weld modelling, benchmark exercises are a common method utilised in examining successful modelling of the residual stresses arising through such processes.

The European Network NeT (157) conducted a round robin exercise examining the residual stresses in a single weld bead on a flat austenitic steel plate through measurement and simulation of the arising residual stresses. This research was undertaken over the course of nine years, with fourteen sets of residual stress measurements, five measurement techniques and over forty finite element simulations. The specimen utilised in this study therefore provides a benchmark and guidance for the simulation and measurement of residual stresses. Highlighted in this study is again the importance of accurate thermal and mechanical material properties varying with temperature and the use of an appropriate material model.

Another example of such a benchmarking exercise is the investigation into the design and manufacture of a pressuriser safety/relief valve nozzle with and without weld overlay (140). This comparative study was undertaken by three organisations, investigating the effect of heat input, manufacturing history and constitutive models on the resulting residual stresses in the simulation model. These values were also compared with experimental residual stress measurements using the deep-hole and incremental deep-hole drilling methods. The three organisations, BE-ANSTO, EMC2 and Westinghouse used 46, 48 and 25 passes respectively for the main weld. It is within the reporting of this research that is has been postulated that the effects of variations in thermal material properties will not greatly impact final residual stress states above a temperature of 800°C due to the lower strength possessed by materials at such high temperatures.

Investigation into accurate weld modelling and the influence of simulation variables on resulting residual stresses predicted by the simulation include factors such as welding heat input, manufacturing history and material constitutive models. These aspects are well introduced in the literature (158), (159).

Weld simulation will often focus either on the thermo-dynamics approach or the thermo-mechanical approach. The former concentrates on the thermal behaviour of the HAZ and models the molten weld pool, while the latter concentrates on the heat source energy, accounting for the thermo-mechanical behaviour on a global scale (160).

The coupling of thermal and mechanical aspects is presented in (158). Heat transfer effects cause deformation which in turn generates heat. The thermal properties of the material are specific to each material depending on the composition and phase changes experienced, these phase changes related to latent heat. Both thermal and deformation related phase changes can occur. It is emphasised that microstructural

effects influence deformation through phase and volume changes. Such material behaviour is temperature dependent as illustrated in the previous chapter in the experimentally obtained data. The ability to determine solid state phase changes through dilatation is illustrated showing the dilatation of a martensitic stainless steel upon heating and the visible phase change from ferrite to austenite. This illustration matches that observed in the case of the heating curve obtained experimentally for 4330 and 17-4 PH. The coefficient of thermal expansion data presented in section 4.4.2 is derived from thermal dilatation data with respect to temperature obtained experimentally using the equipment described. Upon cooling the martensitic transformation is observed at a lower temperature according to the experimental data obtained during testing of 4330 and 17-4 PH and it is emphasised that thermal dilatation and the constraint thereof is the cause for welding stresses with the cooling stage being of most importance with this dominating heating effects. Varying levels of modelling complexity include factors such as including temporal variations in thermal and mechanical material properties. More specifically this can be accounted for through increasing conductivity in the weld pool, modifying the heat capacity to account for phase changes and accounting for the heating and cooling processes.

Development of the modelling process will be investigated in this chapter, accounting for the following characteristics of the weld deposition process:

- Accounting for the deposition of one pass using an axisymmetric representation
- Accounting for weld beads in the deposition of one pass
- Accounting for the deposition of two passes
- Accounting for weld beads in the deposition of two passes
- Accounting for the deposition of two passes in a planar model
- Accounting for weld beads in the deposition of two passes in a planar model
- Accounting for weld beads in the deposition of two passes in a 3D model

5.3 Simulating the weld cladding process using an axisymmetric representation

In modelling the weld cladding process, the overall residual stress state in the model was the key interest. Therefore, a simplified modelling approach was justified as discussed in (158). The initial two-dimensional axisymmetric models simplify the three-dimensional cladding process.

The level of complexity included in accounting for the material behaviour is variable in welding simulation. As has been previously discussed it may be that published material data is utilised or that data is provided by the manufacturer. Material properties can be subject to assumptions such as low values of yield stress and elastic and hardening moduli to account for the low strength and stiffness of materials at high temperatures. This method of altering yield stress and elastic and hardening moduli was applied by Brickstad and Josefson in (161), along with the setting of the coefficient of thermal expansion as a constant throughout the simulation. This constant value was the mean value across the temperature range. The experimental thermal and mechanical properties obtained with temperature and extrapolated to melt temperature herein enable a simplified characterisation of materials for the weld clad simulation, whilst capturing major variations in material properties due to phase changes, for example.

The influence of thermal and mechanical properties on resulting residual stresses has also been discussed in the welding of aluminium plates (162). This study concluded that yield stress has the most notable impact on residual stresses, while it is satisfactory to utilise average values for material properties to achieve a satisfactory indication of residual stresses. This is understandable in the case presented, where the thermal expansion value is essentially constant with temperature. In fact, the data presented in (162) clearly allows the assumption of constant material properties even for density, thermal conductivity and specific heat capacity. However, as highlighted in the previous chapter, this is far from the case with the materials under investigation. This also presents inaccuracies in the deformation produced in the model as thermal dilatation dictates deformation (158). The observation that Young's modulus has a minimal effect on the resulting residual stresses could also be argued in the research presented herein, due to little variation in Young's modulus values in steels. However, there is still a notable variation with temperature in all material properties, both thermal and mechanical. Therefore the experimental testing program discussed in the previous chapter was of utmost importance in preparation for the modelling of the weld cladding process.

It is common to reduce the complexity of the simulation model by decreasing the dimensions accounted for in the model (158). Reducing the number of passes is also a method of decreasing complexity of the model. It was demonstrated by Rossillon and Depradeux (163) that inclusion of the last deposited pass as well as the reduction of the number of passes provides a satisfactory residual stress distribution when compared with multi-pass simulations of austenitic pipe girth welds. This led to the initial simulation model adopting an axisymmetric form with the deposition of the entire clad layer thickness in one step.

The use of an axisymmetric model to simulate the residual stresses arising due to spiral weld cladding of Inconel 625 on SA210 carbon steel showed good agreement with experimental neutron diffraction measurements (164).

The transformation of the clad cylinder into an axisymmetric model is shown in figure 5.1. The applied mesh is also illustrated with the use of the Abaqus element type *CAX4T* with bi-linear displacement and temperature shape functions.

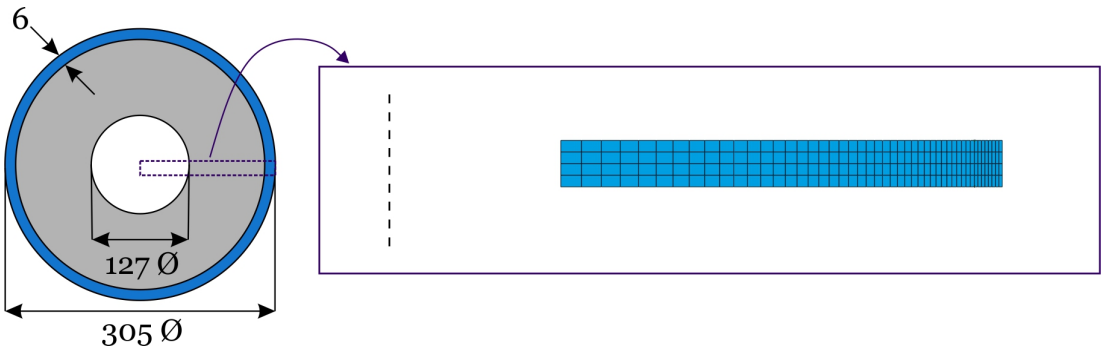

Figure 5.1: Model for clad deposition on outer diameter of cylinder - Illustrating the transformation of the weld clad cylinder into an axisymmetric model. Dimensions in millimetres.

Figure 5.2 shows the cylinder with a clad layer applied onto the inner diameter of the cylinder. This case was also investigated due to the more realistic nature in terms of application of the cladding technology at this location of the components in question. It was found that stresses were of a similar nature and therefore that cladding on the outside diameter of the cylinder, a simpler cladding process in terms of deposition, would provide an indication of the stresses that would be expected generally from utilising the representative geometry and materials.

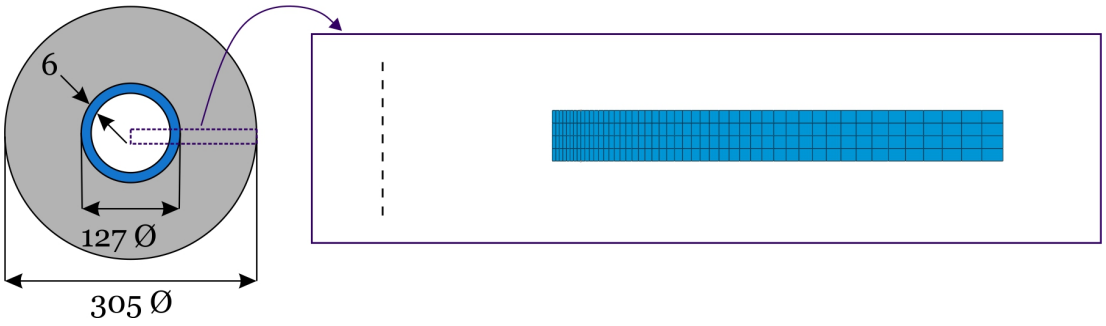

Figure 5.2: Model for clad deposition on inner diameter of cylinder - Illustrating the transformation of the weld clad cylinder into an axisymmetric model. Dimensions in millimetres.

In terms of the model and heat input to model the weld material deposition process, the level of complexity is simplified. This is achieved by carrying out a transient thermal analysis, assigning a temperature to the weld material and assigning appropriate convective heat transfer coefficients and/or insulation boundary conditions

where relative acting as a method of heat input. In the initial axisymmetric model, the entire clad layer is effectively therefore deposited onto the pre-heated cylinder at the beginning of the thermal transient analysis. This creates the assumption of no variation in the temperature or stress fields in the axial and hoop directions as a function of time. Upon commencing the next time step, the entire model begins to cool to room temperature and the material develops stiffness as the model cools. This method has been often utilised, with Carmet et al. prescribing a temperature of 1500°C for the molten weld pool (165) and Goldak et al. prescribing both a maximum temperature and the melt temperature for the analysis (159). The weld material is also set at melt temperature in the investigation of fusion welds by Jones et al. (166). It is noted however, that utilising this approach does not accurately capture the heating characteristics prior to welding, as the material is prescribed at melt temperature from what is viewed as the beginning of the welding process.

Lindgren discusses *cut-off temperatures* used in various published modelling processes, these temperature values being the upper limit for which variation in mechanical material properties are accounted for (158). As was presented in the previous chapter, yield stress and Young's modulus were assigned a zero value at melt temperature, with a linear extrapolation from the last obtained experimental data point. A lower *cut-off temperature* can increase the error in residual transverse stresses, a 2-15% overestimation of stresses arising when the *cut-off temperature* was varied between 600°C and melt temperature (167).

The melt temperatures for the materials investigated are listed in table 4.6. Neither the solid-liquid phase change nor latent heat effects have been accounted for in the analysis.

The momentary heat source utilised, as mentioned, is categorised as a simplified model (158). Thermal boundary conditions, as shown in figure 5.3, have been applied to capture the cooling process applied in the real weld cladding process and the cladding setup. The radial edges of the model were insulated to simulate no axial heat transfer and plane strain conditions applied on the radial lines.

The assumption of plane strain boundary conditions applied herein is highlighted as producing larger longitudinal stresses (158). It is clear that this type of model does not account for the welding speed and therefore it can be considered a weld with infinite speed. This type of model does not capture the transient nature of the welding process in a multi-pass process. It should be noted that the welding simulation discussed in this text is not that of weld cladding, but primarily butt-welds.

Temperature-dependent material properties as experimentally obtained and extrapolated to melt temperature for 4330, Inconel 625 and 17-4 PH were utilised to charac-

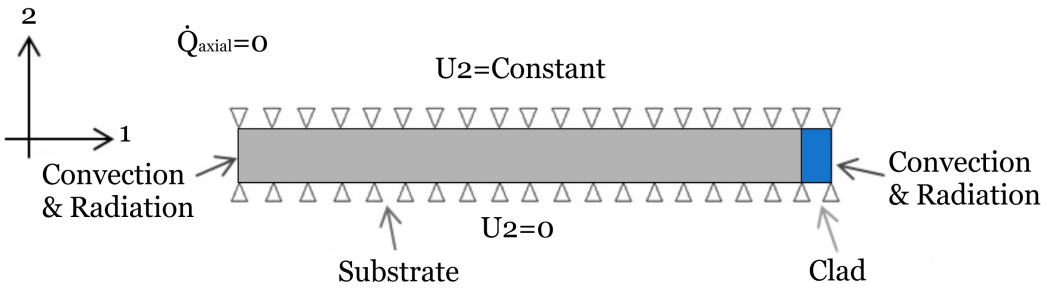

Figure 5.3: Boundary conditions for axisymmetric model - Boundary conditions illustrated for an outer clad cylinder.

terise thermal and mechanical behaviour assuming an elastic-perfectly plastic material model.

The thermal event, degree of constraint and therefore the development of residual stresses due to the weld cladding process are primarily governed by *CTE*, specific heat capacity, thermal conductivity, Young's modulus and yield stress. The finite element software utilised assumes a linear extrapolation between data points and were data not to have been extrapolated to melt temperature, a zero-gradient extrapolation would have been assumed from the last available data point. Therefore, it is not only crucial to ensure accurate values for material properties but also the entire temperature range, especially for the five properties noted above.

Initially density was considered constant, however due to the use of density as a multiplicator with heat capacity in a thermal analysis, temperature-dependent density was accounted for as detailed in section 4.4.5. Poisson's ratio was also initially considered constant, and although this is deemed acceptable, the variation in this property was also accounted for in the simulation as detailed in section 4.4.6.

The entire component was subjected to slow cooling on the inner and outer diameters using a convective heat transfer coefficient of 10 W/m^2K representative of low speed air flow over a surface. A bulk temperature of 25°C was assigned. Emissivity was assumed constant throughout the analysis.

Finite element model data input for all models is provided in Appendix A.

5.3.1 Results

Results are presented for both dissimilar weld clad cases, with the clad material applied on the outside of a low alloy carbon steel thick cylinder using two pre-heat temperatures.

In obtaining residual stress distributions for the axisymmetric model, a path was plotted in the radial direction from the inner to the outer diameter. The path therefore

begins at the bore, this being the substrate material, and traverses towards the clad material at the outside diameter. Figure 5.4 shows the path highlighted in the centre of the axisymmetric model. Meshes utilised are the result of convergence studies.

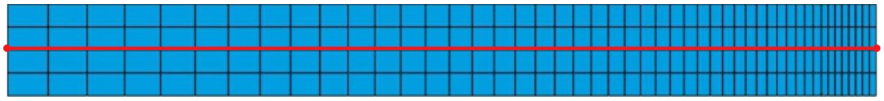

Figure 5.4: Axisymmetric model path - Path utilised in obtaining results data for the axisymmetric model.

In plotting the hoop, radial and axial stress components along this path, the location of the substrate-clad interface has been highlighted using a vertical dotted line to facilitate understanding of the variation in stresses due to respective materials. Likewise, the yield stress of the clad material has been highlighted on each figure using a horizontal dotted line to illustrate the level of residual stress present in the clad layer at the end of the analysis.

Figure 5.5 shows the stress component results at the end of the analysis for the axisymmetric model of 4330 substrate, pre-heated to 150°C and clad in one pass with Inconel 625. It can be seen that radial stresses are compressive along the path, yet lower than hoop and axial stresses. Hoop and axial stresses are compressive in the substrate, with a large discontinuity stress as the path approaches the interface, reaching high into the tensile region. The level of tensile residual stress is not as great as the yield value of the substrate material (869 MPa when clad with Inconel 625). Upon entering the clad layer, these tensile residual stresses decrease to below the level of yield of the clad material (474 MPa). Hoop stresses remain constant throughout the clad layer, whereas axial stresses increase slightly towards the clad surface.

Figure 5.6 illustrates stress component results for the same clad and substrate combination, with a higher pre-heat temperature of 300°C. The stress components are similar to those in figure 5.5 in the substrate, however the discontinuity stress at the interface is much lower in both the hoop and axial components. Hoop and axial stresses are of the same level and trend as in the previous model.

In the case of a 17-4 PH clad with a pre-heat temperature of 150°C, residual stresses are tensile in the substrate material. Figure 5.7 shows that radial stresses are again lower than hoop and axial. A tensile discontinuity stress arises as the path approaches the interface, however again these stress levels are lower than the yield stress of the substrate when clad with 17-4 PH (856 MPa). Both stresses decrease significantly into the compressive region upon entering the clad material. Hoop stresses reach the yield stress value of the clad material (994 MPa) while axial stresses remain at a level slightly lower than yield. Both stress components increase slightly towards the clad surface.

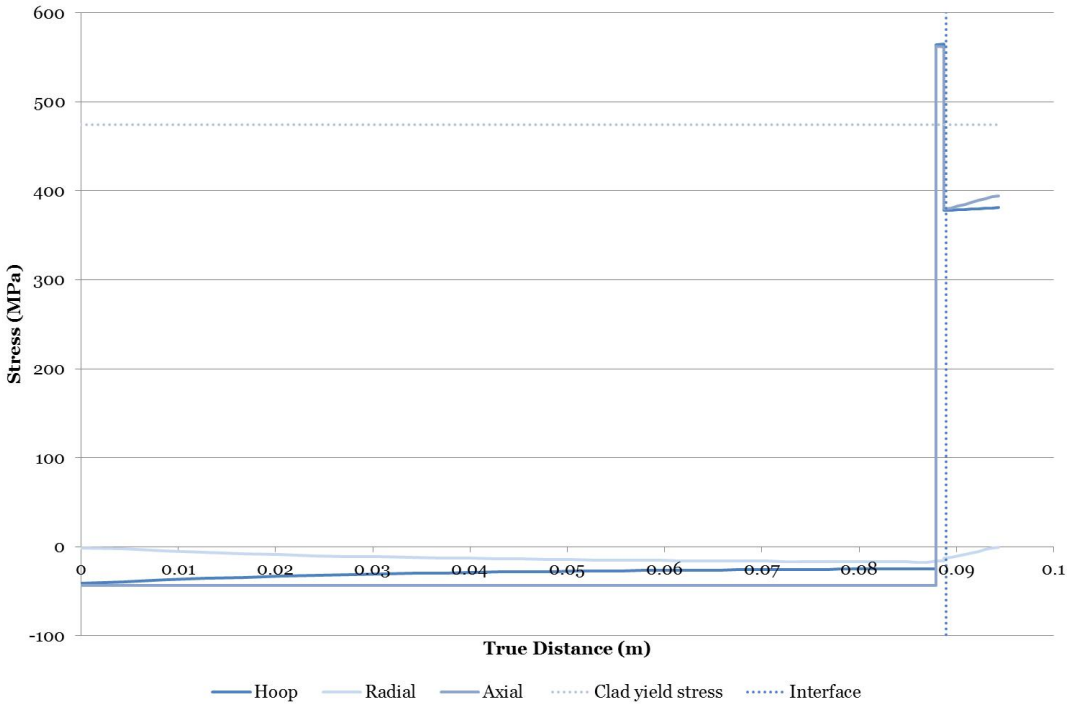

Figure 5.5: Stress components in an axisymmetric model of 4330 substrate and Inconel 625 clad with pre-heat temperature of 150°C - Results shown with the path beginning at the inner diameter, travelling towards the clad surface with the interface highlighted.

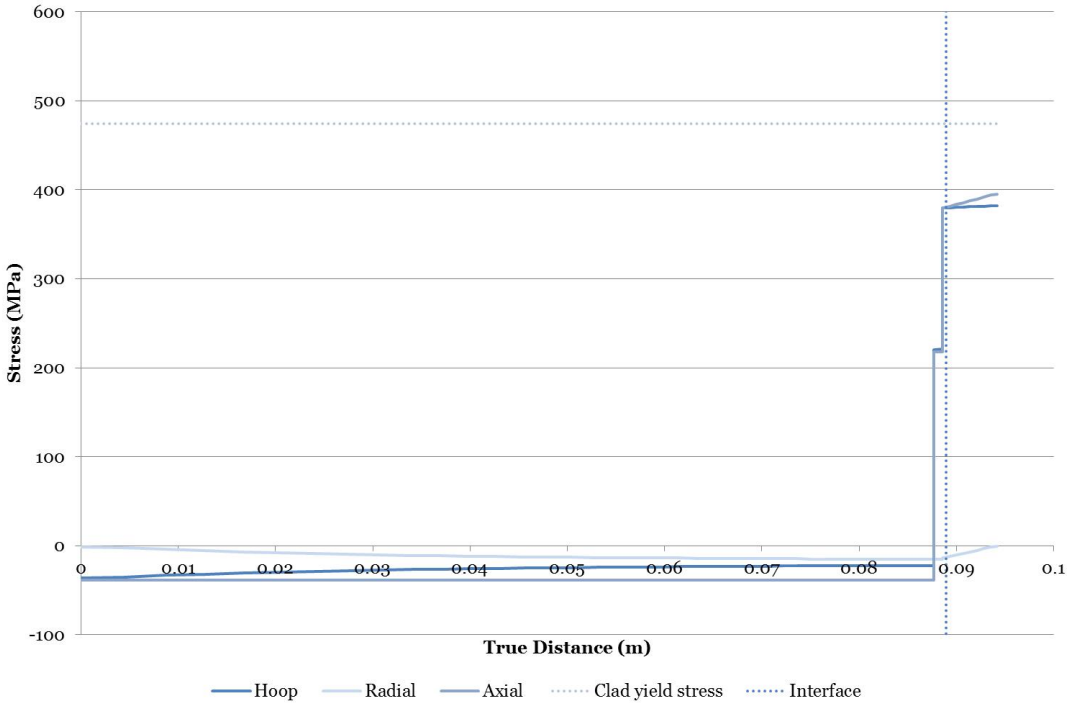

Figure 5.6: Stress components in an axisymmetric model of 4330 substrate and Inconel 625 clad with pre-heat temperature of 300°C - Results shown with the path beginning at the inner diameter, travelling towards the clad surface with the interface highlighted.

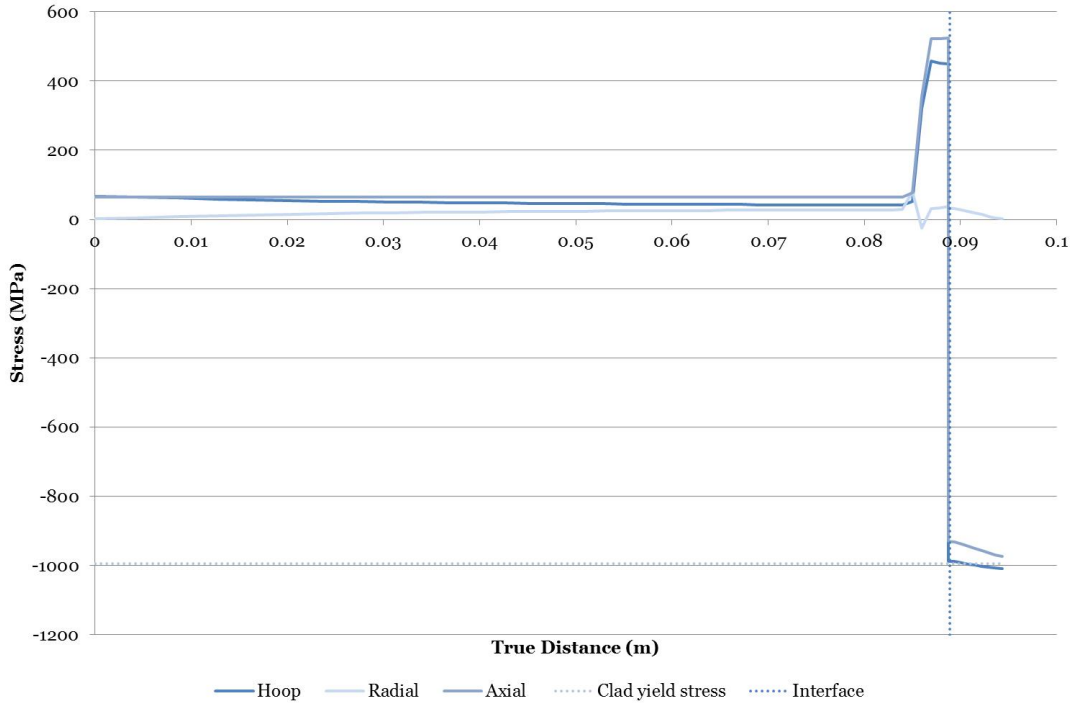

Figure 5.7: Stress components in an axisymmetric model of 4330 substrate and 17-4 PH clad with pre-heat temperature of 150°C - Results shown with the path beginning at the inner diameter, travelling towards the clad surface with the interface highlighted.

Using the same clad material with a higher pre-heat temperature of 300°C (figure 5.8), the radial stress component remains largely unchanged in shape, although slightly less in value. Tensile discontinuity stresses have again decreased, while compressive residual stresses remain at the same level as in the previous model.

Hoop stress values in the substrate material are of similar levels regardless of clad material. Table 5.1 shows the similarity between axial and hoop stress values in each clad material case, highlighting that the pre-heat temperature does not impact the stresses at the clad surface.

Clad material	$T_{PH}(°C)$	$\sigma_{Axial}(MPa)$	$\sigma_{Hoop}(MPa)$
Inconel 625	150	394.3	380.89
Inconel 625	300	393.9	381.96
17-4 PH	150	-972.94	-1009.34
17-4 PH	300	-973.47	-1008.85

Table 5.1: Comparison of axial and hoop stress components at the clad surface in a one-pass model

The model assumed an idealised interface, hence the large discontinuity stresses in the vicinity of the 4330 substrate and clad material for both materials and pre-heat temperatures. Upon reaching the clad material, a transformation in the nature of

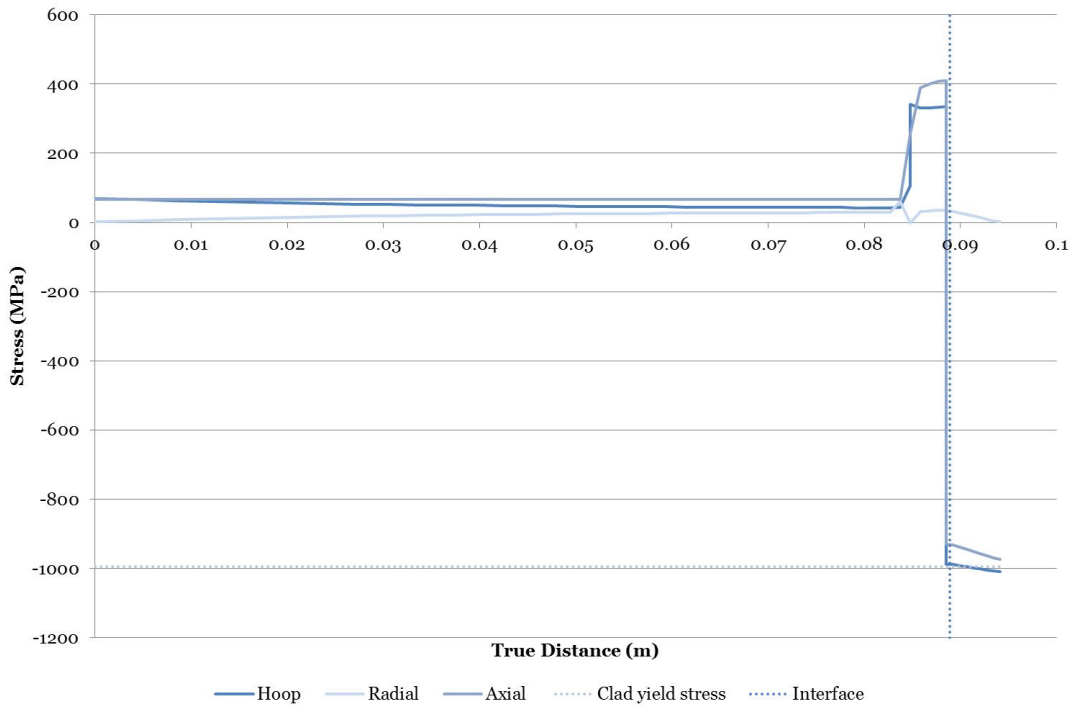

Figure 5.8: Stress components in an axisymmetric model of 4330 substrate and 17-4 PH clad with pre-heat temperature of 300°C - Results shown with the path beginning at the inner diameter, travelling towards the clad surface with the interface highlighted.

stresses occurs in all cases. This is due to the requirement of residual stresses being self-equilibrating, therefore the presence of tensile residual stresses in one region of the component requires a *balancing* of the stresses through the presence of compressive residual stresses elsewhere in the component. The self-equilibrating nature of the stresses were confirmed graphically, taking account of the increase in volume of material with increasing radius. From a fatigue perspective and for the application of this technology, it would be desirable for compressive residual stresses to be present throughout the clad layer of the clad component. Therefore these initial studies indicate that the 4330 and 17-4 PH combination is more desirable when focussing on residual stresses.

Yielding is seen to occur in residual hoop stresses present in a 17-4 PH clad layer, reflecting the elastic-perfectly plastic model utilised. However, stresses remain below yield for hoop and axial components in the Inconel 625 clad case, 20% and 17% below the yield stress level respectively. Yielding however occurs not upon exceeding the yield value in the hoop stress component, nor in the axial or radial components. Rather yielding occurs upon exceeding the Von Mises equivalent stress and therefore it is also beneficial to observe the distribution of this stress component.

The results obtained illustrate the success of the models in capturing the distribution of residual stresses, self-equilibrating in nature, throughout the clad cylinder.

Early studies using published data resulted in tensile residual stresses in the 17-4 PH clad model, confirming the observation that inaccurate material data can completely transform the nature of residual stresses in the finite element model (156).

Although the axisymmetric model presented in this section is a simplification of a process with spatially and temporally varying deposition, it is representative of methods such as evaporative deposition or spray coating followed by sintering.

Residual stresses obtained through the finite element model will be compared with residual stresses obtained experimentally in chapter 6.

5.4 Developing the modelling process

The simplification in the initial models prompted an investigation into the effects of the spatial and temporal variation of the weld cladding process. This is achieved using element *birth and death* to model the activation of elements representing the clad layer.

Accounting for weld beads in the deposition of one pass Using the method of prescribing a temperature to the weld material, the weld section was divided into *beads* to begin to account for the spatial and temporal variation of the weld cladding process. This requires the elements of each bead to be activated at the necessary time step to model the laying of the weld material at this point in the simulation. In this case of the axisymmetric model, it is as if the weld material is being deposited in rings along the length of the cylinder.

The model is completely defined at the beginning of the analysis, with the weld material then removed by deactivating weld clad elements. The weld is deposited by reactivating these elements in a sequential manner. The geometry utilised is illustrated in figure 5.9.

Figure 5.9: Geometry implemented in the representation of weld beads in the deposition of one pass - Geometry illustrated for an axisymmetric model clad on the outer diameter.

The mesh utilised for this model is illustrated in figure 5.10, an increased number of elements introduced to ensure that variations in stress in the *beads* are captured.

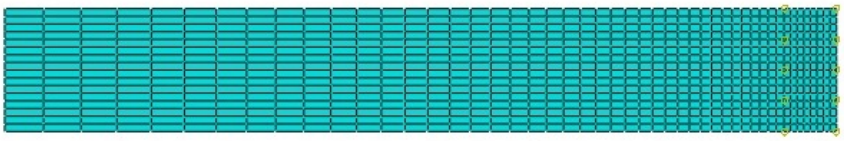

Figure 5.10: Mesh implemented in the representation of weld beads in the deposition of one pass - Mesh illustrated for an axisymmetric model clad on the outer diameter.

Accounting for the deposition of two passes The weld cladding process, as described in chapter 3, was a two-pass weld and therefore this was to be captured and investigated in the finite element model.

Previous studies investigated the laying of multiple passes in thermal coatings, with the particles of the coating forming a layer deposited onto a previously deposited, solidified layer (168). This effectively removes the fluid dynamics aspect of the analysis and results in an analysis solely of a thermo-mechanical nature. This is much like the method utilised in this research, however the second pass is to be laid on the first upon reaching the interpass temperature, with the substrate and first pass being assigned appropriate temperatures and cooling rates to reach the interpass temperature. The maximum interpass temperatures are noted in table 3.3.

The clad layer shown in figure 5.1 was divided into two to introduce the deposition of two passes into the axisymmetric model. This modelling technique effectively lays two 3 mm clad layers along the entire length of the cylinder with a cooling step between these two passes. The same pre-heat temperature values were utilised in the initial step of the analysis. The entire model was then cooled to room temperature after the laying of the second pass.

Accounting for weld beads in the deposition of two passes To further increase correlation between the finite element model and the real cladding process, the two pass model was modified to create *weld beads*. The geometry is shown in figure 5.11. This model then effectively deposits rings around the circumference of the cylinder in two 3 mm passes. The same mesh was utilised as shown in figure 5.10.

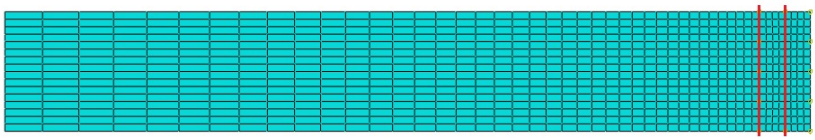

Figure 5.11: Geometry implemented in the representation of weld beads in the deposition of two passes - Geometry illustrated for an axisymmetric model clad on the outer diameter.

Accounting for the deposition of two passes in a planar model The axisymmetric model was then developed into a planar model, depositing two passes at once at melt temperature with a cooling step to the interpass temperature in between. The geometry and mesh utilised in these models is shown in figures 5.12 and 5.13. This creates the same assumption of the clad layers being deposited onto the circumference of the cylinder in rings.

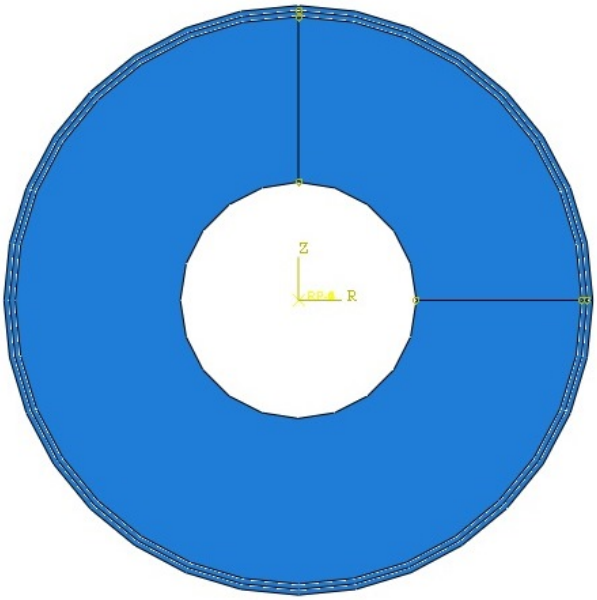

Figure 5.12: Geometry implemented in the deposition of two passes in a planar model - Geometry illustrated for a planar model clad on the outer diameter.

Conclusions The development of the finite element model to more accurately account for the weld deposition process illustrated little variation in residual stresses through the modifications discussed in this section. Therefore focus was placed on investigating the methods most representative of the weld deposition process, namely the deposition of *weld beads* in two passes.

5.4.1 Accounting for weld beads in the deposition of two passes in a planar model

To increase the accuracy and account for the spatial and temporal variation in the two-dimensional planar model, the weld beads were deposited using the information from the welding process. This allowed the simulation to follow the process of laying the first pass considering the speed of the welding process. This was calculated using the data provided by the cladding vendor for the speed of the weld cladding process and this was then utilised to calculate the time to clad the entire circumference. Dividing this value according to the number of elements deposited around the circumference of the cylinder provided the length of time assigned to each time step

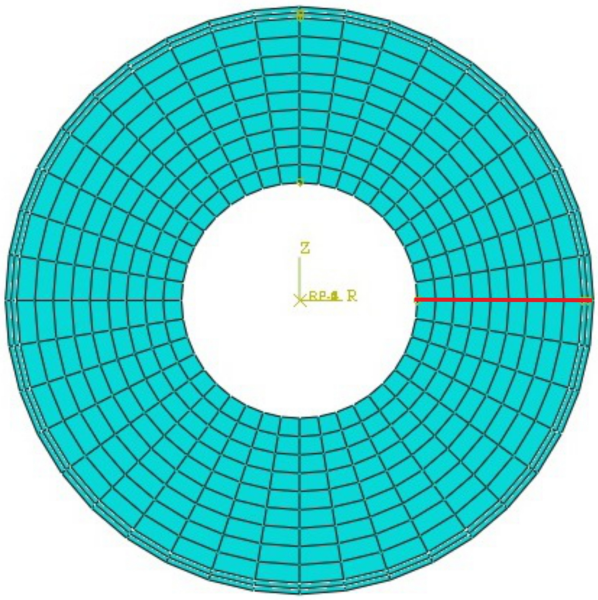

Figure 5.13: Mesh implemented in the deposition of two passes in a planar model - Mesh illustrated for a planar model clad on the outer diameter highlighting also the path utilised in obtaining path plot data.

for the deposition of each bead. The model was then cooled to the interpass temperature appropriate for each model depending on the pre-heat temperature prior to the laying of the second pass. Plane strain conditions were assumed in the axial direction.

Hoop stress contour plots highlight the development of residual stresses throughout the cladding process. Figure 5.14 shows the laying of the first bead in a model of 17-4 PH clad. Compressive residual stresses exist in the substrate with the *weld bead* possessing a tensile nature.

After deposition of the entire first pass, figure 5.15 shows that compressive residual stresses exist in the *HAZ* region. As elements deposited closer to the beginning of the simulation have been allowed more time to cool and therefore for the stress state to develop, it can be seen that stress values differ around the circumference.

Comparing figures 5.15 and 5.16, it can been seen that by the end of the cooling step to reach the interpass temperature, the stress distribution is notably different. Very high compressive residual hoop stresses exist in the substrate, especially in the *HAZ*, with high tensile residual stresses in the clad layer.

Deposition of the second pass creates a similar pattern of stress development as the deposition process develops. Tensile residual stresses are present in the substrate and clad layer, with a region of compressive residual stresses in the *HAZ* (figure 5.17).

Upon commencing cooling to room temperature, as shown in figure 5.18 variations in stresses are seen around the circumference in the clad layer. Upon completion

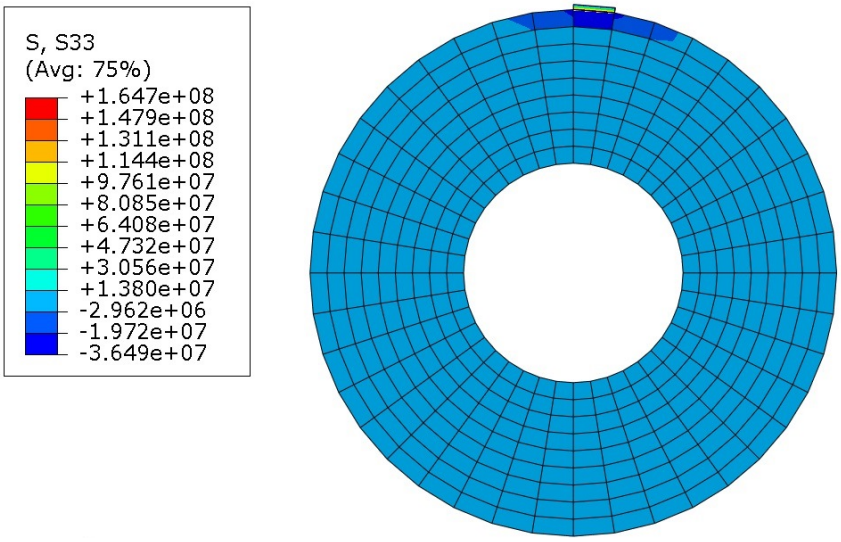

Figure 5.14: Deposition of the first weld bead in a planar model - Example illustrating results for hoop stress in a planar model of 4330 substrate pre-heated to 150°C and clad with 17-4 PH accounting for the deposition of beads in two passes.

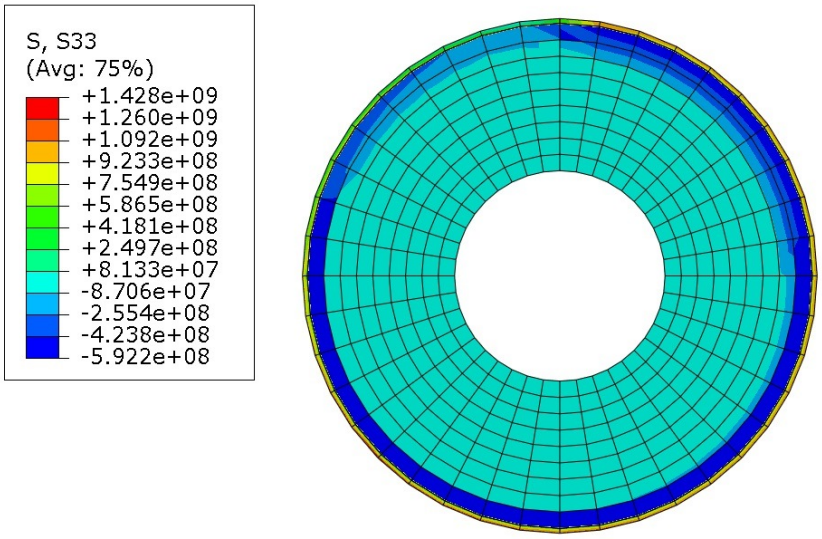

Figure 5.15: Commencing cooling to interpass temperature in a planar model - Example illustrating results for hoop stress in a planar model of 4330 substrate pre-heated to 150°C and clad with 17-4 PH accounting for the deposition of beads in two passes.

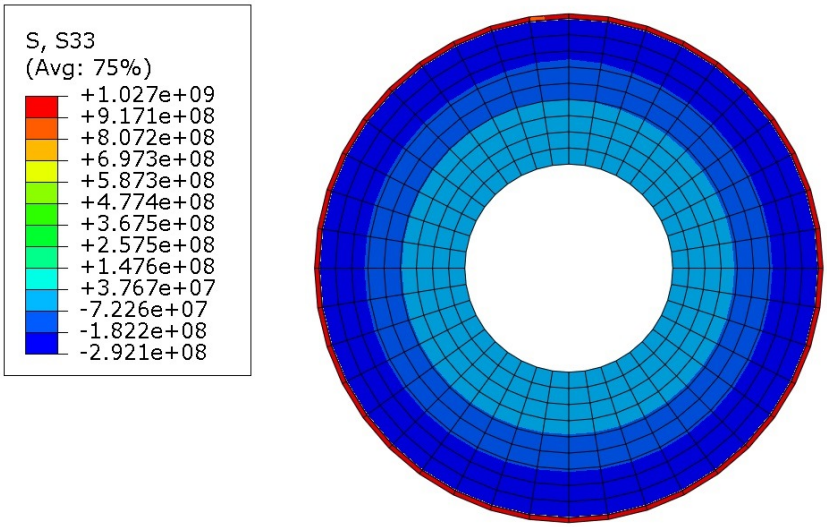

Figure 5.16: Completion of cooling to interpass temperature in a planar model - Example illustrating results for hoop stress in a planar model of 4330 substrate pre-heated to 150°C and clad with 17-4 PH accounting for the deposition of beads in two passes.

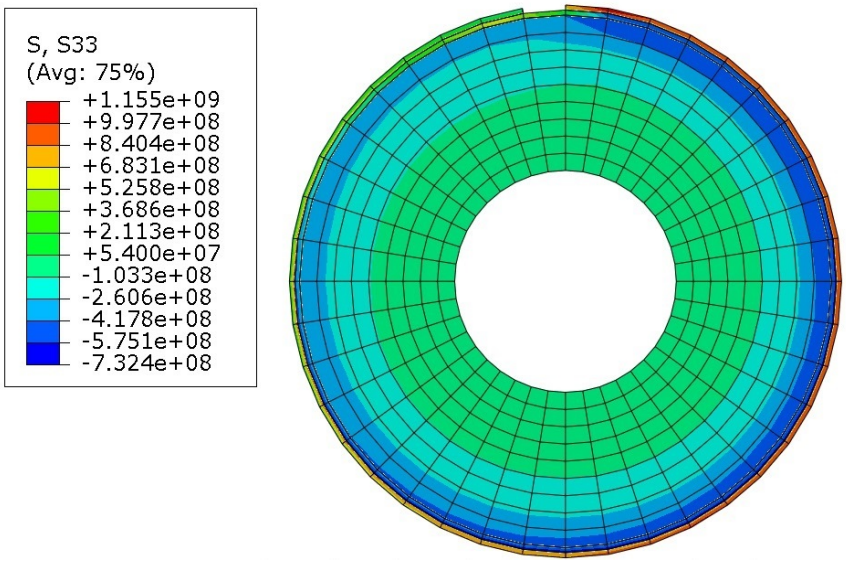

Figure 5.17: Prior to deposition of the last weld bead in a planar model - Example illustrating results for hoop stress in a planar model of 4330 substrate pre-heated to 150°C and clad with 17-4 PH accounting for the deposition of beads in two passes.

of the cooling step when the entire model has reached room temperature, it is seen that the stress distribution throughout the model is uniform in respective clad and substrate regions. Figure 5.19 shows high tensile residual stresses in the substrate and very high compressive residual stresses in the clad layer as indicated by preliminary experimental results in chapter 6.

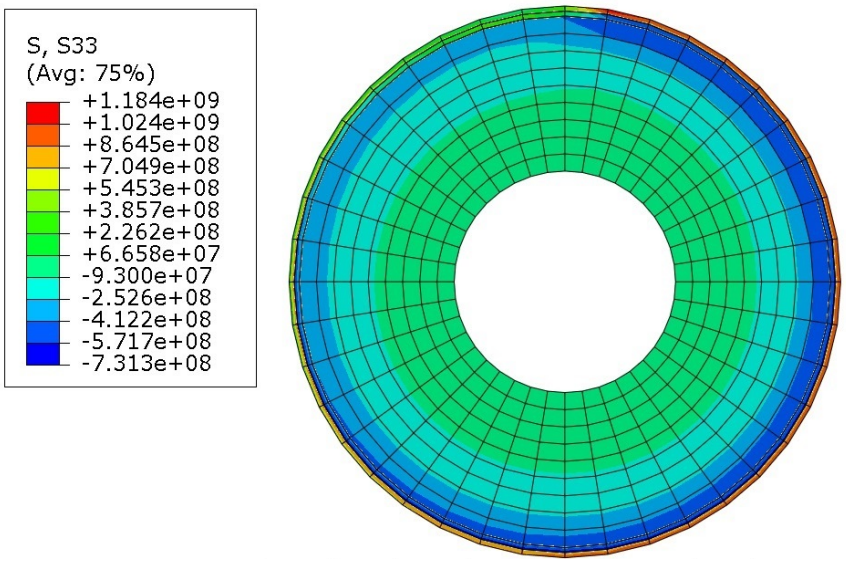

Figure 5.18: Commencing cooling to room temperature in a planar model upon completion of welding process - Example illustrating results for hoop stress in a planar model of 4330 substrate pre-heated to 150°C and clad with 17-4 PH accounting for the deposition of beads in two passes.

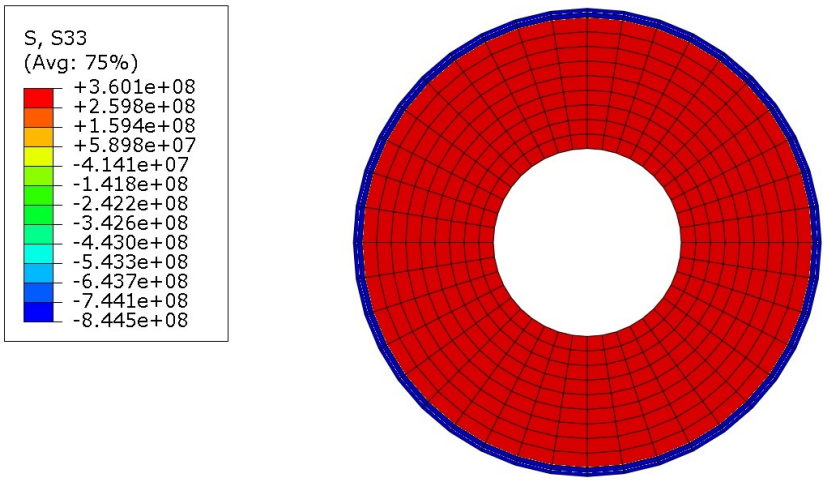

Figure 5.19: Completion of cooling to room temperature in a planar model upon completion of welding process - Example illustrating results for hoop stress in a planar model of 4330 substrate pre-heated to 150°C and clad with 17-4 PH accounting for the deposition of beads in two passes.

A similar stress distribution as in the previous planar model is observed in the case of laying weld beads in a planar model. The path utilised in extracting data for stress components is highlighted in figure 5.13.

Figure 5.20 shows tensile residual hoop stresses in the substrate and a further increase in these stress values to above yield value in an Inconel 625 clad layer. Axial stresses remain compressive in the clad layer and transform into tensile residual stresses in the clad layer.

A higher pre-heat temperature results in doubling of the hoop stresses in the substrate, while in the clad layer the stress level remains the same (figure 5.21). Axial stresses remain similar in nature along the path.

A 17-4 PH clad demonstrates similar stress states with regards to pre-heat temperature effects. Hoop stresses increase in the substrate and decrease in the clad layer with a higher pre-heat temperature when comparing figures 5.22 and 5.23. Axial stresses remain similar in both cases, tensile in the substrate and compressive in the clad layer.

Comparing tables 5.2 and 5.3 illustrates that in all cases the inclusion of *weld beads* has not altered the final residual stress at the clad surface. This is interesting due to the visible development of the stress state shown in figures 5.14-5.19, however confirms the expectation that the effect of spatial and temporal variation is not of utmost importance in the modelling of the weld cladding process in this case.

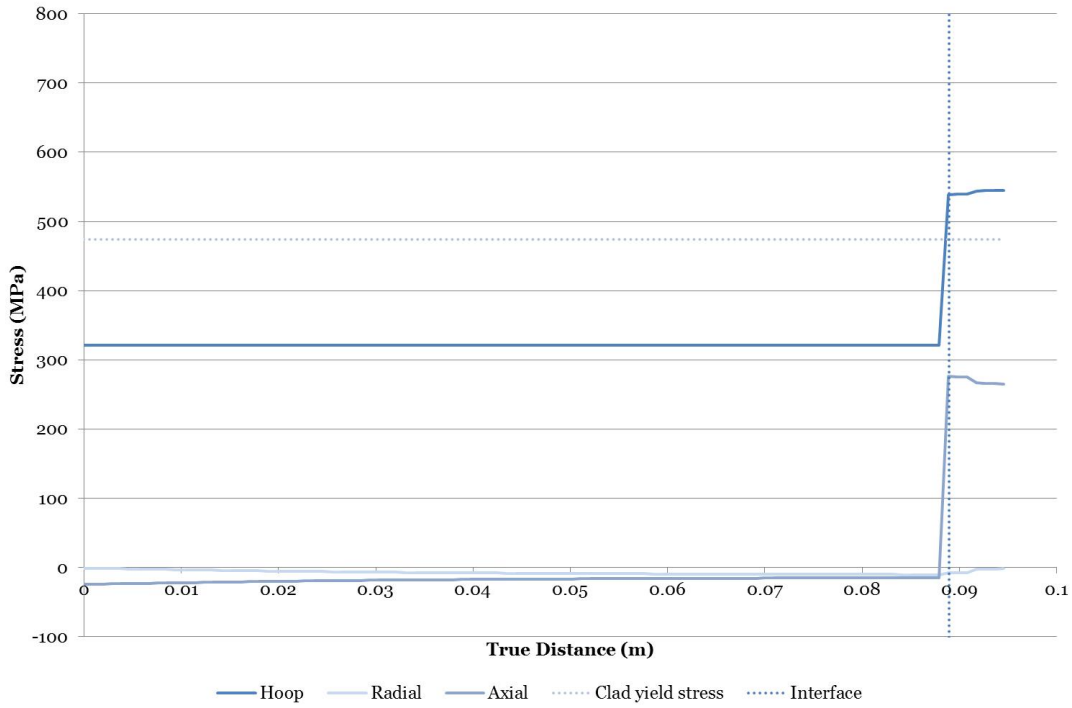

Figure 5.20: Stress components in a planar model of 4330 substrate and Inconel 625 clad with pre-heat temperature of 150°C accounting for the deposition of beads in two passes - Results shown with the path beginning at the inner diameter, travelling towards the clad surface with the interface highlighted.

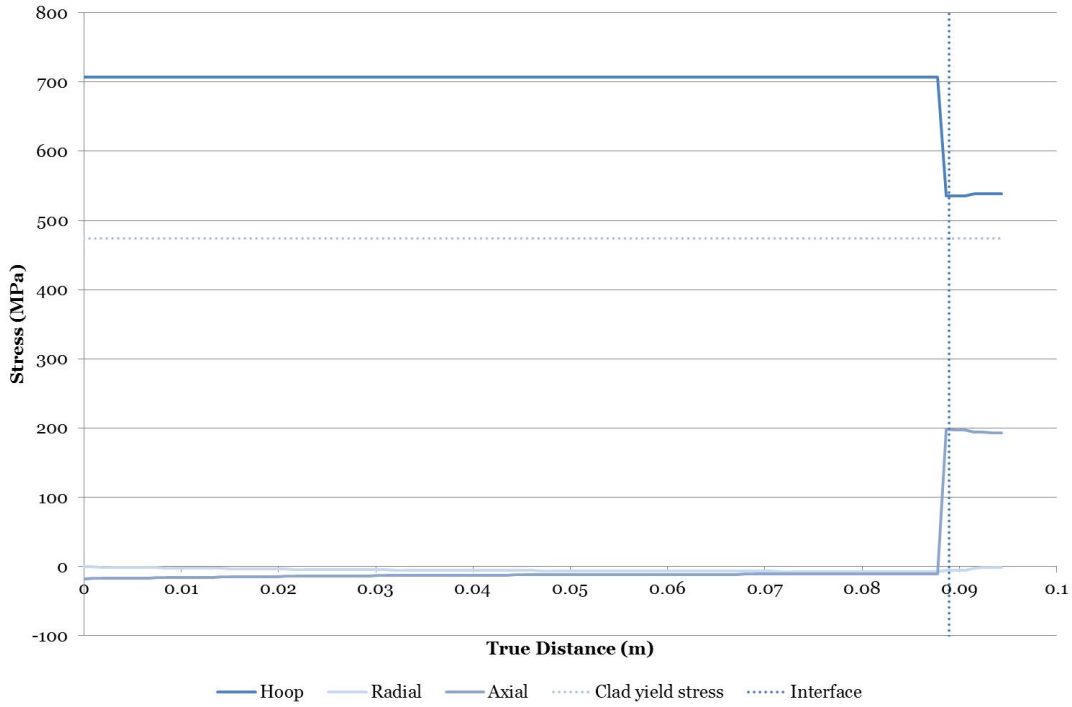

Figure 5.21: Stress components in a planar model of 4330 substrate and Inconel 625 clad with pre-heat temperature of 300°C accounting for the deposition of beads in two passes - Results shown with the path beginning at the inner diameter, travelling towards the clad surface with the interface highlighted.

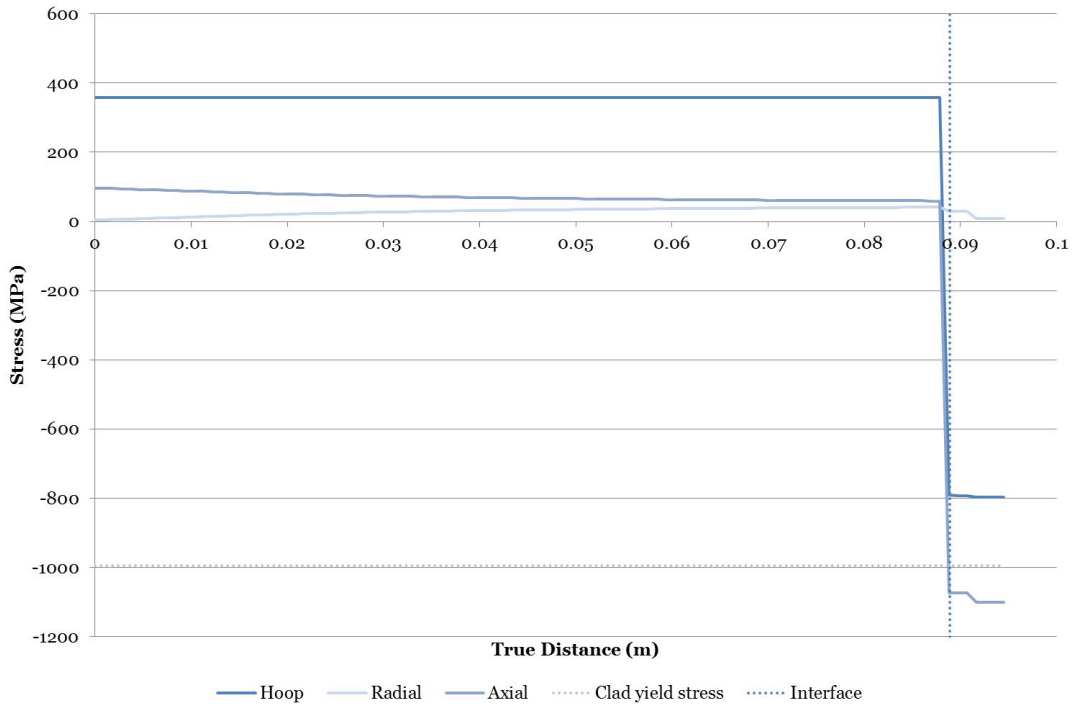

Figure 5.22: Stress components in a planar model of 4330 substrate and 17-4 PH clad with pre-heat temperature of 150°C accounting for the deposition of beads in two passes - Results shown with the path beginning at the inner diameter, travelling towards the clad surface with the interface highlighted.

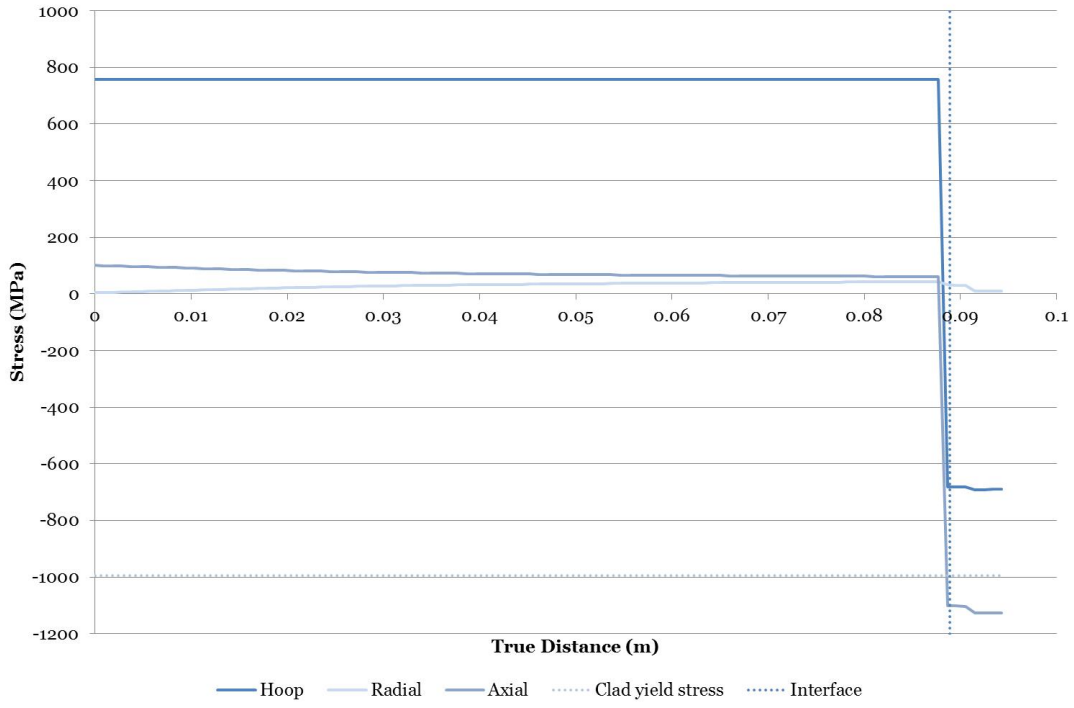

Figure 5.23: Stress components in a planar model of 4330 substrate and 17-4 PH clad with pre-heat temperature of 300°C accounting for the deposition of beads in two passes - Results shown with the path beginning at the inner diameter, travelling towards the clad surface with the interface highlighted.

Clad material	$T_{PH}(^{\circ}C)$	$\sigma_{Axial}(MPa)$	$\sigma_{Hoop}(MPa)$
Inconel 625	150	265.41	544.87
Inconel 625	300	193.94	538.73
17-4 PH	150	-1099.15	-798.97
17-4 PH	300	-1129.31	-676.74

Table 5.2: Comparison of axial and hoop stress components at the clad surface in a two-pass planar model

Clad material	$T_{PH}(^{\circ}C)$	$\sigma_{Axial}(MPa)$	$\sigma_{Hoop}(MPa)$
Inconel 625	150	265.32	544.94
Inconel 625	300	193.14	538.66
17-4 PH	150	-1100.06	-796.62
17-4 PH	300	-1126.94	-689.85

Table 5.3: Comparison of axial and hoop stress components at the clad surface in a two-pass & beads planar model

5.4.2 Accounting for weld beads in the deposition of two passes in a 3D model

Three-dimensional weld modelling is increasing in use, however it is still commonplace to decrease the number of passes as it is clear that accounting for a large number of passes requires a large amount of computational time. For this reason, it was decided to model the three-dimensional model accounting for the accurate thickness of weld bead and the correct number of passes, but to model only one bead thickness to obtain an indication of the residual stresses arising through this deposition process. This was due to the observation that decreasing the complexity in three-dimensional models can lead to the same issue as in two-dimensions, namely an infinite welding speed assumption (158) and therefore cladding the entire circumference of the 3D model was deemed inappropriate in further investigating the weld cladding simulation process.

The restraint arising due to the welding process must always be considered, and although the laying of subsequent beads is not included herein, the weld geometry in terms of weld bead thickness and number of passes is accurate.

The mesh utilised in the 3D model is shown in figures 5.24 and 5.25. Due to the large aspect ratio present due to the mesh utilised it would be recommended to further investigate refinement of the mesh should this model be utilised more thoroughly in the determination of residual stresses due to the weld cladding process. The mesh utilised could lead to erroneous stress values at the interface and therefore as in case

of the axisymmetric model a mesh biased towards the clad layer would be more suitable to ensure that variations in stress in the vicinity of the interface are captured.

The path utilised for obtaining results is as previously defined, highlighted in figure 5.26. Weld beads were deposited onto the pre-heated substrate at melt temperature of the clad material. Due to the large difference in temperature, the bead experienced a rapid quenching effect as shown in figure 5.27. This is in line with expectations comparing to the welding processes, where cooling rates are extremely high at the beginning of the process.

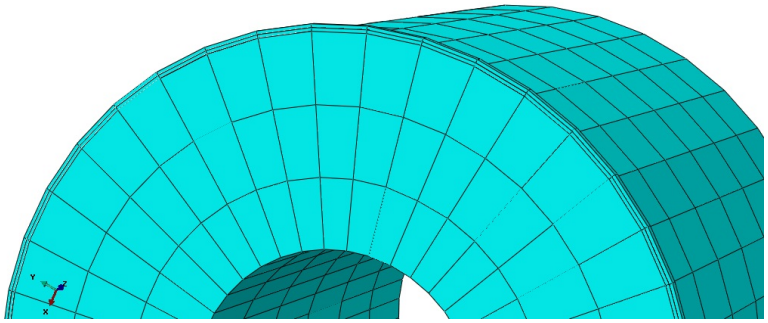

Figure 5.24: Geometry and mesh implemented in the deposition of two passes in a 3D model - Geometry illustrated for a 3D model clad on the outer diameter with two passes of one bead thickness.

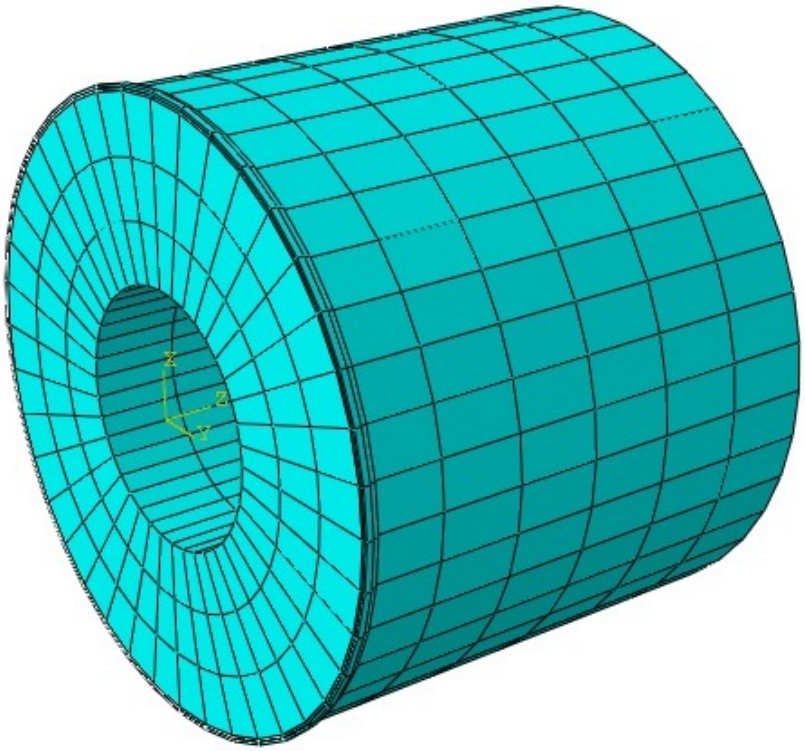

Figure 5.25: Geometry and mesh implemented in the deposition of two passes in a 3D model emphasising bead thickness - Geometry illustrated for a 3D model clad on the outer diameter with two passes of one bead thickness.

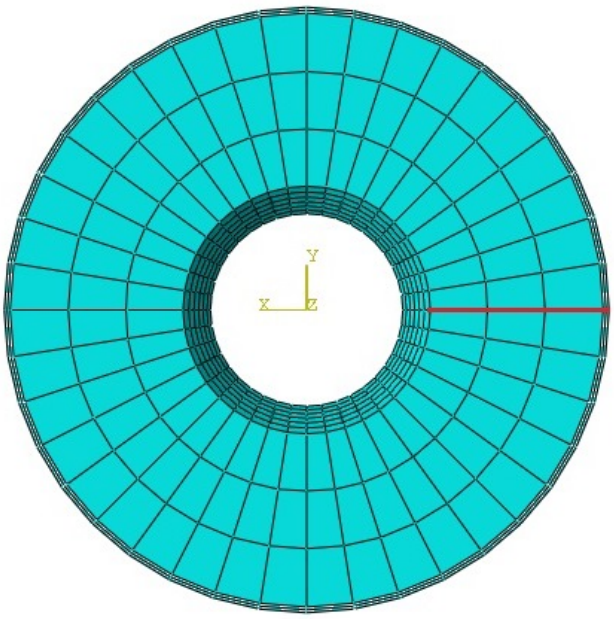

Figure 5.26: Three-dimensional model path - Path utilised in obtaining results data for the 3D model.

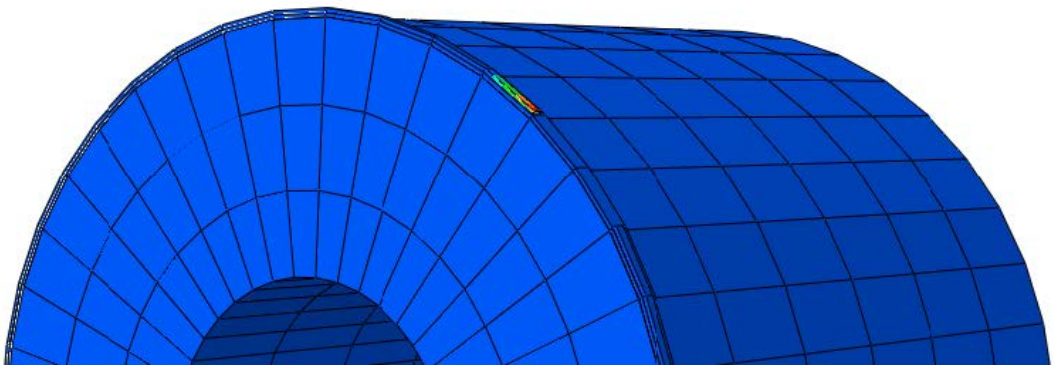

Figure 5.27: Temperature gradient in bead deposition in a 3D model - Geometry illustrated for a 3D model clad on the outer diameter with two passes of one bead thickness.

Figures 5.28-5.31 show that all stress component values are negligible throughout the substrate material. Large discontinuity stresses exist in the vicinity of the interface.

In the case of an Inconel 625 clad, a higher pre-heat temperature results in a slightly higher hoop stress upon entering into the clad material. Hoop stresses drop in both models towards the clad surface. Axial residual stress discontinuity is slightly decreased when using a higher pre-heat temperature. Substantial radial stresses are observed in the clad layer, particularly in the case of a higher pre-heat temperature.

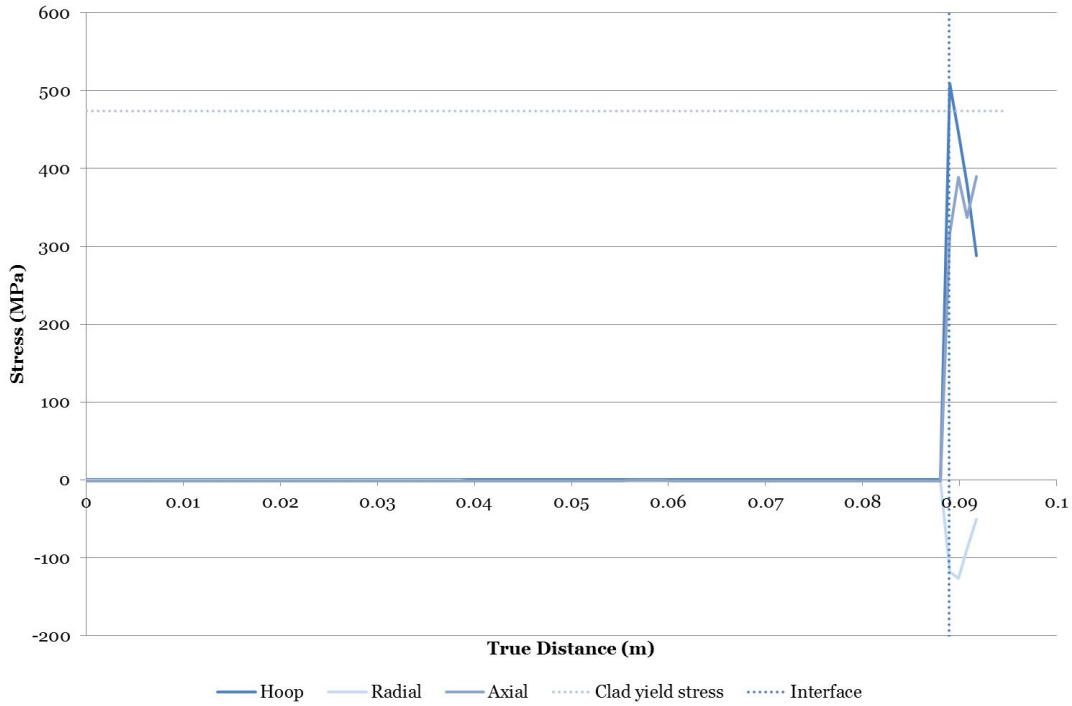

Figure 5.28: Stress components in a 3D model of 4330 substrate and Inconel 625 clad with pre-heat temperature of 150°C accounting for the deposition of two passes - Results shown with the path beginning at the inner diameter, travelling towards the clad surface with the interface highlighted.

Radial stresses in the 17-4 PH clad models are similar in value. Axial stresses are larger in the first pass of the clad layer when a higher pre-heat temperature is applied. The stress discontinuity is therefore larger. However at the clad surface the values are similar. Hoop stresses are compressive in the clad layer, regardless of pre-heat temperature as previously in the two-dimensional models. A lower pre-heat temperature results in a larger discontinuity stress. In both pre-heat temperature cases, the hoop stress decreases towards the clad surface (figures 5.30 and 5.31).

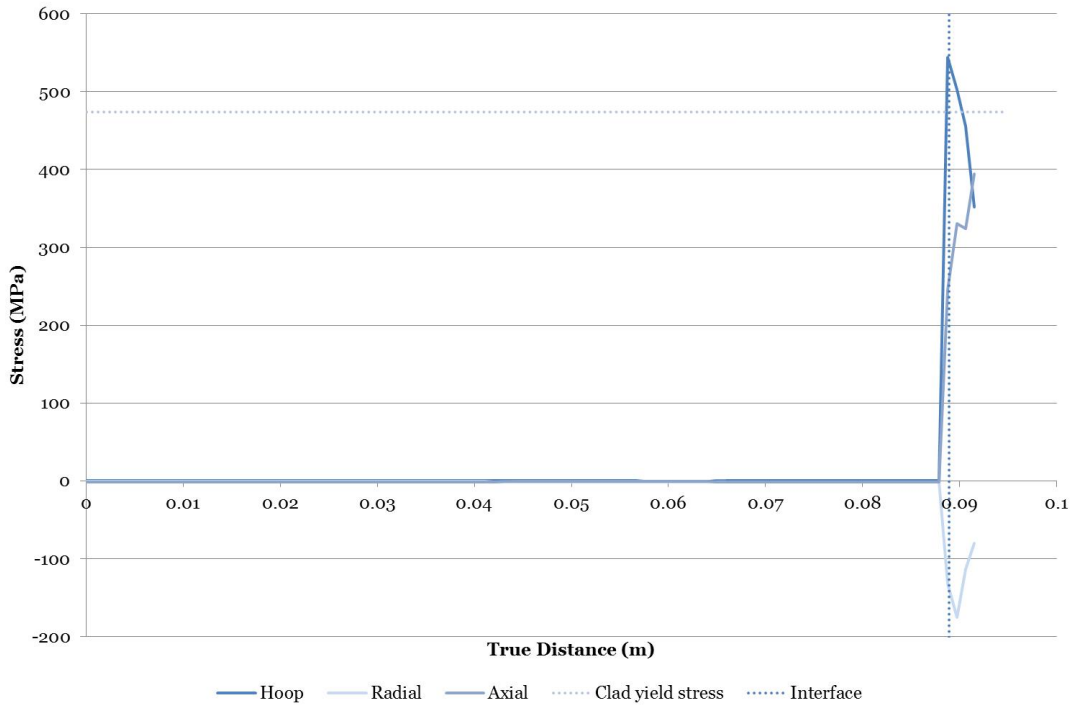

Figure 5.29: Stress components in a 3D model of 4330 substrate and Inconel 625 clad with pre-heat temperature of 300°C accounting for the deposition of two passes - Results shown with the path beginning at the inner diameter, travelling towards the clad surface with the interface highlighted.

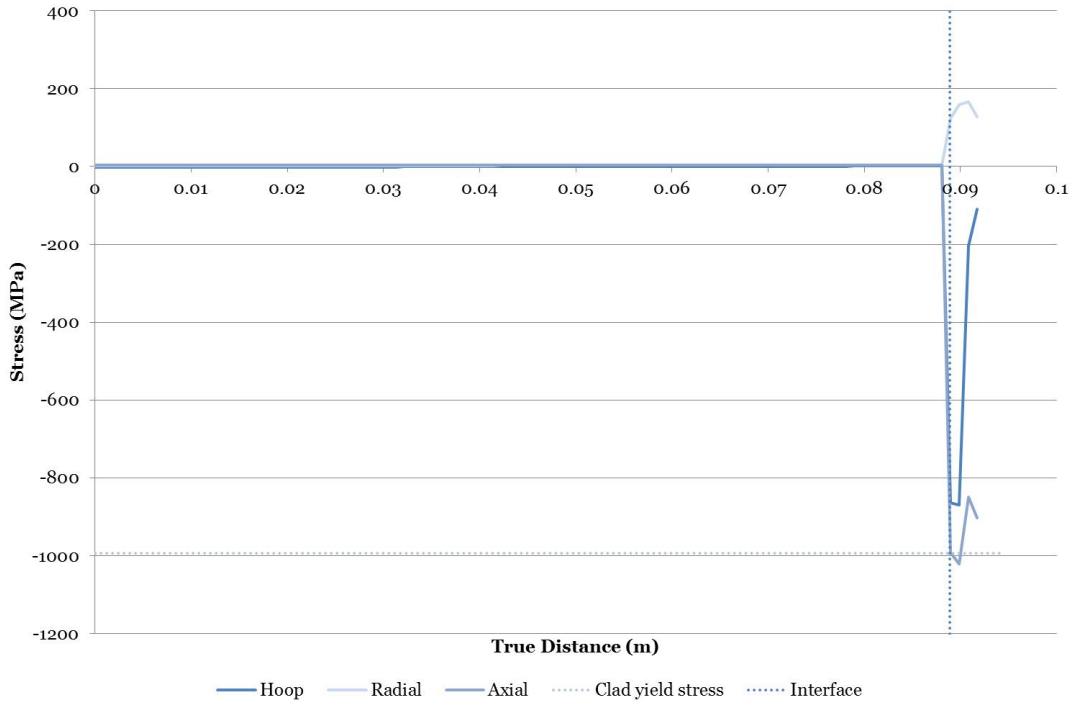

Figure 5.30: Stress components in a 3D model of 4330 substrate and 17-4 PH clad with pre-heat temperature of 150°C accounting for the deposition of two passes - Results shown with the path beginning at the inner diameter, travelling towards the clad surface with the interface highlighted.

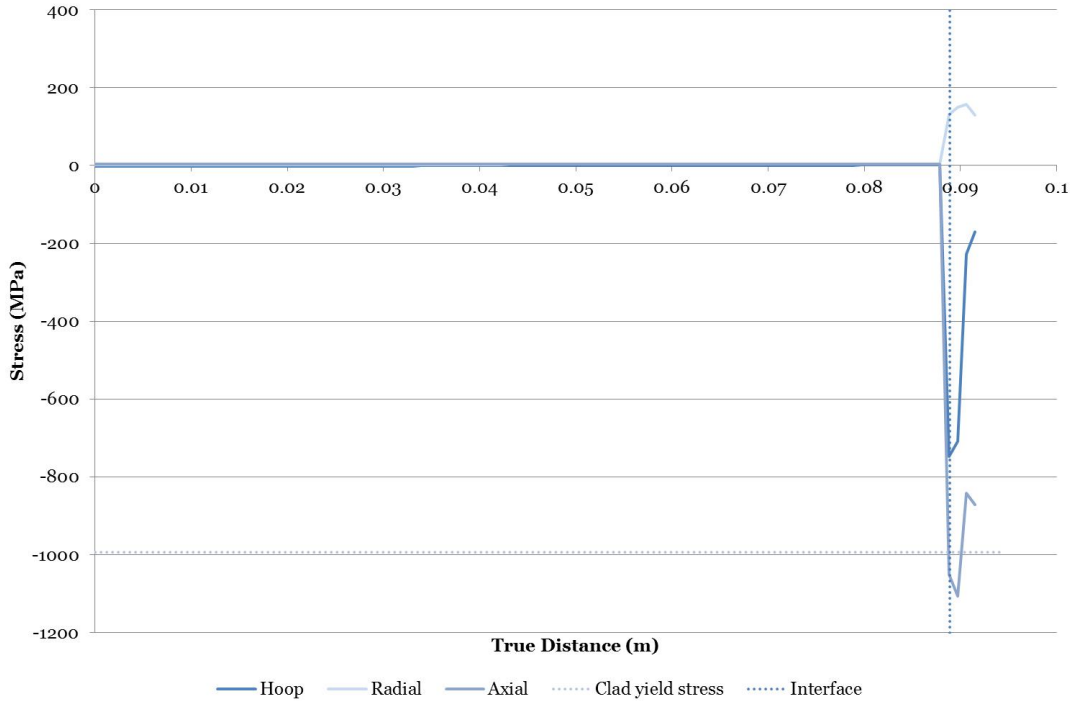

Figure 5.31: Stress components in a 3D model of 4330 substrate and 17-4 PH clad with pre-heat temperature of 300°C accounting for the deposition of two passes - Results shown with the path beginning at the inner diameter, travelling towards the clad surface with the interface highlighted.

Table 5.4 shows that differences between pre-heat temperatures used present only small differences in axial stresses. There are more notable differences in hoop stress values, with larger hoop stresses at the clad surface in both clad materials when a higher pre-heat temperature is used. This is contrary to the previous findings in tables 5.1 and 5.3 in which hoop stresses do not present such differences depending on pre-heat temperature. These results indicate that it would therefore be desirable to use a lower pre-heat temperature in the case of an Inconel 625 clad to minimise the damaging tensile residual stresses, while a higher pre-heat temperature when cladding with 17-4 PH would increase the beneficial compressive residual stresses. To ensure that such measures are appropriate this should also be confirmed with experimental residual stress measurements, presented in chapter 6.

Clad material	$T_{PH}(°C)$	$\sigma_{Axial}(MPa)$	$\sigma_{Hoop}(MPa)$
Inconel 625	150	389.99	288.37
Inconel 625	300	394.82	351.50
17-4 PH	150	-902.65	-110.10
17-4 PH	300	-870.30	-170.06

Table 5.4: Comparison of axial and hoop stress components at the clad surface in a two-pass & beads 3D model

In investigating the modelling of the weld cladding process in three-dimensions, it has been shown that the laying of representative weld bead thickness results in variation in residual stresses through the clad layer, stresses decreasing towards the clad surface. In general however, the nature of residual stresses arising in the clad layer and largely in the substrate has remained consistent throughout the investigation of the modelling process and therefore this development of the modelling process primarily serves as an illustration of the process. It has been highlighted that modelling techniques do not impact the stress state as much as may be expected. Therefore the axisymmetric model was generally utilised throughout the investigation of the simulation of the weld cladding process to minimise computational time and maintain an accurate representation of residual stress generation.

5.5 Effect of pre-heat temperature

Prior to cladding the components, the substrate was heated to a specified temperature as previously described. Two pre-heat temperatures were investigated: 150°C and 300°C. Experimental residual stress measurements were also obtained for components weld clad using these two pre-heat temperature values. These will be presented in chapter 6. Utilising a pre-heat temperature has the purpose of decreasing the thermal gradient between the dissimilar materials. This aids in avoiding brittle martensite formation which can cause thermal fracture (169). It also serves as a drying of the material to avoid hydrogen embrittlement particularly in high strength steels should excessive hydrogen be absorbed (170). The use of a pre-heat temperature can lead to higher levels of plastic deformation through the increase in yield strength of the substrate material (171). This is unfavourable for the residual stress state and highlights that the use of pre-heating should not be considered a favourable solution in all cases. As the aim of pre-heating the substrate is to reduce the heat sink effect, a higher pre-heat temperature would be expected to reduce the resulting residual stresses.

In the previous sections, it has been emphasised that the applied substrate pre-heat temperature did greatly affect the resulting residual stress state in the vicinity of the join. Comparing hoop and axial stresses in an Inconel 625 model shows that values of stress remain the same in the clad layer but the discontinuity stresses are very different as expected. A higher pre-heat temperature decreases the discontinuity stresses by over 150 MPa in both hoop (figure 5.32) and axial (figure 5.33) stress components. This lower discontinuity stress is beneficial from a fatigue point of view due to decreased risk of fatigue cracking. However, these discontinuity stresses are still of a high level and tensile in nature, therefore detrimental for fatigue performance.

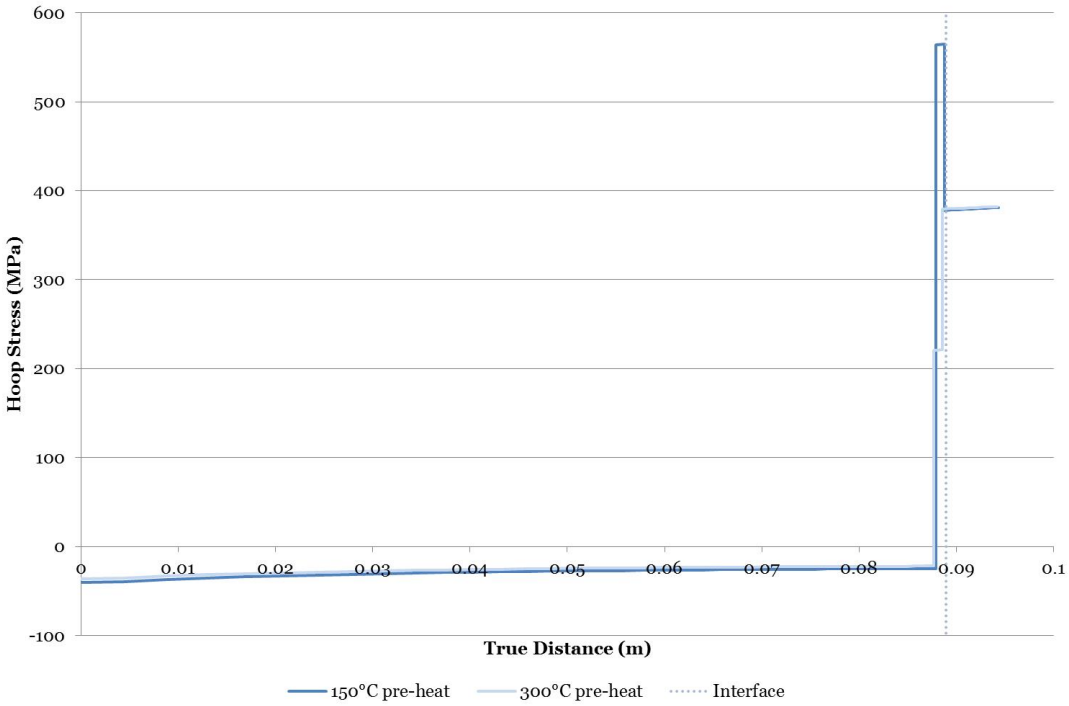

Figure 5.32: Hoop stress in an axisymmetric model of 4330 substrate and Inconel 625 clad - Results shown for two pre-heat temperatures with the path beginning at the inner diameter, travelling towards the clad surface with the interface highlighted.

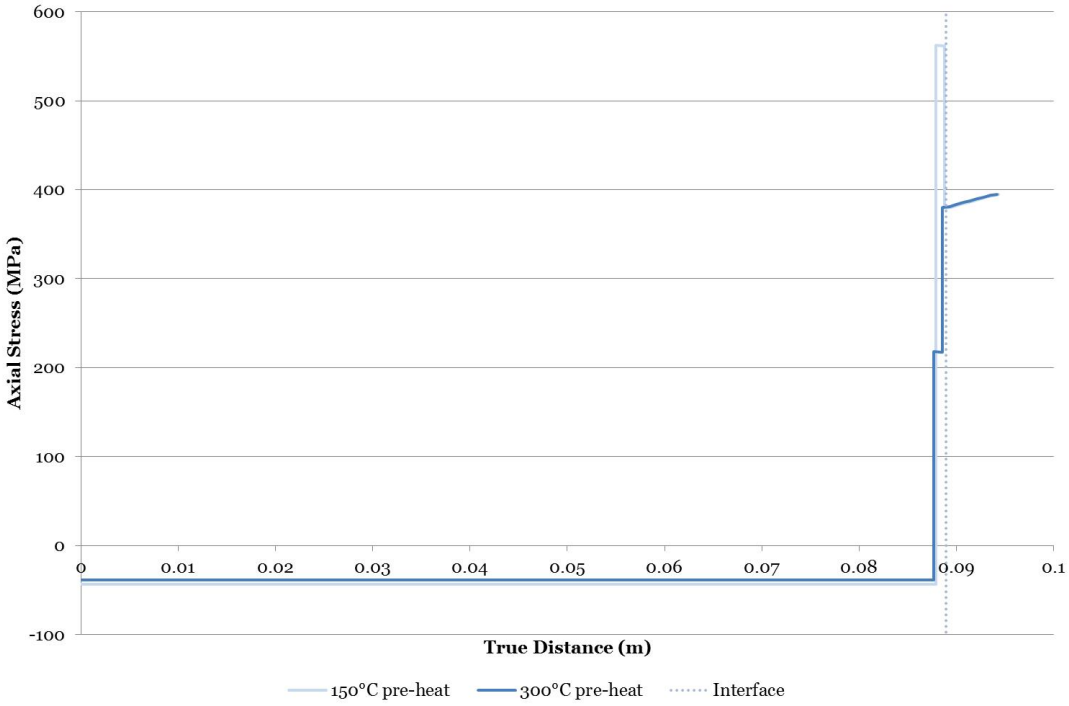

Figure 5.33: Axial stress in an axisymmetric model of 4330 substrate and Inconel 625 clad - Results shown for two pre-heat temperatures with the path beginning at the inner diameter, travelling towards the clad surface with the interface highlighted.

In the case of a 17-4 PH clad, again a higher pre-heat temperature decreases the tensile discontinuity stress in the substrate in both hoop (figure 5.34) and axial (figure 5.35) stress components. Stresses in the clad layer are the same for both pre-heat temperatures.

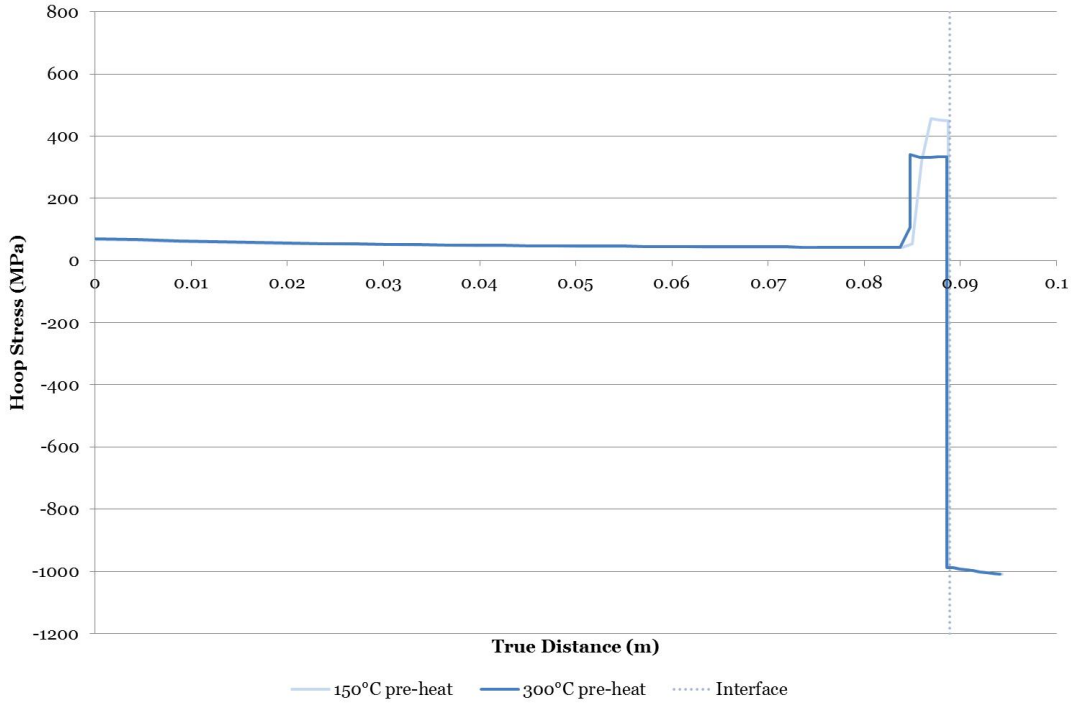

Figure 5.34: Hoop stress in an axisymmetric model of 4330 substrate and 17-4 PH clad - Results shown for two pre-heat temperatures with the path beginning at the inner diameter, travelling towards the clad surface with the interface highlighted.

Ultimately the goal would be to eliminate discontinuity stresses to ensure that fatigue cracking is not encouraged upon reaching the substrate after eroding and corroding of the clad layer. Furthermore, sub-surface cracking could be encouraged in this region and clearly this would be undesirable during component operation.

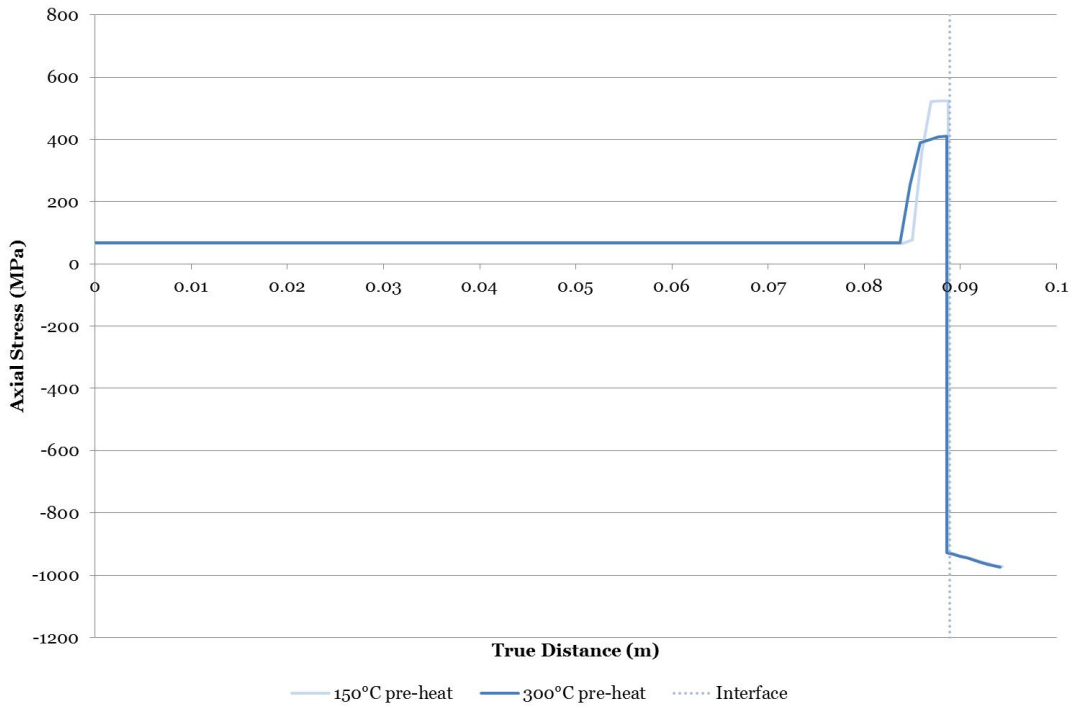

Figure 5.35: Axial stress in an axisymmetric model of 4330 substrate and 17-4 PH clad - Results shown for two pre-heat temperatures with the path beginning at the inner diameter, travelling towards the clad surface with the interface highlighted.

5.6 Nodal cooling rates

The thermal transient nature of the weld cladding process impacts the resulting residual stresses and the development of these stresses with time and therefore investigating the temperature-time variation is of interest.

The resulting constraint due to differences in thermal expansion between materials will result in variations in temperature and coupled with the temperature variations arising due to the prescribed temperature fields in the model it can be expected that cooling rates will greatly differ in the substrate and the clad materials. This is likely to have an impact most notably at the beginning of the process when the thermal transient event is more severe.

The nodes investigated are highlighted in figure 5.36. Nodes *A-D* are located in the substrate while nodes *E-M* are located in the clad layer.

Cooling rates are shown to be rapid at the beginning of the analysis. Clad layer nodes cool more rapidly when a lower pre-heat temperature is applied, shown in figures 5.38 and 5.40. This is to be expected due to the quenching effect of the substrate. A higher pre-heat temperature therefore results in a slower cooling of the nodes with node *D*, in the substrate closest to the clad layer, reaching a higher temperature. The nodes in the substrate, nodes *A-C*, experience a higher heating rate at the beginning

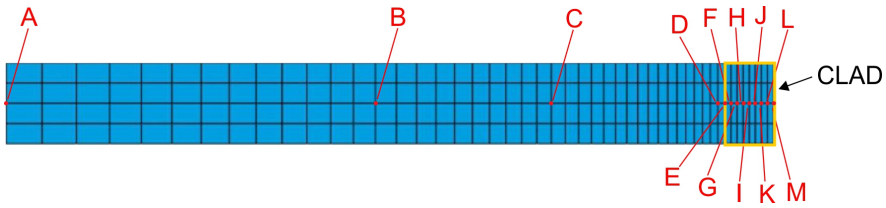

Figure 5.36: Node label assignments - Letters assigned to nodes in the axisymmetric model to investigate cooling rates.

of the analysis when a higher pre-heat temperature is applied.

A lower pre-heat temperature allows the entire model to cool to a consistent temperature quicker as shown in figures 5.37 and 5.39 as cooling of the clad layer nodes is accelerated by the lower pre-heat temperature. A pre-heat temperature of 150°C results in a substrate temperature of approximately 290°C upon commencement of the cladding process, while nodes in the substrate are heated to approximately 405°C with a pre-heat temperature of 300°C. This demonstrates that the molten nature of the clad layer material heats the lower pre-heat temperature nodes to a greater level, an increase of 140°C in comparison to an increase of 105°C in the case of a higher pre-heat temperature. This is with the aim of decreasing the temperature differential between clad and substrate materials.

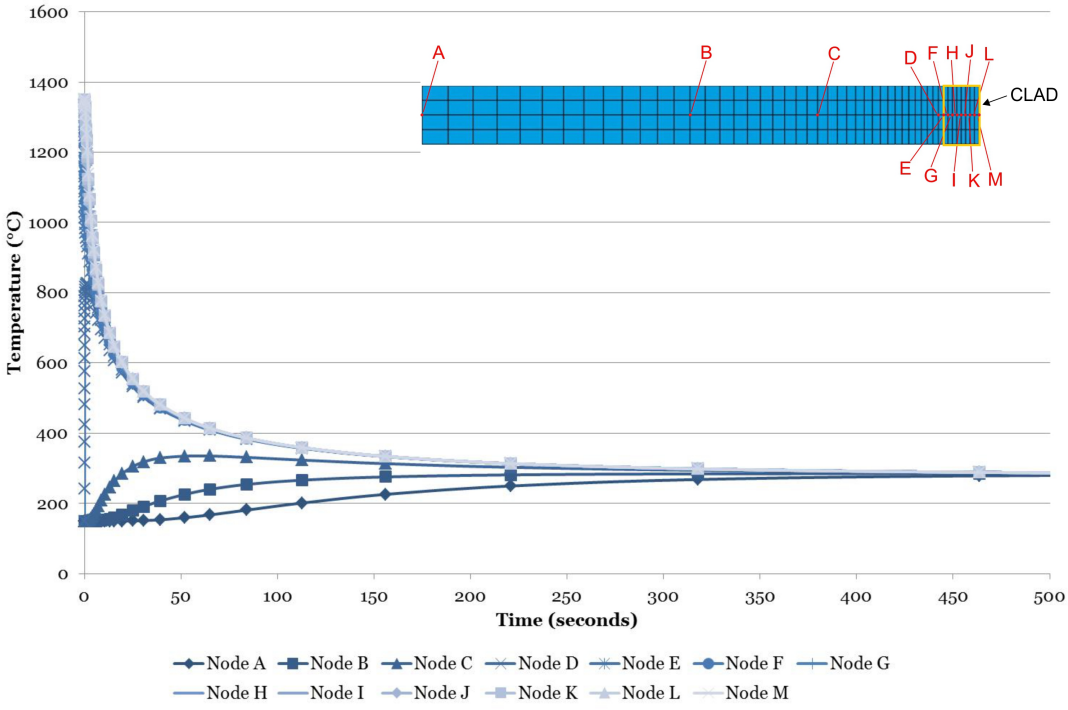

Figure 5.37: Nodal cooling rates for first 500 seconds for an Inconel 625 clad and pre-heat temperature of 150°C - Investigation of nodal cooling rates for an axisymmetric model using nodes highlighted in figure 5.36.

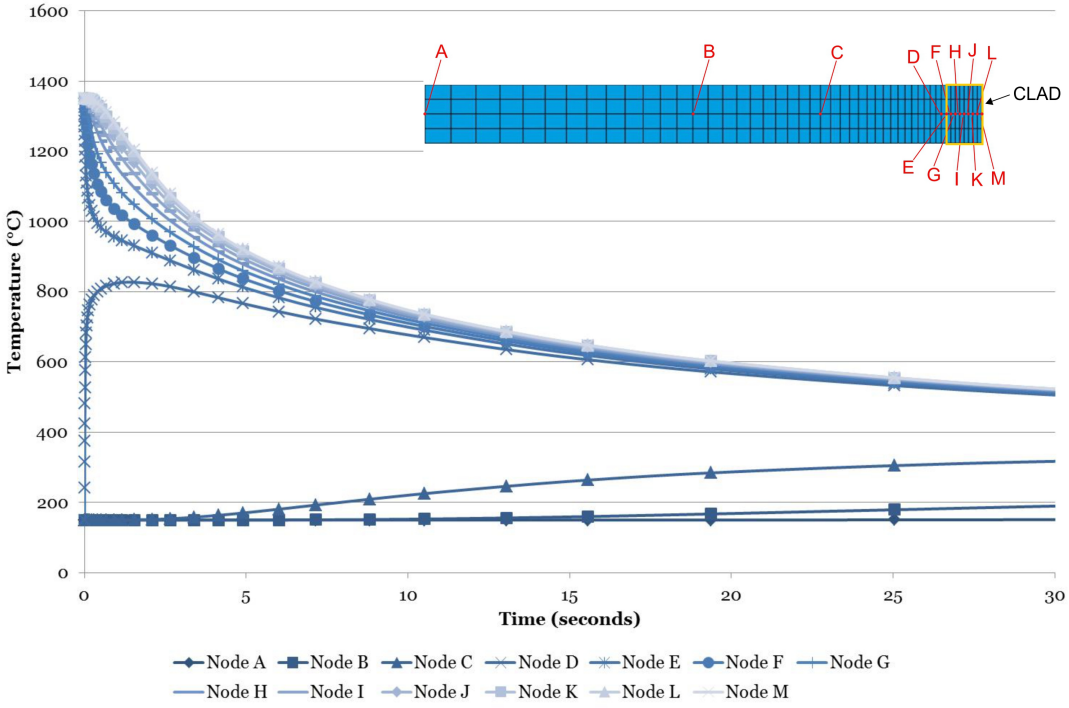

Figure 5.38: Nodal cooling rates for first 30 seconds for an Inconel 625 clad and pre-heat temperature of 150°C - Investigation of nodal cooling rates for an axisymmetric model using nodes highlighted in figure 5.36.

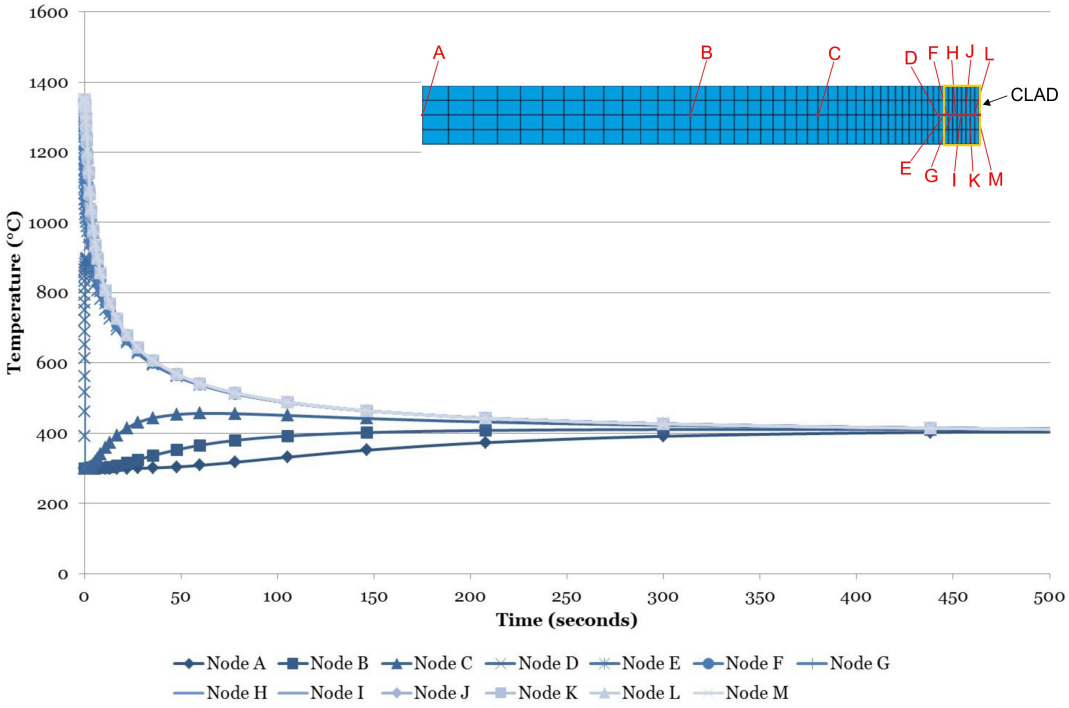

Figure 5.39: Nodal cooling rates for first 500 seconds for an Inconel 625 clad and pre-heat temperature of 300°C - Investigation of nodal cooling rates for an axisymmetric model using nodes highlighted in figure 5.36.

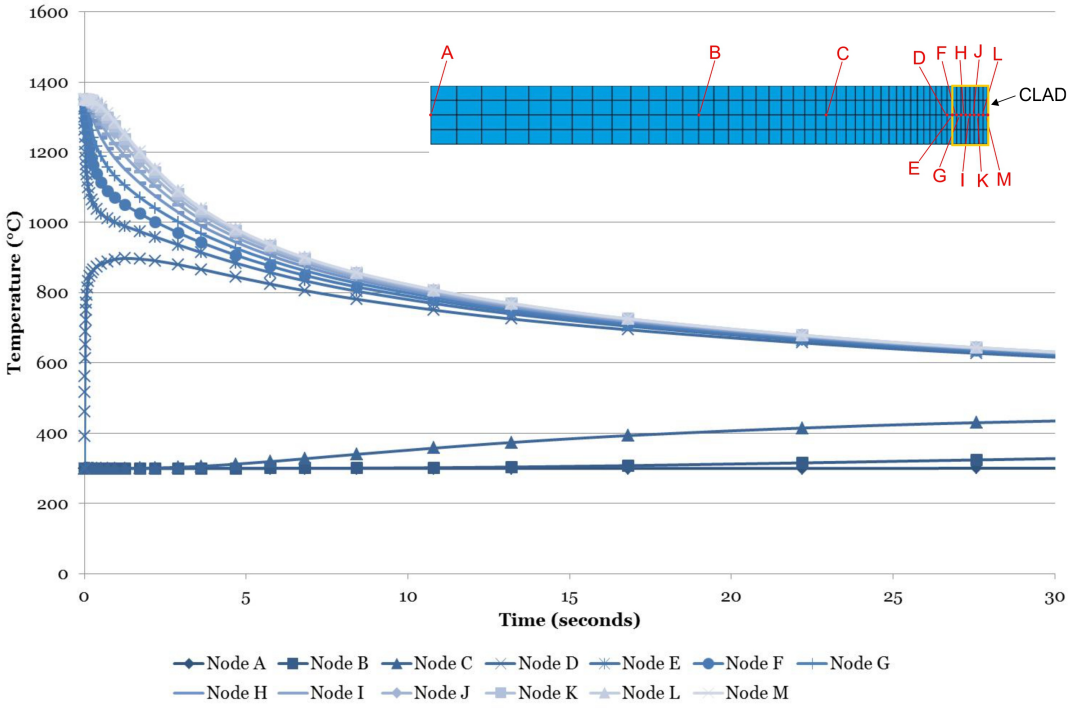

Figure 5.40: Nodal cooling rates for first 30 seconds for an Inconel 625 clad and pre-heat temperature of 300°C - Investigation of nodal cooling rates for an axisymmetric model using nodes highlighted in figure 5.36.

Similar patterns were observed in the case of a 17-4 PH clad. Comparing figures 5.42 and 5.44 illustrates that the clad layer nodes cool more quickly in the case of a lower pre-heat temperature due to the quenching effect of the substrate. Node *D* is likewise heated to a higher temperature when a higher pre-heat temperature is used as would be expected. Nodes *A*-*C* are heated more quickly when a higher pre-heat temperature is applied.

Figures 5.41 and 5.43 show that all nodes reach the same temperature at a slightly earlier time when a lower pre-heat temperature is applied as the clad layer nodes are forced to cool more quickly due to this increased cooling effect arising from the lower pre-heat temperature. In the case of a pre-heat temperature of 150°C nodes in the substrate are heated to a temperature of approximately 325°C, while a pre-heat temperature of 300°C results in nodes in the substrate being heated to approximately 450°C. This again demonstrates that the molten nature of the clad layer material heats the lower pre-heat temperature nodes to a higher level in an aim to decrease the temperature differential. Comparing the temperatures reached by nodes in the substrate when both clad materials are applied shows that in the case of a 17-4 PH clad the substrate nodes are heated to a greater temperature in the case of both pre-heat temperatures.

It would be desirable to utilise cooling rates obtained from the actual cladding pro-

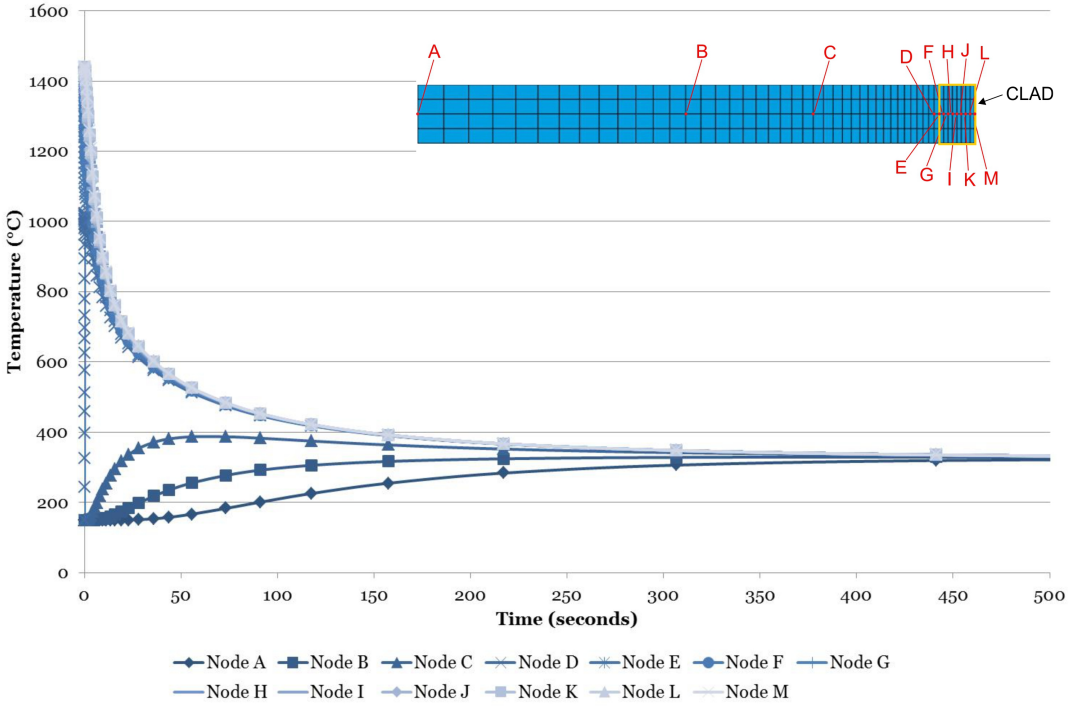

Figure 5.41: Nodal cooling rates for first 500 seconds for a 17-4 PH clad and pre-heat temperature of 150°C - Investigation of nodal cooling rates for an axisymmetric model using nodes highlighted in figure 5.36.

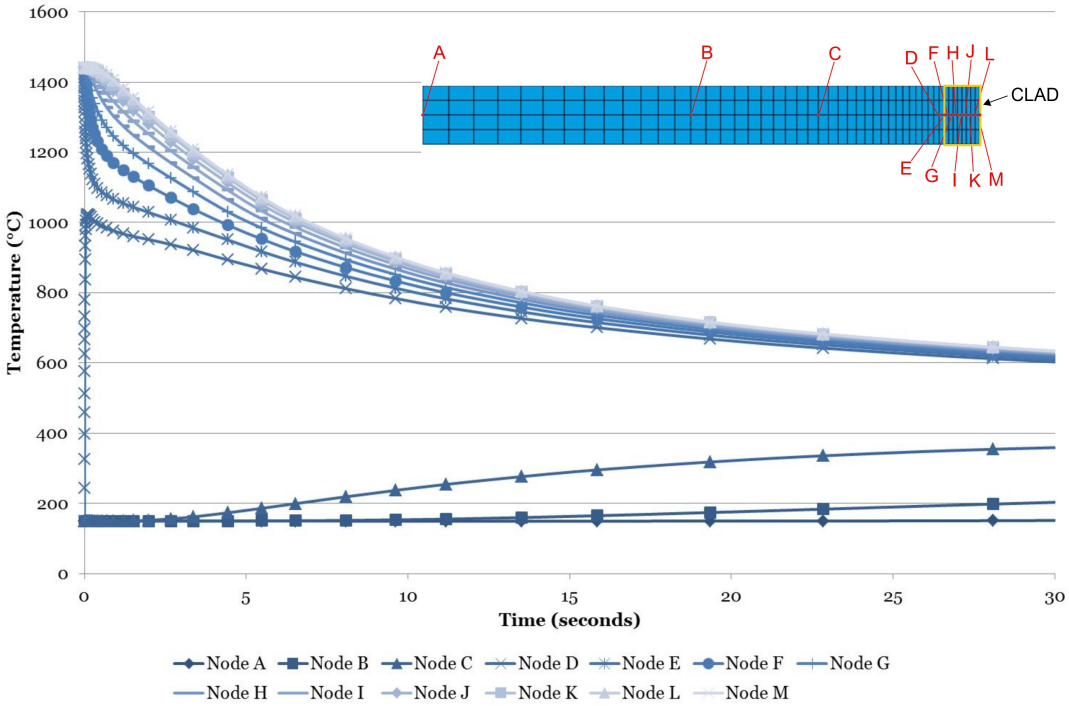

Figure 5.42: Nodal cooling rates for first 30 seconds for a 17-4 PH clad and pre-heat temperature of 150°C - Investigation of nodal cooling rates for an axisymmetric model using nodes highlighted in figure 5.36.

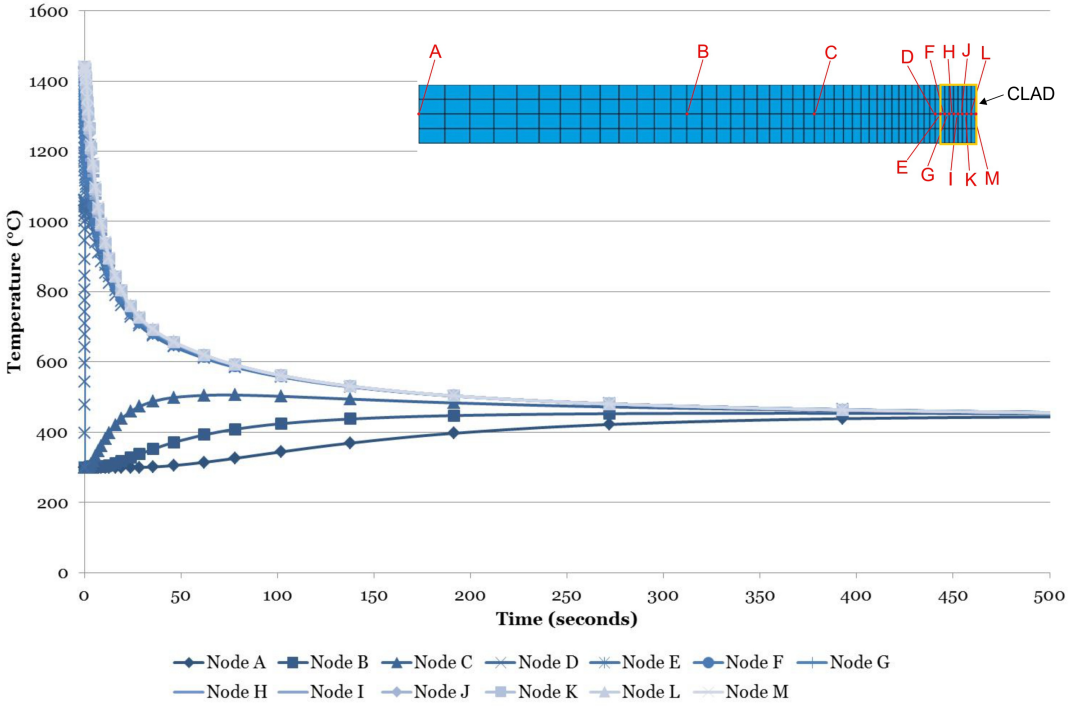

Figure 5.43: Nodal cooling rates for first 500 seconds for a 17-4 PH clad and pre-heat temperature of 300°C - Investigation of nodal cooling rates for an axisymmetric model using nodes highlighted in figure 5.36.

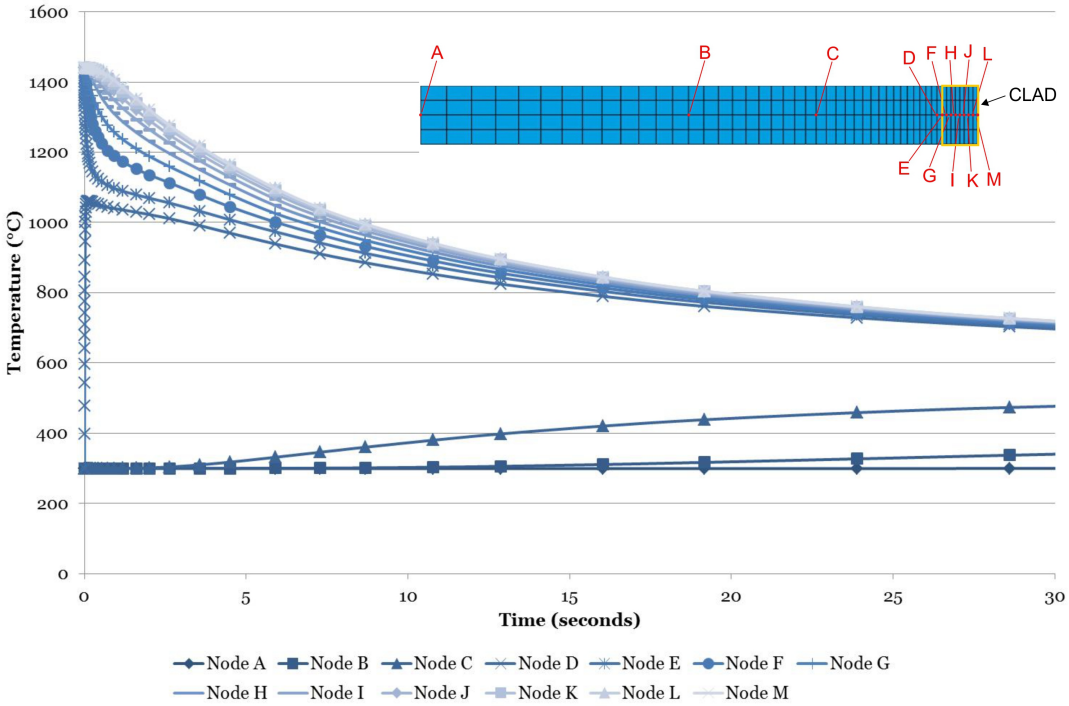

Figure 5.44: Nodal cooling rates for first 30 seconds for a 17-4 PH clad and pre-heat temperature of 300°C - Investigation of nodal cooling rates for an axisymmetric model using nodes highlighted in figure 5.36.

cess to inform testing procedures for material property determination. As was highlighted in the experimental testing program, cooling rates investigated are not representative of the high cooling rates that will be encountered at the beginning of the weld cladding process.

Cooling of the nodes in the substrate is less complex and fairly similar and therefore in obtaining material properties representative of the cooling rate experienced by the material, it would be acceptable to utilise the same data for the three nodes displaced from the clad region. This is expected as the substrate is allowed to cool manually at a rate not required to be as great as that in the clad layer region. In the vicinity of the clad region, and certainly in the clad layer, cooling is of a more complex nature and would require further investigation to understand material behaviour and the effects on material properties, microstructure and ultimately residual stresses.

A relatively slow convective cooling rate, using a heat transfer coefficient of 10 W/m^2K, was applied in these models to accurately capture the weld cladding process utilised to clad the components under investigation. With the use of higher cooling rates, residual stresses could be induced to a higher level, which may or may not be desirable depending on the nature of the stresses.

Correlation of the cooling rate from the weld cladding process with the cooling rate in the simulation is possible through utilising thermocouple measurements obtained during the cladding process.

Rapid cooling rates illustrated also confirm that little time is spent in the high temperature regions during the cladding process and therefore further strengthen the case that material properties at these high temperatures will not greatly impact the final residual stress state (140).

5.7 Discussion

Investigation of the simulation process has indicated that for the present two-pass weld clad axisymmetric component the nature of stresses in the clad layer remains unchanged with increasing mesh layers accounting for spatial and temporal variation. Simulation of the laser cladding process of steel with a metal matrix composite was compared with experimental residual stress determination (172). The study illustrated that although creep effects were not accounted for in the finite element model, good correlation between simulation and experiment was obtained due to the insignificance of creep in this scenario. The effects of creep are only one of the aspects of the simulation, however this supports the neglect of creep in the current simulations. In the cited study, substantial compressive residual stresses were found to remain in the clad layer post-cladding. The models presented in this chapter capture

the tensile or compressive nature of the residual stresses dependent on clad material. All models allow the conclusion to be drawn that tensile residual stresses arise in an Inconel 625 clad layer and compressive residual stresses in a 17-4 PH clad layer.

Previous discussions regarding the complexity of weld clad modelling have emphasised the wide range of possibilities in weld modelling. Figure 5.45 illustrates various constitutive models used in the modelling process. Current modelling is a simplification of constitutive modelling, with the second type being that accounted for herein, where experimental data accounts for variations in material properties. There is clearly scope for increased complexity in the modelling process to account for plasticity, microstructural effects and hardening.

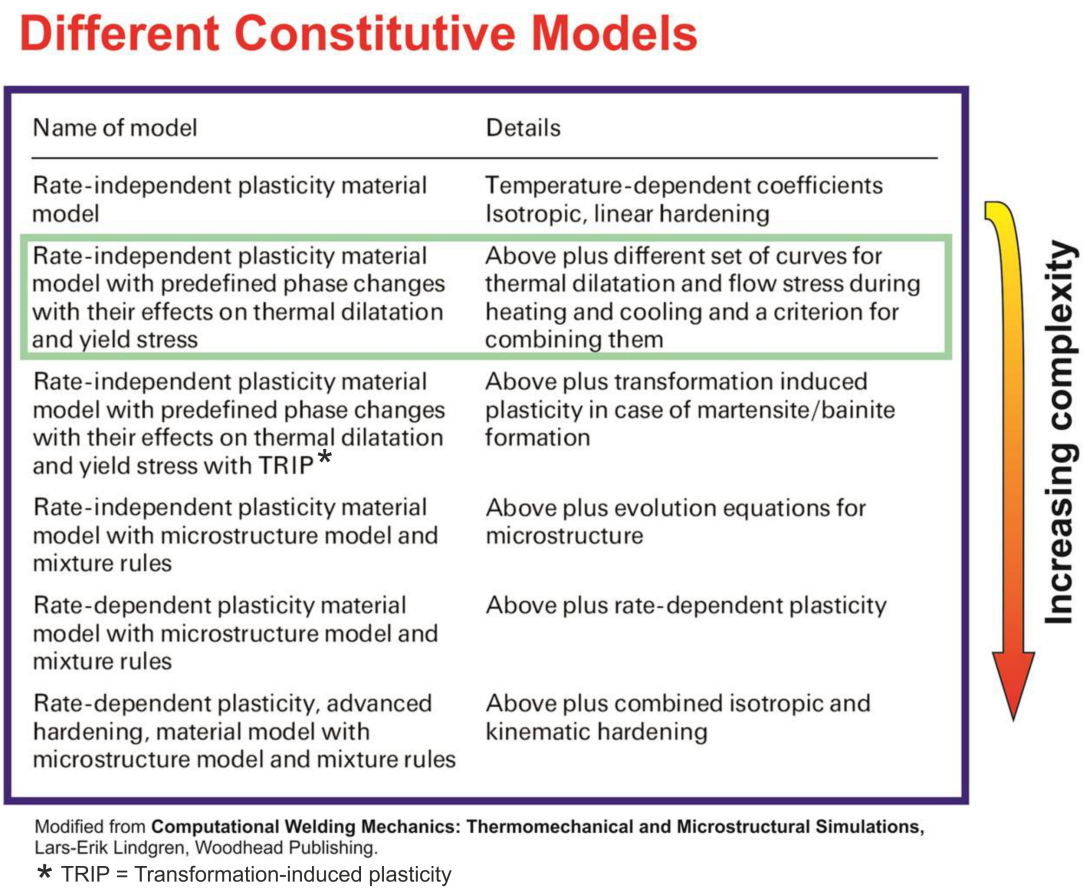

Figure 5.45: Schematic illustrating increasing complexity of computational weld modelling - Modified from (158).

As previously discussed, and also mentioned by Goldak and Akhlaghi (173), the development of the microstructure of the material is dependent on the temperature history experienced. This introduces a coupling between the thermal characteristics of the model and the microstructural. Phase changes may result in volume changes causing a coupling between the microstructural and mechanical aspects of the model. Depending on the deformation occurring in the model, the rate of phase transfor-

mation prescribes the formed microstructure. This time-based process is likewise dependent on the rate of temperature change and not simply the absolute temperature.. Therefore a coupling arises between various aspects of a weld analysis. The extent of inclusion of these aspects determines the level of complexity of the analysis.

Modelling the weld clad case using 17-4 PH is complex due to large differences in data depending on cooling rates. Therefore it would be required to further investigate data at cooling rates appropriate to the cladding process, these being much higher than those utilised in the experimental program.

The assumption of the idealised interface presents discontinuity stresses that are likely to be greater and exist over a narrower zone than those arising in reality. This is due to alloying and diffusion occurring through the weld cladding process, therefore rendering an idealised interface inaccurate, albeit demonstrating a worst case scenario.

Axial stresses in the weld and HAZ have been observed as being strongly correlated with the yield properties of the substrate material. Hoop stresses, however, can be observed to vary depending on the yield properties of the clad material (161). This would require further investigation as to the applicability of this finding in the current research, as axial stresses were found to be similar to hoop stresses throughout.

The *Abaqus Welding Interface* was also utilised in the modelling of the weld cladding process. This allows the analysis to be performed in two steps, firstly a thermal analysis, after which the temperature contours resulting from this first analysis are then used as the input into the structural analysis. Such a loosely coupled analysis presents great potential and would require further investigation, especially with regards to the capability of introducing nodal temperature sensors to mimic thermocouples enabling further calibration of the simulation model with the welding process were more accurate thermocouple measurements to be available from future cladding programs.

Further complexity of the weld cladding process is the cyclic nature of the welding process and although the re-heating effect is being captured in the axisymmetric model, the deposition process could be developed such that weld beads overlap upon deposition therefore introducing a modified heating of previously laid weld material as the *spiralling* of the weld cladding process progresses.

It has been stated (158) that an axisymmetric model does not adequately capture the transient nature of the welding process, although this has been a popular method of decreasing the complexity of the model. The primary factor affected is shrinking in the axial direction due to the effect of the entire circumference welded at once (158). Experimental residual stress determination presented in chapter 6 indicate

good correlation between simulation and experimental residual stresses and through this it is possible to confirm the validity of the axisymmetric models favoured herein.

5.8 Summary

The modelling of the weld cladding process has been investigated indicating that a three-dimensional, multi-pass modelling procedure is of secondary importance. The need for accurate material properties was clearly observed through the use of published data in early simulation models resulting in tensile residual stresses in a 17-4 PH clad layer. Upon inputting experimentally obtained material properties, residual stresses were transformed, being compressive in nature, as confirmed by the experimental results reported in chapter 6. This is concluded to be primarily due to the martensitic phase change upon cooling, captured in thermal property data. This finding was in accordance with the those of Katsuyama et al. (156).

Although the spatial and temporal variation of the weld cladding process has been developed in this research, the laying of weld beads does not take into account the effects of repeated phase changes due to the heating, cooling and re-heating of the weld material and HAZ.

There are various levels of complexity accounted for in weld modelling. In a study, three organisations, BE-ANSTO, EMC2 and Westinghouse used 46, 48 and 25 passes respectively for the simulation of a large weld (140). This is an example of the varying levels of complexity in some weld simulations. In the case of the clad components in this research, a two-pass system was implemented and found to be a reasonable approximation given the axisymmetric nature of the final model.

The assumption of an idealised interface is shown to be inaccurate in chapter 4 and therefore the model should be developed to account for true representation of material properties to obtain an accurate stress distribution and allow for a clearer understanding and more accurate predictions of the effects on fatigue performance. It has been shown previously that the cladding process results in a variation in elemental composition and grain structure and therefore it is expected that material properties will vary with depth. It has also been highlighted that cooling rates differ greatly throughout the model and this will further impact material properties and resulting residual stresses. Therefore, although accurate material data has been obtained from the clad and HAZ regions for both material combinations, simulation models using a step change in such properties at an idealised interface remains a significant approximation to reality.

The discontinuity stresses predicted to be present at the interface of the clad components in the case of both clad materials were found to be very high and could

therefore result in fatigue cracks developing sub-surface. A lower pre-heat temperature resulted in higher discontinuity stresses. It is also supposed that accounting for the alloying and diffusion occurring through the cladding process will accurately model the discontinuity stresses, shown in chapter 6 to be lower in reality than is illustrated in the results presented in this chapter.

Chapter 6

Experimental Determination of Residual Stresses due to Weld Cladding

Experimental techniques of measuring residual stress are discussed in light of the key aspects requiring consideration in selecting an appropriate technique. Focus is placed on incremental centre hole-drilling, the method with which residual stresses present in the weld clad components were obtained experimentally. Considerations such as surface preparation, potential influences from the weld clad profile and the drilling technique are discussed. Results of the experimentally obtained residual stress distribution are presented for a depth of 1 mm from the clad surface. An investigation of the depth of compressive residual stresses in a block clad with 17-4 PH is also presented, illustrating the presence of compressive residual stresses in the 17-4 PH clad layer and into the 4330 HAZ. Potential errors in the incremental centre hole-drilling technique are discussed and consequential uncertainties in residual stress values presented. The experimental residual stresses obtained are compared with the residual stresses obtained in the previous chapter through finite element simulation of the weld cladding process. Good correlation was obtained between experiment and simulation, especially in the case of an Inconel 625 clad. Complexity in obtaining correlation in the case of a 17-4 PH clad is discussed.

6.1 Introduction

The previous chapter presented results of an investigation into the modelling of the weld cladding process. It is very common to validate simulation findings with experimental measurements to obtain correlation and aid in modelling to a level of increased accuracy in the aim of decreasing the need for expensive and time-consuming experimental investigation. In this chapter, experimental residual stress measurements using the incremental centre hole-drilling method will be presented, obtained in the case of both clad materials and both cylindrical and rectangular substrate geometries. These results allow conclusions to be drawn as to the success of the finite element modelling process and the level of correlation obtained. The areas in need of further development are also identified.

6.2 Residual stress measurement

Experimental residual stress measurement includes a wide variety of methods depending on the type of stress requiring measurement. The characteristics of the component and the nature of the stress were introduced in chapter 1. In the case of type 2 and 3 stresses, these stresses being micro stresses, care must be taken to ensure that the volume utilised to obtain such measurements is suitably adequate to characterise these stresses. Methods used to measure macro stresses, on the other hand, do not have the ability to determine micro stresses due to the nature of the technique, for example in the case of hole drilling.

The various techniques to measure residual stresses are well introduced by Rossini et al. (174). The most appropriate technique must be deduced through consideration of the depth of measurement, the required level of material removal and the level of destructiveness of the technique. This is illustrated in figure 6.1. Methods can be categorised as destructive, semi-destructive or non-destructive, with these terms referring to the effects of the measurement procedure on the component.

A method which is destructive releases stresses in the component through a form of material removal, such as the sectioning of the component, to produce deformation in the material encouraging the residual stresses to re-equilibrate.

Semi-destructive methods use a similar principle, however removing smaller amounts of material such as through the drilling of a hole. Therefore the overall structural integrity of the component is not affected to the same degree as with destructive methods, such as the contour method.

Non-destructive methods utilise alternative methods such that the component remains intact and the structural integrity is not affected, for example through the use

of high-energy radiation. This also leads to the ability to define methods according to the method through which stresses are obtained, primarily relaxation or diffraction.

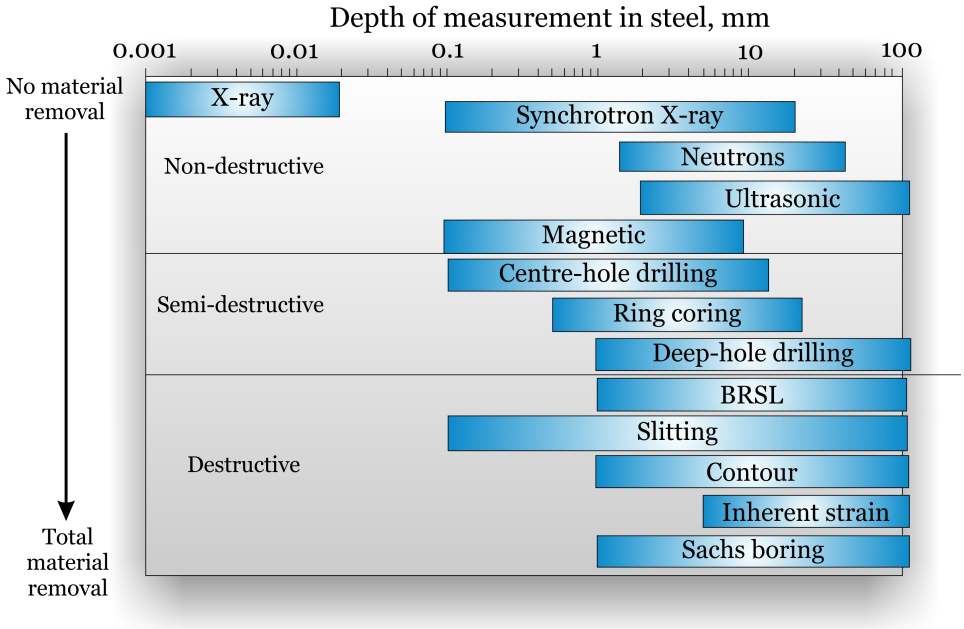

Figure 6.1: Residual stress measurement techniques - Classification of residual stress techniques according to depth of measurement, material removal and destructiveness. Modified from (175).

Kandil et al. (4) present a review of technique selection highlighting the advantages and disadvantages with regards to practical, physical and material aspects for an extensive range of methods.

Residual stresses can be calculated from the measurement of residual strain with the additional knowledge of material properties. The type of stresses and the depth to which stresses are required further directs one towards a selection of appropriate residual stress measurement methods. A selection of methods will be briefly discussed herein. In this chapter focus will be placed on the hole-drilling method and residual stress measurements obtained using this method.

6.2.1 Relaxation techniques

In the case of relaxation techniques, residual stresses are obtained as a result of the relaxation of stresses due to material removal. This relaxation is determined through the displacement of the material, measured as displacement or strain, with the conversion of these strain values into stresses providing the associated residual stresses. Due to the material removal required in these methods, they are generally destructive in nature. However as will be presented in this chapter, material removal can be minimal such that it does not affect the global residual stress distribution, therefore some

relaxation methods can be classed as semi-destructive. Relaxation methods include the hole-drilling, contour and slitting methods.

6.2.1.1 Hole-drilling method

The hole-drilling method as mentioned is a semi-destructive relaxation technique. Stresses are released through the drilling of a hole, with the local displacement of the surface in the close vicinity of the hole measured. A high-speed air turbine is commonly used to drill the hole and remove the material, although air abrasion can also be used (176). The high-speed air turbine, with speeds up to 400,000 *rpm* (177), results in minimal stresses induced through the hole-drilling process. The strain associated with this process of material removal is measured using a strain gauge allowing the residual stresses once present in the hole to be determined. The nature of the drilling process is incremental with the change in residual stress calculated at each incremental stage. To ensure that an accurate stress gradient is obtained drilling increments must be small.

In obtaining residual stress measurements with depth, the method can be referred to as the incremental centre hole-drilling method (*ICHD*). This method was originally introduced by Mathar (178) and is presented and supported in the *ASTM* standard (179). This method of measuring strain relaxation is the most commonly used due to the long-standing history of the method and the ability to utilise this method both in the laboratory or in the field.

The accuracy of the readings obtained through *ICHD* decreases as the hole depth increases as surface changes become less sensitive with material removal at greater depths. The maximum depth for useful strain readings is considered to be one half of the diameter of the drilled hole (180).

Due to the small volume of material removal due to this drilling of a hole, the hole-drilling method is regarded as one of the most favoured techniques to limit component damage and hence described as semi-destructive. *ICHD* is however highly sensitive to user technique, instrumentation errors, applied material constants and hole tapering and roundness. For this reason the radius of the drilled hole is also of utmost interest, to compare the drill diameter with the resulting hole diameter to assess the eccentricity of the hole. Likewise, the radius from the centre of the hole to the centre of the strain gauge is of particular interest.

Schajer presents the hole-drilling theory in (181). In the case of a 45° rectangular strain gauge rosette as shown in figure 6.2, the stress variables can be defined as:

$$P = \frac{\sigma_3 + \sigma_1}{2} \tag{6.1}$$

Figure 6.2: Example of strain gauge utilised in the hole drilling method - Vishay Precision Group strain gauge type EA-06-062RE-120 utilised in the hole drilling measurements (177).

$$Q = \frac{\sigma_3 - \sigma_1}{2} \tag{6.2}$$

$$T = \tau_{13} \tag{6.3}$$

Stress directions are annotated in figure 6.3.

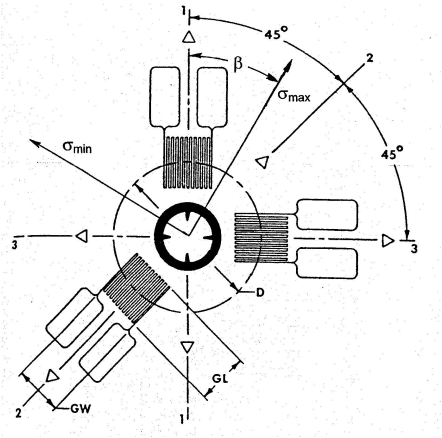

Figure 6.3: Annotated strain gauge rosette - Stress component and principal stress directions annotated on strain gauge rosette. Figure obtained from (182).

Strain variables are likewise defined as:

$$p = \frac{\epsilon_3 + \epsilon_1}{2} \tag{6.4}$$

$$q = \frac{\epsilon_3 - \epsilon_1}{2} \tag{6.5}$$

$$t = \frac{\epsilon_3 + \epsilon_1 - 2\epsilon_2}{2} \tag{6.6}$$

In equations 6.1 and 6.4, P and p effectively represent the pressure of the residual stress present and the associated strain relaxations, while Q, q, T and t represent the shear stress and strain components.

These variables can be transformed to obtain the following equations, introducing the dimensionless coefficients $\bar{a}$ and $\bar{b}$:

$$\bar{a}P = \frac{Ep}{1+\nu} \tag{6.7}$$

$$\bar{b}Q = Eq \tag{6.8}$$

$$\bar{b}T = Et \tag{6.9}$$

These variables can then be used to obtain the Cartesian stress components:

$$\sigma_1 = P - Q \tag{6.10}$$

$$\sigma_3 = P + Q \tag{6.11}$$

$$\tau_{13} = T \tag{6.12}$$

Principal stresses are obtained through combination of the stress variables P, Q and T:

$$\sigma_{max}, \sigma_{min} = P \pm \sqrt{Q^2 + T^2} \tag{6.13}$$

$$\sigma_{max}, \sigma_{min} = \left[\frac{p}{\bar{a}(1+\nu)} \pm \frac{\sqrt{q^2 + t^2}}{b} \right] E \tag{6.14}$$

The angle β between the first gauge as labelled in figure 6.3 and the maximum principal stress direction is determined using either of the following equations, these being equivalent:

$$\beta = \frac{1}{2} tan^{-1} \left(\frac{T}{Q} \right) \tag{6.15}$$

$$\beta = \frac{1}{2} tan^{-1} \left(\frac{t}{q} \right) \tag{6.16}$$

The use of coefficients $\bar{a}$ and $\bar{b}$ in the conversion from measured strains to calculated stresses requires validation and calculation. It is common to conduct experiments in order to achieve this using test samples which are loaded to a known level. This is due to the difficulty of using specimens with residual stresses induced as the exact nature and distribution of these stresses is unknown. This was done by Bynum using the air-abrasive method of material removal and tungsten carbide nozzles with large inner diameters to improve the quality of the hole (183).

The strains measured through the hole-drilling process can be converted into residual stresses using several methods: the uniform stress, the power series, the integral, the Kockelmann or the hole-drilling (*HDM*) methods, amongst others. Depending on the expected stress distribution and the desired degree of accuracy the appropriate method can be selected.

Comparison of the Uniform, Power and Integral methods on measurements obtained on a shot-peened aluminium sample showed that as expected the Uniform stress method did not capture the non-uniform distribution arising due to the shot peening process. The Power method provided an indication of stress variation with depth, although unable to capture the sub-surface peak arising through shot peening. The expected stress profile featuring the sub-surface peak in compressive residual stresses was captured only by the Integral method (180).

The Integral method was utilised in this research due to the expected variation in residual stresses with depth and the general consensus that this method provides the most accurate values for residual stresses (180). The Integral method uses a finite element calculation as a method of calibration. Stresses at the various depths at which measurements are obtained are utilised to consider the overall contribution to the total strain relaxation. The disadvantage of this coupling method is that errors arising in one increment will be carried into the successive increment. Schajer highlights that the Incremental Strain and Average Stress methods are approximations of the Integral method (181).

In drilling incrementally, the first increment considers the relaxation of strain due to the drilling of the hole and relaxation of the material at the component surface. Upon drilling below the surface two factors must be considered: both the relieving of stress associated with drilling at that depth and the effect of this material removal at the strain gauge location at the component surface. This results in additional coefficients for consideration at each depth increment as drilling progresses.

Small increments are preferable to minimise abrupt variations in data. Through applying small increments, the Integral method has the potential to obtain rapidly-varying residual stress fields at the surface of components with complex residual

stress distributions, such as shot peened samples. The optimisation of depth increments has been investigated and presented by Zuccarello (184) and Stefanescu et al. (185). Sensitivity to errors can be reduced by considering the distribution of depth increments, with constant depth increments resulting in large errors. The incrementation chosen also depends on the location at which stress variations are of most interest.

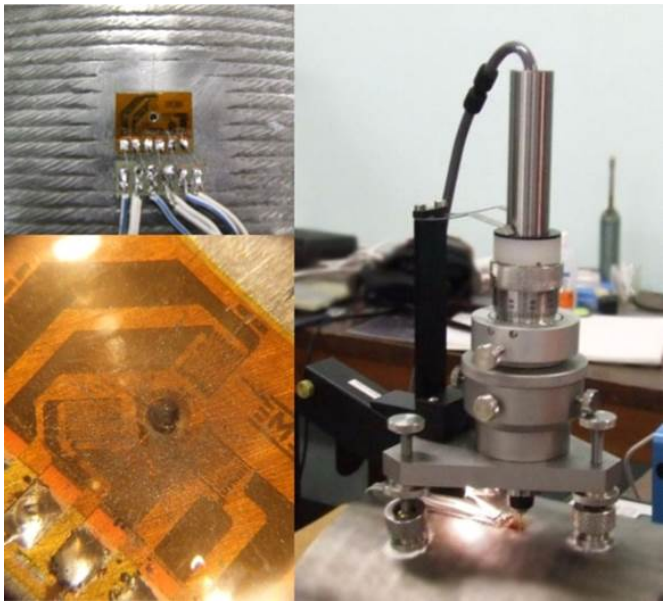

Figure 6.4: Example of the setup utilised in the in-house ICHD process - Showing the Vishay RS-200 precision milling equipment mounted on the weld clad cylinder and an example of a strain gauge utilised in obtaining residual stress measurements.

Electronic speckle pattern interferometry The displacement due to the drilling of the hole can also be observed using electronic speckle pattern interferometry (*ESPI*) (186). This method compares digital interference images obtained during the drilling process, however is more costly and entails a more complex setup with the need for a vibration table to eliminate the potential for errors due to the occurrence of vibration during measurement. However, without the need to install a strain gauge rosette and prepare the component surface in the same way as with *ICHD*, the *ESPI* method can also prove to be more beneficial depending on the specimen in question.

6.2.1.2 Deep-hole drilling

A method of obtaining hole-drilling measurements through the depth of a component has been developed in the form of the deep-hole drilling method (187). Initially a reference hole of small diameter is drilled, the diameter of which is measured by an air probe. Using a trepanning process, material is then removed in a columnar form around the reference hole. Stress relaxation occurs and this in turn results in a

modification of the dimensions of the reference hole and the column drilled. Residual stresses can in this way be obtained in the plane normal to the axis of the hole in a similar manner to the conventional hole-drilling method (188). Although this allows for increased depth of measurements, the process is of course of a higher level of destructiveness than the conventional hole-drilling method.

6.2.1.3 Sectioning methods

Sectioning methods encompass a selection of residual stress measurement methods destructive in nature.

Sachs boring Sachs boring method is an example of this. As the name suggests, this method involves boring through the material, often used in autofrettaged thick-walled cylinders. Strain gauges are installed on the outer diameter of the component to obtain strain readings while the component is subjected to material removal. Relaxed strains are utilised similar to the previous methods described. Although a method typically employed for residual stress determination in autofrettaged thick-walled cylinders, Parker notes that the Sachs' method of material removal does not reliably determine residual stresses, with overestimations in the region of 24-43% (189).

Slitting method The slitting method, also referred to as the crack compliance method focusses on relieved strains in the vicinity of a slit. Strain gauges are installed close to the slit or crack and an incremental slit is cut into the component. Changes in strains are recorded with readings taken as the slit is extended into the component. These are then used to obtain a back calculation resulting in the residual stress distribution. The method assumes uniformity along the length of the slit and solely provides stresses normal to the cut surface (174). This method is highly sensitive with the ability of deducing low magnitudes of residual stress in the region of 10 MPa (190).

Contour method The contour method is also a destructive technique first presented by Prime (191). The displacement of a cut face is accurately measured and a finite element model used in which the opposite of the obtained face profile or contour is applied as a displacement boundary condition. Bueckner's elastic principle of superposition is used to obtain the residual stresses normal to the cutting plane. This method will be described in greater detail in section 8.5 with results of residual stress measurements obtained using this method also presented in this section.

6.2.2 Diffraction techniques

6.2.2.1 X-Ray diffraction

X-ray diffraction (*XRD*) determines the residual stresses in a component through the alteration of lattice plane spacing due to elastic deformation. These deformations cause a change in the stress from the prior stress-less state to the applied stress (174). The surface of the material is penetrated using high energy X-rays, the crystal planes of the material diffracting some of these X-rays. The angular position of the diffracted X-rays are obtained using a detector which notes the ray intensity.

Figure 6.5 illustrates the striking of atoms K and P by the rays on the left-hand side of the figure. Scattering of the beams then occurs as shown on the right-hand side of the figure. These scattered rays are in phase if the path difference between them is a complete wavelength of positive integer n. This relationship between the X-rays and the crystal lattice structure is governed by Bragg's law, shown in equation 6.17 (192). A positive integer n is multiplied by λ, the wavelength of the X-ray, on the left hand side of the equation, this being equal to the product consisting of the distance between crystal lattice planes d, the index hkl representing the Miller index, which describes the family of crystalline planes. The angle between the incoming ray and the crystal lattice plane is θ.

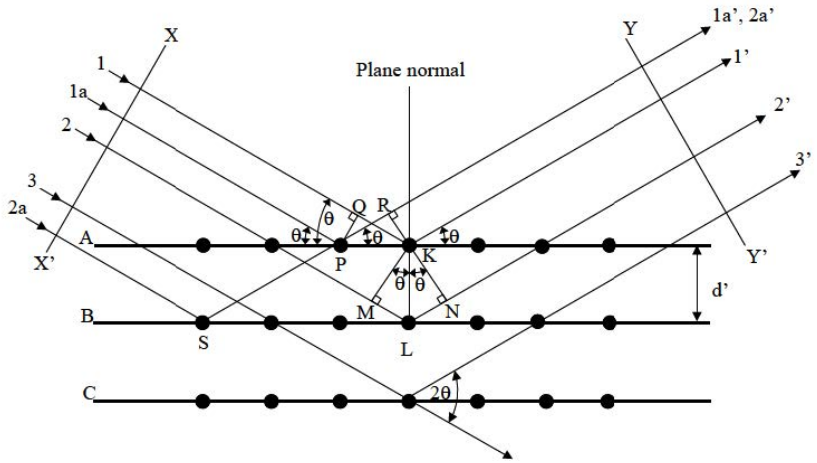

Figure 6.5: X-Ray diffraction - Showing the diffraction of X-rays by a crystal lattice. Figure obtained from (192).

$$n\lambda = 2d_{hkl}sin\theta \tag{6.17}$$

Upon penetration of the material, the atom adopts the frequency of the incoming X-ray. The alignment of the atoms in the crystal lattice will occur at certain angles resulting in an in-phase wave. The intensity of the diffracted beam allows peaks

to be determined, the centre of the peak calculated from the peak width at half maximum. The angle θ at which constructive interference occurs can be obtained when the location of the peaks are known and these values can be used in Bragg's law to calculate the spacing between the crystal planes.

The strain ϵ_{hkl} in the material is determined using the values of the interplanar spacing for the material in the stress-free state d^0_{hkl} and the stressed state d_{hkl}:

$$\epsilon_{hkl} = \frac{d_{hkl} - d^0_{hkl}}{d_{hkl}} \tag{6.18}$$

The higher θ values enable smaller changes in plane spacing to be detected and therefore the setup should ideally allow for an angle of 70-80° to be spanned.

A base value for the diffraction peak for the material is obtained and scanning undertaken at a series of angles as the specimen is rotated. A three dimensional representation of the residual stresses in the specimen is obtained through this rotation of the specimen and observing the location of the peaks and constructive interference with reference to the original diffraction peak obtained (4).

As *XRD* measurements are confined to the surface of the component, measurements with depth can be achieved through electro-polishing the material to remove the material with minimal effects on residual stresses and allow further measurements to be obtained at this depth. In this way, *XRD* can be used to obtain residual stresses with depth, for example using the laboratory or portable equipment manufactured by Proto Manufacturing (193).

XRD also enables insight into the material state, with characteristics such as grain size and the presence and orientation of phases.

6.2.2.2 Neutron diffraction

Neutron diffraction also utilises the elastic deformation in a polycrystalline material and evaluation of the lattice plane spacing in a material to determine the stress change from the stress-free state. However, higher energy neutrons are used instead of X-rays. Neutrons enable a penetration depth of up to many centimetres, providing greater penetration than X-rays (194). Ezeilo and Webster report residual stresses being determined to depths of up to 40 mm (195). However, neutron diffraction possesses very high costs and limited availability to equipment. In measuring residual stresses using XRD and neutron diffraction, the measured area and depth must be considered and the consequential effects on the averaging of the stress value in these regions.

Specimen ID	Gauge No.	Clad material	Weld cladding circumferential/axial location
Strath01	1-XX3.A	Inconel 625	0°
	1-XX3.B	Inconel 625	180°
Strath02	2-XX3.A	17-4 PH	0°
	2-XX3.B	17-4 PH	180°
Strath03	3-3.A	Inconel 625	mid
	3.3.B	Inconel 625	25%
Strath04	4-3.A	17-4 PH	mid
	4-3.B	17-4 PH	25%
Strath05	5-3.A	Inconel 625	mid
	5.3.B	Inconel 625	25%
Strath06	6-3.A	17-4 PH	mid
	6-3.B	17-4 PH	25%
Strath07	7-3.A	Inconel 625	mid
	7-3.B	Inconel 625	25%
Strath08	8-3.A	17-4 PH	mid
	8-3.B	17-4 PH	25%

Table 6.1: Details of residual stress measurements obtained on weld clad specimens

6.3 Experimentally determining residual stresses due to weld cladding

The incremental centre hole-drilling method was utilised to obtain the residual stress distribution in the 4330 cylinders and blocks weld clad with Inconel 625 and 17-4 PH as shown in figures 3.11 and 3.12. Measurements were obtained on the specimens as detailed in table 6.1. Strain gauges were installed on diametrically opposing locations at the centre of the outer diameter of the cylinders. This allowed any non-axisymmetric effects of the cladding and/or any variability in the measurement processes to be deduced if present. On the block specimens strain gauges were installed on the centre-line on the weld clad surface, at the centre point and quarter-length point. This would allow global bending effects to be observed if resulting due to the weld cladding process.

The gauge designations are listed in table 6.1.

The installation of the strain gauge type EA-06-062RE-120 by Vishay Precision Group is shown in figure 6.6 along with the hole-drilling setup. The strain gauges were installed such that element 1 was aligned with the axial direction and element 3 with

the weld direction i.e. the circumferential direction on the cylindrical specimens. On the block specimens element 1 was aligned with the transverse direction and element 3 with the weld direction, i.e. the longitudinal direction.

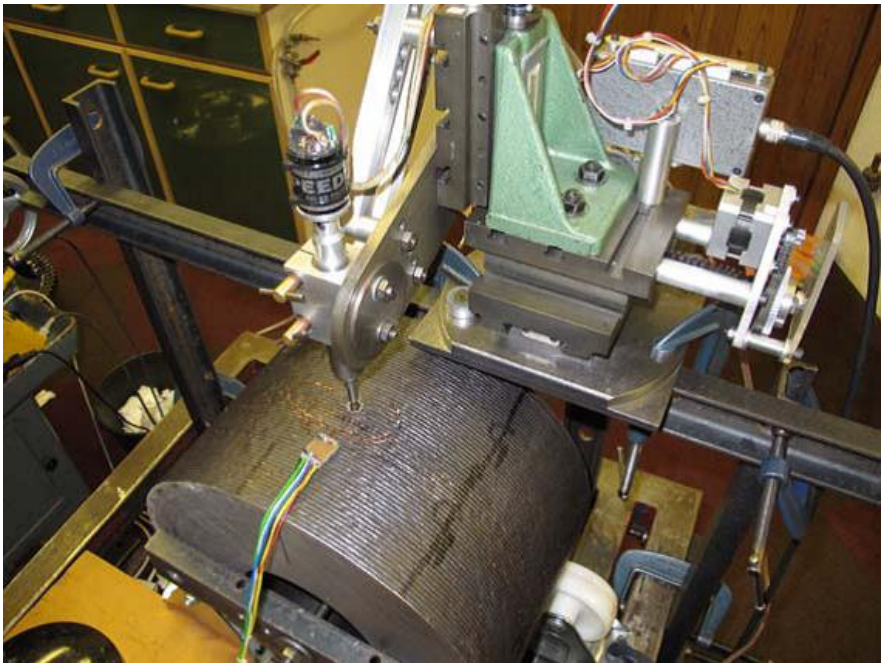

Figure 6.6: Example of the setup utilised in the Stresscraft ICHD process - Showing the customised precision milling equipment positioned around the weld clad cylinder utilised by Stresscraft (196) in obtaining residual stress measurements.

Prior to the laying of the strain gauges, the weld clad profile was machined using a small milling cutter, similar to the drill utilised for drilling the hole. Varying depth increments, beginning with 16μm, then 8μm and lastly 2μm were utilised to minimise the effects of machining on the residual stress distribution. Machining proceeded until complete removal of the weld clad profile such that the strain gauge could be installed without the presence of irregularities on the surface. In this case of the cylindrical specimens the gauge surfaces were machined flat, as opposed to cylindrical.

The amount of material removed for each gauge is listed in table 6.2.

The centre of the strain gauge rosette was positioned at a location where two weld beads previously met i.e. in line with a weld trough. The surface was treated with acetone to degrease, acidic ferric chloride to etch and dilute ammonia to neutralise the area, followed by another degreasing stage prior to the installation of the gauge. The Loctite 407 adhesive was used to install the gauge on the surface of the cylinder as shown in figure 6.7 and the block as shown in figure 6.8.

The zero-depth was determined with initial drilling in 2μm increments until the gauge material and adhesive had been removed.

Specimen	Gauge	Material Removed (μm)
Strath01	1-XX3.A	298
	1-XX3.B	314
Strath02	2-XX3.A	634
	2-XX3.B	538
Strath03	3-3.A	170
	3.3.B	170
Strath04	4-3.A	458
	4-3.B	394
Strath05	5-3.A	218
	5.3.B	298
Strath06	6-3.A	506
	6-3.B	692
Strath07	7-3.A	154
	7-3.B	138
Strath08	8-3.A	362
	8-3.B	522

Table 6.2: Depth of material removal required on weld clad specimens to remove weld clad profile

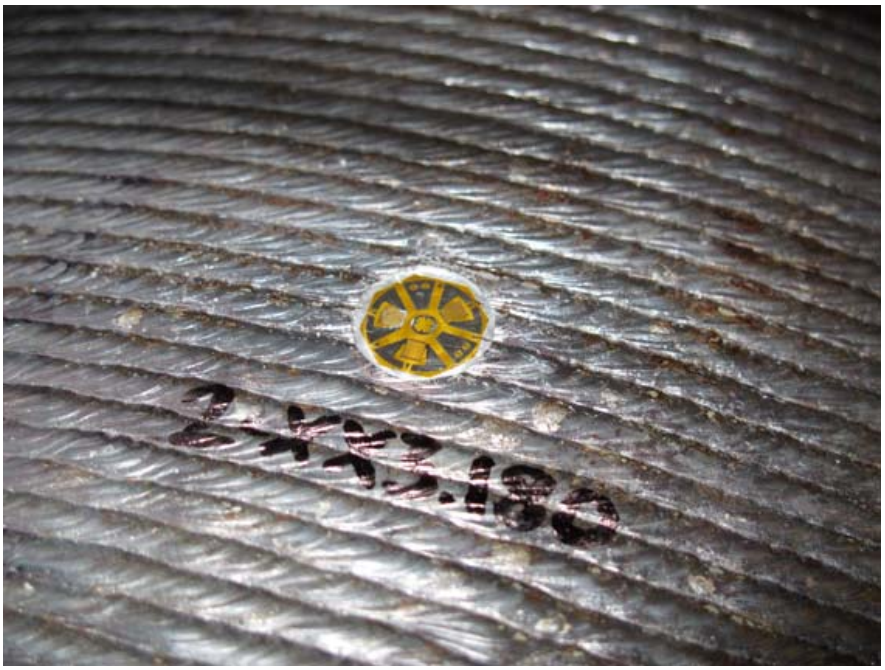

Figure 6.7: Strain gauge installed on weld clad cylinder - Strain gauge type EA-06-062RE-120 by Vishay Precision Group.

Figure 6.8: Strain gauge installed on weld clad block - Strain gauge type EA-06-062RE-120 by Vishay Precision Group.

Tungsten carbide cutters were used to drill the holes with the depth increments utilised in the drilling process noted in table 6.3. Strain values were recorded at each of these increments to a maximum depth of 1408 μm. Combination strains are calculated as detailed in equations 6.4-6.6. Thereafter combination stresses and in-plane Cartesian stresses were calculated to a depth of 1024 μm according to equations 6.1-6.3 and 6.10-6.12. A new drill was used for each hole drilled to ensure that no errors arose due to drill bluntness.

Depth of increment (μm)	No. of increments
32	4
64	4
128	8

Table 6.3: Depth increments utilised in the ICHD process

Figure 6.9 shows the drilling process. Drilling was undertaken in accordance with the guidelines provided in (180).

Young's modulus and Poisson's ratio were used for clad materials as shown in table 6.4 in the conversion of strain to stress values using the Integral method.

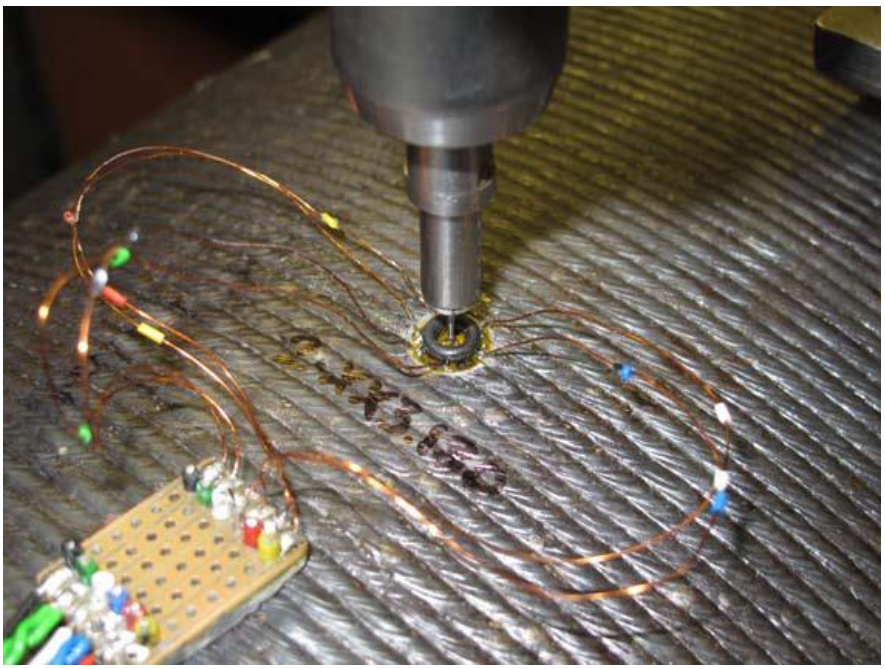

Figure 6.9: ICHD drilling process utilised by Stresscraft - Figure showing the drilling process on the weld clad cylinder, with the strain gauge wired and the drill placed to drill into the centre of the installed strain gauge rosette (196).

	Inconel 625	**17-4 PH**
Youngs modulus (GPa)	205.3	196.4
Poissons ratio	0.312	0.272

Table 6.4: Material properties utilised in the strain-stress conversion process

6.3.1 Considerations

Extensive residual stress measurements were obtained using the *ICHD* method, both in-house and externally, providing a large array of data and therefore confidence in the stress distributions obtained. This measurement program also allowed for the investigation of surface preparation techniques and the effects of curvature in the machining of the surface.

6.3.1.1 Surface preparation

In preparing the weld clad profile for residual stress measurements utilising strain gauge rosettes, the weld clad profile requires machining to provide a smooth surface upon which to lay the strain gauge. Machining of a component will modify the self-equilibrating residual stress distribution in a thin surface layer. The majority of machining processes induce tensile residual stresses, detrimental to fatigue life, potentially increasing susceptibility to stress-corrosion cracking as highlighted by Paxton (11). The effects of these induced tensile residual stresses when superimposed with potential tensile residual stresses resulting from the weld cladding process can result in very high detrimental stresses. In machining a component in which compressive residual stresses have been induced, it should be ensured that these beneficial residual stresses are not removed. It would furthermore be desirable to induce compressive residual stresses through surface preparation as shown to be possible in figure 6.10. The surface of the component is also the most crucial in terms of component operation, as stresses experienced at this location are often highest. Gentle grinding was not possible due to non-availability of suitable *CNC* grinding equipment.

The thermal environment at the surface during machining could also impact the residual stress distribution if the component is heated through temperature gradients arising during machining and therefore measures must be taken to ensure that the component remains cool throughout the process.

Various surface preparation methods were used for the removal of the weld clad profile: hand-grinding, a *CNC* milling method removing material in regular depth increments and a *CNC* milling method with varying depth increments to minimise machining effects. It was found that the latter was most reliable and gave the most consistent results.

Although it was found that using a milling technique with depth varying increments produces the greatest degree of correlation with the finite element simulation, discrepancies still arose close to the surface. This is to be expected due to the machining

of the weld clad profile to allow the installation of the strain gauge rosette modifying the surface residual stress state.

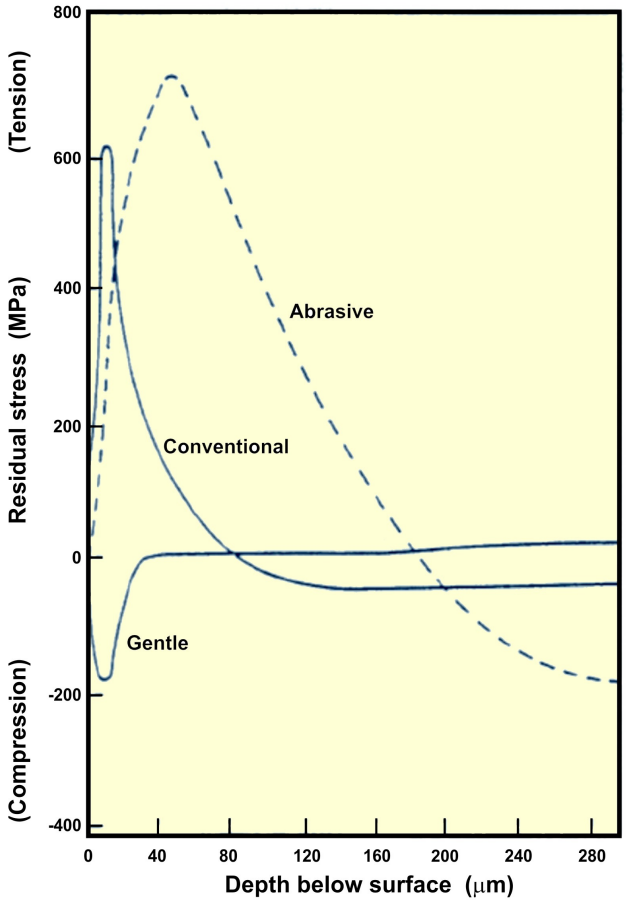

Figure 6.10: Residual stresses induced through grinding processes - Residual stress distributions arising in a hardened steel due to grinding operations. Modified from (4).

Residual stresses due to varying cutting conditions were investigated in (197). Results from this study as shown in figure 6.11 illustrate that when tensile residual stresses and a low surface hardness occur, such as in area *A*, the number of cycles to failure is low. In area *B*, the number of cycles is much greater although the stress level is around zero. Although areas *A* and *C* have hardness values in the same region, the residual stress present in area *C* illustrates the beneficial effects of compressive residual stresses on fatigue life when paired with high hardness levels. This study also concluded that higher hardness values result from the use of a tool with a small radius and a chamfered edge. This provides guidance on the most favourable cutting conditions to increase fatigue performance.

Electropolishing Electropolishing was investigated as a method of surface preparation to minimise residual stresses induced through machining processes. This is one of the processes known to be capable of material removal without inducing ad-

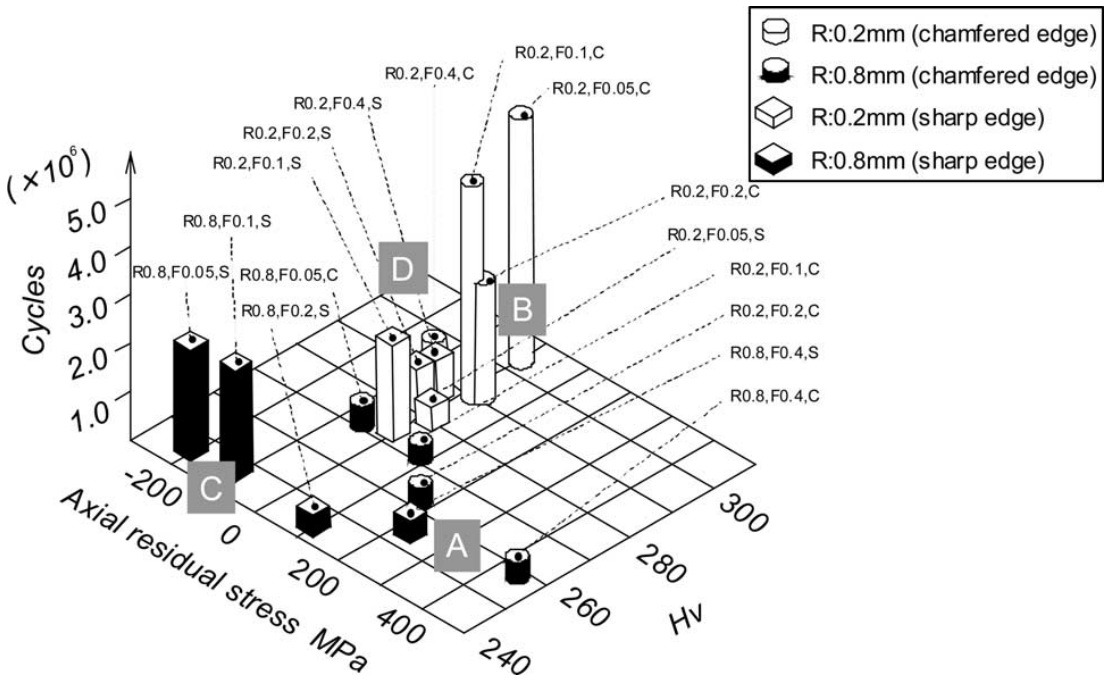

Figure 6.11: Effects of residual stress and surface hardness on fatigue life - Figure obtained from (197)

ditional residual stresses at the macro scale. The use of this technique has also been previously mentioned to facilitate the measurement of residual stresses with depth using *XRD*. The metal to be polished is placed in an electrolytic cell and connected to the positive terminal of an applied voltage, therefore acting as the anode. The cathode connected to the negative terminal is also placed in the electrolytic cell. An applied voltage results in an electrochemical reaction improving the surface finish of the component through material removal due to oxidation.

Various combinations of parameters were investigated for the materials used, altering the applied current, voltage, duration of polishing and the solution. Care must be taken to ensure that pitting does not occur through the process, potentially arising through the application of too large a voltage for example.

Using the Proto Manufacturing PROTO 8818-V3 electropolishing unit, shown in figure 6.12, electropolishing was carried out on weld clad sections. Various electrolytic solutions were used, including the solution shown in table 6.5.

Perchloric acid	62 ml
Ethanol	700 ml
Butyl cellusolve	100 ml
Distilled water	137 ml

Table 6.5: Composition of L1 electrolyte solution

Figure 6.12: PROTO 8818-V3 electropolishing unit by Proto Manufacturing - Image courtesy of Proto Manufacturing (198).

Electropolishing using a voltage of 38 V and a time of 30 seconds produced a typical surface as shown in figure 6.13. The purpose of investigating electropolishing was twofold: as surface preparation for strain gauging and as an etching tool to incrementally remove material for XRD measurement. It was concluded that this process would not be able to remove the weld clad profile in a satisfactory manner due to the differing material removal rates at the peaks and the troughs of the weld clad profile.

From a fatigue point of view, beneficial effects would be expected due to the reduction of stress concentrations present in the weld profile, however this method has been deemed ineffective for the purpose for which it was investigated, namely preparing the surface for the installation of a strain gauge.

6.3.1.2 Weld clad profile

An adaptive-p finite element representation of the weld clad profile is shown in figures 6.14 and 6.15. This model implemented in the Creo Simulate Software served to illustrate the stress concentrations at the peaks and troughs of the profiles when the specimen was subjected to a uniform applied stress of unity.

The analysis converged to 1.5% on the Local Displacement/Energy Index and 2.1% of the Global Root Mean Square Stress Index. Convergence on Maximum Principal Stress was 1.4%. Adaptive refinement was halted, as a 9th order polynomial (maximum) was reached in some areas of adaptive refinement. Further manual seeding of the mesh (h-refinement) was not deemed necessary in this case. Plane

Figure 6.13: Surface of the 4330 machined plate post-electropolishing - Illustrating the machined surface after electropolishing using the L1 solution. Magnification factor: x500.

strain/symmetry boundary conditions were imposed on the section faces with the analysis being of a small displacement and linear elastic nature. The material used was mild steel with a Young's Modulus of 200 GPa and Poissons Ratio of 0.27.

The hoop stress concentration factor (*SCF*) at the selected bead trough was 7.3 while the axial *SCF* at the same locations was only 0.8. The study therefore showed that the stress concentration produced is different for axial and hoop stresses, hoop stresses being larger. Through this model, the complex geometry of the weld clad profile can be reflected upon. Elastic stress concentrations result due to the weld clad geometry when a uniform biaxial stress field is applied. The measurements obtained experimentally will not be representative of the *as-clad* stress field. *XRD* could be utilised without the need for surface preparation to obtain residual stresses of the *as-clad* component, however in practice most fatigue critical applications would involve machining of the clad surface thus further altering the surface layer residual stresses. The focus of this investigation is therefore ensuring beneficial distributions at depth.

6.3.1.3 Drilling technique

An orbital or trepanning drilling technique can be used to further decrease the stresses induced due to the drilling process. This is achieved through using the same drill but offsetting the drill bit such that a larger hole is drilled. This reduces the area upon which the drill is acting at any one time and therefore allows time for the material to cool before the drill approaches the same location again. This method al-

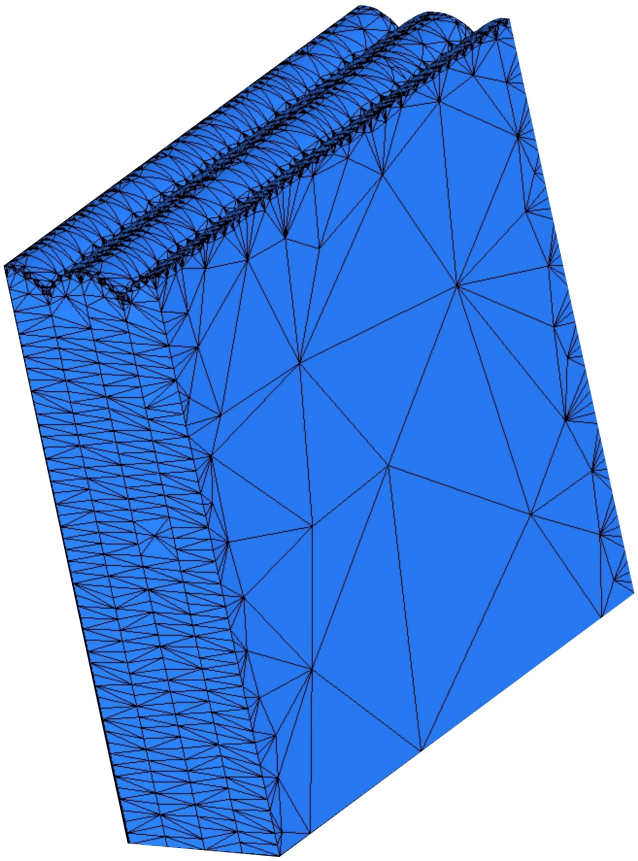

Figure 6.14: Finite element model of weld clad profile - Illustration of peaks and troughs in weld clad profile resulting in stress concentrations.

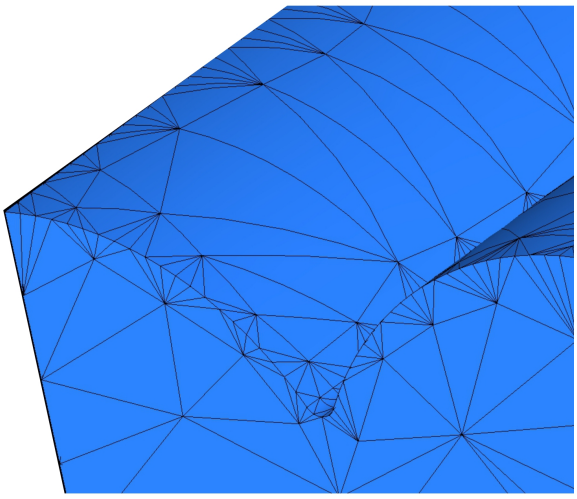

Figure 6.15: Finite element model of weld clad profile emphasising weld peaks and troughs - Illustration of peaks and troughs in weld clad profile resulting in stress concentrations.

Sample ID	Description	Welding consumable	T_{PH} (°C)	$T_{Int.}$ (°C)	Controlled cooling
Strath01	Cylinder	Inconel 625	300	400	Yes
Strath02	Cylinder	17-4 PH	300	400	Yes
Strath03	Plate	Inconel 625	300	400	Yes
Strath04	Plate	17-4 PH	300	400	Yes
Strath05	Plate	Inconel 625	150	250	Yes
Strath06	Plate	17-4 PH	150	250	Yes
Strath07	Plate	Inconel 625	150	250	Yes then $PWSR$
Strath08	Plate	17-4 PH	150	250	Yes then $PWSR$

Table 6.6: Weld cladding sample details

lows both the thermal and mechanical stresses induced due to the drilling process to be reduced. This along with the previous discussion regarding the effects of cutting conditions on residual stresses and fatigue performance (197) indicates that there is scope for further studies into the effects of factors such as machining speeds, feeds and the depth of cutting during machining.

As discussed, the hole-drilling method is highly sensitive to errors and this includes hole geometry. Therefore tapering and roundness of the hole can heavily influence strain readings and in turn resulting residual stresses. For this reason, the method of material removal of air-abrasion (176) is also problematic, in that it is difficult to control the hole geometry to ensure a round, flat-bottomed hole. However, methods of avoiding tapering during deep cuts are available in water jet cutting for example and therefore this may not be an insurmountable problem.

6.4 Results

The designations assigned to the residual stress measurement results are in accordance with those presented in table 6.6.

Variation in the stresses close to the surface was found in the case of an Inconel 625 clad. This is shown in figures 6.16-6.21. This is thought to be related to the machining of the surface to enable the installation of the strain gauge, as discussed in the previous section, or possibly local surface cooling effects, as it is seen that these sharp gradients decrease beyond approximately 200 μm. Stresses are shown to be tensile in all cases, neglecting the case of compression close to the surface. This is in accordance with the findings during the finite element modelling process, although the simulation does not model material property variation through the clad thick-

ness and therefore does not capture the stress gradient at the surface. Experimental measurements are compared with residual stresses obtained through simulation in section 6.5.

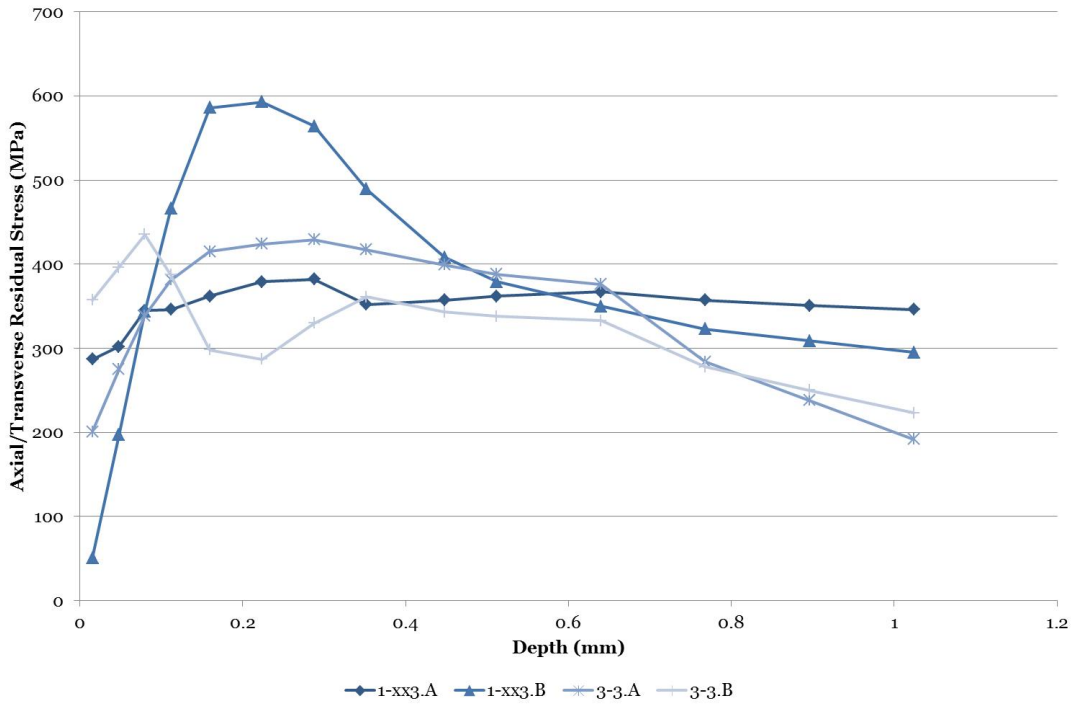

Figure 6.16: Measured axial/transverse residual stresses: Strath01 & Strath03 - ICHD results allowing substrate geometry effects to be deduced for an Inconel 625 clad. Gauges A and B signify two measurements on clad components.

Weld direction stresses, i.e. hoop/longitudinal stresses, in figures 6.17, 6.19 and 6.21 are shown to be slightly less than stresses perpendicular to the weld direction i.e. axial/transverse stresses in figures 6.16, 6.18 and 6.20 at the depth where the stresses adopt a more uniform nature. As the depth of the hole increases, stresses can be seen to fluctuate slightly. At a depth of 512 μm, the maximum tensile residual stress is present in specimen Strath07, a block weld clad with Inconel 625 using a pre-heat temperature of 150°C with *PWSR* applied post-cladding. In this specimen transverse stresses of 449 MPa are present at gauge 7-3.A and 439 MPa at gauge 7-3.B.

The corresponding longitudinal stresses are lower at 286 MPa and 338 MPa respectively. Generally, residual stresses at the maximum depth are smaller than at half of the maximum hole depth, except in the case of Strath05, where stresses at maximum hole depth are σ_1 = 436MPa and σ_3 = 435 MPa. This does not correlate with residual stresses obtained in the simulation models which are uniform throughout the clad layer and highlights the differences in residual stresses due to alloying and diffusion.

Figures 6.16 and 6.17 allow the effects of substrate geometry to be deduced. It is shown that results for a cylinder and a flat rectangular block are very similar hence

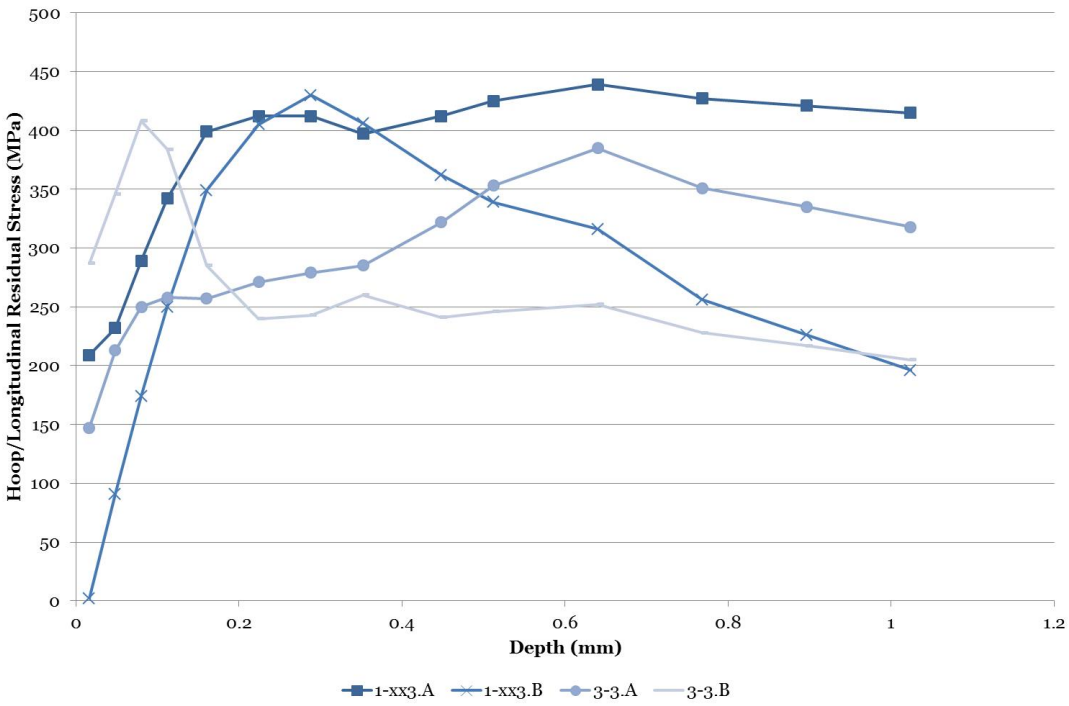

Figure 6.17: Measured hoop/longitudinal residual stresses: Strath01 & Strath03 - ICHD results allowing substrate geometry effects to be deduced for an Inconel 625 clad. Gauges A and B signify two measurements on clad components.

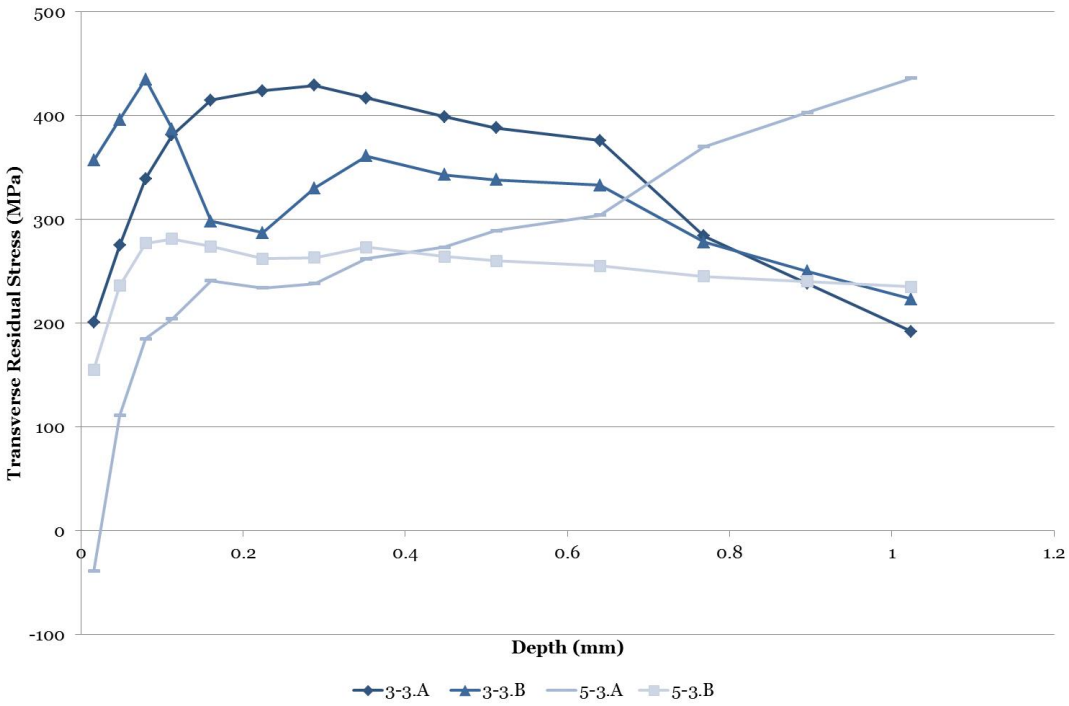

Figure 6.18: Measured transverse residual stresses: Strath03 & Strath05 - ICHD results allowing pre-heat temperature effects to be deduced.

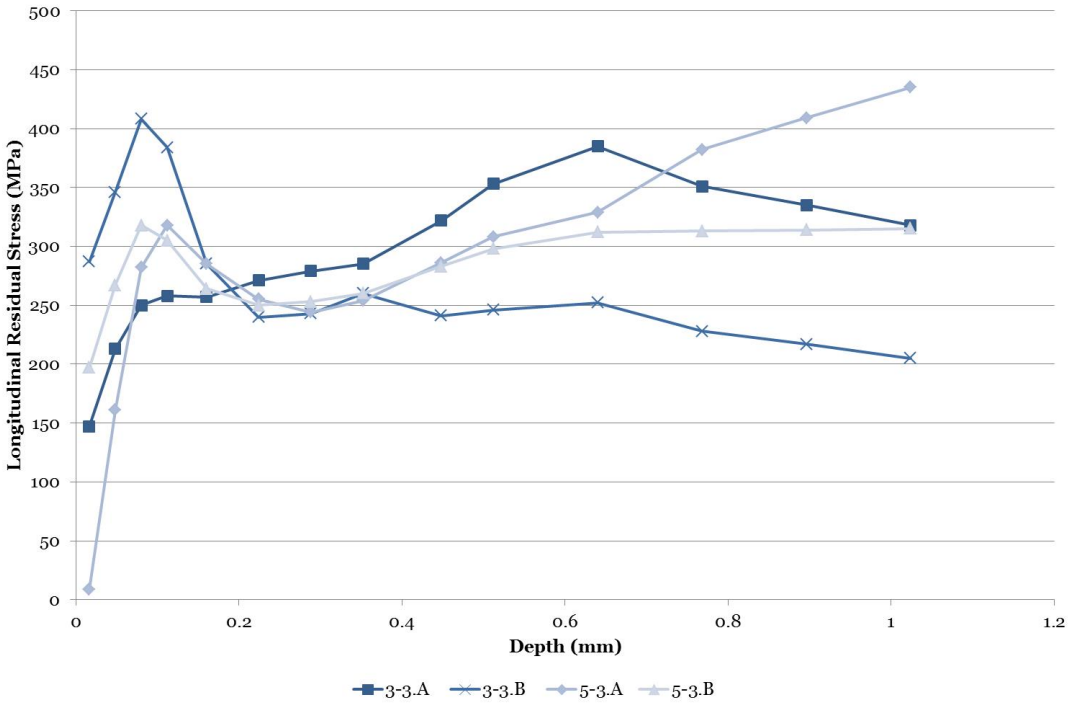

Figure 6.19: Measured longitudinal residual stresses: Strath03 & Strath05 - ICHD results allowing pre-heat temperature effects to be deduced for an Inconel 625 clad. Gauges A and B signify two measurements on clad components.

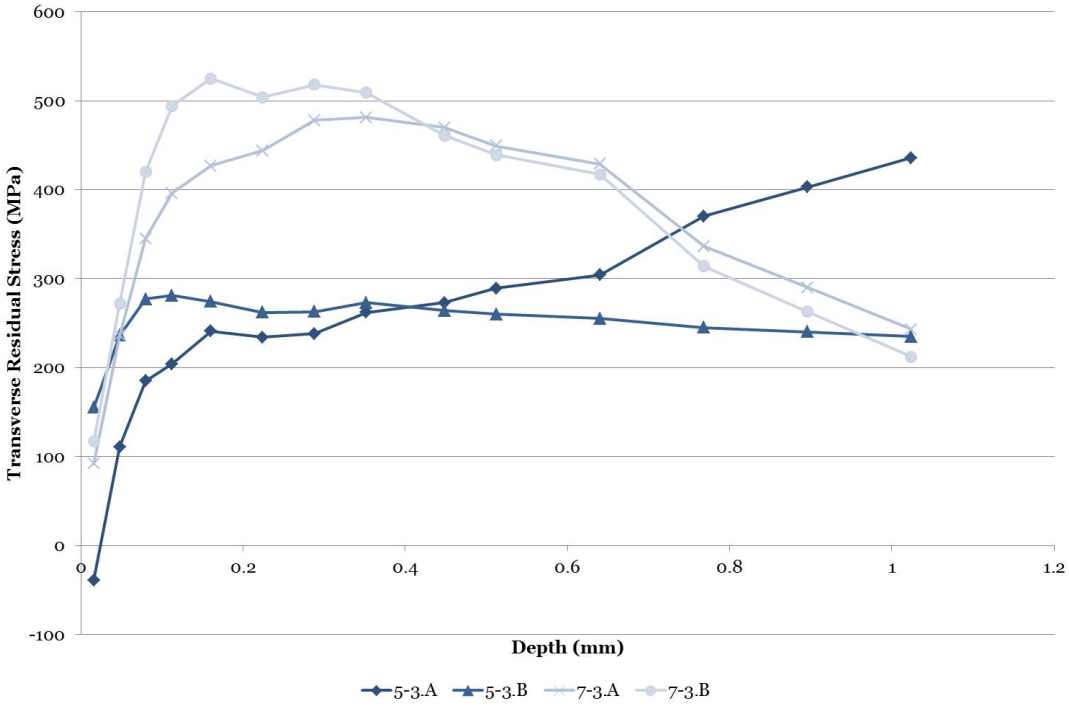

Figure 6.20: Measured transverse residual stresses: Strath05 & Strath07 - ICHD results allowing post-weld stress relief effects to be deduced for an Inconel 625 clad. Gauges A and B signify two measurements on clad components.

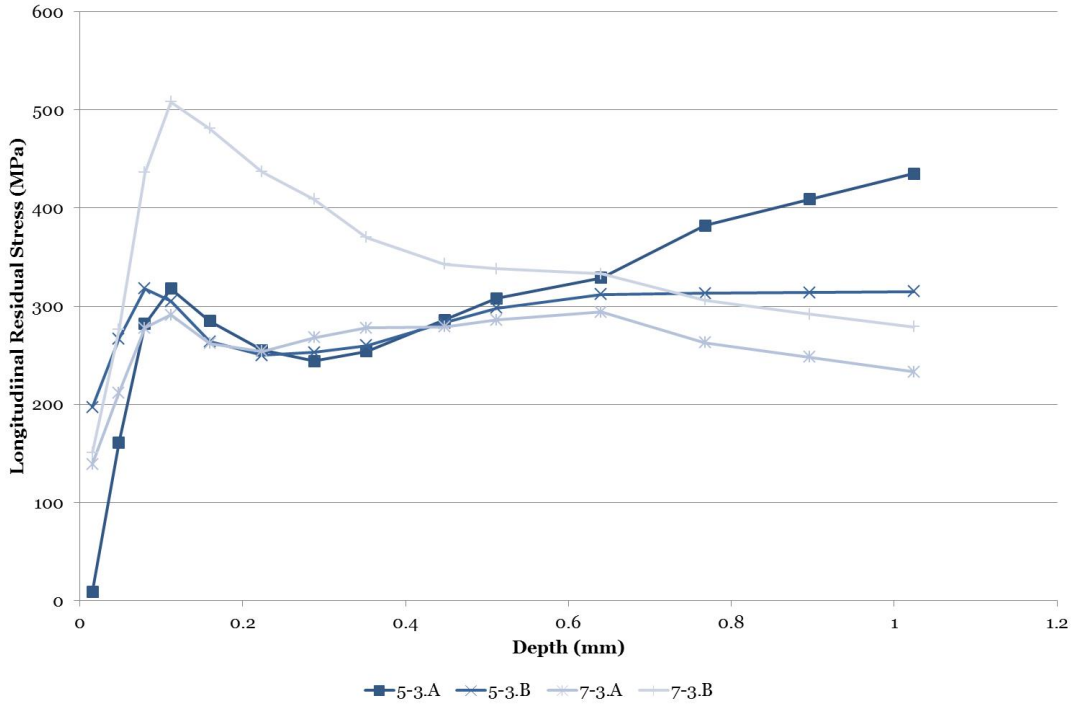

Figure 6.21: Measured longitudinal residual stresses: Strath05 & Strath07 - ICHD results allowing post-weld stress relief effects to be deduced for an Inconel 625 clad. Gauges A and B signify two measurements on clad components.

confirming that residual stresses are predominantly due to local effects as discussed previously. Gauge 1-xx3.B on the cylinder shows a large increase in the initial measurements, this is however thought to be a spurious result due to surface preparation or weld cladding process variability.

The effects of substrate pre-heat can be assessed through reference to figures 6.18 and 6.19. Again variations do arise in measurements, however it is difficult to assign these to the effects of pre-heat temperature, due to the variation in stresses in the initial increments. Towards the maximum depth measurements become more uniform and do not show proof of pre-heat temperature affecting residual stresses in the clad layer as such.

Stress relief is shown in figures 6.20 and 6.21 to have no effect on the level of residual stresses in an Inconel 625 clad. This is thought to be due to the material dissimilarity. *PWHT* will be further discussed in section 11.5.

It is therefore concluded that any effects due to pre-heat and post-heat on macro-level residual stresses is not significant in comparison with the variations inherent in the cladding process and measurement processes used. That is not to say however that pre-heat and post-heat will not have an affect on metallurgy, for example the production of chromium-rich areas as discussed in section 4.2.

In the case of a 17-4 PH clad, compressive residual stresses are observed, shown in

figures 6.22-6.27. This is in stark contrast therefore to the Inconel 625 clad. This is also in accordance with the results on the finite element modelling process and therefore it can be concluded that the nature of residual stresses due to the weld cladding processes has been accurately captured in both clad material cases.

Compressive residual stresses arising in the specimens weld clad with 17-4 PH are compressive at all depths at which measurements were obtained. Machining effects are apparent to a lesser depth of 80 μm. Residual stresses measured in the specimens weld clad with 17-4 PH are also more uniform in nature, with smaller stress gradients across the depth range once machining effects have subsided.

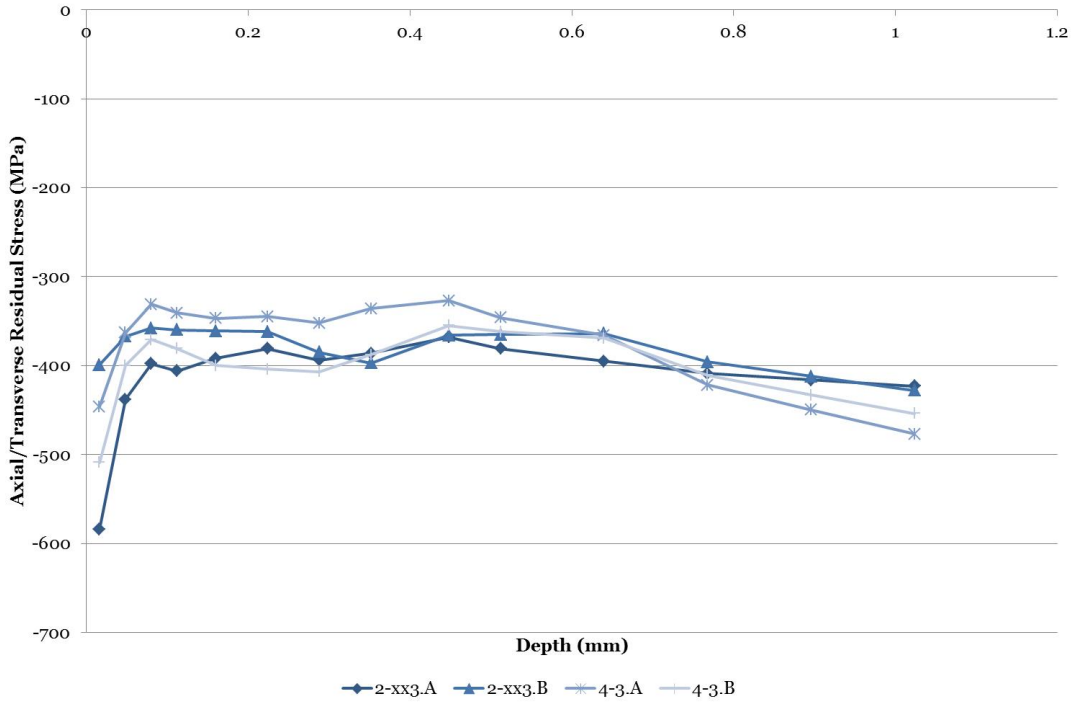

Figure 6.22: Measured axial/transverse residual stresses: Strath02 & Strath04 - ICHD results allowing substrate geometry effects to be deduced for a 17-4 PH clad. Gauges A and B signify two measurements on clad components.

In the case of the 17-4 PH clad residual stresses are larger at the maximum depth than at half the maximum depth, in contrast to the findings for an Inconel 625 clad. It should again be emphasised however that in contrast to these stress gradients in experimental measurements, the finite element models indicated uniform residual stresses throughout the clad layer due to the assumption of an idealised interface and not accounting for machining effects.

Referring to figures 6.22 and 6.23, the effects of substrate geometry are again negligible, more obviously so due to the tighter banding of results.

Figures 6.24 and 6.25 further prove that the pre-heat temperature applied to the substrate does not influence measured residual stresses.

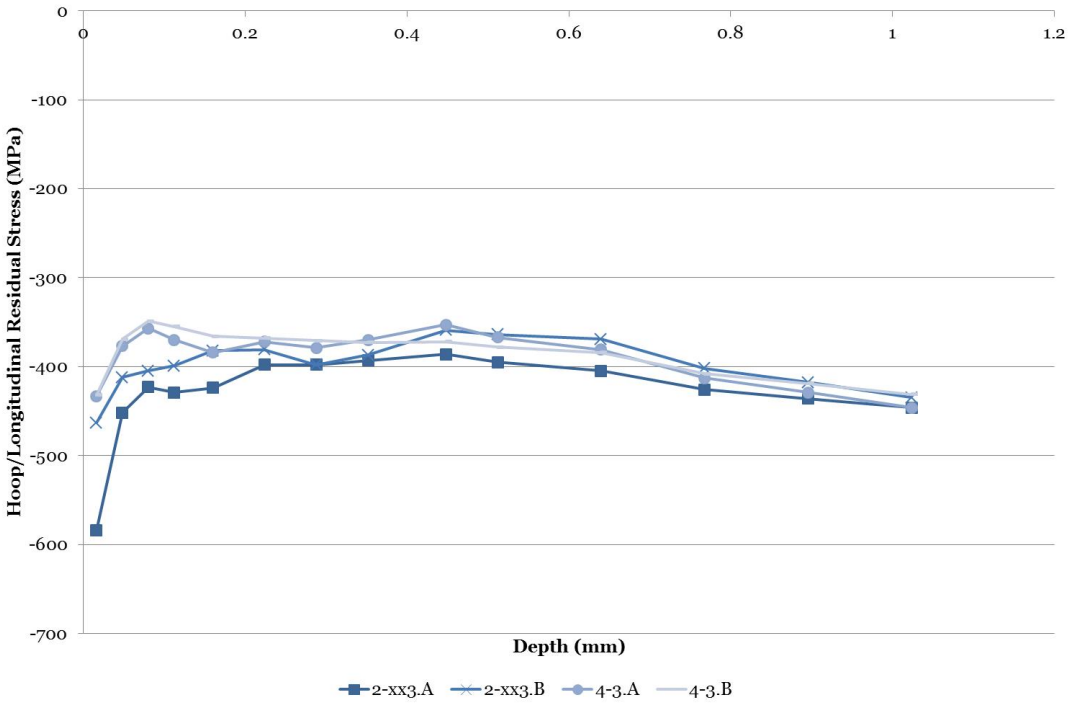

Figure 6.23: Measured hoop/longitudinal residual stresses: Strath02 & Strath04 - ICHD results allowing substrate geometry effects to be deduced for a 17-4 PH clad. Gauges A and B signify two measurements on clad components.

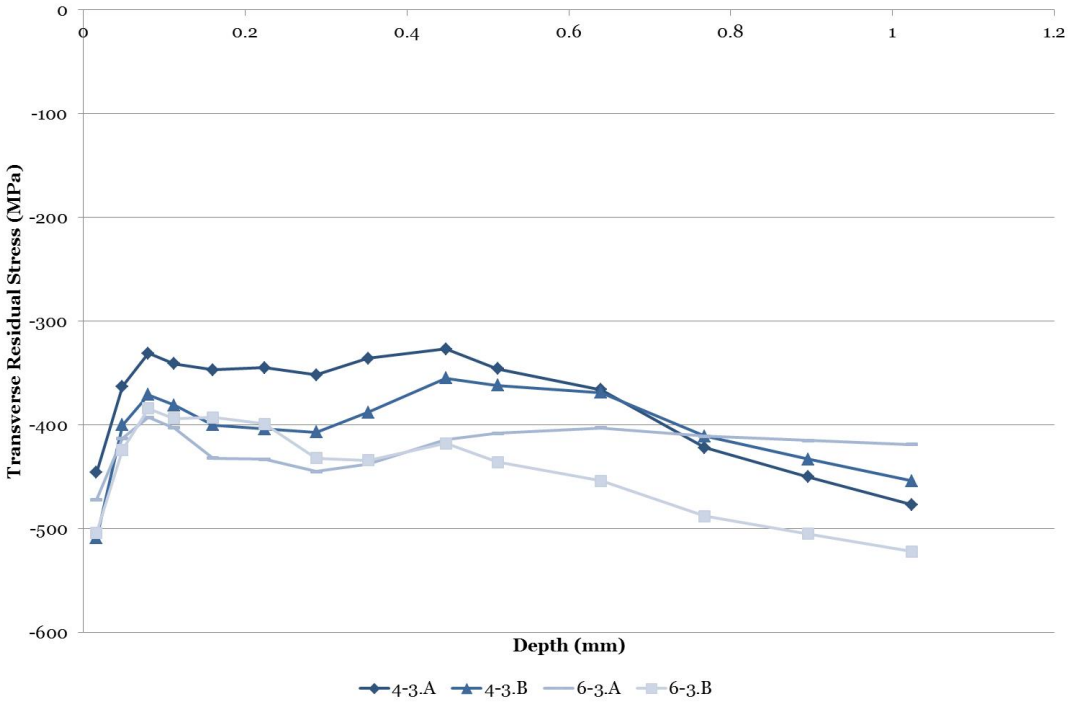

Figure 6.24: Measured transverse residual stresses: Strath04 & Strath06 - ICHD results allowing pre-heat temperature effects to be deduced for a 17-4 PH clad. Gauges A and B signify two measurements on clad components.

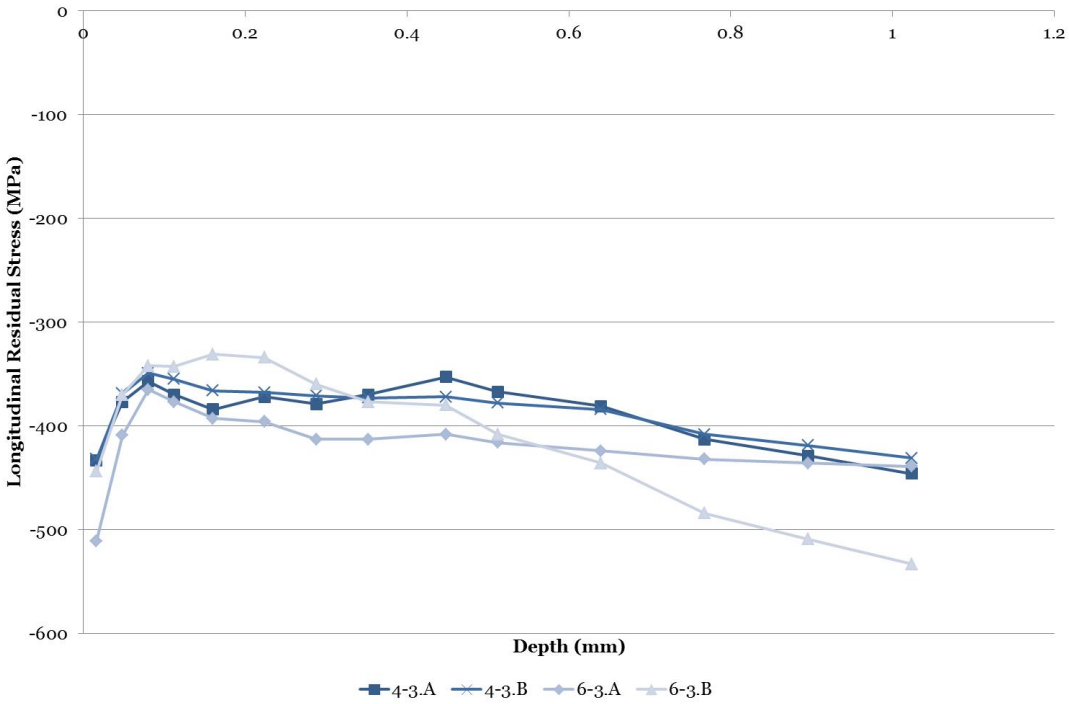

Figure 6.25: Measured longitudinal residual stresses: Strath04 & Strath06 - ICHD results allowing pre-heat temperature effects to be deduced for a 17-4 PH clad. Gauges A and B signify two measurements on clad components.

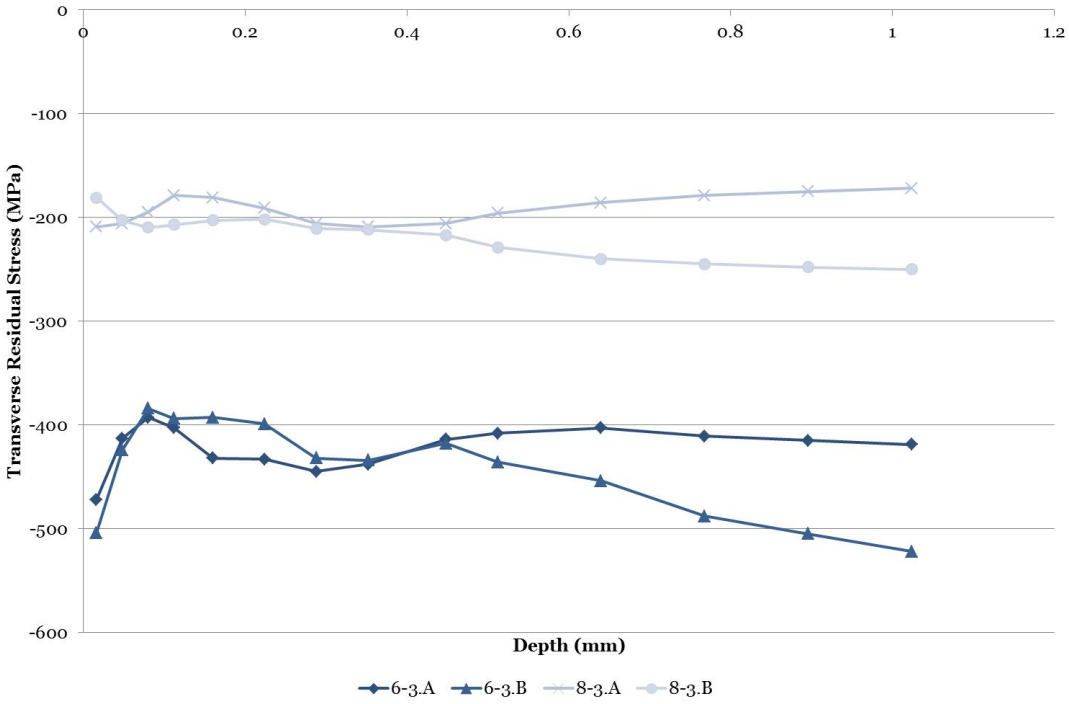

Figure 6.26: Measured transverse residual stresses: Strath06 & Strath08 - ICHD results allowing post-weld stress relief effects to be deduced for a 17-4 PH clad. Gauges A and B signify two measurements on clad components.

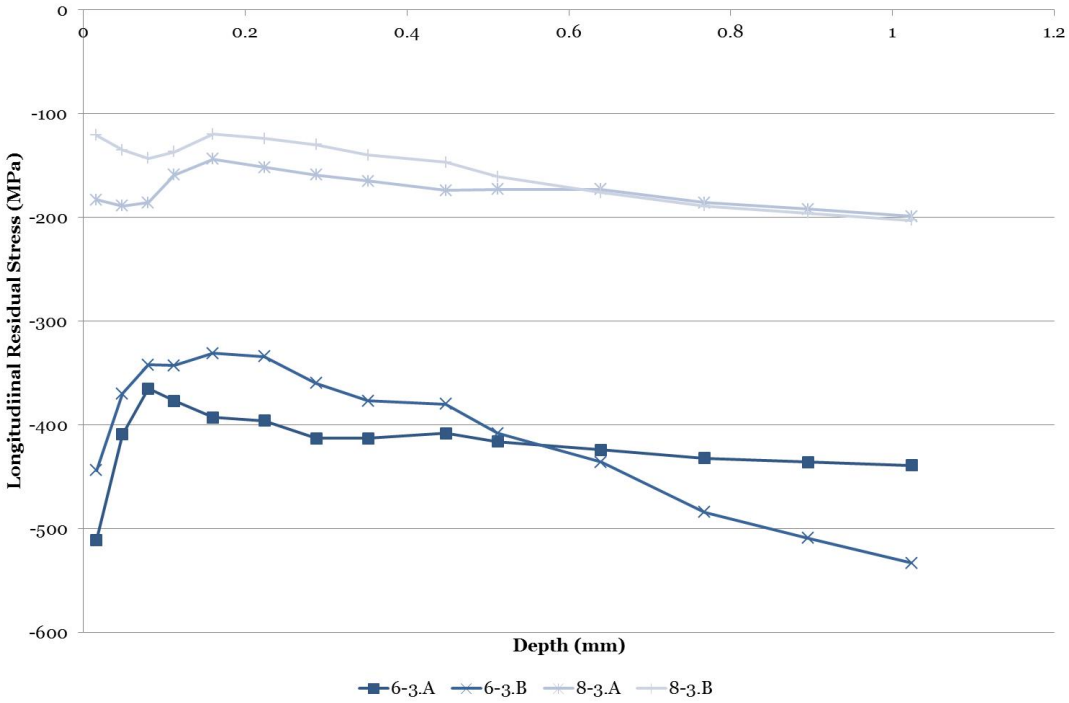

Figure 6.27: Measured longitudinal residual stresses: Strath06 & Strath08 - ICHD results allowing post-weld stress relief effects to be deduced for a 17-4 PH clad. Gauges A and B signify two measurements on clad components.

Stress relief is shown in figure 6.26 and 6.27 to be successful in a 4330 substrate clad with 17-4 PH, however. In this case the materials have a greater degree of similarity, both possessing a high yield strength and experiencing a martensitic transformation upon cooling.

Overall, the results of a 17-4 PH clad produced a tighter banding of results with a greater degree of uniformity with depth over the 1 mm depth for which results were obtained.

6.4.1 Depth of compressive residual stress

In the previous section, the presence of beneficial compressive residual stresses in a 17-4 PH weld clad layer was established. To determine the depth and magnitude of these residual stresses a wire *EDM* machining process was utilised to obtain slices from the specimen Strath06.

The block is shown sectioned in figure 6.28, with the longitudinal and transverse slices shown in figure 6.29.

Etching of the weld region was undertaken using acidic ferric chloride to reveal the weld passes, *HAZ*'s and substrate material as shown in figure 6.30.

Strain gauges were installed on these 4 mm obtained slices with the locations of these

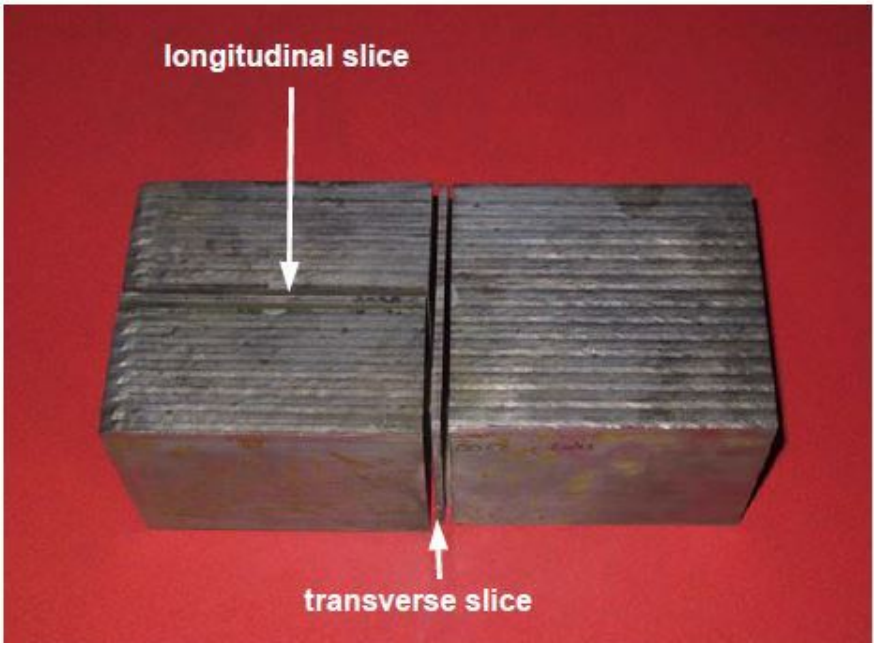

Figure 6.28: Slicing of Strath06 - Slices obtained from 4330 block weld clad with 17-4 PH to obtain longitudinal and transverse slices to determine depth of compressive residual stresses.

Figure 6.29: Longitudinal and transverse slices obtained from Strath06 - Slices obtained from 4330 block weld clad with 17-4 PH to determine depth of compressive residual stresses.

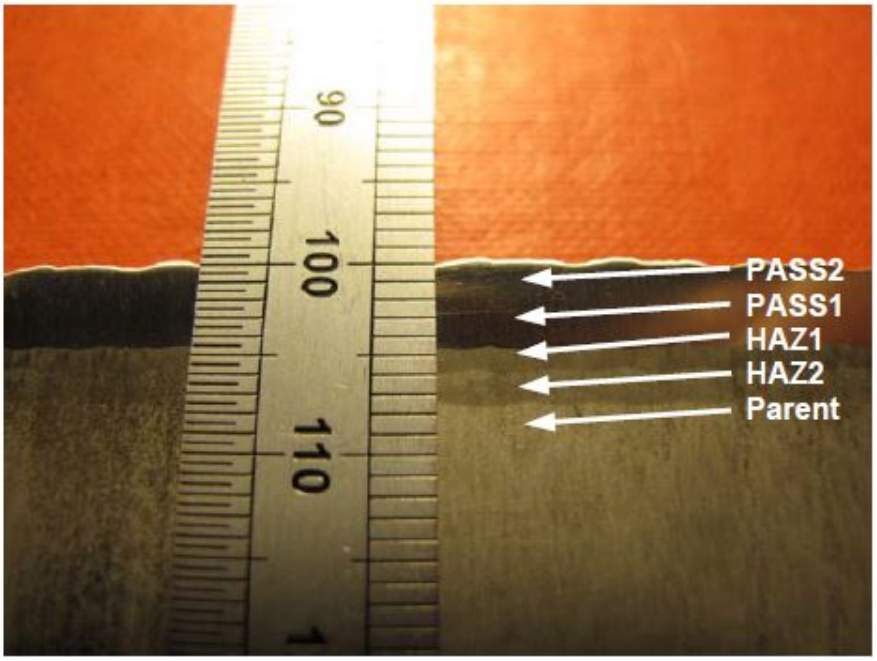

Figure 6.30: Etched Strath06 slice - Etching of slice allows weld features to be observed, with clad passes, HAZ's and parent material highlighted.

gauges detailed in table 6.7 and figures 6.31 and 6.32.

Measurements were obtained either side of the clad/substrate interface and into the parent material.

Gauges were installed such that element 1 of the strain gauge was aligned with the longitudinal direction and element 3 aligned with the vertical direction in the longitudinal slice (figure 6.33).

For the transverse slice, element 1 was aligned with the transverse direction and element 3 aligned with the vertical direction (figure 6.34). These orientations refer therefore also to the stresses σ_1 and σ_3.

Similarly, figure 6.35 shows the strain gauges installed in the locations in the parent material.

The residual stress measurements obtained will be influenced by the machining process and therefore the results obtained must be considered as including effects of stress relaxation in the direction normal to the cut with redistribution of the stresses in the slice plane. The partial relaxation of stresses due to slicing of a specimen has been highlighted in (199). Normal to the slicing plane, the stresses tend to zero. Prior to slicing the stresses in this direction are:

$$\sigma = \frac{E\epsilon}{1-\nu} \tag{6.19}$$

The in-plane stresses transform to a uni-axial state post-slicing:

Gauge No.	Slice	Region	Distance from interface (mm)	Distance from specimen centre (mm)
6-3.L.P1	Longitudinal	Pass 1	-0.7	32
6-3.L.H1	Longitudinal	HAZ 1	0.7	42
6-3.T.P1	Transverse	Pass 1	-0.7	6
6-3.T.H1	Transverse	HAZ 1	0.7	6
6-3.L.Par6	Longitudinal	Substrate	6	37
6-3.L.Par12	Longitudinal	Substrate	12	47

Table 6.7: Installation locations of gauges to determine residual stress distribution in Strath06

Figure 6.31: Strath06 longitudinal slice - Longitudinal slice obtained from 17-4 PH weld clad block shown with strain gauge rosettes installed either side of clad-substrate boundary.

Figure 6.32: Strath06 transverse slice - Transverse slice obtained from 17-4 PH weld clad block shown with strain gauge rosettes installed either side of clad-substrate boundary.

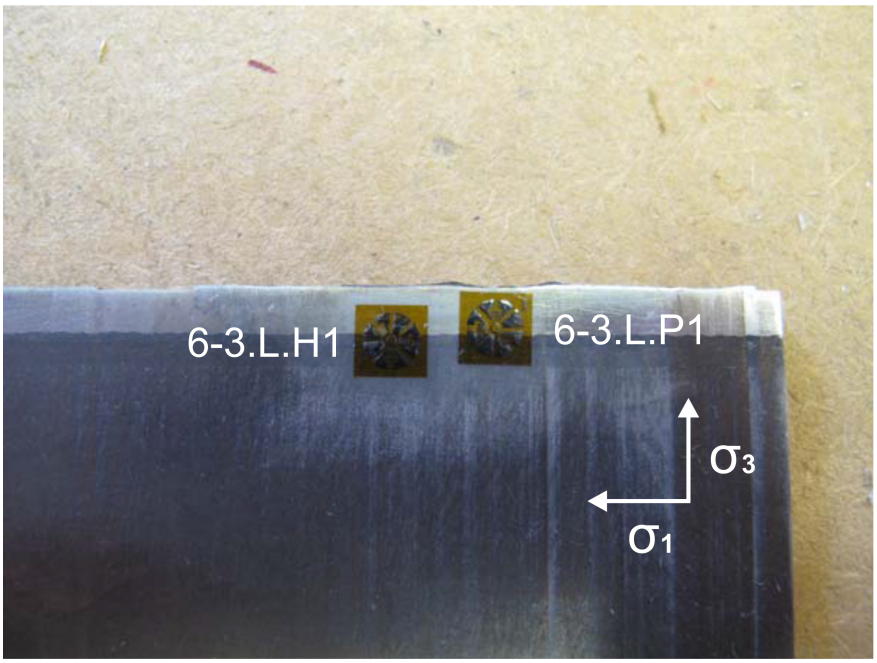

Figure 6.33: Installation of strain gauges on Strath06 longitudinal slice - Strain gauges installed either side of 17-4 PH clad/4330 substrate interface with stress orientations noted.

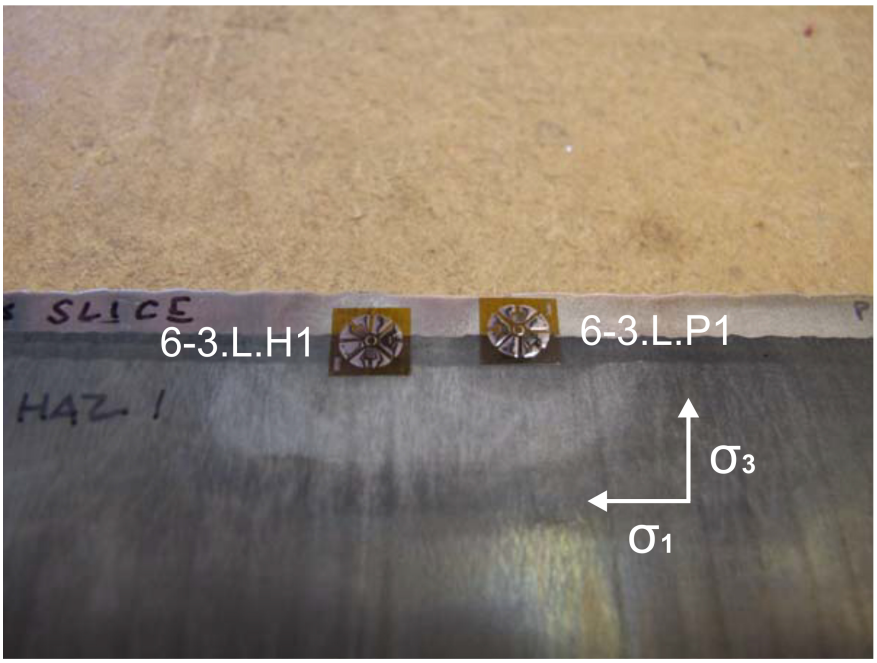

Figure 6.34: Installation of strain gauges on Strath06 transverse slice - Strain gauges installed either side of 17-4 PH clad/4330 substrate interface with stress orientations noted.

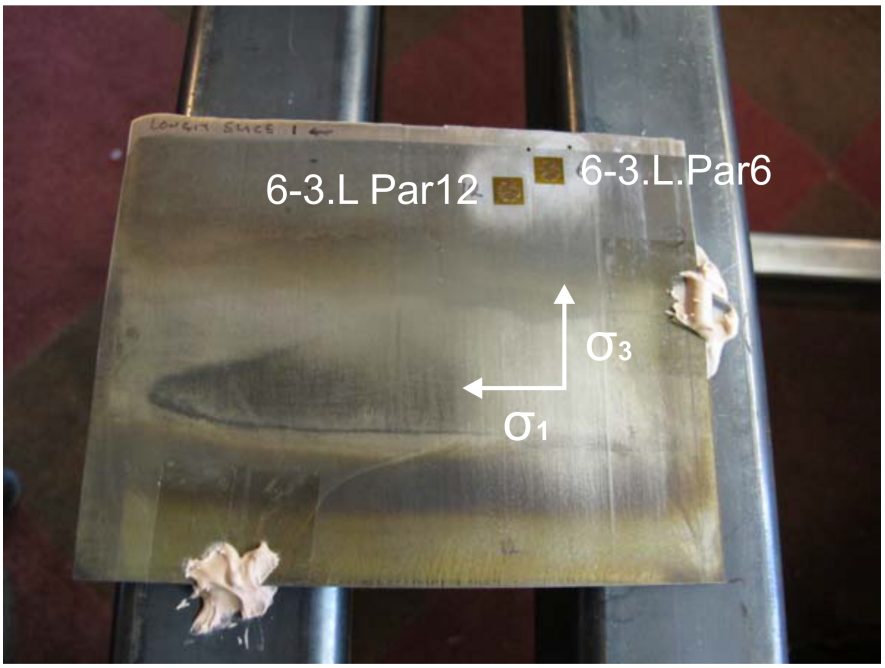

Figure 6.35: Installation of strain gauges in parent material of Strath06 longitudinal slice - Strain gauges installed in parent material with stress orientations noted.

$$\sigma = E\epsilon \tag{6.20}$$

The ratio of stresses of the unsliced and sliced components are therefore approximately:

$$1/(1-\nu) \tag{6.21}$$

To correct for the relaxation of stresses, a multiplication factor

$$1/(1-\nu) = 1.37 \tag{6.22}$$

has been applied to the longitudinal and transverse stresses to indicate the stresses present in the specimen prior to slicing. This factor results in an increase of 37% in the longitudinal and transverse stresses obtained through measurement.

To ensure fixing of the specimen, the slices were cemented to a drilling frame. Tungsten carbide cutters were used with an electric drill head with $2\mu m$ increments utilised to obtain the zero-depth location. Orbital drilling was then carried out to a final depth of 0.7 mm.

The Integral method was used to convert strain relaxation data into residual stresses due to the non-uniform nature of the residual stresses with smoothing applied to the data as appropriate. The results shown in figures 6.36 and 6.37 provide the direct stress components. It is clearly illustrated through the presence of stress gradients that stresses in the region of the cut surface have been influenced by the machining process utilised to obtain the slices. This is especially clear due to the tensile nature of these stresses and the knowledge that many machining processes induce tensile residual stresses. Therefore results should be considered at the depth of 512 μm as this is the maximum depth and the location furthest from the surface subjected to *EDM*. The vertical stress component σ_3 is affected by the relieving of stresses in the longitudinal and transverse directions due to the slicing process.

Through-thickness stress components i.e. σ_3 are largely tensile as shown in figure 6.36. This stress component, normal to the previous strain gauges, has not been previously measured as reported in previous sections.

Figure 6.37 however illustrates that compressive residual stresses exist in the clad layer and into the HAZ for the longitudinal stress component (gauges 6-3.L.P1, 6-3.T.P1, 6-3.L.H1 and 6-3.T.H1). At a depth of 6 mm from the interface, the longitudinal stress component is tensile (gauge 6-3.L.Par6), however at a depth of 12 mm from the interface this component has transformed to fluctuate between tensile and compressive with depth of drilling into the slice (gauge 6-3.L.Par12).

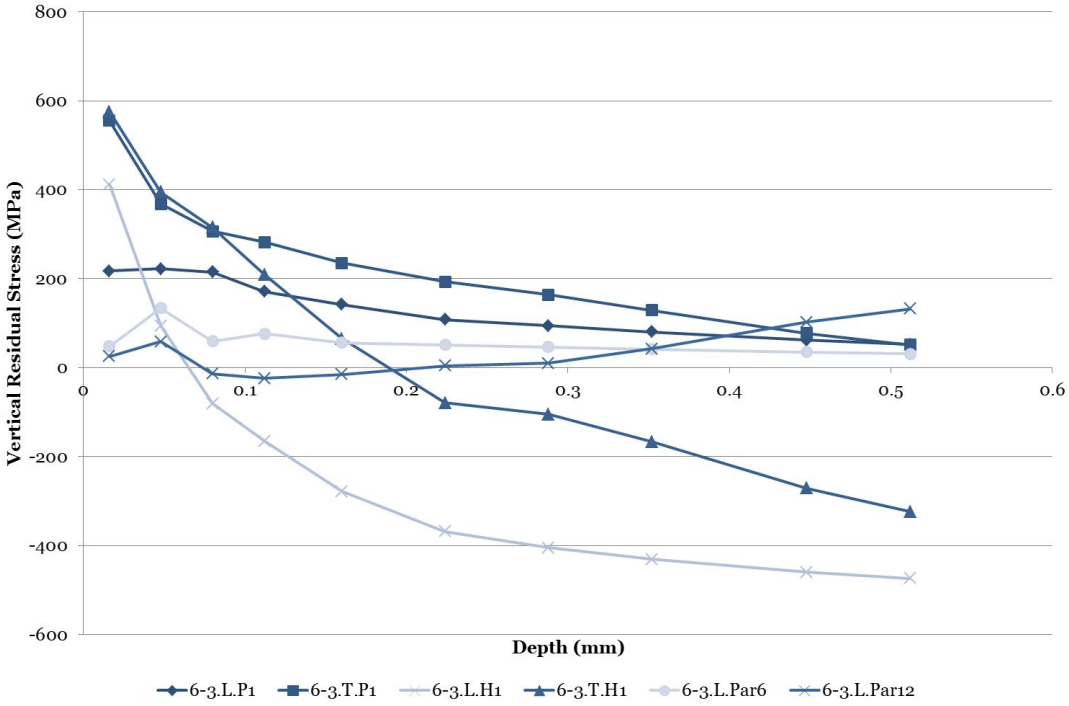

Figure 6.36: Measured vertical residual stresses: Strath06 longitudinal & transverse slices - ICHD results allowing depth of compressive residual stresses in 17-4 PH weld clad block to be deduced. Depth in axial or transverse block direction as appropriate.

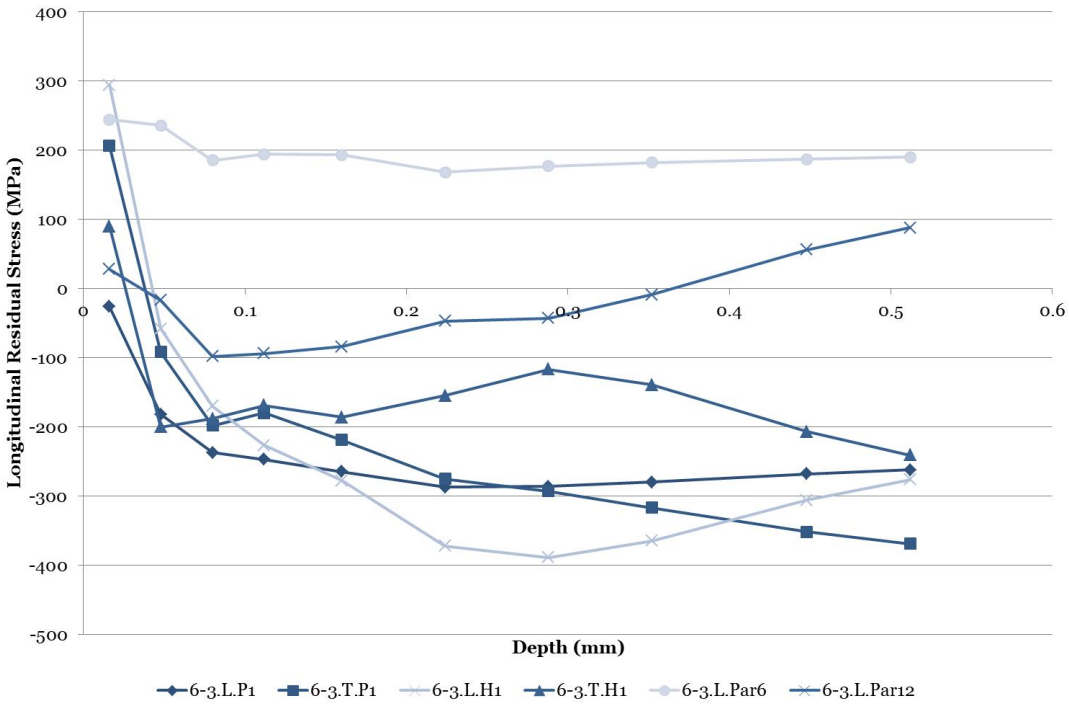

Figure 6.37: Measured longitudinal residual stresses: Strath06 longitudinal & transverse slices - ICHD results allowing depth of compressive residual stresses in 17-4 PH weld clad block to be deduced. Depth in axial or transverse block direction as appropriate.

Initial experimental residual stress measurements were limited to a depth of 1 mm and therefore further measurements as presented in this section were undertaken to examine the depth of compressive residual stresses in a 17-4 weld clad block. These measurements indicated that such beneficial stresses exist into the substrate of the weld clad block to certain depths depending on the stress component investigated and therefore also highlight that the sharp discontinuity stresses observed in the finite element model are in reality also not present.

6.4.2 Errors and uncertainties

As previously discussed, *ICHD* is highly sensitive to errors, whether related to the measurement procedure or the installation of the strain gauge. These are discussed in detail by Schajer and Altus (200):

- Strain measurement errors arising through strains induced during the machining of the surface to install the strain gauge or errors arising due to the instrumentation used to obtain strain readings.
- Hole depth measurement errors due to depth increments or any roundness at the bottom of the hole.
- Hole diameter errors including errors in measurement of the final hole diameter, tapering of the hole or deviation from roundness.
- Eccentricity of the location of the hole where the mean radius of the centre of the hole to each strain gauge differs.
- Material constant errors arising from incorrect Young's modulus and Poisson's ratio values utilised during the strain-stress conversion process.

Kandil et al. present an example of the considerations of all sources of error in the hole-drilling method to obtain an indication of the likely effects these factors have on the resulting uncertainty (4).

Factors contributing to stress uncertainty are also provided in (180). These account for factors attributed to the strain gauge, the strain indicator, specimen preparation and the drilling process. The errors associated with strain measurement are noted as being the greatest sources of uncertainty.

In considering the random strain uncertainty, a value of $\pm 3\mu\epsilon$ is applied to the strain data. This produces uncertainties in the stress components σ_1 and σ_3 as detailed in table 6.8. The largest stress uncertainty is present at the surface due to the effects of surface preparation. An increase in stress uncertainty occurs towards the maximum depth due to decreasing accuracy due to travelling further from the strain gauge. Between these locations stress uncertainties vary linearly, producing the distribution of stress uncertainties shown in figure 6.38. To account for additional sources of error an additional fixed uncertainty of $\pm 7\%$ is estimated.

Smoothing of the strain data obtained can be achieved using the Tikhonov regularisation. This technique uses the principle of standard error estimation, although the smoothing of the obtained strain data can be manually altered. However, this must be carried out appropriately such that the residual stress distribution is not falsely

Depth (μm)	Stress uncertainty (MPa)
16-112	$\pm$60
512	$\pm$11
1024	$\pm$24

Table 6.8: Uncertainties in stress values with depth due to random strain uncertainty

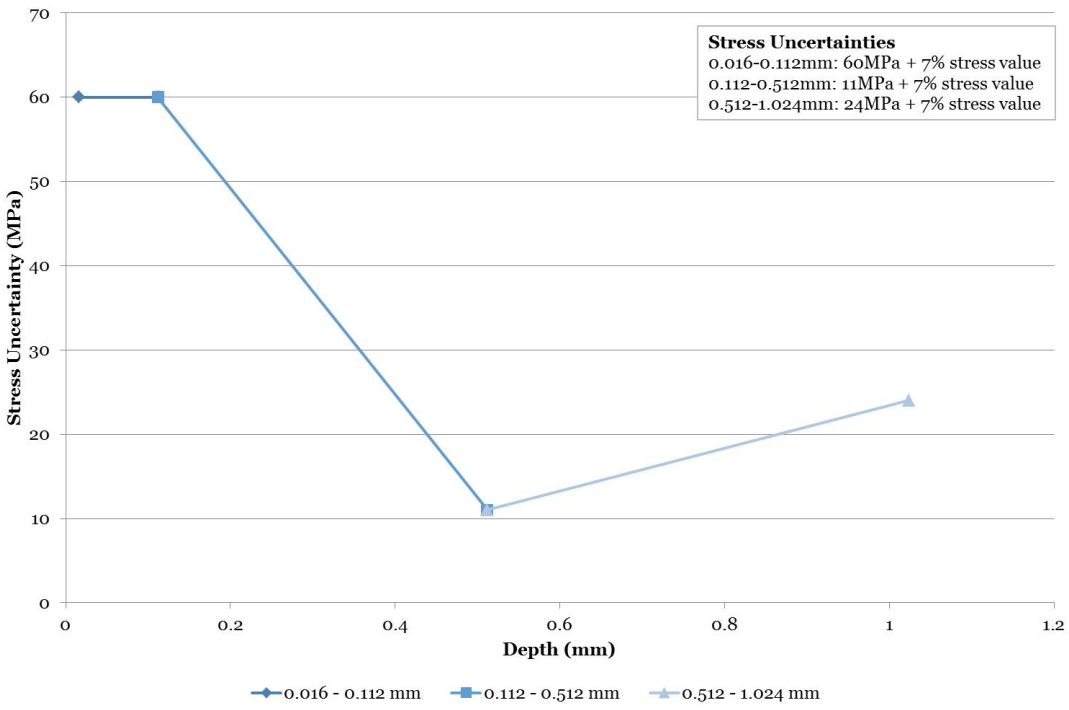

Figure 6.38: Total stress uncertainty with depth for ICHD - Illustrating total stress uncertainty due to errors arising during the ICHD process.

obtained. In the case of extreme variations in strain data, additional consideration must be given to appropriately account for these variations. This was however not the case in these measurements.

6.5 Comparing residual stresses obtained experimentally and through simulation

The finite element axisymmetric models presented in the previous chapter provided predictions for the residual stresses resulting in the ability to capture the residual stress resulting from the weld cladding process. Table 5.1 presented in the previous chapter highlighted the values of axial and hoop stress present at the clad surface in the axisymmetric one-pass model. Figures 6.39-6.46 present comparisons of axial and hoop stresses in Inconel 625 and 17-4 PH weld clad components.

Comparing the experimental results in figures 6.39-6.42 illustrates that the finite element model of an Inconel 625 clad on 4330 steel provides good correlation with experimental residual stress measurements using *ICHD*.

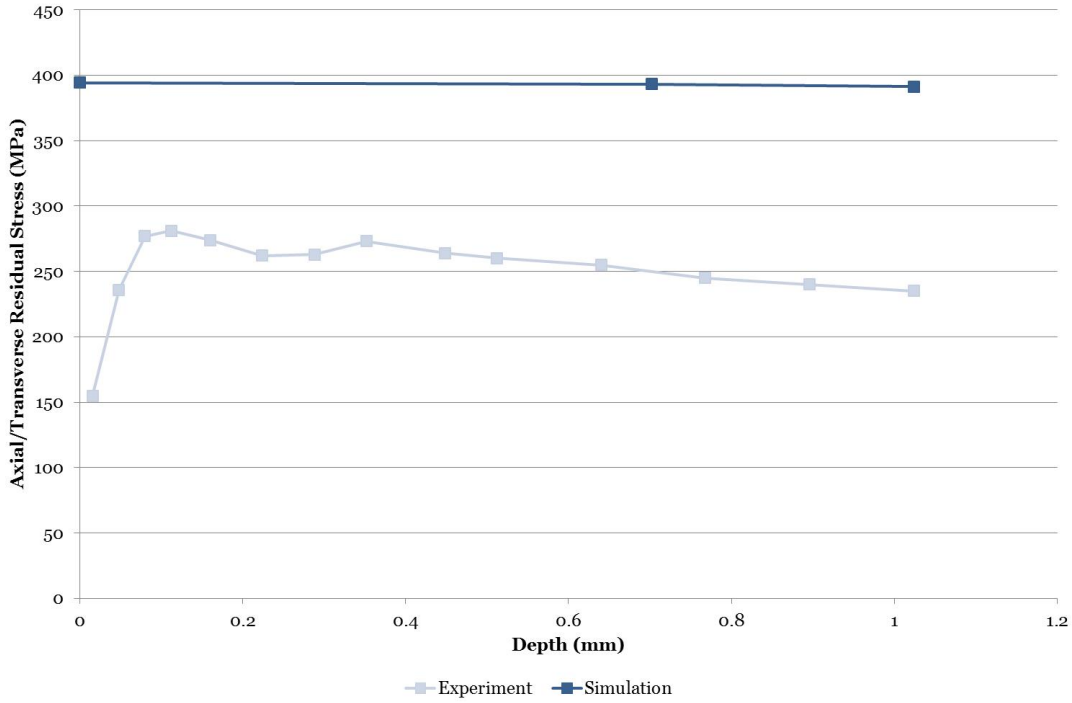

Figure 6.39: Experimental and simulation axial stress comparison for an Inconel 625 weld clad and pre-heat temperature of 150°C - Experimental measurements obtained using ICHD. Simulation results obtained from a one-pass axisymmetric model.

Correlation is particularly good in the case of a 300°C pre-heat temperature as shown in figures 6.41 and 6.42. These measurements show tensile residual stresses in the region of 400 MPa of equi-biaxial nature in the nickel alloy clad layer, with these

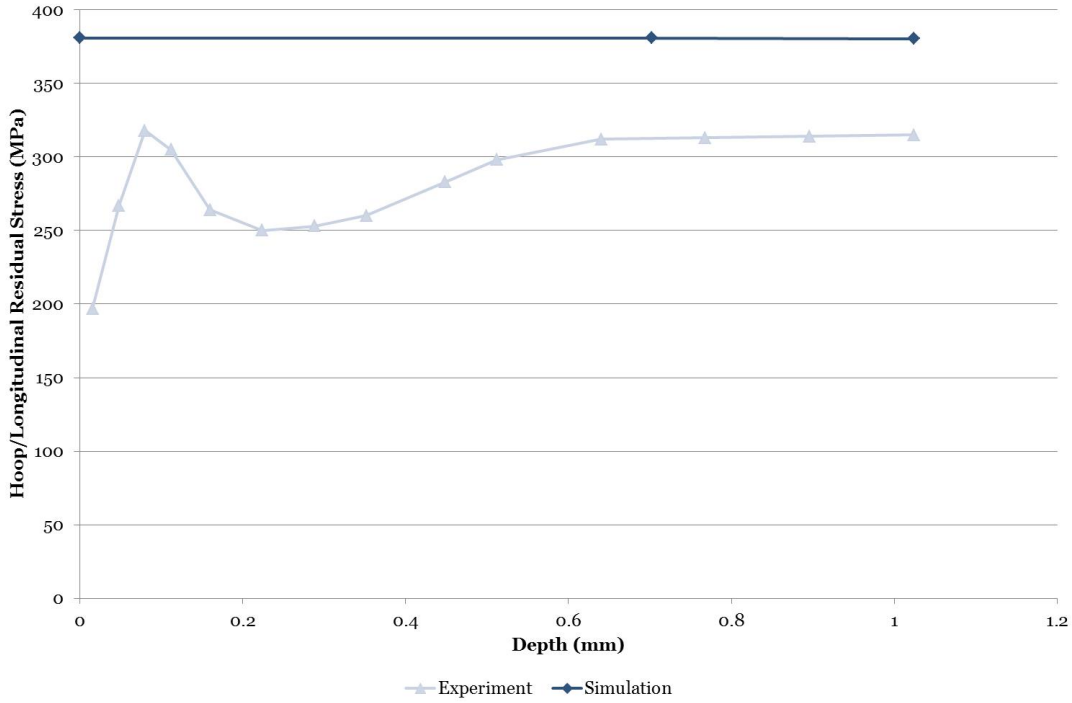

Figure 6.40: Experimental and simulation hoop stress comparison for an Inconel 625 weld clad and pre-heat temperature of 150°C - Experimental measurements obtained using ICHD. Simulation results obtained from a one-pass axisymmetric model.

stresses self-equilibrating, producing compressive residual stresses in the substrate of the finite element model.

Using the same substrate material and a 17-4 PH clad material provided high compressive residual stresses in the clad layer as also indicated in simulation and experimental residual stresses in figures 6.43-6.46. Experimental measurements using *ICHD*, however, indicated much lower compressive residual stresses in the region of 400-500 MPa throughout the clad layer, while stresses obtained in the finite element model are in the region of 1000 MPa.

This poor correlation, thought to be due to inadequate characterisation of the material behaviour of the 17-4 PH material, suggests that further investigation into the effect of material and metallurgical properties on residual stress distribution is critical. Examining the results obtained in the case of a two-pass planar model accounting for the deposition of weld beads in table 6.10 suggests that the modelling process can be used to influence the obtained residual stress distribution. Hoop stresses in this model are significantly lower than in the one-pass axisymmetric model shown in table 6.9. In a model accounting for two passes and weld beads hoop stresses are in the region of 800 and 700 MPa for pre-heat temperatures of 150°C and 300°C respectively compared with 1000 MPa in a one-pass model. The modelling process utilised in this case was presented in section 5.4. This indicates that a combination of improved char-

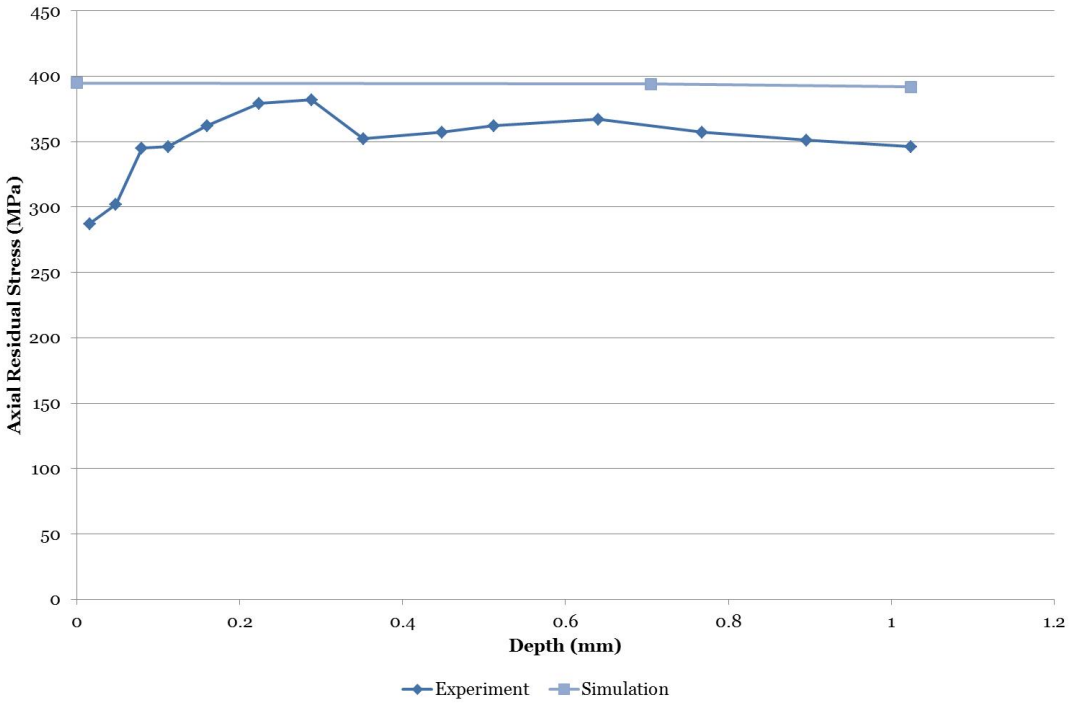

Figure 6.41: Experimental and simulation axial stress comparison for an Inconel 625 weld clad and pre-heat temperature of 300°C - Experimental measurements obtained using ICHD. Simulation results obtained from a one-pass axisymmetric model.

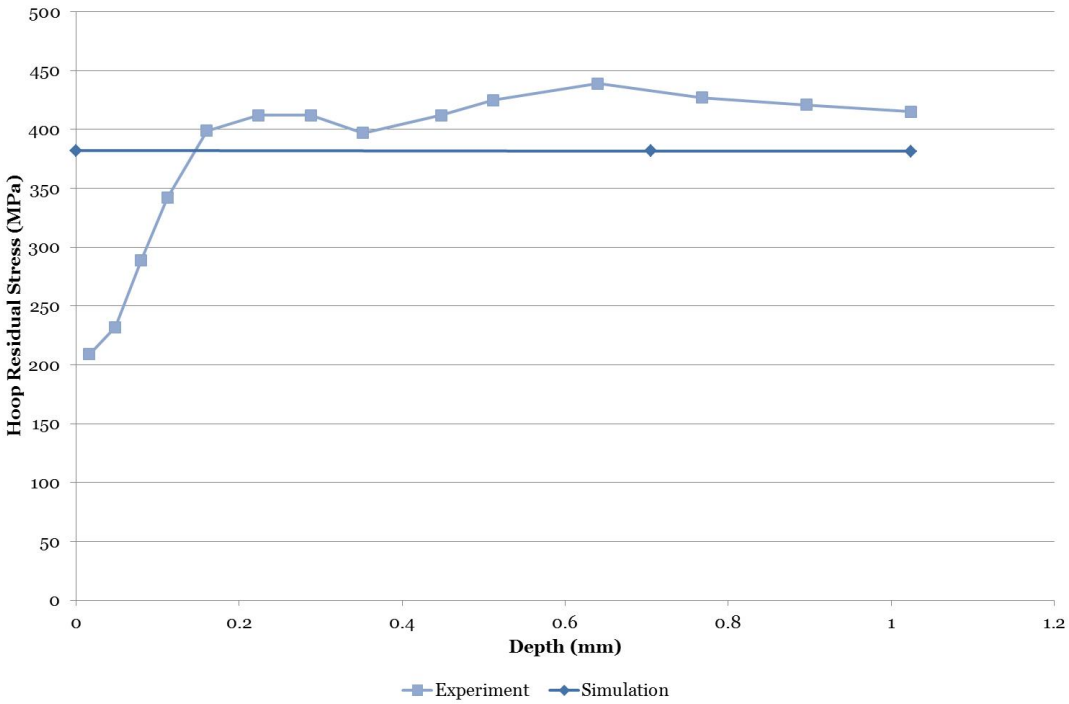

Figure 6.42: Experimental and simulation hoop stress comparison for an Inconel 625 weld clad and pre-heat temperature of 300°C - Experimental measurements obtained using ICHD. Simulation results obtained from a one-pass axisymmetric model.

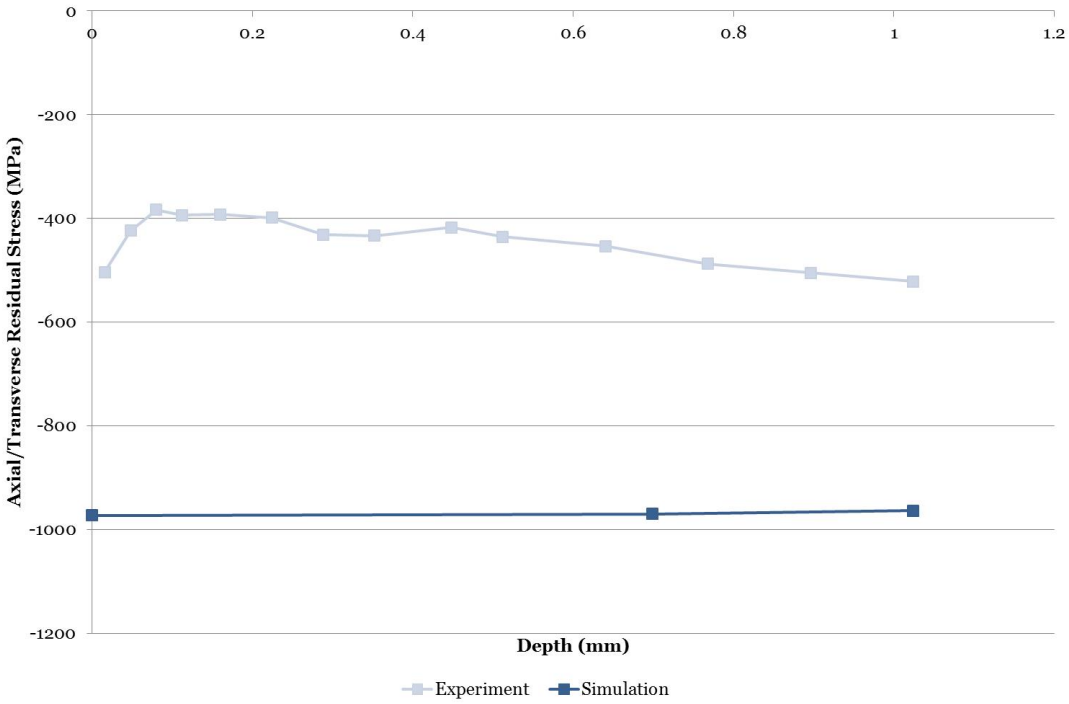

Figure 6.43: Experimental and simulation axial stress comparison for a 17-4 PH weld clad and pre-heat temperature of 150°C - Experimental measurements obtained using ICHD. Simulation results obtained from a one-pass axisymmetric model.

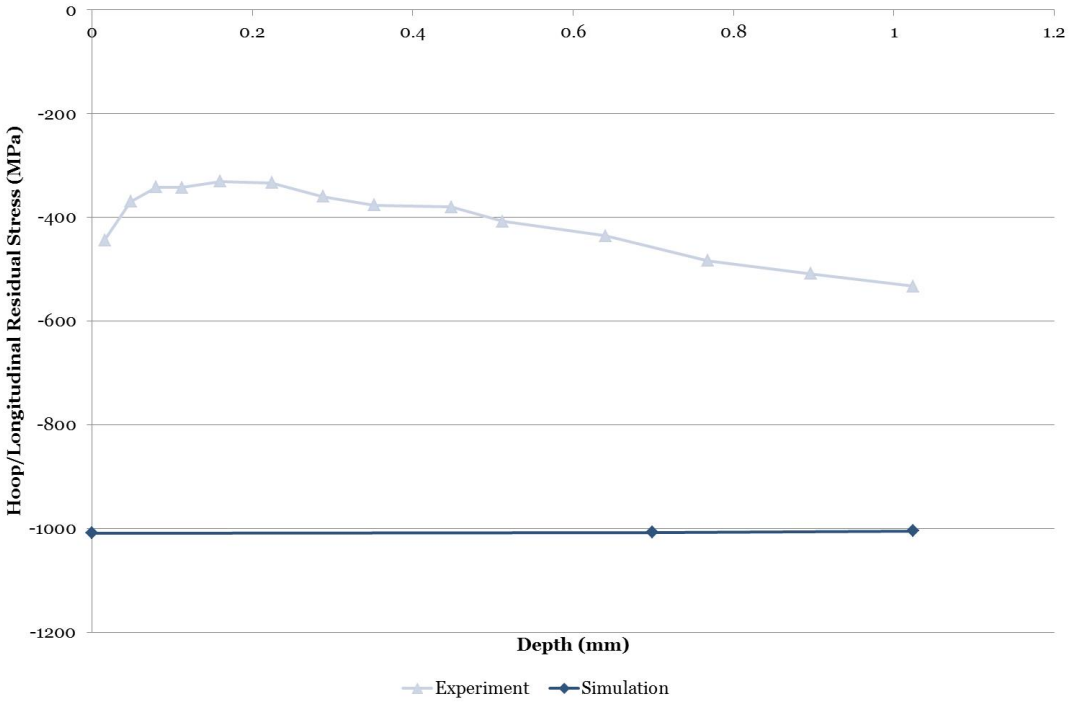

Figure 6.44: Experimental and simulation hoop stress comparison for a 17-4 PH weld clad and pre-heat temperature of 150°C - Experimental measurements obtained using ICHD. Simulation results obtained from a one-pass axisymmetric model.

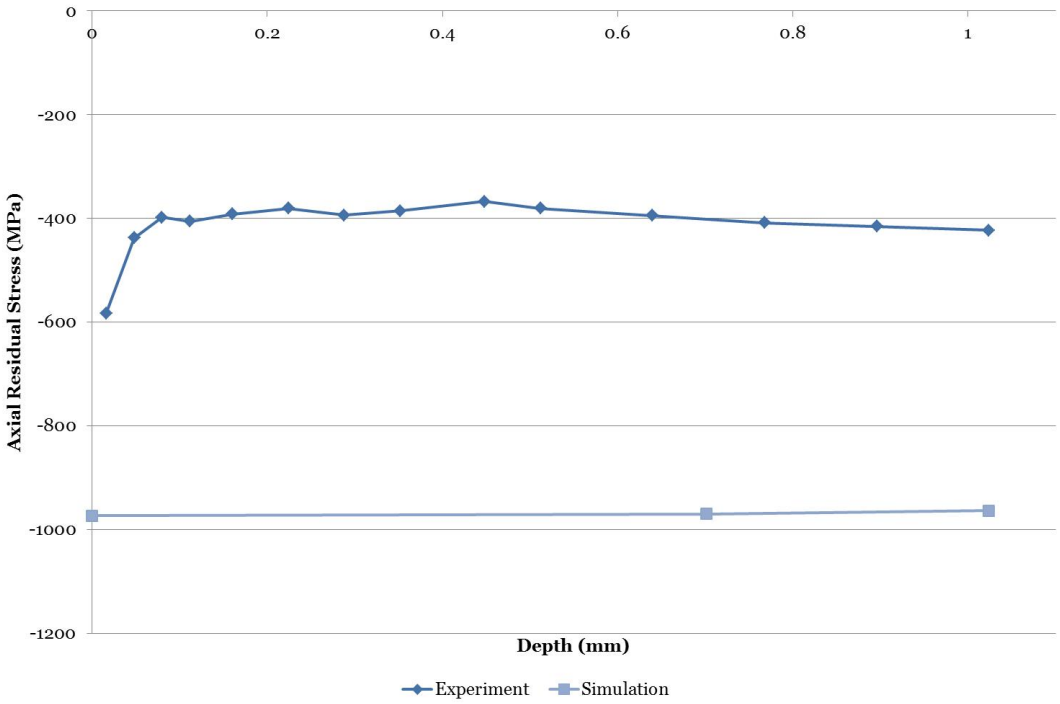

Figure 6.45: Experimental and simulation axial stress comparison for a 17-4 PH weld clad and pre-heat temperature of 300°C - Experimental measurements obtained using ICHD. Simulation results obtained from a one-pass axisymmetric model.

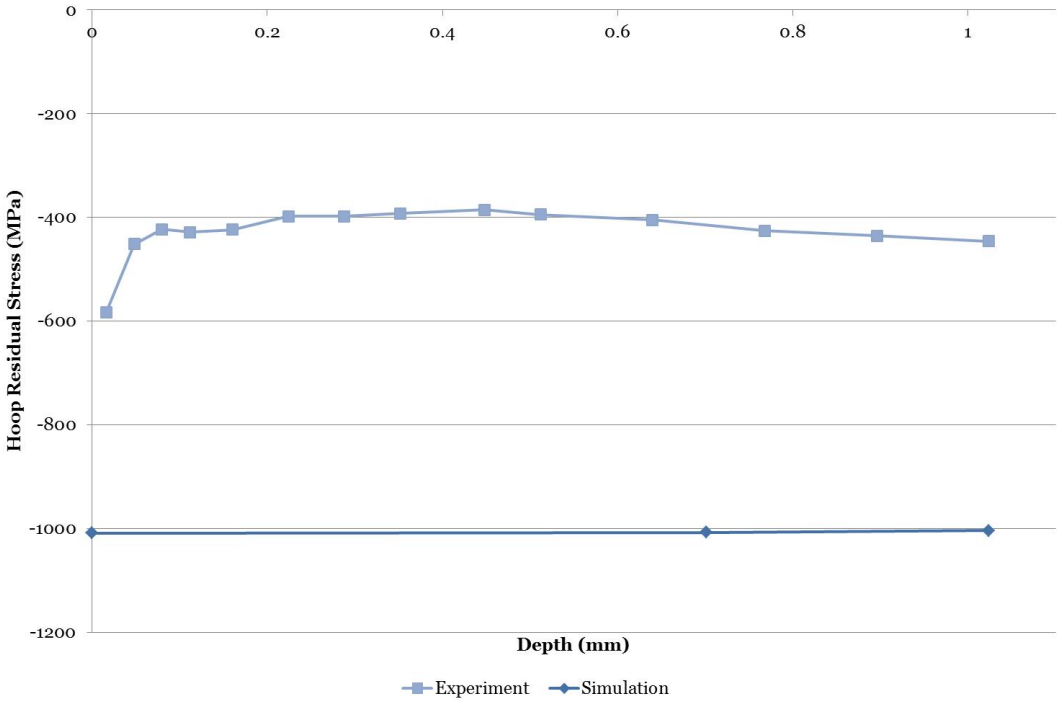

Figure 6.46: Experimental and simulation hoop stress comparison for a 17-4 PH weld clad and pre-heat temperature of 300°C - Experimental measurements obtained using ICHD. Simulation results obtained from a one-pass axisymmetric model.

acterisation of material behaviour and development of the modelling process would enable further improvement in correlation between experiment and simulation.

$T_{PH}(^{\circ}C)$	$\sigma_{Axial}(MPa)$	$\sigma_{Hoop}(MPa)$
150	-972.94	-1009.34
300	-973.47	-1008.85

Table 6.9: Axial and hoop stress components at 17-4 clad surface in a one-pass model

$T_{PH}(^{\circ}C)$	$\sigma_{Axial}(MPa)$	$\sigma_{Hoop}(MPa)$
150	-1100.06	-796.62
300	-1126.94	-689.85

Table 6.10: Axial and hoop stress components at 17-4 clad surface in a two-pass & beads planar model

Simplified weld cladding simulations have however successfully illustrated the development and distribution of residual stresses and the study has highlighted the influence of material property variation with temperature in a simple externally clad thick-walled cylinder. The significance of material behaviour will be discussed in chapter 7, with an emphasis on phase transformations in particular affecting the residual stress state. For one material pairing, that is 4330 and Inconel 625, the correlation between simulation and experiment is seen to be good, with the exception of variations due to machining effects becoming apparent close to the surface, where the weld clad profile has been removed to allow the application of the residual stress strain gauge. For the other pairing of 4330 and 17-4 PH agreement is poor and reasons for this will be discussed.

Extensions to the modelling process, including a full 3D representation of the process accounting for both temporal and spatial deposition of the clad material was shown in the previous chapter to have limited effect on the resulting residual stresses. It is therefore regarded as more beneficial to further investigate obtaining more extensive material properties to support the use of of an algorithm that can accurately predict the extent of martensitic transformation, which in turn is dependent upon accurate cooling rate prediction throughout the model mapped to rate appropriate material phase change data. This is favoured over the development of the modelling process. Discontinuity stresses at the interface between the dissimilar materials may cause fatigue cracking to occur sub-surface and therefore this is also an area of primary concern due to potential failure of a cladding or coating at the interface, the location at which high discontinuity stresses are present.

Numerous studies have shown that often, there is a transition from high tensile residual stresses in the clad layer or coating to compressive residual stresses in the sub-

strate. Gripenberg et al. (88) have investigated this with respect to various residual stress measurement techniques on clad steel and have found that although the magnitude and transition may vary, the overall nature of tensile to compressive transformation can be identified using the measurement techniques of neutron diffraction, ring-core and deep-hole measurements. This study also highlights the difficulties in simulating residual stress distribution mainly due to the inability to easily capture the change in material properties as mentioned previously.

6.6 Summary

It is important, although not usually possible, to ensure that the residual stress state is not altered by surface preparation techniques used to allow installation of the strain gauge rosette. The *ICHD* method is highly sensitive and therefore errors can heavily influence strain readings and in turn residual stress values. The main sources of these errors have been described as being user technique, instrumentation errors, tapering of the hole or hole roundness and material constant errors applied in the conversion process.

The residual stress measurements presented in this chapter, to a depth of 1 mm from the prepared surface, illustrate high biaxial tensile residual stresses in the case of a 4330 substrate weld clad with Inconel 625. High biaxial compressive residual stresses are obtained in a 4330 substrate and 17-4 PH weld clad combination. It is therefore concluded that through selection of specific combinations of clad and substrate materials, residual stress states in the clad layer can be influenced. *PWSR* was shown to be successful in the case of a 17-4 PH clad, however this would be unnecessary from a fatigue point of view, the aim being to maximise compressive residual stresses. The erosion and corrosion characteristics of the clad material should also be considered in selecting the clad and substrate material combination.

Variations in the results for two diametrically opposed positions at the centre of the cylindrical specimen indicate process variability effects, while reductions in measurements over the first 200 μm or so are largely due to machining of weld profile to provide a flat surface for strain gauging.

Compressive residual stresses have been shown to be present below the clad layer into the *HAZ* in the case of a 17-4 PH clad.

Good agreement was obtained, particularly in the case of an Inconel 625 clad, between residual stress distributions obtained experimentally and through the finite element method using a simplified axisymmetric simulation. The complex nature of the material behaviour of 17-4 PH is regarded as the cause of the lesser degree of correlation between experiment and simulation. It was highlighted in the previous

chapter that utilising published data which does not account for the martensitic transformation upon cooling resulted in tensile residual stresses in the clad layer. When experimentally obtained data which reflected the effects of the martensitic transformation in the material properties to some extent was input, these residual stresses in the clad layer were transformed into compressive residual stresses. The model however still did not include the effect of variations in cooling rate throughout the model and hence the extent of the martensitic transformation. This emphasises the need for accurate material properties, however this would require significant further testing to characterise the effect of cooling rate on the martensitic transformation. Including this in the finite element model would also require an extension to the current solution through use of the *UMAT* subroutine in Abaqus or similar. The key aspect in this testing would be to capture accurate cooling rates, as it has been shown that *CTE* values and the form of the *CTE* curve are strongly dependent on the cooling rate at which testing is undertaken.

Similar results for rectangular blocks indicate a geometry independent equi-biaxial residual stress distribution therefore it has been shown that substrate geometry does not affect the resulting residual stress in the weld clad layer. This indicates that the local spatial and temporal variation of the weld cladding process is the dominant factor is the generation of residual stresses in this case.

Chapter 7

Microstructural Effects on Residual Stresses

Residual stresses obtained through simulation of the weld cladding process for an Inconel 625 clad provided good correlation with experimentally obtained residual stresses. In the case of the 17-4 PH clad material, there was some discrepancy between results, thought to be due to the complexity of the behaviour of the martensitic, precipitation hardening stainless steel. In this chapter microstructural effects on residual stresses are investigated, concentrating primarily on martensitic steels. The cooling rate and microstructural effects of 17-4 PH are discussed. Methods of modelling such factors in the simulation model are described. An investigation into varying material properties reveals that the residual stresses generated in the 17-4 PH clad layer are highly sensitive to variations in CTE. Through manipulation of the experimentally obtained data for CTE, residual stresses in the simulation model are obtained such that good correlation results with the residual stresses obtained through ICHD. The relationship between material properties and microstructure presented illustrates that upon utilising a certain chemical composition, the arising phases and material properties must be considered regarding their effects on residual stresses. Methods of deducing material properties using known relationships are discussed for yield and tensile strength and hardness. The contributing strain components are introduced prior to an investigation into the influence of strain hardening on resulting residual stresses. The variation in CTE has proven to significantly influence residual stresses in the 17-4 PH clad material.

7.1 Introduction

In the case of dissimilar joining processes using high heat input, it is clear that depending on the materials and the nature of the join, the residual stresses will vary. The heat input will give rise to varying temperature gradients throughout the join and throughout the process. Finally the differences in present phases also contribute to the residual stress development as has been shown in X70 pipeline steel for example (201).

As has been highlighted in previous chapters, the material properties of the clad and substrate materials greatly influence the residual stresses arising. The materials properties of steels are in turn controllable through the composition of the material and any particular processes in obtaining the end component, for example the cladding process and consequent heat treatments. The phases arising are governed by these factors and it will be the martensitic phase which will be focussed on, primarily in the 17-4 PH stainless steel material. It is common to utilise metallurgical changes involving phase changes to control the residual stress state, with a region of compression being the aim (58).

7.2 Residual stresses in martensitic steels

Upon cooling, austenite transforms into martensite and bainite, associated with dilatational strain, the proportions of which are determined by the amount of time prior to reaching ambient temperature i.e. the cooling rate. The formation of martensite is encouraged by quenching processes, the nature of which arises through the rapid cooling during the weld cladding process. A martensitic microstructure is said to result if the material experiences cooling from the austenitic condition to below the martensite start temperature within less than 10 seconds (158). If this does not occur at this rate then a mixture of martensite and bainite results. An example of the phase transformations experienced in steel during an arbitrary thermal cycle are shown in figure 7.1. The martensite formation at the end of the thermal cycle shows the potential for a mixture of phases present. This diagram does not capture the cooling rate, a contributing factor in the final microstructure due to the varying microstructure depending on the cooling rate, for example the fraction of phases present and the extent of martensitic transformation.

The martensitic transformation, also known as displacive or shear, causes the atomic pattern in the crystal structure to change to that of martensite, in turn altering the macroscopic shape of the crystal (202). The martensitic transformation is a diffu-

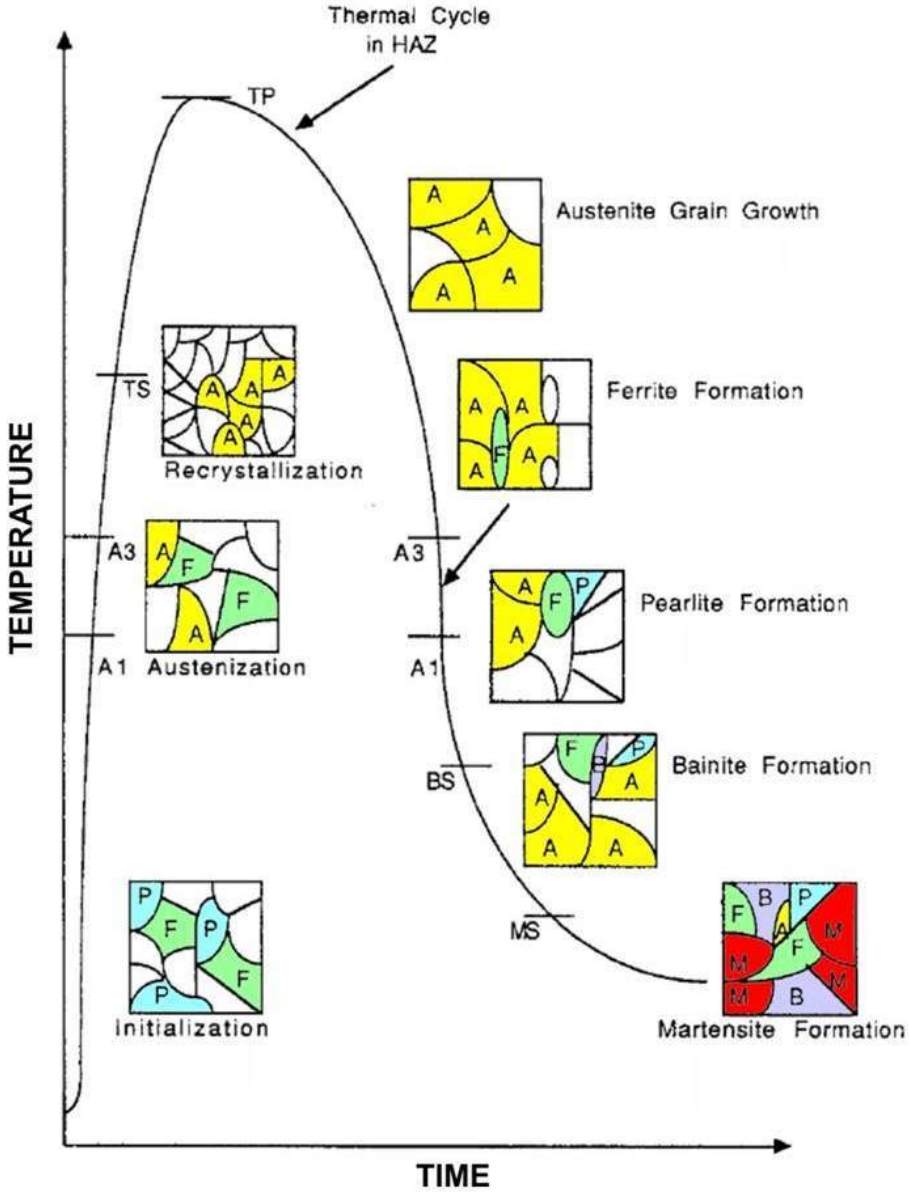

Figure 7.1: Phase transformation occurrence in steel throughout an arbitrary thermal cycle - Figure modified from (173).

sionless process which results in strain due to the shape deformation. Therefore martensite cannot be described through the use of equilibrium phase diagrams.

The temperature at which martensite formation occurs is crucial as the transformation occurring at a low temperature can result in a sharp decrease in residual stresses due to the total strain being occupied primarily with a volumetric change and this therefore being the major influence in resulting residual stresses (158). Applying pre-stress and pre-plastic strain has been shown to effectively modify the martensite start temperature depending on the effect of the applied stress or strain on the energy of austenite. Stabilizing the austenite is achieved through plastic deformation causing a decrease in the start temperature, while the start temperature is increased when the free energy of the austenite is increased through the application of stress (203). A study into welding residual stresses in P91 steel found that the solid-state phase transformation, due to a low martensite start temperature, altered the residual stress sign from tensile to compressive (204). Upon heating of steel the body-centered cubic structure transforms to face-centered cubic accompanied by a decrease in volume. However upon cooling the face-centered cubic structure transforms to body-centered tetragonal and this is accompanied by an increase in volume. These characteristics are reflected in the material properties such as the sharp decrease in the *CTE* curve, highlighted in figure 4.25. The associated phase changes upon heating and cooling, austenitic and martensitic respectively, are illustrated in relation to volume change in figure 7.2. It has been previously shown in section 4.4.2 that *CTE* values reflect such volume changes in the experimentally obtained data. Levels of constraint arising due to varying volume changes and CTE values in dissimilar material joints also impact residual stresses as discussed in chapter 1.

Empirical calculation of the martensite start temperature can be achieved through considering the chemical composition of the material. This temperature can then be utilised in a finite element simulation to model the phase transformation using *Abaqus* subroutines to account for associated volumetric changes and changes in yield stress during this process (205).

The use of an interpass temperature during cladding is common practice. However this also impacts the resulting phases and residual stress states. If the interpass temperature is chosen such that it is above the martensite start temperature then the entire weld material will not undergo martensitic transformation until after the welding process has been completed. This would then encourage compressive residual stresses in the fusion zone. An interpass temperature below that of the martensite start temperature would lead to tempering of previously deposited passes, decreasing the compressive region (207). Throughout the cladding process the cooling rate and time for phase transformation to occur impacts resulting residual stresses.

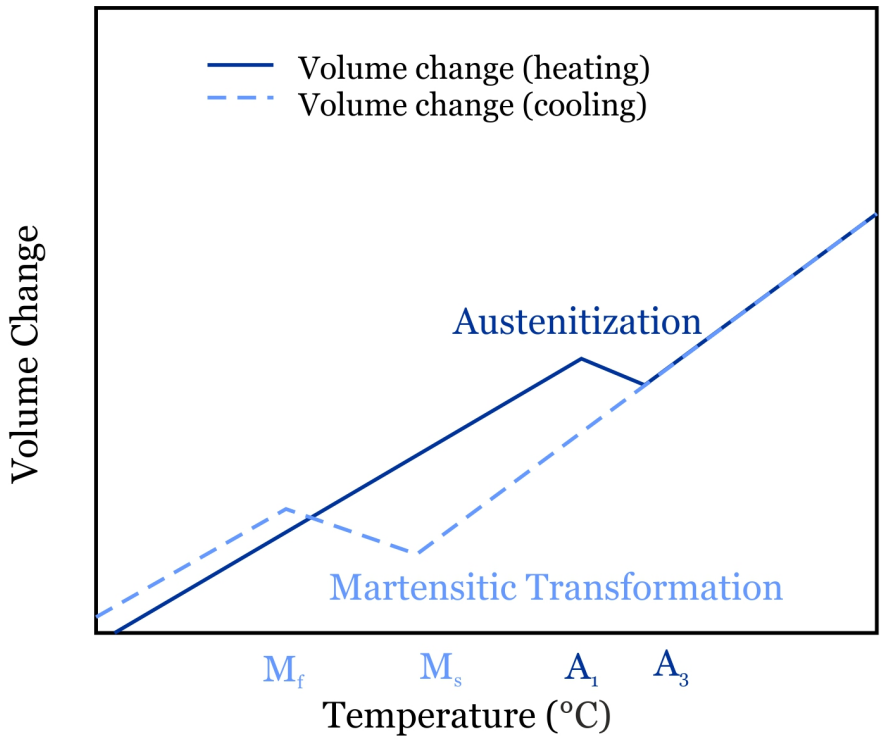

Figure 7.2: Volume changes associated with phase changes upon heating and cooling of steel - Figure modified from (206).

An interpass temperature too close to the martensite end temperature would result in a large level of martensite forming during welding, potentially increasing the brittleness of the material and increasing the chance of the initiation of microcracks. On the other hand, an interpass temperature too close to the martensite start temperature would decrease the level of martensite formation during welding, the transformation from austenite to martensite then occurring during cooling to ambient temperature (205). Ultimately the interpass temperature dictates whether martensitic transformation commences during a multi-pass welding process or whether this transformation occurs only after the welding process is complete and the welded component cools to ambient temperature.

The martensitic transformation does not occur instantaneously, there exists a temperature interval over which the transformation occurs. Quenching for example can be used to control this transformation and in turn the resulting residual stresses. The temperature range over which the transformation occurs must also be captured in the simulation to ensure that the residual stress generation is accurately modelled. Clearly the assumption of an instantaneous transformation will yield a very different stress state to that when considering the martensite start and end temperatures due to the thermal transient nature of the analysis. In the case of the weld cladding process, the temperature gradient, cooling rates and phase transformation duration throughout the weld and substrate materials will be far from uniform and this will result in

variations in the degree of martensitic transformation. Through control of the temperature, the martensitic transformation can be controlled. It has been mentioned by Todinov that the development of compressive residual stresses is hindered through delaying the martensitic transformation at the surface (208). It is likewise mentioned in this study that a uniform transformation in a component cross-section will result in no residual stresses developing. It is further mentioned that a large temperature interval, that is a high transformation start temperature and a low transformation end temperature, minimises the compressive residual stresses resulting due to the transformation (209).

In the welding process, a single phase transformation is not necessarily the case. It is likely that regions of material may undergo several phase changes due to heating and cooling due to the temperature history of the welding process. The rates of cooling are also likely to differ and so it is clear that accounting correctly for the effects of this in a simulation model is a complex process. In this scenario, accounting for the various phase changes is achieved through considering the maximum temperature of elements in a simulation to deduce whether or not martensitic transformation occurs and relationships between martensitic fractions and cooling rate constructed through *CCT* diagrams (206). Martensite fractions are found to be greater in higher carbon content steels.

Upon completion of the martensitic transformation, cooling to room temperature further alters the stress state, with residual stresses increasing due to thermal contraction. It is at this point that tensile residual stresses arise, especially in the welding direction, due to shrinkage of the weld metal (138). Therefore it is favoured that the martensitic transformation is complete upon room temperature, however that completion occurs as close to room temperature as possible.

Similarly, the effects of processes such as annealing can be accounted for in a microstructural model. Phase changes occurring during annealing decrease hardness, reduce dislocation density and decrease flow stress as discussed in (158), this example highlighting the effects of such inclusions or exclusions in an analytical model.

Studies have been conducted to develop weld consumables to encourage compressive residual stress generation, with electrodes possessing lower chromium and nickel contents illustrating the capability of increasing compressive residual stresses (209).

Chromium levels of 6-12% help ensure that the martensitic transformation commences between 100-300°C, while nickel content of 5-11% also aids in controlling the martensite start temperature (210). Modification of the chemical composition and therefore the phase transformation temperature has been shown to have a noticeable effect on the distribution of residual stresses in high-strength steel welds (211). Although it is therefore possible to modify materials to favourably impact

the microstructure and chemical composition, consequent effects on material properties, such as increased hardness must also be considered. This could result in non-compliance with industry standards, such as (110), as was discussed in section 4.4.8.

It has been found that the martensitic transformation does not greatly affect residual stresses due to welding in low alloy carbon steels, however do greatly influence in the case of medium carbon steel (138). This is relevant in the case of the use of 4330, explaining also why characterisation of 4330 is not as crucial as 17-4 PH.

A martensitic transformation is also described as a beneficial process due to the compressive residual stresses resulting from the constraint on the increase in volume increasing resistance to crack propagation in the region of increased hardness (212). In such circumstances again industry standards such as the NACE requirements for hardness levels in welded components must be considered (110).

7.2.1 17-4 PH stainless steel

The 17-4 PH stainless steel utilised in the cladding process is a martensitic precipitation-hardening alloy. Precipitation-hardening stainless steels are often utilised due to the positive characteristics of corrosion resistance and high strength. The former is due to the chromium content and the latter due to the presence of the precipitates. The dispersion of these precipitates can increase not only the yield strength, but also the tensile strength of the material due to the hindrance of dislocation motion caused by the precipitates (66). The selection of a precipitation-hardening steel for welding purposes requires an appropriate welding procedure with a low heat input to ensure toughness and ductility is favourable (213). The microstructure, chemical composition and thermal and mechanical properties for 17-4 PH were presented in chapter 4.

7.2.1.1 Influence of cooling rate

The formation of phases in a steel is dependent, as previously mentioned, on the processes to which the material is subjected. Upon cooling, the cooling rate will determine the extent of phase formation allowed. For example, a rapid cooling rate will limit the extent of alloying and diffusion that occurs before the material reaches ambient temperature. Not only phase fractions, but also transformations temperatures are heavily dependent on the cooling rate during the welding process (156).

Previously, the variation in nodal cooling rates in the axisymmetric model were illustrated as greatly varying in the substrate and clad materials (figures 5.37-5.44).

Instantaneous cooling rates in the 17-4 PH clad layer were examined to aid the investigation of the extent of martensitic transformation. The nodal labels assigned were as previously presented, provided again in figure 7.3. Cooling rates will also be a function of initial model conditions and boundary conditions, with these maintained as those presented previously in chapter 5.

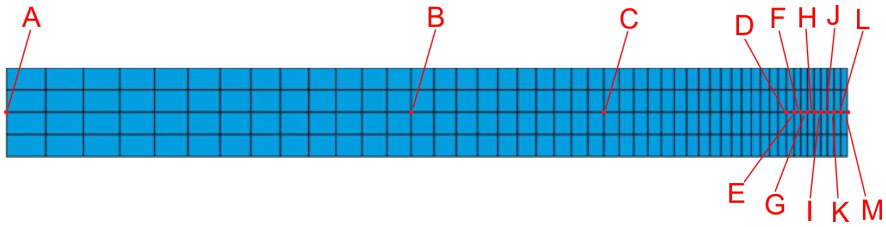

Figure 7.3: Node label assignments - Letters assigned to nodes in the axisymmetric model to investigate cooling rates.

In the experimental data obtained for the *CTE* of 17-4 PH at a cooling rate of 5 K/min, shown in figure 4.25, the martensitic transformation is seen to be at the most extreme point at a temperature of 140°C. The instantaneous cooling rates at this temperature are provided for the clad layer nodes in figure 7.4.

Ideally room temperature would be attained as quickly as possible, resulting in a martensitic microstructure and hindering the increase in residual stresses if the material is not pre-occupied with the martensitic transformation. From this the reasoning for quenching is apparent.

The values observed are however very small, with likewise small variations in cooling rate between nodes within the clad layer. As discussed in section 5.6, cooling rates are most rapid at the beginning of the cooling process, immediately after the weld clad material is deposited. However, it must also be considered that it is not at this temperature that the martensitic transformation occurs. Furthermore, the experimental residual stresses obtained indicated that there was not a significant difference in the resulting level of compressive residual stresses due to varying pre-heat temperature.

The effects of cooling rate should be further investigated. Limitations of the equipment accessible did not allow for investigation of higher cooling rates. During the welding process it is known that initial cooling rates will be very high, studies have been conducted into dilatation during cooling at a rate of 234 K/s (158).

Throughout this research two-dimensional plots have been utilised to provide a means of characterisation of materials. This does not capture the rate of cooling of the material which is changing in a spatial and temporal manner throughout the component. In order to capture the material property variation with both temperature and rate of cooling a three-dimensional representation of the material behaviour

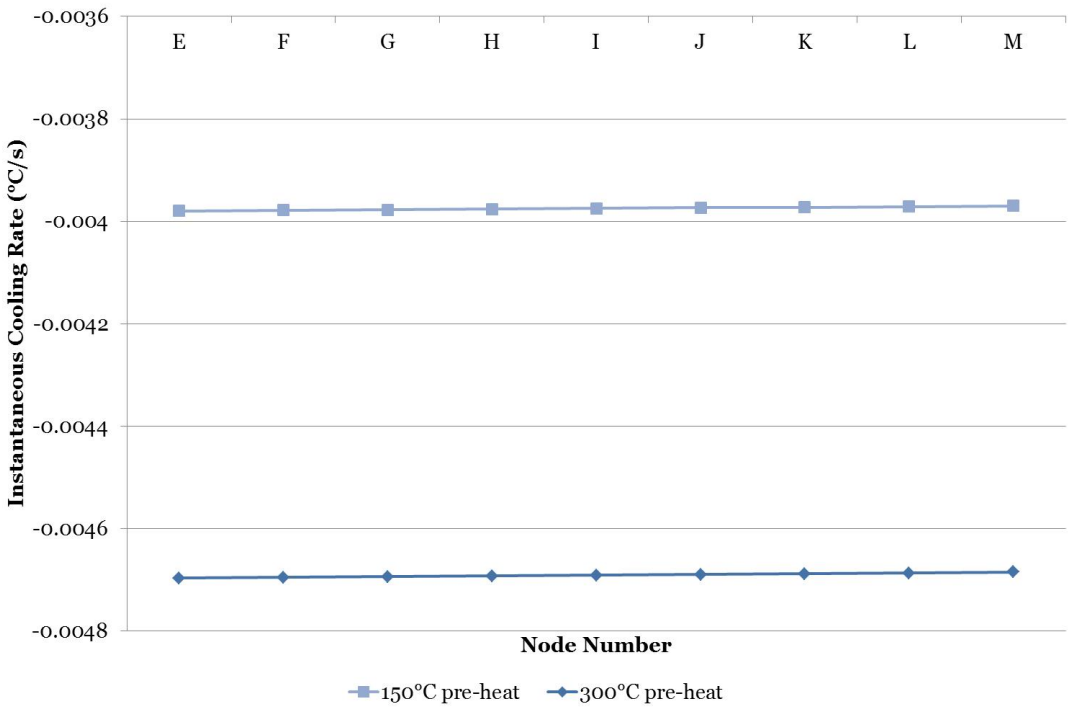

Figure 7.4: Instantaneous cooling rate of 17-4 PH clad layer with pre-heat temperature of 150°C and 300°C - Figure illustrating the instantaneous cooling rate of the clad layer nodes as they pass through 140°C, the temperature at which the lowest point of the CTE curve is reached upon cooling.

would be required. As cooling rate is not a variable in the finite element solver, it would be through these means that this would achieved.

If the temperature and rate of cooling were known for a certain region in the material the necessary material properties could be assigned to this region using this 3D representation of material properties in an iterative manner as per the algorithm used currently with tabulated property-temperature graphs. An example of this is illustrated in figure 7.5 using the *CTE* data trend, indicating movement of each curve depending on the cooling rate.

Rates of cooling were investigated in the finite element model as discussed and therefore an indication of the cooling rates has been obtained as the molten metal is deposited onto the substrate at a certain pre-heat temperature acting like a heat sink. These can be altered through modifying the heat transfer coefficient and appropriate cooling rates applied to regions of the model. The heat transfer due to conductivity is regarded as the most significant effect in influencing the rate of cooling, convection being less significant and radiation less significant again.

Initial studies into the effects of heat treatment suggest that areas of compression arise in the region of the high-temperature material. This was investigated both through the clad and unclad cylinders, indicating that forced cooling has the ability

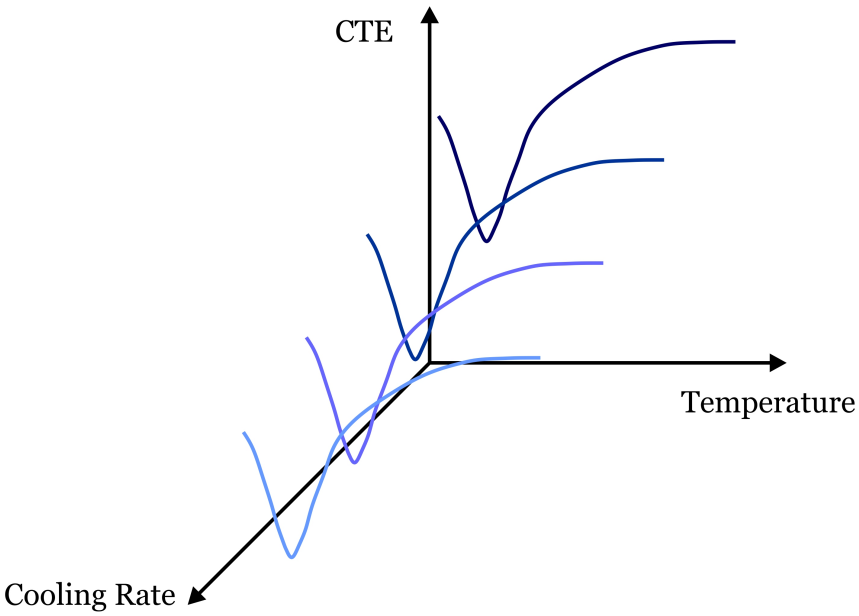

Figure 7.5: 3D representation of material properties - Example of potential CTE variation with temperature and cooling rate.

to generate compressive residual stresses even in unclad cases.

Capturing these effects of cooling rate produces a challenge in both the experimental and simulation aspects of the research. Firstly in obtaining ranges of material property data according to the thermal cycle applied through the weld cladding process and secondly in applying this material data to the simulation model. Due to the limitations of the equipment used, data was obtained for low cooling rates and has been input into the finite element model for one cooling rate. This could be modelled, for example, through the modification of material properties or through user subroutines in *Abaqus*.

The *Abaqus* user subroutine *UMAT* is for example recommended for use when the material models available in *Abaqus* do not adequately represent material behaviour. The data obtained for material properties as a function of temperature and cooling rate could be used in the subroutine. An iterative loop could then be applied such that at every time step, every element is assessed and depending on the temperature and the cooling rate of that element the appropriate material properties would be applied.

In using such a method, certain assumptions would again alter the solution, for example if data was available at two temperature values, whether a linear interpolation could be assumed between the two temperature values or if cooling rate would vary non-linearly hence requiring a more complex definition of the 3D variation of material properties with temperature and cooling rate. An understanding of molecular

physics would be required to allow conclusions to be drawn and accurate implantation to be achieved.

In refining the weld cladding process, a martensitic transformation with the martensite start and end temperatures as low as possible, whilst minimising the temperature range would as discussed maximise the compressive residual stresses. A rapid cooling rate would ensure that there is no time available for the residual stress to increase upon completion of the martensitic transformation.

7.2.1.2 Influence of microstructure

Phase changes will also be influenced by the microstructure of the material, therefore grain size being of interest, as well as the level of carbon content (158). The weldability of low alloy steels can be determined through examination of the grain size, carbon content, precipitation hardening, solid solution hardening and dislocation density of the material. These factors also impact the strength and impact toughness of the material. Reducing the grain size improves strength and toughness, however in the case of the remaining mechanisms increasing strength is accompanied by a decrease in toughness (173).

In tailoring the composition and phase presence of the material, increasing carbon content and encouraging the formation of martensite, the effects on impact toughness must be deduced. It has been shown that increasing the carbon content along with brittle martensite presence can reduce impact toughness (214).

Variations in cooling rate result in varying microstructures. The use of continuous cooling transformation (*CCT*) diagrams allows the phase transformation upon cooling from the austenitic state to room temperature to be illustrated on a diagram according to the cooling rate.

The assumption of a constant cooling rate throughout a phase transformation is however rarely the case in reality. Likewise, throughout the depth of a component the cooling rate will vary, especially clear in the case of the weld cladding applied to the outer diameter of the thick cylinder. The material close to the clad layer will experience a very different temperature history to the material at the cylinder bore. This produces a highly complex scenario, however in terms of the martensitic phase in the clad the cooling rate near the surface in the clad layer is of primary interest.

Variations in the microstructure between pass 1 (figure 4.14) and pass 2 (figure 4.15) of the 17-4 PH clad material illustrate that the thermal loading cycles arising through the two-pass cladding process produce different microstructures. Therefore the extent of the martensitic transformation will differ between passes. Further investigation of the effects of the time allowed for the martensitic transformation would allow insight

into the effects on microstructure, the extent of the martensitic transformation and in turn the effects on residual stresses. Evaluation of the completion of martensitic transformation also shows that in both passes in this case, the presence of ferrite indicates there is potential in modifying the welding and cooling process to encourage increase in the levels of martensite and maximise compressive residual stresses.

In the case of a single-pass weld, the resulting residual stress distribution is governed by the combination of thermal contraction upon cooling and strain changes during the solid-state phase transformation (215). In the two-pass system investigated throughout this study, an added consideration of the effects of reheating the first pass through application of the second will also influence the final stress state.

Multi-pass welds can present the advantage of relaxing phase transformation effects and hence residual stresses through the thermal cycle of heating and cooling of the *HAZ* during deposition (161). The effects of reheating the weld material should be considered to ensure that reheating does not negatively influence the residual stress state through transformational strains experienced. A reduction of yield strength with increased temperature will in turn decrease compressive residual stresses through reheating cycles (206).

Tempered phases arising through the heating of as-welded ferritic steel components clad with austenitic steel resulted in lower mechanical properties in a study by Dupas and Moinereau (216). Therefore tempering of the first pass through the deposition of the second should be carefully considered such that beneficial microstructures and material properties are maintained in both passes.

In the weld material and the *HAZ*, the material properties will be dependent on the grain size. In the case of multi-pass welds, these properties will not remain constant throughout these regions. At higher temperatures grain growth is enhanced and it was shown by Onsoien, M'Hamdi and Akselsen (201) that a higher peak temperature resulted in a higher residual stress due to increased hardening at these elevated temperatures in pipeline steel. It is also mentioned in this study that the hardenability of a material dictates the level of influence of the phase transformation. Grain growth can be encouraged by maintaining a temperature for a period of time prior to cooling (158).

Implementing this metallurgical transformation in the simulation would require consideration of capturing the time taken to cool to ambient temperature amongst other factors such as the extent of the transformation and the start and end transformation temperatures. A means of capturing the link between the phase transformation and time would be required, due to the knowledge that phase transformations are not instantaneous. Constraint on the microstructural transformation may arise through the thermal cycle in phases in close proximity to one another.

To model the evolution of the microstructure, equations are available through which the rate of reaction can be described as being proportional to the deviation from equilibrium (217). Even in these cases however, the tempering effects in multi-pass welding processes are not accounted for.

A thermo-metallurgical-mechanical model was developed for use in *Abaqus* for the simulation of multi-pass butt-welded steel pipes accounting for the temperature field during the welding process and the material microstructure to accurately obtain the resulting residual stresses (218). In this study, assumptions were also made regarding the variation of yield strength with temperature upon heating and cooling.

The finite element code *SYSWELD* has the ability to account for thermal, metallurgical and mechanical variations of the material due to welding processes. This was successfully utilised in the numerical simulation of the laser welding process of butt-joint shipbuilding steel plates providing good correlation with experimental investigation of distortion levels due to welding (219). A material database exists within the program such that properties can be utilised accordingly for common steels and aluminium alloys. However these properties do not account for the welding of the material, but the materials in unwelded form.

7.3 Influence of microstructure on failure mechanisms

The effects of the welding process on the phases resulting due to heating and cooling of the materials require in depth study to appreciate the impact of the thermal cycle on material properties of both the substrate and the clad materials and ultimately component performance.

Failure mechanisms are influenced directly by the mechanical properties and microstructure of a coating, cladding or dissimilar joint. This is in addition to the residual stress state arising through the coating, cladding or joining process and any discontinuity stresses arising through operational loading. The material properties and microstructure will also be affected by alloying and diffusion. The presence of intermetallics and hard spots can also influence fatigue, fracture and stress corrosion cracking. Therefore, in producing a satisfactory cladding or coating, a compromise must be achieved accounting for the design of the dissimilar material join, processing conditions and resulting microstructure and material properties.

Corrosion resistance can also be reduced through phase changes due to the metallurgical changes during the welding process, as reported in a study on welded austenitic stainless steel (220). This could also therefore impact stress-corrosion cracking resistance and fatigue performance.

Fatigue and toughness properties of weld clad stainless steel were investigated with the study concluding that crack growth rate varied throughout the clad layers (221). This clearly indicates that the metallurgy of the clad region has a direct impact on the performance of the clad.

Microstructural defects such as pores and microcracks were discussed in the context of adhesion of thermally sprayed coatings (222). The presence of such defects will result in the inability to accurately determine residual stresses due to the influence the presence of such defects will have on the measured residual stresses and will also clearly have a negative impact on the operation of the component. Thermal integration of coatings and substrates can be improved through post-coating laser treatment (101).

Conversely, micro-cavities present in Inconel 625 *HVOF* coatings blended with tungsten carbide particles deposited on a steel substrate were found to act as stress relaxation regions resulting in the prevention of crack propagation at the surface (118).

Heat treatment is often utilised as a process of encouraging homogeneity in properties and microstructure. A study of clad steel process vessels however reported little variation in as-welded and heat treated microstructures in the case of carbon steel welded with stainless steel. Hardness values though were found to be higher in the first clad layer in all cases, heat treated samples possessing slightly lower hardness values (223).

7.4 Influence of varying material properties on residual stresses

The effects of material properties on resulting residual stresses has been heavily emphasised. It is now apparent that the microstructure also heavily influences the material properties and therefore the residual stresses. In accurately modelling the residual stress distribution, accurate material properties are required. The requirement for including the resulting effects of microstructure on properties is now then also apparent.

In this section a sensitivity study is undertaken to ascertain the likely effects of changing variables in the finite element model, in this case particular material property values.

7.4.1 Investigating the effects of varying coefficient of thermal expansion

Variations in *CTE* values have been clearly observed in the experimental data obtained due to varying cooling rates and chemical compositions. It has been highlighted that the presence of martensite in the material microstructure is illustrated

most clearly in the case of material *CTE* for a stainless steel weld (224). For this reason the influence of varying *CTE* was investigated to deduce the influence of this variation on resulting residual stresses. *CTE* is perhaps the single most important mechanical property directly available in finite element modelling in terms of influencing material expansion and contraction and hence the need for investigation. Constraint on such expansion on the other hand is influenced by modulus and yield stress.

The data obtained for a cooling rate of 5 *K/min* is presented in figure 7.6. This data was manipulated such that two cases resulted for the investigation of the effects of varying *CTE*. This was achieved by dividing the data in the region of the martensitic phase change by 2 and 1.5 for cases *A* and *B* respectively. The form of the curve was manipulated such that the trough decreased towards zero as it was shown in figure 4.25 that with increasing cooling rate data appeared to exhibit less of a sharp decrease in the region of the phase change upon cooling. This data was then utilised in the axisymmetric finite element model of the 4330 cylinder weld clad with 17-4 PH. A pre-heat temperature of 150°C was investigated as it was previously found that there was little variation in the experimental residual stress measurements and therefore the lower pre-heat temperature would provide a more economical process.

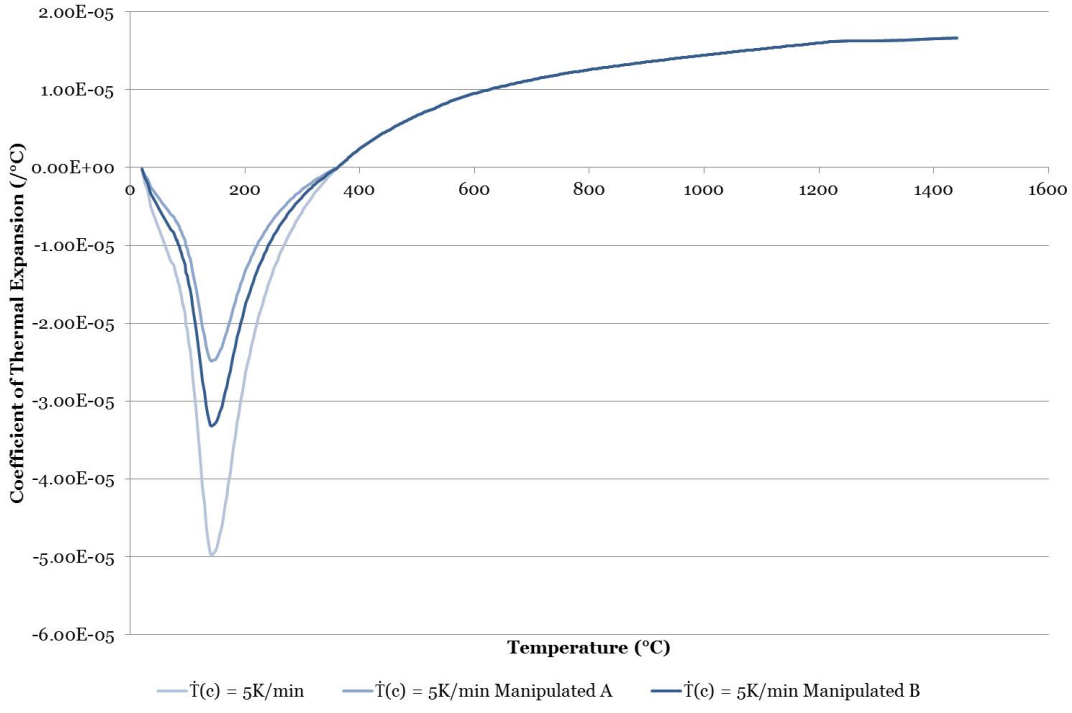

Figure 7.6: Manipulation of coefficient of thermal expansion of 17-4 PH (Clad on 4330) - Data obtained for a cooling rate of 5 K/min manipulated through division of data in the region of the martensitic transformation by 2 and 1.5 to obtain cases A and B respectively.

The stress components were obtained along the radial path from the bore to the outer diameter as previously, the stresses utilising the manipulated data set *A* and *B* and the original data plotted in figures 7.7-7.9. The results show that as the values of *CTE* become less negative in the region of the martensitic transformation, the hoop and axial residual stresses in the clad layer become less compressive.

The manipulated data set *A* provided compressive residual stresses around -200 MPa in both hoop and axial components. The data shown for the residual stresses obtained when utilising data set *B* for the temperature-dependent *CTE* data illustrates that hoop and axial stresses obtained in the clad layer are of the same level as the residual stresses obtained experimentally through *ICHD*. These results indicate that this variable has a significant influence on residual stress results and through the manipulation presented here agreement with experiment has been obtained.

In both cases of manipulated data, the discontinuity stresses at the interface significantly decrease, showing that the material microstructure characterised through variation in material properties can also favourably influence the residual stresses due to weld cladding.

Radial stress components remain lower in stress levels, however also experience a decrease in stress level in the vicinity of the join. Tensile residual stresses decrease in both the substrate and the clad layer.

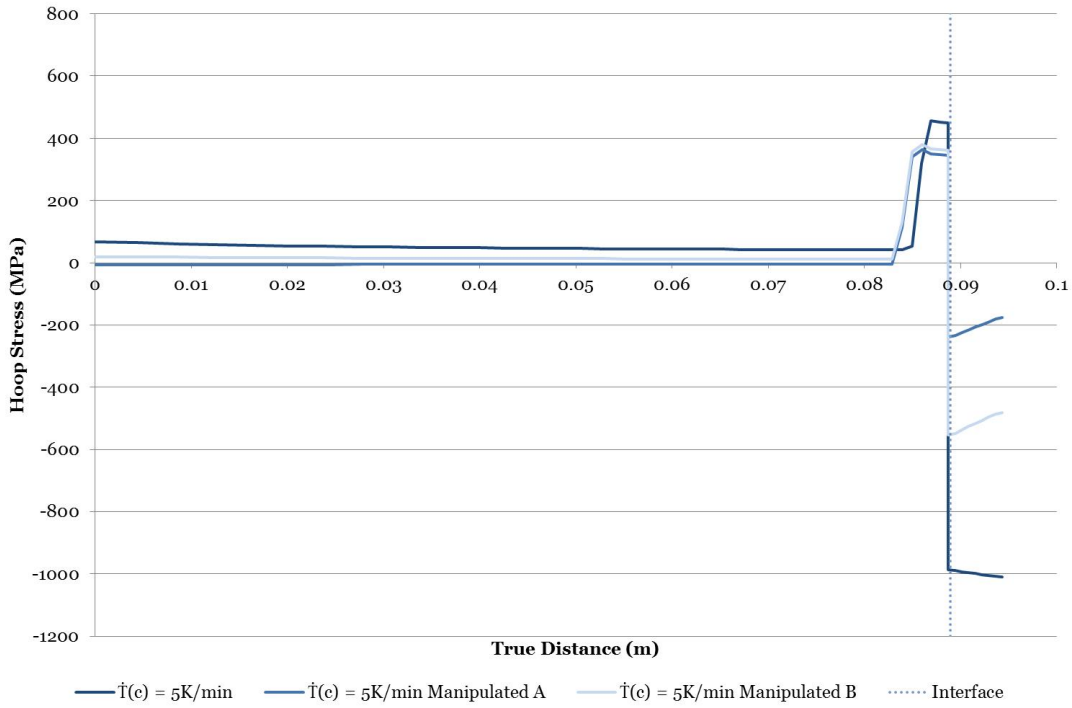

Figure 7.7: Hoop stress component variation due to manipulation of CTE data - Results shown for an axisymmetric model of 4330 substrate and 17-4 PH clad with pre-heat temperature of 150°C utilising the path illustrated in figure 5.4.

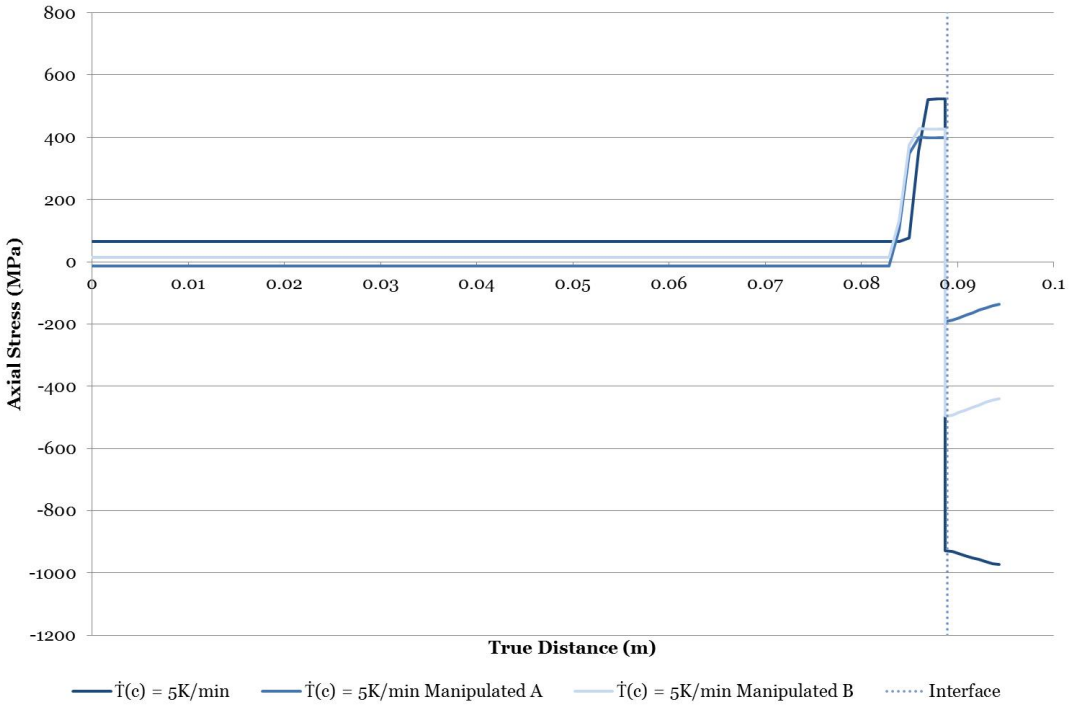

Figure 7.8: Axial stress component variation due to manipulation of CTE data - Results shown for an axisymmetric model of 4330 substrate and 17-4 PH clad with pre-heat temperature of 150°C utilising the path illustrated in figure 5.4.

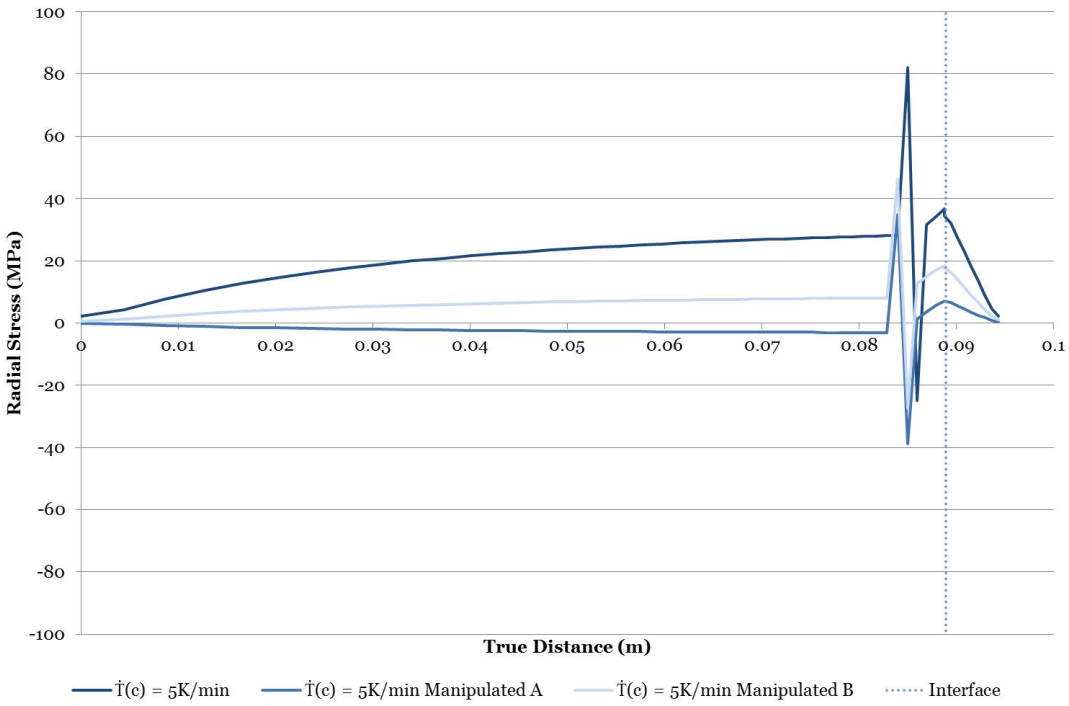

Figure 7.9: Radial stress component variation due to manipulation of CTE data - Results shown for an axisymmetric model of 4330 substrate and 17-4 PH clad with pre-heat temperature of 150°C utilising the path illustrated in figure 5.4.

Investigating the effects of varying the *CTE* upon cooling has successfully demonstrated the ability to tailor the residual stress distribution arising due to weld cladding. It has also further provided evidence of the importance of accurate material properties in obtaining accurate residual stresses through finite element modelling. The phases present in the material will influence material properties. Through knowledge of the chemical composition of the material, phase transformation behaviour can be deduced. Modifying the chemical composition would alter the final microstructure through encouraging variations in phase transformation. This would be reflected in material properties and ultimately residual stresses. In martensitic and ferritic irons and steels, it has been found that chromium has the largest influence on *CTE*. Chromium, nickel, cobalt and silicon decreased *CTE* while titanium, aluminium and copper increased *CTE* (225). It is through such knowledge that the chemical composition of materials can be beneficially utilised to achieve desired material properties and residual stresses.

7.4.2 Comparing simulation and experiment

Comparing the residual stresses obtained experimentally with the newly obtained residual stresses in the axisymmetric model through arbitrary manipulation of *CTE* data shows that residual stress levels in the clad layer to a depth of 1 mm provide a much closer correlation than previously presented in section 6.5. This is particularly the case for the axial stress component shown in figure 7.11.

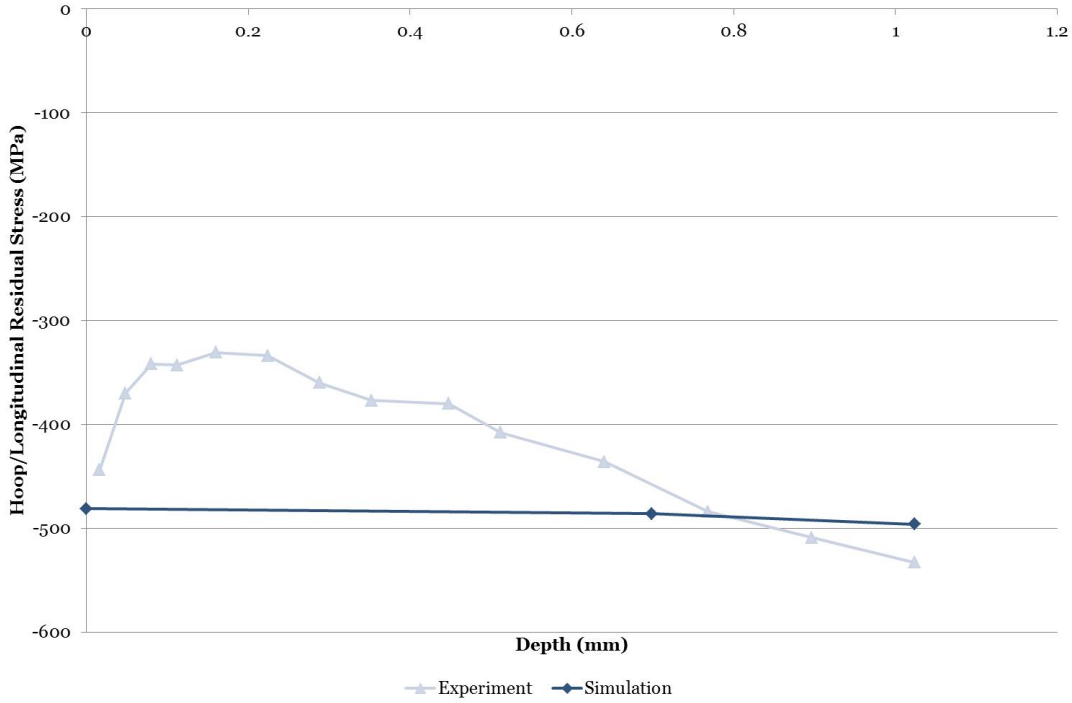

Figure 7.10: Comparison of simulation and experimental hoop/longitudinal stress component when utilising manipulated CTE data - Results shown for a weld clad block and an axisymmetric model of 4330 substrate and 17-4 PH clad with pre-heat temperature of 150°C.

The comparison of experimental and simulation stress components has further indicated that the axisymmetric finite element model is capable of capturing representative residual stress distributions arising due to weld cladding, while the manipulation of data to obtain simulated residual stresses similar to experimentally obtained residual stresses highlights the sensitivity of the finite element model to certain temperature-dependent material properties when these are a function of cooling rate.

7.4.3 Correlation between material properties and microstructure

Increasing the accuracy of the model can be achieved through manipulation of material properties as has been illustrated in varying *CTE*. Accounting for the material microstructure can be achieved through variation in other material properties. Variations in *CTE* and yield stress due to phase transformations can be utilised in *Abaqus*

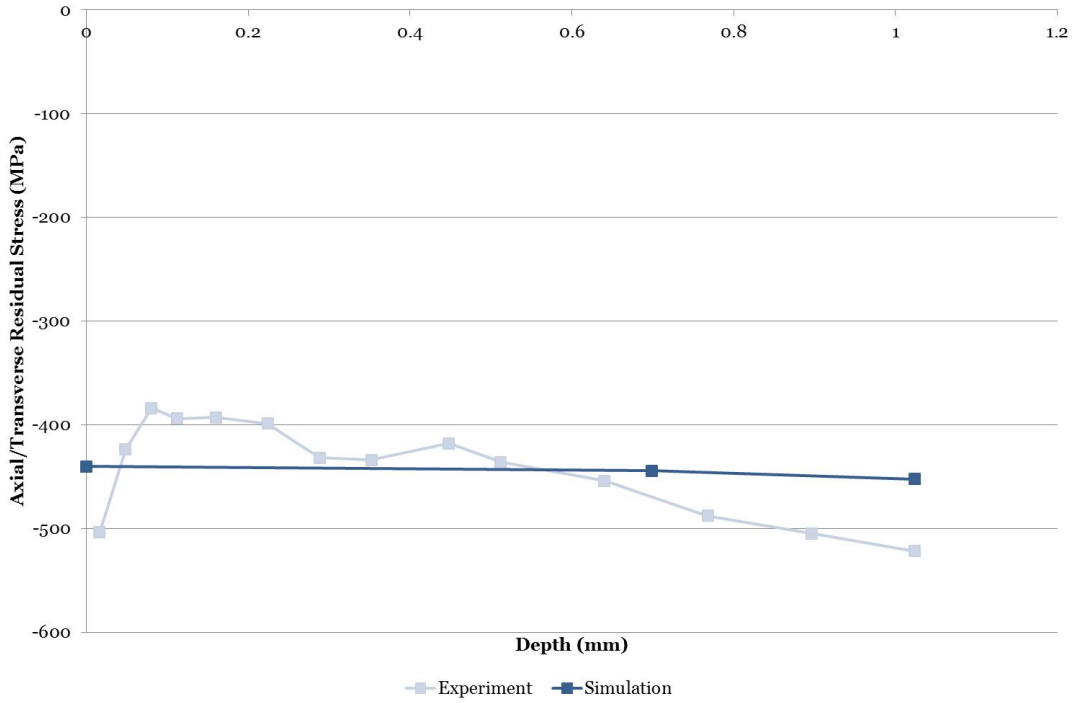

Figure 7.11: Comparison of simulation and experimental axial/transverse stress component when utilising manipulated CTE data - Results shown for a weld clad block and an axisymmetric model of 4330 substrate and 17-4 PH clad with pre-heat temperature of 150°C.

user subroutines to reflect the volumetric changes. This was successfully undertaken by Yaghi et al. in the case of P91 steel with phase transformation plasticity also accounted for (205).

Accounting for the temperature variation at integration points would allow assignment of individual cases of yield stress and *CTE*, the most dominant factors in capturing variations due to phase transformation volumetric changes. Modulus is also a dominant factor, however does not change as greatly with material type and microstructure. Transformation plasticity is modelled through modification of the yield stress. Karlsson modelled a decrease in yield stress in the *HAZ* during the final phase transformation in the modelling of residual stresses in single-pass girth butt welded carbon-manganese pipes (226).

To model the yield stress of phases, a model accounting for the grains of martensite and bainite in the weld and *HAZ* would require development with knowledge of the distribution of the phases. Based on the volume-fraction of phases material properties would then be assigned, for example appropriate yield stress values deduced from the hardness levels in these grains as was undertaken in (156).

7.4.4 Correlating yield and tensile strength with hardness

Variation of yield strength and thermal expansion allow the modelling of representative thermo-plastic behaviour. Calculated phase fractions can be utilised and the known correlation with hardness allows the determination of yield strength of each phase.

The ability to utilise the correlation between hardness and tensile strength was illustrated in section 4.4.10.

The correlation between yield strength and Vickers hardness for a number of steels is given in (227):

$$YS = -90.7 + 2.876H_V \tag{7.1}$$

As this correlation is obtained using a least-squares linear regression, a zero hardness value would not provide a zero yield strength value as expected. The presence of the constant value in the equation results in a standard error which limits the applicability of this relationship to Vickers hardness values above $130H_V$.

Tensile strength and Vickers hardness can also be correlated as previously discussed. This is described in (227) as the following:

$$TS = -99.8 + 3.734H_V \tag{7.2}$$

Again the applicability of this relationship is limited to Vickers hardness values greater than $130H_V$.

In this study, Pavlina and Van Tyne note that the correlation provided for tensile strength and Brinell hardness under-predict strength values in regions of high hardness. When considering material microstructure, the study shows that in the case of complex phases, that is the presence of various phases, the correlation between hardness and yield strength is poorer than that of tensile strength. It is such factors that must be realised when utilising such relationships. For this reason it would be favourable to undertake experimental testing for specific microstructures, however, the benefits of such correlations is clear when limited experimental testing can be undertaken.

Using a variation in yield strength during modelling would also indirectly account then for hardening of the material due to the correlation between these two properties (226).

Due to the temperature-dependent data obtained experimentally for yield stress and ultimate tensile strength and the inability for this method to account for variations due to temperature with the hardness data available, this correlation was not utilised.

7.5 Influence of material strain

In modelling thermo-elastic-plastic behaviour, constitutive models account for the total strain. The components contributing to the total strain are noted in equation 7.3 as contributions due to elastic loading, plastic loading, thermal loading, volumetric change and transformation plasticity. It is clear then from this equation that strains associated with volumetric changes and transformation plasticity will impact residual stress states, the level of influence dependent on the level of strains associated with both.

$$\varepsilon_{Total} = \varepsilon_E + \varepsilon_P + \varepsilon_T + \varepsilon_{VOL} + \varepsilon_{TRP} \tag{7.3}$$

Texture should also be considered, as this also varies with phase transformations. This will therefore cause variation in strain due to transformation, for example the volume and shear strains associated with the phase transformation of austenite and induced plasticity in the austenitic phase dependent on the presence of hard phases, such as martensite (217).

If solid-solid phase transformation effects are not accounted for where relevant, tensile residual stresses resulting from the welding process would increase upon cooling. A compressive plastic strain during heating results in a tensile residual stress upon cooling. Inclusion of the effects of the volume change due to the phase transformation gives rise to compressive residual stresses (228).

It is known that the residual stress state arising due to the welding process is dominated by the volumetric strain changes due to phase transformations. To account for the changes at Gauss points in the model, constitutive equations could be utilised at Gauss points and as time steps progress. This would allow for variations in plasticity effects at these Gauss points. Depending on the stress at a particular Gauss point, values of yield stress, strain rate and deformation characteristics can then be assigned to that point (173).

Stressing of the material will result in a plastic strain during the final phase transformation, known as the transformation plasticity. The purpose of this strain is to maintain compatibility in the material due to the phase change occurring, for example the martensitic transformation due to material deformation. This strain arises at stress values below the material yield stress and therefore it has been common to

utilise a lower yield stress in simplified modelling of the effects of transformation plasticity.

Including the effects of transformation plasticity is commonly achieved using the model by Leblond. It would also be possible to undertake experimental testing of the materials under investigation, cooling the specimen whilst subjected to a particular stress. As the specimen experiences phase changes the experimental data obtained would then provide a representation of the effects of these phase changes.

The inclusion of transformation plasticity has been shown to relax residual stresses in the weld metal. However, in a study of a chromium-nickel type weld metal by Kasuya et al. relaxation of residual stresses in the *HAZ* was not achieved (203). The reasoning for these findings was not elaborated upon. The inclusion of transformation-induced plasticity through consideration of variation in yield strength in the numerical model of welding residual stresses in P91 steel by Bi et al. resulted in better correlation with experimental measurements (204).

The level of constraint experienced by the component will be dependent on the substrate, a large substrate geometry increasing weld constraint, with all stress components influenced by the strain changes associated with the martensitic transformation. Studies undertaken to vary the thickness of the cylinder indicated that increasing pipe thickness could positively influence residual stresses at the interface, with tensile axial stresses decreasing upon increasing the ratio of pipe thickness to cladding thickness (161).

7.5.1 Strain hardening potential

The strain hardening potential of the materials under investigation was considered through calculation of the ratios of tensile strength to yield strength using experimentally obtained data. The resulting values indicating the potential for the material to strain harden are provided in table 7.1.

Material	TS:YS
4330 (Inconel 625 clad)	1.170
4330 (17-4 PH clad)	1.180
Inconel 625	1.626
17-4 PH	1.174

Table 7.1: Ratios of tensile strength to yield strength

Table 7.2 provides the criteria presented in (227). The ranges provided to indicate strain hardening potential show that both 4330 *HAZ*'s and 17-4 PH have a low strain hardening potential, while Inconel 625 has a high strain hardening potential. These

ratios were calculated using experimental data for representative *as-clad* and *HAZ* materials and confirmed the expectation for all materials.

Ratio	Strain Hardening Potential
TS:YS ≤ 1.23	Low
$1.23 <$ TS:YS < 1.56	Medium
TS:YS ≥ 1.56	High

Table 7.2: Strain hardening potential

Good correlation for residual stresses has been presented between simulation and experiment in the case of an Inconel 625 clad, although the simulation model does not account for the strain hardening of the clad material. Although strain hardening potential has been indicated as low, due to the complexity of the modelling of the 17-4 PH clad material the effects of strain hardening were considered.

7.6 Summary

This chapter has introduced various reasons as to the increased complexity including capturing the behaviour of the martensitic, precipitation-hardening stainless steel in cladding simulation.

Key factors clearly requiring accurate definition and data are the effects of the following:

- Phase transformation
- Microstructure
- Material property variation
- Time
- Cooling rate

The effects of these factors have been discussed in this chapter, with recommendations for future investigation also discussed.

The relationship between cooling rate and phase transformation requires further investigation. The extent of the martensitic transformation and the consequential effects on material properties could be experimentally examined, also with a view of capturing these effects in the simulation model.

In harnessing the potential benefits of phase transformations, the consequent effects on thermal and mechanical mechanisms must also be considered as these aspects are

all coupled. For example, it has been shown that in altering the thermal gradient during dilatometry experiments, the *CTE* data obtained greatly varies due to variations in the martensitic transformation. The *FEA* results reported herein shows that variation in phase change *CTE* data can significantly change the magnitude of the resulting residual stresses.

It would also be desirable to develop a manner of incorporating the effects of the martensitic transformation on yield strength and the volumetric change as a means of modelling phase change effects. This has been undertaken through the use of *Abaqus* subroutines in steel butt-welds and concluded that volume change due to the martensitic transformation is of utmost importance (229). The findings of this study were therefore in line with the findings herein, that the neglecting of phase changes can completely transform the nature of the resulting residual stresses from compressive to tensile.

Phase diagrams should be obtained for specific heating and cooling rates, with the latter being more of interest due to the martensitic transformation effects on residual stress generation. The temperature history in the small region of the *HAZ* is likely to possess a constant cooling rate and therefore it would not require as great an experimental program to obtain information regarding phase transformations upon cooling.

In attempting to achieve the best case of a 17-4 PH clad layer, it should be considered that any processes applied to the clad material will also affect the substrate material. Therefore the effects of cooling rate on the substrate should also be borne in mind although likely not as crucial.

It has been assumed that material properties vary only with temperature and therefore the variation in material properties due to the microstructure are not considered. This is acceptable in the case of Inconel 625 due to the similar behaviour upon heating and cooling and upon implementing various rates. However, it has been shown that this is clearly not acceptable in the case of 4330 and 17-4 PH. Surface contours of property data incorporating temperature and cooling rate could also capture the dimension of time in terms of the duration of the martensitic transformation and hence the extent of the transformation. Were various data sets to be available dependent on the temperature history of the material, the simulation could utilise the appropriate data throughout the analysis. The most crucial points to consider are the maximum temperature of the material and the cooling rate between 800°C and 500°C as these dictate the resulting material microstructure (158). A thermal, metallurgical and mechanical model would provide a method of creating sets of material properties depending on the phase composition.

In future it would be desirable to more fully characterise the stress-strain behaviour of the materials investigated at various temperatures. Likewise varying microstructures with varying phase compositions would also ideally be tested due to the difference that arises in resulting properties and stresses depending on the temperature history experienced by the material. Such a full characterisation would most likely however prove impractical from a cost and time point of view.

Welding simulation can be of interest for many reasons and therefore the model required is dependent on the desired outcome of the simulation. The overriding aim in this research has been to demonstrate that useful compressive residual stresses could be generated to a significant depth using weld cladding and a careful choice of clad material. It would also be of interest for the application in question to have a deep understanding of the resulting microstructure of the weld and HAZ, and therefore an obvious area with scope for development is to include a microstructural model.

Chapter 8

Laser Cladding of Low Alloy Carbon Steel

Laser cladding is investigated as an alternative to the weld cladding process. The results indicated good fusion resulted when laser cladding a 4330 substrate with both Inconel 625 and 17-4 PH and investigating two clad layer depths of 2 mm and 6 mm. In comparing weld and laser cladding results, it was shown that a smaller HAZ resulted in the laser cladding process due to lower heat input with HAZ depth found to be independent of clad layer depth. HAZ hardness values were found to be independent of clad material indicating that the cladding process heat cycle is dominant in this case. Dilution levels were found to be lower in the laser cladding process compared with dilution levels in the weld cladding process. Process refinement and controlled cooling should be examined to ensure the most favourable results. Functionally grading the transition is an attractive option, easily obtained in the laser cladding process. Surface finish was found to be smoother when weld cladding as opposed to laser cladding with Inconel 625. However the opposite was the case when cladding with 17-4 PH. Significant compressive residual stresses were measured by ICHD in both a 6 mm and a 2 mm thick clad layer of 17-4 PH and therefore increasing clad layer depth does not appear necessary, unless in the case of a severe erosion-corrosion application. Contour method measurements also indicated high compressive residual stresses in the 17-4 PH clad layer. Good agreement was obtained between ICHD and contour method measurements. Contour method measurements highlighted the importance of accurate data processing, with the smallest knot spacing providing more detailed stress contours. The presence of discontinuity stresses at the interface, obtained previously in the finite element simulation, were confirmed in the contour method results to be present in reality.

8.1 Introduction

The ability to generate beneficial compressive residual stresses has been demonstrated using the weld cladding process. Residual stresses can also been induced through many other cladding or coating processes as discussed in chapter 3. To further investigate the potential of other processes for application of a fatigue-resistant cladding technology, laser cladding of similar block geometries was also undertaken to present an alternative method.

Laser cladding is a process whereby coatings, typically 50 μm to 2 mm in thickness, are applied to a substrate with the aid of a laser beam. De Oliveira (230) describes the three processes by which laser cladding is achieved: applying powder in the form of slurry, wire feeding the clad material to the melt pool or using powder injection. The laser beam energy melts the powder and the clad material is fused with the substrate material through a sintering process whereby the substrate and the clad materials are melted as shown in figure 8.1. De Oliveira also comments that due to the melting and solidification of the laser clad layer high tensile residual stresses may also form which can affect performance.

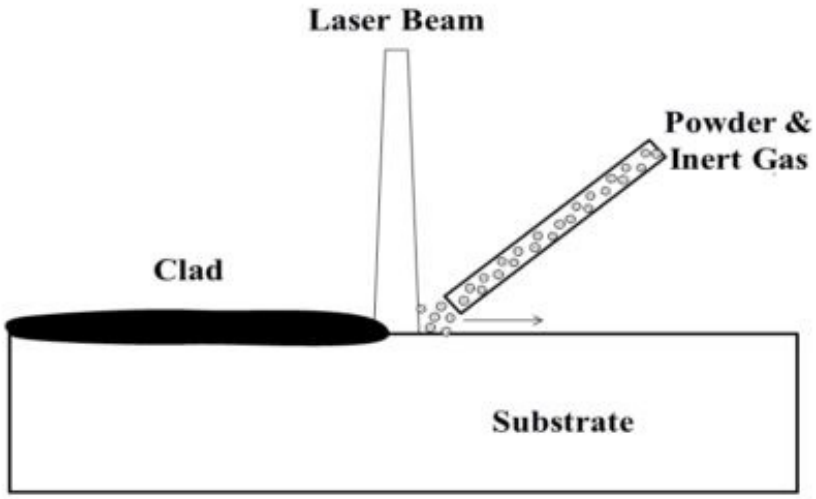

Figure 8.1: Laser cladding process - Figure as presented in (231)

An improvement in the surface properties remains the general aim in the laser cladding process, as was the case with the weld cladding process.

Joint metallurgy is a key aspect to be considered in the application of any cladding or coating. The cladding parameters also heavily influence the resulting residual stresses. Control over the heat input through controlling the energy of the laser is beneficial in controlling the depth of penetration of heat, affecting characteristics such as the depth of the *HAZ*. In this way it can be ensured that sufficient substrate

material is melted to provide a good bond between substrate and clad materials whilst balancing this with a satisfactory *HAZ*, the region of substrate material in which material properties will be altered due to experiencing heating during the deposition process. A poor bond, as with any cladding or coating process, can result in a porous material and potential cracking and delamination.

Simulation models for laser cladding have been developed and compared with experimental testing by Plati et al. (172). In this study of steel laser clad with a metal matrix composite, it was found that while the finite element model did not account for creep effects, good correlation between simulation and experiment was obtained. Substantial compressive residual stresses were found to remain post-cladding, which were also dependent on substrate curvature.

In commencing the laser cladding program, focus was placed on the 17-4 PH clad material due to the beneficial compressive residual stresses which arose in the clad layer when weld cladding with this material. Following the deposition of a 6 mm clad layer during the weld cladding process, two clad layer thicknesses were investigated when using the laser cladding process: 2 mm and 6 mm. The main goal of this study was to determine whether useful residual stresses could be obtained with a different process and in particular with a thinner clad layer. The resulting material microstructure in the clad and *HAZ* was also of interest.

8.2 Laser cladding process

Substrate geometry to be clad consisted of blocks of the same dimensions as were weld clad, with length, breadth and thickness of the blocks being 12, 6 and 4 inches (304.8 mm, 152.4 mm and 101.6 mm) respectively. The blocks to be clad were preheated to 150°C prior to laser cladding with both Inconel 625 and 17-4 PH as previously. Due to the nature of the laser cladding processes, these materials were in powder form prior to deposition.

8.3 Resulting microstructure and material properties

In the previous chapter, the potential of utilising phase changes to tailor the residual stress state was discussed. Phase changes have also been highlighted as a means of ensuring the generation of compressive residual stresses, as in the case of laser cladding nickel cobalt molybdenum powder on maraging steel due to the phase change from austenite to martensite (232).

Zhang et al. (233) investigated the avoidance of cracking in laser cladding. Residual stresses play an important role in cracking as do the properties of the clad and the

bond with the substrate. Cracking was found to occur sub-surface in the clad layer or at the interface with the substrate. The authors recommend careful selection of materials, process parameters and pre- and post-treatments to minimize cracking.

In the investigation of ferrite-based alloy coatings by laser cladding, Yu et al. highlight that hardness and wear resistance can be increased by increasing carbon content, however plasticity and toughness of the coating is negatively affected and cracking susceptibility increased (234).

The combination of materials can be favourably selected by decreasing the difference between *CTE* of the coating and substrate materials to decrease susceptibility to cracking. The criteria to be followed is provided as (235):

$$\frac{-\sigma_{a,UTS}(1-\nu)}{E\Delta T} < \Delta\alpha < \frac{\sigma_{b,UTS}(1-\nu)}{E\Delta T} \tag{8.1}$$

In equation 8.1 $\sigma_{a_{UTS}}$ and $\sigma_{b_{UTS}}$ are the tensile strength values for the coating and the substrate respectively, $\Delta\alpha$ is the difference between *CTE* values, ΔT is the temperature difference, E the Young's modulus and ν the Poisson's ratio.

Cobalt-based superalloys were used to investigate plasma spray, tungsten inert gas, oxyacetylene flame and laser cladding, concluding that laser cladding provided the lowest dilution, no porosity and the benefits of the martensitic transformation to provide compressive residual stresses (236).

A nickel-based tungsten carbide coating deposited onto steel resulted in tensile residual stresses through flame spraying and compressive residual stresses through laser cladding due to the volume change experienced through the chemical-physical reaction, decreasing micro-cracking at the surface (237).

Ocelik, Furar and De Hosson concluded that the method of material deposition can greatly influence the microstructure resulting, with cobalt-based coatings demonstrating that the overlapping of laser tracks results in discontinuities in the microstructure, furthermore observed to be more severe when a higher laser beam velocity is utilised (238).

Laser cladding is advantageous for the low levels of porosity resulting, the potential to control dilution and the good adherence of the cladding with the substrate. A nickel chrome boron silicium ($NiCrBSi$) diode-laser clad provided good sliding wear resistance at high temperature (239). Wear resistance is generally higher when the microhardness of the clad layer is higher. Wear resistance is also influenced by the particle shape in the abrasive fluid. It was found that laser clad WC particles provided increased wear resistance when crushed. In the same study by Huang et al. abrasive wear resistance of tungsten carbide nickel ($WCNi$) clad layers was five to ten times higher than that of the unclad steel substrate (240).

Laser cladding was successfully used to increase erosion-corrosion wear resistance of balance plates in underground mining slurry pumps using a nickel-based alloy on a steel substrate. Flame spraying was previously used in the components studied, however laser cladding provided lower porosity and dilution and a finer grain structure (241).

Supersonic laser deposition using a cold spray process improved bonding at lower velocities due to the heat energy from the laser Stellite 6 on low carbon steel tubes. This process, similar in nature to *HVOF* resulted in no cracks, low porosity, high bond strength, no damage or distortion and improved wear resistance comparing with laser cladding (242).

As part of the present study, to compare the weld and laser cladding processes similar examination of the resulting microstructure was undertaken.

Figure 8.2 shows an example of the metallurgical samples prepared. This figure illustrates a much smaller *HAZ* than in the case of an Inconel 625 6 mm weld clad layer, upon measurement indicating the depth of the *HAZ* was 1 mm. A 17-4 PH 2 mm clad layer, as shown in figure 8.2, was found to result in a *HAZ* of approximately 1 mm. In contrast, in chapter 4 it was shown that the weld clad cases presented *HAZ*'s of 5-6 mm, in the region of the clad layer thickness. Therefore the laser cladding process allows the conclusion to be drawn that in this case the depth of the *HAZ* is not related to the clad layer thickness, resulting in smaller *HAZ*'s due to the lower heat input in the laser cladding process. This is also due to the 6 mm layer being built up in smaller layers hence less heat input compared with for example a larger laser depositing 6 mm in one go. This conclusion could be drawn for both the deposition of Inconel 625 and 17-4 PH using the laser cladding process due to similar methods of powder deposition in both cases. These smaller *HAZ* regions are beneficial in that it is in this region that the material properties of the substrate will be altered due to the cladding process. The ability to control the heat input is a significant parameter in controlling the microstructure in the clad and *HAZ*, which can be a significant advantage in ensuring desirable material properties and microstructure.

The fusion boundary was of interest to draw conclusions as to the adhesion between substrate and clad materials. The fusion boundary was examined in all clad cases with good fusion generally resulting as can be seen in figure 8.3. Alloy rich and alloy lean areas were again observed post-cladding due to the application of preheat and interpass temperatures slowing the cooling rate to encourage diffusion of chromium and nickel in the *HAZ*. Therefore minimising the time at temperature requires balancing with the need to prevent cracking. As previously highlighted, and illustrated left in figure 8.4, this will result in variations in hardness values and therefore ductility in the *HAZ* and ultimately fatigue performance of the cladding

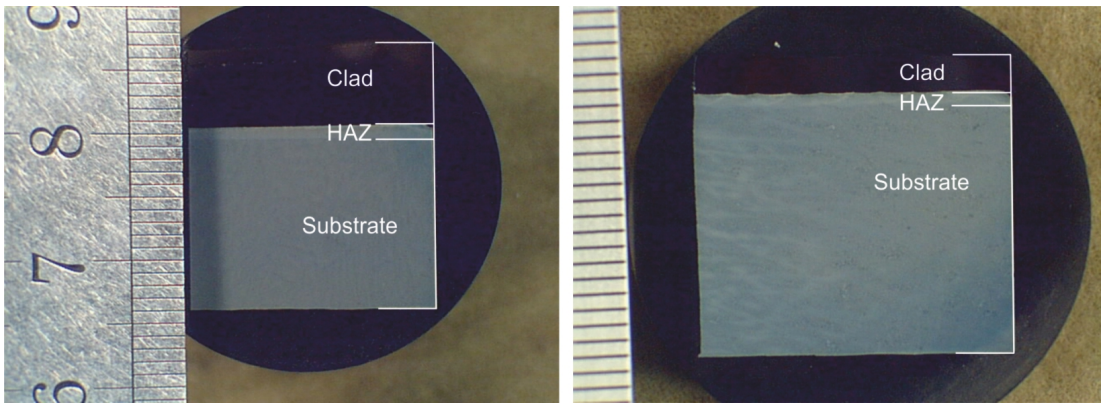

Figure 8.2: Macro section of laser clad specimen with clad layer depth of 6 mm (left) and 2 mm (right) - Showing a 4330 substrate laser clad with Inconel 625 (left) and 17-4 PH (right), both producing a thin HAZ.

and the component on the whole. Examination of the level of dilution of iron in the Inconel 625 clad samples highlighted that the laser cladding process resulted in a lower iron dilution from the substrate into the clad, beneficial from a corrosion perspective as was previously discussed with regards to a maximum dilution level of 5% iron at the surface recommended.

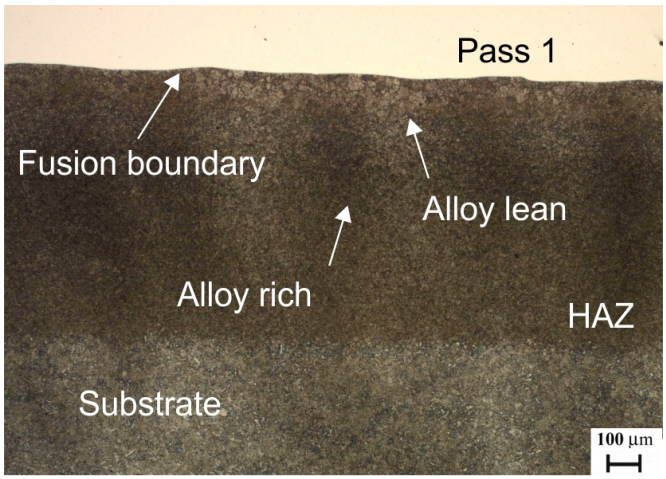

Figure 8.3: Micro section of Inconel 625 laser clad - Figure showing first clad pass, fusion boundary, HAZ with alloy rich and alloy lean areas and substrate material.

Hardness values were obtained to investigate the effects of alloy segregation on material properties using a Vickers diamond indenter with a 200 gram load. Alloy segregation in the *HAZ* gives rise to variations in hardness values in alloy rich and alloy lean areas as highlighted in the right-hand side of figure 8.4. Higher hardness levels are observed in alloy rich areas and lower hardness levels in alloy lean areas. This is in agreement with the findings in weld clad specimens. Areas of alloy segregation were more pronounced in the weld clad specimens, shown left in figure 8.4. Less pronounced alloy segregation in the laser clad specimens is thought to be due to the

decreased heat input compared with the weld cladding process, again the thickness of the substrate geometry slowing the cooling rate by acting like a heat sink.

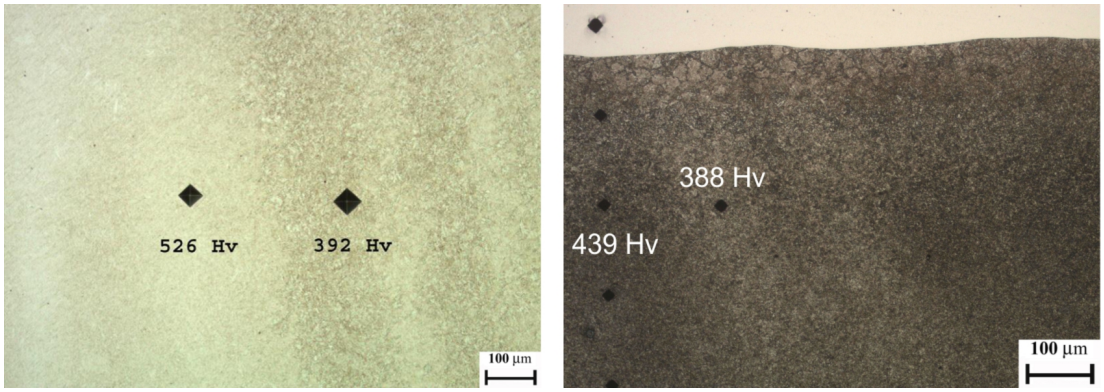

Figure 8.4: Hardness variation in HAZ of weld (left) and laser (right) clad specimen - 4330 substrate laser clad with Inconel 625. Measured using a Vickers diamond indenter with a 200 g load.

Hardness measurements obtained in the case of a 2 mm and 6 mm Inconel 625 laser clad layer deposited onto 4330 *HAZ* are illustrated in figures 8.5 and 8.6 respectively. The effects of the cladding process in increasing hardness levels in the *HAZ* can be observed in both cases, with the depth of the *HAZ* uninfluenced by the thickness of the clad layer. Slightly higher hardness values are observed in the *HAZ* when depositing a 6 mm clad layer.

In both cases the *HAZ* can be seen to be around 1 mm, much smaller than the weld clad specimens as previously mentioned. This may or may not be desirable depending on the resulting effects on material properties and microstructure. An abrupt change in material properties can give rise to a large discontinuity stress, which has been an area that has been heavily discussed herein as requiring elimination. Minimising the diffusion of chromium from the Inconel 625 *HAZ* into the substrate material would be required in both the weld cladding and laser cladding processes to ensure the most favourable *HAZ* properties and prevent the formation of brittle martensite. The consequential effects on residual stresses must of course also be considered. Hardness levels are higher in the case of a 6 mm clad layer due to the additional heat input required to deposit the larger amount of material.

Weld defects were observed in the Inconel 625 specimens. Regions containing impurities at the fusion boundary were observed, highlighted by the dark regions in figure 8.7. These dark regions show the presence of oxides at the fusion boundary due to these impurities. To eliminate this, the laser cladding process would require refinement to ensure a clean substrate upon which deposition takes place and during the deposition process, the shielding gas should be maintained to provide protection from oxide formation. The occurrence of these impurities were found at the surface

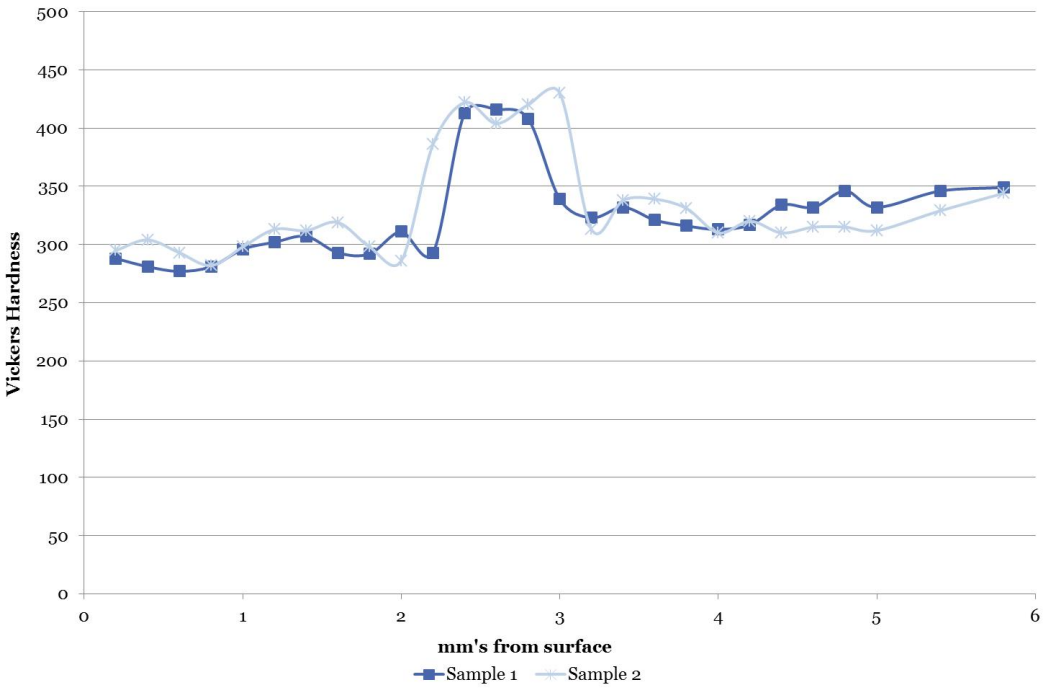

Figure 8.5: Hardness variation in 2 mm Inconel 625 clad layer and 4330 HAZ - Increase in hardness observed upon entering HAZ.

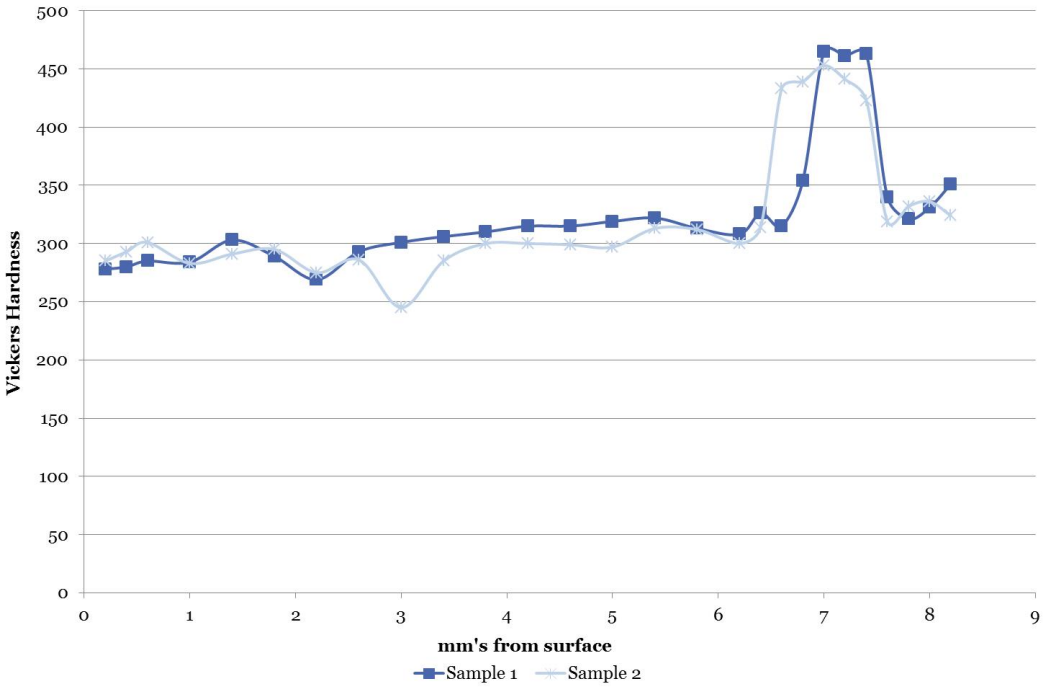

Figure 8.6: Hardness variation in 6 mm Inconel 625 clad layer and 4330 HAZ - Increase in hardness observed upon entering HAZ.

of the 17-4 PH clad and therefore it was concluded that the process utilised to deposit the 17-4 PH clad material provided a more beneficial clad.

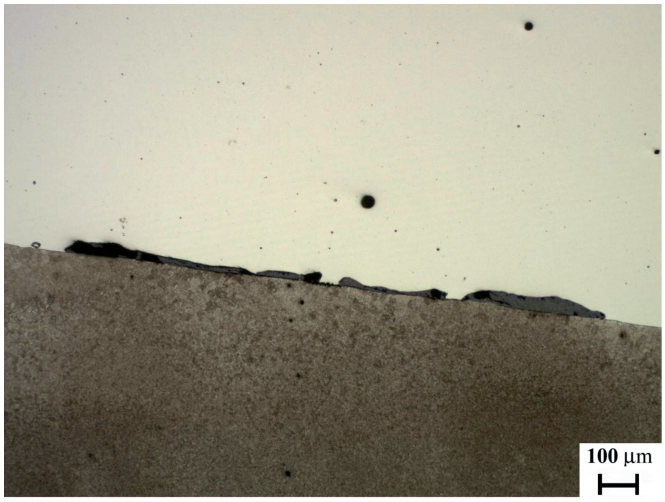

Figure 8.7: Impurities in laser cladding - Impurities present at interface of Inconel 625 laser clad layer and 4330 HAZ. Magnification factor: x50.

Inspection of the clad passes revealed the presence of the same interstitial impurities due to the cladding process as shown in figure 8.8. The spherical nature observed in this figure indicate that formation of these defects occurred during the liquid phase. Chemical analysis of these impurities using a tungsten filament scanning electron microscope (*SEM*) with energy dispersive spectroscopy capability confirmed that these were indeed the presence of oxides in both the Inconel 625 and 17-4 PH clad specimens.

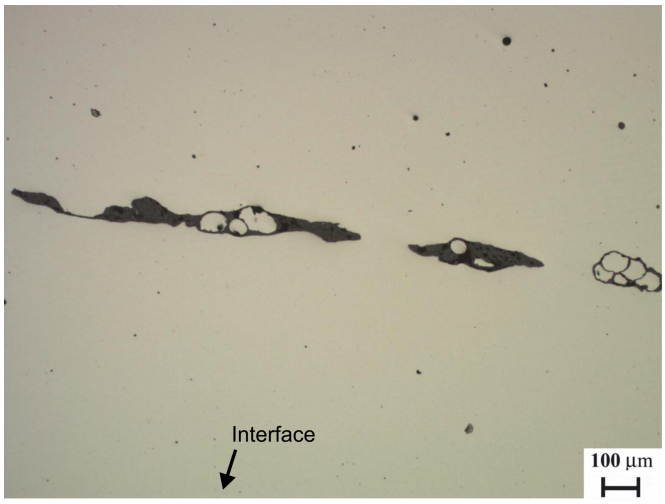

Figure 8.8: Interstitial impurity between clad passes - 6 mm Inconel 625 clad layer deposited using laser cladding process. Magnification factor: x50.

The *HAZ* is clearly observable in the 17-4 PH laser clad specimen shown in figure 8.9, with variations in microstructure arising in the substrate material local to the clad layer and further from the clad layer. Regions of very slight alloy segregation

are also present although not as extreme as in the weld clad specimens or the Inconel 625 laser clad specimens.

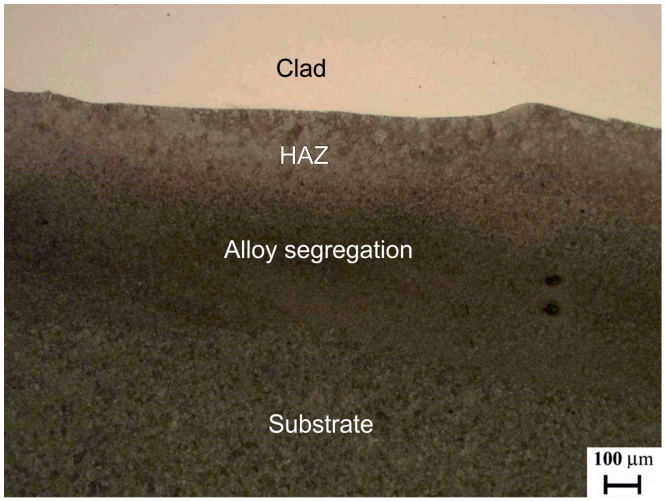

Figure 8.9: Micro section of 17-4 PH laser clad - Figure showing first clad pass, fusion boundary, HAZ with alloy rich and alloy lean areas and substrate material. Magnification factor: x50.

Grain growth is observed in the *HAZ* of a 17-4 PH laser clad specimen due to the material experiencing a high temperature for a prolonged period of time in comparison with the region of the substrate further from the clad layer (figure 8.10).

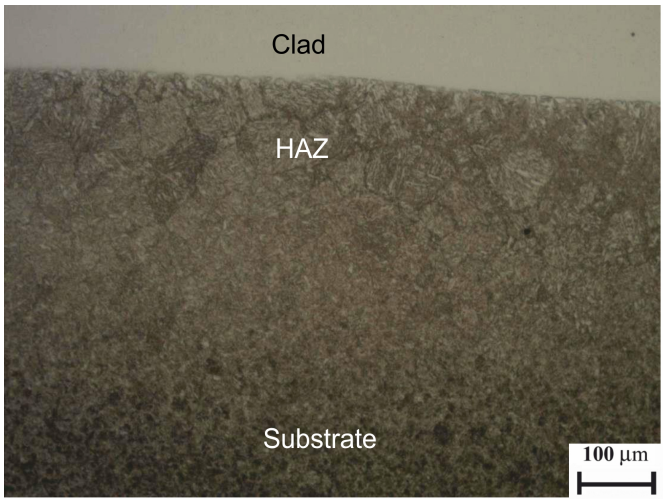

Figure 8.10: Microstructure of 17-4 PH laser clad 4330 HAZ - Differing grain structure in HAZ and unaffected substrate material clearly observable. Magnification factor: x100.

The large increase in hardness values observed upon entering the *HAZ* from the Inconel 625 clad layer is not observed in a 17-4 PH clad which will be beneficial in eliminating discontinuity stresses as abrupt microstructural and property variations in turn result in abrupt variations in stress. Figures 8.11 and 8.12 show that hardness measurements obtained for both clad layer thicknesses generally remain in the same region in the clad layer and *HAZ*. A sharp increase in hardness is observed in one

measurement in the *HAZ* in figure 8.11, which is undesirable due to the increase in brittleness of the material and associated reduced toughness.

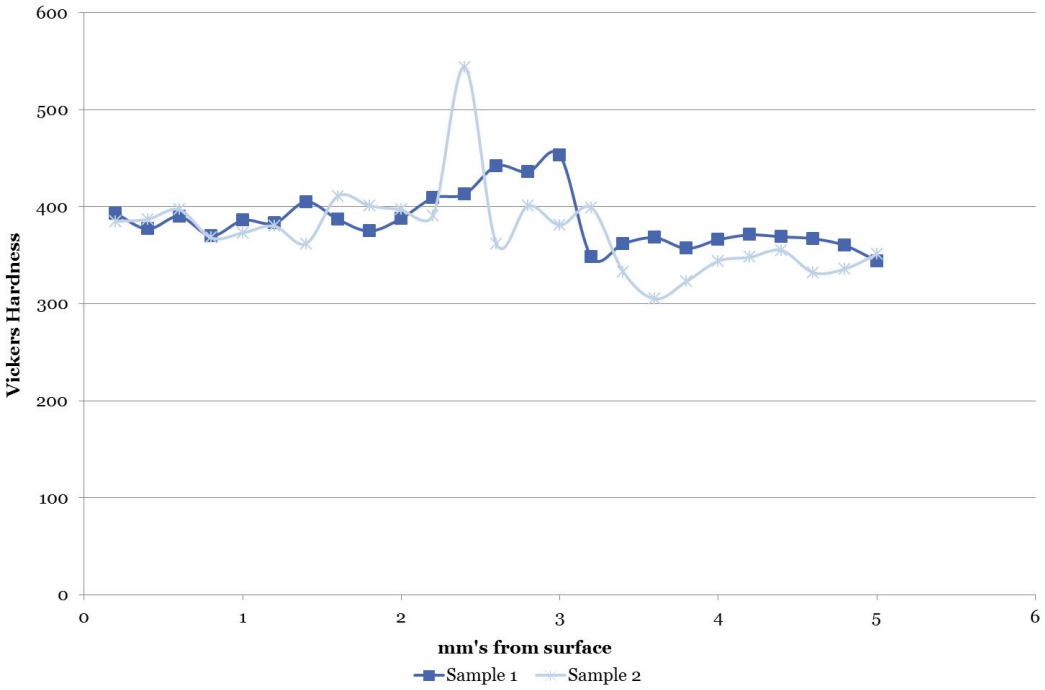

Figure 8.11: Hardness variation in 2 mm 17-4 PH clad layer and 4330 HAZ - Increase in hardness observed upon entering HAZ.

Hardness values for both clad materials have been observed to be similar to those obtained for weld clad specimens in figures 4.48 and 4.49.

Controlled cooling was used during the weld cladding process, presenting the potential to tailor the resulting microstructure and level of martensite formed as discussed in section 7.2. In the laser cladding process, controlled cooling was not implemented and therefore this would be an area worthy of further investigation with a view of lowering the hardness values and producing a more favourable microstructure. Post-weld heat treatment could also be investigated, as it was shown in weld clad specimens that this encouraged increased homogeneity in the *HAZ*.

8.3.1 Functionally graded cladding

The cladding technology would further benefit from a decrease in discontinuity stresses, possible through alteration of the process to a functionally graded deposition (243). The ability to modify as required the thickness of the clad layer and the individual layers creating the clad can also allow optimisation of material properties. In this way, ratios of substrate and clad materials could be utilised such that a gradual transition occurs from the substrate material to the clad material. Sub-surface discontinuity stresses would be reduced without removing the benefits of the compressive

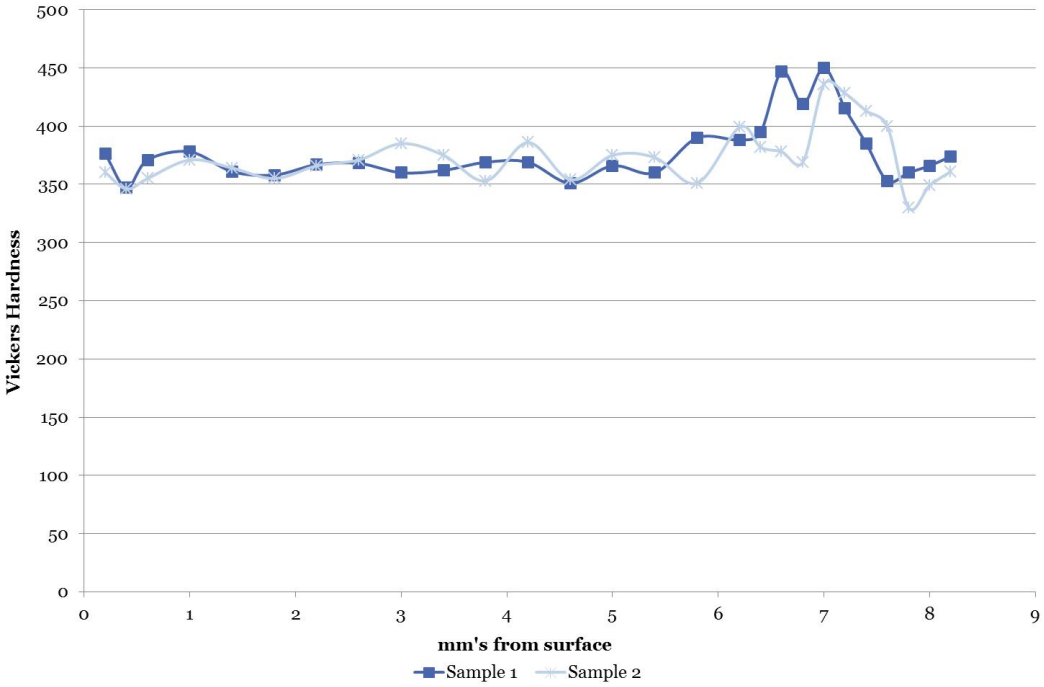

Figure 8.12: Hardness variation in 6 mm 17-4 PH clad layer and 4330 HAZ - Increase in hardness observed upon entering HAZ.

residual stresses arising in the clad layer hence possibly improving fatigue performance. Functionally graded, or multi-layer coatings, have also shown advantages in providing erosion and corrosion resistance such as the reduction of the total wear rate by half when a chromium-nickel/chromium multi-layer coating created by sputtering over stainless steel was implemented compared with bare stainless steel (244). A titanium nitride/titanium coating of total thickness 25 μm was deposited using physical vapour deposition using various layer thicknesses and ratios of materials to improve dry erosion performance in steel turbine components (245).

8.4 Comparing weld and laser clad surfaces

Surface roughness influences fatigue life in terms of potential crack initiation sites and stress-raising regions. Furthermore, corrosion and erosion performance can also be influenced by surface roughness, a rougher surface increasing susceptibility to erosion and corrosion. Weld and laser clad surfaces were examined to enable a comparison between the *as-clad* surfaces to be conducted. Such information also allows post-cladding processes to be determined, for example machining of the clad profile if necessary.

Weld and laser clad specimen information is detailed in table 8.1. This table highlights that laser cladding was undertaken utilising similar temperatures to the weld

cladding process. As these temperatures are similar it allows the influence of solely the cladding process to be deduced.

ID	Cladding Process	Material	Clad Depth (mm)	T_{PH} (°C)	T_{Int} (°C)	Controlled Cooling
LC 625 2	Laser	Inconel 625	2	150	300	No
LC 625 6	Laser	Inconel 625	6	150	300	No
LC 174 2	Laser	17-4 PH	2	150	300	No
LC 174 6	Laser	17-4 PH	6	150	300	No
WC 625 3	Weld	Inconel 625	6	300	400	Yes
WC 174 4	Weld	17-4 PH	6	300	400	Yes
WC 625 5	Weld	Inconel 625	6	150	250	Yes
WC 625 7	Weld	Inconel 625	6	150	250	Yes+PWSR
WC 174 8	Weld	17-4 PH	6	150	250	Yes+PWSR

Table 8.1: Weld and laser clad specimen information

Measurements of the arithmetic average R_a and the maximum profile height R_y were carried out using the Mitutoyo Surftest SV-2000, shown in figure 2.14. Measurements were obtained parallel and perpendicular to the weld direction on the clad surface. The values plotted for all cases in figures 8.13-8.15 are the average values resulting from three measurements.

Weld cladding with Inconel 625 produces overall a less rough surface, with R_a values less than those for laser cladding as shown in measurements parallel (figure 8.13) and perpendicular (figure 8.14) to the weld direction. In contrast, laser cladding with 17-4 PH produces a smoother surface, particularly parallel to the weld direction. Laser cladding with Inconel 625 produces higher R_a and R_y values compared with laser cladding with 17-4 PH, both parallel and perpendicular to the weld direction.

Surface profile measurements were also obtained for all samples in terms of R_a and R_y. Figure 8.15 illustrates that for the materials and process parameters used the majority of measurements obtained for the surface profile of laser clad samples possess similar surface profile values. This is advantageous in that uniformity of the surface profile ensures that regions of stress concentration are not present, critical for component operation. Measurements obtained for Inconel 625 clad layers show that laser clad samples have higher R_a and R_y values than weld clad specimens. Comparing samples weld and laser clad with 17-4 PH shows that laser cladding provides smaller R_a and R_y values, with the most extreme case signalling an R_y value in a 17-4 PH weld clad sample almost twice the laser clad values. The clad profile resulting from

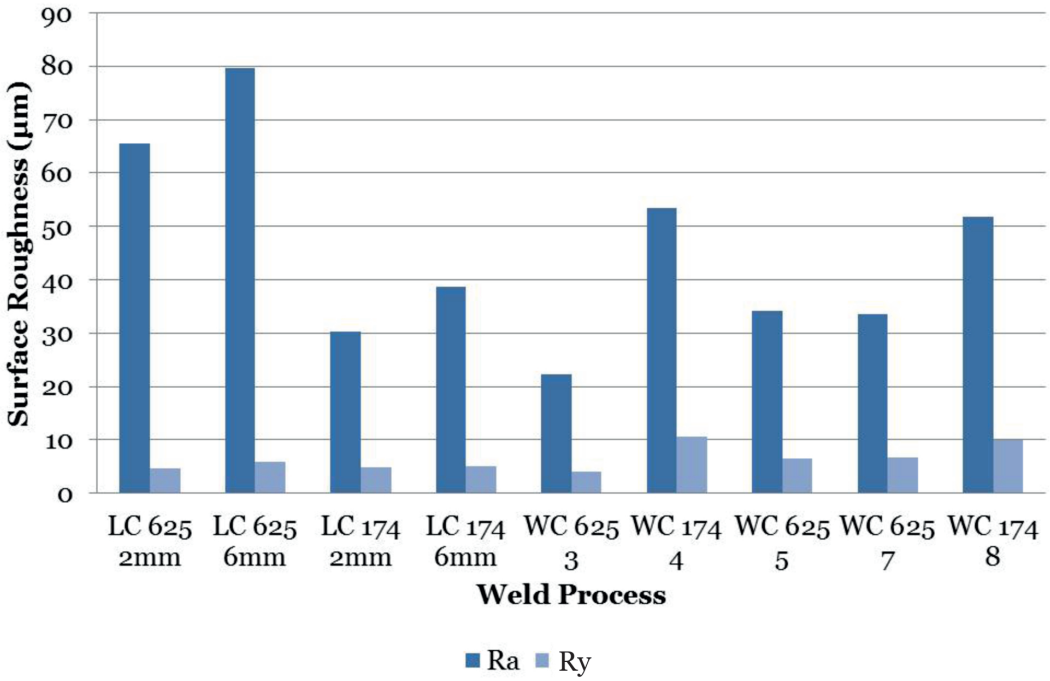

Figure 8.13: Surface roughness parallel to weld direction - Comparison of surface roughness measurements of weld and laser cladding of Inconel 625 and 17-4 PH.

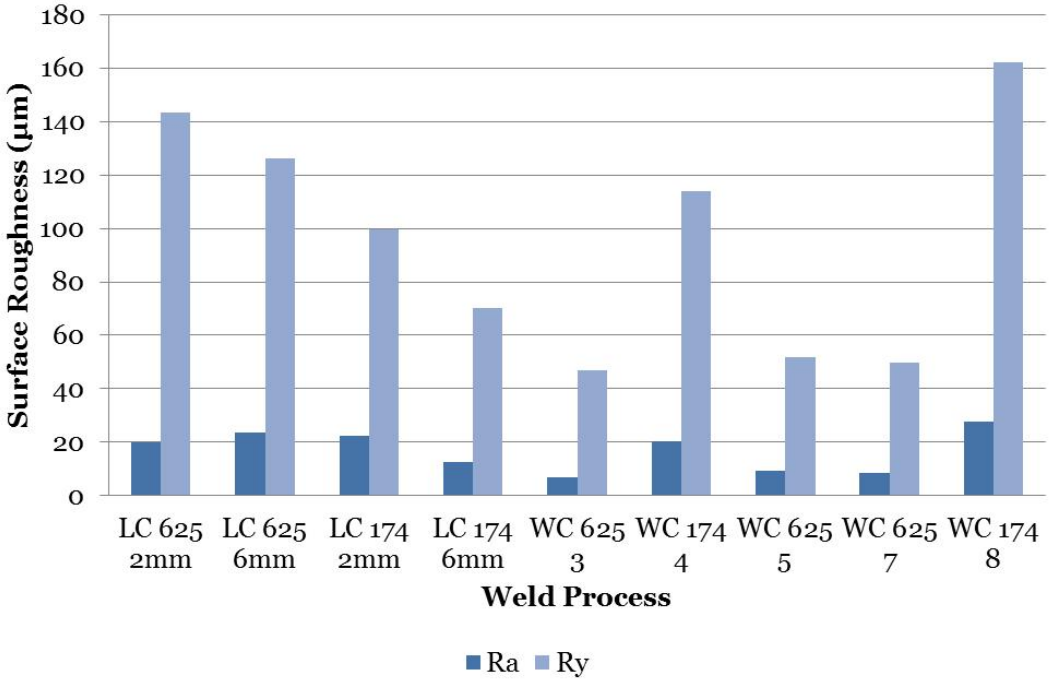

Figure 8.14: Surface roughness perpendicular to weld direction - Comparison of surface roughness measurements of weld and laser cladding of Inconel 625 and 17-4 PH.

the laser cladding process was found to be more uniform when cladding with 17-4 PH compared with Inconel 625.

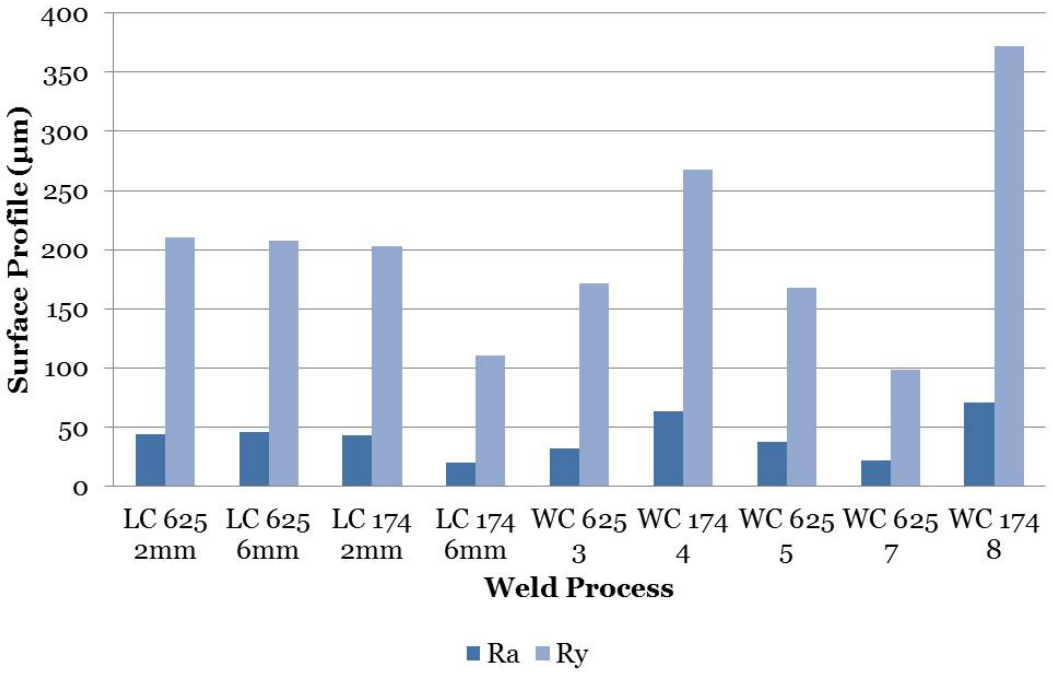

Figure 8.15: Surface profile of clad specimens - Comparison of surface profile measurements of weld and laser cladding of Inconel 625 and 17-4 PH.

Clearly the above investigation applies to the *as-clad* state. It is unlikely that the component would be left in the *as-clad* state prior to application for fatigue demanding applications or flow applications. Smoothing of the clad profile is likely to occur. The data obtained through these measurements then also provides an indication of the level of material removal required to obtain a smooth surface. From this point of view then it would also be preferable to obtain the smoothest surface for minimal material removal. However material removal levels for all cases are in the micron range and therefore this should not present insurmountable problems in many cases. Final *puddling* runs of reheating the clad material can be implemented with the aim of creating a smooth final layer. From a machining point of view however, a more uniform surface profile, as obtained through laser cladding with 17-4 PH, allows material removal across the component to be assumed to be more uniform in comparison with a greatly varying surface profile.

8.5 Residual stress measurement

Experimental residual stress measurements presented in chapter 6 concluded that in weld cladding with Inconel 625 tensile residual stresses were obtained in the clad layer, while weld cladding with 17-4 PH compressive residual stresses were obtained in the clad layer. For the purpose of the fatigue-resistant cladding technology, the 17-4 PH clad material was therefore favoured and in this section focus will be placed on investigating the residual stress distribution arising when laser cladding with 17-4 PH.

Residual stress measurements were obtained using the contour method on the block laser clad with a 6 mm layer of 17-4 PH. This was then compared with residual stress measurements obtained on the block using *ICHD*, as described in section 6.2.1.1.

8.5.1 Contour method

The contour method was briefly introduced in section 6.2.1. This destructive method of residual stress measurement was first introduced by Prime in 2001 (191), based on Bueckner's elastic principle of superposition. This principle considers a cracked body subject to external loading or prescribed displacements and relates forces applied to the cracked surface to close the crack as equivalent to the stress distribution present in the body in an uncracked state, if of the same geometry and experiencing the same external loading.

Figure 8.16 illustrates the contour method procedure. A component unsectioned contains residual stresses σ_x as shown. This component is sectioned normal to the stress component of interest to result in two equal halves and a stress-free cut surface. The component is sectioned in such a way that the cracked body results in a manner as close to brittle fracture as possible i.e. the sectioning procedure does not introduce further residual stresses due to, for example, cold work or heating.

This method is advantageous in that it allows measurement of a two dimensional stress map of a component over the entire cut section (194). The component can be of simple or complex geometry. The contour method measures type I, or macro stresses, as described in section 1.2.

Sectioning the component In terms of the cut conducted, minimal and consistent material removal is desirable in addition to a flat surface and the avoidance of further residual stress. This is most commonly achieved using an *EDM* process, described in section 4.4.1. Submergence of the component in water prior to cutting ensures the minimisation of thermal effects due to the process. The residual stress state of the

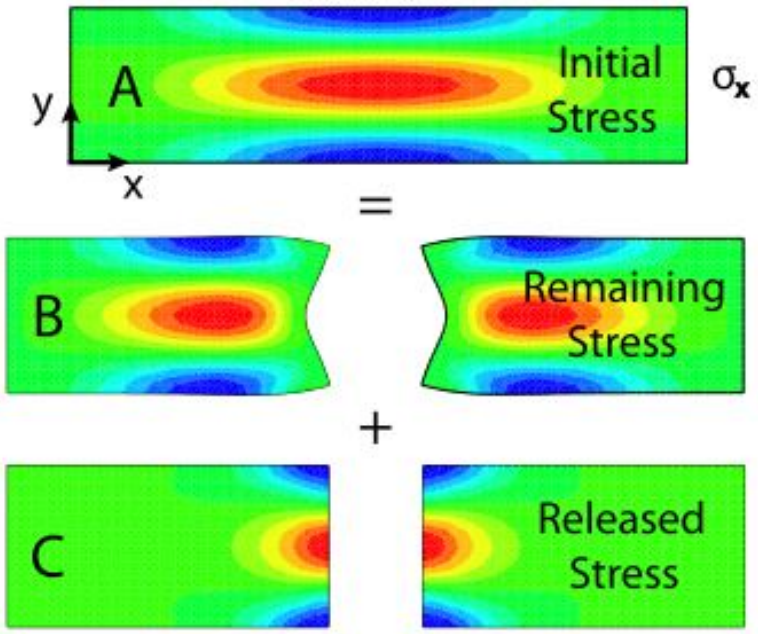

Figure 8.16: Contour method procedure - Figure as presented in (246).

component can influence the cutting procedure, in that the presence of compressive residual stresses can encourage the closing of the cut surfaces after cutting.

Constraining the component Stress relaxation due to the machining process means that the assumption of consistent material removal in sectioning the component is likely to be inaccurate. To minimise the movement of the specimen due to the *EDM* process, it is crucial that the component is appropriately constrained and the cut is conducted such that the wire does not experience jamming. Clamping of the specimen is clearly dependent on the specimen geometry. However, clamping requirements differ from ordinary machining requirements in that both sides of the component should be clamped to ensure that both halves are adequately supported and symmetry remains throughout the process to minimise errors due to the cutting process. This has been highlighted by Bouchard et al. in (247) in a study of various clamping procedures both experimentally and using finite elements simulations. If the clamping procedure does not allow the maintenance of symmetry, variations in shape of measured contours can arise and this will then be carried into the process of averaging and ultimately affecting the resulting measured residual stress distribution.

Measuring distortion Following the *EDM* cut, distortion of the cut surfaces is measured, commonly using a coordinate measurement machine (*CMM*). Laser scanning can also be utilised (248). The accuracy of this measurement is crucial as the data obtained in this step is the raw data that ultimately provides the calculated stress

distribution. It is also dependent upon the complexity of the residual stress distribution to be measured. The number of points, or knots, available for a spline fit influences the accuracy of the resulting stresses. Increasing knot density enables better data fitting. A surface is fitted to the raw data obtained most often and most successfully using polynomials, in particular polynomial splines.

This later allows the production of the stress map. Measurement can be undertaken either *continuously* or in a *pecking* manner. If *continuous*, the probe moves along the surface without retraction from the surface. If *pecking* the probe is raised following each point, producing higher accuracy.

Although the procedure of cutting and measurement of surfaces is simple, the later processing of the data can be complex, with results sensitive to the method applied in this stage.

Data processing Reduction of errors is carried out by investigation of the data and removal of data considered noise, that is data capable of impairing the interpretation of real data. This can be for example data points that clearly lie out with the range of the majority of the data obtained or data points that may be affected by inaccuracies in the experimental procedure. This is commonly undertaken manually or in more complex cases through the use of a script to allow quicker data cleaning. It must be ensured that removal of data points does not remove levels of data to the extent that the data set is no longer representative.

Further data *enhancement* is carried out by processing both cut surfaces and averaging the results so that mirror images of residual stresses are produced. Data obtained on each surface is aligned through defining one surface as the reference surface and aligning the other through mirroring onto the reference surface. This results in both data sets possessing the same global coordinate system and allows the averaging process to commence.

As contour measurements provide information solely regarding the deformation in a direction normal to the cut surface, only these normal stresses can be obtained. The normal stress may or may not be a principal stress, depending on whether the cut plane is a principal plane. Without the in-plane stresses it will not be possible to obtain the principal stresses. To reduce error in measurement, the contours measured are averaged for both surfaces in the case of the presence of shear stresses to allow only the determination of the normal stress (191).

Data must be examined and smoothing and noise removal carried out prior to averaging. This also applies for surface roughness effects.

To cater for the fact that data obtained through the measurement stage is unlikely to correspond with the nodal locations of the finite element model later utilised, a surface is fitted to the measured data post-averaging. This then provides nodal displacement values in the finite element model which are utilised as the boundary conditions in the finite element model i.e. to push the surface back to flat. Using contact surfaces is an alternative way of doing this that avoid large numbers of individual nodal displacements.

The application of polynomials to discrete regions of smoothed data sets ensures that areas of varying stress levels are accounted for providing an accurate representation of the data. This polynomial spline fitting technique combines the fits to each area to provide a complete curve fit.

Obtaining the stress distribution Residual stresses are released in sectioning the component and these stresses normal to the cutting plane can be obtained through considering the reverse of the cutting process and resulting deformation due to the sectioning process. Deformation contours are measured on both cut surfaces. If the face distorts in-plane and this is not captured and included in this process, this will also result in an unknown error in estimating the normal residual stress.

The cut surface can be forced back into its original planar form to obtain the original residual stress distribution. If the assumption is made that the material behaves elastically throughout the stress relief process then with reference to the stresses in figure 8.16, stresses in the initial step A are equal to the sum of those in steps B and C post-sectioning. As the free surface normal and shear stresses must equal zero (B), the stresses σ_x on the cut plane are equal in cases A and C.

A finite element model of the cut surface is created in the stress-free state and the measured contour of the relaxed surface applied to the cut plane using as model boundary conditions the reverse of the coordinates measured to allow the surface to adopt the original flat surface or contact used to push the surface flat (249). In this process, the deformation at each node in the finite element model is evaluated. This finite element model then provides the stresses resulting from the displacement of the cut surface from the flat to the deformed states and these resulting stresses are those residual normal stresses present in the component prior to the performance of the cut.

Validation of the contour method has been often undertaken comparing with other methods of residual stress measurements, such as neutron diffraction and *XRD* (250).

8.5.1.1 Cladding considerations

The contour method assumes that the cut performed possesses a constant width throughout. Due to the variation in stresses, particularly in the vicinity of the join, it is unlikely that this will be the case. The bulge error arises due to the material deformation occurring due to stress relaxation at the location of the cut. Therefore it is likely that such errors will impact results, affecting the results of the obtained stress distribution.

In undertaking the scanning of the surfaces, the component edges must be determined. This can be difficult but especially so in the case of the laser clad components, as the clad surface in particular will present a surface that is not uniform. Manually determining surface edges must be carried out as accurately as possible to ensure the most accurate outline of the specimen.

Additional assumptions to allow this method to be applied are that the cutting process does not influence the deformation contours obtained and induce stresses large enough to require accounting for in the stress calculation procedure and also that the cut plane is assumed to be originally flat (251).

8.5.1.2 Results

Residual stresses were obtained using the contour method on the specimen laser clad with a 6 mm clad layer of 17-4 PH. A representation of the specimen and the cut plane is shown in figure 8.17.

Measurements were obtained at varying knot spacings. This allowed the effects of knot spacing to be deduced and allowed surety in the general residual stress distribution obtained. Surface measurements must be carefully considered as it is in this region that discrepancies in measurement can affect the residual stress distribution obtained. Should these points be of concern, they should be omitted from the data set. While surface stresses are obviously of interest, it should be noted that it is known that actual variations in residual stresses will inevitably result at the surface due to local geometry and heat transfer variables, commonly to referred to as edge effects. *ICHD* showed this to be the case. The contour method however will provide an insight into the residual stresses throughout the clad layer and across the clad-substrate interface.

The contour plots illustrating resulting residual stress distributions are shown in figures 8.18-8.20. It can be seen that the range in the longitudinal stress component decreases with increasing knot spacing. Increased detail in contours are likewise obtained with the smallest knot spacing of 1.5 mm (figure 8.18).

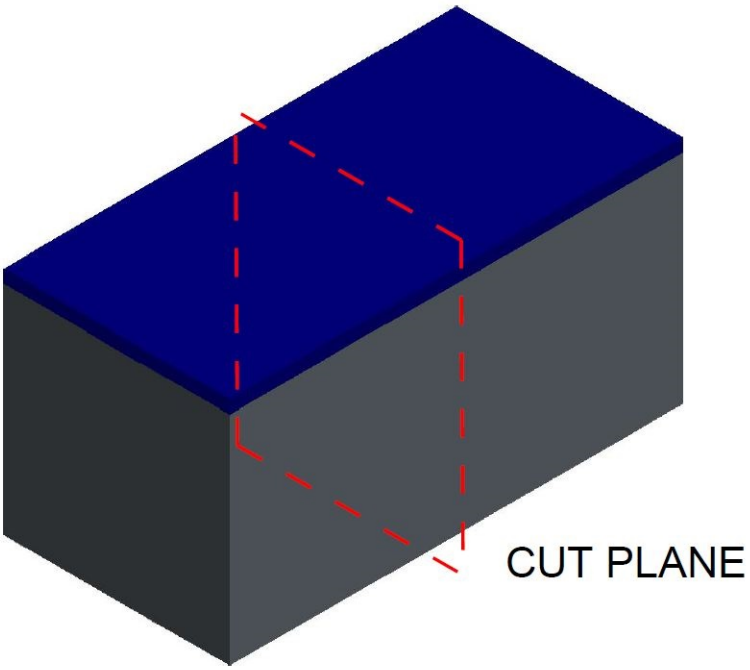

Figure 8.17: Laser clad block - Illustrating surface cut plane.

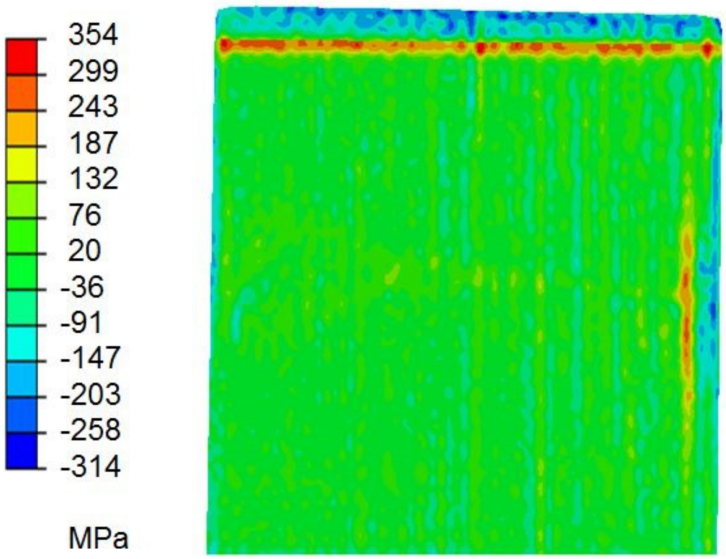

Figure 8.18: Stress contour plot using knot spacing of 1.5 mm - 4330 substrate laser clad with 17-4 PH. Results courtesy of the Open University.

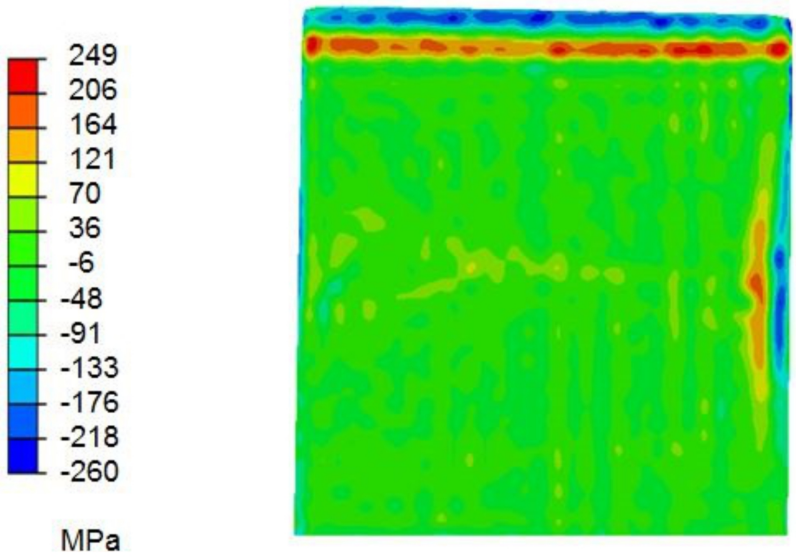

Figure 8.19: Stress contour plot using knot spacing of 3 mm - 4330 substrate laser clad with 17-4 PH. Results courtesy of the Open University.

In the case of a 5 mm knot spacing, the contours are seen to be much larger, unable to capture the detail evident in the previous cases.

The stress contour distributions in all three cases confirm the expected presence of compressive residual stresses in the 17-4 PH clad layer for a laser clad block. It also appears that the expectation of discontinuity stresses observed in the finite element model are in fact present in reality, shown by the presence of high tensile residual stresses in the vicinity of the join.

The presence of unexpected contours to the right of the specimen in the substrate material could be due to a cutting defect for example. This aligns with the wire direction and is visible in figures 8.18-8.20.

Figure 8.21 compares the longitudinal stress component with depth from the clad surface for the 1.5 mm spline, 0 mm being the clad surface. The highest compressive residual stresses are obtained at the clad surface, with the crossover into the tensile stress region in the vicinity of the interface. Stresses are then shown to fluctuate, remaining in the compressive region further into the substrate. Although not shown for clarity, the 3 mm and 5 mm spline results confirm the previous contour observations.

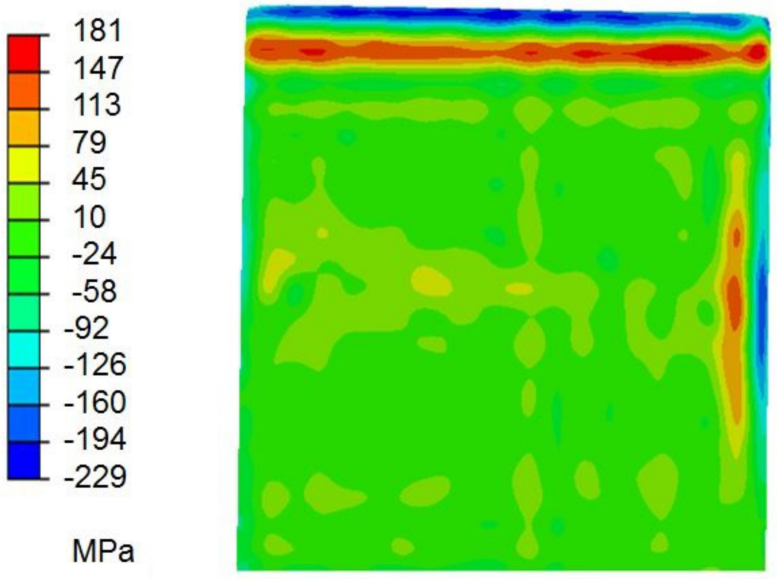

Figure 8.20: Stress contour plot using knot spacing of 5 mm - 4330 substrate laser clad with 17-4 PH. Results courtesy of the Open University.

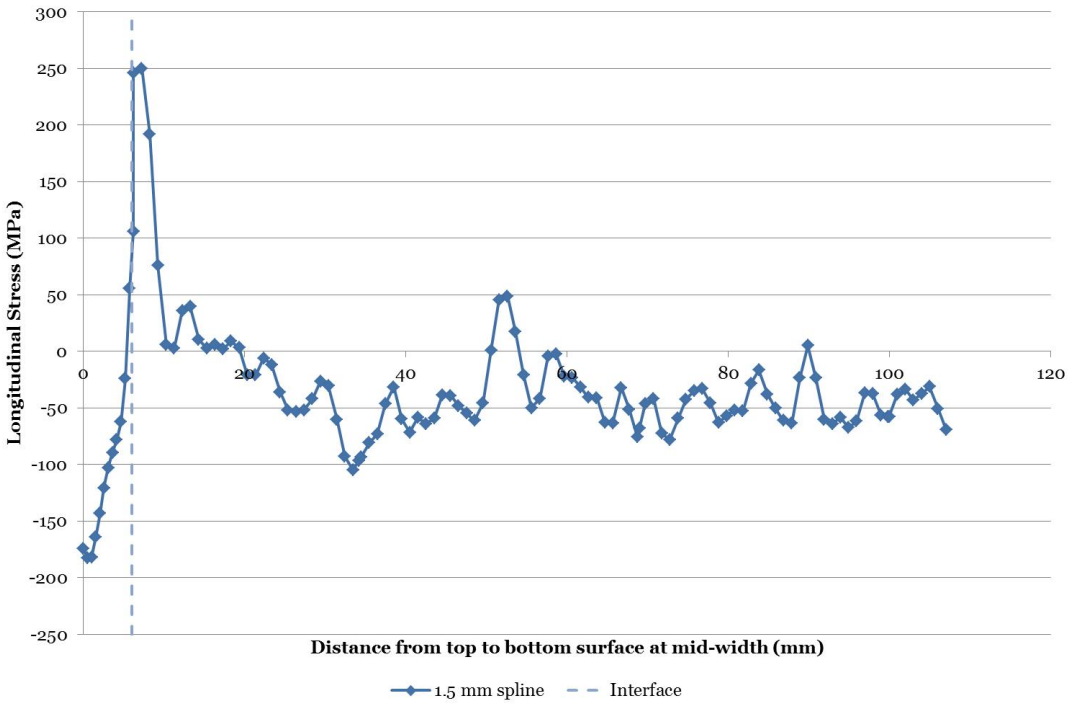

Figure 8.21: Comparison of longitudinal stress in laser clad block - 4330 substrate laser clad with 17-4 PH. Results courtesy of the Open University.

8.5.2 Comparing incremental centre hole-drilling and contour method measurements

Longitudinal stresses obtained through the *ICHD* method to a depth of 1 mm are presented in figure 8.22 alongside stresses obtained using the contour method. Both methods indicate the presence of high compressive residual stresses at the clad surface at the left-hand side of the figure. Higher levels of compressive residual stress are present in the *ICHD* measurement, the increase in stress towards the surface is thought to be, as previously discussed, due to machining effects. The number of measurements close to the surface in the case of the ICHD measurements is greater than those of the contour method. The contour method results have not captured the stress variation close to the surface, emphasising the need for complimentary measurement methods to enable the most accurate indication of the residual stress distribution throughout the component.

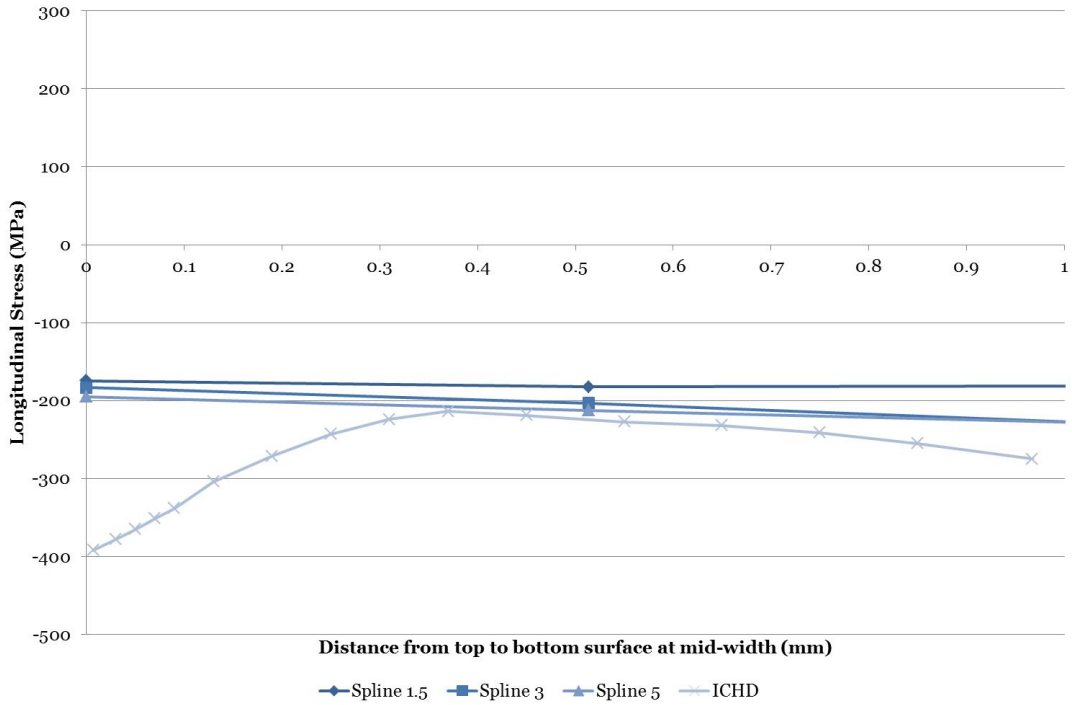

Figure 8.22: Comparing ICHD and contour method stresses to 1 mm depth - 4330 substrate laser clad with 17-4 PH. Results courtesy of the Open University.

Compressive residual stresses are shown in figure 8.23 to remain to a depth of around 5 mm into the clad layer where the transition to tensile residual stresses occurs as the interface is approached. The trend of increasing levels of compressive residual stress towards the center of the clad layer is captured by both the *ICHD* and contour method measurements.

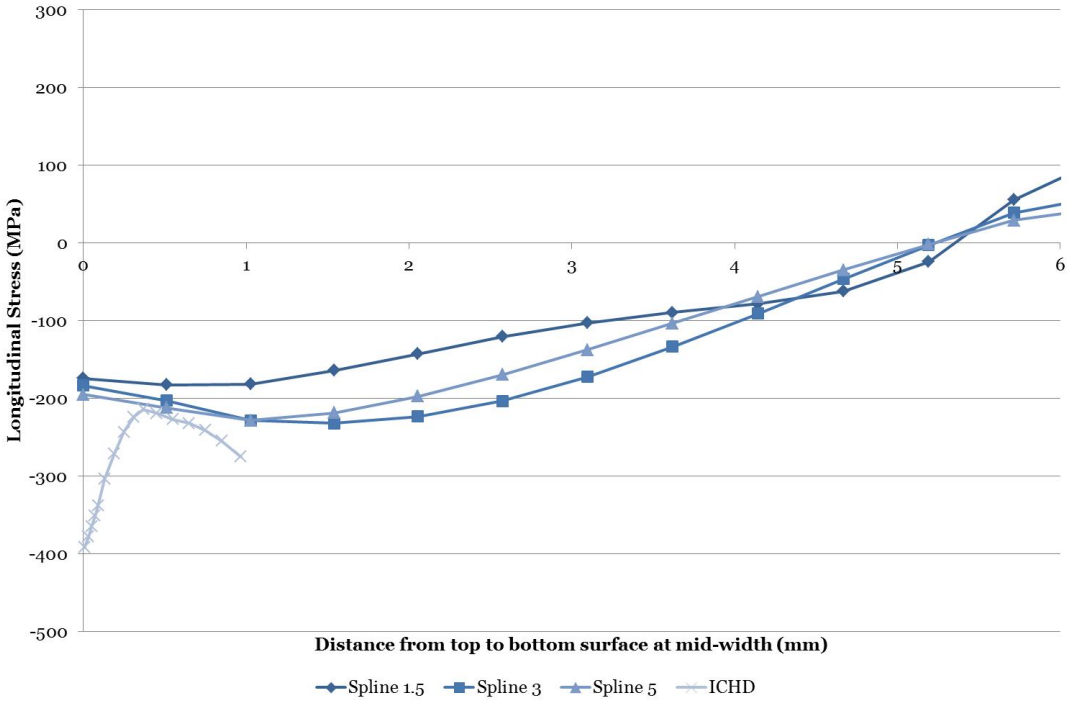

Figure 8.23: Comparing ICHD and contour method stresses throughout entire clad layer - 4330 substrate laser clad with 17-4 PH. Results courtesy of the Open University.

8.6 Summary

Laser cladding using Inconel 625 and 17-4 PH resulted in good fusion between clad and substrate materials. Impurities present due to the lower heat input during the laser cladding process differences in the depth of *HAZ*'s were observed in these specimens. The resulting microstructures and material properties due to these smaller *HAZ*'s should be examined carefully to ensure that damaging levels of discontinuity stresses do not arise. However, a smaller *HAZ* could be beneficial to minimise the alteration of the substrate material through the cladding process. The depth of the *HAZ*'s were found to be independent of the clad layer material and thickness, with 2 mm and 6 mm clad layer thicknesses investigated. This is thought to be due to the deposition of the clad layer in layers using the same heat input rather than deposition of the entire layer using a higher heat input for a thicker clad layer. Hardness values in the 4330 *HAZ* when cladding with Inconel 625 and 17-4 PH were found to be similar and this is also related to the heat cycle experienced by the substrate during the cladding process. Dilution levels were found to be lower in the laser cladding process compared with the weld cladding process. Material properties and microstructure are heavily dependent on the cladding parameters. Modification of the cladding parameters and the introduction of controlled cooling should be examined to refine the cladding process with further potential of the laser cladding process allowing a functionally graded transition, the goal being to achieve this without significantly

reducing any beneficial compressive residual stresses.

It appears that when cladding with Inconel 625 weld cladding provides a better surface finish. When cladding with 17-4 PH laser cladding provides a better surface finish. Therefore the surface roughness is dependent on both cladding process and material. Laser cladding with 17-4 PH resulted in the most uniform surface profile. This would be beneficial due to decreasing regions of stress concentrations, particularly crucial in component operation. Material removal levels to achieve a smooth finish are however in all cases in the micron range. It should also be noted that a smoother finish can always be achieved by a further *puddling* process, where the clad material is simply remelted.

Residual stresses were experimentally obtained for a 4330 substrate laser clad with a 6 mm clad layer of 17-4 PH. Contour method residual stress measurements were obtained through collaboration with the Open University. Both the *ICHD* and contour method measurements indicated the presence of high compressive residual stresses in the 17-4 PH clad layer. Good agreement was obtained between the measurements obtained using these methods.

ICHD measurements indicated that increasing the clad layer depth did not favourably increase compressive residual stresses. Significant compressive residual stresses were present in both a 2 mm and 6 mm 17-4 PH clad layer, though measurements were limited to 1 mm using the *ICHD* method. Therefore both from a stress state and an economical perspective there appears to be no advantage in depositing a deeper clad layer. However from an erosion and corrosion resistance perspective the deposition of additional material is favourable.

Varying knot spacings resulted in varying levels of accuracy in the residual stress distribution obtained using the contour method. This proves that the data processing step can heavily influence results and highlights the need for careful consideration of this step when using the contour method. The contour method also illustrated the presence of discontinuity stresses at the interface, with the presence of high tensile residual stresses at this location. This is in line with the residual stress distribution obtained in the finite element simulation and confirms the presence of discontinuity stresses in reality.

Chapter 9

Improving Fatigue Performance of Weld Clad Low Alloy Carbon Steel through Autofrettage

Autofrettage is investigated in an attempt to favourably modify the tensile residual stress arising through weld cladding in the Inconel 625 case. Finite element simulation models of autofrettage of weld cladding utilise a 4330 cylinder clad with Inconel 625 to provide the as-clad residual stress distribution. Autofrettage is applied to this weld clad component using two values chosen to ensure different degrees of yielding. The results indicate the potentially beneficial effects of autofrettage on the significant tensile residual stresses previously present in the Inconel 625 clad layer with high tensile residual stresses transformed into high compressive residual stresses. With the application of a high autofrettage pressure of 800 MPa compressive residual stresses exist to a depth of 18 mm, or 3 clad layer thicknesses, and discontinuity stresses are almost eliminated. Therefore autofrettage presents a method of improving the fatigue performance of 4330 weld clad with Inconel 625.

9.1 Introduction

The experimental cladding program and the simulation of the cladding process detailed in this thesis has provided a fatigue-resistant cladding technology. The application of such a technology requires in-depth understanding of the materials and processes utilised as has been discussed throughout. The focus on the generation of compressive residual stresses means that Inconel 625 is not as desirable as a clad material in the implementation of this technology. Therefore, consideration was given as to the possibilities of modifying the residual stress distribution arising when cladding with this material.

A 4330 low alloy carbon steel substrate material clad with Inconel 625 nickel-chromium-based superalloy has been shown to produce tensile residual stresses in the clad layer. This has been confirmed through both finite element models in chapter 5 and through experimental residual stress measurements in chapter 6. Therefore, although commonly used in industry, from a fatigue perspective this arising tensile residual stress state is undesirable. It has been highlighted that tensile residual stresses are commonly induced through many welding and machining processes. It is also common that maximum operational stresses occur at the surfaces of components.

Figure 9.1 shows the clad cylinder dimensions in millimetres and the associated axisymmetric finite element model. As discussed in chapter 5 it was this model upon simulating the weld cladding process using an Inconel 625 clad material and 4330 substrate that resulted in high biaxial tensile residual stresses in the clad layer and into the substrate. As has been highlighted throughout, the dissimilarity in materials results in a discontinuity stress at the interface. This stress can be significantly higher than the stress in the clad material which was shown to be the case in figures 5.5 and 5.6. Cracking may subsequently occur at this location depending on the combination of residual and operational stresses and the fatigue strength of the materials involved.

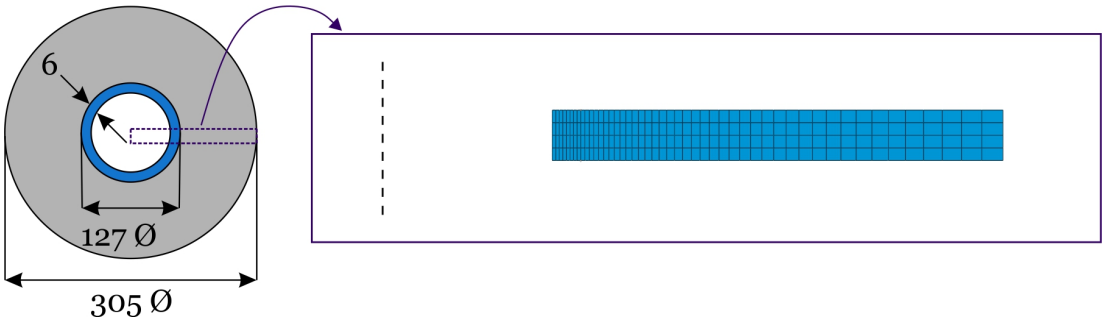

Figure 9.1: Internally clad cylinder axisymmetric finite element model - Dimensions in millimetres.

9.2 Modifying the residual stress distribution

In terms of the *NACE* International regulations (110), the use of Inconel 625 as a weld clad material presents no issues in compliance with the regulations as discussed in section 4.4.8. The beneficial properties of erosion and corrosion resistance provided by Inconel 625 are recognised and therefore post-cladding processes are investigated with a view to improving the residual stress state and ultimately the fatigue-resistance in the case of 4330 steel clad with Inconel 625.

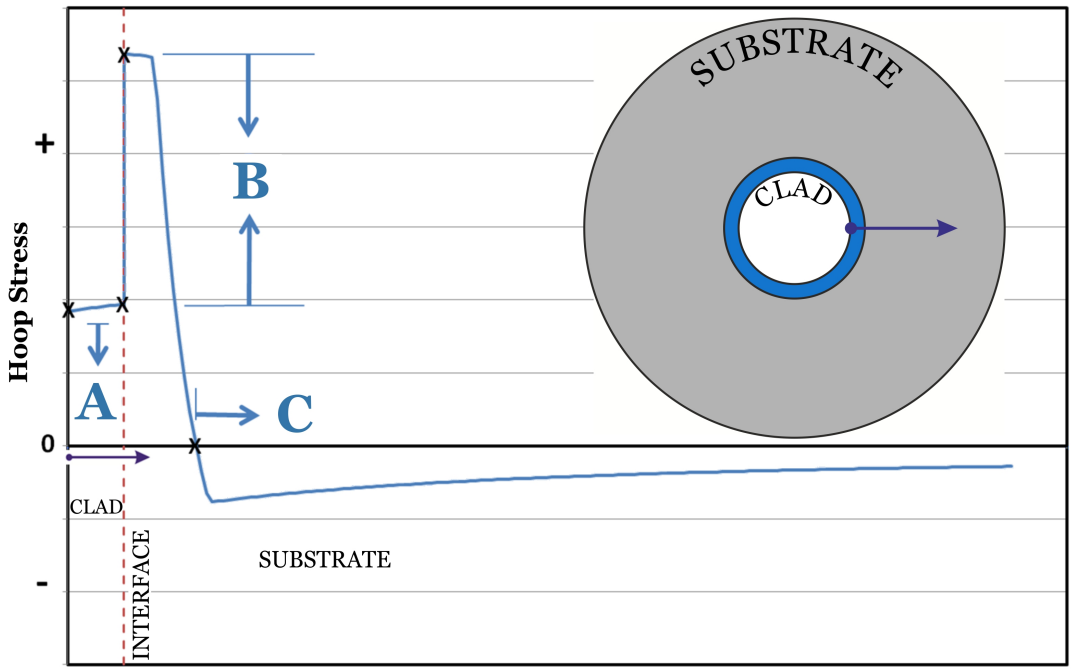

Figure 9.2: Elements of the fatigue resistant cladding concept - Diagram highlighting three characteristics of the obtained residual stress distribution for an Inconel 625 clad.

There are three characteristics of the typical *as-clad* residual stress distribution shown in figure 9.2 that could be modified in a manner that would improve the fatigue performance of the component:

> ***A***: Transformation of the tensile residual stress to a compressive residual stress, with as high a magnitude as possible, throughout the thickness of the clad. This would reduce the likelihood of surface cracks initiating and propagating, with this protection offered in an erosive/corrosive environment until the clad thickness has been removed.
>
> ***B***: Elimination, or at least a decrease in the level, of tensile discontinuity stress at the interface, leading to the reduction of the likelihood of cracks initiating and propagating at the interface between the clad and substrate.
>
> ***C***: Assuming that ***A*** is achieved, it would be desirable for the cross-over point between compressive and tensile residual stresses to be at as great a

depth as possible. While not as significant as ***A*** and ***B*** this would be desirable due to the reduction in crack initiation and propagation potential to a greater depth below the surface and interface. This would also provide protection to a greater depth in an erosive-corrosive environment.

To achieve these three goals, there are various operations that could be implemented depending on the whether this modification should take place in the design, process or post-cladding phase.

Weld and laser cladding investigations have confirmed that goal ***A*** can be achieved through careful selection of substrate and clad materials, with significant compressive residual stresses obtained using a 17-4 PH clad on 4330. Again this was confirmed through both simulation and experimental means in chapters 5 and 6 respectively. Altering process parameters allows further adjustment of the residual stress state in a clad component.

Goal ***B*** would be possible by grading the transition at the interface between the dissimilar materials. The number and thickness of transition layers is a variable that will be both application and process dependent. It is unknown at this point in time as to the effect such grading would have on goal ***A***.

Investigation of the effects of heat-treatment on the simulation model have demonstrated the potential to adjust the magnitude and depth of residual stresses through control of the rate of heat transfer in radial and axial directions in a thick-walled cylinder. The effect of this operation post-cladding is unknown, however. The possibility of generating compressive residual stresses at the surface of the clad component suggests that this would be worthy of further investigation, examining the effects such an operation would have on both the residual stress state and the metallurgy of the joint.

There are various post-cladding operations that could be utilised to impact goals ***A***, ***B*** and ***C*** to varying degrees. Shot peening, for example, is known to induce compressive residual stresses in a thin surface layer, which would therefore achieve goal ***A*** to some extent, however goals ***B*** and ***C*** would be not be achieved through such relatively shallow surface treatments. Due to the effects of shot peening only leading to increased fatigue performance in a thin surface layer, it is unlikely that these effects will be adequate in an aggressive erosive/corrosive environment. One method with potential to introduce significant change is mechanical autofrettage (4).

9.3 Autofrettage of a pressurised plain cylinder

The process of autofrettage induces a compressive residual stress through the application of a pressure in this case to increase the fatigue life of a component. Subjecting a compound cylinder to autofrettage results in that cylinder possessing a higher fatigue resistance compared with a homogeneous cylinder of the same dimensions (22). A clad cylinder is in essence similar to a compound cylinder due to the component consisting of an internally clad cylinder with an external cylinder, namely the substrate, and an internal cylinder, namely the clad layer. During weld cladding a shrinkfit process effectively takes place between the substrate and the clad layer. The difference is of course that in the clad case there is a welded joint between the two cylinders as opposed to a shrink fit. Therefore autofrettage of the clad cylinder is regarded as a beneficial area of study.

The following theory is presented for a plain cylinder to provide insight into the autofrettage process.

To determine the correct autofrettage pressure for a certain component, it must be considered at what pressure the wall of the cylinder will be in a state of plastic flow. A cylinder subjected to internal pressure will initially begin to experience yielding at a pressure $p_{Y.P.}$ given by:

$$p_{Y.P.} = \tau_{Y.P.} \left[\frac{b^2 - a^2}{b^2} \right] \tag{9.1}$$

$\tau_{Y.P.}$ is the shear stress at the yield point, a the inner radius and b the outer radius.

The maximum pressure that the component can withstand, known as the bursting pressure p_{burst}, is related in the following manner to the ultimate tensile strength $\sigma_{ult.}$ and the ratio of outer to inner radii K(252):

$$p_{burst} = \sigma_{ult.} log_e K \tag{9.2}$$

Due to the self-equilibrating nature of residual stresses, cladding residual stresses can be assumed to have no effect on the theoretical burst pressure, likewise is the case with stresses arising through a shrinkfit effect or autofrettage process. Throughout this investigation an elastic-perfectly plastic material has been assumed.

The pressure required for the entire wall of a plain cylinder to be brought into a state of plastic flow is equal to the negative of the radial stress σ_{r_a} at the inner surface (252):

$$p_u = -\sigma_{r_a} = -2\tau_{Y.P.} log_e \frac{a}{b} \tag{9.3}$$

The following two autofrettage pressures were chosen to ensure suitable depths of yielding in the clad cylinder.

The geometric mean radius is given as the greatest depth to which yielding is safely permissible and therefore the maximum autofrettage pressure can be calculated based on the following equation given by Hearn (25):

$$R_p = \sqrt{R_1 R_2} \tag{9.4}$$

The theory presented does not account for the bimetallic nature of the weld clad cylinder. In the clad cylinder, the high-strength substrate will slow the progress of yield through the lower strength clad as there is a greater constraint on the radial expansion of the cylinder. Due to this bimetallic nature of the cylinder, manual adjustment of the input pressures was required to obtain pressures adequate to yield to the desired depth for a stress-free compound cylinder. In the case of a weld-clad model with an induced stress state this requires further adjustment.

For the case of a 17-4 PH clad with a much larger yield stress, the pressure required for autofrettage would be much larger to allow the resulting compressive residual stress field from the cladding operation of around -400 MPa to be taken up to the yield value of 17-4 PH (994MPa). This is vastly different to beginning with a stress-free state.

The Inconel 625 clad has a tensile residual stress of around 400 MPa post-cladding and therefore would not require as high an autofrettage pressure, indicating that autofrettage of this case should be more easily attainable.

9.4 Simulation of the autofrettage process

Initially, an autofrettage pressure is applied to a stress-free cylinder to verify the correct implementation of the autofrettage process. As a benchmark, an unclad 4330 cylinder was analysed and compared to the theoretical solution given in 9.3, providing satisfactory correlation.

An Inconel 625 weld clad model is subjected to a pressure on the inside surface, using the *as-clad* residual stress state shown in figure 5.5.

The cladding simulation is performed as before with the clad material deposited at melt temperature onto the pre-heated cylinder. The whole model is then cooled to room temperature prior to an autofrettage pressure being applied in a ramped manner at the desired value. Model geometry and properties are shown in figure 9.3.

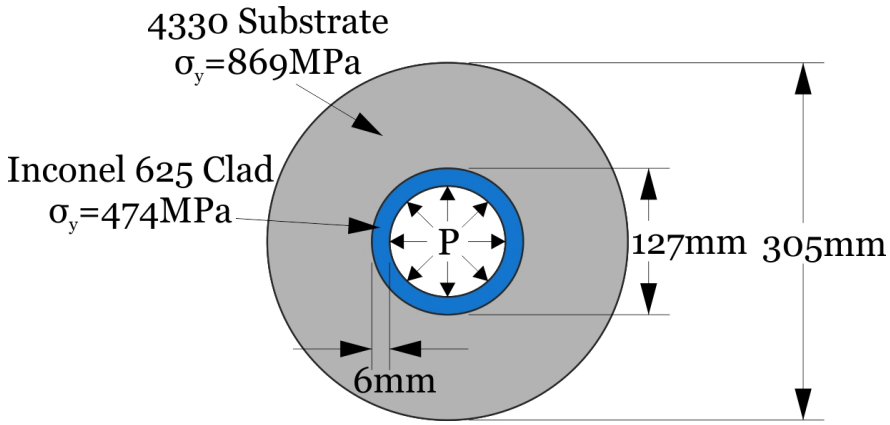

Figure 9.3: Model geometry and properties - Experimentally obtained temperature dependent material properties utilised throughout simulation.

Chosen low and high autofrettage pressures of 400 MPa and 800 MPa respectively are applied as two separate loading scenarios. The pressure is then removed by ramping the pressure back to zero and residual stresses investigated. The Von Mises yield criterion is used in the simulation.

To ensure that constraints on the finite element model cater accordingly, displacement in the axial direction has been fixed. The same plane strain axial boundary conditions were used as with the cladding simulation studies discussed in chapter 5.

9.5 Results

Examining the hoop stress distribution shown in figure 9.4, it is observed that the initial damaging tensile residual stress throughout the clad layer has been transformed to beneficial high compressive levels at both autofrettage pressures.

Applying a low autofrettage pressure of 400 MPa produces high compressive residual stresses in the clad layer and lowers tensile residual stresses in the substrate, with discontinuity stresses at the clad-substrate boundary also reduced.

Applying a high autofrettage pressure of 800 MPa produces high compressive residual stresses in the clad layer and into the substrate alongside a compressive discontinuity stress at the interface as shown in figure 9.4. This compressive discontinuity stress may be desirable depending on the metallurgy of the joint and the resulting mechanical properties achieved for the dissimilar materials at the joint. Although a compressive discontinuity stress may be favourable in preventing crack initiation at this location, the issue of dissimilar materials and therefore dissimilarity in material properties remains.

In observing the effect of autofrettage pressure on hoop stresses, it is seen that an increase in pressure, between low and high pressure values, does not cause a no-

table difference in compressive residual stresses in the clad layer, limited due to the yield stress for the clad material. However the notable difference arises in the effect of autofrettage pressure on the discontinuity stresses at the interface and nature of residual hoop stress in the substrate. A lower autofrettage pressure results in a large discontinuity stress and even the higher autofrettage pressure applied is not large enough to yield the low alloy carbon steel substrate. If the substrate were to yield, it would be of interest to note whether or not the small discontinuity stress arising in the hoop residual stress would also be eliminated due to the effect of plasticity.

Compressive residual hoop stresses exist to a depth of around 18 mm, or three clad layer thicknesses, for the case of high autofrettage pressure. The same level of compressive residual hoop stresses result in the clad layer for both autofrettage pressures as shown in figure 9.4 due to the use of the same yield in tension and compression. Hoop stresses possess their maximum compressive value at the inner surface, reflected in the post-autofrettage curve for a low autofrettage pressure in figure 9.4.

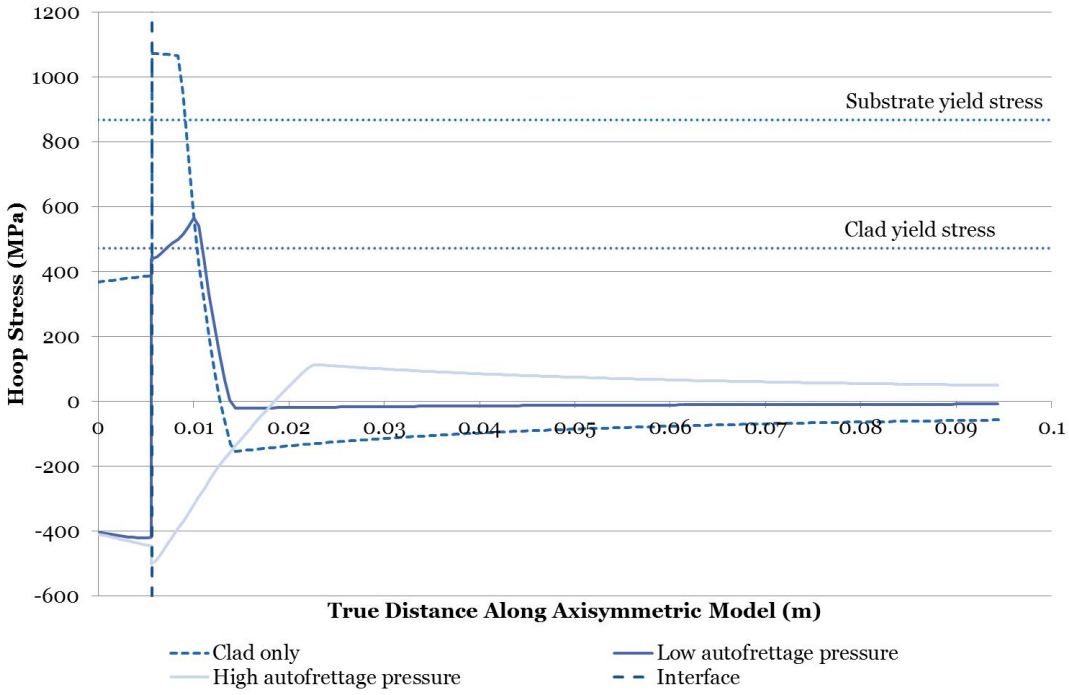

Figure 9.4: Effects of autofrettage on hoop stress - 4330 cylinder pre-heated to 150°C, weld clad with Inconel 625 and subjected to autofrettage post-cladding.

For a pressurized plain cylinder, yielding to any radius R_p can be obtained by applying the appropriate autofrettage pressure P_a, calculated through the equation provided by the High Pressure Technology Association code of practice (25):

$$P_a = \frac{\sigma_y}{2}\left[\frac{K^2 - m^2}{K^2}\right] + \sigma_y log_e m \tag{9.5}$$

$$K = R_2/R_1 \text{ and } m = R_p/R_1.$$

Analytical studies have been undertaken to determine the optimum radius for the elastic-plastic junction arising through the application of the autofrettage process (253), (254). Optimum autofrettage pressures are discussed (253), taking into account the operational pressure and relationship of component dimensions. Therefore, for a particular component, it would be of interest to analyse equivalent stress values with specific operational conditions, component dimensions and material properties in mind. Utilising the optimum autofrettage pressure ensures that the von Mises stress in the component is minimized with the location of the maximum stress also altered depending on autofrettage pressure applied (255).

Axial stresses as shown in figure 9.5 also illustrate a transformation of the tensile residual stresses in the clad layer into compressive residual stresses post-autofrettage for both pressure values.

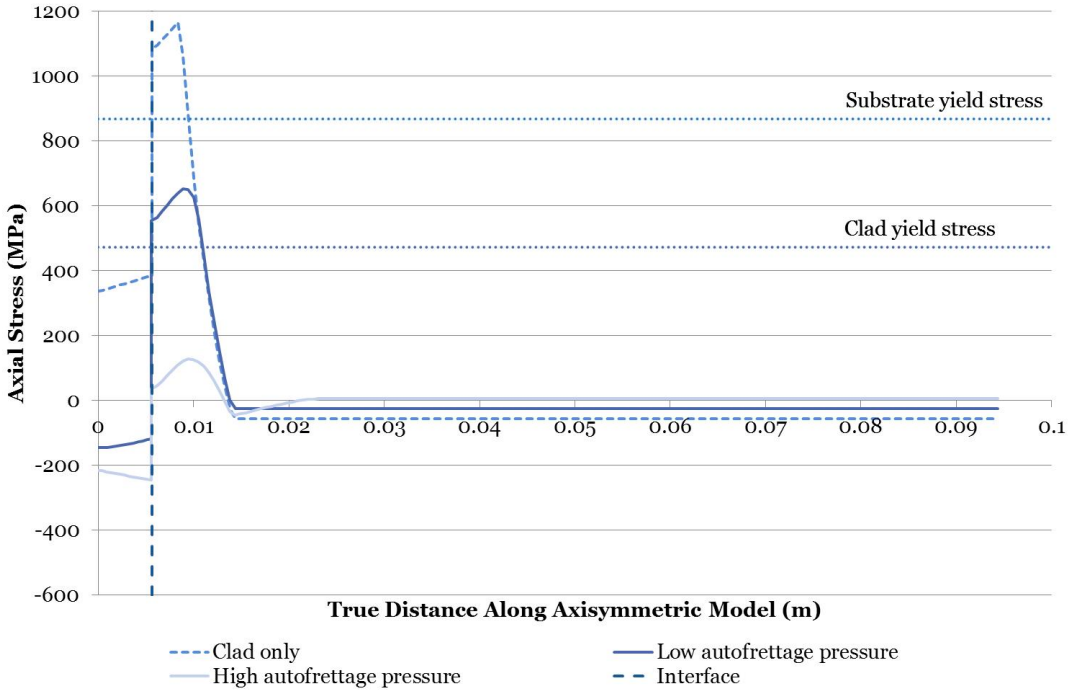

Figure 9.5: Effects of autofrettage on axial stress - 4330 cylinder pre-heated to 150°C, weld clad with Inconel 625 and subjected to autofrettage post-cladding.

Radial stresses as previously are lower, however also experience transformation through the autofrettage process, most notably in the case of the high autofrettage pressure, shown in figure 9.6. It should also be noted that radial stress components are in all cases not self-equilibrating.

As mentioned previously, yielding to the geometric mean radius was also considered as this is generally the maximum allowable autofrettage radius presented in the stan-

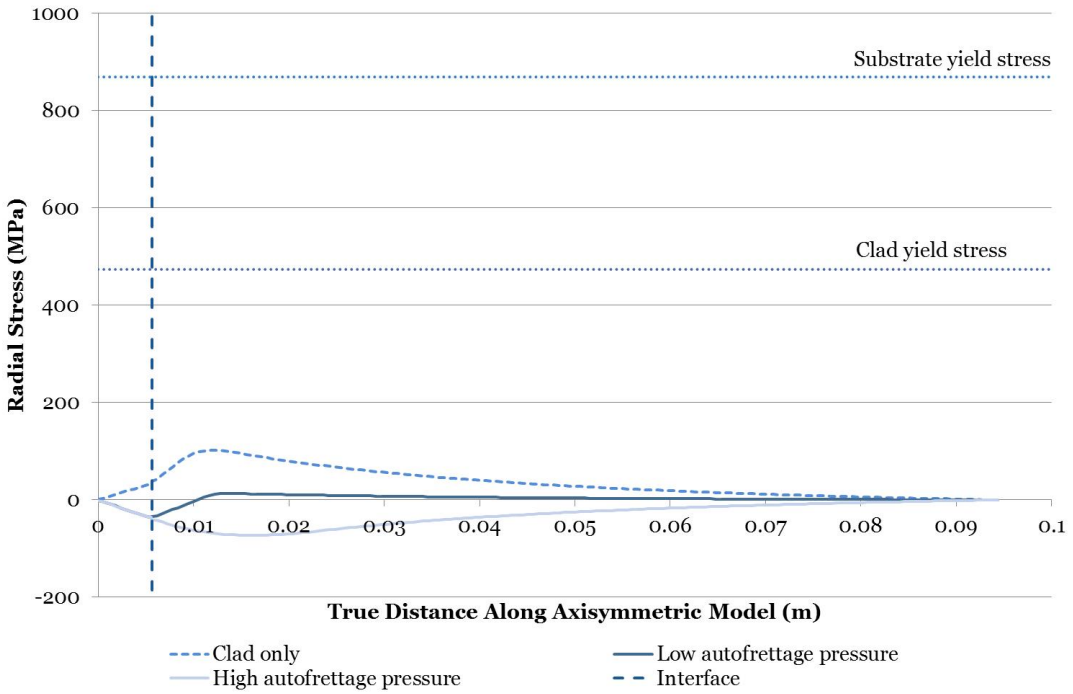

Figure 9.6: Effects of autofrettage on radial stress - 4330 cylinder pre-heated to 150°C, weld clad with Inconel 625 and subjected to autofrettage post-cladding.

dards (25). However, it is recognised that from a practical and economic point of view, the high autofrettage pressure of 800 MPa utilised in this simulation is demanding.

9.6 Discussion

A literature search has shown no (or little) previous published work on the simulation of the autofrettage of weld clad pressure components using finite element analysis.

The present study has shown that autofrettage has the potential to significantly improve the residual stress state in 4330 low alloy carbon steel components weld clad with Inconel 625. This could lead to further fatigue life improvements in an erosive-corrosive environment. The as-clad residual stress state is idealised and therefore in reality the stress distribution is likely to illustrate effects of alloying, for example through a broader discontinuity in stress with reduced peaks and no abrupt transitions. None-the-less the basic tensile residual stress state in the clad is likely to remain throughout the clad layer as demonstrated through ICHD measurements to a depth of 1 mm in chapter 6 in which case autofrettage will result in an improvement in fatigue performance.

While extensive experimental validation of the as-clad residual stresses has been carried out for both materials deposited on a 4330 substrate with both conventional and laser cladding, experimental validation of the autofrettage finite element simulation

results has still to be undertaken.

9.6.1 Application of the Weld Cladding Technology

The cladding technology was successfully applied to fluid ends of hydraulic fracturing pumps. The weld clad component was tested in accordance with standard company testing methods and post-test examination undertaken. Ultrasonic crack detection highlighted the presence of cracking to a significant depth of 61 mm. The cause of cracking was thought to be due to poor substrate geometry prior to the cladding process being applied, presenting discontinuities in geometry and clad layer thickness and therefore areas of stress concentration. These issues are not insurmountable. Therefore, due to the inability to draw conclusions as to the impact of the fatigue-resistant cladding technology on the performance of the component further cladding of the fluid ends would be required.

9.7 Summary

Mechanical autofrettage is shown to be a post-cladding process with the potential to significantly improve the residual stress distribution in a 4330 steel cylinder clad with Inconel 625. Simulation results show the elimination of tensile residual stresses throughout the Inconel 625 weld clad layer. The potential also exists to eliminate the high discontinuity stresses at the clad-substrate boundary and induce compressive residual stresses well into the substrate. High compressive residual stresses exist to a depth of three clad layers thicknesses through the application of a *high* autofrettage pressure. This will significantly enhance the fatigue performance of high strength 4330 components clad with Inconel 625.

For the purpose of a finite element model, pressure values can be adjusted as necessary and provide adequate information regarding the effects of autofrettage. However, in reality, for a real component with more complex geometry, it should be considered whether or not any proposed pressures are feasible, both economically and practically.

Experimental validation of autofrettage of weld cladding is recommended. Likewise, simulation and experimental investigation of the effects of autofrettage of weld cladding with the use of the 17-4 PH clad material would also be of interest.

Chapter 10

Conclusions

A fatigue-resistant cladding technology has been presented aimed at improving the fatigue performance of components subjected to high cyclic loading in an erosive-corrosive environment, through the generation of compressive residual stresses in the clad layer. It was expected that through the thermal deposition of a clad layer onto the bore of a fluid end of a hydraulic fracturing pump using a cladding process that a region of compressive residual stress would result at the surface. The presence of a compressive residual stress would as a result lead to an improvement in fatigue life.

Due to the fluid passing through the component during operation, erosion and corrosion are also areas of concern and therefore materials providing erosion and corrosion resistance in addition to the beneficial effects due to the presence of compressive residual stresses are desirable. Process modifications and material selection have allowed the investigation of the potential applicability and benefits of several options to achieve such an increase in fatigue performance.

- Various cladding and coating processes have been investigated prior to the selection of the weld cladding process to achieve the fatigue-resistant cladding technology.
- The deposition of a weld clad layer induces residual stresses throughout the component, the nature of which is dependent on the combination of substrate and clad materials.
- The benefits of compressive residual stresses on fatigue performance were confirmed through the corrosion fatigue testing of unclad low alloy carbon steel.
- Weld cladding using a hot-wire *TIG* process allowed the deposition of two clad materials, Inconel 625 and 17-4 PH, on a 4330 substrate of varying geometry, both in cylindrical and rectangular block form, with a thickness representative of the component to which the technology is to be applied.
- Resulting metallurgy due to the cladding process was investigated, with a view to identifying potential areas requiring attention in refinement of the cladding technique.
- Specimens harvested from the *HAZ* and clad layers allowed experimental determination of the thermal and mechanical temperature dependent material properties for 4330, Inconel 625 and 17-4 PH.
- Finite element simulation of the weld cladding process allowed the modelling of the generation of residual stresses due to the deposition of the clad material on the substrate material.

- Experimental residual stress measurements using *ICHD* allowed the determination of the nature of the residual stresses induced as a result of the cladding process. This allowed validation of the finite element predictions to a depth of 1 mm from the clad surface.
- Deposition of an Inconel 625 clad layer on a 4330 substrate resulted in high bi-axial tensile residual stresses in the clad layer.
- Inconel 625 is commonly utilised in the oil and gas industry and adheres to standards regarding required hardness values due to the applied welding process, however the presence of tensile residual stresses is undesirable. The material also has measurably better erosion-corrosion properties than 17-4 PH in an oil and gas environment.
- Deposition of a 17-4 PH clad layer on a 4330 substrate resulted in high bi-axial compressive residual stresses in the clad layer.
- The presence of compressive residual stresses in the clad layer when cladding with 17-4 PH is desirable, however issues arise regarding local hard regions due to the welding process and as a result, this clad material arguably does not adhere to industry requirements.
- Microstructural effects were discussed and the impact on material properties and residual stresses examined, particularly in the case of the 17-4 PH clad material. The martensitic phase transformation and associated effects on volume changes and material properties was emphasised as highly influential on the residual stress state when cladding with 17-4 PH.
- Effects of process variables such as the cladding process, materials and parameters were investigated.
- Laser cladding also demonstrated the potential to provide a means of depositing the clad material to improve fatigue performance, with the potential for a thinner clad layer and *HAZ*.
- Modification of the arising residual stress distribution was shown to be possible in the case of an Inconel 625 clad material to transform tensile residual stresses through the application of autofrettage post-cladding.
- Weld cladding and testing of fluid ends of a hydraulic fracturing pump has now been undertaken by Weir SPM, proving the applicability of the technology. Post-test analysis highlighted areas requiring attention to refine and further develop the fatigue-resistant cladding technology.

- Recommendations for further research and development to validate, refine and extend the applicability of the fatigue-resistant cladding technology are presented in the following chapter.

The technology presented does not only provide benefits for the particular application investigated nor solely the process or materials investigated. Other coating and cladding processes and materials could be applied to a substrate with the aim of improving performance from a fatigue, erosion and corrosion perspective particularly in cyclic loading applications.

10.1 Discussion

Corrosion fatigue testing of low alloy carbon steel allowed validation of the hypothesis of a compressive residual stress being beneficial for fatigue performance. This was undertaken through the combined axial fatigue testing and R.R. Moore rotating beam fatigue testing of uncorroded and corroded specimens under tensile and compressive mean stresses, as discussed in chapter 2. This demonstrated that under a suitably high compressive mean stress, fatigue life increased significantly when pre-corrosion pitted and cracked specimens were subjected to an applied cyclic tensile stress of a level that ensured that the maximum stress remained slightly compressive. The investigation of corrosion methods highlighted that aeration during corrosion produces the most favourable corrosion with pitting and cracking present. This provided the introduction to the beneficial effects of compressive residual stresses and initiated the development and validation of the fatigue-resistant cladding technology.

Through the cladding process, dissimilar materials are joined and therefore an understanding of both materials is required along with the resulting material characteristics and residual stresses arising through the cladding process. Various cladding and coating processes were investigated to enable in-depth knowledge of the processes and the resulting effects to be obtained. Erosion and corrosion performance was also of interest throughout the development of the fatigue-resistant cladding technology. The weld cladding process was selected as the primary method of interest. Weld overlay cladding was undertaken using a hot-wire tungsten inert gas (*TIG*) process. A low alloy carbon steel 4330 substrate was weld clad with both nickel-chromium-based superalloy Inconel 625 and martensitic, precipitation hardening stainless steel 17-4 PH. Consideration was given to the welding parameters to ensure a satisfactory process and resulting clad components along with investigation of the effects of substrate geometry, pre-heat temperature and post-weld stress relief.

Post-cladding, metallurgical studies showed good fusion resulting through weld cladding with both Inconel 625 and 17-4 PH. Varying microstructures arose in the two clad

passes deposited with an interpass temperature enabling the temporary halting of the process if the temperature rises too high during any pass. Alloying and diffusion was also evident from the substrate into the clad materials. It was highlighted that significant iron diffusion should not be observed to ensure that corrosion resistance is not negatively impacted through the cladding process. It is such resulting characteristics of a weld clad component that could require refinement to the process to ensure the most favourable result. Specimens were harvested from the clad and heat-affected zone (*HAZ*) layers to allow experimental characterisation of temperature-dependent thermal and mechanical properties. Obtaining these properties allowed for reasonably accurate simulation of the weld cladding process, capturing material behaviour reflected in these properties. This was in spite of the cooling rates inherent of some characterisation being not wholly representative of the actual cladding process. Available published data did not adequately reflect the phase changes upon heating or cooling with some data also not available at elevated temperatures.

Finite element simulation of the weld cladding process was undertaken in *Abaqus*. A variety of modelling techniques were investigated to deduce the effects of material properties, cooling rate and the spatial and temporal variation of the weld cladding process on the resulting residual stresses. An axisymmetric model demonstrated the ability to capture the generation of residual stresses, with the investigation of passes, beads, two-dimensional planar and three-dimensional models providing similar residual stress states. This highlights that simplified modelling is adequate in this case. Accuracy in residual stresses was highlighted as being highly dependent on the material properties defined for the substrate and clad materials. A higher pre-heat temperature was shown to decrease the discontinuity stress at the interface between the substrate and the clad material. The temperature history experienced during the weld cladding process illustrated that the cooling rate is extremely rapid at the beginning followed by a gradual cooling of the entire model upon the clad and substrate reaching the same temperature level.

Experimental determination of residual stress can be undertaken using various methods. These methods are discussed and the characteristics such as the destructive nature and depth of measurement indicated as factors in technique selection. Residual stresses at the clad surface were obtained using incremental centre hole-drilling (*ICHD*). The laying of the strain gauge rosette on the component surface required machining of the weld clad profile to provide a smooth surface. This modifies the residual stress state at the surface of the component and as residual stresses are self-equilibrating this will also impact residual stresses throughout the component. This is a disadvantage of the use of *ICHD* in obtaining residual stress measurements on the weld clad components. *ICHD* is also highly sensitive to user technique. Experimental results showed high bi-axial tensile residual stresses present in an Inconel

625 clad layer and high bi-axial compressive residual stresses in a 17-4 PH clad layer. Sectioning of a 17-4 PH weld clad block allowed residual stress measurements to be obtained either side of the interface, with compressive residual stresses shown to be present into the *HAZ*. Comparing residual stresses obtained experimentally with those obtained in the finite element simulation indicated good correlation, especially in the case of an Inconel 625 clad material. Due to the phase changes occurring upon cooling in the 17-4 PH clad material obtaining correlation proved more difficult.

It is the martensitic, precipitation hardening nature of the 17-4 PH clad material that presents complexity in capturing the behaviour of the material and hence the residual stresses arising when cladding with this material. The cooling rate during welding with such martensitic materials dictates the resulting microstructure. Methods of capturing the effects of microstructure on material properties were investigated through manipulation of the *CTE* curve upon cooling of the material. Residual stresses resulting in the finite element simulation were shown to be highly sensitive to variations in *CTE*. It was through manipulation of the *CTE* data that improvement in correlation between simulation and experimental residual stresses was achieved. This emphasises the need for accurate characterisation of material properties, accounting for the correct cooling rates and chemical compositions which in turn impacts the material microstructure and properties and ultimately the resulting residual stress distribution.

The laser cladding technique was also investigated as an alternative to the weld cladding process. Two clad layer thicknesses, 2 mm and 6 mm, were deposited onto a 4330 substrate with both Inconel 625 and 17-4 PH using the laser cladding process. Good fusion was again obtained through the cladding process along with smaller *HAZ*'s in comparison to those obtained through weld cladding due to lower heat input. The depth of the *HAZ* was found to be independent of clad layer thickness and hardness values independent of clad material. Dilution levels were lower post-laser cladding compared with weld cladding. Useful residual stresses were also obtained with a 2 mm thick clad layer. Refinement of the laser cladding process and the use of controlled cooling provides the potential to further improve the quality of the resulting clad component. Functional grading of the transition is an additional area of interest, possible through the laser cladding process, to decrease discontinuity stresses at the interface. A smoother surface finish is obtained when weld cladding with Inconel 625, although the opposite is the case with 17-4 PH, the laser cladding process providing a smoother surface finish. Experimental residual stress measurements using *ICHD* indicated the presence of tensile residuals stresses in both a 2 mm and a 6 mm Inconel 625 laser clad layer. Compressive residual stresses were present in both a 2 mm and a 6 mm 17-4 PH laser clad layer to a depth of at least 1 mm, which was the limit of the *ICHD* technology used. Therefore, it does not appear

favourable to increase the clad layer thickness. Residual stresses in a 17-4 PH laser clad component were obtained using the contour method to provide the residual stress distribution on a two-dimensional plane due to sectioning of the component. These results also confirmed the presence of high compressive residual stresses in the laser clad layer. Good correlation was obtained between *ICHD* and contour method measurements as presented in chapter 8, illustrating the complimentary nature of these techniques. The presence of discontinuity stresses indicated previously in the simulation model were also confirmed through the contour method to be present in reality with an increase from a longitudinal stress of 0 MPa to 250 MPa at the interface between a 17-4 PH clad and 4330 substrate.

Due to the presence of tensile residual stresses in the Inconel 625 clad layer, methods of modifying this stress state were considered as this material possesses desirable erosion and corrosion resistance characteristics. Simulation of autofrettage of the as-clad component proved successful in transforming tensile residual stresses in the Inconel 625 weld clad layer into compressive residual stresses. The application of a *high* autofrettage pressure resulted in compressive residual stresses to a depth of three clad layer thicknesses, or 18 mm. Discontinuity stresses were also almost eliminated. Hence autofrettage of the weld clad component provides a means of obtaining a fatigue-resistant clad when cladding with Inconel 625.

The fluid end of a hydraulic fracturing pump was weld clad to examine the application of the fatigue-resistant cladding technology. This component was then tested according to standard testing methods. Post-test analysis revealed the presence of cracking in the region of step changes in substrate geometry and clad layer thickness. Through ultrasonic crack detection, the maximum depth of the crack was found to be 61 mm. The presence of such cracking demonstrates the need for a high quality clad to ensure satisfactory component performance. The benefits of the fatigue-resistant cladding technology can only be harnessed through a high quality clad component and likewise assessment of the performance of the fatigue-resistant cladding technology can only be undertaken when there are no areas of stress concentration causing failure due to defects in the clad. To further develop and refine the fatigue-resistant cladding technology, design and manufacture considerations are discussed in the following chapter.

Chapter 11

Recommendations for Further Work

Various aspects of a new fatigue-resistant cladding technology have been successfully developed and validated through the use of weld and laser cladding techniques. While the choice of cladding and substrate largely dictates the nature of residual stresses arising through the cladding process, the presence of tensile residual stresses can also be modified to provide beneficial compressive residual stresses in the clad layer. This has been shown through the application of the process of autofrettage.

Throughout the investigation, key findings have been highlighted along with recommendations for future work. Clearly, there is much potential in further developing and refining the technology and therefore the main areas considered to be of most significant interest will be presented in this chapter. The following topics are not presented in any order of relative importance.

11.1 Functionally grading the transition between substrate and clad layer

As discussed in section 8.3.1, through the use of the laser cladding process, the clad materials in powder form present the potential to functionally grade the transition between substrate and clad materials by creating layers of varying ratios of substrate and clad materials.

In these circumstances there is clearly an interest in not only influencing the residual stress distribution at the surface and throughout the clad but also to influence the magnitude of the discontinuity stresses, both residual and operational. Given the self-equilibrating nature of the residual stress distributions, it should be possible to maintain high beneficial compressive residual stresses throughout the coating or clad layer as well as reducing the high discontinuity stresses at the interface. Interlayers and buttering layers are often used to provide a more gradual transition from one material to another, as well as to improve the bond. The logical development of the use of interlayers is a functionally graded material. Figure 11.1 provides a schematic representation of a transition between two dissimilar materials involving a number of layers where the layer material is gradually changing one to the other. This technology will clearly be more expensive than a simple single bond between two materials. It also requires the availability of layer materials in suitable ratios. This latter requirement generally results in the use of powders, where the constituent materials can be mixed prior to deposition or the mix can be adjusted during deposition. Processes such as hot iso-static pressing and laser cladding find application in this area. Apart from ensuring satisfactory metallurgy, further goals would be to optimise the transition thickness and number of individual layers.

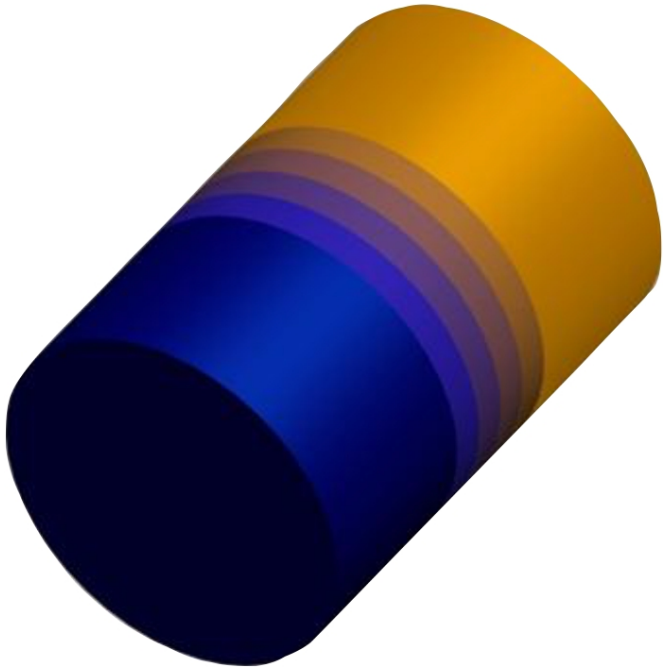

Figure 11.1: Functionally graded transition - Specimen can consist of as many layers as required to create the desired transition.

The development and increasing use of near net-shape layered powdered metal manufacturing equipment, such as *LENS* (Laser Engineered Net Shaping) (256), will no doubt drive down the cost of use of such technology.

Experimental validation of the functionally graded concept and the following repair concept in general is also necessary.

11.2 Repair and reinforcement technology

The fatigue-resistant cladding technology has been presented as a means of cladding the internal geometry of a fluid end of a hydraulic fracturing pump prior to operation. However, the technology does not require application to the entire internal geometry, nor does it require application prior to initial operation. The technology could be applied solely to regions requiring reinforcement or additional strength and could also be applied as a repair technology following a period of operation. This provides the potential to utilise the technology as a reinforcement and repair technology, again with the aim of generating compressive residual stresses in the clad/repair material. Figure 11.2 provides an illustration of the concept.

If utilised as a repair technology, the cracked region or region requiring strengthening would be identified. If a crack were to be present this should be machined and generally the substrate prepared for the deposition of the clad material.

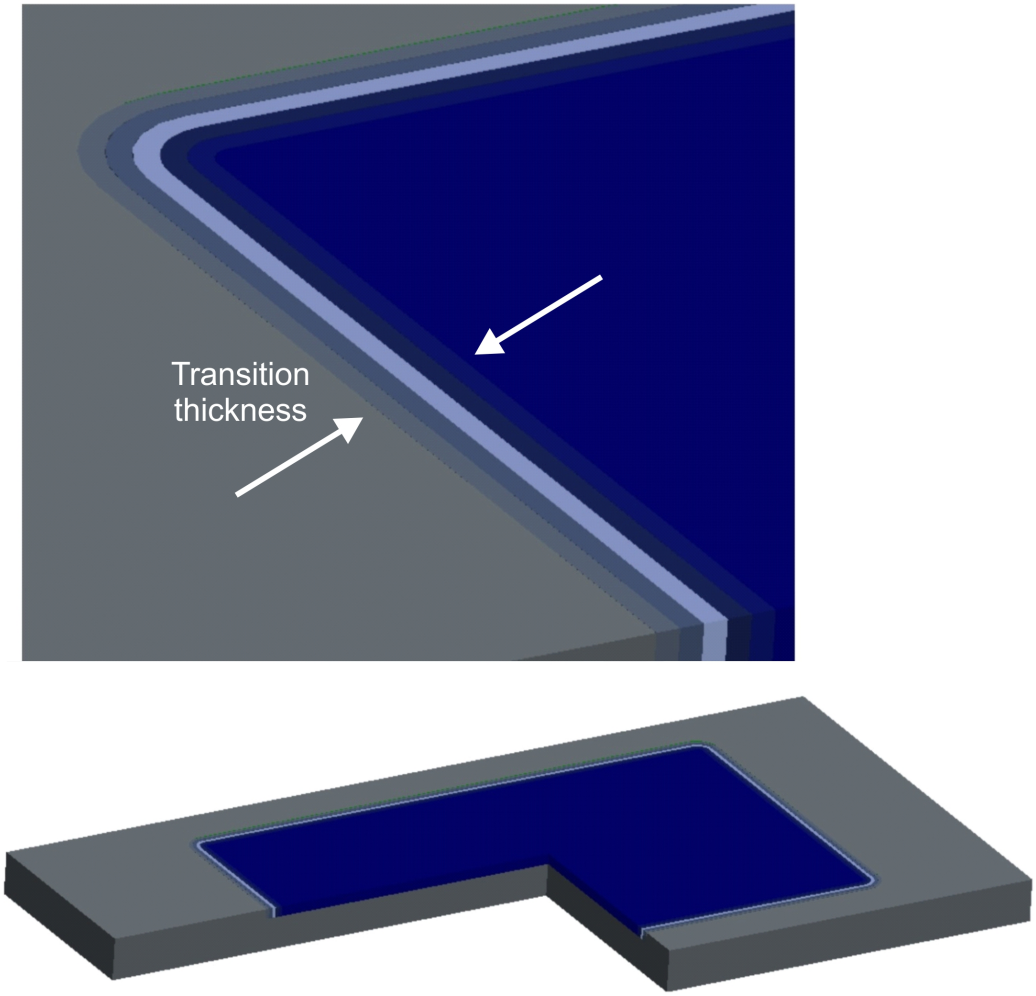

Figure 11.2: Repair and reinforcement technology - Application of the fatigue-resistant cladding technology to localised areas as required.

Potential issues of galvanic corrosion at the boundaries would not be an insurmountable problem. It is within this concept that functional grading could further provide benefit, the variation in flow rates of powders by multiple flow heads creating this grading. Grading the transition around the boundaries would decrease discontinuity stresses and eliminate preferential corrosion. The thickness of the transition and number of layers in the transition could again be altered as appropriate to tailor the stress through the join. A greater transition thickness would reduce discontinuity stresses and therefore positively influence fatigue performance.

Any crack cavity present should be ground out prior to cladding. The clad layer is then deposited to fulfil the repair or strengthening of the component.

Material selection is again of importance, with the generation of compressive residual stresses desired in the deposited material to resist further crack initiation and growth. It would of course again be favourable if the selected material also provide corrosion resistance and compliance with necessary industry standards. Finite element analysis could be used to ensure that the repair boundary lies in areas of low stress, which would also improve the fatigue performance of the repair and help further reduce any galvanic or stress-corrosion effects.

11.3 Material hardening

An elastic-perfectly plastic material model has been used throughout this research and therefore in the future both the weld cladding simulation and the autofrettage process would benefit from investigation into the effects of strain hardening. Ideally, experimental post-yield tensile test data would be used to derive a multi-linear stress-strain graph. Access to limited published data (141) for a true stress-strain curve for non-welded substrate and clad materials would allow preliminary investigation into the effects of hardening on the cladding and autofrettage processes. However, it would also be desirable to experimentally obtain temperature-dependent strain hardening data. This could be undertaken using an electro-thermal mechanical test (*ETMT*) as described in (257). Thermocouples and digital image correlation can be utilised to observe variations in strain during testing and specimens tested at required temperatures to obtain accurate representations of material hardening.

Compressive residual stresses produced in the case of an elastic-perfectly plastic material model are thought to be higher than the stresses that would have been produced had a strain-hardening model been applied, as this was reported by Lee et al. for an autofrettaged compound cylinder due to the Bauschinger effect (22).

A parametric study into multi-pass butt-welded stainless steel pipes highlighted that the hoop stress component appears more complex to capture due to increased sen-

sitivity to constitutive models and the visible effects of phase transformations in this stress component (161). This is the case in non-symmetrical modelling cases. In the case of modelling in an axisymmetric manner, stress components will not demonstrate such variations.

The weld material and material in the vicinity of the weld will experience reverse plastic yielding upon cooling. This requires consideration when implementing a hardening model as stresses will vary depending on the model used. The most commonly used model is the linear isotropic hardening model (158).

A study of Inconel 82/182 weld and buttering with 316L pipe and A508 forging concluded that hoop stresses were most accurately captured when using a mixed isotropic-kinematic hardening constitutive model. This is understandable as the inclusion of the Bauschinger effect and softening of the material will be the case in reality for a cyclically loaded component. Neglecting this will of course impact resulting stresses. Isotropic and kinematic hardening models resulted in conservative hoop stresses, although in the case of isotropic hardening stresses were most conservative (140). This study in fact concluded that the constitutive model is one of the greatest influential factors in successfully modelling residual stress generation due to welding. However, this study investigates pressuriser nozzle dissimilar metal welds and therefore does not possess the same axisymmetric nature of the weld cladding process investigated herein.

A mixed isotropic-kinematic hardening model was further found to provide the most accurate post-weld residual stress field in a stainless steel slot weldment consisting of three passes (258).

Accounting for work hardening in a simulation model was however not found to produce great differences in resulting residual stresses in multi-pass butt-welded austenitic stainless steel pipes (259). Therefore, it is difficult to conclude without further investigation and obtaining of accurate stress-strain data the influence of material hardening in the fatigue-resistant cladding technology.

Inconel 625 is known to be a material which readily work hardens, with a strain hardening coefficient of approximately 0.2 compared to 0.12 for 4330 steel. Pre-cold working the material can be used to reduce the amount of strain hardening during machining. This may be possible using the autofrettage process, inducing compressive residual stresses whilst easing machining, however further investigation is required here. 17-4 PH stainless steel is considered to be less susceptible to work hardening than Inconel 625, although perhaps more so than 4330. The stress gradient in the plastic region is steeper at all temperatures in figure 11.4 than in figure 11.3, demonstrating greater potential for 17-4 PH to strain harden. This further highlights

the requirement to investigate material hardening both in reality and in the finite element model.

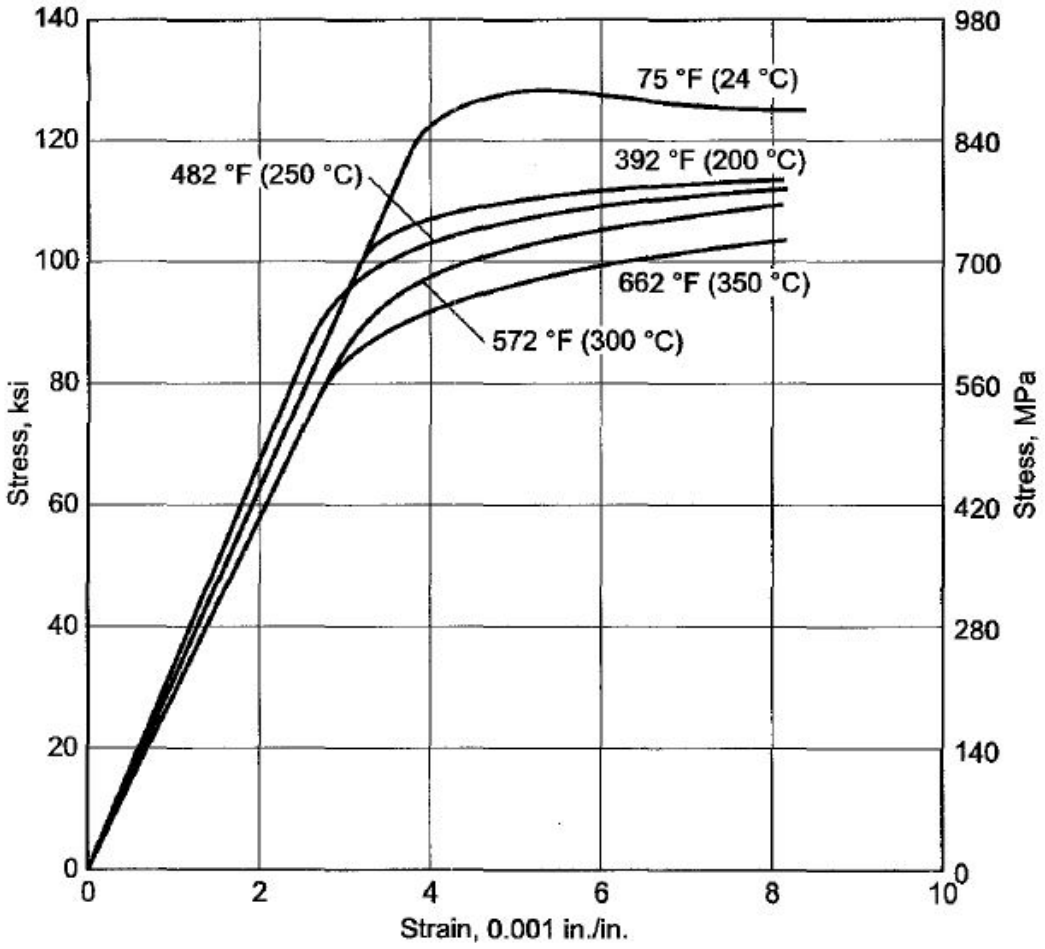

Figure 11.3: Stress strain trends with temperature for 4340 - Figure as published in (260).

Ideally, were material hardening to be implemented with a greater degree of complexity, testing would be carried out at a range of temperatures to obtain accurate stress-strain curves for input into the finite element model as suggested above. A multi-linear hardening model could then be utilised.

With regards to the application of autofrettage to a weld clad cylinder, the finite element model would also be developed to include a material model accounting for strain hardening, possibly Bauschinger effects as well as validatory testing and experimental residual stress measurements. This validated finite element model would then be used to obtain production values for autofrettage pressures.

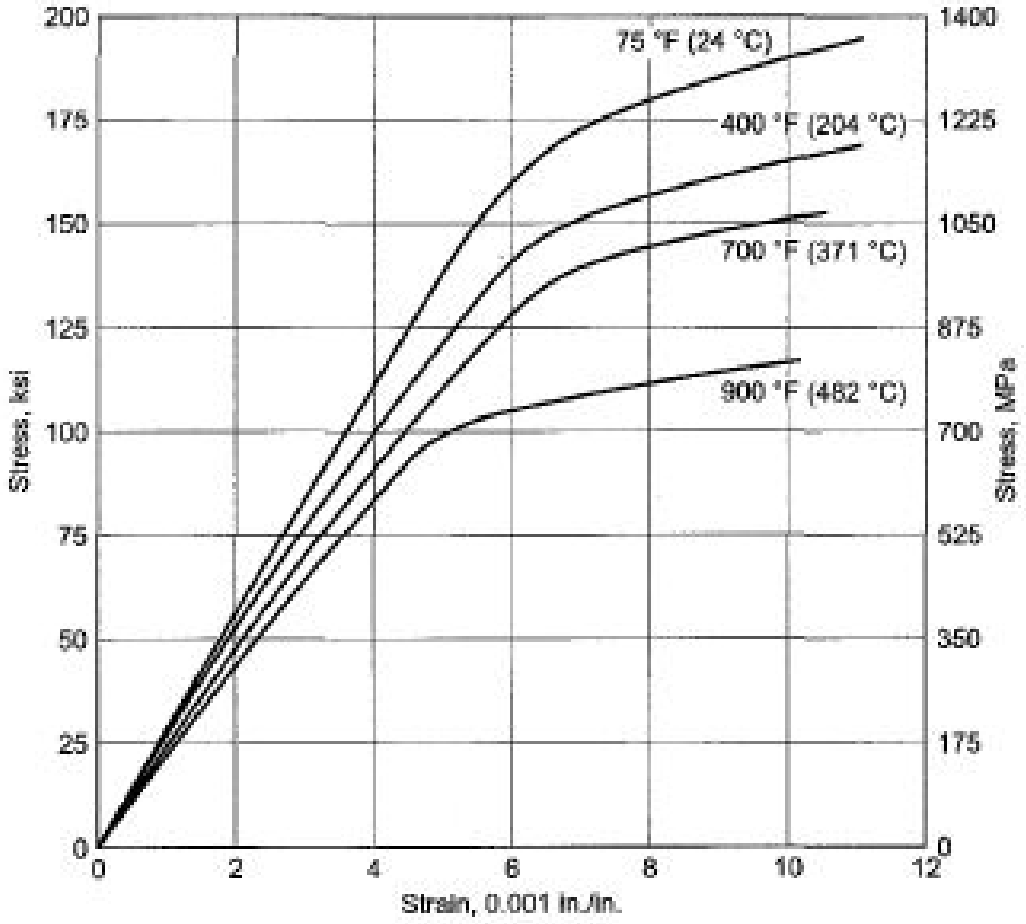

Figure 11.4: Stress strain trends with temperature for 17-4 PH - Figure as published in (260).

11.4 Autofrettage of weld clad components

Inconel 625 is a commonly utilised material in the oil and gas industry due to the erosion and corrosion resistance provided, however the presence of tensile residual stresses is undesirable from the point of view of the fatigue-resistant cladding technology. Section 9.1 presented the concept of applying an autofrettage process to the weld clad component to transform tensile residual stresses in the clad layer into compressive residual stresses.

In applications that are demanding from a fatigue viewpoint, the potential of the above fatigue-resistant coating and cladding concept is clear. While both the as-clad residual stresses to a depth of 1 mm and the autofrettage results for a plain cylinder have been successfully validated against theory also assuming an elastic-perfectly plastic material, it would be of interest to conduct experimental validation of the autofrettage simulation findings of Inconel 625 clad on a 4330 steel thick-walled cylinder. This would include weld cladding of the component followed by the application of autofrettage. Residual stress measurements and investigation of the resulting microstructure and material properties would also be recommended. Throughout this investigation, such detailed understanding required has been continuously emphasised.

From both a simulation and experimental perspective, evaluation is required as to the advantages of using an Inconel 625 clad cylinder subjected to autofrettage, as opposed to a cylinder solely clad with 17-4 PH stainless steel. The effect of autofrettage on thermal residual stresses and discontinuity stresses has been successfully demonstrated, however it is difficult to fully quantify without the implementation of a strain-hardening model.

A 17-4 PH clad produces compressive residual stresses through the cladding process with no need for such a post-cladding operation. *NACE* regulations do not specifically consider the case of a clad layer with significant compressive residual stresses through the thickness. A highly compressive residual stress throughout the clad layer is likely to mitigate effects of cracking in a hydrogen sulphide environment, either completely or to some extent, depending on the extent of autofrettage and the level of operational stresses. Therefore this could be more desirable if materials utilised achieve required standards as dictated by *NACE* (110).

Validation is a key current area of investigation and promise is also shown for studying the effects of autofrettage on a 17-4 PH clad on 4330 steel substrate. The stainless steel clad component does not strictly require autofrettage due to the compressive residual stress field present post-cladding, however it would of interest to investigate the effect of autofrettage on the discontinuity stresses at the clad-substrate boundary.

Due to the initial presence of substantial compressive residual stresses in the clad layer, the necessary level of autofrettage pressure to cause tensile yielding in the clad and interface regions will be substantial.

Likewise autofrettage of laser clad components could also be investigated.

The potential in the combination of weld cladding and autofrettage has been recognised and a patent application filed (261).

Analysis of the fatigue life of a component should be carefully conducted, as the tensile or compressive nature of residual hoop stresses do not necessarily provide accurate indications of improvement in fatigue performance, but rather demonstrate the ability of the component to bear a load (262).

11.5 Effects of post-weld heat treatment

Depending on the nature of residual stresses in components, it may be desirable to influence these stresses to attain the greatest benefit for fatigue life. One of the methods through which this can be achieved is post-weld heat treatment. This involves heating the component to a specified temperature for a set period of time before cooling again.

It was illustrated in section 4.2, that *PWHT* successfully increased the homogeneity of the microstructure of weld clad specimens.

Experimental residual stress measurements presented in section 6.4 demonstrated that compressive residual stresses in the 17-4 PH clad material were reduced through *PWHT*. In this case the substrate and clad materials are well matched, both being high tensile, martensitic steels with similar material properties. Tensile residual stresses in an Inconel 625 weld clad layer were uninfluenced by *PWHT*. Inconel 625 and 4330 are mismatched, the former being an austenitic steel and the latter a martensitic. There is also a large difference in yield stress values. Therefore, stress relief may have some effect at the elevated temperature at which *PWHT* is undertaken, however upon cooling to room temperature residual stresses re-form due to the mismatch in materials and the constraint on thermal contraction. This is not an uncommon observation for residual stresses in welded joints between materials with a significant mismatch in properties and is discussed in a *TWI FAQ* (263) regarding the residual stresses in a dissimilar weld after post-weld heat treatment. Therefore while the residual stresses can be reduced using stress relief, elimination may not be possible if dissimilar materials are involved.

Clearly from a fatigue perspective, it is undesirable to relieve the compressive residual stresses in the 17-4 PH clad component. This process of *PWHT* would generally

only be desirable in the case of tensile residual stresses in the weld, as Barsoum highlighted for welded tubular joints (264). Hansen and Agerskov (265) demonstrated that stress relieving a welded diesel engine possessing compressive residual stresses can also be detrimental, with the fatigue life being halved in this case.

Stress relieving is also possible through a vibratory method which uses a natural resonant process to achieve results relatively quickly compared with traditional natural ageing processes and thermal stress relieving processes. This method of stress relieving allows implementation at any stage of the manufacturing or machining process unlike thermal stress relieving and also claims to avoid the possible decrease in strength and toughness of low carbon steels occurring due to thermal stress relieving (14). Questions are still unanswered however as to the effect of vibratory stress relieving on fatigue life, with suggestions that this process can cause small amounts of fatigue damage. The reduction in stresses are thought to override this effect however. Clearly there is an opportunity to study the effectiveness of this on the as-clad residual stresses in an Inconel 625 clad.

Stress relieving is influenced by three main factors: plasticity, tempering and viscoplasticity (216). The occurrence of creep within the component will influence the transformation of stresses to a more uniform nature, with Hornsey (14) giving the typical stress relieving temperatures for carbon steels as being 570-650°C. Leggatt shows the effects of post weld heat treatment in a butt weld noting that hoop, axial and radial stresses were all greatly reduced (85). In a study of the effects of pre- and post-weld stress relieving, Mukherjee et al. (266) conclude that stress relieving can in some cases increase corrosion resistance in the case of welding and brazing. In welding of steel pipelines in oil and gas systems with Inconel 625 for example, *PWHT* is highlighted as necessary to enable tempering of the *HAZ*. Diffusion of carbon into the weld material encourages the formation of new phases and in turn decreases the level of carbon in the *HAZ*. It is this depletion of carbon that is highlighted in a study by Dodge et al. as being a key area requiring investigation and understanding to allow the resulting welded joint to possess a low susceptibility to hydrogen embrittlement (267).

Marques et al. (223) discuss heat treatment of carbon steel plates clad with stainless steel deposited using submerged arc welding. A heat treatment temperature of 620°C applied for a one hour time period was shown to be more effective than a ten hour period at a temperature of 540°C. Studies have been conducted to determine the method through which heat treatment can be simulated to decrease the need for experimental costs and time (108), (268). However, the main finding from these studies indicate that there is still a great need for experimental data to increase the accuracy of this simulation process.

PWHT, although utilised to improve the stress state in a component, will impact the material microstructure. It has been shown in a study of 17-4 PH that re-transformation of martensite occurs along with a modification of the level of austenite and the hardness value (213). The temperature and duration of *PWHT* determines the extent of these.

From this discussion regarding the effects of *PWHT* and the previous observations regarding the effects of *PWHT* on the clad components, it is crucial that in the application of the fatigue-resistant cladding technology, the process of *PWHT* and indeed the requirement of *PWHT* is carefully considered.

11.6 Residual stress generation and simulation

The effects of residual stresses in the operation of components are dependent on the nature of fatigue. Compressive residual stresses do not generally improve fatigue performance in low cycle fatigue as residual stresses are relaxed through the occurrence of plastic flow (58). Therefore, the most desirable scenario is the presence of compressive residual stresses of sufficient magnitude in a component when subject to operational conditions through which elastic stresses result.

It is recommended that a more detailed study into the heat cycle during deposition is conducted utilising information from the cladding vendor. Should further cladding trials be undertaken, a larger number of thermocouples could be used to provide a larger amount of data to characterise the heat cycle. This would provide a beneficial log of the temperature-time history all over the specimen. This data is likely to prove necessary in any clad simulation of a more complex bore geometry for example, where both spatial and temporal effects would have to be more accurately represented.

Experimental testing to determine temperature-dependent material properties would be desirable at cooling rates representative of the cooling rates occurring during the cladding process. It was highlighted that the equipment available for the present research was unable to test at such high cooling rates.

Furthermore this testing would benefit a deeper insight into the behaviour of the martensitic, precipitation hardening 17-4 PH stainless steel. The martensitic transformation has been discussed and emphasised as being a crucial factor in increasing the accuracy of the finite element model. Presently, it is being assumed that the martensitic transformation manifests itself as a change in material properties at the macro level. Therefore further research is required into modelling the martensitic transformation in grains of the material. Fatigue cracking often occurs in the HAZ due to the coarse grain structure present in this region (173). In obtaining material properties at

additional cooling rates, the cooling rates throughout the martensitic transformation would be of most interest. The accuracy of the thermo-dynamic model is crucial in capturing the cladding process.

The effects of applying heat treatment processes has been discussed, it would be of interest to investigate the effects of quenching on material properties, microstructure and residual stresses.

The influence of factors contributing to thermal stress generation due to the welding process can be obtained through the Satoh test, designed specifically for the very purpose of investigating thermal stress evolution. A bar is heated uniformly and stress history monitored. Constant material properties are assumed and the axial stress rate obtained through observation of the thermoelastic material behaviour (158). The axial stress is obtained through the relationship shown in 11.1, E_W being the Young's modulus, the subscript W signifying the use of the properties for the weld material.

$$\dot{\sigma} = -E_W \alpha_W \dot{T} \tag{11.1}$$

A constant value for Young's modulus, *CTE* and yield stress enable simple calculation of the axial stress. Otherwise variation in these properties must be assessed to consider resulting effects on axial stress. Axial stress will decrease with volume expansion until completion of the martensitic transformation.

It would be of interest to perform such testing to allow a deeper insight and understanding of the generation of residual stresses. A cladding process will involve a variation of cooling rates throughout the model and throughout the process. Ideally therefore temperature-dependent material property data should also be available over the necessary range of cooling rates. Obtaining this data experimentally will generally involve significant effort and cost.

Beneficial effects of high biaxial compressive residual stresses in both clad and unclad materials in a corrosive environment would also be worthwhile, while validation of as-clad residual stresses to a greater depth is also required.

Upon obtaining a deeper knowledge of the materials utilised, the simulation process could be further developed using the *Abaqus Welding Interface*.

11.7 Material selection

The materials utilised in the cladding process presented are by no means the only materials which would find applicability in this technology. As mentioned, issues with the 17-4 PH clad material in adhering to industry standards presents the need

to consider alternative materials capable of inducing compressive residual stresses. However, it should be highlighted that the *NACE* regulations (110) referred to in section 4.4.8 do not consider the case of a clad layer with significant compressive residual stresses through the thickness. It is likely that a highly compressive residual stress throughout the clad layer would mitigate effects of cracking in a hydrogen sulfide environment. As mentioned though, there are likely to be an array of materials that would both generate compressive residual stresses upon cladding and satisfy *NACE* regulations.

Although focus has been placed on clad components, chapter 2 presented the benefits of a compressive mean stress in inhibiting crack propagation through fatigue testing of corroded 4330. Therefore, it would also be of interest to investigate inducing compressive residual stresses in unclad components.

11.8 Material property testing

Although an extensive experimental testing program was undertaken, as presented in chapter 4, discussions highlighted the need for further testing to obtain a more thorough understanding of the variation in material properties throughout the clad and substrate materials due to the weld cladding process. It would be recommended that focus is placed on ensuring adequate cooling rates can be utilised in the testing of *CTE* and yield stress values are obtained at temperatures reflecting accurately the temperature of the specimen. Effects of the martensitic transformation on resulting material properties is crucial in obtaining accurate residual stresses resulting from the weld cladding process and therefore it would also be recommended to further investigate the extent of the martensitic transformation and consequential effects on material properties throughout the clad layer and into the substrate. Additionally, the corrosion fatigue testing undertaken in the early stages of the research would benefit from further investigation. It would be of particular interest to obtain weld clad fatigue specimens to experimentally validate the benefit of cladding on corrosion fatigue performance.

11.9 Application of weld cladding technology to hydraulic fracturing pumps

The intended application of the fatigue-resistant cladding technology reported herein was primarily to that of the fluid ends of a hydraulic fracturing pump. These reciprocating pumps experience high cyclic pressures and as a guideline, stress limits are provided as 10,000-25,000 psi (69-172 MPa), being on the conservative side to cater

for the cycling from suction to discharge pressure (269). These limits are dependent however on the cylinder material, the cycle and the pumped liquid.

In considering the application of the weld cladding technology, the key is to begin with a satisfactory unclad component, of which the geometry and the quality is of acceptable standards. There should be no inconsistencies in the substrate geometry or in the deposited clad layer. Should step changes in substrate geometry or clad layer thickness occur the effects due to these should be investigated and understood. However, it is clearly desirable to eliminate the occurrence of such features.

To assess the performance of the pump, it would be necessary to compare the time to failure with unclad pumps and also a pump clad with both Inconel 625 and 17-4 PH. Detailed information regarding the test rig and the fluid and instrumentation utilised would also be desirable to aid understanding of the process and ensure consistency in testing procedures. Overall, further cladding and testing of high quality components is required to allow assessment of the performance of the components.

11.10 Manufacture and component inspection

A high quality clad is crucial in harnessing the benefits of the fatigue-resistant technology. Crack detection post-testing is of importance, however the inspection of the clad prior to service of the component is also of interest. This would allow weld defects to be located prior to operation and the weld quality assessed. Non-destructive testing is often used for these purposes. Three-dimensional ultrasonic inspection would allow for a more detailed representation of weld defects or cracks present. An example of this is given in figure 11.5.

Automation of such a process to inspect components of complex geometry would surely provide a beneficial tool. This method could be used to determine the requirement for component repair after failure in the field and could also be used as a means of monitoring component operation.

To further inspect cracked components, this method of inspection could also be used to analyse the fracture surfaces and determine crack initiation locations. It would be of interest to evaluate the appearance of the crack and the time-scale over which the crack developed. This could be achieved through monitoring during testing of the component. The location of crack initiation would serve as an indication of areas of concern during operation, for example assessing if crack initiation occurs at the clad/substrate boundary due to the presence of discontinuity stresses. This is a common issue in surface treatments in that the fatigue issue is moved from the free surface to the clad-substrate boundary region.

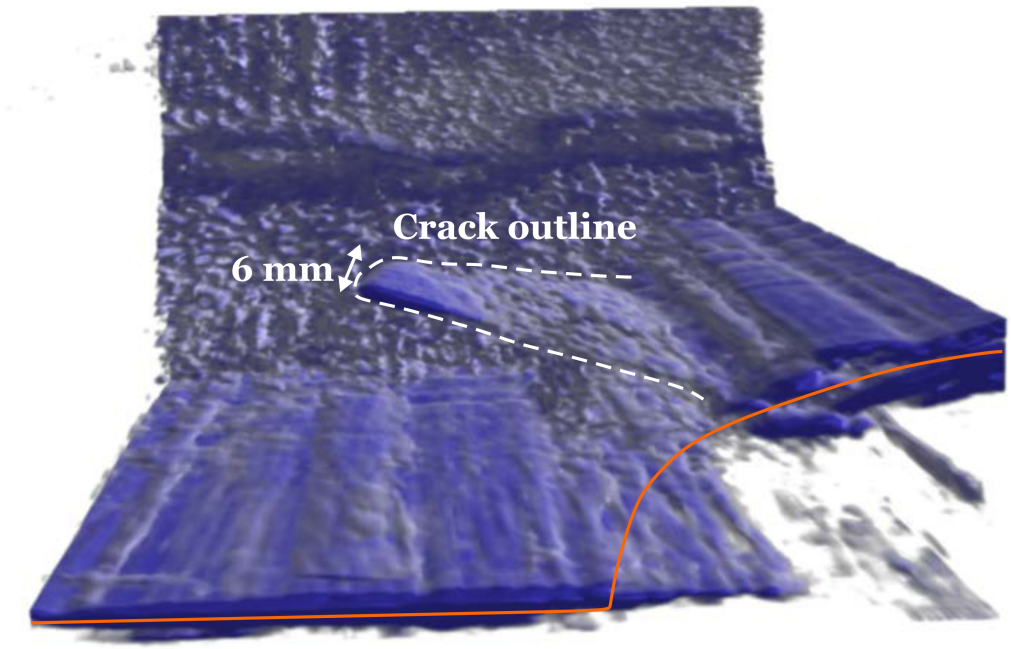

Figure 11.5: 3D ultrasonic inspection of crack in weld clad fluid end - Potential to obtain a full volumetric image of the component to locate weld defects or cracks. Figure courtesy of the Centre for Ultrasonic Engineering, within the department of Electronic & Electrical Engineering at the University of Strathclyde.

11.11 Design and manufacture considerations

In considering the design of the pump, the section thickness should be minimised to minimise the requirement for machining and in turn minimise resulting residual stresses due to machining. The *Pump Handbook* provides recommendations for surface finish, namely that above pressures of 3000 psi (207 bar) the minimum surface finish of internal bores should be 63 rms (269).

From the point of view of the application of the fatigue-resistant cladding technology, it must be considered to what extent cladding of the fluid end would be undertaken. Figure 11.6 shows the internal surfaces of the fluid end. It would be possible to clad the entire internal region of the fluid end, although the effects of cladding on the seals and threads and subsequently on the pump as a whole would require consideration. The fluid bearing regions are most likely of the utmost importance in the cladding operation due to this being the region that is most susceptible to erosion and corrosion, requiring additional protection to increase fatigue performance and life.

Regarding the geometry of the pump body, it would be desirable to remove any step changes in geometry to avoid subsequent step changes in the clad. Therefore recommended modifications to the pump body would be to introduce smooth or tapered bores, therefore avoiding preferential corrosion issues in allowing complete cladding of the internal geometry without abrupt changes in geometry.

The cladding process is limited in cladding internal bores. In deploying a cladding process, the extent of cladding possible must be assessed. Typical values upon enquiring as to the current process limitations revealed that a maximum distance of 500 mm and a minimum bore size of 50 mm could be clad. This would not present any issues in cladding the fluid end geometry in question. However the intersection of bores is problematic as the cladding nozzle cannot follow the step change in geometry in this region. Therefore it would be required that the clad layer is built up and machined to result in the desired geometry.

For mass production of certain components, specifically in the case of this research hydraulic fracturing pumps, a cladding program could be applied. However this would not be an option should components vary in dimensions and geometry.

After completion of the cladding operation, the weld profile would require removal which should be undertaken with a gentle grinding process so as to not impair the beneficial compressive residual stresses induced.

Concerns over the effects of machining have been raised previously and this is particularly the case in manual machining processes. It would be favourable to apply *CNC*

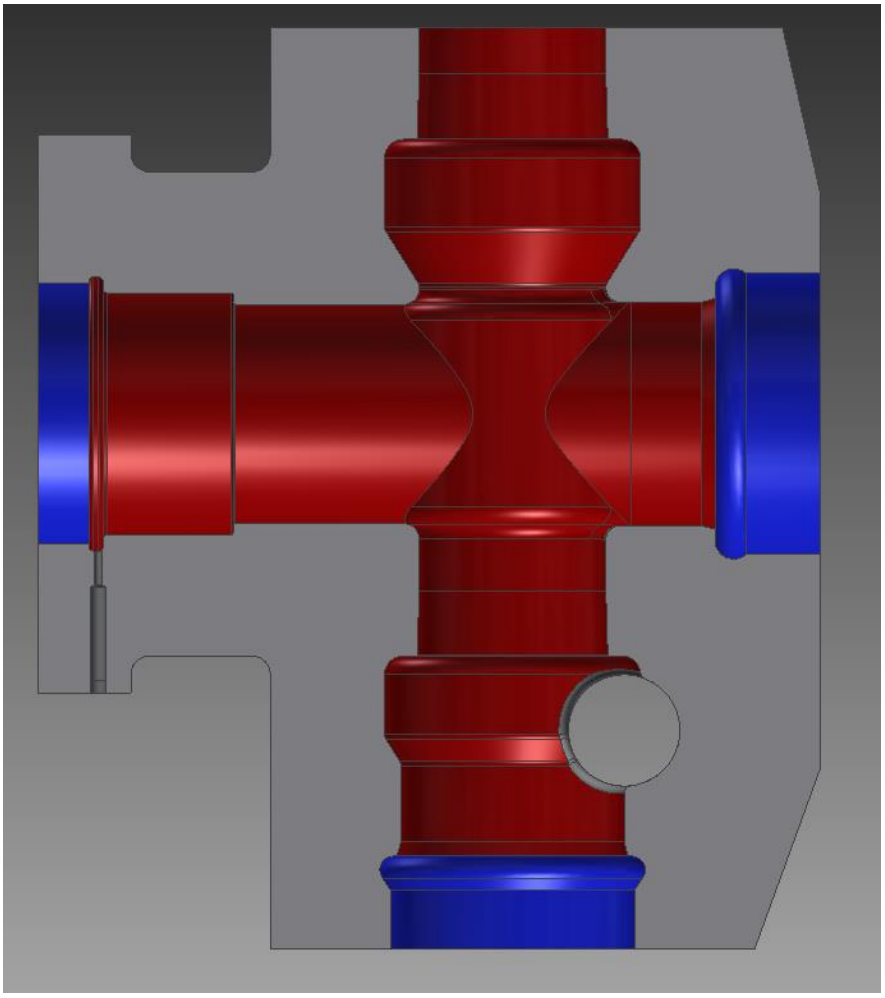

Figure 11.6: Internal fluid end geometry - Potential to clad all internal surfaces of fluid end.

machining processes that would consistently undertake the machining of the component such that variability in residual stress generation due to machining is minimised. Attention must also be given to the cooling and feed rates during machining for these dissimilar materials to ensure that heat dissipation occurs in a satisfactory manner and that temperature values are not greater than desired during machining.

At present, shot peening and autofrettage are applied during manufacture of the fluid ends. This is aimed at the generation of compressive residual stresses through application of these processes with the aim of increasing fatigue life. However, due to the aforementioned limited depth to which these stresses are induced, it appears that cladding would be more beneficial than shot peening. As has been described in this chapter, cladding and autofrettage could potentially be used in conjunction with one another to provide the most beneficial results for an Inconel 625 clad.

11.12 Concluding remarks

The generation of compressive residual stresses through a cladding process has been the focus of this research. Although it is known that compressive residual stresses are beneficial for fatigue performance, it should be noted that an in-depth understanding of residual stress generation and associated effects is required for effective deployment of the technology. Due to the self-equilibrating nature of residual stresses tensile stresses will also be present in the component and their presence must also be understood in terms of effects on component performance. It should be remembered that although compressive residual stresses are of benefit at the surface, at the interface for example superimposing potential tensile residual stresses with operational stresses results in different stress states than at the surface. Therefore attention must be paid to effects during the lifetime of the component and not solely in the early stages of operation.

Development and validation of the fatigue-resistant technology has been the overall aim of this research and this has been successfully achieved. In considering implementation of this technology in industry there will surely be other areas of interest which have not been investigated herein, including extensive testing of the weld clad components. An assessment of the economic and practical viability of the technology as well as the resulting performance of the clad components is of course required to ensure that implementation of the technology is a success. It is clear that there is mileage in further development and refinement of the technology, with the potential to steer further research depending on the main areas of interest.

List of References

[1] K.R. Van Horn. **Residual Stresses Introduced During Metal Fabrication**. *Journal of Metals*, **197**:405–422, 1953. 1

[2] M.B. Prime. **Editorial for Special Issue on Residual Stress in Fatigue & Fracture**. *Fatigue & Fracture of Engineering Materials and Structures*, **30**(3):172–172, March 2007. 1

[3] A. Brown. **Weld Overlay Cladding - The Solution to Pump Corrosion?** *World Pumps*, (October):50–53, October 2005. 2

[4] F.A. Kandil, J.D. Lord, A.T. Fry, and P.V. Grant. **A Review of Residual Stress Measurement Methods - A Guide to Technique Selection**. Technical report, National Physical Laboratory, Teddington, 2001. 3, 4, 56, 211, 219, 226, 248, 313

[5] P.J. Withers and H.K.D.H. Bhadeshia. **Residual Stress: Part 2 - Nature and Origins**. *Materials Science and Technology*, **17**(April):366–375, 2001. 4

[6] A.F. Liu. *Mechanics and Mechanisms of Fracture: An Introduction*. ASM International, Ohio, USA, 2005. 7

[7] L. Wagner. **Mechanical Surface Treatments on Titanium, Aluminum and Magnesium Alloys**. *Materials Science and Engineering A*, **263**:210–216, 1999. 7

[8] R. Specht, F. Harris, L. Lane, D. Jones, L. Hackel, T. Zaleski, J. Halpin, M. Hill, and W. Wübbenhorst. **Process Control Techniques for Laser Peening of Metals**. In L. Wagner, editor, *8th International Conference on Shot Peening*, pages 474–482, Garmisch-Partenkirchen, Germany, 2002. Wiley-VCH. 9

[9] E. Brinksmeier, J.T. Cammett, W. König, P. Leskovar, J. Peters, and H.K. Tönshoff. **Residual Stresses - Measurement and Causes in Machining Processes**. *Annals of the CIRP*, **31**(2):491–510, 1982. 10, 11

[10] J.J. Williams, X. Deng, N. Chawla, B. Lindsley, P. King, and K.S. Narasimhan. **Effects of Residual Surface Stress and Tempering on the Fatigue Behavior of Ancorsteel 4300**. Technical report, Arizona State University & Hoeganaes Corporation, 2006. 10

[11] H.W. Paxton and R.P.M. Procter. **The Effects of Machining and Grinding on the Stress-Corrosion Cracking Susceptibility of Metals and Alloys**. *American Society of Tool and Manufacturing Engineers*, 1968. 10, 225

[12] P. O'Hara. **Stress Corrosion/Corrosion Fatigue Problems Overcome by Pre-Stressing of Surfaces**. *Anti-Corrosion Methods and Materials*, **33**(10):8–10, 1986. 11

[13] K.A. Soady. **Life Assessment Methodologies Incorporating Shot Peening Process Effects: Mechanistic Consideration of Residual Stresses and Strain Hardening: Part 1 - Effect of Shot Peening on Fatigue Resistance**. *Materials Science and Technology*, **29**(6):637–651, June 2013. 11, 22

[14] J.S. Hornsey. **Residual Stresses : Their Causes, and the Effective Means of Treatment to Reduce the Residual Stresses and to Improve the Fatigue Life in Engineering Components**. Technical report, Vibratory Stress Relieving, South Africa, 2006. 11, 57, 338

[15] M. Kobayashi, T. Matsui, and Y. Murakami. **Mechanism of Creation of Compressive Residual Stress by Shot Peening**. *International Journal of Fatigue*, **20**(5):351–357, May 1998. 11

[16] M. Benedetti, T. Bortolamedi, V. Fontanari, and F. Frendo. **Bending Fatigue Behaviour of Differently Shot Peened Al 6082 T5 Alloy**. *International Journal of Fatigue*, **26**:889–897, August 2004. 11

[17] M.A.S. Torres and H.J.C. Voorwald. **An Evaluation of Shot Peening, Residual Stress and Stress Relaxation on the Fatigue Life of AISI 4340 Steel**. *International Journal of Fatigue*, **24**:877–886, August 2002. 12

[18] K.A. Soady, B.G. Mellor, G.D. West, G. Harrison, A. Morris, and P.A.S. Reed. **Evaluating Surface Deformation and Near Surface Strain Hardening Resulting from Shot Peening a Tempered Martensitic Steel and Application to Low Cycle Fatigue**. *International Journal of Fatigue*, **54**:106–117, September 2013. 12

[19] J.-C. Kim, S.-K. Cheong, and H. Noguchi. **Evolution of Residual Stress Redistribution Associated with Localized Surface Microcracking in Shot-Peened Medium-Carbon Steel During Fatigue Test**. *International Journal of Fatigue*, **55**:147–157, October 2013. 12

[20] K. Dalaei, B. Karlsson, and L.-E. Svensson. **Stability of Shot Peening Induced Residual Stresses and their Influence on Fatigue Lifetime**. *Materials Science and Engineering A*, **528**:1008–1015, January 2011. 12

[21] M. Mochizuki. **Control of Welding Residual Stress for Ensuring Integrity Against Fatigue and StressCorrosion Cracking**. *Nuclear Engineering and Design*, **237**(2):107–123, January 2007. 12

[22] E.-Y. Lee, Y.-S. Lee, Q.-M. Yang, J.-H. Kim, K.-U. Cha, and S.-K. Hong. **Autofrettage Process Analysis of a Compound Cylinder Based on the Elastic-Perfectly Plastic and Strain Hardening Stress-Strain Curve**. *Journal of Mechanical Science and Technology*, **23**:3153–3160, January 2009. 13, 314, 332

[23] H.J. Schindler, P. Bertschinger, C.H. Nguyen, and R. Knobel. **Determination and Evaluation of Residual Stresses in Thick-Walled Cylinders due to Autofrettage**. Tech-

nical report, Swiss Federal Laboratories for Materials Testing and Research & Swiss Ordonance Enterprise, 2000. 13

[24] G.H. Farrahi, G.Z. Voyiadjis, S.H. Hoseini, and E. Hosseinian. **Residual Stress Analysis of the Autofrettaged Thick-Walled Tube Using Nonlinear Kinematic Hardening**. *Journal of Pressure Vessel Technology*, **135**(2):021204, March 2013. 13

[25] E.J. Hearn. *Mechanics of Materials 2*. Butterworth-Heinemann, Oxford, third edition, 1997. 13, 315, 317, 319

[26] M. Sedighi and A.H. Jabbari. **Investigation of Residual Stresses in Thick-Walled Vessels with Combination of Autofrettage and Wire-Winding**. *International Journal of Pressure Vessels and Piping*, **111-112**:295–301, November 2013. 13

[27] M.C. Gibson, A. Hameed, and J.G. Hetherington. **Investigation of Residual Stress Development During Swage Autofrettage, Using Finite Element Analysis**. *Journal of Pressure Vessel Technology*, **136**(2):021206, January 2014. 13

[28] R. Bihamta, M.R. Movahhedy, and A.R. Mashreghi. **A Numerical Study of Swage Autofrettage of Thick-Walled Tubes**. *Materials & Design*, **28**(3):804–815, January 2007. 13

[29] K. Genel, M. Demirkol, and M. Çapa. **Effect of Ion Nitriding on Fatigue Behaviour of AISI 4140 Steel**. *Materials Science and Engineering: A*, **279**(1-2):207–216, February 2000. 14

[30] P. Peyre, R. Fabbro, P. Merrien, and H.P. Lieurade. **Laser Shock Processing of Aluminium Alloys. Application to High Cycle Fatigue Behaviour**. *Materials Science and Engineering A*, **210**:102–113, 1996. 14

[31] Y.K. Zhang, J.Z. Lu, X.D. Ren, H.B. Yao, and H.X. Yao. **Effect of Laser Shock Processing on the Mechanical Properties and Fatigue Lives of the Turbojet Engine Blades Manufactured by LY2 Aluminum Alloy**. *Materials and Design*, **30**(5):1697–1703, May 2009. 15

[32] C.S. Montross, T. Wei, L. Ye, G. Clark, and Y.-W. Mai. **Laser Shock Processing and its Effects on Microstructure and Properties of Metal Alloys : A Review**. *International Journal of Fatigue*, **24**:1021–1036, 2002. 15

[33] Y. Zhang, J. Lu, and K. Luo. **Stress Corrosion Cracking Resistance of AISI 304 SS Subjected to Laser Shock Processing**. In *Laser Shock Processing of FCC Metals*, **179** of *Springer Series in Materials Science*, chapter 7, pages 137–152. Springer Berlin Heidelberg, Berlin, Heidelberg, springer edition, 2013. 15

[34] J. Hu, J. Lou, H. Sheng, S. Wu, G. Chen, K. Huang, L. Ye, Z. Liu, Y. Shi, and S. Yin. **The Effects of Laser Shock Peening on Microstructure and Properties of Metals and Alloys: A Review**. *Advanced Materials Research*, **347-353**:1596–1604, October 2012. 15

[35] P.S. Prevéy, N. Jayaraman, and J. Cammett. **Overview of Low Plastcity Burnishing for Mitigation of Fatigue Damage Mechanisms**. In Lambda Technologies, editor, *Proceedings of ICSP 9*, **9**, Paris, France, 2005. 15

[36] J.T. Cammett and P.S. Prevéy. **Fatigue Strength Restoration in Corrosion Pitted 4340 Alloy Steel Via Low Plasticity Burnishing**. Technical report, Lambda Technologies, Cincinnati, OH, USA, 2006. 15

[37] P.S. Prevéy and J. Cammett. **Low Cost Corrosion Damage Mitigation and Improved Fatigue Performance of Low Plasticity Burnished 7075-T6**. *Journal of Materials Engineering and Performance*, **10**(5):548–555, 2001. 15

[38] P.S. Prevéy and N. Jayaraman. **Low Plasticity Burnishing (LPB) Treatment to Mitigate FOD and Corrosion Fatigue Damage in 17-4 PH Stainless Steel**. In Lambda Technologies, editor, *Proceedings of the Tri-Service Corrosion Conference*, number 513, Las Vegas, USA, 2003. 16, 76

[39] J.E. Scheel, P.S. Prevéy, and D.J. Hornbach. **The Effect of Surface Enhancement on the Corrosion Properties, Fatigue Strength, and Degradation of Aircraft Aluminum**. In *NACE International Corrosion Conference & Expo*, number 10087, pages 1–15, 2010. 16

[40] Y.-L. Zhu, K. Wang, L. Li, and Y.-L. Huang. **Evaluation of an Ultrasound-Aided Deep Rolling Process for Anti-Fatigue Applications**. *Journal of Materials Engineering and Performance*, **18**(8):1036–1040, January 2009. 16

[41] A. Cherif, Y. Pyoun, and B. Scholtes. **Effects of Ultrasonic Nanocrystal Surface Modification (UNSM) on Residual Stress State and Fatigue Strength of AISI 304**. *Journal of Materials Engineering and Performance*, **19**(2):282–286, May 2010. 16

[42] Y.M. Xing and J. Lu. **An Experimental Study of Residual Stress Induced by Ultrasonic Shot Peening**. *Journal of Materials Processing Technology*, **152**:56–61, October 2004. 16

[43] V.I. Trufyakov, P.P. Mikheev, Yu.F. Kudryavtsev, and D.N. Reznik. **Fatigue Endurance of Welded Joints, Residual Stresses and Fatigue Improvement Treatments**. In *Ship Structures Synmposium*, page 1993, Arlington, USA. 16

[44] M. Mansoor and J. Lu. **Ultrasonic Surface Mechanical Attrition of Commercially Pure Ti to Induce Nanocrystalline Surface Layer**. *Key Engineering Materials*, **442**:152–157, June 2010. 17

[45] M.R. Sriraman and R. Vasudevan. **Influence of Ultrasonic Cavitation on Surface Residual Stresses in AISI 304 Stainless Steel**. *Journal of Materials Science*, **33**:2899–2904, 1998. 17

[46] S. Roy, J.W. Fisher, and B.T. Yen. **Fatigue Resistance of Welded Details Enhanced by Ultrasonic Impact Treatment (UIT)**. *International Journal of Fatigue*, **25**:1239–1247, September 2003. 17

[47] E.S. Statnikov, V.O. Muktepavel, and A. Blomqvist. **Comparison of Ultrasonic Impact Treatment (UIT) and other Fatigue Life Improvement Methods**. *Welding in the World*, **46**(3/4):20–32, 2002. 17

[48] M. Sticchi, D. Schnubel, N. Kashaev, and N. Huber. **Review of Residual Stress Modification Techniques for Extending the Fatigue Life of Metallic Aircraft Components**. *Applied Mechanics Reviews*, **67**, August 2014. 17

[49] T.N. Chakherlou and J. Vogwell. **A Novel Method of Cold Expansion which Creates Near-Uniform Compressive Tangential Residual Stress around a Fastener Hole**. *Fatigue & Fracture of Engineering Materials & Structures*, **27**:343–351, 2004. 17

[50] S.J. Houghton and S.K. Campbell. **Identifying the Residual Stress Field Developed by Hole Cold Expansion Using Finite Element Analysis**. *Fatigue & Fracture of Engineering Materials & Structures*, **35**:74–83, January 2011. 17

[51] H.D. Gopalakrishna, H.N. Narasimha Murthy, M. Krishna, M.S. Vinod, and A.V. Suresh. **Cold Expansion of Holes and Resulting Fatigue Life Enhancement and Residual Stresses in Al 2024 T3 Alloy An Experimental Study**. *Engineering Failure Analysis*, **17**:361–368, March 2010. 17

[52] L. Yongshou, S. Xiaojun, L. Jun, and Y. Zhufeng. **Finite Element Method and Experimental Investigation on the Residual Stress Fields and Fatigue Performance of Cold Expansion Hole**. *Materials & Design*, **31**(3):1208–1215, March 2010. 18

[53] W.Z. Yan, X.S. Wang, H.S. Gao, and Z.F. Yue. **Effect of Split Sleeve Cold Expansion on Cracking Behaviors of Titanium Alloy TC4 Holes**. *Engineering Fracture Mechanics*, **88**:79–89, July 2012. 18

[54] N. Jayaraman, D. Christensen, and J. Scheel. **LPB as a Crack Initiation Resistant Process for Case Hardened Steels**. Technical report, Lambda Research. 18

[55] N. Tsuji, S. Tanaka, and T. Takasugi. **Evaluation of Surface-Modified Ti6Al4V Alloy by Combination of Plasma-Carburizing and Deep-Rolling**. *Materials Science and Engineering: A*, **488**(1-2):139–145, August 2008. 18

[56] K. Genel, M. Demirkol, and T. Guelmez. **Corrosion Fatigue Behaviour of Ion Nitrided AISI 4140 Steel**. *Materials Science and Engineering A*, **288**:91–100, 2000. 22

[57] W.F. Hosford. *Mechanical Behavior of Materials*. Cambridge University Press, Cambridge, UK, 2005. 22

[58] S.S. Manson and G.R. Halford. *Fatigue and Durability of Structural Materials*. ASM International, Materials Park, OH, USA, 2006. 23, 83, 259, 339

[59] S.J. Maddox. **The Effect of Mean Stress on Fatigue Crack Propagation - A Literature Review**. *International Journal of Fracture*, **11**(3):389–408, 1975. 23, 59

[60] ASM International. **Fatigue**. In F.C. Campbell, editor, *Elements of Metallurgy and Engineering Alloys*, chapter 14, pages 243–264. ASM International, Materials Park, OH, USA, 2008. 23, 27

[61] W. Liu, Z. Wang, and Y. Xia. **Intergranular Fatigue Cracking Behaviour in Aluminium**. *Chin. J. Met. Sci. Technol.*, **5**, 1989. 23

[62] J. Lancaster. *Engineering Catastrophes: Causes and Effects of Major Accidents*. Abington Publishing, 1996. 24

[63] G.H. Koch, M.P.H. Brongers, N.G. Thompson, Y.P. Virmani, and J.H. Payer. **Corrosion Costs and Preventive Strategies in the United States**. Technical report, Federal Highway Administration, CC Technologies, NACE International, 2002. 24

[64] British Standards Institution. **Metallic Materials - Tensile Testing Part 1: Method of Test at Ambient Temperature**. *BSI Standards Publication*, **BS EN ISO**:6892–1:2009, 2009. 25

[65] ASTM Standard. *Standard Practice for Conducting Force Controlled Constant Amplitude Axial Fatigue Tests of Metallic Materials*, **03**. ASTM International, West Conshohocken, PA, USA, e 466-96 edition, 2002. 25, 30, 31, 37

[66] ASM International. **Fatigue and Fracture**. In S. Lampman, editor, *ASM Handbook*, chapter Volume 19. ASM International, USA, 1996. 26, 264

[67] P.E. Weihsmann. **Fatigue Curves Without Testing**. *Materials Engineering*, **March**:52–54, 1980. 26

[68] R.G. Budynas and J.K. Nisbett. *Shigley's Mechanical Engineering Design*. McGraw-Hill Primis, USA, eighth edition, 2008. 30, 139

[69] H.F. Moore and P.E. Henwood. **The Strength of Screw Threads Under Repeated Tension**. *University of Illinois Bulletin*, **XXXI**(28), 1934. 30

[70] ASTM. *Handbook of Fatigue Testing*. Philadelphia, PA, USA, 1974. 31

[71] A. Waughman. *Investigation Into The Effect Of A Compressive Residual Stress Field On The Fatigue Performance Of Corroded 4330 Low Alloy Carbon Steel*. Undergraduate project thesis, University of Strathclyde, 2013. 32

[72] J. Guthrie, B. Battat, and C. Grethlein. **Accelerated Corrosion Testing**. *The AMPTIAC Quarterly*, **6**(3):11–15, 2002. 32

[73] ASTM Standard. *Standard Guide for Examination and Evaluation of Pitting Corrosion*. ASTM International, West Conshohocken, PA, USA, g 46-94 edition, 1999. 32

[74] British Standards Institution. **Corrosion of Metals and Alloys - Corrosion Fatigue Testing - Part 1: Cycles to Failure Testing**. *BSI Standards Publication*, **BS EN ISO**:11782–1:2008, 2008. 36

[75] A. Neville and T. Hodgkiess. **An Assessment of the Corrosion Behaviour of High-Grade Alloys in Seawater at Elevated Temperature and Under a High Velocity Impinging Flow**. *Corrosion Science*, **38**(6):927–956, June 1996. 36

[76] C. Patel. **Cyclic Strain Enhanced Dissolution Behavior of Mild Steel in 10 Pct NH4NO3 and the Correlation with Corrosion Fatigue Properties**. *Metallurgical Transactions A*, **11**(2):301–306, 1980. 36

[77] J. Roszak. *Investigation Into The Effect Of A Compressive Mean Stress On The Fatigue Performance Of Corroded 4330 Low Alloy Carbon Steel*. Undergraduate project thesis, University of Strathclyde, 2014. 37, 56

[78] British Standards Institution. **Metallic Materials - Rotating Bar Bending Fatigue Testing**. *BSI Standards Publication*, **BS ISO**:1143:2010, 2010. 37, 45

[79] European Federation of Corrosion and NACE International. *The Corrosion Performance of Metals for the Marine Environment: A Basic Guide*. Maney Publishing, Leeds, UK, no. 63 edition, 2012. 43

[80] G. Barnard. *Design review and commissioning of an experimental rig for fatigue testing in a corrosive environment*. Undergraduate project thesis, University of Strathclyde, 2014. 43

[81] G. Murtaza and R. Akid. **Empirical Corrosion Fatigue Life Prediction Models of a High Strength Steel**. *Engineering Fracture Mechanics*, **67**(263):461–474, 2000. 48

[82] A. Ragab, H. Alawi, and K. Sorein. **Corrosion Fatigue of Steel in Various Aqueous Environments**. *Fatigue of Engineering Materials*, **12**(6):469–479, 1989. 50

[83] S.I. Rokhlin, J.Y. Kim, H. Nagy, and B. Zoofan. **Effect of Pitting Corrosion on Fatigue Crack Initiation and Fatigue Life**. *Engineering Fracture Mechanics*, **62**:425–444, 1999. 53

[84] R. Ahmed, H. Yu, S. Stewart, L. Edwards, and J. R. Santisteban. **Residual Strain Measurements in Thermal Spray Cermet Coatings via Neutron Diffraction**. *Journal of Tribology*, **129**(2):411, 2007. 57, 58, 64, 165

[85] R.H. Leggatt. **Residual stresses in welded structures**. *International Journal of Pressure Vessels and Piping*, **85**(3):144–151, March 2008. 57, 338

[86] D. Deng, K. Ogawa, S. Kiyoshima, N. Yanagida, and K. Saito. **Prediction of residual stresses in a dissimilar metal welded pipe with considering cladding, buttering and post weld heat treatment**. *Computational Materials Science*, **47**:398–408, December 2009. 57

[87] A. Joseph, S.K. Rai, T. Jayakumar, and N. Murugan. **Evaluation of Residual Stresses in Dissimilar Weld Joints**. *International Journal of Pressure Vessels and Piping*, **82**:700–705, September 2005. 58, 61

[88] H. Gripenberg, H. Keinänen, C. Ohms, H. Hänninen, D. Stefanescu, and D.J. Smith. **Prediction and Measurement of Residual Stresses in Cladded Steel**. *Materials Science Forum*, **404-407**:861–866, 2002. 58, 256

[89] Anthony G. Evans and John W. Hutchinson. **Crack deflection at an interface between dissimilar elastic materials: Role of residual stresses**. *International Journal of Solids and Structures*, **31**(24):3443–3455, December 1994. 59

[90] W Schmitt, D.Z Sun, and J.G Blauel. **Damage mechanics analysis (Gurson model) and experimental verification of the behaviour of a crack in a weld-cladded component**. *Nuclear Engineering and Design*, **174**(3):237–246, October 1997. 59

[91] Xiaoli Zhao, Paul Munroe, Daryoush Habibi, and Zonghan Xie. **Roles of compressive residual stress in enhancing the corrosion resistance of nano nitride composite coatings on steel**. *Journal of Asian Ceramic Societies*, April 2013. 59

[92] A.G. Evans, G.B. Crumley, and R.E. Demaray. **On the Mechanical Behavior of Brittle Coatings and Layers**. *Oxidation of Metals*, **20**(5/6):193–216, 1983. 59

[93] L. Pejryd, J. Wigren, D.J. Greving, J.R. Shadley, and E.F. Rybicki. **Residual Stresses as a Factor in the Selection of Tungsten Carbide Coatings for a Jet Engine Application**. *Journal of Thermal Spray Technology*, **4**(3):268–274, 1995. 59

[94] A.G. Evans, D.R. Mumm, J.W. Hutchinson, G.H. Meier, and F.S. Pettit. **Mechanisms controlling the durability of thermal barrier coatings**. *Progress in Materials Science*, **46**(5):505–553, January 2001. 59

[95] K. Kokini, Y.R. Takeuchi, and B.D. Choules. **Surface thermal cracking of thermal barrier coatings owing to stress relaxation: zirconia vs. mullite**. *Surface and Coatings Technology*, **82**(1-2):77–82, July 1996. 59

[96] W Chen, G Vanboven, and R Rogge. **The role of residual stress in neutral pH stress corrosion cracking of pipeline steels Part II: Crack dormancy**. *Acta Materialia*, **55**(1):43–53, January 2007. 60

[97] Q. Lin, J. Chen, and H. Chen. **Possibility of Inducing Compressive Residual Stresses in Welded Joints of SS400 Steels**. *Journal of Materials Science & Technology*, **17**(6):661–663, 2001. 60

[98] Jarmila Woodtli and Rolf Kieselbach. **Damage due to hydrogen embrittlement and stress corrosion cracking**. *Engineering Failure Analysis*, **7**(6):427–450, December 2000. 60

[99] Masahito Mochizuki, Kunio Enomoto, Noriaki Okamoto, Hideyo Saito, and Eisaku Hayashi. **Welding residual stresses at the intersection of a small diameter pipe penetrating a thick plate**. *Nuclear Engineering and Design*, **144**(3):439–447, November 1993. 60

[100] A Ben Rhouma, C Braham, M E Fitzpatrick, J Ledion, and H Sidhom. **Effects of Surface Preparation on Pitting Resistance , Residual Stress, and Stress Corrosion Cracking in Austenitic Stainless Steels**. *Journal of Materials Engineering and Performance*, **10**(October):507–514, 2001. 60

[101] a.a. Boudi, M.S.J. Hashmi, and B.S. Yilbas. **Fatigue testing of Inconel-625 coatings on carbon and stainless steel after one and three weeks of exposure to aqueous electrolytic solution**. *Industrial Lubrication and Tribology*, **60**(1):24–30, 2008. 60, 64, 271

[102] G Vanboven, W Chen, and R Rogge. **The role of residual stress in neutral pH stress corrosion cracking of pipeline steels. Part I: Pitting and cracking occurrence**. *Acta Materialia*, **55**(1):29–42, January 2007. 60

[103] A.F.M. Arif and B.S. Yilbas. **Three-point bend testing of HVOF Inconel 625 coating: FEM simulation and experimental investigation**. *Surface and Coatings Technology*, **201**(3-4):1873–1879, October 2006. 61

[104] M. Magnani, P.H. Suegama, A.A.C. Recco, J.M. Guilemany, C.S. Fugivara, and A.V. Benedetti. **WC-CoCr Coatings Sprayed by High Velocity Oxygen-Fuel (HVOF) Flame on AA7050 Aluminum Alloy: Electrochemical Behavior in 3.5 % NaCl Solution**. *Materials Research*, **10**(4):377–385, 2007. 61

[105] Tie-Gang Wang, Sheng-Sheng Zhao, Wei-Gang Hua, Jia-Bao Li, Jun Gong, and Chao Sun. **Estimation of residual stress and its effects on the mechanical properties of detonation gun sprayed WCCo coatings**. *Materials Science and Engineering: A*, **527**(3):454–461, January 2010. 61

[106] M.M. Lima, C. Godoy, P.J. Modenesi, J.C. Avelar-Batista, A. Davison, and A. Matthews. **Coating Fracture Toughness Determined by Vickers Indentation: An Important Parameter in Cavitation Erosion Resistance of WC-Co Thermally Sprayed Coatings**. *Surface and Coatings Technology*, **178-178**:489–496, 2004. 61

[107] Jörg Hohe, Marcus Brand, and Dieter Siegele. **Fracture analysis of cladded components considering residual stresses**. *Pamm*, **8**(1):10209–10210, December 2008. 61

[108] H. Alberg. *Simulation of Welding and Heat Treatment: Modelling and Validation*. PhD thesis, Lulea University of Technology, 2005. 61, 338

[109] Y. Li, J. Wang, M. Chen, and X. Shen. **Finite Element Analysis of Residual Stress in the Welded Zone of a High Strength Steel**. *Bulletin of Materials Science*, **27**(2):127–132, April 2004. 61

[110] NACE International. **Metals for Sulfide Stress Cracking and Stress Corrosion Cracking Resistance in Sour Oilfield Environments**. Technical report, NACE Standard MR0175-2003, Houston, Texas, 2003. 62, 122, 124, 164, 264, 312, 336, 341

[111] U. Malayoglu and A. Neville. **Mo and W as Alloying Elements in Co-Based Alloys - Their Effects on Erosion-Corrosion Resistance**. *Wear*, **259**:219–229, July 2005. 63

[112] E.J. Wentzel and C. Allen. **Erosion-Corrosion Resistance of Tungsten Carbide Hard Metals with Different Binder Compositions**. *Wear*, **181-183**:63–69, February 1995. 63

[113] S. Shrestha, T. Hodgkiess, and A. Neville. **The Effect of Post-Treatment of a High-Velocity Oxy-Fuel Ni-Cr-Mo-Si-B Coating Part 2 : Erosion-Corrosion Behavior**. *Journal of Thermal Spray Technology*, **10**(December):656–665, 2001. 63

[114] N. Ahmed, M.S. Bakare, D.G. McCartney, and K.T. Voisey. **The effects of microstructural features on the performance gap in corrosion resistance between bulk and HVOF sprayed Inconel 625**. *Surface and Coatings Technology*, **204**(14):2294–2301, April 2010. 63, 64

[115] E. Chikarakara, S. Aqida, D. Brabazon, S. Naher, J. a. Picas, M. Punset, and A. Forn. **Surface Modification of HVOF Thermal Sprayed WCCoCr Coatings by Laser Treatment**. *International Journal of Material Forming*, **3**:801–804, June 2010. 64

[116] Environmental Security Technology Certification Program. **Cost and Performance Report: Validation of HVOF Thermal Spray Coatings as a Replacement for Hard Chrome Plating on Hydraulic/Pneumatic Actuators**. Technical Report December, U.S. Department of Defense, Alexandria, VA, USA. 64

[117] C.W. Lee, J.H. Han, J. Yoon, M.C. Shin, and S.I. Kwun. **A study on powder mixing for high fracture toughness and wear resistance of WCCoCr coatings sprayed by HVOF**. *Surface and Coatings Technology*, **204**(14):2223–2229, April 2010. 64

[118] Z.Y. Al-Taha, M.S.J. Hashmi, and Bekir Sami Yilbas. **HVOF Coating of Inconel 625 Blended with WC: Fracture Toughness Measurement**. *Advanced Materials Research*, **264-265**:1972–1981, June 2011. 64, 271

[119] Z.Y. Al-Taha, M.S. Hashmi, and B.S. Yilbas. **Effect of WC on the residual stress in the laser treated HVOF coating**. *Journal of Materials Processing Technology*, **209**(7):3172–3181, April 2009. 64

[120] K.O. Legg, B.D. Sartwell, J.-G. Legoux, M. Nestler, C. Dambra, D. Wang, J. Quets, P. Natishan, P. Bretz, and J. Devereaux. **Investigation of Plasma Spray Coatings as an Alternative to Hard Chrome Plating on Internal Surfaces**. Technical report, Naval Research Laboratory, Washington, DC, USA, 2006. 65

[121] C.S. Ramesh, D.S. Devaraj, R. Keshavamurthy, and B.R. Sridhar. **Slurry Erosive Wear Behaviour of Thermally Sprayed Inconel-718 Coatings by APS Process**. *Wear*, **271**:1365–1371, July 2011. 65

[122] B.F. Levin, J.N. Dupont, and a.R. Marder. **Weld overlay coatings for erosion control**. *Wear*, **181-183**:810–820, March 1995. 65

[123] C. Katsich and E. Badisch. **Effect of carbide degradation in a Ni-based hardfacing under abrasive and combined impact/abrasive conditions**. *Surface and Coatings Technology*, **206**(6):1062–1068, December 2011. 66

[124] Abdou Abdel-Samad, E. Lugscheider, K. Bobzin, and M. Maes. **The influence of hot isostatic pressing on plasma sprayed coatings properties**. *Surface and Coatings Technology*, **201**(3-4):1224–1227, October 2006. 66

[125] V. Teixeira, M. Andritschky, W. Fischer, H.P. Buchkremer, and D. Stöver. **Analysis of Residual Stresses in Thermal Barrier Coatings**. *Journal of Materials Processing Technology*, **92-93**:209–216, 1999. 66

[126] O.B. Soroka. **Evaluation of Residual Stresses in PVD-Coatings. Part 1. Review**. *Strength of Materials*, **42**(3):287–296, 2010. 67

[127] Andrew Siao Ming Ang, Christopher C. Berndt, and Philip Cheang. **Deposition effects of WC particle size on cold sprayed WCCo coatings**. *Surface and Coatings Technology*, **205**(10):3260–3267, February 2011. 68

[128] C. Juliot and D.W. Bucholz. **Erosion Resistance of Infiltration Brazed Tungsten Carbide Cladding**. Technical Report 1, Conforma Clad, New Albany, IN, USA, 2005. 68

[129] H.K. Rafi, G.D.J. Ram, G. Phanikumar, and K.P. Rao. **Friction Surfacing of Austenitic Stainless Steel on Low Carbon Steel : Studies on the Effects of Traverse Speed**. In *World Congress on Engineering*, **II**, page Vol II, London, UK, 2010. 69

[130] R.R. Irving. **Tig quality, MIG speed combined in hot wire welding process**. *Iron Age*, **Technical**(October), 1966. 71

[131] B.K. Henon. **Advances in Automatic Hot Wire GTAW (TIG) Welding**. 71

[132] K. Hori, H. Watanabe, T. Myoga, and K. Kusano. **Development of Hot Wire TIG Welding Methods Using Pulsed Current to Heat Filler Wire Research on Pulse Heated Hot Wire TIG Welding Processes**. *Welding International*, **18**(6):456–468, June 2004. 72

[133] IODS Ltd. **IODS International Weld Overlay Specialists**. 74

[134] NiWire Industries Co. Ltd. **Inconel 625**. 76

[135] B.K. Henon. **Technical Paper: Hot Wire Narrow Groove Welding and Cladding with Nickel-Based Alloys**. *Focus on Nuclear Power Generation*, (August):20–23, 2010. 76

[136] The Harris Products Group. **Technical Specification Sheet: 630 (17-4) Stainless Steel Welding Wire**. Technical report, A Lincoln Electric Company, Mason, OH, USA. 76

[137] D.J. Hornbach, P.S. Prevéy, and P.W. Mason. **X-Ray Diffraction Characterization of the Residual Stress and Hardness Distributions in Induction Hardened Gears**. In Gear Research Institute, editor, *First International Conference on Induction Hardened Gears and Critical Components*, pages 69–76, Indianapolis, IN, USA, 1995. Lamda Technologies. 77

[138] Dean Deng. **FEM prediction of welding residual stress and distortion in carbon steel considering phase transformation effects**. *Materials & Design*, **30**(2):359–366, February 2009. 77, 263, 264

[139] S.W. Banovic, J.N. DuPont, and A.R. Marder. **Dilution Control in Gas-Tungsten-Arc Welds Involving Superaustenitic Stainless Steels and Nickel-Based Alloys**. *Metallurgical and Materials Transactions B*, **32B**(December):1171–1176, 2001. 79, 80

[140] M.C. Smith, O. Muransky, A. Goodfellow, E. Kingston, P. Freyer, S. Marlette, G.M. Wilkowski, B. Brust, and S. Do-Jun. **The Impact of Key Simulation Variables on Predicted Residual Stresses in Pressuriser Nozzle Dissimilar Metal Weld Mock-ups. Part 2 - Comparison of Simulation and Measurements**. *ASME PVP*, pages 1–17, 2010. 98, 99, 119, 125, 169, 204, 207, 333

[141] JAHM Software Inc. **MPDB**, 2013. 99, 116, 117, 118, 125, 143, 332

[142] ASTM Standard. *Standard Test Method for Linear Thermal Expansion of Solid Materials With a Push-Rod Dilatometer*. ASTM International, West Conshohocken, PA, USA, e228-11 edition, 2011. 99

[143] ASTM Standard. *Standard Test Method for Thermal Diffusivity by the Flash Method*. ASTM International, West Conshohocken, PA, USA, e1461-13 edition, 2013. 107

[144] ASTM Standard. *Standard Test Method for Determining Specific Heat Capacity by Differential Scanning Calorimetry*. ASTM International, West Conshohocken, PA, USA, e1269-11 edition, 2011. 110, 111

[145] British Stainless Steel Association. **Elevated temperature physical properties of stainless steels**. 116, 118

[146] F. L. Everett and J. Miklowitz. **Poisson's Ratio at High Temperatures**. *Journal of Applied Physics*, **15**:592–598, 1944. 117

[147] ASTM International. *Handbook of Comparative World Steel Standards: DS67B*. Third edition, 2004. 126

[148] ASTM International. *Standard Test Methods for Tension Testing of Metallic Materials [Metric]*. ASTM International, West Conshohocken, PA, USA, e8m-04 edition, 2004. 125, 128

[149] Engineer's Handbook. **Hardness Conversion Table - Brinell, Rockwell, Vickers**, 2006. 154, 155

[150] R.J. Dennis, N.A. Leggatt, M.C. Smith, and P.J. Bouchard. **R6 Weld Modelling Guidelines - Application to Groove Weld Worked Example**. In *ASME 2010 Pressure Vessels & Piping Division*, pages 1–14, Bellevue, Washington, USA, 2010. ASME. 159

[151] W. Vandermeulen, M. Scibetta, A. Leenaers, J. Schuurmans, and R. Gérard. **Measurement of the Young modulus anisotropy of a reactor pressure vessel cladding**. *Journal of Nuclear Materials*, **372**:249–255, January 2008. 159

[152] ASTM Standard. *Standard Test Method for Impact Testing of Miniaturized Charpy V-Notch Specimens*. ASTM International, West Conshohocken, PA, USA, e2248-12 edition, 2012. 162

[153] ASTM Standard. *Standard Test Methods for Notched Bar Impact Testing of Metallic Materials*. ASTM International, West Conshohocken, PA, USA, e23-02a edition, 2003. 162

[154] J. Lesage and D. Chicot. **Role of residual stresses on interface toughness of thermally sprayed coatings**. *Thin Solid Films*, **415**(1-2):143–150, August 2002. 163

[155] S.J. Maddox. *Fatigue Strength of Welded Structures*. Abington Publishing, Cambridge, UK, second edition, 1991. 166

[156] Jinya Katsuyama, Makoto Udagawa, Hiroyuki Nishikawa, Mitsuyuki Nakamura, and Kunio Onizawa. **Evaluation of Weld Residual Stress near the Cladding and J-weld in Reactor Pressure Vessel Head for the assessment of PWSCC Behavior**. *E-Journal of Advanced Maintenance*, **2**:50–64, 2010. 168, 179, 207, 264, 277

[157] M C Smith, A C Smith, and R Wimpory. **Review of the NeT Task Group 1 Single Weld Bead on Plate Benchmark Round Robin**. Technical report, EDF Energy Nuclear Generation Limited, 2011. 169

[158] L.-E. Lindgren. *Computational Welding Mechanics: Thermomechanical and Microstructural Simulations*. Woodhead Publishing Limited, Cambridge, UK, 2007. 169, 170, 171, 173, 189, 205, 206, 259, 261, 263, 265, 268, 269, 282, 333, 340

[159] J. Goldak, J. Zhou, V. Breiguine, and F. Montoya. **Thermal Stress Anlaysis of Welds: From Melting Point to Room Temperature**. *Transactions of JWRI*, **25**(2):185–189, 1996. 169, 173

[160] A. Yaghi and A A Becker. **State of the Art Review - Weld Simulation Using Finite Element Methods**. Technical report, NAFEMS, University of Nottingham, 2005. 169

[161] B. Brickstad and B.L. Josefson. **A parametric study of residual stresses in multi-pass butt-welded stainless steel pipes**. *International Journal of Pressure Vessels and Piping*, **75**:11–25, 1998. 171, 206, 269, 280, 333

[162] X.K. Zhu and Y.J. Chao. **Effects of temperature-dependent material properties on welding simulation**. *Computers & Structures*, **80**:967–976, May 2002. 171

[163] F Rossillon and L Depradeux. **A Time Saving Method to Compute Multi-Pass Weld Residual Stresses**. *SMiRT-22*, pages 413–423, 2013. 171

[164] B. Taljat, T. Zacharia, X.-L. Wang, J. R. Keiser, R. W. Swindeman, Z. Feng, and M. J. Jirinec. **Numerical Analysis of Residual Stress Distribution in Tubes with Spiral Weld Cladding**. *Welding Research Supplement*, (August):328–335, 1998. 172

[165] A. Carmet, S. Debiez, J. Devaux, D. Pont, and J.B. Leblond. **Experimental and numerical study of residual stresses and strains in an electron-beam-welded joint**. In *International Conference on Residual Stresses*, Nancy, France, 1988. 173

[166] B.K. Jones, A.F. Emery, and S.J. Marburger. **An Analytical and Experimental Study of the Effect of Welding Parameters on Fusion Welds**. *Welding Research Supplement*, (February):51–59, 1993. 173

[167] P. Tekriwal and J. Mazumder. **Transient and residual thermal strain-stress analysis of GMAW**. *ASME Journal of Engineering Materials and Technology*, **113**:336–343, 1991. 173

[168] J. Zimmerman. **Finite Element Modelling of the Residual Stresses Induced in Thermally Deposited Coatings**. *Archives of Metallurgy and Materials*, **59**(2), January 2014. 180

[169] H E Coules. **Contemporary approaches to reducing weld-induced residual stress**. *Materials Science and Technology*, **0**(0):1–15, 2012. 195

[170] N. Yurioka and H. Suzuki. **Hydrogen assisted cracking in C-Mn and low alloy steel weldments**. *International Materials Reviews*, **35**(4):217–249, 1990. 195

[171] Y.C. Lin and K.H. Lee. **Effect of preheating on the residual stress in type 304 stainless steel weldment**. *Journal of Materials Processing Technology*, **63**:797–801, 1997. 195

[172] a. Plati, J.C. Tan, I.O. Golosnoy, R. Persoons, K. vanAcker, and T.W. Clyne. **Residual Stress Generation during Laser Cladding of Steel with a Particulate Metal Matrix Composite**. *Advanced Engineering Materials*, **8**(7):619–624, July 2006. 204, 286

[173] J.A. Goldak and M. Akhlaghi. *Computational Welding Mechanics*. Springer, New York, USA, 2005. 205, 260, 268, 279, 339

[174] N.S. Rossini, M. Dassisti, K.Y. Benyounis, and a.G. Olabi. **Methods of measuring residual stresses in components**. *Materials & Design*, **35**:572–588, March 2012. 210, 217, 218

[175] VEQTER. **Overview**. 211

[176] Alan Owens. **Extension to the blind hole drilling technique for residual stress determination with airabrasive hole forming**. *Strain*, pages 159–165, 1984. 212, 231

[177] Micro-Measurements. **Measurement of residual stresses by the hole-drilling strain gage method**. Technical report, Vishay Precision Group, 2010. 212, 213

[178] J. Mathar. **Determination of initial stresses by measuring the deformations around drilled holes**. *Transactions ASME*, **56**(2):249–254, 1934. 212

[179] ASTM Standard. *Standard Test Method for Determining Residual Stresses by the Hole-Drilling Strain-Gage Method*. ASTM International, West Conshohocken, PA, USA, e837-13a edition, 2013. 212

[180] P.V. Grant, J.D. Lord, and P.S. Whitehead. **Measurement Good Practice Guide No. 53 - Issue 2: The Measurement of Residual Stresses by the Incremental Hole Drilling Technique**. Technical Report 53, National Physical Laboratory, Teddington, UK, 2006. 212, 215, 223, 248

[181] G. S. Schajer. **Measurement of Non-Uniform Residual Stresses Using the Hole-Drilling Method . Part I Stress Calculation Procedures**. *Journal of Engineering Materials and Technology*, **110**(October):338–343, 1988. 212, 215

[182] J. Lord. **Hole Drilling Techniques**. In *BCA Structural Materials Workshop*, number September. The NPL Materials Centre, 2000. 213

[183] J.E. Bynum. **Modifications to the Hole-drilling Technique of Measuring Residual Stresses for Improved Accuracy and Reproducibility**. *Experimental Mechanics*, (January):21–30, 1981. 215

[184] B Zuccarello. **Optimal calculation steps for the evaluation of residual stress by the incremental hole-drilling method**. *Experimental mechanics*, pages 117–124, 1999. 216

[185] D. Stefanescu, C. E. Truman, D. J. Smith, and P. S. Whitehead. **Improvements in Residual Stress Measurement by the Incremental Centre Hole Drilling Technique**. *Experimental Mechanics*, **46**(4):417–427, May 2006. 216

[186] C. Barile, C. Casavola, G. Pappalettera, and C. Pappalettere. **Considerations on the choice of experimental parameters in residual stress measurements by hole-drilling and ESPI**. *Frattura ed Integrita Strutturale*, **30**:211–219, 2014. 216

[187] VEQTER. **Deep-Hole Drilling**. 216

[188] D. M. Goudar, C. E. Truman, and D. J. Smith. **Evaluating uncertainty in residual stress measured using the deep-hole drilling technique**. *Strain*, **47**:62–74, 2011. 217

[189] Anthony P. Parker. **A Critical Examination of Sachs Material-Removal Method for Determination of Residual Stress**. *Journal of pressure vessel technology*, **126**(May):234, 2004. 217

[190] C.C. Aydner and M.B. Prime. **Three-Dimensional Constraint Effects on the Slitting Method for Measuring Residual Stress**. *Journal of Engineering Materials and Technology*, **135**:1–10, May 2013. 217

[191] M.B. Prime. **Cross-sectional mapping of residual stresses by measuring the surface contour after a cut**. *Journal of Engineering Materials and Technology*, **123**:162–168, 2001. 217, 299, 301

[192] M.E. Fitzpatrick, A.T. Fry, P. Holdway, F.A. Kandil, J. Shackleton, and L. Suominen. **Measurement Good Practice Guide No. 52: Determination of Residual Stresses by X-ray Diffraction - Issue 2**. Technical Report 52, National Physical Laboratory, Teddington, UK, 2005. 218

[193] Proto Manufacturing. **Residual Stress**. 219

[194] P.J Withers and H.K.D.H. .Bhadeshia. **Residual Stress: Part 1 Measurement Techniques**. *Materials Science and Technology*, **17**(April):355–365, 2001. 219, 299

[195] A.N. Ezeilo and G.A. Webster. **Advances in Neutron Diffraction for Engineering Residual Stress Measurements**. *Textures and Microstructures*, **33**:151–171, 1999. 219

[196] Stresscraft Ltd. **Stresscraft residual stress measurement and stress calculation services**. 221, 224

[197] H. Sasahara. **The Effect on Fatigue Life of Residual Stress and Surface Hardness Resulting from Different Cutting Conditions of 0.45%C Steel**. *International Journal of Machine Tools & Manufacture*, **45**:131–136, February 2005. 226, 227, 231

[198] Proto Manufacturing. **Sample Prep**. 228

[199] A.M. Korsunsky. **Residual elastic strain due to laser shock peening: modelling by eigenstrain distribution**. *The Journal of Strain Analysis for Engineering Design*, **41**(3):195–204, April 2006. 241

[200] G.S. Schajer and E. Altus. **Stress Calculation Error Analysis for Incremental Hole-Drilling Residual Stress Measurements**. *Transactions of the ASME*, **118**(January):120–126, 1996. 248

[201] M I Onsoien, M M'Hamdi, and O M Akselsen. **Residual Stresses in Weld Thermal Cycle Simulated Specimens of X70 Pipeline Steel**. *Welding Journal*, **89**(June):127–s – 132–s, 2010. 259, 269

[202] H. K. D. H. Bhadeshia. **Martensite in Steels**. *Materials Science & Metallurgy*, pages 1–12, 2002. 259

[203] Tadashi Kasuya, Ryouhei Hamamura, Hidekazu Murakawa, Hiroshige Inoue, and Tomoyuki Kakeshita. **Martensite transformation of a Cr-Ni type weld metal and its application to analysis of welded joints**. *Welding in the World*, March 2014. 261, 280

[204] Tao Bi, Dean Deng, Yangang Tong, Xiaozhan Liu, and Yijun Zhou. **Investigation of Influence of Phase Transformation on Welding Residual Stress in P91 Steel**. In *Proceedings of the WSE2013*, Weihai, China, 2013. 261, 280

[205] A.H. Yaghi, T.H. Hyde, A.A. Becker, and W. Sun. **Numerical Simulation of P91 Pipe Welding Including the Effects of Solid-State Phase Transformation on Residual Stresses**. *Proceedings of the Institution of Mechanical Engineers, Part L: Journal of Materials: Design and Applications*, **221**(4):213–224, January 2007. 261, 262, 277

[206] D. Deng, Y. Luo, H. Serizawa, M. Shibahara, and H. Murakawa. **Numerical Simulation of Residual Stress and Deformation Considering Phase Transformation Effect**. *Transactions of JWRI*, **32**(2):325–333, 2003. 262, 263, 269

[207] S.W. Ooi, J.E. Garnham, and T.I. Ramjaun. **Review: Low transformation temperature weld filler for tensile residual stress reduction**. *Materials & Design*, **56**:773–781, April 2014. 261

[208] M T Todinov. **Influence of some parameters on the residual stresses from quenching**. *Modelling Simul. Mater. Sci. Eng.*, **7**:25–41, 1999. 263

[209] M. C. Payares-Asprino, H. Katsumoto, and S. Liu. **Effect of Martensite Start and Finish Temperature on Residual Stress Development in Structural Steel Welds**. *Welding Journal*, **87**(November):279–290, 2008. 263

[210] W Wang, L Huo, Y Zhang, D Wang, and H Jing. **New developed welding electrode for improving the fatigue strength of welded joints**, 2002. 263

[211] Lubos Mraz, Leif Karlsson, Pavol Mikula, and Miroslav Vrána. **Identification of Weld Residual Stresses Using Diffraction Methods and their Effect on Fatigue Strength of High Strength Steels Welds**. *Materials Science Forum*, **768-769**:668–674, September 2013. 263

[212] L.W. Tsay, Y.C. Liu, D.-Y. Lin, and M.C. Young. **The use of laser surface-annealed treatment to retard fatigue crack growth of austenitic stainless steel**. *Materials Science and Engineering: A*, **384**(1-2):177–183, October 2004. 264

[213] A.K. Bhaduri, S. Sujith, G. Srinivasan, T.P.S. Gill, and S.L. Mannan. **Optimized Postweld Heat Treatment Procedures for 17-4 PH Stainless Steels**. *Welding Research Supplement*, (May):153–159, 1995. 264, 339

[214] R. J. Moat, H. J. Stone, a. a. Shirzadi, J. a. Francis, S. Kundu, a. F. Mark, H. K. D. H. Bhadeshia, L. Karlsson, and P. J. Withers. **Design of weld fillers for mitigation of residual stresses in ferritic and austenitic steel welds**. pages 279–284, 2011. 268

[215] Santosh Kumar, a. Kundu, K.a. Venkata, a. Evans, C.E. Truman, J.a. Francis, K. Bhanumurthy, P.J. Bouchard, and G.K. Dey. **Residual Stresses in Laser Welded ASTM A387 Grade 91 Steel Plates**. *Materials Science and Engineering: A*, March 2013. 269

[216] P. Dupas and D. Moinereau. **Evaluation of Cladding Residual Stresses in Clad Blocks by Measurements and Numerical Simulations**. *Journal de Physique IV*, **6**:187–196, 1996. 269, 338

[217] J. A. Francis, H. K. D. H. Bhadeshia, and P. J. Withers. **Welding residual stresses in ferritic power plant steels**. *Materials Science and Technology*, **23**(9):1009–1020, September 2007. 270, 279

[218] Dean Deng and Hidekazu Murakawa. **Finite element analysis of temperature field, microstructure and residual stress in multi-pass butt-welded 2.25Cr1Mo steel pipes**. *Computational Materials Science*, **43**(4):681–695, October 2008. 270

[219] S.A. Tsirkas, P. Papanikos, and Th. Kermanidis. **Numerical simulation of the laser welding process in butt-joint specimens**. *Journal of Materials Processing Technology*, **134**:59–69, 2003. 270

[220] J.P. Moore. **Maintaining the Corrosion Resistance of Welded Stainless Steel**. *Anti-Corrosion Methods and Materials*, **1**(4):92–112, 1954. 270

[221] R. Ahlstrand and P. Rajamfiki. **Toughness and Fatigue Properties of Stainless Steel Submerged Arc Weld Cladding Overlay and Significance of Postulated Flaws in the Cladding Overlay**. *International Journal of Pressure Vessels and Piping*, **33**:129–142, 1988. 271

[222] R. Ahmed, M.E. Fitzpatrick, and N.H. Faisal. **A comparison of neutron diffraction and hole-drilling residual strain measurements in thermally sprayed coatings**. *Surface and Coatings Technology*, **206**(19-20):4180–4185, May 2012. 271

[223] Maria José Marques, António Castanhola Batista, Joana Rebelo-Kornmeier, Michael Hofmann, Joao P. Nobre, and Altino Loureiro. **Residual Stress Fields after Heat Treatment in Cladded Steel of Process Vessels**. *Materials Science Forum*, **681**:364–369, March 2011. 271, 338

[224] J W Elmer, D L Olson, and D K Matlock. **The Thermal Expansion Characteristics of Stainless Steel Weld Metal**. *Welding Research Supplement*, (September):293–301, 1982. 272

[225] F. C. Hull, S. K. Hwang, J. M. Wells, and R. I. Jaffee. **Effect of composition on thermal expansion of alloys used in power generation**. *Journal of Materials Engineering*, **9**(1):81–92, March 1987. 275

[226] C.T. Karlsson. **Finite element analysis of temperatures and stresses in a single-pass butt-welded pipe - influence of mesh density and material modelling**. *Engineering Computations*, **6**(2):133–141, 1989. 277, 278

[227] E.J. Pavlina and C.J. Van Tyne. **Correlation of Yield Strength and Tensile Strength with Hardness for Steels**. *Journal of Materials Engineering and Performance*, **17**(6):888–893, April 2008. 278, 280

[228] Jinya Katsuyama, Hiroyuki Nishikawa, Makoto Udagawa, Mitsuyuki Nakamura, and Kunio Onizawa. **Assessment of Residual Stress Due to Overlay-Welded Cladding and Structural Integrity of a Reactor Pressure Vessel**. *Journal of Pressure Vessel Technology*, **135**(5):051402, September 2013. 279

[229] Dean Deng and Hidekazu Murakawa. **Prediction of welding residual stress in multi-pass butt-welded modified 9Cr1Mo steel pipe considering phase transformation effects**. *Computational Materials Science*, **37**(3):209–219, September 2006. 282

[230] U. O. B. De Oliveira. *Laser Treatment of Alloys: Processing, Microstructure and Structural Properties*. PhD thesis, Rijksuniversiteit Groningen, 2007. 285

[231] Hang Qin, Zhi Hai Cai, Ping Zhang, and Zhen Yang. **Development Status of Laser Cladding Technologies**. *Applied Mechanics and Materials*, **584-586**:1500–1503, July 2014. 285

[232] B. Zoran, S.J. Marko, O.J. Luis, and G. Janez. **Laser Cladding and Heat Treatment of Ni-Co-Mo Maraging Steel**. *Journal of ASTM International*, **8**(5):1–12, 2011. 286

[233] X. Zhang, S. Dong, B. Xu, and Q. Li. **Control measures for clad cracks of laser cladding manufacturing**. Technical report. 286

[234] H. Yu, T. He, and C. Chen. **Advancement in Ferrite-Based Alloy Coatings by Laser Cladding**. *Key Engineering Materials*, **591**:253–257, November 2013. 287

[235] S.J. Bull, A.M. Jones, and A.R. McCabe. **Residual stress in ion-assisted coatings**. *Surface and Coatings Technology*, **5455**(1):173–179, 1992. 287

[236] J.L. de Mol van Otterloo and J.Th.M. De Hosson. **Microstructure and abrasive wear of cobalt-based laser coatings**. *Scripta Materialia*, **36**(2):239–245, January 1997. 287

[237] Zhigang Chen, Dejun Kong, Ling Wang, Xiaoron Zhu, and Xiaobing Zhao. **Study on residual stresses of Ni-based WC coating by laser remelting based on XRD**. In Junhua Pan, James C. Wyant, and Hexin Wang, editors, *Proc. of SPIE Vol. 6723*, **6723**, pages 67230D–1–67230D–6, December 2007. 287

[238] V. Ocelík, I. Furár, and J.Th.M. De Hosson. **Microstructure and properties of laser clad coatings studied by orientation imaging microscopy**. *Acta Materialia*, **58**(20):6763–6772, December 2010. 287

[239] A.H. Garrido, R. González, M. Cadenas, and A.H. Battez. **Tribological Behavior of Laser-Textured NiCrBSi Coatings**. *Wear*, **271**:925–933, June 2011. 287

[240] S.W. Huang, M. Samandi, and M. Brandt. **Abrasive Wear Performance and Microstructure of Laser Clad WC/Ni Layers**. *Wear*, **256**:1095–1105, June 2004. 287

[241] P.-Z. Wang, Y.-S. Yang, G. Ding, J.-X. Qu, and H.-S. Shao. **Laser Cladding Coating Against Erosion-Corrosion Wear and its Application to Mining Machine Parts**. *Wear*, **209**:96–100, 1997. 288

[242] R. Lupoi, A. Cockburn, C. Bryan, M. Sparkes, F. Luo, and W. O'Neill. **Hardfacing Steel with Nanostructured Coatings of Stellite-6 by Supersonic Laser Deposition**. *Light: Science & Applications*, **1**:1–6, May 2012. 288

[243] H.X. Zhao, M. Yamamoto, and M. Matsumura. **Slurry erosion properties of ceramic coatings and functionally gradient materials**. *Wear*, **186-187**(1995):473–479, 1995. 294

[244] J. A. Alegría-Ortega, L. M. Ocampo-Carmona, F. A. Suárez-Bustamante, and J. J. Olaya-Flórez. **Erosion-corrosion wear of Cr/CrN multi-layer coating deposited on AISI-304 stainless steel using the unbalanced magnetron (UBM) sputtering system**. *Wear*, **290-291**(2012):149–153, 2012. 295

[245] B. Borawski, J. Singh, J.A. Todd, and D.E. Wolfe. **Multi-layer coating design architecture for optimum particulate erosion resistance**. *Wear*, **271**:2782–2792, 2011. 295

[246] M. D. Olson, A. T. DeWald, M. B. Prime, and M. R. Hill. **Estimation of Uncertainty for Contour Method Residual Stress Measurements**. *Experimental Mechanics*, December 2014. 300

[247] P. J. Bouchard, P. Ledgard, S. Hiller, and F. Hosseinzadeh. **Making the cut for the contour method**. In J.F. Silva Gomes and M.A.P. Vaz, editors, *15th International Conference on Experimental Mechanics*, Porto, Portugal, 2012. 300

[248] M. B. Prime, R. J. Sebring, J. M. Edwards, D. J. Hughes, and P. J. Webster. **Laser surface-contouring and spline data-smoothing for residual stress measurement**. *Experimental Mechanics*, **44**(2):176–184, 2004. 300

[249] P.J. Withers, M. Turski, L. Edwards, P.J. Bouchard, and D.J. Buttle. **Recent advances in residual stress measurement**. *International Journal of Pressure Vessels and Piping*, **85**(3):118–127, March 2008. 302

[250] M.B Prime, P. Rangaswamy, M.R Daymond, and T.G. Abeln. **Several methods applied to measuring residual stress in a known specimen**. In *SEM Spring Conference on Experimental and Applied Mechanics*, pages 497–499, Houston, Texas, 1998. Society for Experimental Mechanics. 302

[251] M.B. Prime and A.L. Kastengren. **The Contour Method Cutting Assumption: Error Minimization and Correction**. *Experimental and Applied Mechanics*, **6**:233–250, 2011. 303

[252] J.F. Harvey. *Theory and Design of Pressure Vessels*. Van Nostrand Reinhold Company Inc., New York, NY, 1985. 314

[253] A. Ayob and M.K. Elbasheer. **Optimum Autofrettage Pressure in Thick Cylinders**. *Jurnal Mekanikal*, **24**:1–14, 2007. 318

[254] Ruilin Zhu and Jinlai Yang. **Autofrettage of thick cylinders**. *International Journal of Pressure Vessels and Piping*, **75**(6):443–446, May 1998. 318

[255] A. Partovi and S.S. Shamili. *Analysis of Autofrettaged High Pressure Components*. PhD thesis, Blekinge Institute of Technology, Karlskrona, Sweden, 2012. 318

[256] RPM Innovations Inc. **Laser Engineered Net Shaping Advances Additive Manufacturing and Repair**. 330

[257] B. Roebuck, M. Brooks, and M.G. Gee. **Preliminary elevated temperature mechanical tests in the ETMT**. Technical report, NPL, Teddington, UK, 1998. 332

[258] Ondrej Muránsky, Cory J. Hamelin, Mike C. Smith, Phillip J. Bendeich, and Lyndon Edwards. **The Role of Plasticity Theory on the Predicted Residual Stress Field of Weld Structures**. *Materials Science Forum*, **772**:65–71, November 2013. 333

[259] Dean Deng, Hidekazu Murakawa, and Wei Liang. **Numerical and experimental investigations on welding residual stress in multi-pass butt-welded austenitic stainless steel pipe**. *Computational Materials Science*, **42**(2):234–244, April 2008. 333

[260] ASM International. *Atlas of Stress-Strain Curves*. Materials Park, OH, USA, second edition, 2002. 334, 335

[261] J. Wood and G. Schnier. **Autofrettage of Thermally Clad Components**, 2015. 337

[262] O.R. Abdelsalam and R. Sedaghati. **Design Optimization of Compound Cylinders Subjected to Autofrettage and Shrink-Fitting Processes**. *Journal of Pressure Vessel Technology*, **135**:1–11, March 2013. 337

[263] TWI. **What are the residual stresses in a dissimilar metal weld?** 337

[264] Z. Barsoum. **Residual stress analysis and fatigue of multi-pass welded tubular structures**. *Engineering Failure Analysis*, **15**(7):863–874, October 2008. 338

[265] A.V. Hansen and H. Agerskov. **Fatigue Assessment of Root Defects in the Welded Structure of a Large Two-Stroke Diesel Engine**. In *Proceedings of design and analysis of welded high strength steel structures*, pages 373–389, Stockholm, Sweden, 2002. EMAS Publishing. 338

[266] D Mukherjee, K Balamurugan, V Balamurugan, K Balasubramanian, E Kannan, and M Muruganantham. **Corrosion resistance of welded and brazed engineering joints**. *Anti-Corrosion Methods and Materials*, 1995. 338

[267] M. F. Dodge, H. B. Dong, and M. F. Gittos. **Effect of post-weld heat treatment on microstructure evolution in dissimilar joints for subsea oil and gas systems**. *Materials Research Innovations*, **18**(S4):907–913, 2014. 338

[268] Henrik Alberg. *Material Modelling for Simulation of Heat Treatment*. PhD thesis, 2003. 338

[269] I.J. Karassik, J.P. Messina, P. Cooper, and C.C. Heald. *Pump Handbook*. McGraw-Hill, third edition, 2001. 342, 344

List of Publications

G. Schnier, J. Wood, and A. Galloway, *An Experimental Validation of Residual Stresses in Weld Clad Pipelines*, in Research and Applications in Structural Engineering, Mechanics and Computation (Conference Proceedings), A. Zingoni, Cape Town, pp. 613-617, Taylor & Francis Group, London, 2013.

G. Schnier, J. Wood, and A. Galloway, *Investigating the Effects of Process Variables on the Residual Stresses of Weld and Laser Cladding*, Advanced Materials Research, vol. 996, pp. 481-487, 2014.

J. Wood, G. Schnier, UK patent application GB 1501538.1 entitled Autofrettage of Thermally Clad Components filed 30 January 2015.

G. Schnier, J. Wood, *Autofrettage of Weld Clad Components*, in International Conference on Pressure Vessel Technology (Conference Proceedings), Shanghai, *to be presented 23-26 September*, 2015.

Appendix A

Finite Element Model Data Input

A.1 Simulation of the Weld Cladding Process

A.1.1 Axisymmetric Model

Geometry

Plane strain

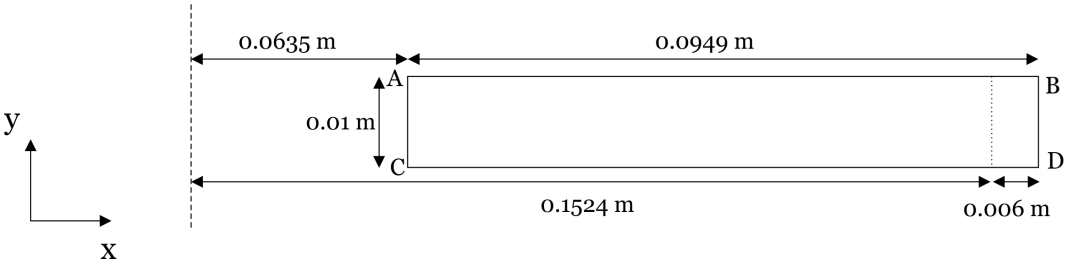

Figure A.1: Finite element model geometry for axisymmetric model - Dimensions in millimetres unless otherwise stated.

Boundary Conditions

Line AB

U_y = constant through equation constraint

Line CD

$U_y = 0$

Loading

Thermal loading through application of clad material at melt temperature onto pre-heated substrate.

Element Type

CAX4T (4-node axisymmetric thermally coupled quadrilateral, bilinear displacement and temperature)

Material Properties

4330 (Inconel 625 clad)

E = 189.8 GPa

ν = 0.289

Perfect plasticity, σ_y = 869 MPa

4330 (17-4 clad)

E = 184.3 GPa

ν = 0.289

Perfect plasticity, σ_y = 856 MPa

Inconel 625

E = 168 GPa

ν = 0.29

Perfect plasticity, σ_y = 474 MPa

17-4 PH E = 179.7 GPa

ν = 0.272

Perfect plasticity, σ_y = 994 MPa

A.1.2 2D Planar Model

Geometry

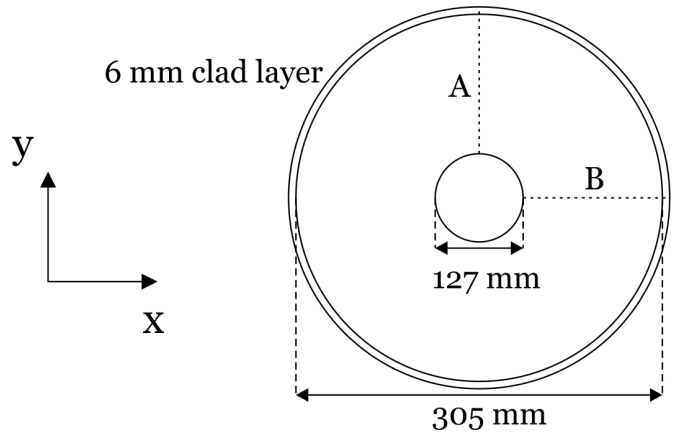

Figure A.2: Finite element model geometry for 2D planar model - Dimensions in millimetres unless otherwise stated.

Boundary Conditions

Line A

$U_x = 0$

Line B

$U_y = 0$

Loading

Thermal loading through application of clad material at melt temperature onto preheated substrate.

Element Type

CPE4T (4-node plane strain thermally coupled quadrilateral, bilinear displacement and temperature)

Material Properties

4330 (Inconel 625 clad)

E = 189.8 GPa

$\nu = 0.289$

Perfect plasticity, σ_y = 869 MPa

4330 (17-4 clad)

E = 184.3 GPa

$\nu = 0.289$

Perfect plasticity, σ_y = 856 MPa

Inconel 625

E = 168 GPa

ν = 0.29

Perfect plasticity, σ_y = 474 MPa

17-4 PH E = 179.7 GPa

ν = 0.272

Perfect plasticity, σ_y = 994 MPa

A.1.3 3D Model

Geometry

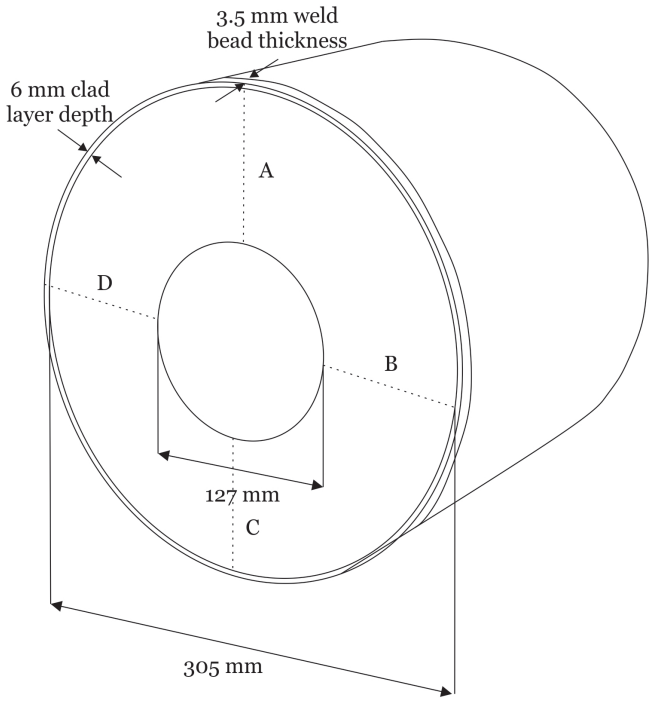

Figure A.3: Finite element model geometry for 3D model - Dimensions in millimetres unless otherwise stated.

Boundary Conditions

Line A

$U_x = 0$

$U_z = 0$

Line B

$U_y = 0$

$U_z = 0$

Line C

$U_x = 0$

$U_z = 0$

Line D

$U_y = 0$

$U_z = 0$

Loading

Thermal loading through application of clad material at melt temperature onto pre-heated substrate.

Element Type

C3D8T (8-node thermally coupled brick, trilinear displacement and temperature)

Material Properties

4330 (Inconel 625 clad)

E = 189.8 GPa

ν = 0.289

Perfect plasticity, σ_y = 869 MPa

4330 (17-4 clad)

E = 184.3 GPa

ν = 0.289

Perfect plasticity, σ_y = 856 MPa

Inconel 625

E = 168 GPa

ν = 0.29

Perfect plasticity, σ_y = 474 MPa

17-4 PH E = 179.7 GPa

ν = 0.272

Perfect plasticity, σ_y = 994 MPa

A.2 Simulation of Autofrettage of a Weld Clad Component

Geometry

Plane strain

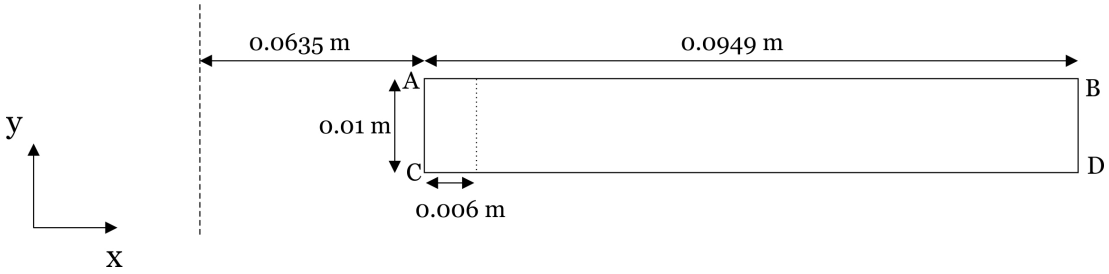

Figure A.4: Finite element model geometry for axisymmetric model - Dimensions in millimetres unless otherwise stated.

Boundary Conditions

Line AB

U_y = constant through equation constraint

Line CD

$U_y = 0$

Loading

Thermal loading through application of clad material at melt temperature onto pre-heated substrate.

Followed by application of pressure on line AC at low or high autofrettage pressure in a ramped manner.

Element Type

CAX4T (4-node axisymmetric thermally coupled quadrilateral, bilinear displacement and temperature)

Material Properties

4330 (Inconel 625 clad)

E = 189.8 GPa

$\nu = 0.289$

Perfect plasticity, σ_y = 869 MPa

4330 (17-4 clad)

E = 184.3 GPa

$\nu = 0.289$

Perfect plasticity, σ_y = 856 MPa

Inconel 625

E = 168 GPa

ν = 0.29

Perfect plasticity, σ_y = 474 MPa

17-4 PH E = 179.7 GPa

ν = 0.272

Perfect plasticity, σ_y = 994 MPa